frontiers | Research Topics

The Role of neuroimaging in cerebral small vessel disease

Edited by
Haitao Li, Yilei Zhao, Tao Liu, Xiaofei Hu and Zhongzhao Teng

Published in
Frontiers in Neurology

ISSN 1664-8714
ISBN 978-2-83251-942-4
DOI 10.3389/978-2-83251-942-4

About Frontiers

Frontiers is more than just an open access publisher of scholarly articles: it is a pioneering approach to the world of academia, radically improving the way scholarly research is managed. The grand vision of Frontiers is a world where all people have an equal opportunity to seek, share and generate knowledge. Frontiers provides immediate and permanent online open access to all its publications, but this alone is not enough to realize our grand goals.

Frontiers journal series

The Frontiers journal series is a multi-tier and interdisciplinary set of open-access, online journals, promising a paradigm shift from the current review, selection and dissemination processes in academic publishing. All Frontiers journals are driven by researchers for researchers; therefore, they constitute a service to the scholarly community. At the same time, the *Frontiers journal series* operates on a revolutionary invention, the tiered publishing system, initially addressing specific communities of scholars, and gradually climbing up to broader public understanding, thus serving the interests of the lay society, too.

Dedication to quality

Each Frontiers article is a landmark of the highest quality, thanks to genuinely collaborative interactions between authors and review editors, who include some of the world's best academicians. Research must be certified by peers before entering a stream of knowledge that may eventually reach the public - and shape society; therefore, Frontiers only applies the most rigorous and unbiased reviews. Frontiers revolutionizes research publishing by freely delivering the most outstanding research, evaluated with no bias from both the academic and social point of view. By applying the most advanced information technologies, Frontiers is catapulting scholarly publishing into a new generation.

What are Frontiers Research Topics?

Frontiers Research Topics are very popular trademarks of the *Frontiers journals series*: they are collections of at least ten articles, all centered on a particular subject. With their unique mix of varied contributions from Original Research to Review Articles, Frontiers Research Topics unify the most influential researchers, the latest key findings and historical advances in a hot research area.

Find out more on how to host your own Frontiers Research Topic or contribute to one as an author by contacting the Frontiers editorial office: frontiersin.org/about/contact

The role of neuroimaging in cerebral small vessel disease

Topic editors
Haitao Li — Army Medical University, China
Yilei Zhao — Zhejiang University, China
Tao Liu — Hainan General Hospital, China
Xiaofei Hu — Army Medical University, China
Zhongzhao Teng — University of Cambridge, United Kingdom

Citation
Li, H., Zhao, Y., Liu, T., Hu, X., Teng, Z., eds. (2023). *The role of neuroimaging in cerebral small vessel disease*. Lausanne: Frontiers Media SA.
doi: 10.3389/978-2-83251-942-4

Table of contents

frontiers in Neurology

METHODS
published: 16 August 2021
doi: 10.3389/fneur.2021.700476

A Processing Pipeline for Quantifying Lenticulostriate Artery Vascular Volume in Subcortical Nuclei

Ning Wei[1], **Xianchang Zhang**[2], **Jing An**[3], **Yan Zhuo**[4,5] **and Zihao Zhang**[4,5]*

[1] China National Clinical Research Center for Neurological Diseases, Beijing Tiantan Hospital, Capital Medical University, Beijing, China, [2] MR Collaboration, Siemens Healthcare Ltd., Beijing, China, [3] Siemens Shenzhen Magnetic Resonance Ltd., Shenzhen, China, [4] State Key Laboratory of Brain and Cognitive Science, Institute of Biophysics, Chinese Academy of Sciences, Beijing, China, [5] University of Chinese Academy of Sciences, Beijing, China

Lenticulostriate arteries (LSAs) supply blood to the basal ganglia region. Its lesion causes lacunar stroke and resulting neurological syndromes. However, due to its small caliber and large individual variance, the evaluation of LSAs was limited to descriptive and objective measurements. In this study, we aimed to develop a post-processing method to quantify LSAs in subcortical regions and compare their vascular volume to conventional LSA measurements. A processing pipeline was designed to extract subcortical areas in individual spaces while screening out vessels. The vascular volume of LSAs in the subcortical region was calculated from time-of-flight-magnetic resonance angiography (TOF-MRA) at 7 Tesla. The reproducibility was tested to be good for the vascular volume ($n = 5$, $\mathrm{ICC_A} = 0.84$). Comparing the results to conventional measurements, the vascular volume was significantly correlated with the number of branches ($r = 0.402$, $p < 0.001$) and the length ($r = 0.246$, $p = 0.032$) of LSAs. By applying the method to a group of healthy volunteers ($n = 40$), we found that most LSAs crossing through the putamen which thereby has the highest vascular density among subcortical nuclei. In general, we proposed a semi-automated processing pipeline for quantifying the vascular volume of LSAs in subcortical regions. The novel method was tested to be robust and provided reasonable results. This method revealed spatial relationships among the perforating arteries and basal ganglia. The vascular volume can be used to evaluated blood supply of subcortical regions, benefiting the radiologic evaluation of neurodegenerative diseases caused by small vascular lesions.

Keywords: TOF-MRA, lenticulostriate artery, subcortical nuclei, 7T, vascular volume

OPEN ACCESS

Edited by:
Xiaofei Hu,
Army Medical University, China

Reviewed by:
Ivan V. Brak,
State Scientific Research Institute of Physiology and Basic Medicine, Russia
Karsten Wrede,
University of Duisburg-Essen, Germany

****Correspondence:***
Zihao Zhang
zhzhang@ibp.ac.cn

Specialty section:
This article was submitted to Applied Neuroimaging, a section of the journal Frontiers in Neurology

Received: *26 April 2021*
Accepted: *08 July 2021*
Published: *16 August 2021*

Citation:
Wei N, Zhang X, An J, Zhuo Y and Zhang Z (2021) A Processing Pipeline for Quantifying Lenticulostriate Artery Vascular Volume in Subcortical Nuclei. Front. Neurol. 12:700476. doi: 10.3389/fneur.2021.700476

INTRODUCTION

Lenticulostriate arteries (LSAs) represent the major microvasculature of the middle cerebral arteries and supply blood to the basal ganglia and internal capsules (1, 2). The occlusion of LSAs will cause lacunar infarcts in subcortical structures, leading to motor deficits, sensory deficits, and cognitive dysfunction (3). Imaging LSAs could be useful for clinical applications and provide insights into the mechanisms underlying cerebral microvascular disease development. Digital subtraction angiography (DSA) has been the gold standard for intracranial vascular imaging (4), but this method requires intravenous contrast and is not suitable for routine evaluations. With advances in imaging techniques, magnetic resonance angiography (MRA) has been widely used in clinical medicine because of its non-invasiveness. In the past decade, time-of-flight magnetic resonance angiography (TOF-MRA) at 7 Tesla (7T) has been shown to produce markedly superior blood-to-tissue contrast, which has enabled the non-invasive visualization of human brain microvasculature, *in vivo*, especially the microvasculature of LSAs (5, 6). Lenticulostriate artery angiography is useful as a diagnostic tool in clinical and research settings for detecting diseases, such as small vessel disease, lacunar infarcts, and vascular dementia. Recent studies have found LSA abnormalities in patients with hypertension (7), lacunar infarcts (8), and vascular dementia (9).

The distribution and morphological characteristics of cerebral small vessels play important roles in diagnosis and treatment of various cerebrovascular diseases (10, 11). However, the analysis tools of LSAs, particularly the quantitative characterization, are still limited. In most studies, the number of LSA stems and branches arising from the first segment of the bilateral ACAs and MCAs are counted manually (7, 9, 12). Some studies have measured the angles, lengths, and curvatures of the longest LSAs on 2D maximum intensity projection (MIP) images (6, 13, 14) or 3D extracted vessels (15, 16). In addition, LSA orifices (8) and vascular densities obtained with rough threshold segmentations (17) have also been proposed. However, due to morphologic variations in LSA structures, these quantification methods have poor sensitivity and stability in being able to evaluate patient groups and sometimes have led to controversial clinical study results (12, 18).

Based on LSA spatial relationships and those of its supplying territories, our study introduces a novel method to quantify LSA vascular volume in subcortical areas to estimate basal ganglia and internal capsule blood supplies. A semi-automatic post-processing pipeline was designed and adjusted to produce LSA vascular volume, objectively. Conventional quantitative indicators, such as the number of branches and lengths of the LSAs were compared with LSA vascular volume.

MATERIALS AND METHODS

Participants

A total of 45 participants were enrolled in this study, separated into validation group (G_{val}) and application group (G_{app}). G_{val} was used to validate the method and assess its robustness and reproducibility. It included five healthy participants (Aged 25 ± 2.3 years, 3 males). These participants underwent MRI acquisition twice on the same day, with repositioning between two scans. G_{app} was applied to find the prevalence of LSAs in basal ganglia region and formed by 40 healthy volunteers (Aged 40.7 ± 9.7 years, 21 males). Informed consent was obtained from all participants and was approved by the local institutional review board.

Magnetic Resonance Imaging

All MRI scans were performed on a 7T whole-body research MR scanner (Siemens Healthcare, Erlangen, Germany). A birdcage transmission and a 32-channel receiving head coil (Nova Medical, MA, USA) were used for all scanning procedures. T1-weighted magnetization-prepared rapid gradient echo (T1w MPRAGE) and TOF-MRA were collected for every participant.

Two protocols of TOF-MRA sequence were optimized to visualize LSAs. To evaluate the reproducibility of our method, whole-brain TOF-MRA with isotropic 0.40 mm resolution was acquired in G_{val} with the following parameters: field of view (FOV) = 205 × 175 × 107 mm^3, number of slabs = 6, repetition time (TR) = 18 ms, echo time (TE) = 4.03 ms, flip angle (FA) = 22°, bandwidth (BW) = 158 Hz/Px, generalized auto-calibrating partial parallel acquisition (GRAPPA) factor = 3, time of acquisition (TA) = 9 min 28 s. For the G_{app}, single-slab TOF-MRA was optimized to shorten the acquisition time (9). The imaging slab was positioned obliquely axial covering the bottom of the MCA and basal ganglia. Detailed parameters were FOV = 180 × 135 × 52 mm^3, resolution = 0.23 × 0.23 × 0.36 mm^3, TR = 15 ms, TE = 3.57 ms, FA = 20°, BW = 151 Hz/Px, GRAPPA factor = 2, TA = 8 min 20 s. The T1w MPRAGE was obtained for structural images in both groups, with the following parameters: FOV = 224 × 224 × 179 mm^3, resolution = 0.70 × 0.70 × 0.70 mm^3, TR = 3,000 ms, TE = 3.23 ms, inversion time = 1,050 ms, FA = 8°, BW = 320 Hz/Px, GRAPPA factor = 3, TA = 5 min 54 s.

Image Analysis

Pre-processing

The pre-processing was performed in FSL software, a comprehensive library of analytic tools (19). The processing workflow is shown in **Figure 1**. First, the T1w anatomical dataset was registered to the Montreal Neurological Institute (MNI) brain atlas. Non-linear registrations (FNIRT) were used following affine linear transformations (FLIRT) for maximal accuracy. Second, we chose the regions of interest (ROI) indicating the LSA supply territories to build a mask in the MNI space. The selected areas included the putamen, globus pallidus, and caudate nuclei from the Harvard-Oxford Subcortical Structural Atlas and the posterior limbs of the internal capsule from the JHU ICBM-DTI-81 White-Matter labels. On the other hand, the TOF-MRA dataset was aligned to its corresponding T1w anatomical dataset. The N4 bias correction was applied to resolve signal inhomogeneity caused by the dielectric effects of ultra-high fields (20). Finally, rigid and non-linear transformations were concatenated to transform the ROI masks into individual TOF-MRA spaces.

Vessel Enhancement and Filtering

To enhance vessel-to-tissue contrast and suppress non-vascular structures and image noise, we used vessel enhancement filters from the Vascular Modeling Toolkit (21). One voxel of LSA was selected as a seed point. Based on the morphology of LSAs and spatial resolutions of TOF-MRA, vessel enhancement filter parameters were optimized as: minimum vessel diameter = 1 voxel, maximum vessel diameter = 5 voxels, vessel contrast = 100, suppress plates = 10%, and suppress blobs = 40%. Then, we used the previously generated ROI masks to extract enhanced vasculatures to calculate the volume of LSAs, as shown in **Figure 1**.

Blood vessel volume was analyzed with the MATLAB 2016 software program. We applied a volume ratio scheme to find

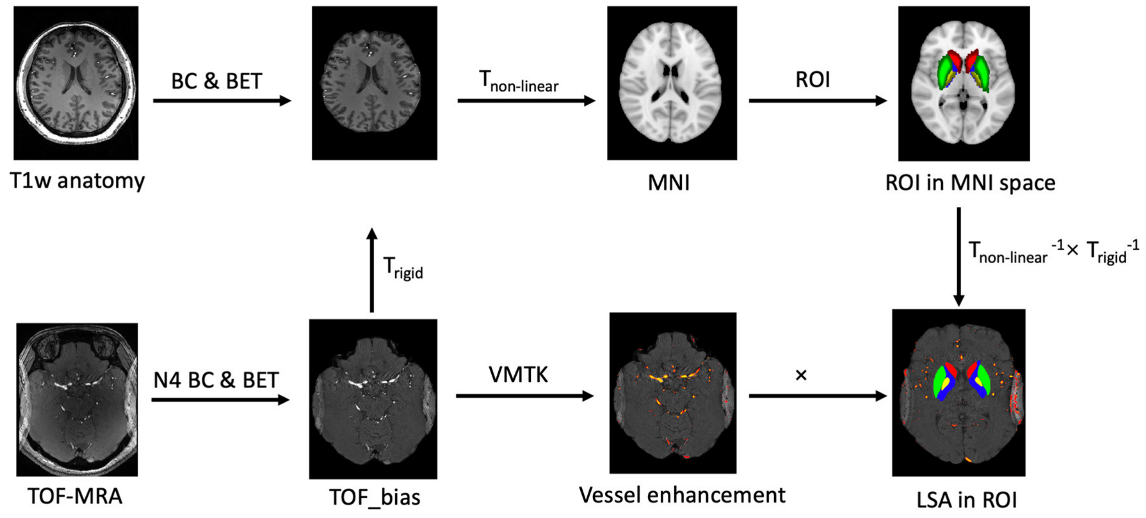

FIGURE 1 | The workflow for calculating lenticulostriate artery (LSA) vascular volume. BC, bias correction; BET, brain extraction tool using FSL software; VMTK, Vascular Modeling Toolkit.

an appropriate threshold for screening out complete vessels while filtering out noise from the parenchymal tissues. The thresholds were adjusted until vessel-to-tissue volume ratios changed >0.2%. The vascular volume was defined as the number of voxels above the threshold multiplied by the imaging resolution.

Quantifying the Morphologic Characteristics of Lenticulostriate Arteries

Three dimensional (3D) MRA image reconstructions and analyses were performed using a free and open-source code software from Horos (https://horosproject.org). We counted the number of LSA stems and branches arising from the first segment of the bilateral ACAs (A1) and MCAs (M1). Only blood vessels of the LSA-supplying territories (the previously mentioned ROIs) were counted. Stems were defined as LSAs directly connected to A1s or M1s. Branches were defined as daughter vessels arising from parent LSA stems without any subordinate branches. If a trunk had no branches, it was recorded as both stem and branch. To measure the maximal length of the LSAs, MIP was reconstructed in the coronal view with a slab thickness of 28 mm covering the LSAs and MCAs. The maximal length was determined as the distance from MCA to the visible end of the longest LSA.

Statistical Analyses

The inter-class correlation coefficient (ICC) was used as the measure for reproducibility, assessing the absolute agreement (ICC_A) between both scans of G_{val}. In addition, the data of G_{app} was used for quantitative analysis. All the quantitative data were presented as means ± standard deviations (SDs). The level of significance was set at $p < 0.05$. The volume of LSAs calculated with our new method was compared with conventional LSA measurements using Pearson's correlation coefficient. All statistical analyses were carried out using SPSS vision 21 software.

RESULTS

Figure 2 shows an example of subcortical ROIs and LSA voxels. The subcortical nuclei and basal ganglia were well-segmented according to the anatomic images. The LSA vasculature was clearly demonstrated after vessel enhancement and filtering. The volumes of subcortical ROIs have an $ICC_A = 0.98$ (95% CI = 0.88–0.99), confirming excellent registration for ROI definition. The inter-scan reproducibility of quantifying LSA volume was good with an $ICC_A = 0.84$ (95% CI = 0.47–0.96). An example of reproducibility test was exhibited in **Figure 3**. The discrepancies between the repeated scans occurred mostly for tiny branches of LSA which was sensitive to partial volume effect.

Two participants in G_{app} were excluded from the analyses because voxels of large arteries were involved in the basilar ROI and contaminated the results. In total, 38 participants (76 hemispheres) were used for the statistical analyses. The LSA voxel numbers in the subcortical nuclei and internal capsules were 998.01 ± 206.88, which corresponded to a volume of 19.01 ± 0.45 mm^3. There were 5.71 ± 1.41 LSA branches and 3.39 ± 1.07 stems in each hemisphere, and the length of the longest branch was 3.44 ± 0.53 cm. The vascular volume was significantly correlated with the number of LSA branches ($r = 0.402$, $p < 0.001$) and the LSA lengths ($r = 0.246$, $p = 0.032$), but no correlation was found between the vascular volume and the number of LSA stems ($r = 0.062$, $p = 0.596$), as shown in **Figure 4**. The LSA voxel numbers in different subcortical regions (putamen, globus pallidus, caudate nucleus, and internal capsule) were further analyzed. We found that 90% of the visible perforating branches funneled through the putamen, which can be observed in **Figure 2**.

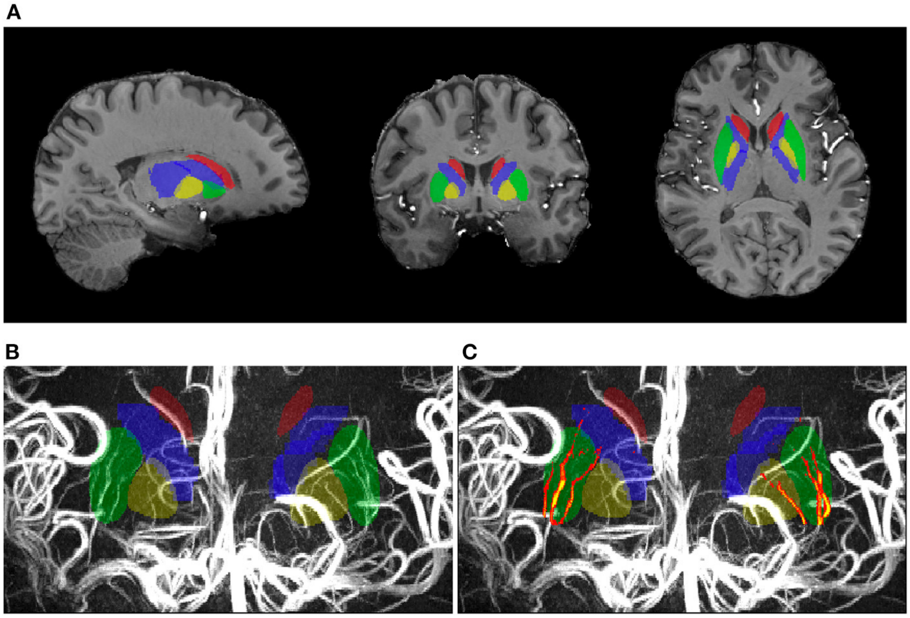

FIGURE 2 | The subcortical regions of interest (ROIs) and LSA vascular volume in one participant. **(A)** The ROIs in the anatomical image; **(B,C)** The vascular voxels identified in the ROIs concide well with the vasculature in the raw image.

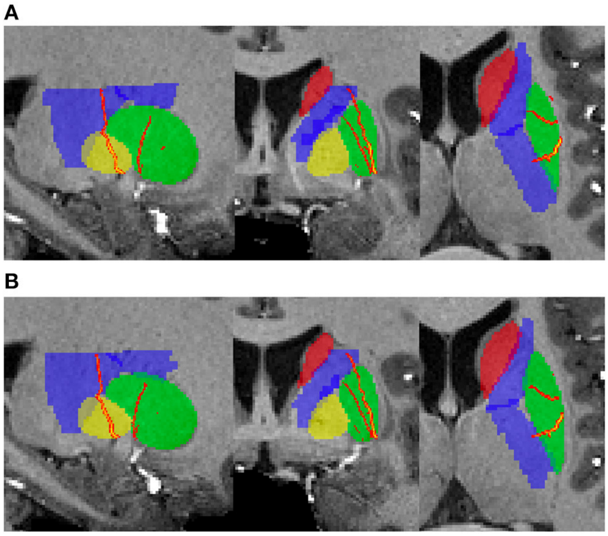

FIGURE 3 | The extracted LSA vasculatures of one hemisphere in the reproducibility testing. **(A)** The first scan; **(B)** The second scan.

DISCUSSION

Our study proposed a novel method for quantifying perforating arteries in subcortical regions. LSA vascular volume, equivalent to voxel numbers, reflected regions of subcortical blood supply. In previous studies, stems, branches, and lengths were used to describe LSA morphologies. Compared with these traditional measurements, the vascular volume in subcortical ROIs was significantly correlated with the number of LSA branches and the LSA lengths. Conversely, LSA vascular volume was not correlated with the number of LSA stems, which could be explained by larger perforating arteries dividing into numerous branches before entering the brain substance (22, 23). Lenticulostriate artery volume assessments were able to estimate blood supplies in the subcortical regions more appropriately.

This new analytic method has two main advantages over traditional methods. First, the vascular volume is comprehensive representations of LSA numbers, lengths, and diameters. In a previous study, negative correlations were reported between LSA numbers and diameters (the higher the number of branches, the smaller the branch diameters, and vice versa) (24). Vascular volume measurements provided more comprehensive LSA quantifications in the subcortical regions, which was likely related to the blood perfusion in this area. In addition, the analytic methods represent an automatic post-processing pipeline that avoids the subjective bias of traditional measurements. In previous studies, investigators had to manually count the number of branches and draw curves to obtain diameter lengths. These operations depended more or less on subjective vasculature definitions. However, our new method extracted LSAs in an automated way eliminating subjective influence. The reproducibility testing gave robust and consistent results, owing to its fixed and deterministic behavior. Therefore, this novel method would be suitable for perforating artery analyses in studies with larger populations.

According to previous studies, a consensus has been reached that LSA imaging has important clinical implications and provides insights into the mechanisms underlying the

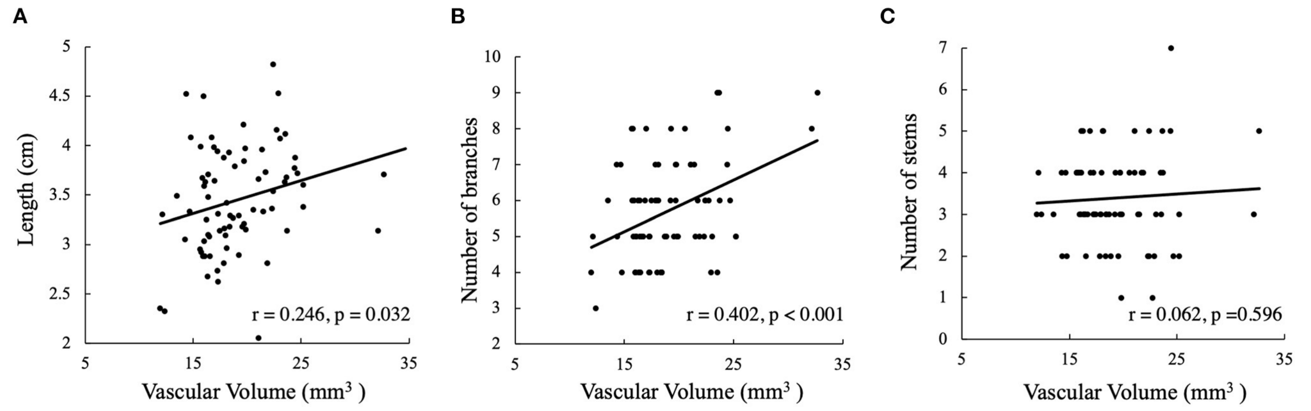

FIGURE 4 | Correlation analyses of lenticulostriate artery (LSA) volume and conventional measurements; LSA vascular volume vs. **(A)** LSA lengths, **(B)** the number of LSA branches, and **(C)** the number of LSA stems.

development of cerebral small vessel disease. However, radiologic studies investigating the associations between vasculature and basal ganglia are still lacking. Huge morphologic differences in LSA appearances among different individuals could be an important reason for the current limits of research on this topic, since currently available LSA imaging characteristics have poor sensitivity in being able to detect LSA abnormalities. In this study, the proposed method identified LSA vasculature and its supplying territories automatically. We showed a relationship between perforating arteries and the basal ganglia. The quantification of LSA vascular volume in subcortical areas could be used in both neurovascular studies and clinical diagnostic settings. LSA vascular volume reflects the density of perforating arteries and can be used to evaluate the impacts of lacunar infarcts, explore the causes of vascular dementia, and facilitate the etiologic studies of cerebral small vessel disease.

There are two major limitations to our study. First, large arteries were observed in the subcortical ROIs in 2 of 40 subjects, which interfered with the screening of LSA voxels and were thus removed from the analysis. These large vessels arose from the second MCA segments and crept along the surface of the brains without entering the parenchyma. Inclusion of these large arteries could be explained by misregistering subcortical ROIs from the templates to the individual spaces and should be improved upon in future studies. Second, when analyzing data from different subcortical areas, most vascular volume was found in the putamen, while very few voxels existed in other nuclei, especially the caudate nucleus. However, anatomic studies showed that LSAs arc around and course through the putamen and then travel superomedially through the superior part of the internal capsule and much of the caudate nucleus. The caudate nucleus is located superior to the putamen and other subcortical nuclei. The weakened in-flow of blood could have resulted in limited TOF-MRA sensitivity in the superior part of the scanning slab, and thus, miss small vessels in the caudate nucleus. However, the bias should not affect the results when comparing vascular volume in similar areas among different individuals.

CONCLUSION

In conclusion, we proposed an automatic processing pipeline for quantifying LSA vascular volume in subcortical regions. The results provided a general knowledge of the relationship between perforating arteries and basal ganglia. This method introduces a new dimension for interpreting LSA imaging findings, and could potentially assist in the radiologic evaluation of neurodegenerative diseases caused by small vascular lesions.

DATA AVAILABILITY STATEMENT

The raw data supporting the conclusions of this article will be made available by the authors, without undue reservation.

ETHICS STATEMENT

The studies involving human participants were reviewed and approved by The Institutional Review Board of Beijing MRI Center for Brain Research. The patients/participants provided their written informed consent to participate in this study.

AUTHOR CONTRIBUTIONS

NW and ZZ contributed to the conception and design of the study, analysis and interpretation of the data, and drafting of the manuscript. XZ and JA contributed to the acquisition of data. YZ contributed to the funding acquisition and supervision. All the authors approved the publication of the study.

FUNDING

This work was supported by the National Key R&D Program of China (No. 2017YFC1307900, 2017YFC1307904), National Natural Science Foundation of China (82001804, 81961128030), Beijing Natural Science Foundation (7191003), Strategic Priority Research Program of Chinese Academy of Science (XDB32010300), and Capital's Funds for Health Improvement and Research (CFH2020-2-5115).

REFERENCES

1. Marinković S, Gibo H, Milisavljević M, Cetković M. Anatomic and clinical correlations of the lenticulostriate arteries. *Clin Anat*. (2001) 14:190–5. doi: 10.1002/ca.1032
2. Alexander L. The vascular supply of the strio-pallidum. *Res Publ Assoc Res Nerv Ment Dis*. (1942) 21:77–132.
3. Decavel P, Vuillier F, Moulin T. Lenticulostriate infarction. *Front Neurol Neurosci*. (2012) 30:115–9. doi: 10.1159/000333606
4. Jeans WD. The development and use of digital subtraction angiography. *Brit J Radiol*. (1990) 63:161–8. doi: 10.1259/0007-1285-63-747-161
5. Cho ZH, Kang CK, Han JY, Kim SH, Kim KN, Hong SM, et al. Observation of the lenticulostriate arteries in the human brain *in vivo* using 7.0T MR angiography. *Stroke*. (2008) 39:1604–6. doi: 10.1161/STROKEAHA.107.508002
6. Kang CK, Park CA, Lee H, Kim SH, Park CW, Kim YB, et al. Hypertension correlates with lenticulostriate arteries visualized by 7T magnetic resonance angiography. *Hypertension*. (2009) 54:1050–6. doi: 10.1161/HYPERTENSIONAHA.109.140350
7. Kang CK, Park CW, Han JY, Kim SH, Park CA, Kim KN, et al. Imaging and analysis of lenticulostriate arteries using 7.0-Tesla magnetic resonance angiography. *Magn Reson Med*. (2009) 61:136–44. doi: 10.1002/mrm.21786
8. Kong Q, Zhang Z, Yang Q, Fan Z, Wang B, An J, et al. 7T TOF-MRA shows modulated orifices of lenticulostriate arteries associated with atherosclerotic plaques in patients with lacunar infarcts. *Eur J Radiol*. (2019) 118:271–6. doi: 10.1016/j.ejrad.2019.07.032
9. Seo SW, Kang CK, Kim SH, Yoon DS, Liao W, Worz S, et al. Measurements of lenticulostriate arteries using 7T MRI: new imaging markers for subcortical vascular dementia. *J Neurol Sci*. (2012) 322:200–5. doi: 10.1016/j.jns.2012.05.032
10. Matsushige T, Chen B, Dammann P, Johst S, Quick HH, Ladd ME, et al. Microanatomy of the subcallosal artery: an *in-vivo* 7 T magnetic resonance angiography study. *Eur Radiol*. (2016) 26:2908–14. doi: 10.1007/s00330-015-4117-1
11. Matsushige T, Kraemer M, Sato T, Berlit P, Forsting M, Ladd ME, et al. Visualization and classification of deeply seated collateral networks in moyamoya angiopathy with 7T MRI. *AJNR Am J Neuroradiol*. (2018) 39:1248–54. doi: 10.3174/ajnr.A5700
12. Ling C, Fang X, Kong Q, Sun Y, Wang B, Zhuo Y, et al. Lenticulostriate arteries and basal ganglia changes in cerebral autosomal dominant arteriopathy with subcortical infarcts and leukoencephalopathy, a high-field MRI study. *Front Neurol*. (2019) 10:870. doi: 10.3389/fneur.2019.00870
13. Kang CK, Park CA, Park CW, Lee YB, Cho ZH, Kim YB. Lenticulostriate arteries in chronic stroke patients visualised by 7 T magnetic resonance angiography. *Int J Stroke*. (2010) 5:374–80. doi: 10.1111/j.1747-4949.2010.00464.x
14. Yashiro S, Kameda H, Chida A, Todate Y, Hasegawa Y, Nagasawa K, et al. Evaluation of lenticulostriate arteries changes by 7 T magnetic resonance angiography in Type 2 diabetes. *J Atheroscler Thromb*. (2018) 25:1067–75. doi: 10.5551/jat.43869
15. Ma SJ, Sarabi MS, Yan L, Shao X, Chen Y, Yang Q, et al. Characterization of lenticulostriate arteries with high resolution black-blood T1-weighted turbo spin echo with variable flip angles at 3 and 7 Tesla. *Neuroimage*. (2019) 199:184–93. doi: 10.1016/j.neuroimage.2019.05.065
16. Zhang Z, Fan Z, Kong Q, Xiao J, Wu F, An J, et al. Visualization of the lenticulostriate arteries at 3T using black-blood T1-weighted intracranial vessel wall imaging: comparison with 7T TOF-MRA. *Eur Radiol*. (2019) 29:1452–9. doi: 10.1007/s00330-018-5701-y
17. Cho ZH, Lee YB, Kang CK, Yang JW, Jung IH, Park CA, et al. Microvascular imaging of asymptomatic MCA steno-occlusive patients using ultra-high-field 7T MRI. *J Neurol*. (2013) 260:144–50. doi: 10.1007/s00415-012-6604-5
18. Liem MK, van der Grond J, Versluis MJ, Haan J, Webb AG, Ferrari MD, et al. Lenticulostriate arterial lumina are normal in cerebral autosomal-dominant arteriopathy with subcortical infarcts and leukoencephalopathy: a high-field *in vivo* MRI study. *Stroke*. (2010) 41:2812–6. doi: 10.1161/STROKEAHA.110.586883
19. Jenkinson M, Beckmann CF, Behrens TE, Woolrich MW, Smith SM. Fsl. *Neuroimage*. (2012) 62:782–90. doi: 10.1016/j.neuroimage.2011.09.015
20. Tustison NJ, Avants BB, Cook PA, Zheng Y, Egan A, Yushkevich PA, et al. N4ITK: improved N3 bias correction. *IEEE Trans Med Imaging*. (2010) 29:1310–20. doi: 10.1109/TMI.2010.2046908
21. Antiga L, Piccinelli M, Botti L, Ene-Iordache B, Remuzzi A, Steinman DA. An image-based modeling framework for patient-specific computational hemodynamics. *Med Biol Eng Comput*. (2008) 46:1097–112. doi: 10.1007/s11517-008-0420-1
22. Kaplan HA, Ford DH. *The Brain Vascular System*. Amsterdam: Elsevier Publishing Company (1966).
23. Rosner SS, Rhoton AL, Ono M, Barry M. Microsurgical anatomy of the anterior perforating arteries. *J Neurosurg*. (1984) 61:468–85. doi: 10.3171/jns.1984.61.3.0468
24. Marinković SV, Kovačević MS, Marinković JM. Perforating branches of the middle cerebral artery: microsurgical anatomy of their extracerebral segments. *J Neurosurg*. (1985) 63:266–71. doi: 10.3171/jns.1985.63.2.0266

Conflict of Interest: XZ is an employee of Siemens Healthcare and JA is an employee of Siemens Shenzhen Magnetic Resonance Ltd. The Institute of Biophysics (Chinese Academy of Sciences) holds a research agreement with Siemens Healthcare.

The remaining authors declare that the research was conducted in the absence of any commercial or financial relationships that could be construed as a potential conflict of interest.

frontiers in Neurology

SYSTEMATIC REVIEW
published: 22 September 2021
doi: 10.3389/fneur.2021.649233

An ALE Meta-Analysis of Specific Functional MRI Studies on Subcortical Vascular Cognitive Impairment

Wenwen Xu[1†], *Yu Song*[1†], *Shanshan Chen*[1], *Chen Xue*[2], *Guanjie Hu*[3], *Wenzhang Qi*[2], *Wenying Ma*[1], *Xingjian Lin*[1*] and *Jiu Chen*[3,4*]

[1] Department of Neurology, The Affiliated Brain Hospital of Nanjing Medical University, Nanjing, China, [2] Department of Radiology, The Affiliated Brain Hospital of Nanjing Medical University, Nanjing, China, [3] Institute of Brain Functional Imaging, Nanjing Medical University, Nanjing, China, [4] Institute of Neuropsychiatry, The Affiliated Brain Hospital of Nanjing Medical University, Nanjing, China

Edited by:
Xiaofei Hu,
Army Medical University, China

Reviewed by:
Feng Chen,
Zhejiang Chinese Medical University, China
Zhenghua Hou,
Southeast University, China

Correspondence:
Xingjian Lin
linxingjian@njmu.edu.cn
Jiu Chen
ericcst@aliyun.com

[†] These authors have contributed equally to this work and share first authorship

Specialty section:
This article was submitted to Applied Neuroimaging, a section of the journal Frontiers in Neurology

Received: *06 January 2021*
Accepted: *28 July 2021*
Published: *22 September 2021*

Citation:
Xu W, Song Y, Chen S, Xue C, Hu G, Qi W, Ma W, Lin X and Chen J (2021) An ALE Meta-Analysis of Specific Functional MRI Studies on Subcortical Vascular Cognitive Impairment. Front. Neurol. 12:649233. doi: 10.3389/fneur.2021.649233

Background: Subcortical vascular cognitive impairment (sVCI), caused by cerebral small vessel disease, accounts for the majority of vascular cognitive impairment, and is characterized by an insidious onset and impaired memory and executive function. If not recognized early, it inevitably develops into vascular dementia. Several quantitative studies have reported the consistent results of brain regions in sVCI patients that can be used to predict dementia conversion. The purpose of the study was to explore the exact abnormalities within the brain in sVCI patients by combining the coordinates reported in previous studies.

Methods: The PubMed, Embase, and Web of Science databases were thoroughly searched to obtain neuroimaging articles on the amplitude of low-frequency fluctuation, regional homogeneity, and functional connectivity in sVCI patients. According to the activation likelihood estimation (ALE) algorithm, a meta-analysis based on coordinate and functional connectivity modeling was conducted.

Results: The quantitative meta-analysis included 20 functional imaging studies on sVCI patients. Alterations in specific brain regions were mainly concentrated in the frontal lobes including the middle frontal gyrus, superior frontal gyrus, medial frontal gyrus, and precentral gyrus; parietal lobes including the precuneus, angular gyrus, postcentral gyrus, and inferior parietal lobule; occipital lobes including the lingual gyrus and cuneus; temporal lobes including the fusiform gyrus and middle temporal gyrus; and the limbic system including the cingulate gyrus. These specific brain regions belonged to important networks known as the default mode network, the executive control network, and the visual network.

Conclusion: The present study determined specific abnormal brain regions in sVCI patients, and these brain regions with specific changes were found to belong to important brain functional networks. The findings objectively present the exact abnormalities within the brain, which help further understand the pathogenesis of sVCI and identify them as potential imaging biomarkers. The results may also provide a basis for new approaches to treatment.

Keywords: subcortical vascular cognitive impairment, resting state, ALE, amplitude of low-frequency fluctuation, regional homogeneity, functional connectivity

INTRODUCTION

Cerebral small vessel disease (CSVD), referring to the series of neuropathological processes related to heredity and age, continuously damages the small perforating arteries, arterioles, capillaries, and venules (1). The cerebral white and deep gray matter are inevitably damaged, which further results in the onset of occult cognitive impairment (1). Vascular cognitive impairment (VCI), including VCI non-dementia (VCIND), vascular dementia (VD), and mixed dementia with VCI, is a potentially preventable and treatable cognitive impairment (2). Accounting for about 36–67% of VCI, subcortical vascular cognitive impairment (sVCI) caused by CSVD needs early recognition and intervention, which is the key to reducing the incidence of VD (3). Topics surrounding sVCI such as cognitive impairment, imaging features, and biological markers have gradually become the focus of today's international stroke and domestic research (4). It is well known that dementia is a group of syndromes involving memory loss, judgment, reasoning, mood changes, behavior, and communication (5). However, compared with AD, the cognitive characteristics of sVCI, involve the domains of executive function impairment and attention deficit, rather than more prominent memory impairment (6). It is reasonable to deduce that the main damaged brain area in AD and the main damaged brain area in sVCI are dissimilar because of the difference in cognitive impairment between the two neurodegenerative diseases, which is a point worthy of further study.

CSVD can be divided into three disease subtypes as follows (7). Subtype 1 is composed of sporadic arteriolosclerosis accompanied by aging and several vascular risk factors, which include systemic arterial hypertension and diabetes mellitus (7). Subtype 2 is defined by cerebral amyloid angiopathy (CAA) linked to hereditary (7). Subtype 3 refers to all inherited or genetic CSVD subtypes without CAA (7). Among them, the most common disease is cerebral autosomal dominant arteriopathy with subcortical ischemic strokes and leukoencephalopathy (8). The common feature of the different subtypes is hemorrhage or ischemia of the subcortical small cerebral vessels. Therefore, it is necessary to clarify the characteristics and types of CSVD by searching original studies and conducting comprehensive quantitative analysis.

In terms of neuroimaging, CSVD appears as white matter lesions, lacunar infarcts, enlarged perivascular spaces, and cerebral microbleeds (8). Resting-state functional magnetic resonance imaging (fMRI) has made it possible for researchers to detect alterations in brain functional networks and local spontaneous neuronal activity, which provides new insight into the pathogenesis of neurological diseases (9). At present, there are three reliable technical means widely used in fMRI, including the amplitude of low-frequency fluctuation (ALFF), regional homogeneity (ReHo), and functional connectivity (FC) (10–12). The ALFF is used to describe spontaneous regional brain activity and ReHo is used to demonstrate the consistency of brain activity (10). FC reveals whether there is connectivity disruption or compensation in the brain regions (12). In the field of neuroimaging, the known networks for cognitive impairment include the default mode network (DMN), the executive control network (ECN), and the visual network (VN). Different networks interact and coordinate with each other to maintain the cognitive level (13). When cognitive impairment occurs, these networks are undoubtedly affected, and vice versa (13). Since the clinical cognitive impairment of sVCI involves multiple aspects, impairment in different networks is likely to occur.

Anatomical Likelihood Estimation (ALE) is a coordinate-based meta-analysis method whose principle is that a 3D Gaussian probability distribution is derived from each coordinate of the research (14). ALE maps are formed by synthesizing the distribution of all eligible studies with a threshold of $p < 0.05$ (15). ALE has demonstrated statistically significant results in studies of various neurological or psychiatric disorders (16). There are no original articles on sVCI in the study of resting-state FC and spontaneous neuronal activity. However, a rare meta-analysis was conducted on specific functional alterations of the brain regions in sVCI patients. Therefore, it is necessary to summarize the previously published articles on sVCI caused by CSVD to determine the specific cognitive domains and brain regions damaged using the ALE algorithm. This study was conducted to investigate the potential targets of sVCI and further discover the pathogenesis. Hence, we made assumptions that in sVCI: (1) specific brain functional markers associated with cognitive impairment would be revealed in sVCI patients and (2) these specific markers would belong to important networks whose interruption has been associated with cognitive decline.

METHOD

The meta-analysis of the present studies was based on the PRISMA statement guidelines.

Literature Retrieval and Research Selection

Retrieval Strategies

Two researchers thoroughly and systematically searched the PubMed, Embase, and Web of Science databases using the keywords (1) ("functional magnetic resonance imaging [MeSH] OR "RESTING STATE" [MeSH]) AND ("subcortical vascular cognitive impairment" [MeSH]) AND ("Functional connectivity"); (2) ("functional magnetic resonance imaging [MeSH] OR "RESTING STATE" [MeSH]) AND ("subcortical vascular cognitive impairment" [MeSH] AND "regional homogeneity"); (3) ("functional magnetic resonance imaging" [MeSH] OR "RESTING STATE" [MeSH]) AND ("subcortical vascular cognitive impairment" [MeSH] AND ("amplitude of low frequency fluctuation") (**Supplementary Table 1**). **Figure 1** shows the flowchart of the literature search and selection strategy.

Inclusion and Exclusion Criteria

Inclusion Criteria

The inclusion criteria were (1) lacunar infarction (LI), cerebral microinfarct, hemorrhage (CMB), leukoencephalopathy (WML), lacunae, and enlarged perivascular gaps on head magnetic resonance imaging (MRI) (17); (2) diagnostic criteria for CSVD

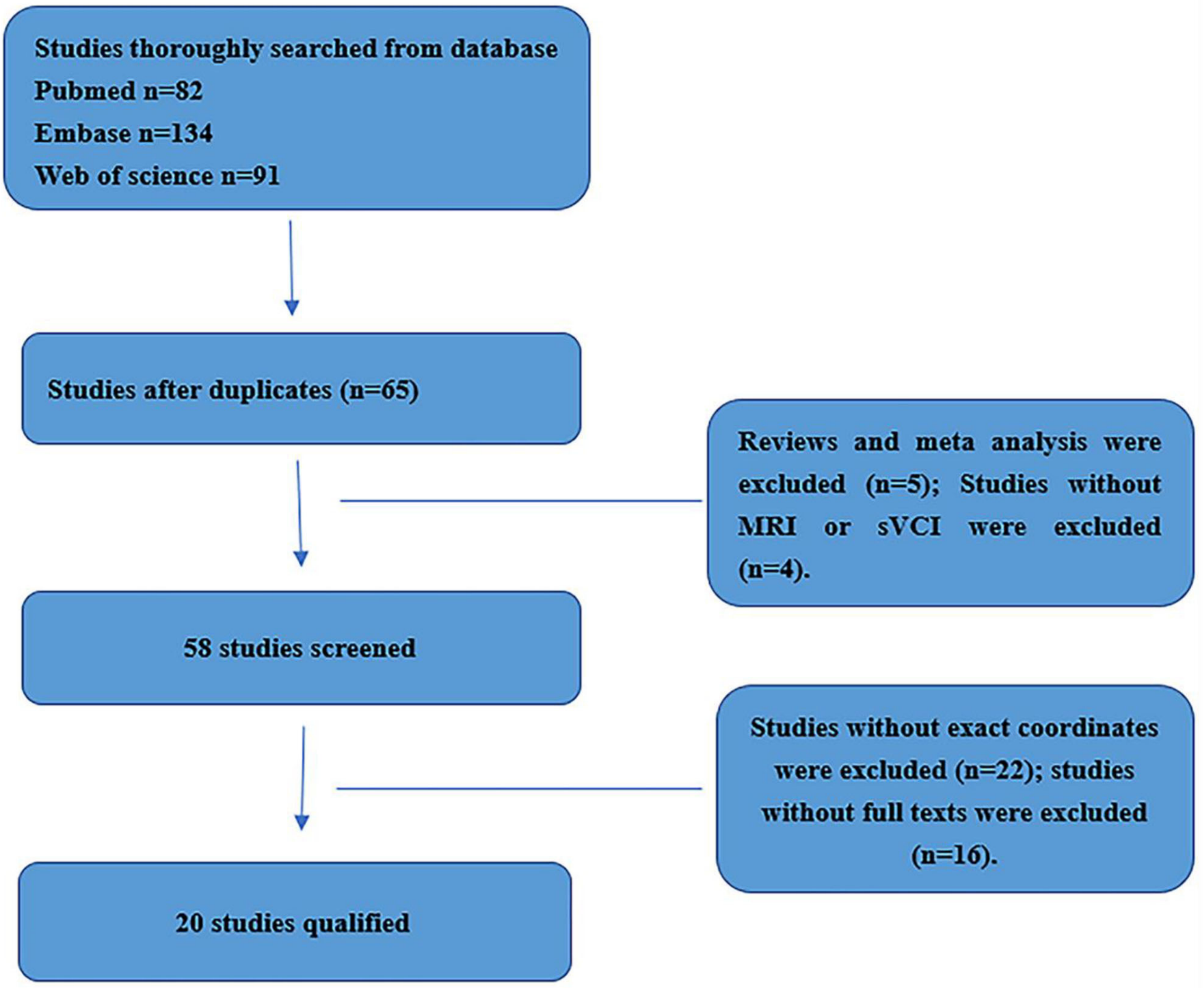

FIGURE 1 | The flowchart of meta-analysis.

based on CSVD expert consensus (18); and (3) the results of the assessment of all the enrolled patients were within the range of cognitive impairment.

Exclusion Criteria

The exclusion criteria were (1) existing or past infarction, hemorrhage, and derma in 1/3 of the cerebral lobe; (2) obvious cerebral artery stenosis or occlusion (18); (3) other diseases of the brain that cause leukinopathy (e.g., hypoglycemia, poisoning, and immune disorders (18)); (4) patients with intracranial tumors and major organ dysfunction (18); and (5) patients with dementia, mental symptoms, audiovisual impairment, and the inability to cooperate (18).

Article Requirements

The articles needed to contain resting-state functional MRI and present Talairach or Montreal Neurologic Institute (MNI) information. We only selected articles in English. Literature such as reviews and meta-analysis articles were excluded. Articles with incomplete information or secondary processing were also excluded.

Data Extraction

Two researchers independently selected, extracted, and checked the data. When there is any disagreement, a third reviewer participated in the decision. All of the abnormal brain region coordinates were derived from the consistent text.

Data Analysis Program

We identified both increased and decreased indicators. The ALFF/fALFF ratio was increased in 32 foci ($n = 169$) and decreased in 11 foci ($n = 202$); ReHo was increased in 6 foci ($n = 95$) and decreased in 7 foci ($n = 95$); and FC was increased in 24 foci ($n = 122$) and decreased in 44 foci ($n = 136$).

TABLE 1 | Demographic data and clinical information.

Study	G	*N*	Age (SD)	Gender (male/female)	MMSE (SD)	Group contrasts	Foci	Correction for multiple comparisons
ALFF								
(19)	sVCI	11	40.2 (11.2)	4/7	19.6 (4.3)	sVCI>HC	15	$p < 0.05$ (cor)
	HC	22	40.2 (87.2)	10/12	28.5 (1.5)	sVCI<HC	3	
(20)	sVCI	30	69.0 (7.8)	19/11	68.0 (5.8)	sVCI>HC	6	$p < 0.01$ (cor)
	HC	35	68.0 (5.8)	22/13	28.4 (1.1)	sVCI<HC	2	
(21)	sVCI	30	69.0 (7.8)	19/11	16.1 (5.1)	sVCI>HC	3	$p < 0.01$ (cor)
	HC	35	68.0 (5.8)	22/13	28.4 (1.1)	sVCI<HC	1	
(22)	sVCI	22	79 (6)	16/6	25 (2.05)	sVCI>HC	2	$p < 0.05$(cor)
	HC	28	70 (9)	17/11	29 (1.09)	sVCI<HC	2	
(23)	sVCI	22	49.0 (14.2)	13/9	23.3 (6.3)	sVCI>HC	3	$p < 0.05$ (cor)
	HC	44	48.5 (13.7)	26/18	28.6 (1.1)	sVCI<HC	1	
(24)	sVCI	46	59.99 (8.59)	22/24	23.23 (2.70)	sVCI>HC	1	$p < 0.05$ (cor)
	HC	28	58.35 (6.82)	13/15	29.46 (1.07)	sVCI<HC	1	
(25)	sVCI	28	65.3 (8.1)	12/16	29.1 (1.2)	sVCI>HC	2	$p < 0.01$ (cor)
	HC	26	66.7 (9.5)	11/15	25.7 (2.7)	sVCI<HC	1	
FC								
(26)	sVCI	32	70.09 (8.26)	14/18	23.78 (2.66)	sVCI>HC	2	$p < 0.05$ (cor)
	HC	23	68.87 (7.05)	14/9	27.96 (0.98)	sVCI<HC	8	
(27)	sVCI	22	48.9 (14.2)	13/9	23.5 (5.7)	sVCI>HC	3	$p < 0.05$ (cor)
	HC	44	48.4 (13.7)	26/18	28.2 (1.3)	sVCI<HC	6	
(28)	sVCI	29	71.07 (6.72)	19/10	25.90 (3.09)	sVCI>HC	3	$p < 0.05$ (cor)
	HC	22	67.78 (6.75)	14/8	28.61 (1.23)	sVCI<HC	7	
(29)	sVCI	16	69.1 (7.8)	14/2	28.1 (1.4)	sVCI>HC	5	$p < 0.01$ (cor)
	HC	18	66.2 (7.7)	16/2	28.9 (1.3)	sVCI<HC	5	
(30)	SVCI	54	70.48 (4.81)	32/22	25.80 (2.48)	sVCI>HC	6	$p < 0.05$ (cor)
	NC	27	67.63 (8.19)	10/17	27.93 (1.03)	sVCI<HC	5	
(23)	sVCI	22	49.0 (14.2)	13/9	23.3 (6.3)	sVCI>HC	0	$p < 0.05$ (cor)
	HC	44	48.5 (13.7)	26/18	28.6 (1.1)	sVCI<HC	8	
(31)	sVCI	14	66.00 (5.13)	7/7	26.86 (2.66)	sVCI>HC	5	
	HC	33	62.03 (7.53)	16/17	28.47 (1.49)	sVCI<HC	0	
(32)	sVCI	31	63.84 (14.1)	18/13	26.32 (2.06)	sVCI>HC	0	$p < 0.05$ (cor)
	HC	32	62.72 (8.22)	18/14	28.75 (1.39)	sVCI<HC	5	
ReHo								
(32)	sVCI	31	63.84 (14.1)	18/13	26.32 (2.06)	sVCI>HC	0	$p < 0.05$ (cor)
	HC	32	62.72 (8.22)	18/14	28.75 (1.39)	sVCI<HC	2	
(31)	sVCI	14	66.00 (5.13)	7/7	26.86 (2.66)	sVCI>HC	3	$p < 0.05$ (cor)
	HC	33	62.03 (7.53)	16/17	28.47 (1.49)	sVCI<HC	0	
(33)	SIVD	20	75.8 (7.67)	13/7	20.1 (5.88)	sVCI>HC	2	$p < 0.05$ (cor)
	HC	23	65.1 (6.97)	11/12	27.9 (1.60)	sVCI<HC	1	
(22)	sVCI	22	79 (6)	16/6	25 (2.05)	sVCI>HC	1	$p < 0.05$ (cor)
	HC	28	70 (9)	17/11	29 (1.09)	sVCI<HC	3	
(27)	sVCI	22	48.9 (14.2)	13/9	23.5 (5.7)	sVCI>HC	0	$p < 0.05$(cor)
	HC	44	48.4 (13.7)	26/18	28.2 (1.3)	sVCI<HC	1	

We used a Java-based version of Ginger ALE 2.3.6 (http://www.brainmap.org/ale) to perform the ALE meta-analysis. The convergence of the difference in foci was assessed between the sVCI and HC groups. The steps were as follows: (1) import a text file used to read the data into the software; (2) set a threshold at $p < 0.05$; (3) input the maps into the MNI template and view the image with dpabi software (http://fmri.org/dpabi).

RESULTS

Research Results

The study characteristics and results are summarized in **Table 1**.

Meta-Analysis Results

Compared to the HC groups, sVCI patients had no increased ALFF in the specific brain regions. In contrast, the brain regions

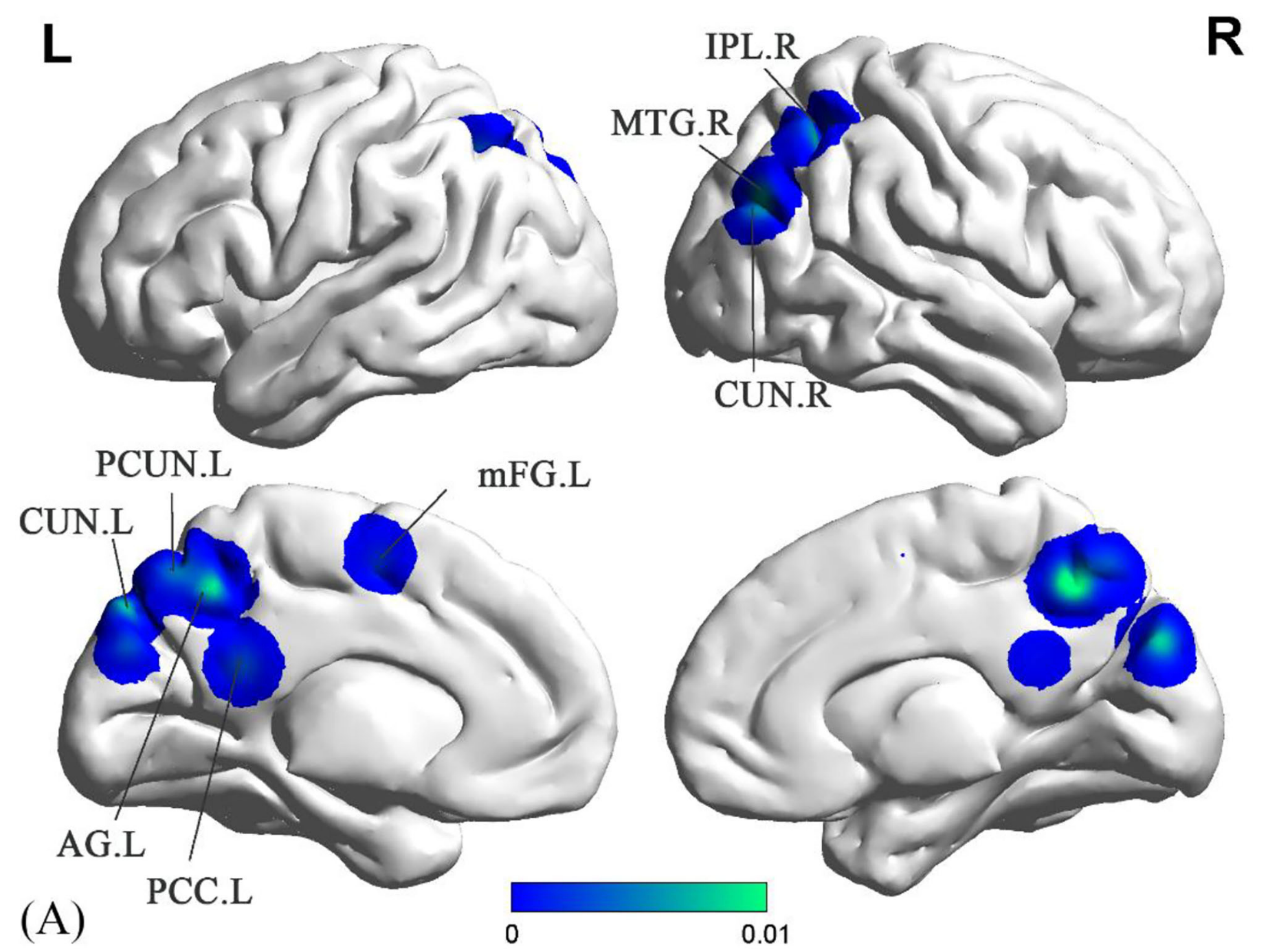

FIGURE 2 | Decreased ALFF in sVCI patients compared with HCs. sVCI, subcortical cognitive impairment; HCs, healthy controls; ALFF, amplitude of low-frequency fluctuation; PCUN, precuneus; PCC, posterior cingulate cortex; CUN, cuneus; MTG, middle temporal gyrus; IPL, inferior parietal lobule; AG, angular gyrus; Mfg, medial frontal gyrus; R, right; L, left.

with a significant decrease in ALFF values mainly included the precuneus (PCUN), posterior cingulate cortex (PCC), cuneus (CUN), middle temporal gyrus (MTG), inferior parietal lobule (IPL), angular gyrus (AG), and the medial frontal gyrus (mFG) (**Figure 2** and **Table 2**).

sVCI patients had increased ReHo in the PCUN, IPL, cingulate gyrus (CG), fusiform gyrus (FFG), and middle frontal gyrus (MFG) (**Figure 3** and **Table 2**). In addition, sVCI patients presented with decreased ReHo in the PCUN, lingual gyrus (LING), insula, posterior lobe, lentiform nucleus, and MFG (**Figure 3** and **Table 2**).

Compared to the HC groups, sVCI patients showed increased FC in the precentral gyrus (PreCG), superior frontal gyrus (SFG), and MFG (**Figure 4** and **Table 2**). sVCI patients showed decreased FC in the MFG, postcentral gyrus (PosCG), PreCG, sub-gyral, mFG, and MFG (**Figure 4** and **Table 2**).

DISCUSSION

The present study was the first meta-analysis conducted to explore the specific functional alterations in brain regions in sVCI patients. We determined different patterns of spontaneous brain activity through two indicators, ALFF and ReHo, and found different brain functional connections by comparing the results. In patients with sVCI, the areas most affected in the brain were the frontal lobes, parietal lobes, and occipital lobes. Additionally, the significant difference in the limbic system may indicate spatially distinct patterns of brain function in sVCI patients.

Decreases in ALFF were found in the PCUN, PCC, MTG, IPL, and AG. ReHo was also decreased in the PCUN and increased in the PCUN and IPL. As the medial aspect of the parietal lobe, the PCUN is considered the hub of multiple brain networks (34). The PCUN has three separate areas that participate in different functional networks (35). The anterior PCUN mainly links to

TABLE 2 | All brain regions and clusters derived from meta-analysis.

Cluster	**Volume (mm^3)**	**MNI**			**Anatomical regions**	**Maximum ALE value**	**Side**	**BA**
		X	**Y**	**Z**				
ALFF								
sVCI>HC								
None								
sVCI<HC								
1	44,904	2	−54	48	Precuneus	0.017697	Left	7
1	44,904	−6	−45	24	Posterior cingulate cortex	0.008758	Left	30
1	44,904	6	−81	30	Cuneus	0.008326	Right	18
1	44,904	−8	−80	42	Cuneus	0.008056	Left	19
1	44,904	0	−66	54	Precuneus	0.006929	Left	7
2	17,440	48	−72	30	Middle temporal gyrus	0.00918	Right	39
2	17,440	42	−54	50	Inferior parietal lobule	0.006901	Right	40
3	11,360	−30	−60	44	Angular gyrus	0.006901	Left	39
4	9,664	−9	−3	57	Medial frontal gyrus	0.007794	Left	6
ReHo								
sVCI>HC								
1	30,608	24	−68	36	Precuneus	0.007556	Right	7
1	30,608	42	−51	39	Inferior parietal lobule	0.007112	Right	40
2	15,872	−18	−60	51	Cingulate gyrus	0.007331	Left	7
3	14,400	−12	21	30	Precuneus	0.008136	Left	32
4	13,576	53	−31	−23	Fusiform gyrus	0.007794	Right	20
5	12,872	39	51	15	Middle frontal gyrus	0.007624	Right	10
sVCI<HC								
1	32,920	2	−76	30	Precuneus	0.011713	Left	31
1	32,920	15	−87	6	Lingual gyrus	0.008056	Right	17
2	14,400	−39	0	12	Insula	0.008326	Left	13
3	13,216	−21	−78	−33	Pyramis	0.008618	Left	-
4	13,216	21	3	6	Lentiform nucleus	0.008618	Right	-
5	12,872	39	51	15	Middle frontal gyrus	0.007624	Right	10
FC								
sVCI>HC								
1	19,800	40	6	28	Precentral gyrus	0.00901	Right	6
1	19,800	48	44	24	Superior frontal gyrus	0.008695	Right	9
1	19,800	50	24	22	Middle frontal gyrus	0.008292	Right	6
1	19,800	28	50	24	Superior frontal gyrus	0.007415	Right	9
sVCI<HC								
1	14,976	−34	−6	42	Middle frontal gyrus	0.008927	Left	6
1	14,976	−36	−18	50	Postcentral gyrus	0.008331	Left	3
1	14,976	−50	−20	38	Postcentral gyrus	0.007795	Left	2
1	14,976	−36	0	28	Precentral gyrus	0.007652	Left	6
2	13,800	48	6	48	Middle frontal gyrus	0.009673	Left	6
2	13,800	42	14	30	Precentral gyrus	0.009003	Right	9
2	13,800	48	8	40	Middle frontal gyrus	0.008929	Right	6
2	13,800	64	2	12	Precentral gyrus	0.008695	Right	6
2	13,800	48	4	22	Precentral gyrus	0.00806	Right	6
4	8,736	22	28	36	Sub-gyral	0.008695	Right	8
4	8,736	10	36	42	Medial frontal gyrus	0.008695	Right	8
4	8,736	32	38	30	Middle frontal gyrus	0.008621	Right	9

BA, Brodmann Area; ALE, Anatomical/Activation Likelihood Estimation; MNI, Montreal Neurologic Institute; sVCI, subcortical vascular cognitive impairment; HCs, healthy controls; ALFF, the amplitude of low-frequency fluctuation; ReHo, regional homogeneity; FC, functional connectivity.

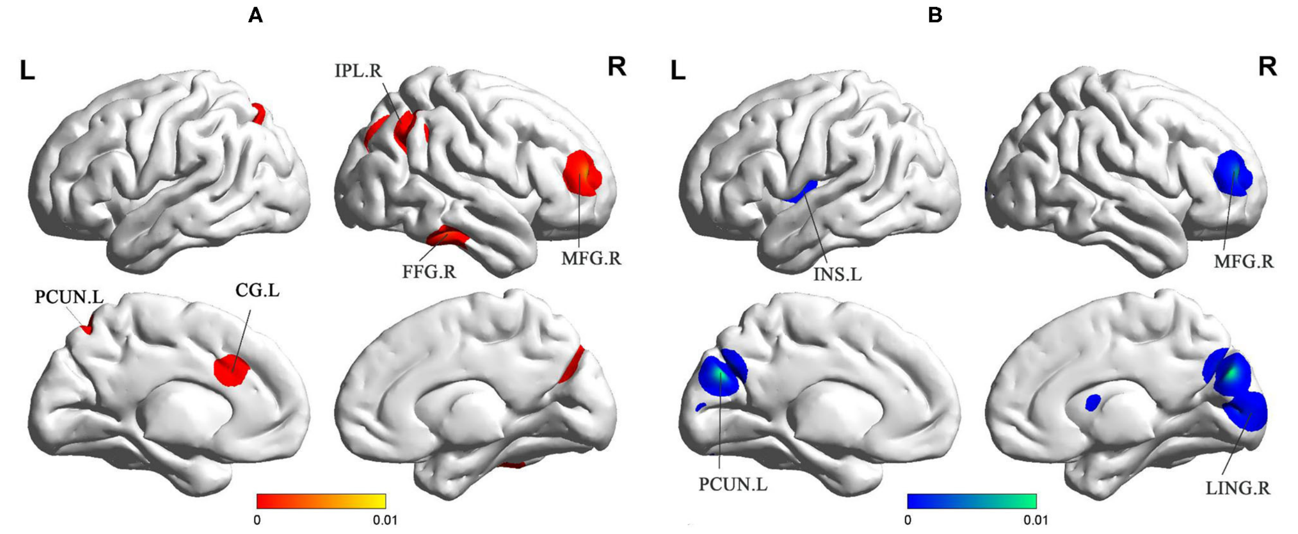

FIGURE 3 | (A) Increased ReHo in sVCI patients compared with HCs. **(B)** Decreased ReHo in sVCI patients compared with HCs. sVCI, subcortical cognitive impairment; HCs, healthy controls; ReHo, regional homogeneity; PCUN, precuneus; IPL, inferior parietal lobule; CG, cingulate gyrus; INS, insula; FFG, fusiform gyrus; MFG, middle frontal gyrus; LING, lingual gyrus; R, right; L, left.

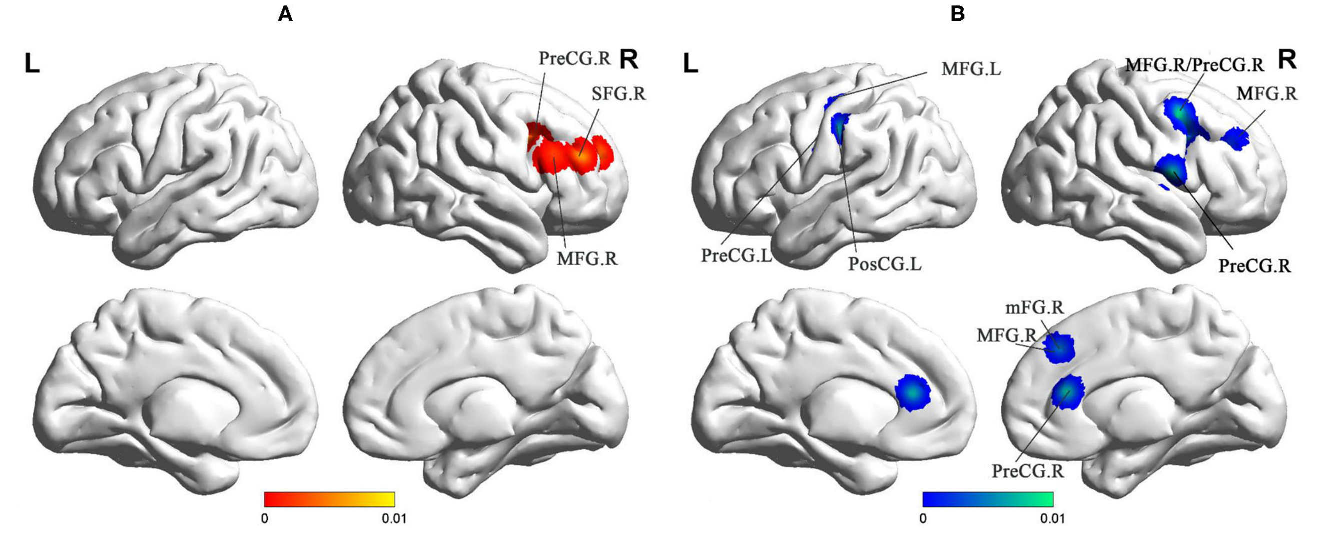

FIGURE 4 | (A) Increased FC in sVCI patients compared with HCs. **(B)** Increased FC in sVCI patients compared with HCs. sVCI, subcortical cognitive impairment; HCs, healthy controls; FC, functional connectivity; PreCG, precentral gyrus; SFG, superior frontal gyrus; MFG, middle frontal gyrus; PosCG, postcentral gyrus; mFG, medial frontal gyrus; MFG, middle frontal gyrus; R, right; L, left.

sensorimotor areas and projects into the insula. The central PCUN is related to the hippocampus and the posterior PCUN joins with regions of the visual cortex (35). Previous evidence reported in a positron emission tomography (PET) study showed hypometabolism of the PCUN in sVCI patients (36). It is known that the IPL is responsible for maintaining attention control and dealing with information (37). The AG is involved in language, number processing, and memory retrieval (38). As an important part of the limbic system, the PCC has extensive functional connections with many brain areas in the prefrontal lobe. Weak signal values in this region, which is responsible for monitoring sensation, stereotyping, and memory, suggest that cognitive impairment in sVCI patients is closely related to this important brain region (39). A recent study revealed that the PCC and PCUN appeared to have the most structural and functional alterations in sVCI patients (40). Some studies reported that the language understanding network, centered on the dominant hemisphere of the MTG, is the neural basis of the brain's language understanding function (41). As we know, language impairment is an important manifestation of vascular dementia (42).

All of the brain regions mentioned above are part of the DMN, the main function of which is to extract the process of episodic memory, cognition, and emotion (43). As for both rising and falling signals in the same brain region, this is due to different stages of the disease (44). It has been shown that during the development of sVCI, some brain regions are compensated for to coordinate cognitive functions (45). Thus, it is not hard to explain why there are elevated signals in certain brain regions. In summary, brain function damage caused by sVCI was concentrated in the DMN, which is consistent with the impairment of episodic memory shown in sVCI patients. However, the within-group analysis showed no significant differences in the increased ALFF values.

Brain regions such as the MFG, SFG, mFG, and PreCG exhibited abnormal FC. These brain regions were located in the ECN, which aims at integrating sensory and memory information and regulating cognition and behavior (30). The ECN, whose core is the prefrontal lobe, is in charge of the integration of sensation, memory information, and the regulation of cognition and behavior (46). Executive function has been confirmed to be the main cognitive domain that shows degeneration in sVCI (29). A structural equation model on CSVD showed that the main neuropsychological symptom, executive dysfunction, may predict both reductions in awareness and the quality of life (47). The pathogenesis of sVCI is mainly the long-term damage of gray matter and white matter. Naturally, the course of the disease shows a trend of gradual aggravation. As a result, it is significant to conclude that the involved brain regions were located in the ECN based on the existing literature. Recent findings pointed out that the employment of transcranial magnetic stimulation could promote an increase in global excitability in sVCI (42). Our research can provide meaningful potential targets for transcranial magnetic stimulation (TMS) to enhance cortical excitability and synaptic plasticity.

Our study showed decreased ALFF in the cuneus and decreased ReHo in the LING. Located at the center of the visual cortex, the LING and the cuneus are in charge of visual function processes (48). A randomized controlled trial confirmed that visual dysfunction may exist in sVCI and regular ophthalmological exams can help improve the quality of life (49). Our findings were consistent with the clinical symptoms. There was a synergistic effect between the networks. When the DMN and ECN are abnormal, the VN will also be functionally damaged (49). As for the compensatory increase in the VN in the later period, more experiments are needed to prove this. Regardless, ReHo tends to demonstrate the coherence of neural activity. Interestingly, a decrease in ReHo in the insula was a unique and important discovery in sVCI patients (50). Covered by the frontal and temporal opercula, the insula contains several functional regions involved in attention, language, speech, and working memory. It is also the hub of several important networks (51). As mentioned in the DMN above, the insula is connected to the anterior PCUN, both of which are reduced. Thus, brain regions and brain networks interact with each other in sVCI patients (49).

LIMITATIONS

Although the results of this study are valuable, limitations were inevitable. The heterogeneity of the data sources is clear. Different threshold settings and preprocessing methods used in the studies would affect our results to different extents (52). However, these differences were negligible with respect to the neuroimaging changes. Since CSVD is a broad concept that includes a wide range of diseases, there were limitations in this area even though the pathogenesis was similar. Due to the small number of studies, it was difficult to study the detailed unified classification. Another limitation was confounding factors such as load of white matter lesions, the presence of microbleeds, and infarcts, which influenced the resting-state indexes to some degree. Besides, as the domains of cognitive impairment were different in the included papers, the heterogeneity of the article was undeniable. Finally, because it is difficult to get the full text of several literatures, this is also the limitation of this paper.

CLINICAL IMPLICATIONS

Although a single study can provide valuable information, it still lacks uniformity and precision. Considering this, our quantitative analysis was very necessary. Core brain areas such as the PCUN, LING, frontal gyrus, and insula were regarded as neuroimaging markers in sVCI. The findings also provide a valuable basis for TMS and drug treatment. Having identified which functions were impaired, we can follow up regularly, such as focusing on visual function, to improve the patients' quality of life. In conclusion, our results showed disease-specific brain area damage characteristics and provide information for follow-up care and treatment.

CONCLUSION

By synthesizing the published literature on sVCI caused by cerebral microvascular disease, we obtained special imaging markers, which were concentrated on the frontal lobes including the middle frontal gyrus, superior frontal gyrus, medial frontal gyrus, precentral gyrus; parietal lobes including the precuneus, angular gyrus, postcentral gyrus, and inferior parietal lobule; occipital lobes including the lingual gyrus and cuneus; temporal lobes including the fusiform gyrus and middle temporal gyrus; and the limbic system including the cingulate gyrus. By dividing these brain regions, the brain networks to which they belonged were also identified. Multiple brain functional networks such as the DMN, ECN, and VN showed abnormal performance consistent with sVCI patients. These findings objectively present the exact abnormalities within the brain, which can help to further understand the pathogenesis of sVCI and suggest imaging findings as a potential biomarker. It may also provide a basis for new treatment approaches.

DATA AVAILABILITY STATEMENT

The original contributions presented in the study are included in the article/**Supplementary Materials**, further inquiries can be directed to the corresponding author.

AUTHOR CONTRIBUTIONS

JC and XL designed the study and revised it critically for important content. WX performed the research and drafted the manuscript. YS and SC helped in data analyses. CX, GH, and WM helped in clinical data collection and analyses.

FUNDING

This study was supported by the National Natural Science Foundation of China (No. 81701675); the Key Project supported by the Medical Science and Technology Development Foundation, Nanjing Department of Health (No. JQX18005); the Cooperative Research Project of Southeast University-Nanjing Medical University (No. 2018DN0031); the Key Research and Development Plan (Social Development) Project of Jiangsu Province (No. BE2018608); and the Innovation and Entrepreneurship Training Program for College Students in Jiangsu Province (Nos. 201810312061X and 201910312035Z).

SUPPLEMENTARY MATERIAL

The Supplementary Material for this article can be found online at: https://www.frontiersin.org/articles/10.3389/fneur.2021.649233/full#supplementary-material

REFERENCES

1. Pasi M, Cordonnier C. Clinical relevance of cerebral small vessel diseases. *Stroke.* (2020) 51:47–53. doi: 10.1161/STROKEAHA.119.024148
2. Gorelick PB, Counts SE, Nyenhuis D. Vascular cognitive impairment and dementia. *Biochim Biophys Acta.* (2016) 1862:860–8. doi: 10.1016/j.bbadis.2015.12.015
3. Jang H, Kim HJ, Park S, Park YH, Choe Y, Cho H, et al. Application of an amyloid and tau classification system in subcortical vascular cognitive impairment patients. *Eur J Nuclear Med Mol Imaging.* (2020) 47:292–303. doi: 10.1007/s00259-019-04498-y
4. Sun Y, Cao W, Ding W, Wang Y, Han X, Zhou Y, et al. Cerebral blood flow alterations as assessed by 3D ASL in cognitive impairment in patients with subcortical vascular cognitive impairment: a marker for disease severity. *Front Aging Neurosci.* (2016) 8:211. doi: 10.3389/fnagi.2016.00211
5. Kalaria RN, Akinyemi R, Ihara M. Stroke injury, cognitive impairment and vascular dementia. *Biochim Biophys Acta.* (2016) 1862:915–25. doi: 10.1016/j.bbadis.2016.01.015
6. Yang Y, Kimura-Ohba S, Thompson J, Rosenberg GA. Rodent models of vascular cognitive impairment. *Transl Stroke Res.* (2016) 7:407–14. doi: 10.1007/s12975-016-0486-2
7. Müller K, Courtois G, Ursini MV, Schwaninger M. New insight into the pathogenesis of cerebral small-vessel diseases. *Stroke.* (2017) 48:520–7. doi: 10.1161/STROKEAHA.116.012888
8. Zhu S, Nahas SJ. CADASIL: imaging characteristics and clinical correlation. *Curr Pain Headache Rep.* (2016) 20:57. doi: 10.1007/s11916-016-0584-6
9. Smitha KA, Akhil Raja K, Arun KM, Rajesh PG, Thomas B, Kapilamoorthy TR, et al. Resting state fMRI: a review on methods in resting state connectivity analysis and resting state networks. *Neuroradiol J.* (2017) 30:305–17. doi: 10.1177/1971400917697342
10. Wang JJ, Chen X, Sah SK, Zeng C, Li YM, Li N, et al. Amplitude of low-frequency fluctuation (ALFF) and fractional ALFF in migraine patients: a resting-state functional MRI study. *Clin Radiol.* (2016) 71:558–64. doi: 10.1016/j.crad.2016.03.004
11. Zang Y, Jiang T, Lu Y, He Y, Tian L. Regional homogeneity approach to fMRI data analysis. *NeuroImage.* (2004) 22:394–400. doi: 10.1016/j.neuroimage.2003.12.030
12. Shen X, Wu J, Wang Z, Chen T. Characterization of in vitro neural functional connectivity on a neurofluidic device. *Electrophoresis.* (2019) 40:2996–3004. doi: 10.1002/elps.201900168
13. Zhu Y, Gong L, He C, Wang Q, Ren Q, Xie C. Default mode network connectivity moderates the relationship between the APOE genotype and cognition and individualizes identification across the Alzheimer's disease spectrum. *J Alzheimers Dis.* (2019) 70:843–60. doi: 10.3233/JAD-190254
14. DeRamus TP, Kana RK. Anatomical likelihood estimation meta-analysis of grey and white matter anomalies in autism spectrum disorders. *Neuroimage Clin.* (2015) 7:525–36. doi: 10.1016/j.nicl.2014.11.004
15. Fornito A, Yücel M, Patti J, Wood SJ, Pantelis C. Mapping grey matter reductions in schizophrenia: an anatomical likelihood estimation analysis of voxel-based morphometry studies. *Schizophr Res.* (2009) 108:104–13. doi: 10.1016/j.schres.2008.12.011
16. Robinson JL, Laird AR, Glahn DC, Blangero J, Sanghera MK, Pessoa L, et al. The functional connectivity of the human caudate: an application of meta-analytic connectivity modeling with behavioral filtering. *NeuroImage.* (2012) 60:117–29. doi: 10.1016/j.neuroimage.2011.12.010
17. Li Q, Yang Y, Reis C, Tao T, Li W, Li X, et al. Cerebral small vessel disease. *Cell Transpl.* (2018) 27:1711–22. doi: 10.1177/0963689718795148
18. Teng Z, Dong Y, Zhang D, An J, Lv P. Cerebral small vessel disease and post-stroke cognitive impairment. *Int J Neurosci.* (2017) 127:824–30. doi: 10.1080/00207454.2016.1261291
19. Lei Y, Li Y, Ni W, Jiang H, Yang Z, Guo Q, et al. Spontaneous brain activity in adult patients with moyamoya disease: a resting-state fMRI study. *Brain Res.* (2014) 1546:27–33. doi: 10.1016/j.brainres.2013.12.022
20. Li C, Liu C, Yin X, Yang J, Gui L, Wei L, et al. Frequency-dependent changes in the amplitude of low-frequency fluctuations in subcortical ischemic vascular disease (SIVD): a resting-state fMRI study. *Behav Brain Res.* (2014) 274:205–10. doi: 10.1016/j.bbr.2014.08.019
21. Liu C, Li C, Yin X, Yang J, Zhou D, Gui L, et al. Abnormal intrinsic brain activity patterns in patients with subcortical ischemic vascular dementia. *PLoS ONE.* (2014) 9:e87880. doi: 10.1371/journal.pone.0087880
22. Ni L, Liu R, Yin Z, Zhao H, Nedelska Z, Hort J, et al. Aberrant spontaneous brain activity in patients with mild cognitive impairment and concomitant lacunar infarction: a resting-state functional mri study. *J Alzheimers Dis.* (2016) 50:1243–54. doi: 10.3233/JAD-150622
23. Su J, Wang M, Ban S, Wang L, Cheng X, Hua F, et al. Relationship between changes in resting-state spontaneous brain activity and cognitive impairment in patients with CADASIL. *J Headache Pain.* (2019) 20:36. doi: 10.1186/s10194-019-0982-3
24. Wang J, Chen H, Liang H, Wang W, Liang Y, Liang Y, et al. Low-frequency fluctuations amplitude signals exhibit abnormalities of intrinsic brain activities and reflect cognitive impairment in leukoaraiosis patients. *Med Sci Monit.* (2019) 25:5219–28. doi: 10.12659/MSM.915528
25. Yi L, Wang J, Jia L, Zhao Z, Lu J, Li K, et al. Structural and functional changes in subcortical vascular mild cognitive impairment: a combined voxel-based morphometry and resting-state fMRI study. *PLoS ONE.* (2012) 7:e44758. doi: 10.1371/journal.pone.0044758
26. Zhou X, Hu X, Zhang C, Wang H, Zhu X, Xu L, et al. Aberrant functional connectivity and structural atrophy in subcortical vascular cognitive impairment: relationship with cognitive impairments. *Front Aging Neurosci.* (2016) 8:14. doi: 10.3389/fnagi.2016.00014
27. Su J, Ban S, Wang M, Hua F, Wang L, Cheng X, et al. Reduced resting-state brain functional network connectivity and poor regional homogeneity in patients with CADASIL. *J Headache Pain.* (2019) 20:103. doi: 10.1186/s10194-019-1052-6
28. Ding W, Cao W, Wang Y, Sun Y, Chen X, Zhou Y, et al. Altered functional connectivity in patients with subcortical vascular cognitive impairment–a resting-state functional magnetic resonance imaging study. *PLoS ONE.* (2015) 10:e0138180. doi: 10.1371/journal.pone.0138180

29. Sun YW, Qin LD, Zhou Y, Xu Q, Qian LJ, Tao J, et al. Abnormal functional connectivity in patients with vascular cognitive impairment, no dementia: a resting-state functional magnetic resonance imaging study. *Behav Brain Res.* (2011) 223:388–94. doi: 10.1016/j.bbr.2011.05.006
30. Liu X, Chen L, Cheng R, Luo T, Lv F, Fang W, et al. Altered functional connectivity in patients with subcortical ischemic vascular disease: a resting-state fMRI study. *Brain Res.* (2019) 1715:126–33. doi: 10.1016/j.brainres.2019.03.022
31. Ye Q, Chen X, Qin R, Huang L, Yang D, Liu R, et al. Enhanced regional homogeneity and functional connectivity in subjects with white matter hyperintensities and cognitive impairment. *Front Neurosci.* (2019) 13:695. doi: 10.3389/fnins.2019.00695
32. Zuo M, Xu Y, Zhang X, Li M, Jia X, Niu J, et al. Aberrant brain regional homogeneity and functional connectivity of entorhinal cortex in vascular mild cognitive impairment: a resting-state functional MRI study. *Front Neurol.* (2018) 9:1177. doi: 10.3389/fneur.2018.01177
33. Tu MC, Hsu YH, Yang JJ, Huang WH, Deng JF, Lin SY, et al. Attention and functional connectivity among patients with early-stage subcortical ischemic vascular disease and Alzheimer's disease. *Front Aging Neurosci.* (2020) 12:239. doi: 10.3389/fnagi.2020.00239
34. Cunningham SI, Tomasi D, Volkow ND. Structural and functional connectivity of the precuneus and thalamus to the default mode network. *Hum Brain Mapping.* (2017) 38:938–56. doi: 10.1002/hbm.23429
35. Wang Z, Fei L, Sun Y, Li J, Wang F, Lu Z. The role of the precuneus and posterior cingulate cortex in the neural routes to action. *Comput Assist Surg (Abingdon).* (2019) 24:113–20. doi: 10.1080/24699322.2018.1557903
36. Kato T, Inui Y, Nakamura A, Ito K. Brain fluorodeoxyglucose (FDG) PET in dementia. *Ageing Res Rev.* (2016) 30:73–84. doi: 10.1016/j.arr.2016.02.003
37. Igelström KM, Graziano MSA. The inferior parietal lobule and temporoparietal junction: a network perspective. *Neuropsychologia.* (2017) 105:70–83. doi: 10.1016/j.neuropsychologia.2017.01.001
38. Seghier ML. The angular gyrus: multiple functions and multiple subdivisions. *Neuroscientist.* (2013) 19:43–61. doi: 10.1177/1073858412440596
39. Fu Z, Caprihan A, Chen J, Du Y, Adair JC, Sui J, et al. Altered static and dynamic functional network connectivity in Alzheimer's disease and subcortical ischemic vascular disease: shared and specific brain connectivity abnormalities. *Hum Brain Mapp.* (2019) 40:3203–21. doi: 10.1002/hbm.24591
40. Noh Y, Seo SW, Jeon S, Lee JM, Kim JS, Lee JH, et al. The role of cerebrovascular disease in amyloid deposition. *J Alzheimers Dis.* (2016) 54:1015–26. doi: 10.3233/JAD-150832
41. Jabbour RA, Penovich PE, Risse GL, Kispert DE, Dunn MB, Gates JR. Atypical language cortex in the left temporal lobe: relationship to bilateral language. *Neurology.* (2004) 63:1833–7. doi: 10.1212/01.WNL.0000144273.82654.96
42. Cantone M, Lanza G, Fisicaro F, Pennisi M, Bella R, Di Lazzaro V, et al. Evaluation and treatment of vascular cognitive impairment by transcranial magnetic stimulation. *Neural Plasticity.* (2020) 2020:8820881. doi: 10.1155/2020/8820881
43. Yuan B, Chen J, Gong L, Shu H, Liao W, Wang Z, et al. Mediation of episodic memory performance by the executive function network in patients with amnestic mild cognitive impairment: a resting-state functional MRI study. *Oncotarget.* (2016) 7:64711–25. doi: 10.18632/oncotarget.11775
44. Simó M, Rifà-Ros X, Vaquero L, Ripollés P, Cayuela N, Jové J, et al. Brain functional connectivity in lung cancer population: an exploratory study. *Brain Imaging Behav.* (2018) 12:369–82. doi: 10.1007/s11682-017-9697-8
45. Liu Y, Chen Y, Liang X, Li D, Zheng Y, Zhang H, et al. Altered resting-state functional connectivity of multiple networks and disrupted correlation with executive function in major depressive disorder. *Front Neurol.* (2020) 11:272. doi: 10.3389/fneur.2020.00272
46. Hojjati SH, Ebrahimzadeh A, Khazaee A, Babajani-Feremi A. Predicting conversion from MCI to AD by integrating rs-fMRI and structural MRI. *Comput Biol Med.* (2018) 102:30–9. doi: 10.1016/j.compbiomed.2018.09.004
47. Brookes RL, Herbert V, Paul S, Hannesdottir K, Markus HS, Morris RG. Executive dysfunction, awareness deficits and quality of life in patients with cerebral small vessel disease: a structural equation model. *Neuropsychology.* (2014) 28:247–53. doi: 10.1037/neu0000015
48. Li S, Lv P, He M, Zhang W, Liu J, Gong Y, et al. Cerebral regional and network characteristics in asthma patients: a resting-state fMRI study. *Front Med.* (2020) 14:792–801. doi: 10.1007/s11684-020-0745-1
49. Kidoh M, Utsunomiya D, Funama Y, Ashikaga H, Nakaura T, Oda S, et al. Vectors through a cross-sectional image (VCI): a visualization method for four-dimensional motion analysis for cardiac computed tomography. *J Cardiovasc Comput Tomogr.* (2017) 11:468–73. doi: 10.1016/j.jcct.2017.09.010
50. Xu X, Li W, Mei J, Tao M, Wang X, Zhao Q, et al. Feature selection and combination of information in the functional brain connectome for discrimination of mild cognitive impairment and analyses of altered brain patterns. *Front Aging Neurosci.* (2020) 12:28. doi: 10.3389/fnagi.2020.00028
51. Gasquoine PG. Contributions of the insula to cognition and emotion. *Neuropsychol Rev.* (2014) 24:77–87. doi: 10.1007/s11065-014-9246-9
52. Pardoe H, Pell GS, Abbott DF, Berg AT, Jackson GD. Multi-site voxel-based morphometry: methods and a feasibility demonstration with childhood absence epilepsy. *Neuroimage.* (2008) 42:611–6. doi: 10.1016/j.neuroimage.2008.05.007

Conflict of Interest: The authors declare that the research was conducted in the absence of any commercial or financial relationships that could be construed as a potential conflict of interest.

frontiers in Neurology

ORIGINAL RESEARCH
published: 14 October 2021
doi: 10.3389/fneur.2021.731237

Cerebral Small Vessel Disease Burden Related to Carotid Intraplaque Hemorrhage Serves as an Imaging Marker for Clinical Symptoms in Carotid Stenosis

Xiaoyuan Fan[1†], *Xiaoqian Zhang*[1†], *Zhichao Lai*[2], *Tianye Lin*[1], *Hui You*[1], *Changwei Liu*[2] *and Feng Feng*[1,3*]

[1] Department of Radiology, Peking Union Medical College Hospital, Chinese Academy of Medical Sciences and Peking Union Medical College, Beijing, China, [2] Department of Vascular Surgery, Peking Union Medical College Hospital, Chinese Academy of Medical Sciences and Peking Union Medical College, Beijing, China, [3] State Key Laboratory of Difficult, Severe and Rare Diseases, Peking Union Medical College Hospital, Chinese Academy of Medical Sciences and Peking Union Medical College, Beijing, China

Edited by:
Xiaofei Hu,
Army Medical University, China

Reviewed by:
Bruno J. Weder,
University of Bern, Switzerland
Zhao Jian,
Chinese People's Liberation Army General Hospital, China
Wei Zhang,
Sichuan Armed Police Corps Hospital, China

***Correspondence:**
Feng Feng
cjr.fengfeng@vip.163.com

[†] These authors have contributed equally to this work and share first authorship

Specialty section:
This article was submitted to Applied Neuroimaging, a section of the journal Frontiers in Neurology

Received: *26 June 2021*
Accepted: *07 September 2021*
Published: *14 October 2021*

Citation:
Fan X, Zhang X, Lai Z, Lin T, You H, Liu C and Feng F (2021) Cerebral Small Vessel Disease Burden Related to Carotid Intraplaque Hemorrhage Serves as an Imaging Marker for Clinical Symptoms in Carotid Stenosis. Front. Neurol. 12:731237. doi: 10.3389/fneur.2021.731237

Objectives: In patients with carotid stenosis, to investigate the relationship between carotid intraplaque hemorrhage (IPH) and total burden of cerebral small vessel disease (CSVD) and preliminarily explore whether the total CSVD burden as an imaging marker can distinguish the severity of clinical symptoms.

Methods: A total of 108 patients (the mean age was 66 ± 7 years, and 85.2% were male) with unilateral carotid stenosis $\geq$50% underwent brain MRI and high-resolution MRI for carotid plaque characterization. The total burden of CSVD was calculated by accumulating one point according to the presence or severity of each of the four MRI markers: white matter hyperintensities, lacunes, perivascular spaces, and cerebral microbleeds. Recent clinical symptoms including transient ischemic attack, amaurosis fugax, and ischemic stroke were recorded. The association between intraplaque hemorrhage (IPH) and total CSVD burden was examined adjusted for other risk factors. The symmetry of CSVD burdens between the ipsilateral and contralateral hemispheres of IPH was tested. Imaging features (CSVD score, IPH, degree of stenosis, and completeness of the circle of Willis) were correlated with clinical symptoms by Kruskal–Wallis H test, Chi-square test, and Fisher's exact test.

Results: Multivariable logistic regression analysis showed that IPH (OR = 2.98, 95% CI [1.39, 6.40], $p = 0.005$) was independently associated with a higher CSVD score. The presence of unilateral IPH was associated with the inter-hemispheric CSVD score difference ($p = 0.004$). Patients with stroke had a higher ipsilateral CSVD score than asymptomatic patients ($p = 0.004$) and those with transient ischemic attack/amaurosis fugax ($p = 0.008$). The statistical difference was marginally significant between symptoms and IPH ($p = 0.057$). No statistical difference was found between the symptoms and degree of stenosis and the completeness of the circle of Willis ($p > 0.05$).

Conclusions: Carotid IPH is associated with an elevated total burden of CSVD in patients with carotid stenosis. Compared with the degree of stenosis, primary collaterals, and IPH, the total CSVD score might be a more effective imaging marker linked with clinical symptoms.

Keywords: cerebral small vessel disease, carotid stenosis, carotid intraplaque hemorrhage, magnetic resonance imaging, stroke

INTRODUCTION

Cerebral small vessel disease (CSVD) often coexists with large artery atherosclerosis (LAA) (1, 2). CSVD can be observed in about two-thirds of patients with carotid stenosis (3). In patients with carotid stenosis, CSVD is associated with increased risks of long-term cardiovascular death (3) and future stroke (4, 5) and adversely affects postoperative cognition (6). Therefore, a better understanding of the pathogenesis for CSVD in carotid stenosis would help improve patients' prognosis.

MRI-defined carotid intraplaque hemorrhage (IPH) is in strong agreement with the histologically defined vulnerable plaque (7) and considered as a reliable marker of thromboembolic plaque activity (8). By releasing emboli into the cerebral vascular system, IPH may be an important risk factor for CSVD. Previous researches (9–13) and meta-analyses (14, 15) reached controversial conclusions on the association between plaque characteristics and CSVD. Most previous studies (9–13) did not provide an adequate control of confounders, possibly interrelated and patient-related. Moreover, previous studies (9–13) often focused on an isolated CSVD marker. Actually, multiple CSVD imaging features are often present simultaneously or sequentially; thus, CSVD should be treated as a whole brain disease (16). A prevailing scoring system called the "total burden of CSVD" expressed by the cooccurrence of white matter hyperintensities (WMHs), lacunes, perivascular spaces (PVSs), and cerebral microbleeds (CMBs) has been proposed for capturing the overall brain damage resulting from CSVD, rather than estimating only one or two individual CSVD markers separately (17). However, the association between carotid IPH and total CSVD score has not been confirmed in carotid stenosis patients.

In addition, although IPH is a strong predictor of stroke in carotid stenosis patients (18), carotid plaque MRI examination is not often performed in clinical practice. If the total CSVD burden is associated with presence of IPH, it may be another effective imaging marker for indicating clinical symptoms. Actually, previous longitudinal studies (4, 5) demonstrated that WMHs and lacunes can identify a high-risk group for ischemic events in patients with carotid stenosis. Similarly, whether "the total CSVD burden" can distinguish the severity of symptoms in carotid stenosis has not been reported.

Therefore, the main purpose of our study was to investigate the relationship between carotid IPH and the total burden of CSVD by adding a within-patient design. The additional purpose was to preliminarily test whether the total CSVD score was an effective imaging marker linked with clinical symptoms.

METHODS AND MATERIALS

Participants

This study was approved by the Medical Ethics Committee of the Peking Union Medical College Hospital, in line with the Declaration of Helsinki. All participants provided written informed consent for this study. Patients were recruited from a cohort study in vascular surgery, designed to explore the application value of multimodal MRI in carotid stenosis patients (19). Patients with unilateral carotid stenosis ≥50% diagnosed with computed tomography angiography (CTA) were included. The exclusion criteria included: (a) patients with intracranial large artery stenosis (≥50%) or occlusion; (b) patients with MR scanning contraindications or who refused MR scanning; and (c) incomplete MR images or MR images with artifacts. From January 2017 to March 2021, a total of 196 patients were diagnosed with carotid stenosis by CTA, and 137 patients had unilateral carotid stenosis. There were 5 patients who had intracranial middle cerebral artery occlusion, 15 patients who had MR scanning contraindications or refused MR scanning, and 9

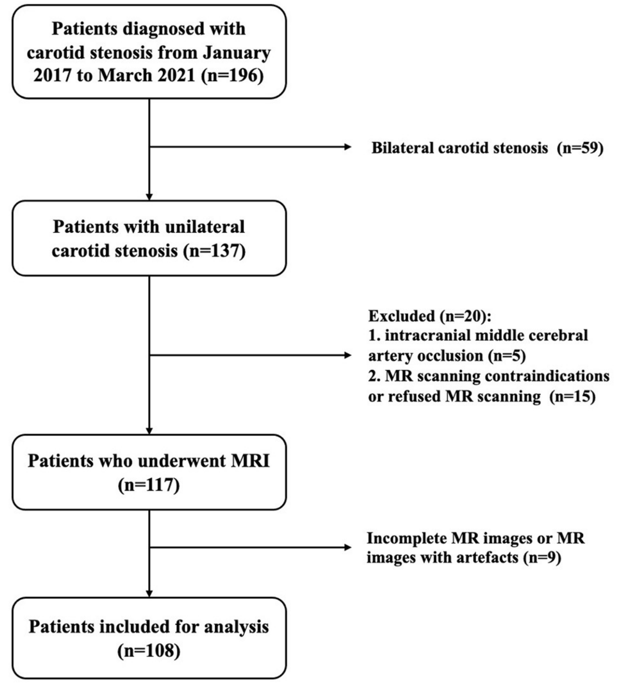

FIGURE 1 | Flowchart of patient enrollment.

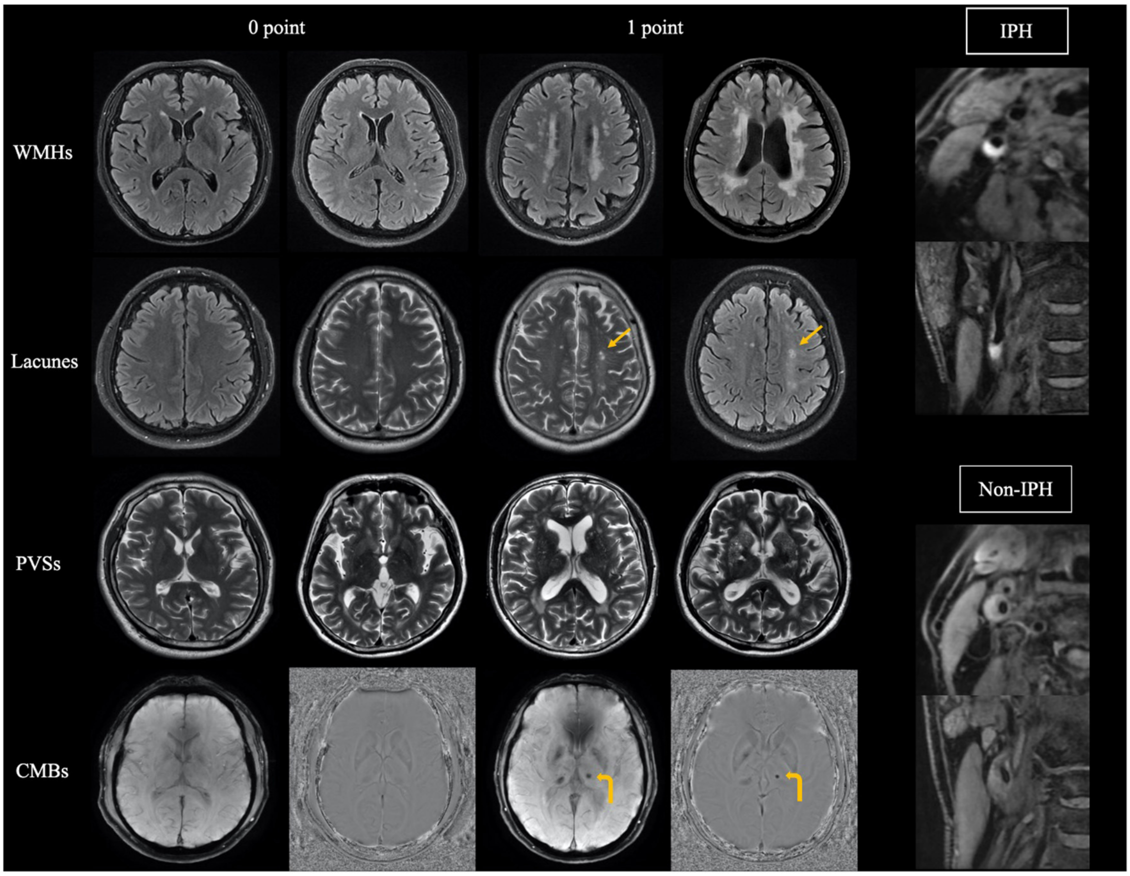

FIGURE 2 | Reference images of total cerebral small vessel disease burden and carotid intraplaque hemorrhage (IPH). Arrow indicates lacunes, and curved arrow indicates cerebral microbleeds. WMHs, white matter hyperintensities; PVSs, perivascular spaces; CMBs, cerebral microbleeds.

patients who met incomplete MR images or MR images with artifacts to be excluded. Finally, 108 patients were included in our study (**Figure 1**).

Data on systemic vascular risk factors were obtained from medical records. Clinical symptoms were recorded by a vascular surgeon with more than 10 years of experience. Symptomatic carotid stenosis was defined as the presence of recent (<6 months since onset) ipsilateral anterior circulation transient ischemic attack (TIA), amaurosis fugax, and non-disabling ischemic stroke (20).

Magnetic Resonance Imaging

All MR examinations were performed on a 3.0 T scanner (GE Discovery 750). Brain MRI was performed with an 8-channel phased-array head coil, and carotid plaque MRI was performed with 8-channel or 32-channel phased-array head and neck coil. High-resolution MRI for carotid plaque characterization was performed with 3D fat-suppressed fast-spin-echo T1-weighted black blood sequence: slice thickness = 0.8 mm, time of repetition = 800 ms, echo time = 15.7 ms, flip angle = 90°, field of view = 204 × 184 mm^2, and acquisition matrix = 320 × 256. The parameters of conventional MRI sequences are shown in **Supplementary Table 1**.

Evaluation of CSVD and IPH

All four MRI markers of CSVD (lacunes, WMHs, PVSs, and CMBs) were identified according to the previously reported neuroimaging standards (21). The detailed evaluation criteria of each CSVD marker and the total CSVD burden score are shown in **Supplementary Table 2**. Briefly, the deep white matter and periventricular white matter were graded separately according to the Fazekas scale (22). We graded the number of PVSs in the basal ganglia with a three-category ordinal scale as follows: 0–10 (category 1); 11–25 (category 2); >25 (category 3) (23). The number of lacunes and CMBs was also recorded. CMBs strictly located in lobes were not recorded. For each patient, an overall CSVD burden score was calculated by counting one point according to the presence of four CSVD markers (17). The overall CSVD score ranged from 0 to 4. The CSVD scores in ipsilateral and contralateral hemispheres were scored separately.

IPH was identified according to the presence of a hyperintense region in the atherosclerotic plaque on the high-resolution MRI for carotid plaque characterization. The presence of hyperintensity was defined on the basis of a signal intensity ≥150% of that of the adjacent skeletal muscle (24).

Reference images of the total CSVD burden and IPH are shown in **Figure 2**. Two radiologists (H. You and T. Lin, with

TABLE 1 | Characteristics of the study population.

	Total ($n = 108$)
Clinical characteristics	
Age, years, mean (SD)	66.3 (7.2)
Male, *n* (%)	92 (85.2)
Hypertension, *n* (%)	73 (67.6)
Diabetes mellitus, *n* (%)	46 (42.6)
Hyperlipidemia, *n* (%)	47 (43.5)
Coronary artery disease, *n* (%)	31 (28.7)
Smoking, *n* (%)	58 (53.7)
Imaging characteristics	
Ipsilateral intraplaque hemorrhage, *n* (%)	38 (35.2)
Unilateral intraplaque hemorrhage, *n* (%)	31 (28.7)
Degree of stenosis	
Moderate stenosis, *n* (%)	16 (14.8)
Severe stenosis, *n* (%)	66 (61.1)
Near-occlusion, *n* (%)	26 (24.1)
Complete circle of Willis, *n* (%)	39 (36.1)
Ipsilateral CSVD score	
0, *n* (%)	41 (38)
1 point, *n* (%)	23 (21.3)
2 points, *n* (%)	23 (21.3)
3 points, *n* (%)	14 (13)
4 points, *n* (%)	7 (6.5)
Contralateral CSVD score	
0, *n* (%)	39 (36.1)
1 point, *n* (%)	31 (28.7)
2 points, *n* (%)	23 (21.3)
3 points, *n* (%)	7 (6.5)
4 points, *n* (%)	8 (7.4)
Clinical symptoms	
Absent/non-specific symptoms, *n* (%)	68 (63)
TIA/ amaurosis fugax, *n* (%)	21 (19.4)
Stroke, *n* (%)	19 (17.6)

CSVD, cerebral small vessel disease; TIA, transient ischemic attack; n, number; SD, standard deviation.

19 years and 7 years of neuroradiology experience, respectively) evaluated the CSVD score and the presence of IPH. They were trained before evaluation and viewed the MRI images blinded for the clinical information. Disagreements were resolved by consensus.

Other Imaging Features

The degree of stenosis was measured with CTA. Moderate or severe stenosis was determined according to the North American Symptomatic Carotid Endarterectomy Trial criteria (NASCET) grading (25), and we also carefully performed the diagnosis of carotid near-occlusion based on previous studies (26).

The completeness of the circle of Willis was evaluated based on the presence of anterior communicating artery and the first segments of bilateral anterior cerebral arteries (A1) on CTA. A complete circle of Willis was defined if both anterior communicating artery and bilateral A1 were visualized. An incomplete circle of Willis was defined if any of the three arterial segments was absent or hypoplastic (<0.8 mm in diameter) (27). Since the presence of posterior communicating artery had little effect on cerebral hemodynamics and clinical symptoms (28), posterior circulation arterial segments were not included.

Statistical Analysis

The data were analyzed using IBM SPSS 25.0. Cohen's κ-value was calculated for the inter-observer agreement on the presence of IPH. Linear-weighted κ-value was calculated for the inter-observer agreement on the CSVD score. The $\kappa \leq 0.40$ represented poor agreement, values >0.40 and ≤ 0.65 represented general agreement, values >0.65 and ≤ 0.75 represented good agreement, and values >0.75 represented excellent agreement.

To investigate the association between IPH and CSVD adjusted for other factors, logistic regression models were used for the univariable and multivariable analyses. IPH was entered as the predictor variable, and CSVD score was entered as dependent variable. We entered baseline characteristics into multivariable models according to the $p < 0.15$ in univariable model. The results are reported as odds ratios (ORs) with 95% confidence intervals (CIs). The paired Wilcoxon signed-rank test was used to test the symmetry of CSVD burdens between bilateral cerebral hemispheres. In patients with unilateral IPH, CSVD scores between ipsilateral and contralateral hemispheres of IPH were compared, while in patients with bilateral or non-IPH, the CSVD scores between ipsilateral and contralateral hemispheres of stenosis were compared. Finally, imaging markers, including ipsilateral CSVD score, IPH, the degree of stenosis, and the completeness of the circle of Willis, were compared between groups with different clinical symptoms by using Kruskal–Wallis *H*-test, Chi-square test, and Fisher's exact test adjusted by the Bonferroni correction. All *p*-values were calculated using two-tailed tests, and $p < 0.05$ was considered as statistically significant.

RESULTS

Characteristics of Patients

The clinical characteristics and imaging features of patients are shown in **Table 1**. The mean age of patients was 66 ± 7 years, and 85.2% were male. Of the 108 patients, 66 (61.1%) had severe carotid stenosis, 26 (24.1%) had carotid near-occlusion, and 38 (35.2%) were observed with IPH. In terms of ipsilateral CSVD score, there were 41 (38%) cases of 0 point, 23 (21.3%) cases of 1 point, 23 (21.3%) cases of 2 points, 14 (13%) cases of 3 points, and 7 (6.5%) cases of 4 points. Sixty-eight (63%) patients were asymptomatic, 21 (19.4%) patients presented with TIA or amaurosis fugax, and 19 (17.6%) patients presented with stroke. Moreover, the degree of stenosis was not statistically different between patients with and without IPH ($p = 0.293$).

The inter-observer agreements on the presence of IPH and CSVD score were excellent and good with κ values of 0.84 and 0.71, respectively.

TABLE 2 | Multivariable logistic regression analysis for factors associated with cerebral small vessel disease burden.

	Univariable model		Multivariate model	
	OR (95% CI)	***P*-value**	**OR (95% CI)**	***P*-value**
Age, years	1.07 (1.02, 1.12)	0.009	1.06 (1.01, 1.12)	**0.020**
Gender				
Male	2.14 (0.78, 5.84)	0.138	1.49 (0.53, 4.22)	0.450
Female	1[a]	—	1[a]	—
Hypertension	1.81 (0.86, 3.79)	0.118	1.71 (0.76, 3.82)	0.194
Diabetes mellitus	0.93 (0.47, 1.86)	0.840	—	—
Hyperlipidemia	0.69 (0.35, 1.37)	0.289	—	—
Coronary artery disease	2.18 (1.03, 4.60)	0.042	1.67 (0.75, 3.72)	0.209
Smoking	1.57 (0.79, 3.13)	0.197	—	—
Ipsilateral intraplaque hemorrhage	3.59 (1.72, 7.52)	0.001	2.98 (1.39, 6.40)	**0.005**
Degree of stenosis				
Near-occlusion	0.77 (0.25, 2.39)	0.651	—	—
Severe stenosis	1.15 (0.43, 3.07)	0.785	—	—
Moderate stenosis	1[a]	—	—	—
Complete circle of Willis	1.45 (0.71, 2.94)	0.306	—	—

OR, odds ratio; CI, confidence interval.

[a] *Used as reference category.*

The bold font indicates that the difference achieved statistical significance.

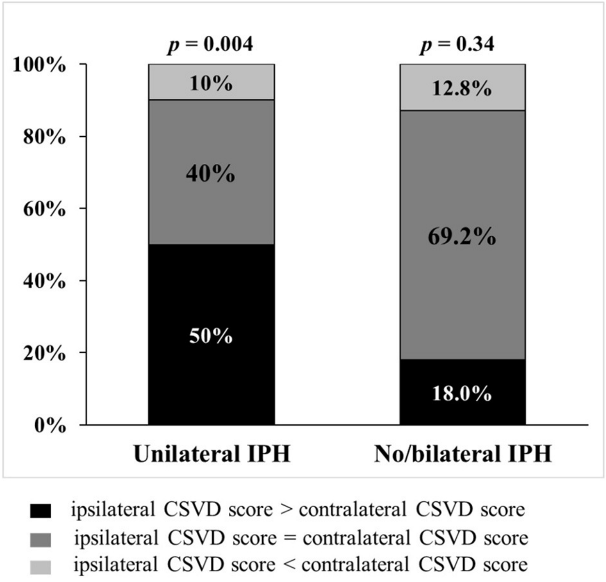

FIGURE 3 | The symmetry of CSVD burden in patients with and without unilateral IPH. In 31 patients with unilateral intraplaque hemorrhage (IPH), the total cerebral small vessel disease (CSVD) scores were higher on the IPH-side ($p = 0.004$). In 77 patients with bilateral or non-IPH, CSVD scores were largely similar between ipsilateral and contralateral hemispheres of stenosis ($p = 0.34$).

Association Between IPH and Total CSVD Burdens

The results of univariable and multivariable logistic regression analyses for independent risk factors of ipsilateral CSVD burdens are shown in **Table 2**. Age, sex, hypertension, coronary artery disease, and IPH were entered into the multivariable logistic regression model. After adjustment for other risk factors, IPH (OR = 2.98, 95% CI [1.39, 6.40], $p = 0.005$) was still associated with higher CSVD burdens. There was no significant difference in the degree of stenosis (severe stenosis: $p = 0.785$; carotid near-occlusion: $p = 0.651$), completeness of the circle of Willis ($p = 0.306$), and other clinical characteristics.

IPH was associated with the asymmetry of CSVD burden between ipsilateral and contralateral hemispheres (**Figure 3**): In patients with unilateral carotid IPH, the CSVD scores were higher on the IPH-side ($p = 0.004$). In contrast, the CSVD scores were largely similar between ipsilateral and contralateral hemispheres of stenosis in patients with bilateral presence or absence of IPH ($p = 0.34$). Representative examples are shown in **Figure 4**.

Comparison of Imaging Markers Between Groups With Different Clinical Symptoms

The comparison of imaging markers between groups with different clinical symptoms is shown in **Table 3**. Patients with stroke had a higher ipsilateral CSVD score than asymptomatic patients ($p = 0.004$) and those with TIA/amaurosis fugax ($p = 0.008$). IPH was observed in more than half of the patients with stroke (11 of 19, 57.9%). The statistical difference was marginally significant between symptoms and IPH ($p = 0.057$). No statistical difference was found between the degree of stenosis, the integrity of the circle of Willis, and clinical symptoms.

DISCUSSION

In a group of patients with unilateral carotid stenosis, we found that a significant association existed between carotid IPH and the total burden of CSVD. Moreover, compared with the degree of stenosis, primary collaterals, and IPH, the total CSVD score was a more effective imaging marker linked with clinical symptoms.

In the present study, multiple parameters including vascular risk factors, the degree of stenosis, collaterals, and carotid IPH were included to provide a comprehensive analysis on the relationship between CSVD and carotid stenosis. Theoretically, the association between LAA and CSVD may be indirect through common vascular risk factors or causative with arterial thromboembolism and impaired hemodynamics being two possible mechanisms (29). In order to better expose the effect of LAA on CSVD, we only included patients with unilateral carotid stenosis and evaluated the relationship between IPH and inter-hemispheric CSVD differences by using a within-patient design, which allowed the control of variability among individuals that may confuse the association between carotid stenosis and CSVD. By using this method, it can be further determined that the effect of carotid IPH on CSVD was independent of vascular risk factors shared by LAA and CSVD. As a reliable marker of thromboembolic plaque activity (8),

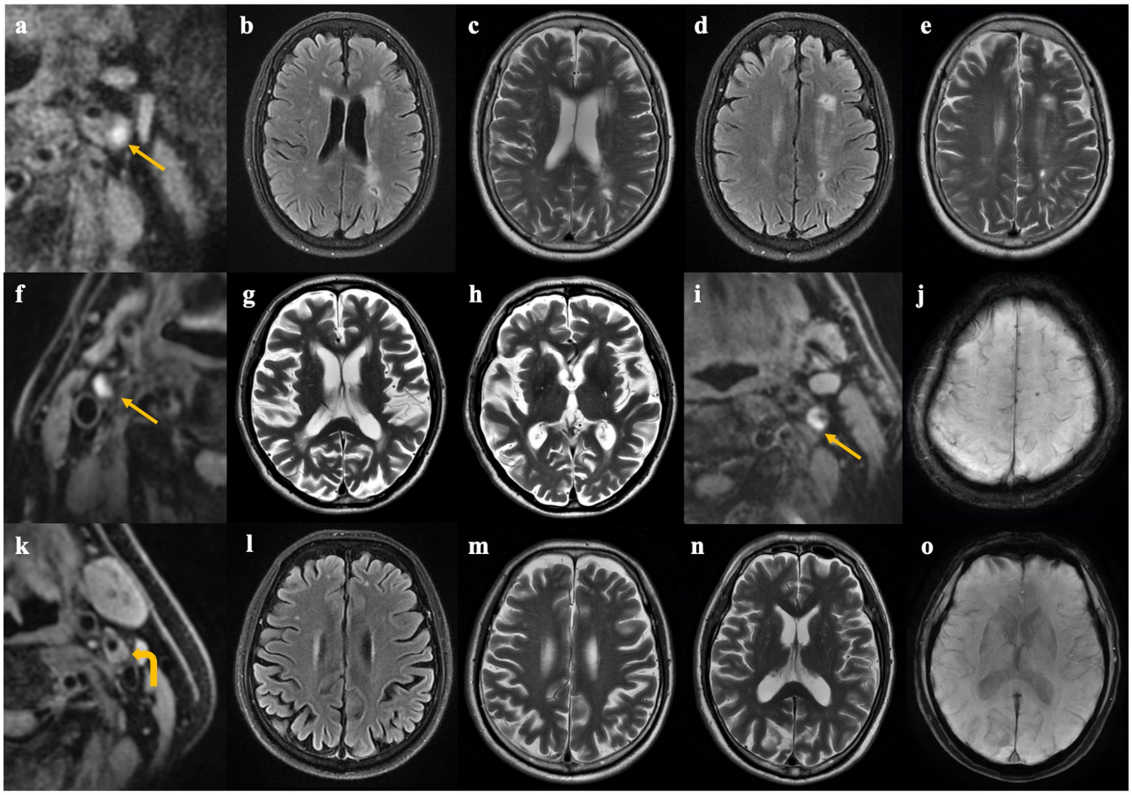

FIGURE 4 | Representative cases of patients with and without unilateral carotid IPH. Case 1 **(a–e)**. A 68-year-old female complained of weakness of right limbs, and high-resolution MRI for carotid plaque showed carotid intraplaque hemorrhage (IPH) on the left side **(a)**. Brain MRI showed more severe white matter hyperintensities and lacunes on the left hemisphere than that on the contralateral hemisphere **(b–e)**. Case 2 **(f–h)**. An 82-year-old male complained of transient weakness of lower limbs. High-resolution MRI for carotid plaque showed IPH on the right side **(f)**. Brain MRI showed category-1 perivascular spaces (PVSs) in the left basal ganglia and category-2 PVSs in the right basal ganglia **(g,h)**. Case 3 **(i,j)**. An 85-year-old male complained of dizziness for 1 month. High-resolution MRI for carotid plaque showed IPH on the left side **(i)**, and a cerebral microbleed lesion was found on the ipsilateral hemisphere **(j)**. Case 4 **(k–o)**. A 71-year-old male with asymptomatic carotid stenosis. Carotid plaque without hemorrhage on the left side was shown on carotid MRI **(k)**, and cerebral small vessel disease was symmetrical between two hemispheres **(l–o)**. Arrow indicates carotid IPH, and curved arrow indicates carotid non-IPH.

the association of IPH with CSVD means that artery-to-artery thromboembolism may be an underlying mechanism through which LAA can aggravate CSVD. A previous study (30) found that IPH was also associated with decreased lumen size, which may be another source for CSVD in theory. However, in our study, the stenosis degree was not statistically different between patients with and with IPH; thus, the effect of IPH on CSVD was not driven by the association of IPH with decreased lumen size.

Our results were consistent with some previous studies evaluating the effects of carotid IPH on certain CSVD markers such as WMHs, lacunes, and CMBs (13–15). Certainly, our study also partly conflicted some studies that did not detect the association between carotid IPH and WMHs or lacunes (9–12). For example, the study by Ammirati et al. (11) examined the association between the progression of WMHs and plaque characteristics by using carotid ultrasound in asymptomatic patients with <70% stenosis, and they reached negative results. The population-based Rotterdam Study (9) involving 951 participants (only 13.1% with lacunes) also showed no association between MRI-defined carotid IPH and lacunes on MRI. The discrepancies between previous studies (9–12) and our study may stem from the different selections of study subjects, a more accurate imaging of plaque by MRI than that by ultrasound, within-subject design, and the notion of "total burden of CSVD" used in our study.

A systematic review and meta-analysis (14) of 32 studies ($n = 17{,}721$) showed no association of WMHs with simple carotid stenosis. Similarly, no significant association was found between the degree of stenosis, integrity of the circle of Willis, and total CSVD burden in our study. However, our results cannot negate the effect of impaired hemodynamics on CSVD because no data on cerebral blood flow or cerebrovascular reactivity were available in the present study.

In addition, our findings suggested that compared with the integrity of the circle of Willis, the degree of stenosis, and IPH, the total CSVD score was a more effective imaging marker linked with clinical manifestation. There are two main mechanisms for the occurrence of ischemic events caused by carotid stenosis; one is the downstream hypoperfusion secondary to stenosis,

TABLE 3 | Comparison of imaging markers between groups with different clinical symptoms.

	Asymptomatic ($n = 68$)	TIA/amaurosis fugax ($n = 21$)	Stroke ($n = 19$)	P-value
Ipsilateral CSVD score	1 [0,2]	0 [0,2]	2 [2,3][a]	**0.003**
Intraplaque hemorrhage, n (%)	22 (32.4)	5 (23.8)	11 (57.9)	0.057
Degree of stenosis				0.989
Moderate stenosis, n (%)	11 (16.2)	3 (14.3)	2 (10.5)	
Severe stenosis, n (%)	41 (60.3)	13 (61.9)	12 (63.2)	
Near-occlusion, n (%)	16 (23.5)	5 (23.8)	5 (26.3)	
Complete circle of Willis, n (%)	26 (38.2)	7 (33.3)	6 (31.6)	0.830

TIA, transient ischemic attack; CSVD, cerebral small vessel disease.

[a] *Patients with stroke had higher ipsilateral CSVD score than asymptomatic patients (adjusted p = 0.004) and those with TIA/amaurosis fugax (adjusted p = 0.008).*

The bold font indicates that the difference achieved statistical significance.

and the other is artery-to-artery embolism (31). The degree of stenosis, collateral circulation, or IPH can only explain a certain mechanism, while the total CSVD score can comprehensively reflect brain microstructure damage influenced by both the two mechanisms. That can partly explain why the total CSVD score was a more efficient imaging marker for the indication of clinical symptoms. Moreover, CSVD itself may accelerate the stroke process caused by carotid stenosis. The presence of CSVD often indicates impaired cerebrovascular reserve (16). When faced with decreased cerebral perfusion pressure caused by carotid stenosis, patients with CSVD would suffer from lower cerebral blood flow due to the inadequate vasodilation of cerebral micro-vessels, which promotes the occurrence of ischemic events or stroke (32).

In patients with carotid stenosis, WMHs and lacunes were reported to be associated with the risk of ischemic stroke in longitudinal studies (4, 5). Our study preliminarily extended the notion of "total burden of CSVD" to the severity of symptoms in patients with carotid stenosis. Although the present study cannot determine the predictive value of total CSVD burden for stroke, the results showed that the CSVD score can best distinguish between patients with and without stroke. That gave a hint that the total CSVD score might be a potential imaging marker for predicting clinical symptoms, which needs to be verified by future longitudinal studies.

An innovation of the present study was that we used the notion of total CSVD burden to evaluate the association between IPH, CSVD, and ischemic events. Considering the high possibility that these CSVD markers coexist with each other, merging them into the total CSVD burden can provide a more comprehensive information about the status of CSVD (17). Moreover, the total CSVD score is reliable and easy to collect as long as the standardized definition of each feature is adopted (21). When high-resolution MRI for carotid plaque characterization is not performed in patients with carotid stenosis in clinical practice, the total CSVD score evaluated on brain MRI can help indicate the stability of the plaque.

Our study also had several limitations. First, the main limitation was the cross-sectional design, and thus the causality between CSVD and clinical symptoms cannot be determined. As we mentioned above, CSVD may participate in the stroke progress caused by carotid stenosis, or their association stems from the common pathogenesis. Second, the degree of stenosis and integrity of the circle of Willis were indirect measurements of hemodynamics. Therefore, the effect of hemodynamics on CSVD or clinical symptoms cannot be directly concluded in present study. Although cerebral blood flow and cerebrovascular reactivity are more accurate indicators for cerebral hemodynamic changes, the degree of stenosis and collaterals are the commonly used imaging markers when determining treatment strategies or intraoperative procedures (25, 33). Third, our findings were only applicable to patients with carotid stenosis $\geq$50%. The relative contributions of IPH and hemodynamics may differ in pre-clinical subjects with $<$50% stenosis.

CONCLUSION

In conclusion, our study demonstrated that in patients with carotid stenosis, the total burden of CSVD was associated with IPH and can be an effective imaging marker linked with clinical symptoms. Our study adumbrates the potential value of total CSVD score for risk stratification in patients with carotid stenosis. Future longitudinal studies are needed to investigate the predictive value of the total CSVD burden in patients with carotid stenosis, by which the total CSVD burden may participate in formulating treatment strategies.

DATA AVAILABILITY STATEMENT

The data that support the findings of this study are available from the corresponding author upon reasonable request.

ETHICS STATEMENT

The studies involving human participants were reviewed and approved by Medical Ethics Committee of the Peking Union Medical College Hospital. The patients/participants provided their written informed consent to participate in this study.

AUTHOR CONTRIBUTIONS

XF, XZ, and ZL designed the study. XF performed the statistical analyses. XF and XZ contributed to data preparation and drafting the original manuscript. ZL was responsible for clinical evaluation. TL and XF are responsible for MR scanning. TL and HY evaluated MR images. FF and CL managed the subject recruitment. FF modified and confirmed the final article. All authors contributed to the article and approved the submitted version.

FUNDING

This work was supported in part by the National Nature Science Foundation of China grant (82071899), the Beijing NaturalScience Foundation grant (L182067), and the Fundamental Research Funds for the Central Universities (3332020009).

ACKNOWLEDGMENTS

We thank Lifang Zhang from Clinical Epidemiology Unit, International Epidemiology Network, Peking Union Medical College Hospital, Chinese Academy of Medical Science for statistical advice, and Juan Wei from GE Healthcare Beijing for the MR technical help.

SUPPLEMENTARY MATERIAL

The Supplementary Material for this article can be found online at: https://www.frontiersin.org/articles/10.3389/fneur.2021.731237/full#supplementary-material

REFERENCES

1. Brisset M, Boutouyrie P, Pico F, Zhu Y, Zureik M, Schilling S et al. Large-vessel correlates of cerebral small-vessel disease. *Neurology.* (2013) 80:662–9. doi: 10.1212/WNL.0b013e318281ccc2
2. Lu T, Liang J, Wei N, Pan L, Yang H, Weng B, et al. Extracranial artery stenosis is associated with total MRI burden of cerebral small vessel disease in ischemic stroke patients of suspected small or large artery origins. *Front Neurol.* (2019) 10:243. doi: 10.3389/fneur.2019.00243
3. Timmerman N, Rots ML, van Koeverden ID, Haitjema S, van Laarhoven CJHCM, Vuurens AM, et al. Cerebral small vessel disease in standard pre-operative imaging reports is independently associated with increased risk of cardiovascular death following carotid endarterectomy. *Eur J Vasc Endovasc Surg.* (2020) 59:872–80. doi: 10.1016/j.ejvs.2020.02.004
4. Song J, Kim KH, Jeon P, Kim YW, Kim DI, Park YJ, et al. White matter hyperintensity determines ischemic stroke severity in symptomatic carotid artery stenosis. *Neurol Sci.* (2021) 42:3367–74. doi: 10.1007/s10072-020-04958-6
5. Kakkos SK, Sabetai M, Tegos T, Stevens J, Thomas D, Griffin M, et al. Silent embolic infarcts on computed tomography brain scans and risk of ipsilateral hemispheric events in patients with asymptomatic internal carotid artery stenosis. *J Vasc Surg.* (2009) 49:902–9. doi: 10.1016/j.jvs.2008.10.059
6. Yoshida J, Yamashita F, Sasaki M Jun, Yoshioka K, Fujiwara S, Kobayashi M, et al. Adverse effects of pre-existing cerebral small vessel disease on cognitive improvement after carotid endarterectomy. *Int J Stroke.* (2020) 15:657–65. doi: 10.1177/1747493019874732
7. Bitar R, Moody AR, Leung G, Symons S, Crisp S, Butany J, et al. In vivo 3D high-spatial-resolution MR imaging of intraplaque hemorrhage. *Radiology.* (2008) 249:259–67. doi: 10.1148/radiol.2491071517
8. Altaf N, Goode SD, Beech A, Gladman JR, Morgan PS, MacSweeney ST,, et al. Plaque hemorrhage is a marker of thromboembolic activity in patients with symptomatic carotid disease. *Radiology.* (2011) 258:538–45. doi: 10.1148/radiol.10100198
9. van den Bouwhuijsen QJA, Vernooij MW, Verhaaren BFJ, Vrooman HA, Niessen WJ, Krestin GP, et al. Carotid plaque morphology and ischemic vascular brain disease on MRI. *Am J Neuroradiol.* (2017) 38:1776–82. doi: 10.3174/ajnr.A5288
10. Patterson AJ, U-King-Im JM, Tang TY, Scoffings DJ, Howarth SP, Graves MJ, et al. Association between white matter ischaemia and carotid plaque morphology as defined by high-resolution in vivo MRI. *Eur J Vasc Endovasc Surg.* (2009) 38:149–54. doi: 10.1016/j.ejvs.2009.04.005
11. Ammirati E, Moroni F, Magnoni M, Rocca MA, Anzalone N, Cacciaguerra L, et al. Progression of brain white matter hyperintensities in asymptomatic patients with carotid atherosclerotic plaques and no indication for revascularization. *Atherosclerosis.* (2019) 287:171–8. doi: 10.1016/j.atherosclerosis.2019.04.230
12. Kwee RM, Hofman PA, Gronenschild EH, van Oostenbrugge RJ, Mess WH, ter Berg JW, et al. Association between carotid plaque characteristics and cerebral white matter lesions: one-year follow-up study by MRI. *PLoS ONE.* (2011) 6:e17070. doi: 10.1371/journal.pone.0103924
13. Hori S, Hori E, Shibata T, Umemura K, Okamoto S, Kubo M,, et al. Correlation between cerebral microbleeds and vulnerable plaque in patients with severe carotid artery stenosis; comparative magnetic resonance imaging study. *J Stroke Cerebrovasc Dis.* (2019) 28:104300. doi: 10.1016/j.jstrokecerebrovasdis.2019.07.016
14. Liao SQ, Li JC, Zhang M, Wang YJ, Li BH, Yin YW, et al. The association between leukoaraiosis and carotid atherosclerosis: a systematic review and meta-analysis. *Int J Neurosci.* (2015) 125:493–500. doi: 10.3109/00207454.2014.949703
15. Moroni F, Ammirati E, Magnoni M, D'Ascenzo F, Anselmino M, Anzalone N, et al. Carotid atherosclerosis, silent ischemic brain damage and brain atrophy: a systematic review and meta-analysis. *Int J Cardiol.* (2016) 223:681–7. doi: 10.1016/j.ijcard.2016.08.234
16. Wardlaw JM, Smith C, Dichgans M. Small vessel disease: mechanisms and clinical implications. *Lancet Neurol.* (2019) 18:684–96. doi: 10.1016/S1474-4422(19)30079-1
17. Staals J, Makin SD, Doubal FN, Dennis MS, Wardlaw JM. Stroke subtype, vascular risk factors, and total MRI brain small-vessel disease burden. *Neurology.* (2014) 83:1228–34. doi: 10.1212/Wnl.0000000000000837
18. Schindler A, Schinner R, Altaf N, Hosseini AA, Simpson RJ, Esposito-Bauer L, et al. Prediction of stroke risk by detection of hemorrhage in carotid plaques: meta-analysis of individual patient data. *JACC Cardiovasc Imaging.* (2020) 13:395–406. doi: 10.1016/j.jcmg.2019.03.028
19. Lin T, Lai Z, Lv Y, Qu J, Zuo Z, You H, et al. Effective collateral circulation may indicate improved perfusion territory restoration after carotid endarterectomy. *Eur Radiol.* (2018) 28:727–35. doi: 10.1007/s00330-017-5020-8
20. Brott TG, Hobson RW 2nd, Howard G, Roubin GS, Clark WM, Brooks W, et al. Stenting versus endarterectomy for treatment of carotid-artery stenosis. *N Engl J Med.* (2010) 363:11–23. doi: 10.1056/NEJMoa0912321
21. Wardlaw JM, Smith EE, Biessels GJ, Cordonnier C, Fazekas F, Frayne R, et al. Neuroimaging standards for research into small vessel disease and its contribution to ageing and neurodegeneration. *Lancet Neurol.* (2013) 12:822–38. doi: 10.1016/s1474-4422(13)70124-8
22. Fazekas F, Chawluk JB, Alavi A, Hurtig HI, Zimmerman RA. MR signal abnormalities at 1.5T in Alzheimer's dementia and normal aging. *AJNR Am J Neuroradiol.* (1987) 8:421–6. doi: 10.2214/ajr.149.2.351
23. Klarenbeek P, van Oostenbrugge RJ, Lodder J, Rouhl RP, Knottnerus IL, Staals J. Higher ambulatory blood pressure relates to enlarged Virchow-Robin spaces in first-ever lacunar stroke patients. *J Neurol.* (2013) 260:115–21. doi: 10.1007/s00415-012-6598-z
24. Altaf N, MacSweeney S, Gladman J, Auer D. Carotid intraplaque hemorrhage predicts recurrent symptoms in patients with high grade carotid stenosis. *Stroke.* (2007) 38:1633–5. doi: 10.1161/STROKEAHA.106.473066
25. Barnett HJM, Taylor DW, Eliasziw M, Fox AJ, Ferguson GG, Haynes RB, et al. Benefit of carotid endarterectomy in patients with symptomatic moderate or severe stenosis. North American Symptomatic Carotid

Endarterectomy Trial Collaborators. *N Engl J Med.* (1998) 339:1415–25. doi: 10.1056/NEJM199811123392002

26. Johansson E, Gu T, Aviv RI, Fox AJ. Carotid near-occlusion is often overlooked when CT angiography is assessed in routine practice. *Eur Radiol.* (2020) 30:2543–51. doi: 10.1007/s00330-019-06636-4
27. Katano H, Mase M, Sakurai K, Miyachi S, Yamada K. Revaluation of collateral pathways as escape routes from hyperemia/ hyperperfusion following surgical treatment for carotid stenosis. *Acta Neurochir.* (2012) 154:2139–48; discussion: 2148–39. doi: 10.1007/s00701-012-1498-7
28. Di Napoli A, Cheng SF, Gregson J, Atkinson D, Markus JE, Richards T, et al. Arterial spin labeling MRI in carotid stenosis: arterial transit artifacts may predict symptoms. *Radiology.* (2020) 297:652–60. doi: 10.1148/radiol.2020200225
29. Altaf N, Morgan PS, Moody A, MacSweeney ST, Gladman JR, Auer DP. Brain white matter hyperintensities are associated with carotid intraplaque hemorrhage. *Radiology.* (2008) 248:202–9. doi: 10.1148/radiol.2481070300
30. Takaya N, Yuan C, Chu B, Saam T, Polissar NL, Jarvik GP, et al. Presence of intraplaque hemorrhage stimulates progression of carotid atherosclerotic plaques: a high-resolution magnetic resonance imaging study. *Circulation.* (2005) 111:2768–75. doi: 10.1161/CIRCULATIONAHA.104.504167
31. Baradaran H, Gupta A. Brain imaging biomarkers of carotid artery disease. *Ann Transl Med.* (2020) 8:1277. doi: 10.21037/atm-20-1939
32. Gupta A, Chazen JL, Hartman M, Delgado D, Anumula N, Shao H, et al. Cerebrovascular reserve and stroke risk in patients with carotid stenosis or occlusion: a systematic review and meta-analysis. *Stroke.* (2012) 43:2884–91. doi: 10.1161/Strokeaha.112.663716
33. Pennekamp CW, van Laar PJ, Hendrikse J, den Ruijter HM, Bots ML, van der Worp HB, et al. Incompleteness of the circle of Willis is related to EEG-based shunting during carotid endarterectomy. *Eur J Vasc Endovasc Surg.* (2013) 46:631–7. doi: 10.1016/j.ejvs.2013.09.007

Conflict of Interest: The authors declare that the research was conducted in the absence of any commercial or financial relationships that could be construed as a potential conflict of interest.

frontiers in Neurology

ORIGINAL RESEARCH
published: 20 October 2021
doi: 10.3389/fneur.2021.752762

Abnormal Cerebral Blood Flow and Functional Connectivity Strength in Subjects With White Matter Hyperintensities

Hao Huang[1], **Kun Zhao**[2], **Wenzhen Zhu**[3], **Hui Li**[1] **and Wenhao Zhu**[1]*

[1] Department of Neurology, Tongji Hospital, Tongji Medical College, Huazhong University of Science and Technology, Wuhan, China, [2] School of Biological Science & Medical Engineering, Beijing Advanced Innovation Center for Biomedical Engineering, Beihang University, Beijing, China, [3] Department of Radiology, Tongji Hospital, Tongji Medical College, Huazhong University of Science and Technology, Wuhan, China

White matter hyperintensities (WMHs) are common neuroimaging findings in the aging population and are associated with various clinical symptoms, especially cognitive impairment. Abnormal global cerebral blood flow (CBF) and specific functional connections have been reported in subjects with higher WMH loads. Nevertheless, the comprehensive functional mechanisms underlying WMH are yet to be established. In this study, by combining resting-state functional magnetic resonance imaging and arterial spin labeling, we investigated the neurovascular dysfunction in subjects with WMH in CBF, functional connectivity strength (FCS), and CBF–FCS coupling. The whole-brain alterations of all these measures were explored among non-dementia subjects with different WMH loads using a fine-grained Human Brainnetome Atlas. In addition, exploratory mediation analyses were conducted to further determine the relationships between these neuroimaging indicators, WMH load, and cognition. The results showed that subjects with higher WMH loads displayed decreased CBF and FCS mainly in regions involving the cognitive- and emotional-related brain networks, including the default mode network, salience network, and central executive network. Notably, subjects with higher WMH loads also showed an abnormal regional CBF–FCS coupling in several regions of the thalamus, posterior cingulate cortex, and parahippocampal gyrus involving the default mode network. Furthermore, regional CBF in the right inferior temporal gyrus and right dorsal caudate may mediate the relationship between WMH load and cognition in WMH subjects. These findings indicated characteristic changes in cerebral blood supply, brain activity, and neurovascular coupling in regions involving specific brain networks with the development of WMH, providing further information on pathophysiology underpinnings of the WMH and related cognitive impairment.

Keywords: white matter hyperintensities, arterial spin labeling, cerebral blood flow, functional magnetic resonance imaging, functional connectivity strength, neurovascular coupling

Edited by:
Tao Liu,
Hainan General Hospital, China

Reviewed by:
Pilar Maria Ferraro,
IRCCS Ospedale Policlinico San Martino, Italy
Jiajia Zhu,
First Affiliated Hospital of Anhui Medical University, China
Tianyu Tang,
Southeast University, China

***Correspondence:**
Wenhao Zhu
tianyalinghu@126.com;
whzhu@tjh.tjmu.edu.cn

Specialty section:
This article was submitted to Applied Neuroimaging, a section of the journal Frontiers in Neurology

Received: *03 August 2021*
Accepted: *13 September 2021*
Published: *20 October 2021*

Citation:
Huang H, Zhao K, Zhu W, Li H and Zhu W (2021) Abnormal Cerebral Blood Flow and Functional Connectivity Strength in Subjects With White Matter Hyperintensities. Front. Neurol. 12:752762. doi: 10.3389/fneur.2021.752762

INTRODUCTION

White matter hyperintensities (WMHs), also known as leukoaraiosis or white matter (WM) lesions, are common neuroimaging findings in the aging population, which are typically described as hyperintensities on fluid-attenuated inversion recovery (FLAIR) magnetic resonance images (MRIs) (1, 2). Considered as established markers of cerebral small vessel disease (CSVD), WMHs are demonstrated to be associated with mood disorders, gait disturbance, and, particularly, cognitive impairment in various domains (1–3). Neuroimaging studies could directly investigate the structural and functional abnormalities in subjects with WMH *in vivo* and have provided important information on understanding the pathophysiological mechanisms underlying WMH (4–7). In the past decades, convergent evidence has identified the disruption of WM microstructural integrity and structural networks with the development of WMH and the related cognitive decline (6, 8, 9). However, compared with structural abnormalities, functional changes in subjects with WMH were much less reported *in vivo*, and a comprehensive picture of functional mechanisms underlying WMH is still far from clarified.

Previous studies at the cellular and the tissue level suggested that neurovascular dysfunction may be involved in the increase of WMH burden (10–13). Hence, hemodynamic indicators in neuroimaging studies, such as cerebral blood flow (CBF) and blood-oxygen-level-dependent (BOLD) functional magnetic resonance imaging (fMRI), may provide new perspectives for further elucidating the potential functional underpinnings of WMH (14). CBF is an important indicator that can reflect brain functional metabolism in respect of glucose utilization, oxygen consumption, and aerobic glycolysis (15). Using invasive imaging techniques of single-photon emission computed tomography, Xeon-computed tomography, or positron emission tomography, previous studies have indicated that subjects with higher WMH loads showed a decreased global CBF reduction in the whole brain, WM, and gray matter (GM) (16–20). Furthermore, a few recent studies have attempted to investigate CBF changes in WMH subjects using arterial spin labeling (ASL) MRI, which is a non-invasive technique without contrast and revealed a relationship between WMH load and CBF in WM, especially in the areas of WMH and normal-appearing WM around WMH (19–23). Nevertheless, these studies mainly focused on the global CBF changes of the whole brain or large brain areas in subjects with WMH, yet the characteristic alteration map of regional CBF in subjects with different WMH loads has not been evaluated. Resting-state BOLD fMRI is another promising neuroimaging tool for evaluating the aberrant functional architecture underlying the increase of WMH burden, which reflects the neuronal activity and intrinsic functional interactions and integrations among anatomically separated brain regions (24–27). Based on resting-state fMRI, previous studies have revealed aberrant functional connectivity (FC) in specific regions involving the default mode network (DMN) in subjects with higher WMH loads, which was associated with cognitive decline (25, 26, 28). As a data-driven, newly developed measure for FC calculation, the functional connectivity strength (FCS) represents the connectivity of each voxel with all other voxels in the brain (29–31). Hence, different from the seed-based FC analysis and independent component analysis approach used in previous studies (25, 26, 32), FCS analysis may be used to delineate overall functional alterations of each brain region underlying the increase of WMH burden.

Brain regions with higher neuronal activity usually tend to have higher perfusion and energy supply, indicating a neurovascular coupling that plays a critical role in maintaining normal brain function (33). Combined ASL and fMRI, previous studies have demonstrated a striking correlation between resting-state FCS and CBF in the normal brain (30, 34), further supporting the hypothesis of neurovascular coupling. Moreover, abnormal global and characteristic regional CBF–FCS coupling has been identified in several neuropsychiatric diseases, including schizophrenia, Wilson's disease, primary open-angle glaucoma, and generalized anxiety disorder (34–37). However, the relationship between CBF and FCS in subjects with different WMH loads remains unknown, which may provide complementary evidence for clarifying potential functional mechanisms in WMH.

Here, we hypothesized that the changes of not only CBF and FCS but also CBF–FCS coupling could contribute to the increase of WMH burden and the related cognitive impairment. To test this hypothesis, resting-state ASL and fMRI data were acquired to compute CBF, FCS, and correlation between CBF and FCS from 86 non-dementia subjects with WMH. Furthermore, to obtain the precise alteration information of CBF, FCS, and CBF–FCS coupling in both the whole GM and each brain subregion, we investigated the global and local alteration patterns of these neuroimaging measures among subjects with different grades of WMH using a fine-grained Human Brainnetome Atlas (38). In addition, we performed exploratory correlation and mediation analyses to evaluate the relationships between these neuroimaging indicators, WMH load, and cognition.

MATERIALS AND METHODS

Subjects

Eighty-six non-dementia subjects with WMH on MRI scans were recruited from the outpatient service of the Department of Neurology, Tongji Hospital, Wuhan, China. The inclusion criteria for the participants were as follows: (1) 50–80 years old, right-handedness; (2) mild to severe WMH; (3) >5 years of education; (4) no dementia based on the criteria of the Diagnostic and Statistical Manual of Mental Disorders, Fourth Edition; (5) no MRI contraindication. The exclusion criteria were as follows: (1) cerebral infarcts with the diameter

---

Abbreviations: ACC, anterior cingulate cortex; ANOVA, one-way analysis of variance; ASL, arterial spin labeling; BOLD, blood-oxygen-level-dependent; CBF, cerebral blood flow; CEN, central executive network; CSVD, cerebral small vessel disease; DLPFC, dorsolateral prefrontal cortex; DMN, default mode network; FC, functional connectivity; FCS, functional connectivity strength; fMRI, functional magnetic resonance imaging; GM, gray matter; LPFC, lateral prefrontal cortex; IPL, inferior parietal lobule; ITG, inferior temporal gyrus; MRI, magnetic resonance imaging; PCC, post-cingulate cortex; SN, salience network; TMT, Trail Making Test; WM, white matter; WMH, white matter hyperintensities.

>15 mm or cerebral hemorrhage; (2) WMH mimics (e.g., leukodystrophy and multiple sclerosis); (3) severe large vessel diseases, such as carotid artery stenosis (>50%); (4) systematic diseases (e.g., cancer, connective tissue diseases); (5) a history of epilepsy, degenerative diseases, such as Alzheimer's disease and Parkinson's disease, or psychiatric diseases; (6) could not fulfill the MRI scan or the neuropsychological tests. The severity of WMH was visually rated on FLAIR images according to the Fazekas rating scale by two experienced neurologists (W.H.Z. and H.H.) blinded to the clinical information. The final score was the sum of the deep WMH score (0—absent, 1—punctuate foci, 2—beginning confluence of foci, 3—large confluent areas) and the periventricular WMH score (0—absent, 1—caps or pencil lining, 2—smooth halo, 3—irregular periventricular hyperintensities extending into deep WM) (39, 40). The correlation coefficient of the results from the two observers and the inter-rater coefficient was higher than 0.9. When the two observers failed to reach an agreement on the WMH score, another experienced neurologist (S.B.X., with 20 years of experience) would evaluate the Fazekas score of the case independently. A definite evaluation would be made if two of the three observers agreed; otherwise, they would discuss the case to make the final decision. Furthermore, according to the different WMH loads, the participants were divided into three groups: the mild WMH group (the total Fazekas scores of 1 or 2, $n = 32$), the moderate WMH group (the total Fazekas scores of 3 or 4, $n = 24$), and the severe WMH group (the total Fazekas scores of 5 or 6, $n = 30$). The Ethics Committee of Tongji Hospital, Tongji Medical College, Huazhong University of Science and Technology, approved the study (ID: TJ-C20131216). Written informed consent was obtained from each participant.

Neuropsychological Tests

All participants received a series of neuropsychological tests to examine the performance of various cognitive domains, including (1) global cognition: the Mini-Mental State Examination; (2) processing speed: the Trail Making Test Part A; (3) executive function: Trail Making Test Part B; (4) episodic memory: the Auditory Verbal Learning Test long-delayed recall (20 min); (5) and language: the Verbal Fluency Test (41). For comparisons of performance across each cognitive domain, raw scores for these neuropsychological tests were transformed to z-scores based on the means and standard deviations across all the WMH subjects included in the present study and were then presented as the cognitive performance of each domain (42).

Data Acquisition

MRIs were acquired on a 3.0-T MR scanner (Discovery MR750, GE Healthcare, Milwaukee, WI, USA) using a 32-channel head array coil. T1-weighted images were collected using a BRAVO sequence with a repetition time (TR) of 8.16 ms, echo time (TE) of 3.18 ms, inversion time (TI) of 50 ms, flip angle (FA) of 12°, a matrix of 256 × 256, a field of view (FOV) of 256 × 256 mm, a slice thickness of 1 mm, and 188 slices. FLAIR images were acquired using a TR/TE of 8,000/160 ms, a TI of 2,100 ms, an FA of 111°, a 512 × 512 matrix, a 240 × 240-mm FOV, a slice thickness of 5.0 mm, and a slice gap of 1.5 mm. Resting-state fMRI data were obtained by an axial gradient echo-planar imaging sequence with a TR/TE of 2,000/35 ms, an FA of 90°, a 64 × 64 matrix, a 220 × 220-mm FOV, a slice thickness of 3.0 mm, a slice gap of 1.0 mm, and an acquisition time of 7 min. ASL MRI data were collected using a pseudo-continuous ASL technique, with a TR/TE of 5,086/15 ms, a TI of 2,025 ms, an FA of 111°, a 128 × 128 matrix, a 240 × 240-mm FOV, a slice thickness of 4.0 mm, and 50 slices. All the subjects were asked to relax, move as little as possible, and keep their eyes closed during the scan. Foam pads were used to minimize head movement, and earplugs were used to attenuate scanner noise.

Cerebral Blood Flow Analysis

The ASL data were pre-processed using the CAT12 toolbox (Computational Anatomy Toolbox; http://www.neuro.uni-jena.de/cat) implemented in SPM12 (Statistical Parametric Mapping, Institute of Neurology, London, UK). First, the ASL images were calculated by subtraction of the label images and control images based on the single-compartment model; after that, the images were then converted to the CBF images combined with the proton-density-weighted reference images (34, 43). Second, the skulled structural three-dimensional T1-weighted images were registered to the standard Montreal Neurological Institute (MNI) space to obtain the deformation parameters. Furthermore, the proton-density-weighted reference images were registered to the subject's T1-weighted images and written to the standard MNI space using before obtained deformation parameters, then applied to the CBF images and resliced to a 3 × 3 × 3-mm cubic voxel.

Functional Magnetic Resonance Imaging Data Pre-processing

The fMRI data were pre-processed by the Brainnetome fMRI toolkit (BRANT, http://brant.brainnetome.org) (44). The first 10 volumes were removed because of the magnetization equilibration effect, and the remaining images were corrected by the slice timing procedure to solve the acquisition time delay between different slices. The images were then realigned to the first volume to correct for head motion. Of note, we restricted the further analysis in participants with no more than 3° angular rotation on any axis or 3-mm translation, and no subjects were excluded according to the criteria. Next, the images were normalized to the MNI space and resampled to 3 × 3 × 3-mm voxels. Furthermore, a linear regression analysis was conducted to remove nuisance variables, including the linear shift, the mean signals from CSF and WM, and the head motion at the x-, y-, and z-axes. Finally, to eliminate the effect of low-frequency drifts and high-frequency noise, the temporal band-pass filter (0.01–0.08 Hz) was applied.

Functional Connectivity Strength Analysis

The Pearson's correlation coefficients were calculated between all pairs of the whole GM voxels, and the functional connectivity (FC) matrix was obtained from each participant. To reduce the influence of background noise, we restricted the analysis to positive correlations above a threshold of 0.2, according to previous studies that reported specific alterations of resting-state FCS in several neuropsychological diseases (34, 36, 37, 45–47). If the value of an FC was lower than 0.2, it would be set to zero. The FCS of a given voxel was calculated as the average of the FC between the voxel and all the remaining voxels (30, 45).

Cerebral Blood Flow–Functional Connectivity Strength Coupling Analysis

To quantitatively explore the relationship between CBF and FCS in subjects with WMH, we conducted correlation analyses across voxels and subjects, according to the protocols proposed by Liang et al. (30). Before the CBF–FCS coupling analysis, both ASL and BOLD images were smoothed by a 6-mm full width half maximum Gaussian kernel, and for each participant, CBF and FCS values were transferred into *z*-scores by subtracting mean and dividing by the standard deviation of global values within the GM as previous studies reported (30, 34). A distinctive CBF–FCS correlation coefficient was generated for each subject at the global GM level. Similarly, regional CBF–FCS coupling for each subject was calculated by averaging the CBF–FCS correlation coefficients of all voxels containing in a certain brain region. To delineate the whole-brain CBF–FCS decoupling maps with the increase of WMH burden, both the global and regional CBF–FCS correlations were further compared among the three groups in the study.

Statistical Analyses

Between-Group Differences in Demographic and Clinical Data

The differences in demographic and clinical data, including medical history and neuropsychological scores among the three groups, were evaluated by one-way analysis of variance (ANOVA), the Kruskal–Wallis test, and the χ^2 test using SPSS 20.0 (IBM Corp., Armonk, NY, USA). To explore the potential effects of head motion, we also compared framewise displacement (48), a representative metric for head motion among the three groups. The relationship between the WMH scale and the z-score of each cognitive test was also determined by partial correlation analysis, controlling for age, sex, and years of education.

Atlas-Based Comparison in Cerebral Blood Flow, Functional Connectivity Strength, and Cerebral Blood Flow–Functional Connectivity Strength Coupling

We performed one-way ANOVA and *post-hoc* analysis to identify differences in the FCS, CBF, and correlation coefficient between CBF and FCS among the three WMH groups at the whole GM level ($p < 0.01$, permutation test for 1,000 times), with age and sex as confounding variables. To further characterize the regional changes of these neuroimaging measures of each subject, the human Brainnetome Atlas consists of 246 subregions in the cerebrum (210 cortical and 36 subcortical regions) (http://atlas.brainnetome.org) and has been widely used in previous neuroimaging studies that were used (38). The cerebellum regions were not included in the analysis in the study. One-way ANOVA and *post-hoc* analysis were also performed to evaluate the characteristic regional changes in all these neuroimaging measures among the three WMH groups, with age and sex as covariates ($p < 0.01$, permutation test for 1,000 times).

Exploratory Mediation Analyses

We performed Pearson's correlation analyses to evaluate the relationships between the CBF, FCS, and coefficient of CBF–FCS correlation in different brain regions and the z-scores of each cognitive domain in all subjects with WMH, controlling for age, sex, and years of education ($p < 0.05$). Furthermore, to determine whether the relationship between WMH load and cognitive decline in WMH subjects can be explained by the changes of hemodynamic measures revealed in our study, exploratory mediation analyses were implemented using the PROCESS macro v3.1 in SPSS (49). In all mediation models, the altered neuroimaging measures identified in the between-group comparisons, including CBF, FCS, and correlation coefficient between CBF and FCS, were separately entered as the mediators, whereas the WMH scale of each individual was entered into the models as the predictor and the z-score of each cognitive domain as the outcome, age, sex, and years of education as confounding variables. Mediation analyses were evaluated using a bootstrap method ($n = 5{,}000$), and significant indirect effects were defined by a 95% confidence interval, not including zero.

Control Analysis

To verify the stability of our main results, we repeated the between-group comparisons by adding hypertension and diabetes as covariates to investigate the potential confusion of the two risk factors. Furthermore, 16 matched healthy controls (HCs) from the in-house database with no visible WMH on FLAIR images were additionally included in the analysis to validate the alteration patterns of CBF, FCS, and CBF–FCS coupling in subjects with higher WMH loads (the details can be found in the **Supplementary Material**).

RESULTS

Demographic, Structural Magnetic Resonance Imaging, and Neuropsychological Data Analysis

Demographic, neuropsychological, and structural MRI characteristics of the participants are summarized in **Table 1**, **Supplementary Table 1**. There were no significant differences in age, gender, years of education, global gray matter volume, and framewise displacement among the three groups. The subjects in the moderate WMH and the severe WMH groups showed more proportion of hypertension and diabetes history than the subjects in the mild WMH group, whereas no significant differences were observed in these metrics between the moderate WMH group and the severe WMH group. Subjects in the severe WMH group exhibited worse performance in global cognitive function, executive function, and episodic memory compared with the other two groups and exhibited worse performance in processing speed compared with the moderate WMH group. No difference in language was observed among the three groups.

TABLE 1 | Demographic and clinical features of subjects.

	Mild WMH ($n = 32$)	Moderate WMH ($n = 24$)	Severe WMH ($n = 30$)	p-value
Demographic data				
Age (years)	63.69 ± 5.47	64.33 ± 6.65	66.43 ± 5.07	0.126[a]
Gender (male/female)	16/16	13/11	18/12	0.731[b]
Education (years)	10.78 ± 3.13	11.08 ± 3.69	9.10 ± 3.89	0.078[a]
Hypertension (yes/no)	6/26	17/7[d]	21/9[e]	<0.001[b]
Diabetes (yes/no)	3/29	4/20	8/22	0.199[b]
Smoking history (yes/no)	5/27	7/17	10/20	0.250 [b]
Drinking history (yes/no)	8/24	3/21	3/27	0.234[b]
MRI features				
Gray matter volume (ml)	614.96 ± 38.54	615.65 ± 31.16	626.83 ± 57.33	0.517[c]
Framewise displacement	0.18 ± 0.16	0.18 ± 0.10	0.17 ± 0.08	0.957[c]
Cognitive performance				
Global cognitive function	0.28 ± 0.69	0.32 ± 0.79	−0.56 ± 1.19[e,f]	<0.001[c]
Processing speed	0.18 ± 0.88	0.26 ± 0.89	−0.39 ± 1.11 [f]	0.026[c]
Executive function	0.33 ± 0.76	0.20 ± 0.95	−0.52 ± 1.08[e,f]	0.001[c]
Episodic memory	0.34 ± 0.88	0.12 ± 1.00	−0.46 ± 0.98[e,f]	0.005[c]
Language	0.25 ± 0.85	0.09 ± 1.12	−0.33 ± 0.99	0.061[c]

[a] *Kruskal–Wallis test.*
[b] *χ^2 test.*
[c] *One-way analysis of variance.*
[d] *Significant difference between mild WMH and moderate WMH groups.*
[e] *Significant difference between mild WMH and severe WMH groups.*
[f] *Significant difference between moderate WMH and severe WMH groups.*
WMH, white matter hyperintensities.

Spatial Distribution of Cerebral Blood Flow and Functional Connectivity Strength

Visually, the distributions of CBF and FCS were similar among the three WMH groups (**Figure 1**). All of the three groups exhibited higher values of CBF in the posterior cingulate gyrus (PCC)/precuneus (PCu), anterior cingulate cortex (ACC), bilateral medial frontal cortex, lateral parietal cortex, lateral pre-frontal cortex (LPFC), lateral temporal cortex, insula, and several thalamus regions, most of which were core brain regions of the DMN and salience network (SN). Brain regions with higher FCS values were primarily located in the DMN regions, LPFC, insula, and visual cortex, showing a similar distribution pattern with CBF.

Cerebral Blood Flow and Functional Connectivity Strength Changes Among Subjects With Different White Matter Hyperintensity Loads

From the mild WMH group to the severe WMH group, both global CBF and global FCS showed a decreasing trend in whole GM. Particularly, subjects in the severe WMH group displayed a prominent decrease of both global CBF and global FCS in whole GM compared with the mild WMH group (**Supplementary Table 2**).

The identified brain regions showing altered CBF among the three groups mainly included the widespread cortical regions covering the PCC, ACC, bilateral inferior parietal lobule (IPL), dorsolateral pre-frontal cortex (DLPFC), frontal operculum, insula, and several regions of the temporal cortex, and subcortical regions of the bilateral thalamus and right dorsal caudate. Compared with the mild WMH group, subjects in the severe WMH group showed significantly decreased CBF in all these regions, whereas patients in the severe WMH group also showed lower CBF in the bilateral insula, thalamus, and a few regions of the frontal and temporal cortex, PCC, and caudate compared with the moderate WMH group. Significant altered CBF between the moderate WMH group and mild WMH group was observed in only one sub-region of the temporal cortex (**Figure 2**, **Supplementary Table 3**).

The FCS alteration map among the three WMH groups is shown in **Figure 3**. Relative to the mild WMH group, the patients in the severe WMH group exhibited lower FCS primarily in the bilateral IPL, inferior temporal gyrus (ITG), left anterior insula, left DLPFC, and PCun. Different from the CBF change pattern, lower FCS values in the moderate WMH group could also be observed in several regions of the IPL, ITG, and left DLPFC as compared with the mild WMH group. Furthermore, the subjects in the severe WMH group showed significantly decreased FCS in the left anterior insula and showed significantly increased FCS in the left DLPFC, compared with the moderate WMH group. In addition, the full overlap of the CBF and FCS changes was located in several regions of the IPL and anterior insula (**Supplementary Table 4**).

Global and Regional Cerebral Blood Flow–Functional Connectivity Strength Coupling Changes Among Subjects With Different White Matter Hyperintensity Loads

In all of the three WMH groups, CBF was significantly correlated with FCS across voxels of the whole GM (**Figure 4A**).

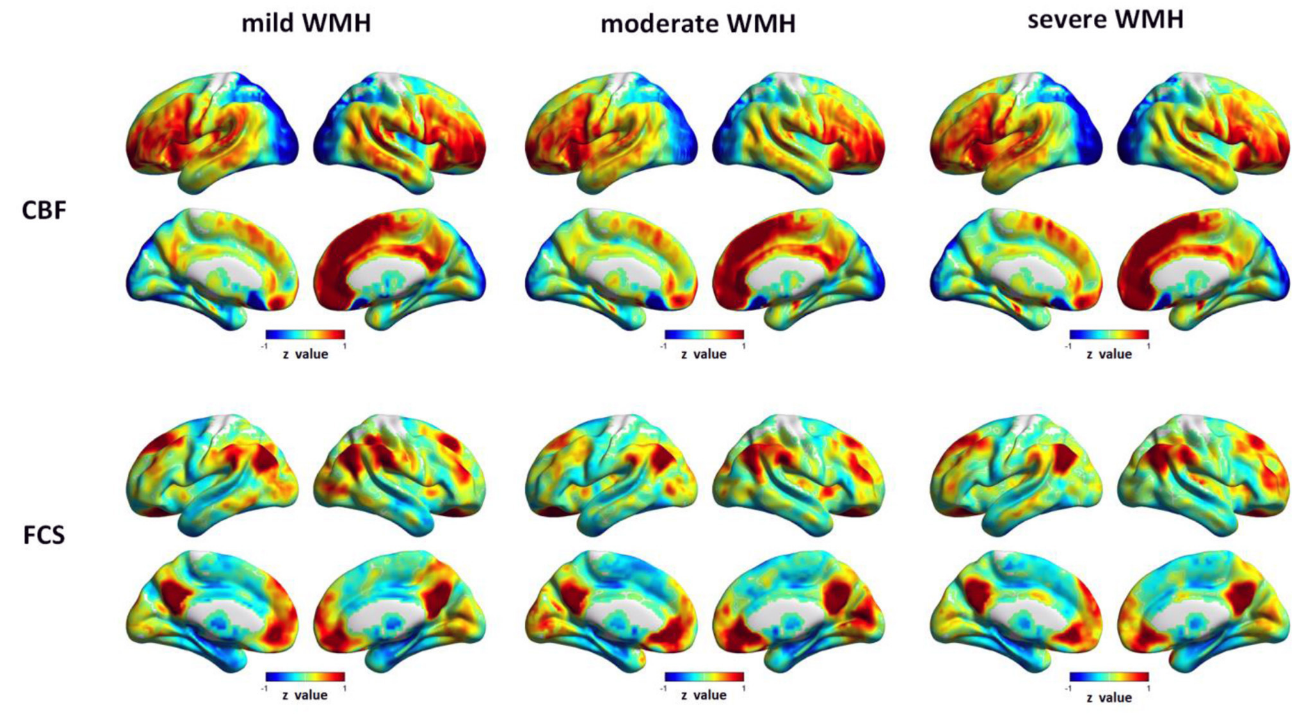

FIGURE 1 | Spatial distribution maps CBF and FCS in subjects with different WMH grades. CBF and FCS maps are normalized to *z*-values and averaged among subjects within each group. CBF, cerebral blood flow; FCS, functional connectivity strength; WMH, white matter hyperintensities.

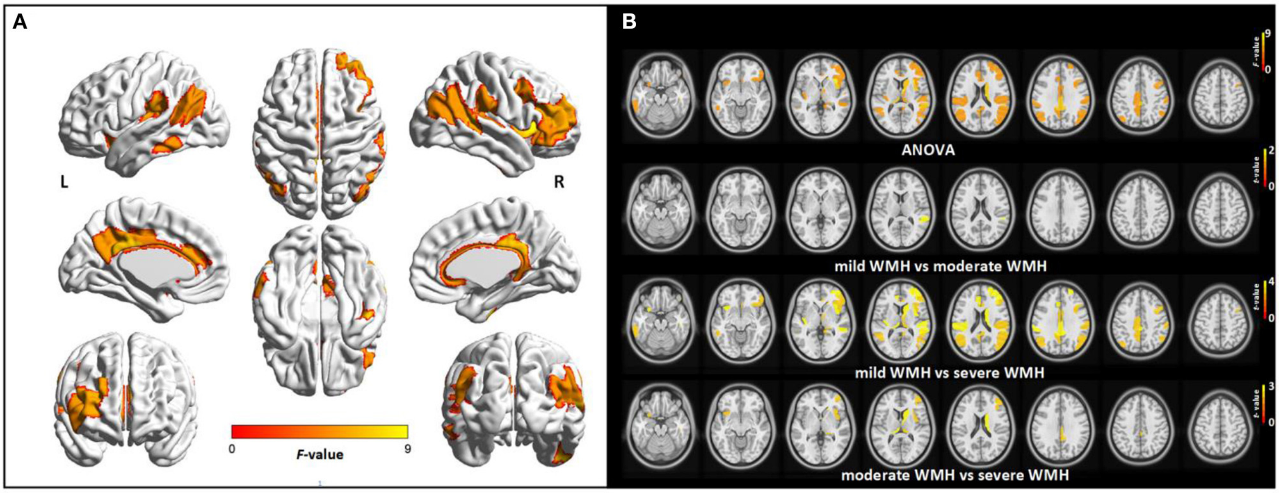

FIGURE 2 | Group differences in regional CBF among subjects with different WMH loads controlling for age and sex. **(A)** Surface statistical maps displaying *F*-scores of ANOVA for altered CBF among three groups ($p < 0.01$, with permutation test for 1,000 times). **(B)** Axial statistical maps displaying *F*-scores of ANOVA and *t*-scores of *post-hoc* analysis between every two groups. In statistical maps of ANOVA, warmer colors indicate significant differences in local CBF among three groups. In statistical maps of *post-hoc* analysis between every two groups, warm colors represent regional CBF decrease in moderate WMH group compared with mild WMH group, or in severe WMH group compared with mild WMH group, or in WMH3 group compared with moderate WMH group, respectively. L, left; R, right.

However, the global CBF–FCS coupling showed a decreasing trend with the increase of WMH load, although no significant difference was identified in the correlation coefficient among the three groups (**Figure 4B**). The severe WMH group showed significantly reduced CBF–FCS coupling in several regions of the bilateral thalamus compared with the other two WMH groups and showed significantly reduced CBF–FCS coupling in the PCC compared with the mild WMH group. In

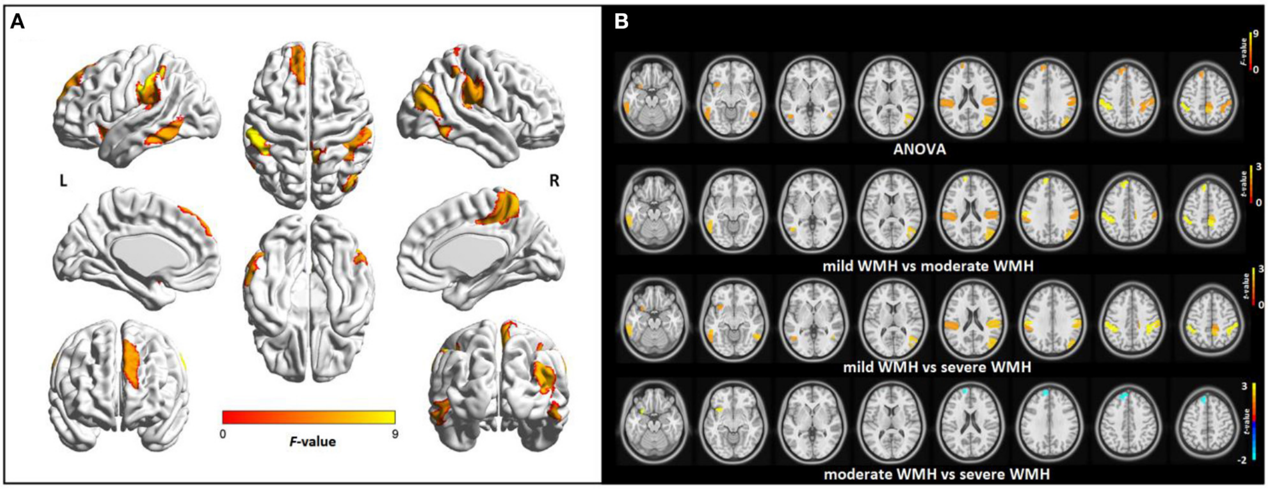

FIGURE 3 | Group differences in regional FCS among subjects with different WMH loads controlling for age and sex. **(A)** Surface statistical maps displaying *F*-scores of ANOVA for altered FCS among three groups ($p < 0.01$, with permutation test for 1,000 times). **(B)** Axial statistical maps displaying *F*-scores of ANOVA and *t*-scores of *post-hoc* analysis between every two groups. In statistical maps of ANOVA, warmer colors indicate significant differences in regional FCS among three groups. In statistical maps of *post-hoc* analysis between every two groups, warm colors represent regional FCS decrease in moderate WMH group compared with mild WMH group, or in severe WMH group compared with mild WMH group, or in WMH3 group compared with moderate WMH group, respectively, and cold colors represent regional FCS increase in severe WMH group compared with moderate WMH group. No significant increased FCS was found in severe WMH group relative to mild WMH group, or moderate WMH group when compared with mild WMH group. L, left; R, right.

addition, compared to the other two groups, the severe WMH group showed a significantly altered CBF–FCS correlation pattern that CBF was negatively associated with FCS in a sub-region of the left parahippocampal gyrus (**Figures 4C**,**D**, **Supplementary Table 5**).

Relationships Between Neuroimaging Measures, White Matter Hyperintensity Load, and Cognitive Performance

In all WMH subjects, there were significant associations between WMH Fazekas score and global cognitive function ($r = -0.299$, $p = 0.006$), executive function ($r = -0.323$, $p = 0.003$), episodic memory ($r = -0.244$, $p = 0.026$), and language ($r = -0.217$, $p = 0.049$), and no significant association was identified between Fazekas score and processing speed ($r = -0.188$, $p = 0.089$). CBF in several regions of frontal, temporal, parietal, insular, cingulate cortices, and caudate was found to be positively associated with cognitive decline in various domains, especially processing speed and executive function (**Supplementary Table 6**). Meanwhile, the FCS–cognition relationship was observed only between regional FCS in a sub-region of IPL and executive function, and the correlation coefficient between CBF and FCS in a sub-region of the thalamus was significantly associated with global cognitive performance (**Supplementary Table 6**). Because no significant correlation was identified between WMH load and processing speed, here mediation models were established only for the cognitive performance of other domains. Significant mediation effects of WMH on the cognitive decline were observed via regional CBF in a sub-region of ITG (for episodic memory and executive function) and right dorsal caudate (for executive function) (**Figure 5**, **Supplementary Table 7**).

Control Results

For all of the three neuroimaging measures (CBF, FCS, and CBF–FCS coupling), significant correlations between the *F*-scores or *t*-scores in the main results with and without controlling for hypertension and diabetes were observed (**Supplementary Figures 1–3**), indicating that other risk factors, such as hypertension and diabetes, are unlikely to provide a convincing explanation of alterations in the hemodynamic measures underlying the increase of WMH burden revealed in this study. The patterns of differences in all the three measures between the HC group and the moderate/severe WMH group were spatially consistent with alteration patterns in these measures between the mild WMH group and the other two WMH groups (**Supplementary Figures 4–6**, **Supplementary Table 8**), emphasizing the robustness of our main results that revealed characteristic alteration patterns of these measures in subjects with higher WMH loads.

DISCUSSION

To the best of our knowledge, this is the first study to depict the whole-brain CBF, FCS, and CBF–FCS coupling alteration maps among subjects with different WMH loads by combining ASL and BOLD fMRI techniques. Subjects with higher WMH loads showed decreased CBF and FCS in subcortical and cortical regions involving several important large-scale brain networks, especially the DMN, SN, and CEN. Notably, patients with severe WMH load showed abnormal regional CBF–FCS coupling in several regions of the thalamus, PCC, and parahippocampal gyrus. Furthermore, exploratory mediation analyses identified

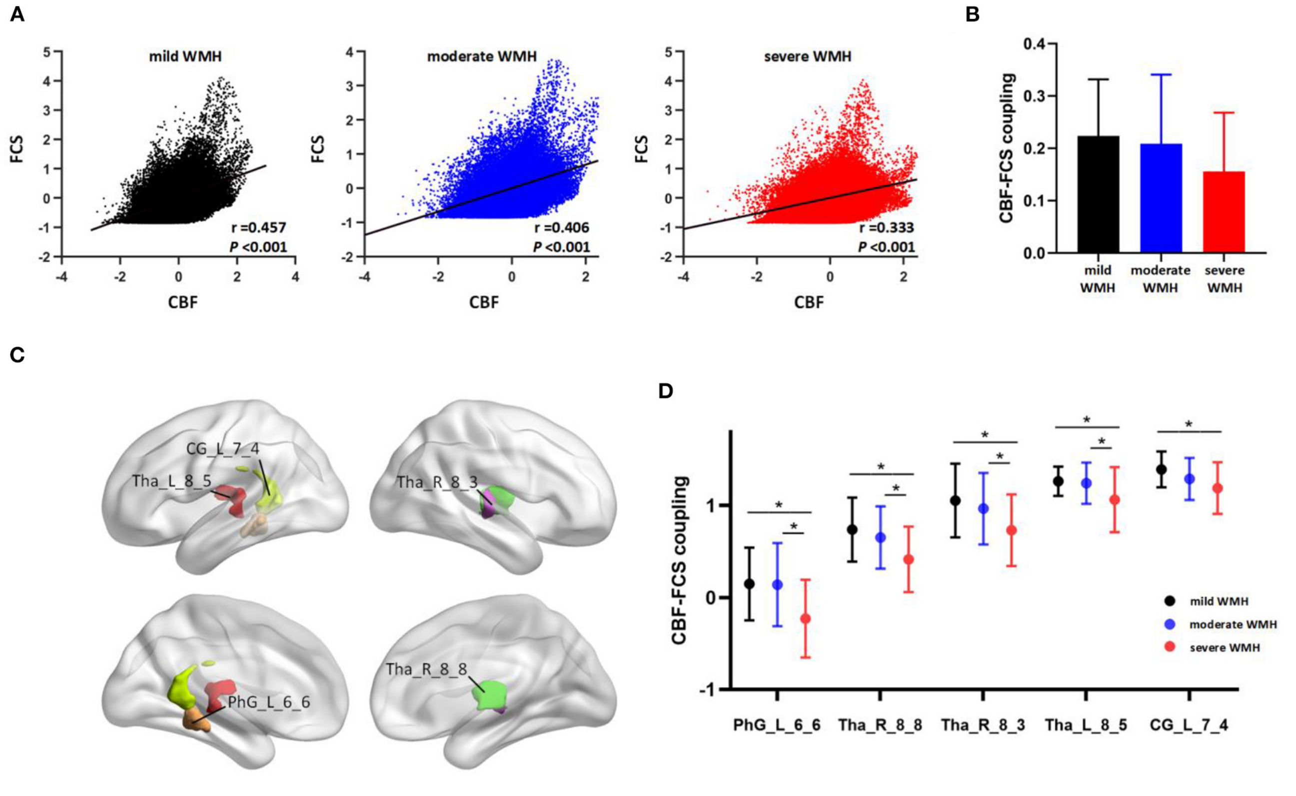

FIGURE 4 | Global and regional CBF–FCS coupling changes among subjects with different WMH loads. **(A)** Whole-brain CBF–FCS coupling alterations across voxels in samples of subjects with different WMH loads. **(B)** Between-group comparisons exhibited a decreasing trend in global CBF–FCS coupling from mild WMH group to severe WMH group (mild WMH group: $r = 0.225 \pm 0.108$; moderate WMH group: $r = 0.209 \pm 0.132$; severe WMH group: $r = 0.156 \pm 0.112$), whereas no significant differences were identified in global CBF–FCS coupling among three WMH groups ($F = 1.645$, $p = 0.199$). **(C,D)** Altered regional CBF–FCS coupling among three WMH groups. Compared with mild WMH and moderate WMH group, severe WMH group showed significant aberrant CBF–FCS coupling in bilateral thalamus, ACC, and left parahippocampal gyrus. Data were shown as adjusted correlation coefficients between CBF and FCS controlling for age and sex. Error bars represent the SD. $^*p < 0.05$. ACC, anterior cingulate cortex; PhG, parahippocampal gyrus; Tha, thalamus; WMH, white matter hyperintensities. L, left; R, right. Detailed information on brain regions is available at http://atlas.brainnetome.org/.

the crucial role of specific CBF reduction underlying cognitive impairment in subjects with WMH. Altogether, these findings provide further information on dysfunctional mechanisms underlying WMH and related cognitive impairment from the comprehensive perspective of blood supply, brain activity, and neurovascular decoupling.

In the present study, we found a significant trend of both CBF and FCS reduction with the increase of WMH load. As neuroimaging measures reflecting distinct brain functional aspects of metabolic demand and neuronal activity, respectively, both CBF and FCS can be affected by structural damages (50, 51). Prior works have demonstrated that the disruption of WM fibers underlay the increase of WMH burden and was associated with various clinical symptoms related to WMH, including cognitive impairment, gait disturbance, and depression (6, 52, 53). Severe and extensive WM disconnections can result in the degeneration and hypometabolism of the GM connected to the impaired WM fibers, which may be an important explanation for the recorded CBF and FCS reduction in subjects with more severe WMH (54, 55). Another possible mechanism for CBF and FCS changes is the abnormalities in GM attributed to CSVD directly. Considered to be the primary neuroimaging manifestations of CSVD, WMHs are usually accompanied by other damages in GM, including cortical microinfarcts, cerebral microbleeds, and GM atrophy, which may lead to the lower blood supply required by GM tissues as well as the decreased neuronal activity (56). In addition, aberrant inflammatory factors, which are considered to be involved in the pathophysiological mechanisms of WMH, would also contribute to the abnormal modulation of CBF and FCS in subjects with higher WMH loads (13).

Of note, our results showed a characteristic regional CBF decrease in cortical functional hub regions, which exhibited higher values of CBF in all the three groups, mainly covering the core component of the DMN (PCC/PCu, bilateral IPL, and lateral temporal cortex) (57, 58), SN (ACC, bilateral frontal operculum, and insula) (58, 59), and CEN (bilateral DLPFC and posterior parietal cortex) (58), as well as subcortical nuclei, which also serve as integrative hubs for brain networks (bilateral thalamus and right dorsal caudate) (60, 61) in subjects with more WMH. Similarly, significantly decreased FCS in subjects

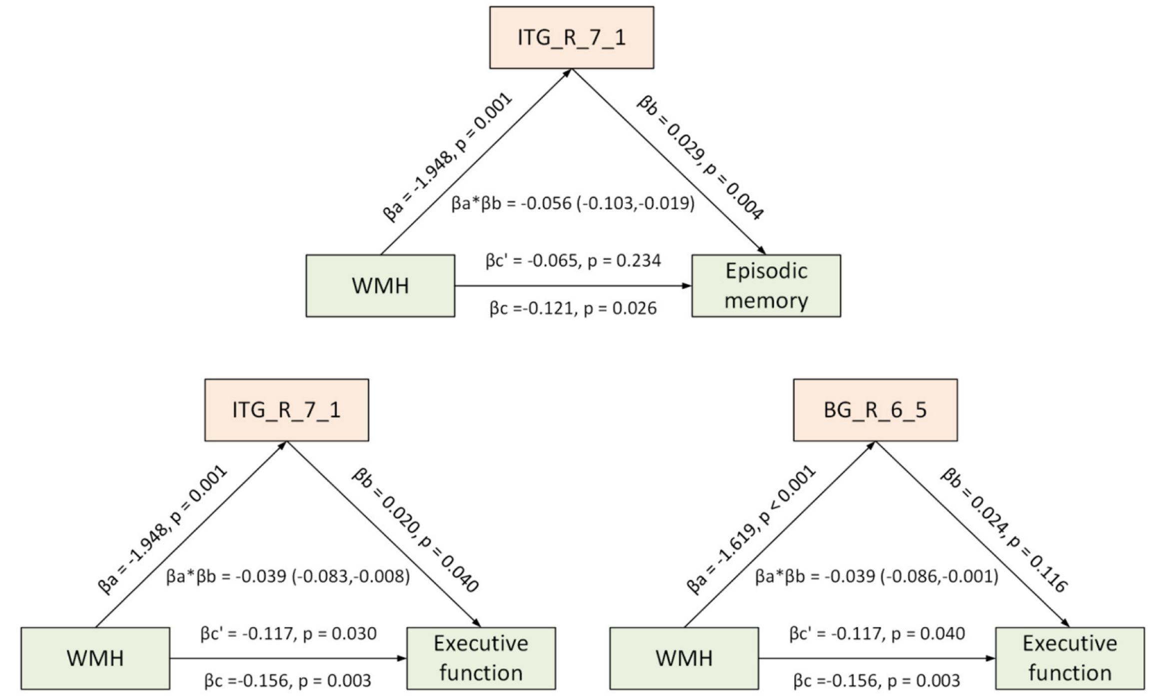

FIGURE 5 | Mediation effect of regional CBF between WMH load and cognitive function. Diagrams show areas of CBF mediating relationship between WMH load (represented as Fazekas score) and cognitive performance (executive function or episodic memory), and mediation models of pathways from WMH load to CBF reduction in right ITG and right caudate to reduce cognitive performance. In each model, age, sex, and years of education were entered as covariates. βa and βb represent coefficients of relationships between WMH load and regional CBF, and associations between region CBF and cognition (when both WMH load and CBF were both entered into model as predicting variables). Total effect (βc) = Direct effect (βc') + Mediation effect (βa*βb). Mediating role of regional CBF reduction on association between WMH and cognition is defined when 95% confidence interval did not conclude 0 for 5,000 bootstrapping iterations. BG, basal ganglia; CBF, cerebral blood flow; FCS, functional connectivity strength; ITG, inferior temporal gyrus; WMH, white matter hyperintensities. L, left; R, right. Detailed information on brain regions is available at http://atlas.brainnetome.org/.

with moderate and severe WMH were detected mainly in core nodes of the DMN (PCu, bilateral IPL, and lateral temporal cortex) (57, 58), ECN (bilateral posterior parietal cortex and right DLPFC) (58), and SN (left anterior insula) (58, 59). Particularly, a full overlap of the CBF and FCS changes in subjects with higher WMH loads was identified in several of these regions, including IPL and anterior insula. The DMN, CEN, and SN are the most robust intrinsic large-scale networks that account for a wide range of cognitive and emotional processing (58). Consistent with previous studies focused on the structural and functional abnormalities in WMH (25, 26, 28, 62), the characteristic alteration patterns of both CBF and FCS among subjects with different WMH loads emphasized that the dysfunction of these intrinsic brain networks may play a crucial role in the pathophysiology of WMH. It is worth noting that there were also some differences in the alteration patterns of CBF and FCS among subjects with diverse WMH loads. Altered CBF was mainly identified between the severe WMH group and the other two groups, whereas FCS alterations were mainly detected in the comparisons between the mild WMH group and the two groups with higher WMH loads. Because only subjects in the severe WMH group showed significantly impaired cognitive performance, one could speculate that the disconnections of functional networks may appear earlier than CBF reduction with the increase of WMH burden, and extensive WM disconnections, as well as microvasculature damage associated with neuroinflammation, may further generate hypoperfusion in cognitive-related networks, resulting in cognitive impairment in subjects with WMH. Another possible explanation is that referred to as the "degree centrality" of weighted networks, FCS could not fully reflect the whole alteration picture of dissociable intrinsic brain networks independently (31). For example, FCS may be normal when significantly increased FCs and decreased FCs coexist involving a certain voxel or region. Hence, more information of aberrant intra- and inter-network connectivity architecture, which may attribute to the further increase of WMH burden and the subsequent cognitive decline, would not be completely revealed by FCS alterations. In addition, in the severe WMH group, the values of FCS in the left DLPFC were significantly higher than those in the moderate WMH group but were still significantly lower than those in the mild WMH group, which might be explained as a compensatory mechanism to the structural impairments of the DLPFC in the patients with severe WMH; on the other hand, DLPFC plays important roles not only in a wide range of cognitive domains but also in modulating emotional processing (59, 63–65). Thus, in line with previous studies focused on major depression and schizophrenia (63, 66), this result may be related to emotion dysregulation in patients with severe WMH as reported.

Another strength of our study is that we explored the alterations of both the global and regional CBF–FCS coupling among the subjects with different WMH loads. The whole-brain CBF–FCS coupling showed a decreasing trend from the mild WMH group to the severe WMH group, and importantly, subjects with severe WMH load showed significantly altered regional CBF–FCS correlations in several core nodes of the DMN, including the thalamus, PCC, and parahippocampal gyrus (57, 67). The altered associations between CBF and FCS within the DMN in the subjects with more WMH, which were first discovered by our study from the novel aspect of neurovascular decoupling, further emphasized that the selective functional abnormalities in the DMN may play a key role in the increase of WMH burden in addition to our results of CBF and FCS alterations. The neurovascular coupling depends on various components and their interaction of neurovascular unit, including neurons, astrocytes, and vessels (68). One possible explanation for neurovascular decoupling in subjects with a high WMH load is the prominent astrocyte dysfunction, as previous studies reported, which may impede the interaction between neuronal activity and vascular response (13, 33). Second, the vascular factors, especially endothelial cell dysfunction together with a series of concomitant inflammatory processes, which have been considered as another important pathological basis for WMH, may lead to the dysregulation of the CBF and neuronal activity (10–13, 69). Finally, GM atrophy in WMH subjects due to the denervation associated with WM disconnections and the microvasculature damages in GM, which has been demonstrated in various structural neuroimaging studies (5, 70–72), may also contribute to the reduced neurovascular coupling in subjects with higher WMH loads. Because no difference in global gray matter volume was found among the three groups in our study, further investigations with a larger sample size are needed to verify this hypothesis.

Previous studies have reported that resting-state functional connectivity within the DMN was associated with cognitive decline in subjects with WMH (26, 28). Consisting with and further extending their findings, our results showed significant correlations between cognitive performance and all the functional neuroimaging measures investigated in our study (CBF, FCS, and CBF–FCS coupling) in several cortical and subcortical hub regions involving cognitive networks in subjects with WMH. In particular, the results of mediation analyses indicated that CBF in the right ITG and right dorsal caudate might mediate the relationship between WMH load and cognition. Thought to be a constituent of the DMN, the ITG is well-known to be involved in various high-cognitive functions, including visual perception, language comprehensions, and memory (73–75). The right dorsal caudate has also been demonstrated to constitute a core circuit supporting the integration of diverse cognitive networks and is involved in the process of executive function (60, 76). Thus, we infer that cortical and subcortical hub regions involving essential cognitive and emotional networks would be more vulnerable to the neurovascular damage caused by WMH, resulting in a series of emotional and cognitive impairment, and specific regional CBF may serve as a potential neuroimaging marker for detecting an early cognitive decline in the future. However, no mediation effect of either regional FCS or CBF–FCS coupling between WMH and cognitive function was identified, which may partly be attributed to relatively simple neuropsychological scales to reflect cognitive performance in each domain and the selection of threshold in the FCS calculation. Because this is the first time to investigate the alterations of FCS and CBF–FCS coupling in the subjects with WMH, these findings should be further evaluated in the future. In addition, it is worth noting that many factors could contribute to cognitive decline in older adults, and the relationship between WMH load and cognitive impairment revealed by our study as well as previous works would only be considered as a correlation but not causality. Hence, our results may only provide a possible explanation to the association between WMH burden and cognitive impairment using mathematical models, and the detailed mechanisms of how hemodynamic changes regulate the WMH progression and lead to cognitive impairment should be further investigated.

The current study has several limitations that should be addressed. First, as CBF at rest varies greatly with time, it may be insufficient to provide precise information on regional cerebral perfusion and the real demand of blood supply by tissues (69, 77). Other alternative measures, for instance, cerebrovascular reactivity, may be applied to explore further the adequacy of tissue-level CBF in the subjects with different WMH loads (78, 79). Second, this is an exploratory study with relatively small sample size, and few regions can survive with a strict multiple comparison correction in this study. Here, we added to introduce a permutation test (for 1,000 times, $p < 0.01$) for the comparison of each measure among the three groups to increase the reliability of the results. Third, the control analysis showed that whether compared with the mild WMH group or the HC group, regional CBF, FCS, and CBF–FCS coupling in subjects with higher WMH loads exhibited very similar alteration patterns, highlighting the important role of dysfunction in brain regions involving large-scale networks underlying the increase of WMH load. Nevertheless, given the very small sample size in the additional HC group, there were still limitations in these findings. Fourth, in line with several previous studies (30, 34–37, 47), the procedure of partial volume correction was not implemented in this study. Also, in the between-group CBF analysis, we did not conduct a mean-centering of CBF at the individual level to compare the differences in absolute regional CBF among subjects with different WMH loads. Finally, we did not collect the information on emotional and gait disturbance common in subjects with a high WMH load. Large-scale longitudinal studies with more detailed clinical information will be warranted to determine further the exact role of neurovascular dysfunction in the increase of WMH burden and related clinical symptoms.

In conclusion, we investigated dysfunctional architectures in WMH subjects in the alterations in CBF, FCS, and coupling between CBF and FCS among the subjects with diverse WMH loads. Specifically, we found decreased regional CBF, FCS, and disrupted CBF–FCS coupling in hub regions involving cognitive- and emotional-related networks in subjects with higher WMH loads. These findings provide novel insights into the pathophysiology underpinnings of WMH and related cognitive impairment.

DATA AVAILABILITY STATEMENT

The original contributions presented in the study are included in the article/**Supplementary Material**, further inquiries can be directed to the corresponding author/s.

ETHICS STATEMENT

The studies involving human participants were reviewed and approved by the Ethics Committee of Tongji Hospital, Tongji Medical College, Huazhong University of Science and Technology. The patients/participants provided their written informed consent to participate in this study.

AUTHOR CONTRIBUTIONS

WenhZ conceived and designed the experiments. WenhZ, HH, and HL recruited the subjects and collected the clinical and neuropsychological information of the subjects. WenzZ was responsible for MRI data acquisition. HH, KZ, and WenhZ performed data analysis. WenhZ and HH wrote the manuscript. All authors contributed to the article and approved the submitted version.

FUNDING

This work was supported by the National Natural Science Foundation of China (81801146, 81871438, and 81771341) and the Beijing Natural Science Funds for Distinguished Young Scholars (JQ200036).

ACKNOWLEDGMENTS

We are grateful to Prof. Shabei Xu for the assessment of WMH, and we are grateful to all the participants in the study.

SUPPLEMENTARY MATERIAL

The Supplementary Material for this article can be found online at: https://www.frontiersin.org/articles/10.3389/fneur.2021.752762/full#supplementary-material

REFERENCES

1. Prins ND, Scheltens P. White matter hyperintensities, cognitive impairment and dementia: an update. *Nat Rev Neurol.* (2015) 11:157–65. doi: 10.1038/nrneurol.2015.10
2. Debette S, Markus HS. The clinical importance of white matter hyperintensities on brain magnetic resonance imaging: systematic review and meta-analysis. *BMJ.* (2010) 341:c3666. doi: 10.1136/bmj.c3666
3. Wardlaw JM, Smith EE, Biessels GJ, Cordonnier C, Fazekas F, Frayne R, et al. Neuroimaging standards for research into small vessel disease and its contribution to ageing and neurodegeneration. *Lancet Neurol.* (2013) 12:822–38. doi: 10.1016/S1474-4422(13)70124-8
4. Bernbaum M, Menon BK, Fick G, Smith EE, Goyal M, Frayne R, et al. Reduced blood flow in normal white matter predicts development of leukoaraiosis. *J Cereb Blood Flow Metab.* (2015) 35:1610–5. doi: 10.1038/jcbfm.2015.92
5. Zhu W, Huang H, Yang S, Luo X, Zhu W, Xu S, et al. Cortical and subcortical grey matter abnormalities in white matter hyperintensities and subsequent cognitive impairment. *Neurosci Bull.* (2021) 37:789–803. doi: 10.1007/s12264-021-00657-0
6. van Leijsen EMC, Bergkamp MI, van Uden IWM, Ghafoorian M, van der Holst HM, Norris DG, et al. Progression of white matter hyperintensities preceded by heterogeneous decline of microstructural integrity. *Stroke.* (2018) 49:1386–93. doi: 10.1161/STROKEAHA.118.020980
7. Wong SM, Jansen JFA, Zhang CE, Hoff EI, Staals J, van Oostenbrugge RJ, et al. Blood-brain barrier impairment and hypoperfusion are linked in cerebral small vessel disease. *Neurology.* (2019) 92:e1669–77. doi: 10.1212/WNL.0000000000007263
8. Lawrence AJ, Chung AW, Morris RG, Markus HS, Barrick TR. Structural network efficiency is associated with cognitive impairment in small-vessel disease. *Neurology.* (2014) 83:304–11. doi: 10.1212/WNL.0000000000000612
9. Liu C, Zou L, Tang X, Zhu W, Zhang G, Qin Y, et al. Changes of white matter integrity and structural network connectivity in nondemented cerebral small-vessel disease. *J Magn Reson Imaging.* (2020) 51:1162–9. doi: 10.1002/jmri.26906
10. Rajani RM, Quick S, Ruigrok SR, Graham D, Harris SE, Verhaaren BFJ, et al. Reversal of endothelial dysfunction reduces white matter vulnerability in cerebral small vessel disease in rats. *Sci Transl Med.* (2018) 10:eaam9507. doi: 10.1126/scitranslmed.aam9507
11. Hainsworth AH, Oommen AT, Bridges LR. Endothelial cells and human cerebral small vessel disease. *Brain Pathol.* (2015) 25:44–50. doi: 10.1111/bpa.12224
12. Ghosh M, Balbi M, Hellal F, Dichgans M, Lindauer U, Plesnila N. Pericytes are involved in the pathogenesis of cerebral autosomal dominant arteriopathy with subcortical infarcts and leukoencephalopathy. *Ann Neurol.* (2015) 78:887–900. doi: 10.1002/ana.24512
13. Wardlaw JM, Smith C, Dichgans M. Small vessel disease: mechanisms and clinical implications. *Lancet Neurol.* (2019) 18:684–96. doi: 10.1016/S1474-4422(19)30079-1
14. Shi L, Miao X, Lou W, Liu K, Abrigo J, Wong A, et al. The spatial associations of cerebral blood flow and spontaneous brain activities with white matter hyperintensities-an exploratory study using multimodal magnetic resonance imaging. *Front Neurol.* (2017) 8:593. doi: 10.3389/fneur.2017.00593
15. Vaishnavi SN, Vlassenko AG, Rundle MM, Snyder AZ, Mintun MA, Raichle ME. Regional aerobic glycolysis in the human brain. *Proc Natl Acad Sci USA.* (2010) 107:17757–62. doi: 10.1073/pnas.1010459107
16. Fu J, Tang J, Han J, Hong Z. The reduction of regional cerebral blood flow in normal-appearing white matter is associated with the severity of white matter lesions in elderly: a Xeon-CT study. *PLoS ONE.* (2014) 9:e112832. doi: 10.1371/journal.pone.0112832
17. Ishibashi M, Kimura N, Aso Y, Matsubara E. Effects of white matter lesions on brain perfusion in patients with mild cognitive impairment. *Clin Neurol Neurosurg.* (2018) 168:7–11. doi: 10.1016/j.clineuro.2018.02.030
18. O'Sullivan M, Lythgoe DJ, Pereira AC, Summers PE, Jarosz JM, Williams SC, et al. Patterns of cerebral blood flow reduction in patients with ischemic leukoaraiosis. *Neurology.* (2002) 59:321–6. doi: 10.1212/WNL.59.3.321
19. Stewart CR, Stringer MS, Shi Y, Thrippleton MJ, Wardlaw JM. Associations between white matter hyperintensity burden, cerebral blood flow and transit time in small vessel disease: an updated meta-analysis. *Front Neurol.* (2021) 12:647848. doi: 10.3389/fneur.2021.647848
20. Shi Y, Thrippleton MJ, Makin SD, Marshall I, Geerlings MI, de Craen AJM, et al. Cerebral blood flow in small vessel disease: a systematic

review and meta-analysis. *J Cereb Blood Flow Metab.* (2016) 36:1653–67. doi: 10.1177/0271678X16662891

21. Crane DE, Black SE, Ganda A, Mikulis DJ, Nestor SM, Donahue MJ, et al. Gray matter blood flow and volume are reduced in association with white matter hyperintensity lesion burden: a cross-sectional MRI study. *Front Aging Neurosci.* (2015) 7:131. doi: 10.3389/fnagi.2015.00131
22. Kim CM, Alvarado RL, Stephens K, Wey HY, Wang DJJ, Leritz EC, et al. Associations between cerebral blood flow and structural and functional brain imaging measures in individuals with neuropsychologically defined mild cognitive impairment. *Neurobiol Aging.* (2020) 86:64–74. doi: 10.1016/j.neurobiolaging.2019.10.023
23. Dolui S, Tisdall D, Vidorreta M, Jacobs DR, Jr., Nasrallah IM, Bryan RN, et al. Characterizing a perfusion-based periventricular small vessel region of interest. *Neuroimage. Clin.* (2019) 23:101897. doi: 10.1016/j.nicl.2019.101897
24. Buckner RL, Sepulcre J, Talukdar T, Krienen FM, Liu H, Hedden T, et al. Cortical hubs revealed by intrinsic functional connectivity: mapping, assessment of stability, and relation to Alzheimer's disease. *J Neurosci.* (2009) 29:1860–73. doi: 10.1523/JNEUROSCI.5062-08.2009
25. Zhu W, Huang H, Yang S, Luo X, Zhu W, Xu S, et al. Dysfunctional architecture underlies white matter hyperintensities with and without cognitive impairment. *J Alzheimers Dis.* (2019) 71:461–76. doi: 10.3233/JAD-190174
26. Chen X, Huang L, Ye Q, Yang D, Qin R, Luo C, et al. Disrupted functional and structural connectivity within default mode network contribute to WMH-related cognitive impairment. *Neuroimage Clin.* (2019) 24:102088. doi: 10.1016/j.nicl.2019.102088
27. Cole MW, Bassett DS, Power JD, Braver TS, Petersen SE. Intrinsic and task-evoked network architectures of the human brain. *Neuron.* (2014) 83:238–51. doi: 10.1016/j.neuron.2014.05.014
28. Reijmer YD, Schultz AP, Leemans A, O'Sullivan MJ, Gurol ME, Sperling R, et al. Decoupling of structural and functional brain connectivity in older adults with white matter hyperintensities. *Neuroimage.* (2015) 117:222–9. doi: 10.1016/j.neuroimage.2015.05.054
29. Zuo XN, Ehmke R, Mennes M, Imperati D, Castellanos FX, Sporns O, et al. Network centrality in the human functional connectome. *Cereb Cortex.* (2012) 22:1862–75. doi: 10.1093/cercor/bhr269
30. Liang X, Zou Q, He Y, Yang Y. Coupling of functional connectivity and regional cerebral blood flow reveals a physiological basis for network hubs of the human brain. *Proc Natl Acad Sci USA.* (2013) 110:1929–34. doi: 10.1073/pnas.1214900110
31. Rubinov M, Sporns O. Complex network measures of brain connectivity: uses and interpretations. *Neuroimage.* (2010) 52:1059–69. doi: 10.1016/j.neuroimage.2009.10.003
32. Yi LY, Liang X, Liu DM, Sun B, Ying S, Yang DB, et al. Disrupted topological organization of resting-state functional brain network in subcortical vascular mild cognitive impairment. *CNS Neurosci Ther.* (2015) 21:846–54. doi: 10.1111/cns.12424
33. Iadecola C. The neurovascular unit coming of age: a journey through neurovascular coupling in health and disease. *Neuron.* (2017) 96:17–42. doi: 10.1016/j.neuron.2017.07.030
34. Zhu J, Zhuo C, Xu L, Liu F, Qin W, Yu C. Altered coupling between resting-state cerebral blood flow and functional connectivity in schizophrenia. *Schizophr Bull.* (2017) 43:1363–74. doi: 10.1093/schbul/sbx051
35. Hu S, Wu H, Xu C, Wang A, Wang Y, Shen T, et al. Aberrant coupling between resting-state cerebral blood flow and functional connectivity in Wilson's disease. *Front Neural Circuits.* (2019) 13:25. doi: 10.3389/fncir.2019.00025
36. Chen Y, Cui Q, Sheng W, Tang Q, Lu F, Pang Y, et al. Anomalous neurovascular coupling in patients with generalized anxiety disorder evaluated by combining cerebral blood flow and functional connectivity strength. *Prog Neuropsychopharmacol Biol Psychiatry.* (2021) 111:110379. doi: 10.1016/j.pnpbp.2021.110379
37. Wang Q, Qu X, Chen W, Wang H, Huang C, Li T, et al. Altered coupling of cerebral blood flow and functional connectivity strength in visual and higher order cognitive cortices in primary open angle glaucoma. *J Cereb Blood Flow Metab.* (2021) 41:901–13. doi: 10.1177/0271678X20935274
38. Fan L, Li H, Zhuo J, Zhang Y, Wang J, Chen L, et al. The human brainnetome atlas: a new brain atlas based on connectional architecture. *Cereb Cortex.* (2016) 26:3508–26. doi: 10.1093/cercor/bhw157
39. Helenius J, Henninger N. Leukoaraiosis burden significantly modulates the association between infarct volume and national institutes of health stroke scale in ischemic stroke. *Stroke.* (2015) 46:1857–63. doi: 10.1161/STROKEAHA.115.009258
40. Fazekas F, Chawluk JB, Alavi A, Hurtig HI, Zimmerman RA. MR signal abnormalities at 1.5 T in Alzheimer's dementia and normal aging. *AJR Am J Roentgenol.* (1987) 149:351–6. doi: 10.2214/ajr.149.2.351
41. Jia J, Wang F, Wei C, Zhou A, Jia X, Li F, et al. The prevalence of dementia in urban and rural areas of China. *Alzheimers Dement.* (2014) 10:1–9. doi: 10.1016/j.jalz.2013.01.012
42. Papma JM, de Groot M, de Koning I, Mattace-Raso FU, van der Lugt A, Vernooij MW, et al. Cerebral small vessel disease affects white matter microstructure in mild cognitive impairment. *Hum Brain Mapp.* (2014) 35:2836–51. doi: 10.1002/hbm.22370
43. Xu G, Rowley HA, Wu G, Alsop DC, Shankaranarayanan A, Dowling M, et al. Reliability and precision of pseudo-continuous arterial spin labeling perfusion MRI on 3.0 T and comparison with 15O-water PET in elderly subjects at risk for Alzheimer's disease. *NMR Biomed.* (2010) 23:286–93. doi: 10.1002/nbm.1462
44. Xu K, Liu Y, Zhan Y, Ren J, Jiang T. BRANT: a versatile and extendable resting-state fMRI toolkit. *Front Neuroinform.* (2018) 12:52. doi: 10.3389/fninf.2018.00052
45. Wang L, Dai Z, Peng H, Tan L, Ding Y, He Z, et al. Overlapping and segregated resting-state functional connectivity in patients with major depressive disorder with and without childhood neglect. *Hum Brain Mapp.* (2014) 35:1154–66. doi: 10.1002/hbm.22241
46. Liu F, Zhu C, Wang Y, Guo W, Li M, Wang W, et al. Disrupted cortical hubs in functional brain networks in social anxiety disorder. *Clin Neurophysiol.* (2015) 126:1711–6. doi: 10.1016/j.clinph.2014.11.014
47. Zhang Y, Zhou T, Feng S, Wang W, Liu H, Wang P, et al. The chronic effect of cortisol on orchestrating cerebral blood flow and brain functional connectivity: evidence from Cushing's disease. *Metabolism.* (2021) 115:154432. doi: 10.1016/j.metabol.2020.154432
48. Power JD, Barnes KA, Snyder AZ, Schlaggar BL, Petersen SE. Spurious but systematic correlations in functional connectivity MRI networks arise from subject motion. *Neuroimage.* (2012) 59:2142–54. doi: 10.1016/j.neuroimage.2011.10.018
49. Hayes AF. *Introduction to Mediation, Moderation, and Conditional Process Analysis: A Regression-Based Approach.* 1st ed. New York: The Guilford Press (2013).
50. Hagmann P, Cammoun L, Gigandet X, Meuli R, Honey CJ, Wedeen VJ, et al. Mapping the structural core of human cerebral cortex. *PLoS Biol.* (2008) 6:e159. doi: 10.1371/journal.pbio.0060159
51. Várkuti B, Cavusoglu M, Kullik A, Schiffler B, Veit R, Yilmaz Ö, et al. Quantifying the link between anatomical connectivity, gray matter volume and regional cerebral blood flow: an integrative MRI study. *PLoS ONE.* (2011) 6:e14801. doi: 10.1371/journal.pone.0014801
52. Su N, Liang X, Zhai FF, Zhou LX, Ni J, Yao M, et al. The consequence of cerebral small vessel disease: linking brain atrophy to motor impairment in the elderly. *Hum Brain Mapp.* (2018) 39:4452–61. doi: 10.1002/hbm.24284
53. van Uden IW, Tuladhar AM, de Laat KF, van Norden AG, Norris DG, van Dijk EJ, et al. White matter integrity and depressive symptoms in cerebral small vessel disease: the RUN DMC study. *Am J Geriatr Psychiatry.* (2015) 23:525–35. doi: 10.1016/j.jagp.2014.07.002
54. Tuladhar AM, Reid AT, Shumskaya E, de Laat KF, van Norden AG, van Dijk EJ, et al. Relationship between white matter hyperintensities, cortical thickness, and cognition. *Stroke.* (2015) 46:425–32. doi: 10.1161/STROKEAHA.114.007146
55. Du AT, Schuff N, Chao LL, Kornak J, Ezekiel F, Jagust WJ, et al. White matter lesions are associated with cortical atrophy more than entorhinal and hippocampal atrophy. *Neurobiol Aging.* (2005) 26:553–9. doi: 10.1016/j.neurobiolaging.2004.05.002
56. Ter Telgte A, van Leijsen EMC, Wiegertjes K, Klijn CJM, Tuladhar AM, de Leeuw FE. Cerebral small vessel disease: from a focal to a global perspective. *Nat Rev Neurol.* (2018) 14:387–98. doi: 10.1038/s41582-018-0014-y

57. Buckner RL, Andrews-Hanna JR, Schacter DL. The brain's default network: anatomy, function, and relevance to disease. *Ann N Y Acad Sci.* (2008) 1124:1–38. doi: 10.1196/annals.1440.011
58. Menon V. Large-scale brain networks and psychopathology: a unifying triple network model. *Trends Cogn Sci.* (2011) 15:483–506. doi: 10.1016/j.tics.2011.08.003
59. Seeley WW, Menon V, Schatzberg AF, Keller J, Glover GH, Kenna H, et al. Dissociable intrinsic connectivity networks for salience processing and executive control. *J Neurosci.* (2007) 27:2349–56. doi: 10.1523/JNEUROSCI.5587-06.2007
60. Bell PT, Shine JM. Subcortical contributions to large-scale network communication. *Neurosci Biobehav Rev.* (2016) 71:313–22. doi: 10.1016/j.neubiorev.2016.08.036
61. Hwang K, Bertolero MA, Liu WB, D'Esposito M. The human thalamus is an integrative hub for functional brain networks. *J Neurosci.* (2017) 37:5594–607. doi: 10.1523/JNEUROSCI.0067-17.2017
62. Chen H, Li Y, Liu Q, Shi Q, Wang J, Shen H, et al. Abnormal interactions of the salience network, central executive network, and default-mode network in patients with different cognitive impairment loads caused by leukoaraiosis. *Front Neural Circuits.* (2019) 13:42. doi: 10.3389/fncir.2019.00042
63. Shen T, Li C, Wang B, Yang WM, Zhang C, Wu Z, et al. Increased cognition connectivity network in major depression disorder: a FMRI study. *Psychiatry Investig.* (2015) 12:227–34. doi: 10.4306/pi.2015.12.2.227
64. Herrington JD, Mohanty A, Koven NS, Fisher JE, Stewart JL, Banich MT, et al. Emotion-modulated performance and activity in left dorsolateral prefrontal cortex. *Emotion.* (2005) 5:200–7. doi: 10.1037/1528-3542.5.2.200
65. Yang Y, Raine A. Prefrontal structural and functional brain imaging findings in antisocial, violent, and psychopathic individuals: a meta-analysis. *Psychiatry Res.* (2009) 174:81–8. doi: 10.1016/j.pscychresns.2009.03.012
66. van Veelen NM, Vink M, Ramsey NF, Kahn RS. Left dorsolateral prefrontal cortex dysfunction in medication-naive schizophrenia. *Schizophr Res.* (2010) 123:22–9. doi: 10.1016/j.schres.2010.07.004
67. Raichle ME. The restless brain. *Brain Connect.* (2011) 1:3–12. doi: 10.1089/brain.2011.0019
68. Muoio V, Persson PB, Sendeski MM. The neurovascular unit - concept review. *Acta Physiol.* (2014) 210:790–8. doi: 10.1111/apha.12250
69. Østergaard L, Engedal TS, Moreton F, Hansen MB, Wardlaw JM, Dalkara T, et al. Cerebral small vessel disease: capillary pathways to stroke and cognitive decline. *J Cereb Blood Flow Metab.* (2016) 36:302–25. doi: 10.1177/0271678X15606723
70. Wang J, Liang Y, Chen H, Wang W, Wang Y, Liang Y, et al. Structural changes in white matter lesion patients and their correlation with cognitive impairment. *Neuropsychiatr Dis Treat.* (2019) 15:1355–63. doi: 10.2147/NDT.S194803
71. Mok V, Wong KK, Xiong Y, Wong A, Schmidt R, Chu W, et al. Cortical and frontal atrophy are associated with cognitive impairment in age-related confluent white-matter lesion. *J Neurol Neurosurg Psychiatry.* (2011) 82:52–7. doi: 10.1136/jnnp.2009.201665
72. Peres R, De Guio F, Chabriat H, Jouvent E. Alterations of the cerebral cortex in sporadic small vessel disease: a systematic review of *in vivo* MRI data. *J Cereb Blood Flow Metab.* (2016) 36:681–95. doi: 10.1177/0271678X15625352
73. Greicius MD, Krasnow B, Reiss AL, Menon V. Functional connectivity in the resting brain: a network analysis of the default mode hypothesis. *Proc Natl Acad Sci USA.* (2003) 100:253–8. doi: 10.1073/pnas.0135058100
74. Bullmore E, Sporns O. Complex brain networks: graph theoretical analysis of structural and functional systems. *Nat Rev Neurosci.* (2009) 10:186–98. doi: 10.1038/nrn2575
75. Su Q, Yao D, Jiang M, Liu F, Jiang J, Xu C, et al. Increased functional connectivity strength of right inferior temporal gyrus in first-episode, drug-naive somatization disorder. *Austral N Zeal J Psychiatry.* (2015) 49:74–81. doi: 10.1177/0004867414553949
76. Arsalidou M, Duerden EG, Taylor MJ. The centre of the brain: topographical model of motor, cognitive, affective, and somatosensory functions of the basal ganglia. *Hum Brain Mapp.* (2013) 34:3031–54. doi: 10.1002/hbm.22124
77. Promjunyakul NO, Dodge HH, Lahna D, Boespflug EL, Kaye JA, Rooney WD, et al. Baseline NAWM structural integrity and CBF predict periventricular WMH expansion over time. *Neurology.* (2018) 90:e2119–26. doi: 10.1212/WNL.0000000000005684
78. Thrippleton MJ, Shi Y, Blair G, Hamilton I, Waiter G, Schwarzbauer C, et al. Cerebrovascular reactivity measurement in cerebral small vessel disease: rationale and reproducibility of a protocol for MRI acquisition and image processing. *Int J Stroke.* (2018) 13:195–206. doi: 10.1177/1747493017730740
79. Sam K, Crawley AP, Conklin J, Poublanc J, Sobczyk O, Mandell DM, et al. Development of white matter hyperintensity is preceded by reduced cerebrovascular reactivity. *Ann Neurol.* (2016) 80:277–85. doi: 10.1002/ana.24712

Conflict of Interest: The authors declare that the research was conducted in the absence of any commercial or financial relationships that could be construed as a potential conflict of interest.

Publisher's Note: All claims expressed in this article are solely those of the authors and do not necessarily represent those of their affiliated organizations, or those of the publisher, the editors and the reviewers. Any product that may be evaluated in this article, or claim that may be made by its manufacturer, is not guaranteed or endorsed by the publisher.

frontiers in Neurology

REVIEW
published: 24 November 2021
doi: 10.3389/fneur.2021.736309

Endothelial Dysfunction and Hyperhomocysteinemia-Linked Cerebral Small Vessel Disease: Underlying Mechanisms and Treatment Timing

Shuang Li[1,2†], **Guangjian Li**[3†], **Xia Luo**[1,2], **Yan Huang**[1,2], **Lan Wen**[4*] **and Jinglun Li**[1,2*]

[1] Department of Neurology, The Affiliated Hospital of Southwest Medical University, Luzhou, China, [2] Laboratory of Neurological Diseases and Brain Function, The Affiliated Hospital of Southwest Medical University, Luzhou, China, [3] Department of Neurology, Southwest Hospital, Third Military Medical University (Army Medical University), Chongqing, China, [4] Department of Neurosurgery, West China Hospital, Sichuan University, Chengdu, China

Edited by:
Tao Liu,
Hainan General Hospital, China

Reviewed by:
Ivan V. Brak,
State Scientific Research Institute of Physiology and Basic Medicine, Russia
Yuzhen Xu,
Tongji University, China

***Correspondence:**
Lan Wen
l_wen1225@163.com
Jinglun Li
ljl031611@163.com

† These authors have contributed equally to this work and share first authorship

Specialty section:
This article was submitted to Applied Neuroimaging, a section of the journal Frontiers in Neurology

Received: 09 July 2021
Accepted: 01 November 2021
Published: 24 November 2021

Citation:
Li S, Li G, Luo X, Huang Y, Wen L and Li J (2021) Endothelial Dysfunction and Hyperhomocysteinemia-Linked Cerebral Small Vessel Disease: Underlying Mechanisms and Treatment Timing. Front. Neurol. 12:736309. doi: 10.3389/fneur.2021.736309

Cerebral small vessel disease (cSVD)—a common cause of stroke and vascular dementia—is a group of clinical syndromes that affects the brain's small vessels, including arterioles, capillaries, and venules. Its pathogenesis is not fully understood, and effective treatments are limited. Increasing evidence indicates that an elevated total serum homocysteine level is directly and indirectly associated with cSVD, and endothelial dysfunction plays an active role in this association. Hyperhomocysteinemia affects endothelial function through oxidative stress, inflammatory pathways, and epigenetic alterations at an early stage, even before the onset of small vessel injuries and the disease. Therefore, hyperhomocysteinemia is potentially an important therapeutic target for cSVD. However, decreasing the homocysteine level is not sufficiently effective, possibly due to delayed treatment, which underlying reason remains unclear. In this review, we examined endothelial dysfunction to understand the close relationship between hyperhomocysteinemia and cSVD and identify the optimal timing for the therapy.

Keywords: cerebral small vessel disease, homocysteine, hyperhomocysteinemia, endothelial dysfunction, homocysteine-lowering therapy

INTRODUCTION

Cerebral small vessel disease (cSVD) refers to a series of clinical, imaging, and pathological syndromes caused by various etiological factors affecting small arteries, capillaries, and venules in the brain. As an age-dependent disease, the cSVD incidence is predicted to increase with the aging population (1). Several factors can contribute to the occurrence of cSVD, such as age, hypertension, diabetes, hyperlipidemia, small artery sclerosis, cerebrovascular amyloid, gene mutations, immune-mediated vasculitis, and certain infections (2); arteriolar sclerosis is the most common factor in older individuals (3, 4).

Globally, cSVD causes up to 45% of dementia and accounts for approximately 20% of all strokes. Twenty-five percent of these stroke cases are of the ischemic (or lacunar) type, of which in about 20% patients left disabled (3), putting an enormous burden on the society and families of these patients. Evidence regarding the efficacy of treatment with antiplatelets, anticoagulants, lipid-regulating drugs, and other methods in cSVD is lacking (5–7). Therefore, early detection and intervention of the risk factors is currently a beneficial strategy (8). The characteristic magnetic resonance imaging (MRI) markers are white matter hyperintensities (WMH), lacunes of presumed vascular origin, cerebral microbleeds (CMBs), enlarged perivascular spaces (EPVS), and cerebral atrophy (9, 10). Apart from imaging markers, sensitive, specific, and simple serum markers, such as homocysteine (Hcy), intercellular adhesion molecule-1 (ICAM-1), C-reactive protein (CRP), and interleukin-6 (IL-6) are also valuable in diagnosing cSVD (11).

Homocysteine (Hcy) is also an age-dependent indicator, and an elevated serum total Hcy (tHcy) level is associated with cardiovascular diseases, atherosclerosis, cerebrovascular diseases, and neurodegenerative disorders (12). Therefore, Hcy-lowering treatment is gradually becoming a therapeutic target for these diseases. However, contradictory results have been reported in cSVD. Several trials reported that primary prevention with Hcy-lowering therapy could reduce the incidence of cerebrovascular diseases (13–15). Unfortunately, a few trials using vitamin B supplementation to reduce Hcy levels failed to demonstrate the benefit of reducing stroke and cognitive impairment events (16–18). Understanding the mechanism behind Hcy-lowering therapy could help elucidate these findings. Endothelial dysfunction (ED) is a core mechanism of hyperhomocysteinemia (HHcy) affecting cSVD. Reducing Hcy levels alleviates ED, and early intervention of ED could reverse cSVD progression. Therefore, it is critical to identify the correct timing of lowering serum Hcy levels for treating ED and improving cSVD patient's prognosis.

HYPERHOMOCYSTEINEMIA

Homocysteine Metabolism and HHcy

Hcy is an intermediate metabolite in the methionine cycle, and the only Hcy sources are methionine-containing foods, such as eggs, sesame seeds, nuts, and meat. Plasma Hcy concentrations increase with age and are higher in men than in women (12, 19, 20). Hcy is primarily involved in methyl transfer (or one-carbon metabolism) and can undergo three metabolic pathways (21–23) (**Figure 1**): (a) *Remethylation:* Hcy is remethylated with the participation of 5-methyltetrahydrofolate and vitamin B12 (cobalamin) and catalyzed by methionine synthase (MS) to form methionine. Alternatively, betaine provides methyl to produce methionine catalyzed by betaine-homocysteine methyltransferase (BHMT); (b) *Transsulfuration Pathway:* Hcy is formed as cysteine is catalyzed by cystathionine beta-synthase (CBS) and its coenzyme, vitamin B6; (c) a small amount of Hcy is released directly into the extracellular fluid to perform physiological functions.

Vitamins B2, B6, B9 (folic acid), and B12 are indispensable coenzymes in the metabolism of the amino acid Hcy, and their deficiency could disturb the aforementioned pathways, leading to Hcy accumulation and elevated levels of Hcy in the plasma that triggers HHcy (24).

HHcy is defined by the plasma Hcy level of more than 15 μmol/L, and can be categorized into mild (Hcy = 15–30 μmol/L), moderate (Hcy = 30–100 μmol/L), and severe (Hcy >100 μmol/L) (24). HHcy can be classified as primary or secondary. Primary HHcy is mainly caused by mutations in the *MTHFR* (C677T or A1298C) and *MTRR* (A2756G) genes (25, 26). A higher *MTHFR* mutation rate is observed in the Chinese population than the others (27). The frequency of C677T mutation varies between 23.2 and 45.2% in the Chinese population (25), contributing to higher plasma-Hcy levels in Chinese than in Americans and Koreans (28–30). Secondary HHcy is mainly caused by impaired Hcy metabolism due to the deficiency of vitamin B2, B6, B9 (folic acid), or B12, renal failure, hypothyroidism, tumors, certain drugs, among several other causes (31). Dietary overdose may also lead to HHcy.

HHcy and Disease Condition

As a characteristic feature of aging, HHcy is causally linked to the development of age-associated disorders, such as ischemic heart diseases, atherosclerosis, cerebrovascular diseases, neurodegeneration, glomerular filtration rate decline, bone fractures, and venous thrombosis (12, 32). In particular, the focus has been on cardiocerebrovascular events. Several studies have shown that interventions to reduce tHcy, such as B-vitamin supplementation alone or in combination, had no effect on myocardial infarction and death from any cause or adverse event; however, statistical differences were observed in the stroke group (33, 34). These results suggested that the nervous system may be more sensitive to the toxic effects of HHcy than the cardiovascular system. Similarly, a study on the secondary prevention of stroke found that the use of B-vitamin supplements to lower Hcy significantly reduced stroke events and recurrence (13–15). Regardless of a history of acute ischemic stroke, patients with higher plasma-Hcy concentrations are more likely to develop cognitive impairments and depression than patients with normal levels (35, 36). Consequently, HHcy is a significant risk factor for nervous system disorders, especially cerebrovascular diseases.

HHcy Damages Brain Small Vessel Through Affecting Endothelial Function

There is an abundance of evidence that HHcy can damage brain small vessel, which increases the incidence of cSVD. The mechanisms include inflammation, atherosclerotic plaque formation, endothelial dysfunction, smooth muscle cell proliferation and oxidative stress response (37, 38). Among these pathological injury mechanisms, endothelial dysfunction plays a major role and determines the occurrence, development, and prognosis of cSVD (39). Hcy accumulation can interfere with the normal functioning of endothelial cells (ECs) through many pathological pathways (40–50). These include (a) oxidative stress resulting from the uncoupling of nitric oxide (NO) synthase, upregulation of the oxidation system, and decline of the antioxidant system; (b) competitive inhibition of NO synthase due to accumulation of asymmetric dimethylarginine (AMDA), resulting in decreased production of NO; (c) reduced hydrogen sulfide production, leading to abnormal vascular relaxation; (d)

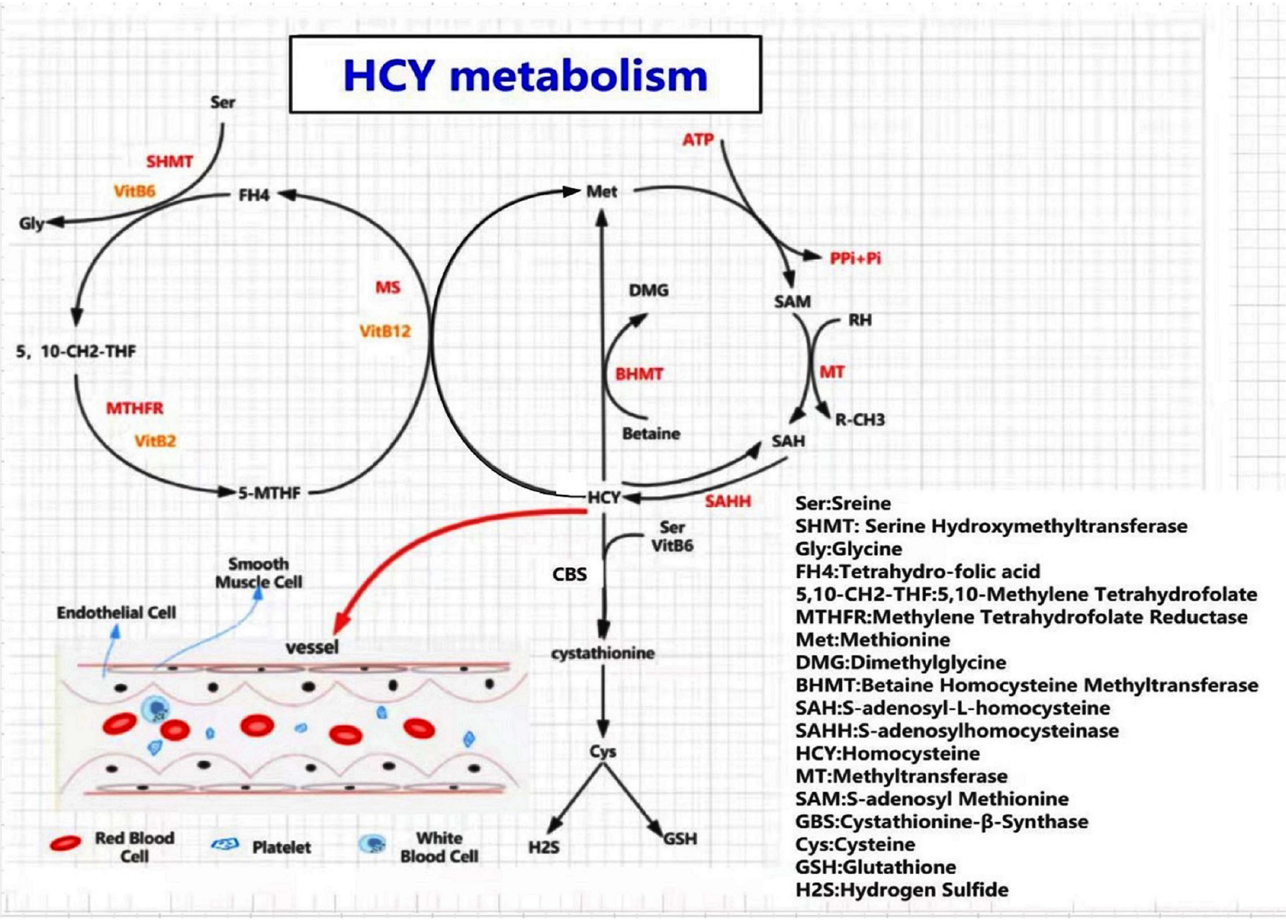

FIGURE 1 | A diagram of homocysteine (Hcy) and methionine metabolism. Three pathways involved in Hcy meatabolism, including remethylation pathway, transsulfuration pathway, and a small amount of Hcy released directly into the extracellular fluid. When a deficiency of MTHFR, CBS, MS, or B-vitamins occurs, an excess of homocysteine enters the blood, causing HHcy, resulting in damage to the corresponding target organs. SAM is the only donor of methyl in all of the metabolic pathways. HHcy leads to hypomethylation of biomolecules, such as proteins, lipids, and nucleic acids, which contributes to metabolic abnormalities and promotes disease occurrence.

endoplasmic reticulum stress and unfolded protein response with eventual EC apoptosis; (e) chronic inflammation and prothrombotic conditions; and (f) epigenetic alterations, including hypomethylation and protein N-homocysteinylation. These mechanisms result in endothelial dysfunction and apoptosis, broken intercellular tight connections, and chronic hypoperfusion, which could be conducive to the formation and progression of cSVD.

ENDOTHELIAL DYSFUNCTION AND cSVD

ED' Relevance in cSVD

Pathological changes in the small vessels vary during different periods of the cSVD process, including ED, blood-brain-barrier (BBB) injury, inflammatory response, smooth muscle proliferation, and small vessel sclerosis (3). Although different pathological changes play different roles in cSVD, they overlap and affect each other. ED triggers the first step of small blood vessel damage and plays a crucial role during the entire disease development process (39, 51). The significance of ED in cSVD has been well-established by population studies. A case-control study showed a worsening cerebral vasoreactivity in symptomatic lacunar stroke patients compared to that in matched controls, while cerebrovascular reactivity was used as a marker of endothelial function, indicating that ED severity in the cerebral artery may be a predisposing factor of symptomatic lacunar stroke in cSVD patients (51). Abnormal endothelial secretion of soluble ICAM-1, promotes the adhesion of leucocytes, which causes small vessels to occlude, and leads to incidence of silent brain infarctions and periventricular white matter lesions, implying ED in relation to progression of ischemic cerebral small vessel disease in type 2 diabetes (52). Markers of endothelial activation and damage, such as ICAM-1, thrombomodulin (TM), tissue factor (TF), and tissue factor pathway inhibitor (TFPI), were associated with the number of lacunes and severity of leukoaraiosis in the cSVD group in a prospective series of patients suffering from a lacunar strokes (53).

How ED Affects cSVD

ECs in the brain maintain BBB's integrity and regulate transmembrane transport functions. In addition, ECs are functionally active in controlling normal physiological processes, such as blood clotting, matching blood flow to neural activity, inflammatory reaction, and angiogenesis (54). When ischemic attacks, immune inflammation, or oxidative stress damage the endothelium, various abnormally released molecules (e.g., vasomotor factors, adhesion molecules, inflammatory cytokines, factors involved in the coagulation process, and enzymes) from ECs lead to impaired endothelium-dependent vasodilation, BBB destruction, and pre-thrombotic state, and exacerbates cSVD progression (11).

ED is the first step in cSVD pathogenesis. It is associated with leukoaraiosis, lacuna infarctions, and microbleeds through multiple underlying mechanisms (**Figure 2**). Firstly, the imbalance of vasomotor factors leads to pathological vasoconstriction and blood flow reduction, eventually leading to ischemia in the corresponding regions. Endothelially-derived NO, a key factor of vasodilation, is produced by L-arginine in a reaction catalyzed by endothelial-type NO synthase (eNOS), released into smooth muscle cells, wherein it activates guanylate cyclase to relax the vessel mediated by the cGMP pathway (55). In eNOS-deficient ED mice, NO reduction leads to pathological vasoconstriction and cerebral hypoperfusion, which exhibits similar MRI findings to those of cSVD, such as microhemorrhage, microinfarction, and white matter changes (56). In a cSVD rat model, ED, subsequent NO reduction, and BBB injury were associated with WMH burden (57). In addition, dysfunctional ECs can increase the secretion of endothelin-1, a vasoconstrictor, resulting in the pathological process of vasoconstriction (39).

Secondly, ECs and their tight junction (TJ) protein complexes are required to form a complete BBB. TJ protein complexes between ECs maintain BBB integrity and control the passage of cells and molecules. Damaged ECs and broken tight junctions can decrease BBB's integrity and increase its penetrability, leading to inflammation and edema of the surrounding tissue; corresponding signal changes can be observed on an MRI (58). The destruction of TJs caused by ECs dysfunction mainly results from the abnormal secretion of NO, matrix metalloproteinases (MMPs), and claudin proteins, inhibiting the modification of TJ proteins via nitrosylation or nitrosation, promoting TJ loss and accelerating BBB leakage (59). MMP-2 and MMP-9 also show increased expression, leading to decreased TJ proteins and transmembrane protein, claudin-5, which increases BBB's permeability (60). In addition, ED reduces the release of claudin-5, which adversely affects the tight connections between ECs and causes BBB injuries, which can impair brain function (61).

Thirdly, the survival and maturation of oligodendrocytes could be affected by ED and eventually interfere with white matter myelination. In an ATP11B-knockout rat model of cSVD, dysfunctional vascular endothelium secretes MMP chaperone protein, heat shock protein 90α (HSP90α), which leads to the maturation of oligodendrocyte precursor cells, contributing to white matter changes (57). Excessive MMPs, especially MMP-3 and MMP-9, secreted from dysfunctional ECs into the brain tissue cause and accelerate myelin breakdown (62). Moreover, dysfunctional ECs secrete increased CRP, IL-6, ICAM1, and e-selectin, leading to oligodendrocyte damage, and even apoptosis (4).

Finally, ED can participate in cSVD pathogenesis in multiple ways. Elevated plasma adhesion factors (ICAM-1 and vascular cell adhesion molecule-1 [VCAM-1]) and endothelial microparticles result from ED activating circulating inflammatory cells and causing vascular inflammation (63–65). Increased release of von Willebrand factor (vWF) caused by ED, which acts as a bridge to connect the process of platelets and inflammation, could lead to small vessel occlusion and further stimulate inflammation (66). These changes affect the structure and function of small vessels, contributing to the occurrence of cSVD and participating in its progression.

ED and Disease Reversal in the Early cSVD Stage

ED could be reversed through therapeutic interventions targeting the risk factors and inhibiting endothelial oxidative stress and inflammation. Previously, relieving eNOS uncoupling has been shown to reverse ED (54). This theory is also suitable for cSVD. Drug treatment to stabilize ED reverses the endothelial and oligodendroglial pathologies. Improved endothelial function can reverse ED itself, WMH, and oligodendroglial changes in the early disease state (57). Evidence suggests that in the early stage of cSVD, punctate lesions and a small number of white matter lesions caused by impaired interstitial fluid circulation may be quiescent and reversible. In contrast, fused and massive white matter lesions caused by demyelination and chronic hypoperfusion at later stages generally appear progressive and irreversible (67, 68). Thus, reversal of ED is a crucial therapeutic mechanism of cSVD, and the time window is notable and worth considering.

HHcy AND cSVD

Several population-based experiments confirmed that elevated baseline Hcy levels are positively associated with cSVD incidence and the subsequent severity and disease progression, independent of vascular risk factors and severity of the atherosclerotic disease. The relevance of the presence and number of lacunar infarcts, WMH volume, and progression to high baseline Hcy levels (32, 69–71) provides a more intuitive view of the correlation between HHcy and cSVD. In patients with dementia caused by small vessel lesions, higher tHcy levels were used to predict WMH progression, and the level was associated with deep CMBs and lacunes (32). In cSVD-related stroke, serum Hcy levels were significantly higher in patients with large WMH volumes than those with small WMH volumes (69, 70). The association between Hcy and WMH burden suggested that the degree of ED may be greater in patients with increased WMH volume and may, in part, explain that ED acts as a bridge between HHcy and cSVD (72). Similar results were obtained in recent observational studies, where WMH volume and EPVS number were positively correlated with plasma Hcy concentrations. EPVS may be specifically associated with BBB leakage led by injured

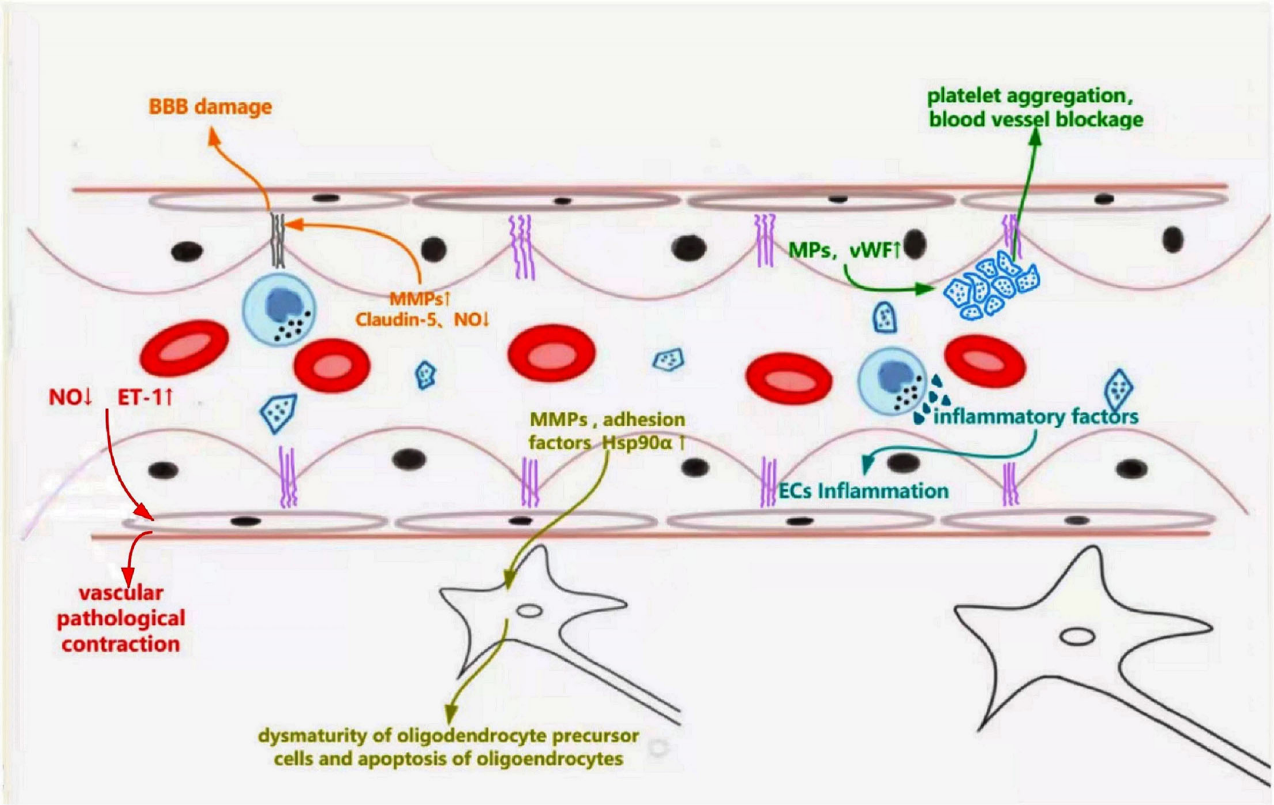

FIGURE 2 | Schematic representation of dysfunctional ECs linking to specific features of cerebral small vessel disease. Dysfunctional ECs induce abnormal secretion of NO and endothelin-1, which leads pathological vascular contraction. Increased secretion of MMPs and decreased production of claudin-5 destroy the tight connections, leading to blood-brain barrier leakage. Abnormally released MMPs, adhesion factors (ICAM-1, VCAM-1), and Hsp90α result in dysmaturity of oligodendrocyte precursor cells and apoptosis of oligodendrocytes, which affects the myelination. Endothelial microparticles and vWF are released from the damaged ECs, causing platelet aggregation and inflammatory response.

ECs and is considered as an important marker of BBB disruption (68, 73, 74).

ED in Hcy-Linked cSVD

As mentioned earlier, ED is a major mechanism of HHcy-linked cSVD, which mainly manifests as NO reduction, TJ breakage, BBB leakage, platelet aggregation, and pre-thrombotic state (**Figure 3**). The decrease in NO production and bioavailability predominates in Hcy-induced endothelial injury models, which exhibits vasoconstriction, vascular smooth muscle proliferation, and small arteriosclerosis; inadequate perfusion eventually develops cerebral white matter damage, acute small infarctions, and hemorrhages (44, 45). In addition, HHcy damages ECs and induces abnormal secretion of MMPs and transmembrane proteins, disrupting endothelial junctions, leading to BBB leakage, providing an important pathological basis for WMH, EPVS, lacunes, and CMB (75, 76). Furthermore, HHcy can also induce a pre-thrombotic state by modifying fibrinogen or enhancing platelet activation and coagulation and weakening fibrinolysis, which is prone to thrombosis and leads to ischemic stroke (42, 77). Naturally, Hcy-lowering therapy acts by ameliorating ED. AVE3085, a specific eNOS-targeting enhancer, prevents Hcy-induced ED by increasing NO production and reversing eNOS reduction in human ECs. The protective effects of AVE3085 translate into improved endothelium-dependent relaxation in the aorta of spontaneously hypertensive rats and significantly improved endothelium-dependent vasorelaxation in the Hcy-exposed human internal mammary artery (54). However, these studies indicate that ameliorating ED could reverse disease progression, which seems to be working just at early stage.

Hcy-Lowering Therapy in cSVD

In HHcy patients, several trials, reviews, and meta-analyses evaluating primary prevention with treatment, have shown that Hcy-lowering therapy with B-vitamin supplementation reduces the incidence of cerebrovascular diseases (13–15), in contrast to studies that have shown no such association (16–18). Thus, the main question might be at what stage of the disease can cSVD lesions be reversed or stopped from progressing using proper Hcy-lowering treatment. Some studies did not observe positive results due to malabsorption and other individual factors. Patients with chronic kidney disease

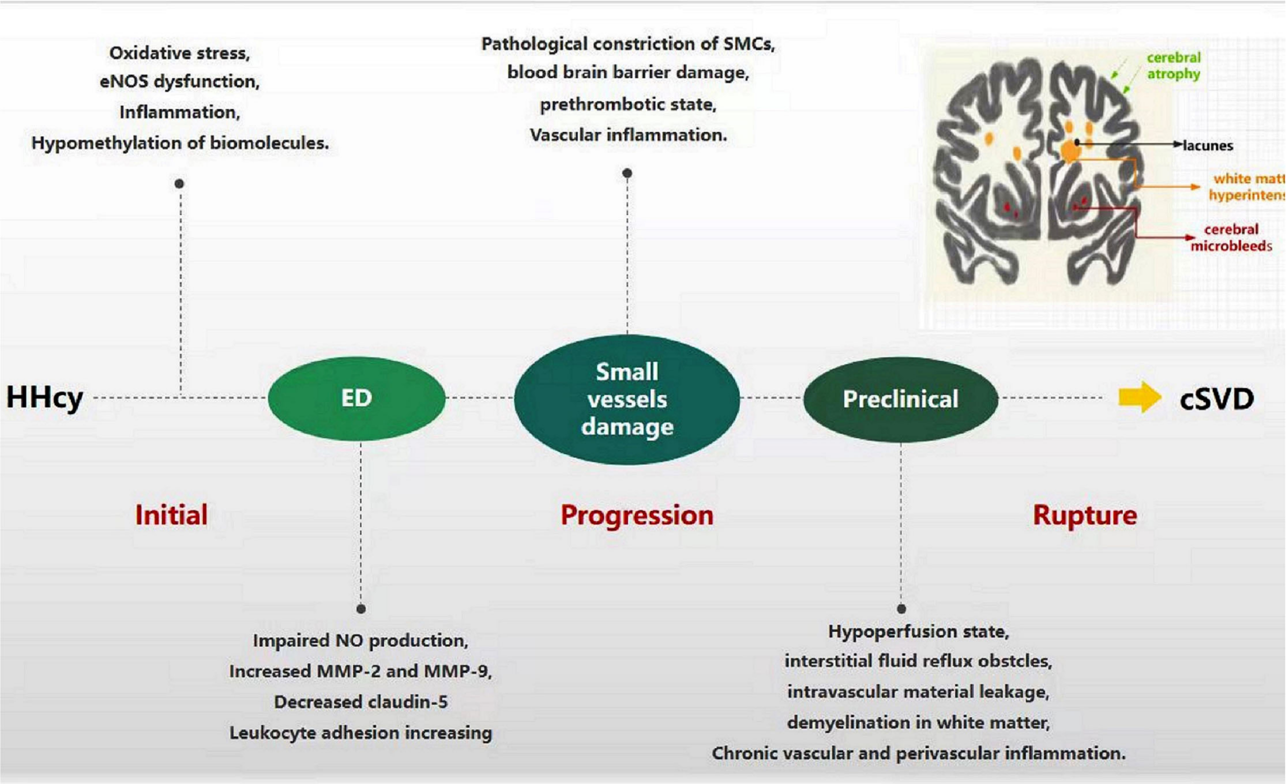

FIGURE 3 | Progression of HHcy-induced cSVD through ED. In the beginning, HHcy induces endothelial cell injury through oxidative stress, eNOS dysfunction, inflammation, and hypomethylation of biomolecules. Dysfunctional endothelia release the molecules abnormally, such as impaired NO production, increased MMPs and adhesion factors, decreased claudin-5. The process facilitates the damage of small vessels, including pathological vasoconstriction, SMCs injury, blood-brain barrier damage, pre-thrombotic state and vascular inflammation. Along with these pathological changes progression, hypoperfusion, intravascular material leakage, demyelination, chronic vascular and perivascular inflammation appear successively, which eventually develop into cSVD.

and those on antiplatelet therapy had reduced effects of B-vitamin supplementation on Hcy-associated cerebrovascular events (78). Older patients with gastrointestinal diseases failed to reach therapeutic concentrations of B-vitamins due to malabsorption and Hcy-lowering therapy may not be effective for hereditary cSVD (79). Moreover, delayed treatment may be a significant cause of a poor response to treatment. Nam et al. showed that if an ischemic stroke occurs in cSVD patients, disease progression might not be reversed by treatments meant to lower the tHcy levels, which suggest that patients with early or preclinical cSVD are more likely to benefit from Hcy-lowering therapy, and the curative effect was closely related to the timing of the treatment (68). In the stroke prevention trial, patients with low baseline Hcy levels had better outcomes than those with high levels (80). It indicates that Hcy-lowering treatment is similar to statin therapy for lowering lipid levels, and the underlying disease mechanisms are independent of the original baseline Hcy level. Considering that Hcy levels are associated with disease severity, it is also possible that patients with lower levels are more likely to be at an early stage of the disease and are more likely to benefit from treatment.

DISCUSSION

Both cSVD and HHcy are age-dependent diseases, and as a risk factor of cSVD, HHcy contributes to its onset and progression. Nonetheless, the use of Hcy-lowering therapy is controversial. Therefore, it is unclear whether Hcy can be considered as an early indicator of cSVD and whether reducing Hcy levels is necessary for the treatment. Considering the prevalence of HHcy in older individuals and their vulnerability to cSVD, monitoring of tHcy levels is recommended. In consideration of the limited treatment time window, active measures should be taken sooner rather than later. ECs were injured when first exposed to elevated tHcy conditions; once Hcy is elevated, damage to the endothelium begins, which precedes cerebral small vessel injury years before the onset of cSVD. As mentioned above, ameliorating ED could reverse the progression of the disease in its early stage, which is the primary purpose of Hcy-lowering therapy. Since effective therapy relies on early intervention, immediate steps should be taken upon detection of HHcy. Currently, most pathological states are described as early or later stages; therefore, the critical point of the irreversible stage remains unclear. Further studies are needed to evaluate the relationship between different manifestations of endothelial injury and determine the timeline of brain damage in patients with cSVD.

AUTHOR CONTRIBUTIONS

All authors listed have made a substantial, direct and intellectual contribution to the work, and got involved in the process of preparation, correction, and modification of the manuscript. All of them approved it for publication.

FUNDING

LW was a post-doctoral fellow from the West China Hospital of Sichuan University and was supported by Postdoctoral Research Found of China (2021M692285).

ACKNOWLEDGMENTS

We would like to thank Editage (www.editage.com) for English language editing.

REFERENCES

1. De Silva TM, Faraci FM. Contributions of aging to cerebral small vessel disease. *Annu Rev Physiol.* (2020) 82:275–95. doi: 10.1146/annurev-physiol-021119-034338
2. Cannistraro RJ, Badi M, Eidelman BH, Dickson DW, Middlebrooks EH, Meschia JF. CNS small vessel disease: a clinical review. *Neurology.* (2019) 92:1146–56. doi: 10.1212/WNL.0000000000007654
3. Pantoni L. Cerebral small vessel disease: from pathogenesis and clinical characteristics to therapeutic challenges. *Lancet Neurol.* (2010) 9:689–701. doi: 10.1016/S1474-4422(10)70104-6
4. Mustapha M, Nassir C, Aminuddin N, Safri AA, Ghazali MM. Cerebral small vessel disease (CSVD) - lessons from the animal models. *Front Physiol.* (2019) 10:1317. doi: 10.3389/fphys.2019.01317
5. Eng CM, Guffon N, Wilcox WR, Germain DP, Lee P, Waldek S, et al. Safety and efficacy of recombinant human α-galactosidase a replacement therapy in Fabry's disease. *N Engl J Med.* (2001) 345:9–16. doi: 10.1056/NEJM200107053450102
6. Du H, Wilson D, Ambler G, Banerjee G, Shakeshaft C, Cohen H, et al. Small vessel disease and ischemic stroke risk during anticoagulation for atrial fibrillation after cerebral ischemia. *Stroke.* (2021) 52:91–9. doi: 10.1161/STROKEAHA.120.029474
7. Amarenco P, Benavente O, Goldstein LB, Callahan A, 3rd, Sillesen H, Hennerici MG, et al. Results of the stroke prevention by aggressive reduction in cholesterol levels (SPARCL) trial by stroke subtypes. *Stroke.* (2009) 40:1405–9. doi: 10.1161/STROKEAHA.108.534107
8. Hilal S, Mok V, Youn YC, Wong A, Ikram MK, Chen CL. Prevalence, risk factors and consequences of cerebral small vessel diseases: data from three Asian countries. *J Neurol Neurosurg Psychiatry.* (2017) 88:669–74. doi: 10.1136/jnnp-2016-315324
9. Cuadrado-Godia E, Dwivedi P, Sharma S, Ois Santiago A, Roquer Gonzalez J, Balcells M, et al. Cerebral small vessel disease: a review focusing on pathophysiology, biomarkers, and machine learning strategies. *J Stroke.* (2018) 20:302–20. doi: 10.5853/jos.2017.02922
10. Wardlaw JM, Smith EE, Biessels GJ, Cordonnier C, Fazekas F, Frayne R, et al. Neuroimaging standards for research into small vessel disease and its contribution to ageing and neurodegeneration. *Lancet Neurol.* (2013) 12:822–38. doi: 10.1016/S1474-4422(13)70124-8
11. Poggesi A, Pasi M, Pescini F, Pantoni L, Inzitari D. Circulating biologic markers of endothelial dysfunction in cerebral small vessel disease: a review. *J Cereb Blood Flow Metab.* (2016) 36:72–94. doi: 10.1038/jcbfm.2015.116
12. Ostrakhovitch EA, Tabibzadeh S. Homocysteine and age-associated disorders. *Ageing Res Rev.* (2019) 49:144–64. doi: 10.1016/j.arr.2018.10.010
13. Ji Y, Tan S, Xu Y, Chandra A, Shi C, Song B, et al. Vitamin B supplementation, homocysteine levels, and the risk of cerebrovascular disease: a meta-analysis. *Neurology.* (2013) 81:1298–307. doi: 10.1212/WNL.0b013e3182a823cc
14. Huo Y, Li J, Qin X, Huang Y, Wang X, Gottesman RF, et al. Efficacy of folic acid therapy in primary prevention of stroke among adults with hypertension in China: the CSPPT randomized clinical trial. *JAMA.* (2015) 313:1325–35. doi: 10.1001/jama.2015.2274
15. Park JH, Saposnik G, Ovbiagele B, Markovic D, Towfighi A. Effect of B-vitamins on stroke risk among individuals with vascular disease who are not on antiplatelets: a meta-analysis. *Int J Stroke.* (2016) 11:206–11. doi: 10.1177/1747493015616512
16. Lee M, Hong KS, Chang SC, Saver JL. Efficacy of homocysteine-lowering therapy with folic acid in stroke prevention: a meta-analysis. *Stroke.* (2010) 41:1205–12. doi: 10.1161/STROKEAHA.109.573410
17. Hsu CY, Chiu SW, Hong KS, Saver JL, Wu YL, Lee JD, et al. Folic acid in stroke prevention in countries without mandatory folic acid food fortification: a meta-analysis of randomized controlled trials. *J Stroke.* (2018) 20:99–109. doi: 10.5853/jos.2017.01522
18. McMahon JA, Green TJ, Skeaff CM, Knight RG, Mann JI, Williams SM. A controlled trial of homocysteine lowering and cognitive performance. *N Engl J Med.* (2006) 354:2764–72. doi: 10.1056/NEJMoa054025
19. Dankner R, Chetrit A, Lubin F, Sela BA. Life-style habits and homocysteine levels in an elderly population. *Aging Clin Exp Res.* (2004) 16:437–42. doi: 10.1007/BF03327398
20. Feng C, Bai X, Xu Y, Hua T, Huang J, Liu XY. Hyperhomocysteinemia associates with small vessel disease more closely than large vessel disease. *Int J Med Sci.* (2013) 10:408–12. doi: 10.7150/ijms.5272
21. Stipanuk MH, Ueki I. Dealing with methionine/homocysteine sulfur: cysteine metabolism to taurine and inorganic sulfur. *J Inherit Metab Dis.* (2011) 34:17–32. doi: 10.1007/s10545-009-9006-9
22. Castro R, Rivera I, Blom HJ, Jakobs C, Tavares de Almeida I. Homocysteine metabolism, hyperhomocysteinaemia and vascular disease: an overview. *J Inherit Metab Dis.* (2006) 29:3–20. doi: 10.1007/s10545-006-0106-5
23. Tchantchou F. Homocysteine metabolism and various consequences of folate deficiency. *J Alzheimers Dis.* (2006) 9:421–7. doi: 10.3233/JAD-2006-9408
24. Huang YC, Chang SJ, Chiu YT, Chang HH, Cheng CH. The status of plasma homocysteine and related B-vitamins in healthy young vegetarians and nonvegetarians. *Eur J Nutr.* (2003) 42:84–90. doi: 10.1007/s00394-003-0387-5
25. Yang B, Liu Y, Li Y, Fan S, Zhi X, Lu X, et al. Geographical distribution of MTHFR C677T, A1298C and MTRR A66G gene polymorphisms in China: findings from 15357 adults of han nationality. *PLoS ONE.* (2013) 8:e57917. doi: 10.1371/journal.pone.0057917
26. Cao Y, Su N, Zhang D, Zhou L, Yao M, Zhang S, et al. Correlation between total homocysteine and cerebral small vessel disease: a mendelian randomization study. *Eur J Neurol.* (2021) 28:1931–8. doi: 10.1111/ene.14708
27. Pepe G, Camacho Vanegas O, Giusti B, Brunelli T, Marcucci R, Attanasio M, et al. Heterogeneity in world distribution of the thermolabile C677T mutation in 5,10-methylenetetrahydrofolate reductase. *Am J Hum Genet.* (1998) 63:917–20. doi: 10.1086/302015
28. Xu R, Huang F, Wang Y, Liu Q, Lv Y, Zhang Q. Gender- and age-related differences in homocysteine concentration: a cross-sectional study of the general population of China. *Sci Rep.* (2020) 10:17401. doi: 10.1038/s41598-020-74596-7
29. Lim HS, Heo YR. Plasma total homocysteine, folate, and vitamin B12 status in Korean adults. *J Nutr Science Vitaminol.* (2002) 48:290–7. doi: 10.3177/jnsv.48.290
30. Jacques PF, Rosenberg IH, Rogers G, Selhub J, Bowman BA, Gunter EW, et al. Serum total homocysteine concentrations in adolescent and adult Americans: results from the third national health and nutrition examination survey. *Am J Clin Nutr.* (1999) 69:482–9. doi: 10.1093/ajcn/69.3.482
31. Selhub J. Homocysteine metabolism. *Annu Rev Nutr.* (1999) 19:217–46. doi: 10.1146/annurev.nutr.19.1.217

32. Miwa K, Tanaka M, Okazaki S, Yagita Y, Sakaguchi M, Mochizuki H, et al. Increased total homocysteine levels predict the risk of incident dementia independent of cerebral small-vessel diseases and vascular risk factors. *J Alzheimers Dis.* (2016) 49:503–13. doi: 10.3233/JAD-150458
33. Spence JD. Homocysteine-lowering therapy: a role in stroke prevention? *Lancet Neurol.* (2007) 6:830–8. doi: 10.1016/S1474-4422(07)70219-3
34. Marti-Carvajal AJ, Sola I, Lathyris D, Dayer M. Homocysteine-lowering interventions for preventing cardiovascular events. *Cochrane Database Syst Rev.* (2017) 8:CD006612. doi: 10.1002/14651858.CD006612.pub5
35. Refsum H, Nurk E, Smith AD, Ueland PM, Gjesdal CG, Bjelland I, et al. The hordaland homocysteine study: a community-based study of homocysteine, its determinants, and associations with disease. *J Nutr.* (2006) 136:1731S40. doi: 10.1093/jn/136.6.1731S
36. Kwon HM, Lee YS, Bae HJ, Kang DW. Homocysteine as a predictor of early neurological deterioration in acute ischemic stroke. *Stroke.* (2014) 45:871–3. doi: 10.1161/STROKEAHA.113.004099
37. Balint B, Jepchumba VK, Gueant JL, Gueant-Rodriguez RM. Mechanisms of homocysteine-induced damage to the endothelial, medial and adventitial layers of the arterial wall. *Biochimie.* (2020) 173:100–6. doi: 10.1016/j.biochi.2020.02.012
38. Hainsworth AH, Oommen AT, Bridges LR. Endothelial cells and human cerebral small vessel disease. *Brain Pathol.* (2015) 25:44–50. doi: 10.1111/bpa.12224
39. Quick S, Moss J, Rajani RM, Williams A. A vessel for change: endothelial dysfunction in cerebral small vessel disease. *Trends Neurosci.* (2021) 44:289–305. doi: 10.1016/j.tins.2020.11.003
40. Lai WK, Kan MY. Homocysteine-induced endothelial dysfunction. *Ann Nutr Metab.* (2015) 67:1–12. doi: 10.1159/000437098
41. Esse R, Barroso M, Tavares de Almeida I, Castro R. The contribution of homocysteine metabolism disruption to endothelial dysfunction: state-of-the-art. *Int J Mol Sci.* (2019) 20:867. doi: 10.3390/ijms20040867
42. Dayal S, Wilson KM, Leo L, Arning E, Bottiglieri T, Lentz SR. Enhanced susceptibility to arterial thrombosis in a murine model of hyperhomocysteinemia. *Blood.* (2006) 108:2237–43. doi: 10.1182/blood-2006-02-005991
43. Di Minno MN, Tremoli E, Coppola A, Lupoli R, Di Minno G. Homocysteine and arterial thrombosis: challenge and opportunity. *Thromb Haemost.* (2010) 103:942–61. doi: 10.1160/TH09-06-0393
44. Kaur K, Singh N, Dhawan RK. Exploring the role of dimethylarginine dimethylaminohydrolase-mediated reduction in tissue asymmetrical dimethylarginine levels in cardio-protective mechanism of ischaemic postconditioning in rats. *Iran J Basic Med Sci.* (2019) 22:1415–23. doi: 10.22038/IJBMS.2019.14067
45. Stanger O, Weger M. Interactions of homocysteine, nitric oxide, folate and radicals in the progressively damaged endothelium. *Clin Chem Lab Med.* (2003) 41:1444–54. doi: 10.1515/CCLM.2003.222
46. Yang Q, He GW. Imbalance of homocysteine and h2s: significance, mechanisms, and therapeutic promise in vascular injury. *Oxid Med Cell Longev.* (2019) 2019:7629673. doi: 10.1155/2019/7629673
47. Wang R, Szabo C, Ichinose F, Ahmed A, Whiteman M, Papapetropoulos A. The role of H2S bioavailability in endothelial dysfunction. *Trends Pharmacol Sci.* (2015) 36:568–78. doi: 10.1016/j.tips.2015.05.007
48. Chan SH, Hung CH, Shih JY, Chu PM, Cheng YH, Lin HC, et al. Exercise intervention attenuates hyperhomocysteinemia-induced aortic endothelial oxidative injury by regulating SIRT1 through mitigating NADPH oxidase/LOX-1 signaling. *Redox Biol.* (2018) 14:116–25. doi: 10.1016/j.redox.2017.08.016
49. Xiao Y, Xia J, Cheng J, Huang H, Zhou Y, Yang X, et al. Inhibition of S-adenosylhomocysteine hydrolase induces endothelial dysfunction via epigenetic regulation of p66shc-mediated oxidative stress pathway. *Circulation.* (2019) 139:2260–77. doi: 10.1161/CIRCULATIONAHA.118.036336
50. Jamaluddin MD, Chen I, Yang F, Jiang X, Jan M, Liu X, et al. Homocysteine inhibits endothelial cell growth via DNA hypomethylation of the cyclin A gene. *Blood.* (2007) 110:3648–55. doi: 10.1182/blood-2007-06-096701
51. Deplanque D, Lavallee PC, Labreuche J, Gongora-Rivera F, Jaramillo A, Brenner D, et al. Cerebral and extracerebral vasoreactivity in symptomatic lacunar stroke patients: a case-control study. *Int J Stroke.* (2013) 8:413–21. doi: 10.1111/j.1747-4949.2011.00755.x
52. Umemura T, Kawamura T, Umegaki H, Mashita S, Kanai A, Sakakibara T, et al. Endothelial and inflammatory markers in relation to progression of ischaemic cerebral small-vessel disease and cognitive impairment: a 6-year longitudinal study in patients with type 2 diabetes mellitus. *J Neurol Neurosurg Psychiatry.* (2011) 82:1186–94. doi: 10.1136/jnnp.2010.217380
53. Hassan A, Hunt BJ, O'Sullivan M, Parmar K, Bamford JM, Briley D, et al. Markers of endothelial dysfunction in lacunar infarction and ischaemic leukoaraiosis. *Brain.* (2003) 126:424–32. doi: 10.1093/brain/awg040
54. Xu S, Ilyas I, Little PJ, Li H, Kamato D, Zheng X, et al. Endothelial dysfunction in atherosclerotic cardiovascular diseases and beyond: from mechanism to pharmacotherapies. *Pharmacol Rev.* (2021) 73:924–67. doi: 10.1124/pharmrev.120.000096
55. Vanhoutte PM, Shimokawa H, Feletou M, Tang EH. Endothelial dysfunction and vascular disease - a 30th anniversary update. *Acta Physiol.* (2017) 219:22–96. doi: 10.1111/apha.12646
56. Liao FF, Lin G, Chen X, Chen L, Zheng W, Raghow R, et al. Endothelial nitric oxide synthase-deficient mice: a model of spontaneous cerebral small vessel disease. *Am J Pathol.* (2021) 191:1932–45. doi: 10.1016/j.ajpath.2021.02.022
57. Rajani RM, Quick S, Ruigrok SR, Graham D, Harris SE, Verhaaren BF, et al. Reversal of endothelial dysfunction reduces white matter vulnerability in cerebral small vessel disease in rats. *Sci Transl Med.* (2018) 10:eaam9507. doi: 10.1126/scitranslmed.aam9507
58. Zhang CE, Wong SM, van de Haar HJ, Staals J, Jansen JF, Jeukens CR, et al. Blood–brain barrier leakage is more widespread in patients with cerebral small vessel disease. *Neurology.* (2017) 88:426–32. doi: 10.1212/WNL.0000000000003556
59. Daneman R, Prat A. The blood-brain barrier. *Cold Spring Harb Perspect Biol.* (2015) 7:a020412. doi: 10.1101/cshperspect.a020412
60. Yang Y, Estrada EY, Thompson JF, Liu W, Rosenberg GA. Matrix metalloproteinase-mediated disruption of tight junction proteins in cerebral vessels is reversed by synthetic matrix metalloproteinase inhibitor in focal ischemia in rat. *J Cereb Blood Flow Metab.* (2007) 27:697–709. doi: 10.1038/sj.jcbfm.9600375
61. Nitta T, Hata M, Gotoh S, Seo Y, Sasaki H, Hashimoto N, et al. Size-selective loosening of the blood-brain barrier in claudin-5-deficient mice. *J Cell Biol.* (2003) 161:653–60. doi: 10.1083/jcb.200302070
62. Jalal FY, Yang Y, Thompson J, Lopez AC, Rosenberg GA. Myelin loss associated with neuroinflammation in hypertensive rats. *Stroke.* (2012) 43:1115–22. doi: 10.1161/STROKEAHA.111.643080
63. Huang Y, Zhang W, Lin L, Feng J, Chen F, Wei W, et al. Is endothelial dysfunction of cerebral small vessel responsible for white matter lesions after chronic cerebral hypoperfusion in rats? *J Neurol Sci.* (2010) 299:72–80. doi: 10.1016/j.jns.2010.08.035
64. Porro C, Trotta T, Panaro MA. Microvesicles in the brain: biomarker, messenger or mediator? *J Neuroimmunol.* (2015) 288:70–8. doi: 10.1016/j.jneuroim.2015.09.006
65. Vion AC, Ramkhelawon B, Loyer X, Chironi G, Devue C, Loirand G, et al. Shear stress regulates endothelial microparticle release. *Circ Res.* (2013) 112:1323–33. doi: 10.1161/CIRCRESAHA.112.300818
66. Denorme F, Vanhoorelbeke K, De Meyer SF. von Willebrand factor and platelet glycoprotein ib: a thromboinflammatory axis in stroke. *Front Immunol.* (2019) 10:2884. doi: 10.3389/fimmu.2019.02884
67. Shi Y, Wardlaw JM. Update on cerebral small vessel disease: a dynamic whole-brain disease. *Stroke Vasc Neurol.* (2016) 1:83–92. doi: 10.1136/svn-2016-000035
68. Nam KW, Kwon HM, Jeong HY, Park JH, Kwon H, Jeong SM. Serum homocysteine level is related to cerebral small vessel disease in a healthy population. *Neurology.* (2019) 92:e317–25. doi: 10.1212/WNL.0000000000006816
69. Wong A, Mok V, Fan YH, Lam WW, Liang KS, Wong KS. Hyperhomocysteinemia is associated with volumetric white matter change in patients with small vessel disease. *J Neurol.* (2006) 253:441–7. doi: 10.1007/s00415-005-0022-x
70. Kloppenborg RP, Geerlings MI, Visseren FL, Mali WP, Vermeulen M, van der Graaf Y, et al. Homocysteine and progression of generalized

small-vessel disease: the SMART-MR study. *Neurology.* (2014) 82:777–83. doi: 10.1212/WNL.0000000000000168

71. Naka H, Nomura E, Takahashi T, Wakabayashi S, Kajikawa H, Kohriyama T, et al. Plasma total homocysteine levels are associated with advanced leukoaraiosis but not with asymptomatic microbleeds on T2*-weighted MRI in patients with stroke. *Eur J Neurol.* (2006) 13:261–5. doi: 10.1111/j.1468-1331.2006.01205.x
72. Cloonan L, Fitzpatrick KM, Kanakis AS, Furie KL, Rosand J, Rost NS. Metabolic determinants of white matter hyperintensity burden in patients with ischemic stroke. *Atherosclerosis.* (2015) 240:149–53. doi: 10.1016/j.atherosclerosis.2015.02.052
73. Wardlaw JM, Doubal F, Armitage P, Chappell F, Carpenter T, Munoz Maniega S, et al. Lacunar stroke is associated with diffuse blood-brain barrier dysfunction. *Ann Neurol.* (2009) 65:194–202. doi: 10.1002/ana.21549
74. Wardlaw JM. Blood-brain barrier and cerebral small vessel disease. *J Neurol Sci.* (2010) 299:66–71. doi: 10.1016/j.jns.2010.08.042
75. Beard RS, Jr., Reynolds JJ, Bearden SE. Hyperhomocysteinemia increases permeability of the blood-brain barrier by NMDA receptor-dependent regulation of adherens and tight junctions. *Blood.* (2011) 118:2007–14. doi: 10.1182/blood-2011-02-338269
76. Muradashvili N, Tyagi R, Metreveli N, Tyagi SC, Lominadze D. Ablation of MMP9 gene ameliorates paracellular permeability and fibrinogen-amyloid beta complex formation during hyperhomocysteinemia. *J Cereb Blood Flow Metab.* (2014) 34:1472–82. doi: 10.1038/jcbfm.2014.102
77. Wardlaw JM, Smith C, Dichgans M. Small vessel disease: mechanisms and clinical implications. *Lancet Neurol.* (2019) 18:684–96. doi: 10.1016/S1474-4422(19)30079-1
78. Vermeer SE, Van Dijk EJ, Koudstaal PJ, Oudkerk M, Hofman A, Clarke R, et al. Homocysteine, silent brain infarcts, and white matter lesions: the rotterdam scan study. *Ann Neurol.* (2002) 51:285–9. doi: 10.1002/ana.10111
79. Rutten-Jacobs LC, Traylor M, Adib-Samii P, Thijs V, Sudlow C, Rothwell PM, et al. Association of MTHFR C677T genotype with ischemic stroke is confined to cerebral small vessel disease subtype. *Stroke.* (2016) 47:646–51. doi: 10.1161/STROKEAHA.115.011545
80. Spence JD, Bang H, Chambless LE, Stampfer MJ. Vitamin intervention for stroke prevention trial: an efficacy analysis. *Stroke.* (2005) 36:2404–9. doi: 10.1161/01.STR.0000185929.38534.f3

Conflict of Interest: The authors declare that the research was conducted in the absence of any commercial or financial relationships that could be construed as a potential conflict of interest.

frontiers
in Neurology

ORIGINAL RESEARCH
published: 06 December 2021
doi: 10.3389/fneur.2021.735033

Altered Default Mode Network Is Associated With Cognitive Impairment in CADASIL as Revealed by Multimodal Neuroimaging

Panlong Li[1†], *Qi Huang*[2†], *Shiyu Ban*[3], *Yuan Qiao*[4], *Jing Wu*[4], *Yu Zhai*[4], *Xiaoxia Du*[3*], *Fengchun Hua*[5*] and *Jingjing Su*[4*]

[1] *School of Electrical and Information Engineering, Zhengzhou University of Light Industry, Zhengzhou, China,* [2] *Positron Emission Tomography (PET) Center, Huashan Hospital, Fudan University, Shanghai, China,* [3] *Shanghai Key Laboratory of Magnetic Resonance and Department of Physics, School of Physics and Materials Science, East China Normal University, Shanghai, China,* [4] *Department of Neurology, Shanghai Ninth People's Hospital, Shanghai Jiao Tong University School of Medicine, Shanghai, China,* [5] *Department of Nuclear Medicine, Longhua Hospital, Shanghai University of Traditional Chinese Medicine, Shanghai, China*

OPEN ACCESS

Edited by:
Xiaofei Hu,
Army Medical University, China

Reviewed by:
Ling He,
Children's Hospital of Chongqing Medical University, China
Yuting Zhang,
Children's Hospital of Chongqing Medical University, China

***Correspondence:**
Jingjing Su
jingjingsu2000@163.com
Fengchun Hua
huafc@hotmail.com
Xiaoxia Du
xxdu@phy.ecnu.edu.cn

†*These authors have contributed equally to this work and share first authorship*

Specialty section:
This article was submitted to Applied Neuroimaging, a section of the journal Frontiers in Neurology

Received: *02 July 2021*
Accepted: *08 October 2021*
Published: *06 December 2021*

Citation:
Li P, Huang Q, Ban S, Qiao Y, Wu J, Zhai Y, Du X, Hua F and Su J (2021) Altered Default Mode Network Is Associated With Cognitive Impairment in CADASIL as Revealed by Multimodal Neuroimaging. Front. Neurol. 12:735033. doi: 10.3389/fneur.2021.735033

Background and Purpose: Cerebral autosomal dominant arteriopathy with subcortical infarcts and leukoencephalopathy caused by mutations in the NOTCH3 gene is a hereditary cerebral small vessel disease, manifesting with stroke, cognitive impairment, and mood disturbances. Functional or structural changes in the default mode network (DMN), which plays important role in cognitive and mental maintenance, have been found in several neurological and mental diseases. However, it remains unclear whether DMN is altered in patients with cerebral autosomal dominant arteriopathy with subcortical infarcts and leukoencephalopathy (CADASIL).

Methods: Multimodal imaging methods, including MRI and positron emission tomography (PET), were applied to evaluate the functional, structural, and metabolic characteristics of DMN in 25 patients with CADASIL and 42 healthy controls.

Results: Compared with controls, patients with CADASIL had decreased nodal efficiency and degree centrality of the dorsal medial pre-frontal cortex and hippocampal formation within DMN. Structural MRI and diffusion tensor imaging (DTI) showed decreased gray matter volume and fiber tracks presented in the bilateral hippocampal formation. Meanwhile, PET imaging showed decreased metabolism within the whole DMN in CADASIL. Furthermore, correlation analyses showed that these nodal characteristics, gray matter volume, and metabolic signals of DMN were related to cognitive scores in CADASIL.

Conclusions: Our results suggested that altered network characteristics of DMN might play important roles in cognitive deficits of CADASIL.

Keywords: CADASIL, default mode network, cognitive impairment, MRI, PET

INTRODUCTION

Cerebral autosomal dominant arteriopathy with subcortical infarcts and leukoencephalopathy is the most common hereditary cerebrovascular disease (1). It is caused by the pathogenic mutations in the NOTCH3 gene on chromosome 19 and, therefore, shows familial inheritance. The typical clinical manifestations of cerebral autosomal dominant arteriopathy with subcortical infarcts and leukoencephalopathy (CADASIL) are migraine with aura, stroke, mood disturbances, and progressive cognitive impairments, including deficits in executive function, processing speed, attention, and memory (2).

Default mode network is a notable network that shows greater activity during the resting state than when performing tasks. It was first addressed by Raichle in a positron emission tomography (PET) study in 2001 (3). The component brain areas of default mode network (DMN) mainly include posterior cingulate cortex and precuneus (PCC/PCU), medial pre-frontal cortex (MPFC), medial and inferior temporal lobes, and inferior parietal lobe (IPL), and play important roles in a great variety of cognitive domains, such as working memory, visuomotor, visual language, and mental imagery (4). DMN has become a central research theme in neuropsychiatric disorders, including stroke, dementia, migraine, traumatic brain injury, depression, anxiety, and schizophrenia (5–10). A series of important research results about changed DMN characteristics in these disorders have been reported by using magnetic resonance imaging (MRI) and PET methods (5–10). However, as a focus of research into cognition, whether DMN is altered in patients with CADASIL remains unclear.

Several studies have demonstrated brain alterations in functional and structural imaging parameters in patients with CADASIL. Our previous resting-state functional MRI (fMRI) studies showed that altered functional activity and connectivity in PCC/PCU and para-hippocampal cortex (PHC) were associated with cognitive impairment in CADASIL (11, 12). Diffusion tensor imaging (DTI) studies have demonstrated widespread white matter lesions associated with cognitive deficits in CADASIL (13–15). Moreover, a case study using diffusion tensor tractography indicated that neural tract injuries were mainly located in the frontal lobe in a patient with CADASIL (16). Furthermore, a recent ^{18}F-2-fluoro-2-deoxy-D-glucose PET (^{18}F-FDG PET) study showed that decreased metabolism in the limbic lobe, including the hippocampus and PHC, was positively associated with a cognitive score in patients with CADASIL (17). Several regions involved in CADASIL belong to the hub nodes of DMN, and the DMN has a high degree of connectivity across the above-involved regions, including the PCC/PCU, MPFC, hippocampus, and PHC (5, 18). Though promising initial results from different neuroimaging studies have shown considerable overlap with areas typically considered part of the DMN, few studies explored the DMN in patients with CADASIL. Thus, based on the brain regions highlighted in these CADASIL studies, we assumed DMN modifications in patients with CADASIL.

Therefore, in the present study, we focused on multimodal imaging outcomes of DMN in CADASIL. To characterize the DMN comprehensively, resting-state fMRI, T1-weighted MRI, DTI, and ^{18}F-FDG PET were employed to assess functional network properties, gray matter volume (GMV), structural connectivity, and metabolism in DMN, and the associations with cognitive deficits.

MATERIALS AND METHODS

Participants

The study protocol was approved by the ethics committee in the Shanghai Ninth People's Hospital. All participants were fully informed of the study procedures and signed the informed consent. A total of 25 patients with CADASIL from 14 families evaluated at Shanghai Ninth People's Hospital between May 2016 and January 2019 were recruited for this study. For all patients, the diagnosis was confirmed by the identification of pathogenic mutations in the NOTCH3 gene (19). All subjects underwent detailed standard neurological examinations. Subjects were excluded from the study if they had severe depression or anxiety according to evaluation by two trained neuropsychologists using the Hamilton Depression Scale (HAMD) and the Hamilton Anxiety Scale (HAMA) (20, 21). Subjects were diagnosed with severe depression and anxiety based on HAMD and HAMA scores >17 and >14, respectively. Neurological deficits in all subjects were assessed using the National Institutes of Health Stroke Scale (NIHSS) and the modified Rankin scale (mRs). Cognitive scores in all subjects were recorded by the Montreal Cognitive Assessment (MoCA) and Mini-Mental State Examination (MMSE). Most of the patients underwent both MRI and PET/computed tomography (PET/CT), but four underwent only MRI and another four underwent only PET/CT.

Forty-two healthy subjects were recruited as a control group based on the following criteria: no history of stroke, headache, cognitive impairment, or vascular disease risk factors; no family history of cerebrovascular diseases or vascular disease risk factors; not taking medications and no substance addiction, such as drugs, cigarettes, or alcohol. All of the healthy subjects had normal results on neurological and general examinations. Among the 42 controls, 21 underwent only MRI and the remaining 21 controls underwent only PET/CT. The sample size and demographic information of each group were listed in **Table 1**.

MRI Acquisition

Subjects in the first control group and 21 patients with CADASIL underwent MRI, including resting-state fMRI, structural MRI (T1-weighted, T2-weighted, and fluid-attenuated inversion recovery [FLAIR] imaging), and DTI on a 3 Tesla system (Trio Tim; Siemens Healthcare, Malvern, PA, USA) with a 12-channel head coil at East China Normal University. Soft earplugs and custom-fit foam were applied to reduce noise and movement artifacts. Resting-state fMRI was performed using a T2*-weighted gradient-echo echo-planar imaging pulse sequence with the following parameters: repetition time/echo time (TR/TE) $= 2{,}000/30$ ms; flip angle $= 90°$; field of view (FOV) $= 220$ mm $\times$ 220 mm; number of slices $= 33$; resolution $=$ 3.44 mm $\times$ 3.44 mm $\times$ 4.38 mm; total volume $= 210$. The fMRI acquisition time was 7 min and 6 s for each subject. During the

TABLE 1 | Demographic information of CADASIL and control.

	CADASIL (n = 25)		**Controls (n = 42)**		***p*-values**	
	MRI (n = 21), PET (n = 21)		**MRI (n = 21), PET (n = 21)**		***p1***	***p2***
Male/female	13/8	14/7	13/8	14/7	1	1
Age (years), mean ± SD	48.4 ± 14.2	46.3 ± 14.0	48.7 ± 14.3	45.8 ± 12.1	0.9	0.9
Education (years), mean ± SD	8.7 ± 3.5	8.9 ± 3.3	9.1 ± 3.2	9.3 ± 3.0	0.8	0.8
Family history, *n* (%)	20 (95.2)	21 (100)	–	–	–	–
Migraine, *n* (%)	3 (14.3)	3 (14.3)	–	–	–	–
Migraine with aura, *n* (%)	2 (9.5)	2 (9.5)	–	–	–	–
Migraine without aura, *n* (%)	1 (4.8)	1 (4.8)	–	–	–	–
WMH volume (cm^3), mean ± SD (n = 19)	78.3 ± 55.7	–	–	–	–	–
Lacunar volume (cm^3), mean ± SD (n = 17)	1.9 ± 1.8	–	–	–	–	–
Microbleeds (number), mean ± SD (n = 6)	6.0 ± 1.8	–	–	–	–	–
O'Sullivan sign, *n* (%)	9 (42.9)					
HAMD, median ± IQR	4 ± 6	4 ± 5	3 ± 4	3 ± 3	0.3	0.3
HAMA, median ± IQR	3 ± 1	3 ± 1	3 ± 1	3 ± 2	0.7	0.7
NIHSS, median ± IQR	0 ± 1	0 ± 1	0 ± 0	0 ± 0	0.01	0.006
mRs, median ± IQR	1 ± 2	1 ± 2	0 ± 0	0 ± 0	0.001	0.001
MoCA, median ± IQR	21 ± 15	20 ± 11	26 ± 3	27 ± 1	0.000	0.000
MMSE, median ± IQR	24 ± 12	24 ± 11	28 ± 1	28 ± 2	0.001	0.002

SD and IQR represent standard deviation and interquartile range, respectively. P1 represents p-values of the comparisons between patients and controls in the MRI group, and p2 represents p-values of the comparisons between patients and controls in the PET group. CADASIL, cerebral autosomal dominant arteriopathy with subcortical infarcts and leukoencephalopathy; MRI, magnetic resonance imaging; PET, positron emission tomography; WMH, white matter hyperintensities; TIA, transient ischemic attack; HAMD, Hamilton Depression Scale; HAMA, Hamilton Anxiety Scale; NIHSS, National Institute of Health Stroke Scale; mRS, modified Rankin scale; MoCA, Montreal Cognitive Assessment; MMSE, Mini-Mental State Examination.

fMRI scan, the subjects kept their eyes closed but did not fall asleep. The whole-brain anatomical volume was obtained using a high-resolution T1-weighted 3D magnetization-prepared rapid-acquisition gradient-echo pulse sequence with the following parameters: TR = 2,530 ms; TE = 2.34 ms; flip angle = 7°; FOV = 256 mm × 256 mm; number of slices = 192; resolution = 1 mm × 1 mm × 1 mm. The T1-weighted image acquisition time was 6 min and 3 s for each subject. T2-weighted imaging was obtained using turbo spin-echo dark fluid sequence with the following parameters: TR/TE = 5,500/83 ms; FOV = 220 mm × 220 mm; number of slices = 35; resolution = 0.38 mm × 0.38 mm × 5.2 mm. The T2-weighted image scanning time was 1 min and 26 s for each subject. The parameters of FLAIR imaging were: TR/TE = 9,000/93 ms; FOV = 220 mm × 220 mm; number of slices = 30; resolution = 0.43 mm × 0.43 mm × 4.55 mm. The FLAIR image scanning time was 4 min and 50 s for each subject. DTI was performed using a single-shot, spin-echo planar imaging sequence acquired in contiguous axial planes with the following parameters: 64 non-collinear directions, diffusion weighting of b = 1,000 s/m^2, an acquisition without diffusion weighting of b = 0; TR/TE = 8,900/86 ms; FOV = 256 mm × 256 mm, covered the whole brain; 70 contiguous slices; resolution = 2 mm × 2 mm × 2 mm. The DTI scanning time was 10 min and 7 s for each subject. The total MRI acquisition time was 29 min and 38 s for each subject.

PET Acquisition

^{18}F-2-fluoro-2-deoxy-D-glucose PET data were acquired using a Siemens Biograph Truepoint HD 64 PET/CT is made by Simens in Germany at the PET Center of Huashan Hospital, Fudan University. ^{18}F-FDG was synthesized and radiolabeled at the PET Center according to the protocol of the manufacturer under the inspection by the Chinese Food and Drug Administration. Before ^{18}F-FDG injection, subjects were asked to avoid strenuous physical activity and fast for about 6 h to maintain blood glucose level <8 mmol/L. After receiving an injection of ^{18}F-FDG at a dose of 5.55 MBq/kg (0.15 mCi/kg), subjects rested in a dimly lit room for 50 min. Before PET acquisition, a low-dose CT scan was performed for attenuation correction, and then 10-min PET images were reconstructed using a filtered back-projection algorithm. The matrix size of the reconstructed images was 168 × 168 × 148 with a resolution of 2.04 mm × 2.04 mm × 1.5 mm.

Data Processing

Prior to preprocessing, all the raw DICOM data were converted to the Neuroimaging Informatics Technology Initiative format (NII) using MRICRON software (https://people.cas.sc.edu/rorden/mricron/install.html) and the quality of the images was checked visually.

fMRI Data Processing

The resting-state fMRI data were preprocessed using Data Processing Assistant for Resting-State fMRI (DPARSF; http://www.restfmri.net) (22, 23). Data were preprocessed starting with the removal of the first 10 volumes to ameliorate possible effects of scanner instability and the adaptation of subjects to the environment. Then, slice time correction was applied to reduce the effects of within-scan acquisition time differences between

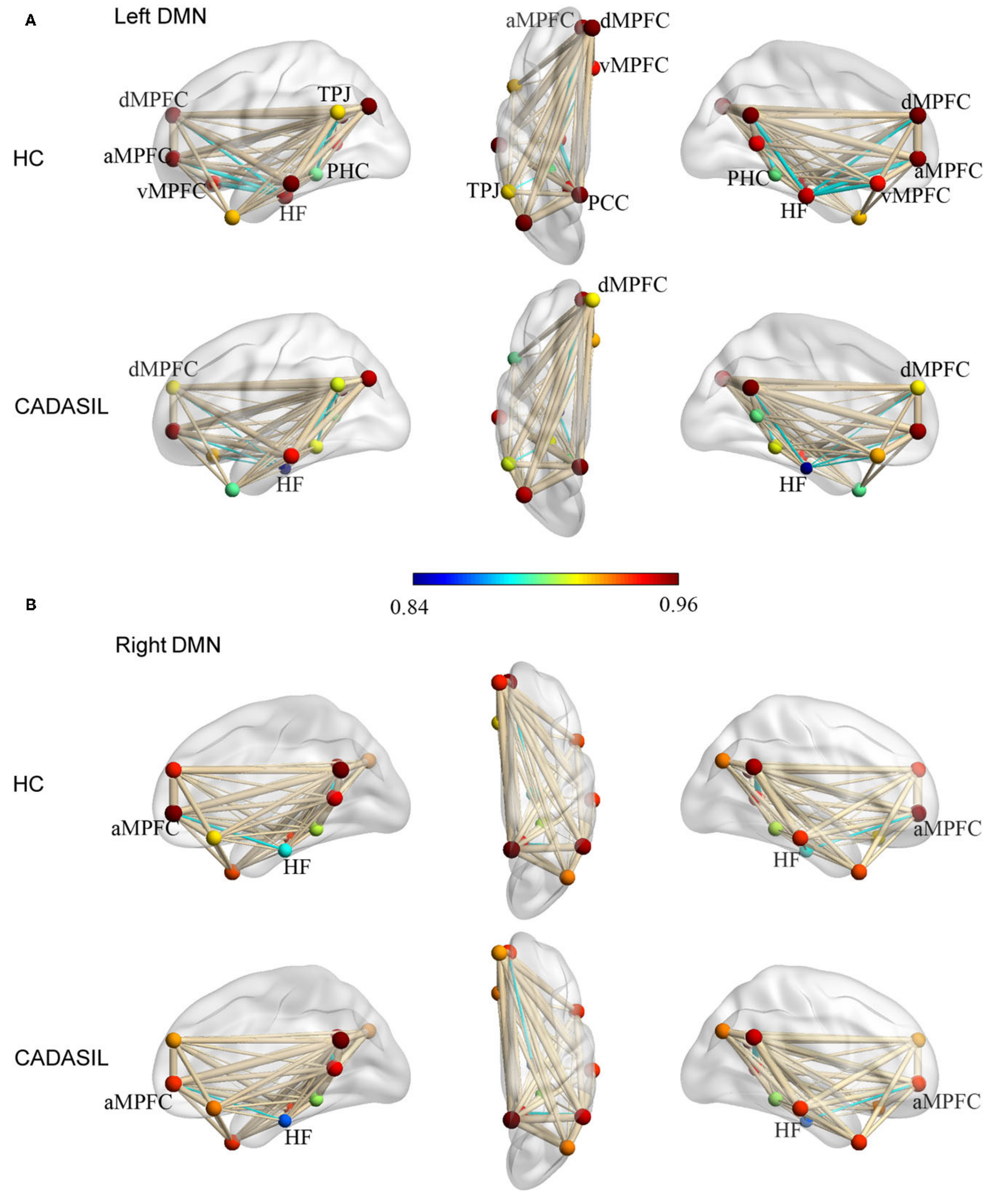

FIGURE 1 | Topological properties of DMN in CADASIL and control groups in the left **(A)** and right **(B)** hemisphere. The color bar corresponded to nodal color, representing the mean nodal efficiency in the corresponding group. Nodal size represented the mean degree of centrality in the corresponding group. The thickness of edges reflected the strength of FC between regions. FC showing significant differences between the two groups was indicated in cyan ($p < 0.05$). DMN, default mode network; CADASIL, cerebral autosomal dominant arteriopathy with subcortical infarcts and leukoencephalopathy; FC, functional connectivity; HC, healthy control; *(Continued)*

FIGURE 1 | a MPFC, anterior medial pre-frontal cortex; dMPFC, dorsal medial pre-frontal cortex; vMPFC, ventral medial pre-frontal cortex; HF, hippocampal formation; PCC, posterior cingulate cortex; PHC, parahippocampal cortex; TPJ, temporal-parietal junction.

slices. To correct the effects of head motion, the fMRI images of each subject were realigned and registered. All subjects had head motions <1.5° of rotation or 0.5 mm of mean frame-wise displacement (24). The fMRI images were then normalized into the Montreal Neurological Institute (MNI) space using the EPI template and smoothed by a full-width at half-maximum (FWHM) 8 mm Gaussian kernel. Following spatial smoothing, linear detrend was performed to remove noise due to long-term physiological shifts, movement-related noise remaining after realignment, and instrumental instability. To reduce further the effects of noise, the fMRI images were filtered with a temporal band-pass filter (0.01–0.08 Hz). Finally, the six head motion parameters, global mean signal, white matter signal, and cerebrospinal fluid signal were regressed out as nuisance covariates to remove these unwanted signals.

With reference to previous studies (18, 25, 26), 11 separate regions comprising the left DMN and 11 mirrored regions comprising the right DMN were defined as regions of interest (ROIs). The 11 ROIs were spheres of radius 8 mm in the dorsal MPFC (dMPFC), anterior MPFC (aMPFC), ventral MPFC (vMPFC), posterior IPL (pIPL), temporal-parietal junction (TPJ), lateral temporal cortex (LTC), temporal pole (TempP), PCC, retrosplenial cortex (RSC), PHC, and hippocampal formation (HF) (see **Supplementary Table 1** and **Supplementary Figure 1** for coordinates and spatial positions). Average fMRI time-series were calculated across every voxel in each ROI. The absolute value of Fisher's z-transformed Pearson's correlation coefficient between each pair of time-series was defined as the functional connectivity (FC) strength.

Graph analysis of the pairwise (11 × 11) correlation matrixes was performed using GRETNA (v2.0.0; https://www.nitrc.org/projects/gretna/) (27). Global and nodal network properties, including nodal degree centrality, nodal shortest path length, nodal clustering coefficient, nodal efficiency, nodal local efficiency, betweenness centrality, global efficiency, assortativity coefficient, and small-worldness, were calculated to delineate the integrative and local topological architecture of the DMN, respectively. Their definitions and calculations of the nodal and global network properties were summarized in **Supplementary Table 2**.

T1-Weighted Data Processing

The T1-weighted MRI data were preprocessed using the Computational Anatomy Toolbox (CAT12; http://dbm.neuro.uni-jena.de/cat12) implemented in statistical parametric mapping software (SPM12; htttp://www.fil.ion.ucl.ac.uk/spm/). First, all T1-weighted MRI data were normalized into the MNI space using the Diffeomorphic Anatomic Registration Through Exponentiated Lie algebra algorithm (DARTEL). The bias field inhomogeneities were corrected to remove non-uniform intensities. Normalized images were then segmented into gray matter, white matter, and cerebrospinal fluid components. The total intracranial volume (TIV) of each participant was evaluated to correct for the effects of differences in brain size. The internal gray matter threshold was set to 0.2 to exclude artifacts on the gray-white matter border. Thereafter, all preprocessed scans were smoothed with the FWHM 6 mm Gaussian kernel. Finally, the average GMV was calculated across every voxel in each ROI.

DTI Data Processing

The raw DTI data were preprocessed using FMRIB Software Library (FSL; http://www.fmrib.ox.ac.uk/fsl/index.html.) First, eddy current correction was performed to correct for head motion artifacts and eddy current distortions. Then, the brain of each subject was extracted using the FSL Brain Extraction Tool (BET). Tensor reconstruction and fiber tracking were applied by Diffusion Toolkit TrackVis (https://www.nitrc.org/projects/trackvis.) The Fiber Association Continuous Tracking (FACT) algorithm in Diffusion Toolkit was applied to obtain the whole-brain fiber tracts. The main parameters in fiber tractography were as follows: maximum turning angle threshold at 35°; minimum fractional anisotropy (FA) threshold of 0.2. Then, SPM12 was applied to bring all the individual tracts into the MNI space by non-linear transformation methods. In the normalization step, tracts were spatially normalized by: co-registering T1-weighted MRI to the corresponding FA image; calculating the deformation field of the individual coregistered T1-weighted image space to the MNI space; applying the deformation field to tracts and bringing them into the MNI space. Thereafter, TrackVis was used to record the number of tracts (NT) passing through each ROI.

PET Data Processing

First, PET images of each subject were processed using SPM12 software with spatial normalization and smoothing. The PET template in SPM12 was used in the spatial normalization step. The FWHM 8 mm Gaussian kernel was applied in the smoothing step. The average glucose metabolism was then calculated across every voxel in each ROI.

Statistical Analysis

Statistical analysis was performed using IBM SPSS Statistics for Windows (SPSS, Chicago, IL, USA). The Chi-square tests and permutation tests (permutation times = 10,000) were used to compare demographic, clinical, and imaging characteristics between the CADASIL and control groups, as appropriate. Furthermore, the two-sample *t*-test was applied for voxel-wise metabolism comparisons between the CADASIL and corresponding control groups using SPM12 software. Subsequently, partial correlations were established to estimate the relations between the cognitive deficits and the imaging characteristics showing significant between-group differences. Age, sex, and education levels were entered as covariates in partial correlation analysis. Benjamini-Hochberg false discovery rate (FDR) correction was further used to avoid type-I errors in

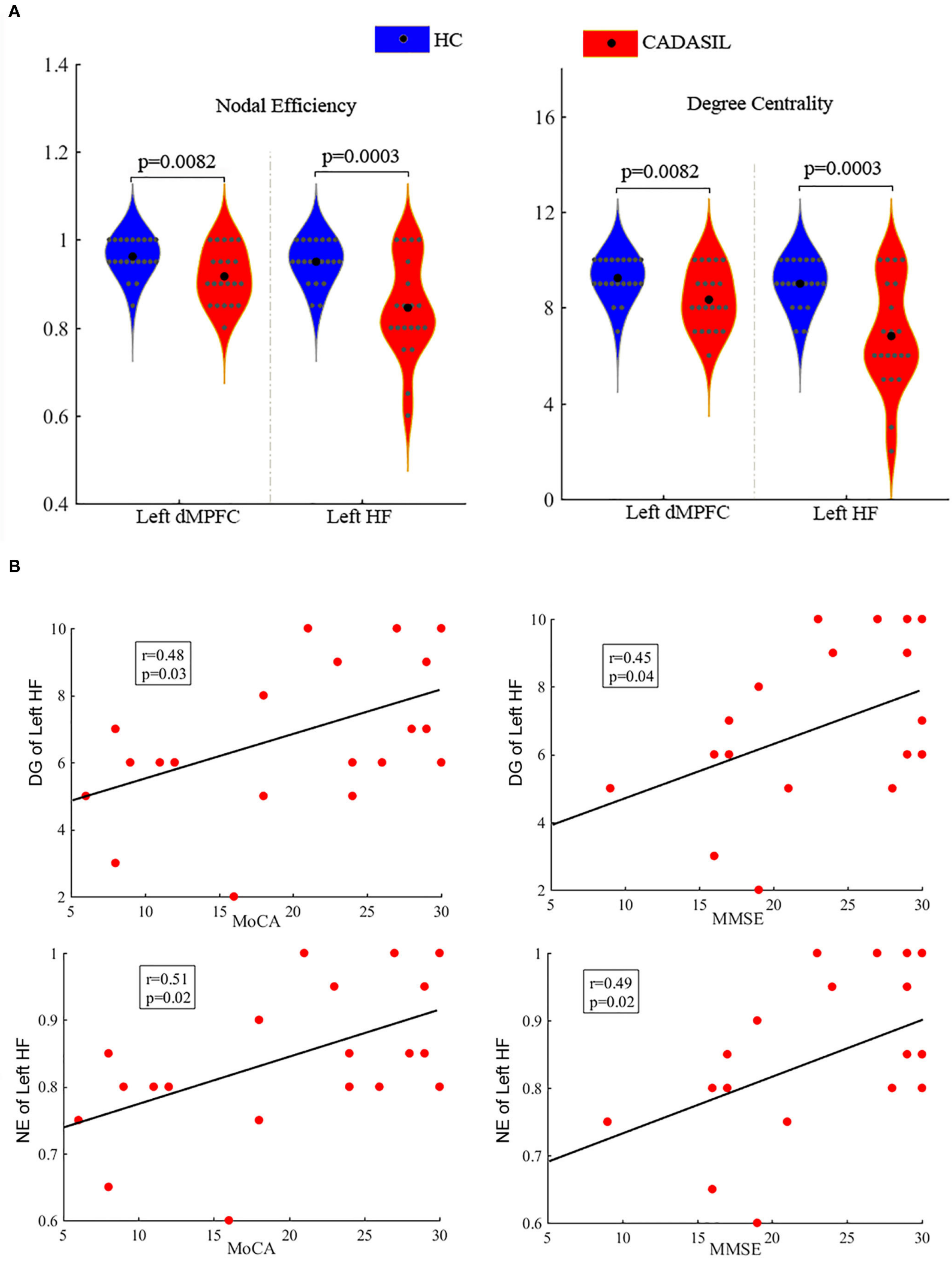

FIGURE 2 | Differences between CADASIL and control groups in topological properties and correlations between the properties and cognitive scores in the DMN. **(A)** Nodal efficiency and degree centrality were significantly different between the CADASIL and healthy control groups in the left DMN. The CADASIL had decreased nodal efficiency and degree centrality in the left dMPFC and HF. **(B)** Linear correlations between network properties in the DMN and cognitive scores in CADASIL.

(Continued)

FIGURE 2 | CADASIL, cerebral autosomal dominant arteriopathy with subcortical infarcts and leukoencephalopathy; DMN, default mode network; dMPFC, dorsal medial pre-frontal cortex; HF, hippocampal formation; HC, healthy control; DG, degree centrality; NE, nodal efficiency; MoCA, Montreal Cognitive Assessment; MMSE, Mini-Mental State Examination.

the multiple comparisons and correlations. The results of two-sample comparisons and partial correlations were regarded as significant at $p < 0.05$ (two-tailed) with FDR correction.

RESULTS

Demographic and Clinical Data

Table 1 showed comparisons of the demographic and clinical data of the CADASIL and healthy control groups. There were significant differences between the two groups in terms of neurological deficits and cognitive scores, but no differences in sex, age, education levels, or depression and anxiety symptom scores.

Network Analysis of DMN

Compared with the healthy control group, the CADASIL group had decreased FC between the HF and the MPFC (aMPFC, dMPFC, and vMPFC), as well as increased FC between the TPJ and PHC within the left DMN (**Figure 1A** and **Supplementary Figure 2**). Further network analysis showed that the nodal characteristics of the left dMPFC and HF, including nodal efficiency and degree centrality, were significantly different between the CADASIL and healthy control groups (**Figure 2A**). The integrative topological architecture of the left DMN was not significantly different between the two groups.

In the right DMN, the CADASIL group showed decreased FC between the HF and the aMPFC as well as the dMPFC, and increased FC between the TPJ and RSC in comparison to the healthy control group (**Figure 1B** and **Supplementary Figure 2**). There were no significant differences in the global or local topological architecture of the right DMN between the two groups.

GMV Analysis of DMN

There was no significant difference in TIV between the CADASIL group and the healthy control group. Compared with the healthy control group, the patients with CADASIL had decreased GMV in the left PHC (0.58 ± 0.1 vs. 0.66 ± 0.12, respectively, $p = 0.02$) and bilateral HF (left: 0.38 ± 0.04 vs. 0.41 ± 0.05, respectively, $p = 0.035$; right: 0.40 ± 0.05 vs. 0.44 ± 0.06, respectively, $p = 0.04$) (**Figure 3A**).

Fiber Tracks Analysis of DMN

Compared with the healthy control group, the patients with CADASIL had reduced NT in the bilateral HF (left: 198.86 ± 85.86 vs. 263.33 ± 64.18, respectively, $p = 0.008$; right: 208.05 ± 72.68 vs. 290.24 ± 84.01, respectively, $p = 0.001$) (**Figure 4**). There was no significant increase in tracks between the CADASIL and healthy control groups.

Metabolism Analysis of DMN

Compared with the healthy control group, the patients with CADASIL had decreased glucose metabolism across the ROIs ($p < 0.00001$) (**Figure 5A**). There was a significant decrease in global metabolism across the whole brain ($p < 0.00001$) (**Figure 5A**). There was no significant increase in regional metabolism between the two groups.

Correlation Analysis

In fMRI, the nodal efficiency and degree centrality in the bilateral HF were positively correlated with MoCA and MMSE scores in the patients with CADASIL ($p < 0.05$) (**Figure 2B**). Similar correlations between the GMV of the bilateral HF and left PHC, and cognitive scores were also detected in the CADASIL group (**Figure 3B**). There was no significant correlation between the number of tracks and cognitive scores. The levels of metabolism in most ROIs with decreased glucose metabolism were positively correlated with the cognitive scores in the CADASIL group ($p < 0.01$) (**Figure 5B** and **Supplementary Table 3**).

DISCUSSION

The present study was performed to investigate whether the DMN was altered in patients with CADASIL. We integrated the results of multimodal imaging methods, including fMRI, T1-weighted MRI, DTI, and PET, to investigate the changes in functional network properties, GMV, fiber tracks, and glucose metabolism within the DMN in patients with CADASIL. Consistent with our initial hypothesis, the characteristics of DMN represented by these images in the CADASIL group were significantly different compared with those in the healthy control group. Correlation analysis showed that these modifications were associated with cognitive deficits in the CADASIL group. These findings had important implications for the further understanding of CADASIL-related cognitive deficits and could provide potential brain markers for CADASIL.

Previous neuroimaging studies have focused on the whole brain functional or structural changes in CADASIL by a single imaging modality (15, 17, 28). In our study, we focused on the DMN by multi-modal imaging methods. The results in this study corresponded with previous MRI studies on stroke, dementia, migraine, and WMH that showed that functional or structural modifications of DMN are associated with cognitive deficits. In this study, more than 90% of CADASIL subjects had WMH. Although the ratio of migraine, dementia, and migraine was not as high as WMH, these symptoms are also typical of the later clinical manifestations of CADASIL. Notably, in order to fully and thoroughly explore the DMN alterations in CADASIL, except for three MRI modalities, one PET modality which represents the glucose metabolism in the brain was applied to evaluate the network characteristics of DMN. In order to reduce the influence

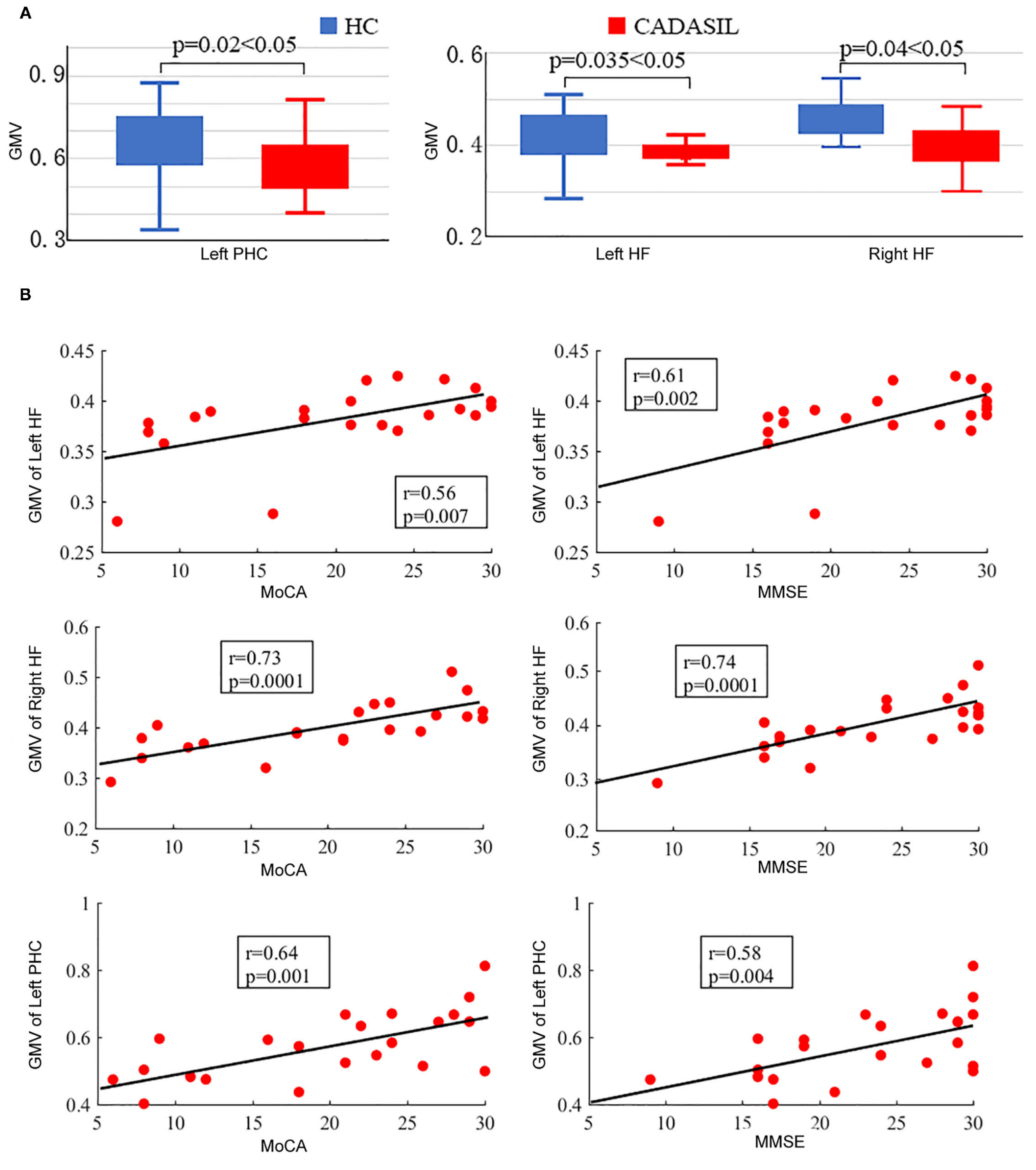

FIGURE 3 | Results of GMV analysis in CADASIL and control groups. **(A)** Alterations in GMV of the DMN in CADASIL. Patients with CADASIL had decreased GMV in the left PHC and bilateral HF compared with healthy controls. **(B)** Correlations between GMV of ROIs within the DMN and cognitive scores in CADASIL. GMV, gray matter volume; CADASIL, cerebral autosomal dominant arteriopathy with subcortical infarcts and leukoencephalopathy; DMN, default mode network; PHC, parahippocampal cortex; HF, hippocampal formation; ROI, region of interest; HC, healthy control; MoCA, Montreal Cognitive Assessment; MMSE, Mini-Mental State Examination.

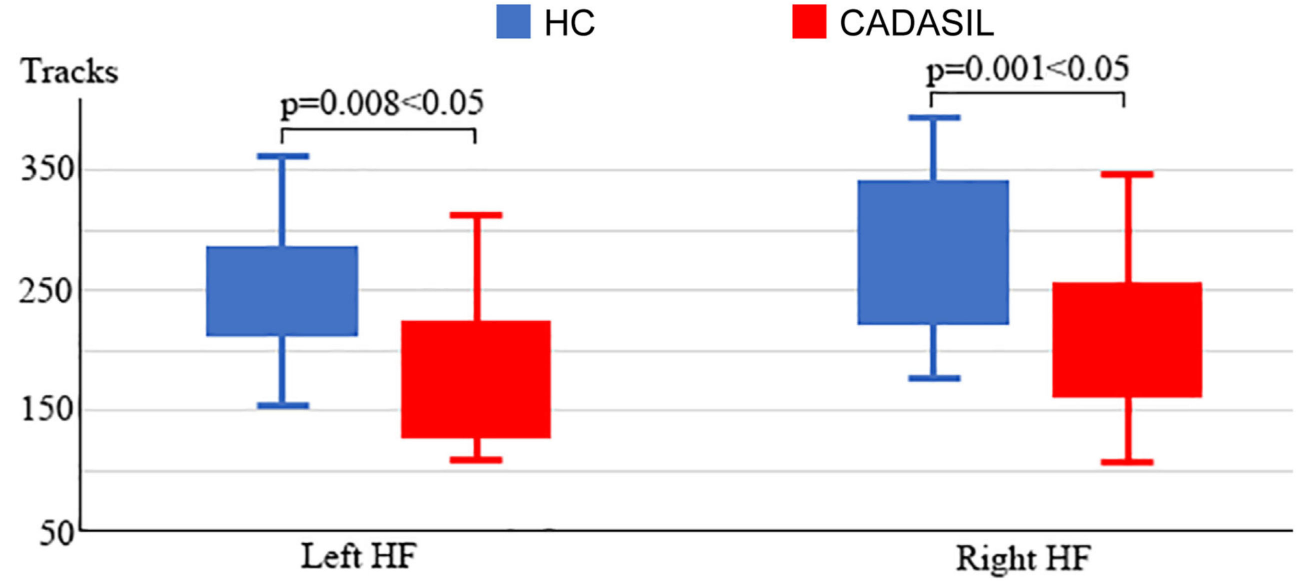

FIGURE 4 | Analysis of fiber tracks in the DMN in CADASIL and control groups. Patients with CADASIL had decreased fiber tracks in the bilateral HF. DMN, default mode network; CADASIL, cerebral autosomal dominant arteriopathy with subcortical infarcts and leukoencephalopathy; HF, hippocampal formation; HC, healthy control.

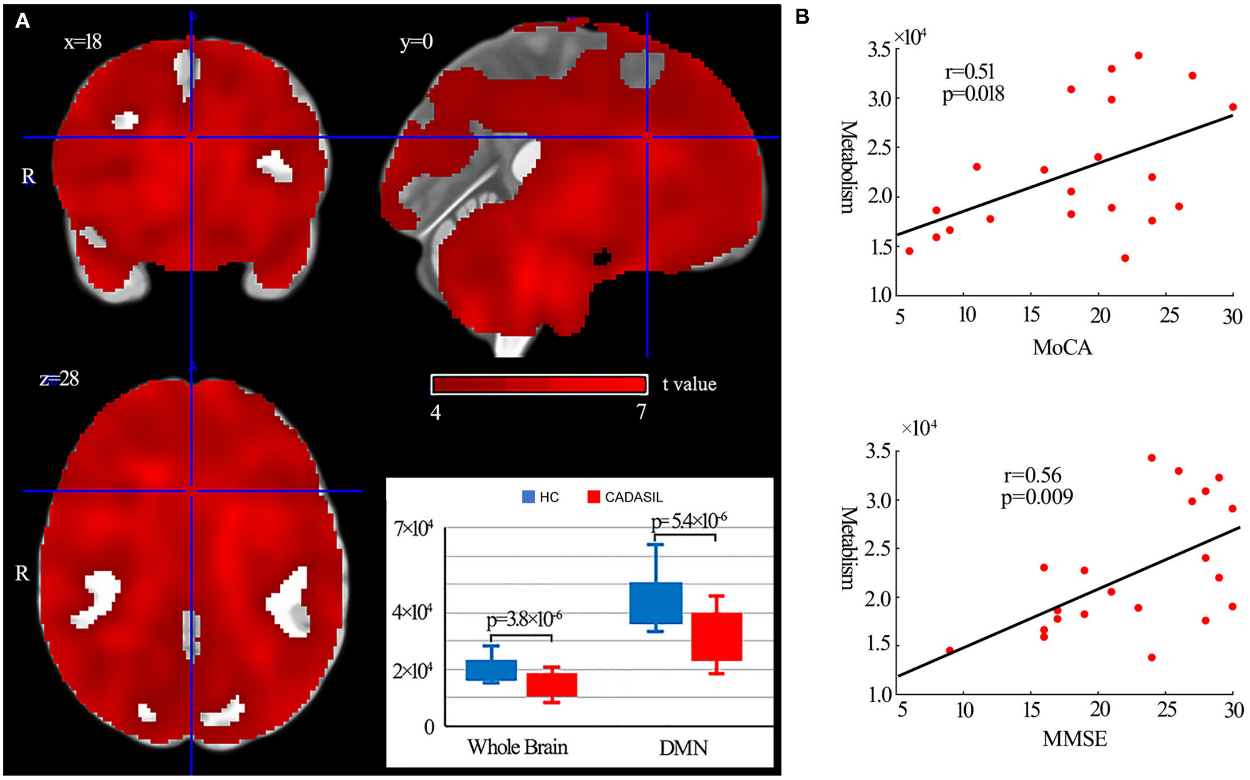

FIGURE 5 | Results of metabolism analysis in the DMN in CADASIL and control groups. **(A)** Metabolism alterations in the CADASIL group. **(B)** Correlations between metabolism across ROIs within the DMN and cognitive scores in the CADASIL group. Patients with CADASIL had decreased metabolism across the whole brain, including the ROIs within the DMN, compared with healthy controls. DMN, default mode network; CADASIL, cerebral autosomal dominant arteriopathy with subcortical infarcts and leukoencephalopathy; ROI, region of interest; HC, healthy control; MoCA, Montreal Cognitive Assessment; MMSE, Mini-Mental State Examination.

of different subjects on the results, most of the patients with CADASIL (17 of 21) had both PET and MRI modalities.

In the FC analysis, weakened interactions between the HF and MPFC (aMPFC and dMPFC) were detected in both the left and right DMN in patients with CADASIL. Further graph theory analysis of the FC matrixes showed that the changed FC resulted in decreased nodal efficiency and degree centrality of HF and dMPFC in the CADASIL group. These observations indicated that HF and dMPFC within the DMN in the patients with CADASIL have a poor capacity for information propagation, and reduced functional interactions with other regions within the network. Indeed, the HF plays a central node in memory function (29–31) and the dMPFC plays a key role in cognitive performance, including decision making, reward processing, mentalizing, memory, and conceptual processing (6, 31, 32). In addition, functional interactions between the HF and MPFC have been demonstrated to form an important neural circuit for spatial working memory (33–35). Furthermore, functional alterations in the HF or MPFC have been shown to be associated with cognitive deficits in other diseases (36–40). Therefore, our fMRI results demonstrated that the changed FC strength as a particular locus of dysfunction affected the nodal properties of the DMN, which may contribute to cognitive deficits in patients with CADASIL.

To examine structural changes within the DMN in CADASIL, differences between the two groups in GMV and NT of the ROIs were examined. Analyses of both the GMV and NT showed that patients with CADASIL had decreased GMV and NT in the ROI of HF. Further, decreased GMV was found in the left PHC and the bilateral HF in the CADASIL group. Both the PHC and HF are key regions for memory-related cognition (31, 41, 42). In addition, decreased GMV as well as changed FA in the two regions have been reported to be associated with cognitive deficits (15, 43–45). The significant associations between the GMV of HF and cognitive scores were consistent with the results of a previous MRI study in a large cohort (46). The HF belongs to the medial temporal subsystem of the DMN, which, through its interactions with the MPFC, plays a role in a wide range of associative or constructive aspects of mental simulation (6). Indeed, decreased interactions between the MPFC and medial temporal lobe including the hippocampus in resting-state fMRI data, and decreased GMV in the two regions, have been suggested to be associated with cognitive deficits, including working memory, social and emotional processing, and executive function deficits (39, 40, 43–45, 47, 48). The two regions have been suggested to play hub roles in DMN, which is a hub network for advanced cognition (18, 25). Cognitive performance relies on the coordination and collaboration of the activation and deactivation response; if one component fails, the whole system is jeopardized (49, 50). Therefore, the overlap between the results of fMRI and structural MRI indicates that changes of HF within the DMN may play important roles in the cognitive deficits seen in patients with CADASIL, and HF may be a potential brain marker. These MRI results corresponded with a previous DMN study in Fabry disease that showed functional DMN modifications and white matter damage were associated with cognitive deficits (51). However, contrary to the pattern of reduced DMN FC and decreased GMV found in our results, there were no significant differences in GMV, and increased DMN FC was observed in patients with Fabry disease. These differences between CADASIL and Fabry disease implied different pathogenic mechanisms underlying the two conditions, which can be further investigated. In marked contrast to the local variation in MRI results, ^{18}F-FDG PET showed that glucose metabolism of each ROI within the whole DMN, and even the whole brain, was decreased in the CADASIL group. Although there have been few PET studies in CADASIL, two independent PET studies reported hypometabolism across the whole brain in the resting state in patients with CADASIL (52, 53), which was consistent with our findings. Furthermore, similar to the results of MRI, metabolism was positively correlated with the cognitive scores in the CADASIL group. These correlations between characteristics of DMN revealed by different imaging modalities and cognitive scores suggested that interior relations may underlie the functional and structural changes within the DMN in patients with CADASIL. However, regional functional or structural disconnection can affect metabolism in other regions and vice versa. Further longitudinal multimodal imaging studies are required to determine the underlying mechanisms.

This study has some limitations, as only resting-state fMRI or PET data were collected, and it is, therefore, unclear whether there were altered patterns of DMN activity or connectivity during task performance in CADASIL, which had been demonstrated in other disorders or with aging (54–57).

CONCLUSIONS

In conclusion, altered functional and structural properties of the DMN were found in patients with CADASIL by multimodal imaging. These cognition-associated changes of HF within the DMN may play important roles in cognitive deficits in CADASIL.

DATA AVAILABILITY STATEMENT

The raw data supporting the conclusions of this article will be made available by the authors, without undue reservation.

ETHICS STATEMENT

The studies involving human participants were reviewed and approved by Independent Ethics Committee of Shanghai Ninth Hospital, Shanghai Jiao Tong University School of Medicine. The patients/participants provided their written informed consent to participate in this study.

AUTHOR CONTRIBUTIONS

JS, FH, and XD: study conception and design. PL, QH, JW, YQ, and YZ: acquisition of data. PL and SB: analysis and interpretation of data. All authors drafting the article and final approval of the version to be published.

FUNDING

This research was supported by grants from the National Natural Science Foundation of China (82071282 to JS), the Rare Disease Registration Platform of Shanghai Ninth People's Hospital, Shanghai Jiao Tong University School of Medicine (JYHJB08 to JS), and the Horizontal Research Project from Shanghai Ninth People's Hospital (JYHX2021001 to JS).

ACKNOWLEDGMENTS

We would like to gratefully thank the patients and healthy volunteers taking part in this study.

SUPPLEMENTARY MATERIAL

The Supplementary Material for this article can be found online at: https://www.frontiersin.org/articles/10.3389/fneur.2021.735033/full#supplementary-material

REFERENCES

1. Di Donato I, Bianchi S, De Stefano N, Dichgans M, Dotti MT, Duering M, et al. Cerebral autosomal dominant arteriopathy with subcortical infarcts and leukoencephalopathy (CADASIL) as a model of small vessel disease: update on clinical, diagnostic, and management aspects. *BMC Med.* (2017) 15:41. doi: 10.1186/s12916-017-0778-8
2. Davous P. CADASIL: a review with proposed diagnostic criteria. *Eur J Neurol.* (1998) 5:219–33. doi: 10.1046/j.1468-1331.1998.530219.x
3. Raichle ME, MacLeod AM, Snyder AZ, Power WJ, Gusnard DA, Shulman GL. A default mode of brain function. *Proc Natl Acad Sci USA.* (2001) 98:676–82. doi: 10.1073/pnas.98.2.676
4. Hu ML, Zong XF, Mann JJ, Zheng JJ, Liao YH, Li ZC, et al. a review of the functional and anatomical default mode network in schizophrenia. *Neurosci Bull.* (2017) 33:73–84. doi: 10.1007/s12264-016-0090-1
5. Menon V. Large-scale brain networks and psychopathology: a unifying triple network model. *Trends Cogn Sci.* (2011) 15:483–506. doi: 10.1016/j.tics.2011.08.003
6. Andrews-Hanna JR, Smallwood J, Spreng RN. The default network and self-generated thought: component processes, dynamic control, and clinical relevance. *Ann N Y Acad Sci.* (2014) 1316:29–52. doi: 10.1111/nyas.12360
7. Rodriguez-Cano E, Alonso-Lana S, Sarro S, Fernandez-Corcuera P, Goikolea JM, Vieta E, et al. Differential failure to deactivate the default mode network in unipolar and bipolar depression. *Bipolar Disord.* (2017) 19:386–95. doi: 10.1111/bdi.12517
8. Messina R, Filippi M, Goadsby PJ. Recent advances in headache neuroimaging. *Curr Opin Neurol.* (2018) 31:379–85. doi: 10.1097/WCO.0000000000000573
9. Guo X, Duan X, Suckling J, Chen H, Liao W, Cui Q, et al. Partially impaired functional connectivity states between right anterior insula and default mode network in autism spectrum disorder. *Hum Brain Mapp.* (2019) 40:1264–75. doi: 10.1002/hbm.24447
10. Zong X, Hu M, Pantazatos SP, Mann JJ, Wang G, Liao Y, et al. A dissociation in effects of risperidone monotherapy on functional and anatomical connectivity within the default mode network. *Schizophr Bull.* (2019) 45:1309–18. doi: 10.1093/schbul/sby175
11. Su J, Ban S, Wang M, Hua F, Wang L, Cheng X, et al. Reduced resting-state brain functional network connectivity and poor regional homogeneity in patients with CADASIL. *J Headache Pain.* (2019) 20:103. doi: 10.1186/s10194-019-1052-6
12. Su J, Wang M, Ban S, Wang L, Cheng X, Hua F, et al. Relationship between changes in resting-state spontaneous brain activity and cognitive impairment in patients with CADASIL. *J Headache Pain.* (2019) 20:36. doi: 10.1186/s10194-019-0982-3
13. Molko N, Pappata S, Mangin JF, Poupon F, LeBihan D, Bousser MG, et al. Monitoring disease progression in CADASIL with diffusion magnetic resonance imaging: a study with whole brain histogram analysis. *Stroke.* (2002) 33:2902–8. doi: 10.1161/01.STR.0000041681.25514.22
14. Viswanathan A, Godin O, Jouvent E, O'Sullivan M, Gschwendtner A, Peters N, et al. Impact of MRI markers in subcortical vascular dementia: a multi-modal analysis in CADASIL. *Neurobiol Aging.* (2010) 31:1629–36. doi: 10.1016/j.neurobiolaging.2008.09.001
15. Ban S, Wang H, Wang M, Xu S, Qin Z, Su J, et al. Diffuse tract damage in CADASIL is correlated with global cognitive impairment. *Eur Neurol.* (2019) 81:294–301. doi: 10.1159/000501612
16. Jang SH, Seo YS. Injuries of neural tracts in a patient with CADASIL: a diffusion tensor imaging study. *BMC Neurol.* (2015) 15:176. doi: 10.1186/s12883-015-0434-x
17. Su J, Huang Q, Ren S, Xie F, Zhai Y, Guan Y, et al. Altered brain glucose metabolism assessed by F-FDG PET imaging is associated with the cognitive impairment of CADASIL. *Neuroscience.* (2019) 417:35–44. doi: 10.1016/j.neuroscience.2019.07.048
18. Andrews-Hanna JR, Reidler JS, Sepulcre J, Poulin R, Buckner RL. Functional-anatomic fractionation of the brain's default network. *Neuron.* (2010) 65:550–62. doi: 10.1016/j.neuron.2010.02.005
19. Joutel A, Corpechot C, Ducros A, Vahedi K, Chabriat H, Mouton P, et al. Nothc3 mutations in CADASIL, a hereditary adult-onset condition causing stroke and dementia. *Nature.* (1996) 383:707–10. doi: 10.1038/383707a0
20. Mozen-Zadeh E, Bayanati S, Ziafat K, Rezaei F, Mesgarpour B, Akhondzadeh S. Vortioxetine as adjunctive therapy to risperidone for treatment of patients with chronic schizophrenia: a randomised, double-blind, placebo-controlled clinical trial. *Journal of Psychopharm.* (2020) 34:506–13. doi: 10.1177/0269881120909416
21. Zimmerman M, Thompson JS, Diehl JM, Balling C, Kiefer R. Is the DSM-5 Anxious Distress Specifier Interview a valid measure of anxiety in patients with generalized anxiety disorder: a comparison to the Hamilton Anxiety Scale. *Psychiatry Res.* (2020) 286:112859. doi: 10.1016/j.psychres.2020.112859
22. Chao-Gan Y, Yu-Feng Z. DPARSF: A MATLAB Toolbox for "Pipeline" data analysis of resting-state fMRI. *Front Syst Neurosci.* (2010) 4:13. doi: 10.3389/fnsys.2010.00013
23. Yan CG, Wang XD, Zuo XN, Zang YF. DPABI: Data processing & analysis for (Resting-State) brain imaging. *Neuroinformatics.* (2016) 14:339–51. doi: 10.1007/s12021-016-9299-4
24. Power JD, Barnes KA, Snyder AZ, Schlaggar BL, Petersen SE. Spurious but systematic correlations in functional connectivity MRI networks arise from subject motion. *Neuroimage.* (2012) 59:2142–54. doi: 10.1016/j.neuroimage.2011.10.018
25. Buckner RL, Andrews-Hanna JR, Schacter DL. The brain's default network: anatomy, function, and relevance to disease. *Ann N Y Acad Sci.* (2008) 1124:1–38. doi: 10.1196/annals.1440.011
26. Buckner RL, Sepulcre J, Talukdar T, Krienen FM, Liu H, Hedden T, et al. Cortical hubs revealed by intrinsic functional connectivity: mapping, assessment of stability, and relation to Alzheimer's disease. *J Neurosci.* (2009) 29:1860–73. doi: 10.1523/JNEUROSCI.5062-08.2009
27. Wang J, Wang X, Xia M, Liao X, Evans A, He Y. GRETNA: a graph theoretical network analysis toolbox for imaging connectomics. *Front Hum Neurosci.* (2015) 9:386. doi: 10.3389/fnhum.2015.00458
28. Pan H, Huang Q, Ban S, Du X, Su J, Liu J. Brain structural changes in CADASIL patients: a morphometric magnetic resonance imaging study. *Neurosci Lett.* (2020) 738:135388. doi: 10.1016/j.neulet.2020.135388
29. Eichenbaum H. Does the hippocampus preplay memories? *Nat Neurosci.* (2015) 18:1701–2. doi: 10.1038/nn.4180
30. Bird CM. The role of the hippocampus in recognition memory. *Cortex.* (2017) 93:155–65. doi: 10.1016/j.cortex.2017.05.016

31. Hainmueller T, Bartos M. Parallel emergence of stable and dynamic memory engrams in the hippocampus. *Nature.* (2018) 558:292–6. doi: 10.1038/s41586-018-0191-2
32. Lv C, Wang Q, Chen C, Xue G, He Q. Activation patterns of the dorsal medial prefrontal cortex and frontal pole predict individual differences in decision impulsivity. *Brain Imaging Behav*. (2020) 15:421–9. doi: 10.1007/s11682-020-00270-1
33. Benchenane K, Peyrache A, Khamassi M, Tierney PL, Gioanni Y, Battaglia FP, et al. Coherent theta oscillations and reorganization of spike timing in the hippocampal- prefrontal network upon learning. *Neuron.* (2010) 66:921–36. doi: 10.1016/j.neuron.2010.05.013
34. Hyman JM, Zilli EA, Paley AM, Hasselmo ME. Working memory performance correlates with prefrontal-hippocampal theta interactions but not with prefrontal neuron firing rates. *Front Integr Neurosci*. (2010) 4:2. doi: 10.3389/neuro.07.002.2010
35. Wirt RA, Hyman JM. integrating spatial working memory and remote memory: interactions between the medial prefrontal cortex and hippocampus. *Brain Sci.* (2017) 7:43. doi: 10.3390/brainsci7040043
36. Moran JM, Jolly E, Mitchell JP. Social-cognitive deficits in normal aging. *J Neurosci.* (2012) 32:5553–61. doi: 10.1523/JNEUROSCI.5511-11.2012
37. Pasquini L, Scherr M, Tahmasian M, Meng C, Myers NE, Ortner M, et al. Link between hippocampus' raised local and eased global intrinsic connectivity in AD. *Alzheimers Dement.* (2015) 11:475–84. doi: 10.1016/j.jalz.2014.02.007
38. Zhu L, Shu H, Liu D, Guo Q, Wang Z, Zhang Z. Apolipoprotein E epsilon4 specifically modulates the hippocampus functional connectivity network in patients with amnestic mild cognitive impairment. *Front Aging Neurosci.* (2018) 10:289. doi: 10.3389/fnagi.2018.00289
39. Tao J, Liu J, Chen X, Xia R, Li M, Huang M, et al. Mind-body exercise improves cognitive function and modulates the function and structure of the hippocampus and anterior cingulate cortex in patients with mild cognitive impairment. *Neuroimage Clin.* (2019) 23:101834. doi: 10.1016/j.nicl.2019.101834
40. Liang L, Zhao L, Wei Y, Mai W, Duan G, Su J, et al. Structural and functional hippocampal changes in subjective cognitive decline from the community. *Front Aging Neurosci.* (2020) 12:64. doi: 10.3389/fnagi.2020.00064
41. Brown TI, Stern CE. Contributions of medial temporal lobe and striatal memory systems to learning and retrieving overlapping spatial memories. *Cereb Cortex.* (2014) 24:1906–22. doi: 10.1093/cercor/bht041
42. Eichenbaum H. On the integration of space, time, and memory. *Neuron.* (2017) 95:1007–18. doi: 10.1016/j.neuron.2017.06.036
43. Chen B, Fan GG, Liu H, Wang S. Changes in anatomical and functional connectivity of Parkinson's disease patients according to cognitive status. *Eur J Radiol.* (2015) 84:1318–24. doi: 10.1016/j.ejrad.2015.04.014
44. Konishi K, McKenzie S, Etchamendy N, Roy S, Bohbot VD. Hippocampus-dependent spatial learning is associated with higher global cognition among healthy older adults. *Neuropsychologia.* (2017) 106:310–21. doi: 10.1016/j.neuropsychologia.2017.09.025
45. Jirsaraie RJ, Sheffield JM, Barch DM. Neural correlates of global and specific cognitive deficits in schizophrenia. *Schizophr Res.* (2018) 201:237–42. doi: 10.1016/j.schres.2018.06.017
46. O'Sullivan M, Ngo E, Viswanathan A, Jouvent E, Gschwendtner A, Saemann PG, et al. Hippocampal volume is an independent predictor of cognitive performance in CADASIL. *Neurobiol Aging.* (2009) 30:890–7. doi: 10.1016/j.neurobiolaging.2007.09.002
47. Wang L, Zang Y, He Y, Liang M, Zhang X, Tian L, et al. Changes in hippocampal connectivity in the early stages of Alzheimer's disease: evidence from resting state fMRI. *Neuroimage.* (2006) 31:496–504. doi: 10.1016/j.neuroimage.2005.12.033
48. Kennedy DP, Courchesne E. The intrinsic functional organization of the brain is altered in autism. *Neuroimage.* (2008) 39:1877–85. doi: 10.1016/j.neuroimage.2007.10.052
49. Wermke M, Sorg C, Wohlschlager AM, Drzezga A. A new integrative model of cerebral activation, deactivation and default mode function in Alzheimer's disease. *Eur J Nucl Med Mol Imaging.* (2008) 35(Suppl. 1):S12–24. doi: 10.1007/s00259-007-0698-5
50. Broyd SJ, Demanuele C, Debener S, Helps SK, James CJ, Sonuga-Barke EJ. Default-mode brain dysfunction in mental disorders: a systematic review. *Neurosci Biobehav Rev.* (2009) 33:279–96. doi: 10.1016/j.neubiorev.2008.09.002
51. Cocozza S, Pontillo G, Quarantelli M, Sacca F, Riccio E, Costabile T, et al. Default mode network modifications in Fabry disease: a resting-state fMRI study with structural correlations. *Hum Brain Mapp.* (2018) 39:1755–64. doi: 10.1002/hbm.23949
52. Tatsch K, Koch W, Linke R, Poepperl G, Peters N, Holtmannspoetter M, et al. Cortical hypometabolism and crossed cerebellar diaschisis suggest subcortically induced disconnection in CADASIL: An ^{18}F-FDG PET study. *J Nuclear Med.* (2003) 44:862–9.
53. Tuominen S, Miao Q, Kurki T, Tuisku S, Pöyhönen M, Kalimo H, et al. Positron emission tomography examination of cerebral blood flow and glucose metabolism in young CADASIL patients. *Stroke.* (2004) 35:1063–7. doi: 10.1161/01.STR.0000124124.69842.2d
54. Kennedy DP, Redcay E, Courchesne E. Falling to deactivate: Resting functional abnormalities in autism. *Proc Nat Acad Sci USA*. (2006) 103:8275–80. doi: 10.1073/pnas.0600674103
55. Andrews-Hanna JR, Snyder AZ, Vincent JL, Lustig C, Head D, Raichle ME, et al. Disruption of large-scale brain systems in advanced aging. *Neuron.* (2007) 56:924–35. doi: 10.1016/j.neuron.2007.10.038
56. Li LM, Violante IR, Leech R, Ross E, Hampshire A, Opitz A, et al. Brain state and polarity dependent modulation of brain networks by transcranial direct current stimulation. *Hum Brain Mapp.* (2018) 40:904–15. doi: 10.1002/hbm.24420
57. Hughes C, Faskowitz J, Cassidy BS, Sporns O, Krendl AC. Aging relates to a disproportionately weaker functional architecture of brain networks during rest and task states. *Neuroimage.* (2020) 209:116521. doi: 10.1016/j.neuroimage.2020.116521

Conflict of Interest: The authors declare that the research was conducted in the absence of any commercial or financial relationships that could be construed as a potential conflict of interest.

frontiers
in Neurology

ORIGINAL RESEARCH
published: 04 January 2022
doi: 10.3389/fneur.2021.789918

Associations Among Diffusion Tensor Image Along the Perivascular Space (DTI-ALPS), Enlarged Perivascular Space (ePVS), and Cognitive Functions in Asymptomatic Patients With Carotid Plaque

Hui Liu[1,2†], **Shuai Yang**[1,2†], **Wei He**[2,3], **Xiaojuan Liu**[2,4], **Shanyi Sun**[4], **Song Wang**[4], **Yang Wang**[2,5], **Xiaoliang Zhou**[2,4], **Tao Tang**[2,5,6], **Jian Xia**[2,4,6], **Yunhai Liu**[2,4,6] **and Qing Huang**[2,4,6]*

[1] Department of Radiology, Xiangya Hospital, Central South University, Changsha, China, [2] Hunan Clinical Research Center for Cerebrovascular Disease, Xiangya Hospital, Central South University, Changsha, China, [3] Department of Emergency, Xiangya Hospital, Central South University, Changsha, China, [4] Department of Neurology, Stroke Center, Xiangya Hospital, Central South University, Changsha, China, [5] Department of Integrated Traditional and Western, Xiangya Hospital, Central South University, Changsha, China, [6] National Clinical Research Center for Geriatric Disorders, Xiangya Hospital, Central South University, Changsha, China

Edited by:
Tao Liu,
Hainan General Hospital, China

Reviewed by:
Yunxia Li,
Huazhong University of Science and Technology, China
Swati Rane,
University of Washington, United States
Yuzhen Xu,
Tongji University, China

***Correspondence:**
Qing Huang
xyneuro@126.com

[†] These authors have contributed equally to this work and share first authorship

Specialty section:
This article was submitted to Applied Neuroimaging, a section of the journal Frontiers in Neurology

Received: *05 October 2021*
Accepted: *17 November 2021*
Published: *04 January 2022*

Citation:
Liu H, Yang S, He W, Liu X, Sun S, Wang S, Wang Y, Zhou X, Tang T, Xia J, Liu Y and Huang Q (2022) Associations Among Diffusion Tensor Image Along the Perivascular Space (DTI-ALPS), Enlarged Perivascular Space (ePVS), and Cognitive Functions in Asymptomatic Patients With Carotid Plaque. Front. Neurol. 12:789918. doi: 10.3389/fneur.2021.789918

Background and Aim: Carotid atherosclerosis (CAS) is a common pathogenesis of cerebrovascular disease closely related to stroke and silent cerebrovascular disease (SCD), while the insufficient brain perfusion mechanism cannot quite explain the mechanism. The purpose of this study was to utilize diffusion tensor image analysis along the perivascular space (DTI-ALPS) to evaluate the glymphatic system activity and correlated DTI-ALPS with enlarged perivascular spaces (ePVS), carotid intima-media thickening (CIMT), mini-mental state examination (MMSE), and serological indicator in individuals with carotid plaque.

Methods: Routine MRI and diffusion tensor images scan of the brain, carotid ultrasound, and blood examination were conducted on 74 individuals (52 carotid plaque subjects, 22 non-carotid plaque subjects), whose demographic and clinical characteristics were also recorded. DTI-ALPS index between patients with carotid plaque and normal controls were acquired and the correlations with other variables were analyzed.

Results: The values of ALPS-index in the carotid plaque group was significantly lower compared to normal controls (2.12 ± 0.39, 1.95 ± 0.28, respectively, $p = 0.034$). The ALPS-index was negatively correlated with the basal ganglia (BG)-ePVS score ($r = -0.242$, $p = 0.038$) while there was no significant difference in the centrum semiovale (CSO)-ePVS score. Further analysis showed that there are more high-grade ePVS in the BG compared to the carotid plaque group than in the non-carotid plaque group (84.6% vs. 40.9%, $p = 0.001$).

Conclusions: ALPS-index reflects the glymphatic system of the brain, which is associated with early high-risk cerebrovascular diseases. There may be damage in the function of the glymphatic system which induces the expansion of the perivascular space (PVS) in the BG in individuals with carotid plaque.

Keywords: carotid plaque, carotid atherosclerosis, glymphatic system, DTI-ALPS, ePVS

INTRODUCTION

Carotid atherosclerosis (CAS) can lead to stroke, vascular cognitive impairment, and silent cerebrovascular disease (SCD) (1, 2). CAS is a dynamic evolution which can be divided into three main stages, including carotid intima-media thickening (CIMT), carotid plaque formation, and carotid stenosis. CIMT or carotid plaque formation is a subclinical state of CAS. Studies have shown that the two states may be correlated with cognitive impairment in the high-risk asymptomatic individuals who develop stroke. However, the mechanism has not been fully explained (3, 4). A more recent study has shown that enlarged perivascular space (ePVS) is an early neuroimaging diagnostic biomarker of mild cognitive impairment (5). PVS refers to the normal fluid-filled anatomical structure surrounding the small blood vessels in the brain. Recent studies have shown that PVS is a drainage channel, that plays a critical role not only in the fluid exchange, but also in the removal of waste in the brain and in the maintenance of brain homeostasis and immune regulation. Studies have shown that ePVS increases with age and blood pressure, especially in intracranial atherosclerosis (6, 7). Some cross-sectional studies have also shown that the more ePVS, the more severe white matter hyperintensity (WMH) and lacunar infarction are found in the brain. Furthermore, ePVS are more common in patients with dementia than in the normal people. However, the formation mechanisms of ePVS is still unclear (8, 9).

A recently discovered waste drainage system in the central nervous system, the glymphatic system, has been found to play a significant role in the movement of the cerebrospinal fluid (CSF) along the PVS. This system not only promotes the clearance of accumulated soluble proteins, but also assists in the distribution of nutrients and neuromodulators in the brain. In this glymphatic loop circuit, CSF and interstitial fluid (ISF) interchange by the influx of CSF along the PVS (10–12). The impairment of the glymphatic system has been suggested to cause SCD, cerebral vascular atherosclerosis, neurodegenerative diseases, and other diseases related to aging (13–15).

There is also a growing interest in the potential imaging-marker for glymphatic activity [the diffusion tensor image analysis along the perivascular space (DTI-ALPS) parameter] using diffusion MRI imaging (16, 17). The DTI-ALPS showed promising results in its ability to differentiate glymphatic system impairment in patients with Parkinson's disease, idiopathic normal pressure hydrocephalus, and Type 2 diabetes mellitus (T2DM) (18–20). Previous studies also showed significant positive correlations between DTI-ALPS and cognitive functions assessed with the MMSE in individuals who are cognitively normal and who have Alzheimer's disease (21).

Carotid atherosclerosis, the causative roles of the cerebrovascular dysfunction mechanism, following abnormal vascular endothelial cell damage, lipid deposition, release of inflammatory factors, results in artery stenosis, or even occlusion. Not only stable plaque but also vulnerable plaque cause wide health problems and established risk factors for stroke and vascular cognitive decline in elderly people and in people with vascular Parkinsonism (3, 4, 22).

Previous studies of our group have shown that the cognitive score of patients with carotid artery vulnerable plaque were different from that of the group with stable carotid plaque, while there was no significant difference in the blood pressure and cerebral blood flow perfusion between the two groups (9, 21). By comparing different brain regions in the resting state, the functional MRI (fMRI) between the two groups and local consistency in patients with carotid artery vulnerable plaque were higher than in the stable plaque group, and functional connections in the default network were significantly enhanced. These studies indicated that the corresponding brain regions in the vulnerable plaque group are not in a state of low activity due to insufficient blood supply (6); thus we speculated that cognitive impairment might be induced not only based on hemodynamic changes, but might be due to a new mechanism that causes the changes. We hypothesize that subclinical state of CAS, the carotid plaque, which can be used to assess the vascular risk of asymptomatic individuals and SCD, may induce changes in the glymphatic function of the brain. Therefore, we aimed to evaluate the activities of glymphatic system in patients with DTI, who have carotid plaque, using the DTI-ALPS method. We also investigated whether there were any relationship between the DTI-ALPS-index and ePVS, as well as with MMSE score and the inflammation factors.

To our knowledge, up to now, there is no research to evaluate the function of the glymphatic system in patients with carotid plaque. This study is based on the hypothesis that the state of carotid artery plaque may not change the cerebral perfusion, but the cause of early white matter fiber damage may be caused by the impaired function of the glymphatic system in the group with carotid artery plaque.

MATERIALS AND METHODS

Study Subjects

From December 2015 to December 2017, all subjects were recruited from the project of Stroke Risk Screening and Prevention Project in Hunan Province. A total of 2,275 subjects were surveyed to collect the data regarding their gender, age, educational level, smoking status, and previous medical and medication history. Blood samples were also collected. Physical examination and neuropsychological tests (MMSE) were also performed by professional neurologists. All subjects came from the Wujialing community, Changsha city, Hunan province. About 1,251 of the subjects were at high-risk of stroke (participants who were over 40 years old and preserved

≥3 of traditional vascular risk factors were defined as high-risk of stroke) and completed carotid ultrasound examination. According to the inclusion and exclusion criteria, as defined in the following standard, a total of 107 subjects underwent brain multimodal MRI scanning (i.e., T1WI, T2WI, and FLAIR DTI sequences) (**Figure 1**). The inclusion criteria were as follows: (1) subjects aged from 40 to 75 years old; (2) right handedness; (3) single type of carotid plaque, hypoechoic, isoechoic, or hyperechoic; (4) carotid stenosis <50%; (5) no previous history of stroke or transient ischemic attack; (6) no other organic or mental diseases in the nervous system; (7) no serious heart disease, such as atrial fibrillation; (8) no drug dependence, and (9) education level >6 years. The exclusion criteria were as follows: (1) MRI contraindications; (2) with subclavian artery plaque; (3) have a history of carotid endarterectomy; (4) a history of nervous system trauma; (5) using hormone contraceptive or in pregnancy and lactation; (6) Fazekas scores >2. According to the inclusion and exclusion criteria, 107 subjects were scanned by carotid ultrasound and MRI (i.e., DTI-ALPS). In the end, 74 people (32 men and 42 women; mean of 60.8 years old; age range of 46–76 years) were enrolled in this study. All procedures were approved by the ethics committee of Xiangya Hospital of Central South University. Each participant had given a written informed consent.

Clinical Information at Baseline

Age, gender, hypertension, diabetes mellitus (DM), hyperlipidemia, body mass index (BMI), coronary heart disease, and smoking status were recorded. Hypertension was defined as the mean systolic blood pressure (SBP) ≥140 mmHg and/or mean diastolic blood pressure (DBP) ≥90 mmHg at two consecutive non-invasive measurements with an interval of at least 15 min, or with a medical history of oral medication with blood pressure lowering drugs. The DM was defined as fasting plasma glucose (FPG) ≥7.9 mmol/L, plasma glucose at any time of ≥11.0 mmol/L, or a history of oral medication of glucose lowering drugs. Hyperlipidemia was defined as low density lipoprotein ≥160 mg/dL, total cholesterol of ≥240 mg/dL, triglycerides of ≥150 mg/dL, or a history of oral medication with lipid-lowering drugs. Coronary heart disease was defined as the presence of clinical manifestations of myocardial infarction, angina, or ischemic heart failure as well as coronary atherosclerosis. Smoking was defined as smoking ≥10 cigarettes per day or smoking for >1 year. Each subject was scored with MMSE by the neurologist trained in professional neuropsychological scoring. MMSE total score was 30 points (23), where the score <27 was considered to be a cognitive impairment.

Blood Examination

Venous blood was collected from the antecubital vein in the morning before the participants ate breakfast, following an overnight fast of 12–14 h. All subjects underwent routine laboratory tests, including assays for FPG, serum total cholesterol, serum triglycerides (TG), serum low density lipoprotein cholesterol (LDL-c), high-sensitivity C-reactive protein (hsCRP), and interleukin-6 (IL-6).

Carotid Ultrasound Examination

Carotid ultrasound was carried out with an ultrasound scanner (5-MHz Sector Array transducer; iU22, Philips Ultrasound, Bothell, WA, USA) in both the right and left common carotid arteries (CCAs) and bifurcations by an experienced ultrasound doctor. The distance from the media-adventitia interface to the intima-lumen interface was defined as the intima-media thickness (IMT). A plaque was defined as a focal structure with an IMT >1.5 mm (24). The carotid intima-media thickness (CIMT) was defined as the average IMT and was calculated from the bilateral IMTs of the CCAs, carotid bulb, and bifurcations in a region free of plaque (25).

MRI Protocol

Magnetic resonance imaging was acquired by using a 3.0-T scanner (SIGNA HDX, GE, Boston, USA) with a 12-channel

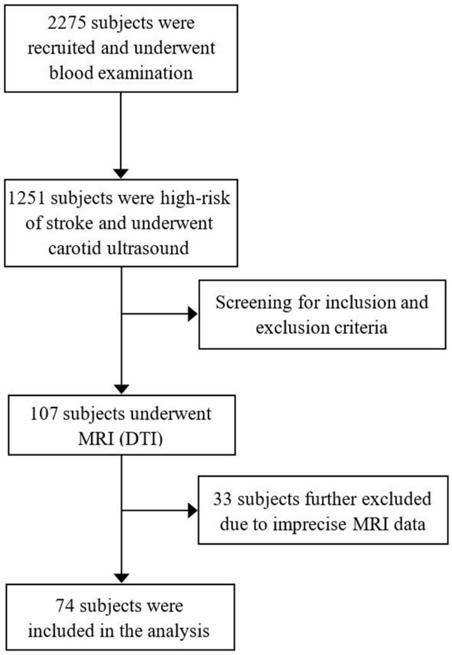

FIGURE 1 | Procedure for checking the enrolled population.

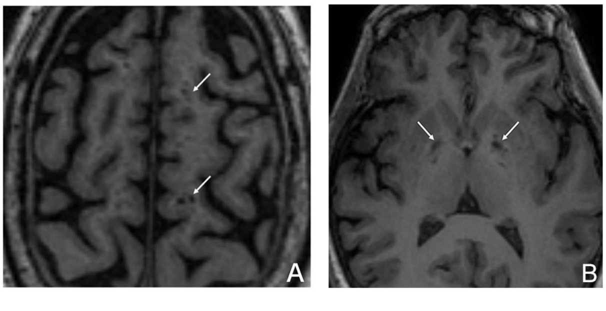

FIGURE 2 | ePVS in the centrum ovale **(A)** and in the basal ganglia **(B)** (arrow).

head coil. The MRI scanning included T1-weighted imaging (T1WI), T2-weighted imaging (T2WI), and fluid attenuated inversion recovery (FLAIR) sequences. Each scan involved a three-dimensional sagittal brain volume imaging (BRAVO) sequence with the following parameters: repetition time (TR) = 7.792 ms, echo time (TE) = 2.984 ms, flip angle = 7°, 188 slices, slice thickness = 1 mm, slice spacing = 1 mm, acquisition matrix = 256 × 256, voxel size = 111 mm^3. Diffusion tensor imaging (DTI) parameters are as follows: repetition time (TR) = 12,000 ms, echo time (TE) = 72.5 ms, acquisition matrix = 256 × 256, field of view (FOV) = 230 × 230 mm, slice thickness = 3 mm, flip angle = 90, gradient direction = 32, diffusion sensitivity coefficient (b) = 0.1000 s/mm^2. All the digital imaging and communications in medicine (DICOM) images are imported to RadiAnt DICOM Viewer.

Enlarged Perivascular Space Scoring

The layer with the largest number of ePVS was selected independently in the centrum ovale and in the BG. The ePVS was determined according to the following criteria: (1) depending on the image plane, the ePVS was spotty or strip-like, with clear and smooth borders and usually <3 mm in diameter; (2) the ePVS was consistent with the passage of the perforating vessels; and (3) on all MRI sequences, the density of the ePVS was equal to that of the CSF (**Figure 2**). The ePVS of each region was graded as follows: 0, none; 1, ≤10; 2, 11–20; 3, 21–40; 4, ≥40 (26, 27).

DTI-ALPS Processing and Image Analysis

The ALPS-index was calculated to assess the activity of the glymphatic system. We adopted the method for DTI-ALPS processing and measurement from the previous publication (7–9, 21, 28, 29). Diffusion metric images were generated by using dTV.II.13k+ software (Department of Biomedical Information Sciences, Graduate School of Information Sciences, Hiroshima City University) (30). The software creates computational images of the diffusion tensor including a color-coded fractional anisotropy (FA) map and diffusivity map, and in addition, has

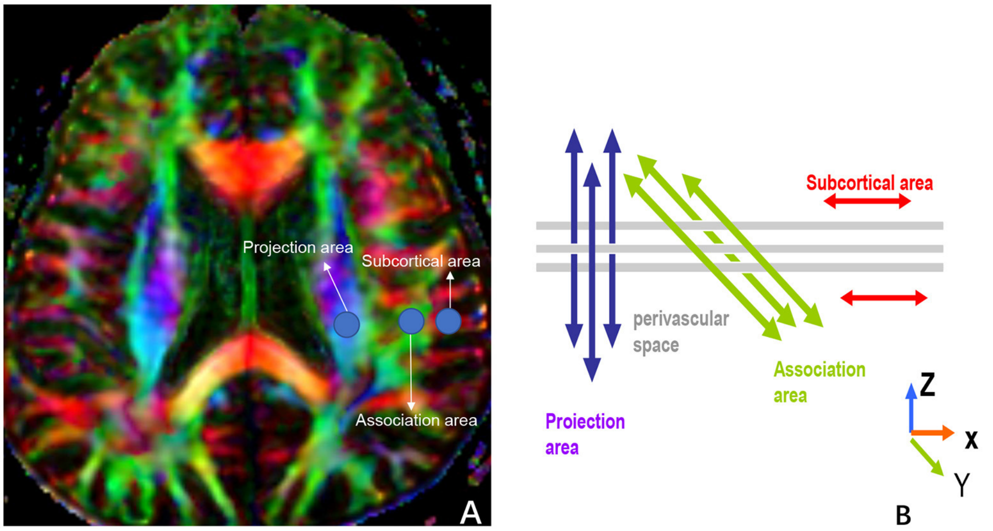

FIGURE 3 | (A) shows three ROIs that are placed in the area with projection fibers (projection area), association fibers (association area), and subcortical fibers (subcortical area) to measure diffusivities of the three directions (x, y, z). **(B)** indicates the relationship between the direction of the perivascular space (gray cylinders) and the directions of the fibers [**(B)** uses Figure 2b in the paper, "*Evaluation of glymphatic system activity with the diffusion MR technique: diffusion tensor image analysis along the perivascular space (DTI-ALPS) in Alzheimer's disease cases*" for reference].

TABLE 1 | Demographic and clinical characteristics of the patients.

	Non-carotid plaque group (*n* = 22)	Carotid plaque group (*n* = 52)	χ^2/*t* value/ *z* value	*P*-value
Age (year), mean (SD)	58.77 ± 71.16	61.65 ± 6.79	−1.641	0.105
Male sex no. (%)	11 (50)	11 (21)	0.582	0.445
Current cigarette smoker no. (%)	5 (22.7)	15 (28.8)	0.293	0.588
Hypertension no. (%)	15 (68.2)	32 (61.5)	0.294	0.587
Diabetes no. (%)	7 (31.8)	20 (38.5)	0.294	0.792
Hyperlipidemia no. (%)	21 (95.5)	41 (78.8)	3.139	0.587
Coronary heart disease no. (%)	0 (0)	2 (3.8)	0.870	0.351
BMI of 30 or more no. (%)	3 (13.6)	3 (5.8)	1.284	0.257

TABLE 2 | Imaging index and blood examination.

	Non-carotid plaque group ($n = 22$)	Carotid plaque group ($n = 52$)	χ^2/t value/ z value	P-value
ALPS-index	2.12 ± 0.39	1.95 ± 0.28	2.167	0.034*
BG-ePVS (high grade) no. (%)	9 (40.9)	44 (84.6)	14.529	0.000*
CSO-ePVS (high grade) no. (%)	6 (27.3)	7 (13.5)	2.036	0.154
BG-ePVS score	25.68	42.50	−3.127	0.001*
CSO-ePVS score	41.45	35.83	−1.085	0.278
Mean arterial pressure	102.86 ± 10.80	104.81 ± 11.64	−0.670	0.505
Pulse pressure	50.32 ± 9.54	50.94 ± 15.00	−0.18	0.858
IMT	0.72 ± 0.08	0.80 ± 0.10	−3.415	0.001*
MMSE	29.05 ± 1.00	28.58 ± 1.16	1.651	0.103
FPG	6.32 ± 0.26	6.25 ± 2.22	0.120	0.905
TG	2.31 ± 1.80	1.95 ± 0.81	1.204	0.232
LDL-c	3.34 ± 1.03	3.42 ± 0.88	−0.373	0.711
IL-6	72.27 ± 37.55	69.24 ± 26.88	0.392	0.696
hsCRP	1.54 ± 1.14	1.18 ± 1.26	−1.009	0.316

** represents that the difference is statistically significant.*

the capability to calculate diffusivity in the direction of the x-, y-, and z-axes on each image. We selected the slice at the level of the lateral ventricle body (**Figure 3A**). At this level, the direction of the perivascular space is perpendicular to the ventricle wall and is thus mostly in the right-left direction (x-axis) on the axial plane. The direction is also perpendicular to the direction of both the projection fibers (mostly in the z-axis) and the association fibers (mostly in the y-axis). Thus, the diffusivity along the x-axis at regions with projection/association fibers will at least partly represent the diffusivity along the perivascular space. A 5-mm diameter spherical region of interest (ROI) was placed in the area of the projection fibers, the area of the association fibers, and the area of the subcortical fibers in the left hemisphere (**Figure 3B**). For each area, we calculated the diffusivity in the directions of the x-, y-, and z-axes and the index value was derived from the ratio of the two diffusivity value sets that are perpendicular to the main fibers in the tissue: that is, the ratio of the average values of the x-axis diffusivity in the area of the projection fibers (Dxproj) and the x-axis diffusivity in the area of the association fibers (Dxassoc) to the average value of the y-axis diffusivity in the area of the projection fibers (Dyproj), and the z-axis diffusivity in the areas of the association fibers (Dzassoc), as shown below:

$$ALPS - index = mean(Dxproj,\ Dxassoc)/(mean\ (Dyproj,\ Dzassoc)$$

Repeatability Assessment

The ePVS SCORING and ALPS-index in our project were measured by two radiologists (with 10 and 15 years of experience in neuroimaging, respectively). Intra-class correlation coefficient (ICC) and Bland-Altman plot (mean difference, 95% limits of agreement) were used to assess the agreement between the two radiologists. For ePVS SCORING, The ICC coefficients of inter-class and intra-class were 0.93 and 0.91, respectively. For ALPS-index, The ICC coefficients of inter-class and intra-class were 0.86 and 0.81, respectively. Bland-Altman plot showed that only 1 plot is outside of the 95% conformance limitation for ePVS SCORING and ALPS-index, respectively. At last, the two radiologists compared their ratings and decided on the final data together.

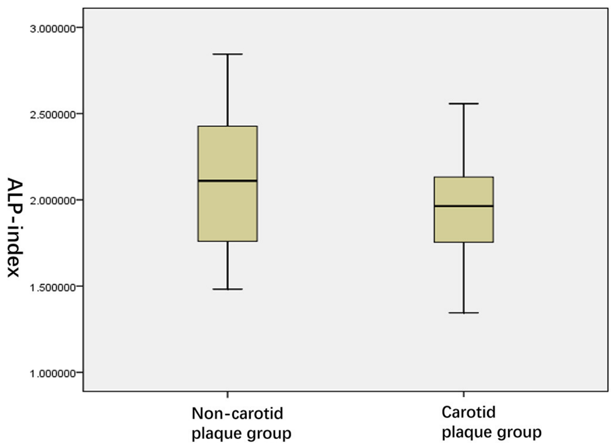

FIGURE 4 | ALPS-index in two groups.

Statistical Analysis

All the data were analyzed by SPSS 22.0 software, the continuous variables were expressed by mean value ± standard deviation. Shapiro Wilk (S–W) test was used to test the normally distributed variables, independent sample T-test was used for two sample variables, Mann–Whitney U-test for non-normal distribution variables, and χ^2 test for type variables. Pearson's correlation analysis was used to analyze the correlation between the two sample variables, and Spearman's correlation was used to analyze the rank variables. The value, $P < 0.05$ means that the difference is statistically significant. An independent samples t-test and Wilcoxon rank-sum test were used for evaluating

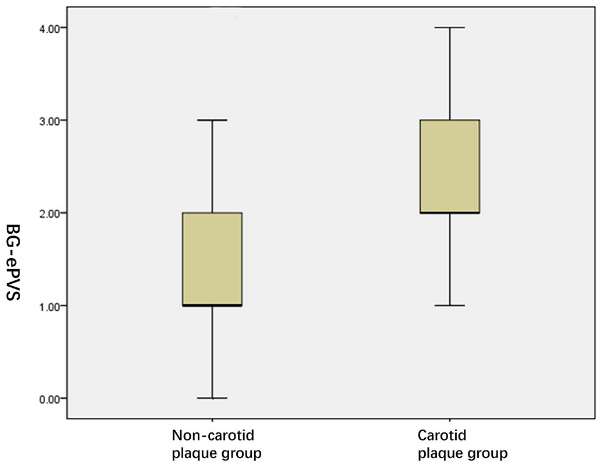

FIGURE 5 | High grade BG-ePVS in two groups.

patient characteristics. The statistical significance levels of the report were two-sided, with the statistical significance set at 0.05.

RESULTS

According to the carotid ultrasound examination, 74 people (32 men and 42 women; mean of 60.8 years old; age range of 66–76 years) were allocated into two groups (non-carotid plaque group and carotid plaque group). Demographic and clinical characteristics of the two groups are shown in **Table 1**.

Table 1 shows that 22 patients have no carotid plaque and 52 patients belonged to the carotid plaque group; there were no significant differences found between the groups in years, gender, diabetes, hypertension, hyperlipidemia, coronary heart disease, and BMI.

As shown in **Table 2**, between the two groups, ALPS-index values in carotid plaque group were significantly lower than that of the non-carotid plaque group ($P = 0.034$, **Figure 4**); conversely, IMT in carotid plaque group were significantly higher than that of non-carotid plaque group ($P = 0.034$, **Figure 4**). Moreover, compared with non-carotid plaque group, there were more ePVS high grade and score in BG ($P = 0.000$, **Figure 5**).

Table 3 demonstrates that ALPS-index was negatively correlated with IMT ($r = -0.262$, $P = 0.024$) and BG-ePVS score ($r = -0.242$, $P = 0.038$) whereas no significant correlation was found between ALPS-index and CSO-ePVS score ($r = -1.085$, $P = 0.278$). Meanwhile, ALPS-index showed no significant correlations with FPG, IL-6, hsCRP, cognitive function score (MMSE), pulse pressure, etc. ALPS-index has no significant correlations with gentle either, as shown in **Table 4**.

Table 5 shows that the effect of IMT and BG-ePVS score on ALPS-index was statistically significant ($P < 0.05$).

TABLE 3 | Relationship between ALPS-index and other variables.

	Variable	*R*	*P*-value
ALPS-index	BG-ePVS score	−0.242*	0.038*
	CSO-ePVS score	−0.006	0.960
	Systolic pressure	0.059	0.619
	Diastolic blood pressure	−0.003	0.983
	Pulse pressure	−0.078	0.509
	FPG	−0.071	0.549
	IMT	−0.262*	0.024*
	IL-6	0.003	0.980
	hsCRP	−0.054	0.645
	Cholesterol	0.091	0.443
	MMSE	0.041	0.730
	Age	0.084	0.477

** represents that the difference is statistically significant.*

TABLE 4 | ALPS-index in different sex groups.

	Male (*n* = 32)	Female (*n* = 42)	*t*-value	*P*-value
ALPS-index	1.97 ± 0.35	2.02 ± 0.30	−0.652	0.516

TABLE 5 | Multiple linear regression analysis of ALPS-index and other variables.

Variable	Coefficients	*t*-value	*P*-value
Age	0.040	0.345	0.731
MMSE	0.181	1.579	0.119
IMT	−0.249	−2.238	0.028*
BG-ePVS score	0.256	2.257	0.027*

** represents that the difference is statistically significant.*

DISCUSSION

There are growing interests in the fluid loop circuit in the glymphatic system and driving mechanisms for this interchange. Transmission in the PVS is believed to be an advection and it is generated by the cardio-cerebrovascular pulsatility in each cardiac cycle on the brain parenchyma (10, 11, 31, 32).

Recently, there are several studies that have made use of the ALPS-index to evaluate the function of cerebral glymphatic system (16, 18–20). We calculated the ALPS-index in order to clarify the activity of the glymphatic system in asymptomatic patients with carotid plaque and controls. There are several important findings in this study. First of all, we found that there were significant differences in ALPS-index between carotid plaque group and non-carotid plaque group using the means of the groups in an independent-sample *t*-test (**Table 2**). ALPS-index in the carotid plaque group is lower than that in the non-carotid plaque group. This finding is evident of the dysfunction of glymphatic system in the early and middle stages of CAS. This result is similar to the results of the research by Yang et al. on T2DM (20). Asymptomatic patients with carotid plaque might have a common feature of cortical atherothrombotic embolism and lacunar stroke; the coexisting macrovascular and microvascular damage can be induced by different degrees of carotid plaque, increasing the risk of developing small vessel disease with the enlargement of the PVS (11, 33). The results were consistent with those of previous studies, specifically those that showed that carotid atherosclerosis is associated with brain changes (34, 35). Our research supports the hypothesis that CAS is related to changes in the brain injury and the cardiovascular and cerebrovascular diseases can affect the brain structure and brain function (25, 36), which might be achieved by affecting the function of the glymphatic system. It is interesting to note that comparing asymptomatic patients with carotid plaque and non-carotid plaque, the correlation analysis showed that the ALPS-index was not a significant sign correlated with sex, age, MBP, FBS, TG, LDL-c, cognitive function score (MMSE), pulse pressure, history of hypertension, diabetes, and hypercholesterolemia.

Our study suggested that CAS is directly related to the glymphatic system of the brain (37). Previous studies have speculated that the expansion of the PVS is evident of intracranial imaging lesions caused by the dysfunction of the glymphatic system (38). However, so far, studies using the DTI-ALPS method assessing the function of the glymphatic system lack the analysis of ePVS of the study subjects. Our study examined the relationship between MRI-visible ePVS and DTI-ALPS. Further analysis showed that there are more high-grade ePVS in the BG area compared to the carotid plaque group with the non-carotid plaque group; the ALPS-index showed significantly negative correlation with the BG-ePVS score while there was no significant difference in the CSO-ePVS score. This result further confirms the hypothesis that CAS affects the function of the glymphatic system and causes PVS in BG-ePVS. We know that the expansion of PVS in the BG is related to blood pressure variability (39) and is related to deep perforating atherosclerosis (40). In our study, there was no significant difference in the variability of blood pressure or pulse pressure between the two groups. The reasons may be as follows: First, there may be other mechanisms involved in carotid plaque, deep perforating artery atherosclerosis, DTI-ALPS changes and glymphatic system dysfunction, BG-ePVS. Second, due to the deviation of the study, for example, the sample size is too small. The sample will be expanded for further research in the future, but it cannot be ignored that it is very likely that CAS itself can mediate the decrease in the clearance of the glymphatic system.

Clinical research data have proved that ePVS is a risk factor for cognitive impairment and dementia. The ePVS is an important risk factor for cognitive decline in Parkinson's disease and Alzheimer's disease, as well as vascular cognitive impairment and vascular dementia (21, 41–43). However, we found no significant difference between MMSE and BG-ePVS score and CSO-ePVS score. The correlation analysis also showed that the ALPS-index had no significant signs correlated with the MMSE score. The glymphatic system is a covert discovered waste drainage system in the brain parenchyma that involves the movement of the CSF along the PVS. This study further confirms that cognitive dysfunction is the result of abnormalities in the glymphatic system rather than the cause. In the early stages of atherosclerosis, MMSE score is not a sensitive indicator of vascular cognitive decline. Previous research findings of our studies (44), using ASL technique to evaluate mean CBF of the whole brain, found normal cognitive functions and CBF in two groups. In other words, the phenomenon that CAS affects the function of the glymphatic system and causes the perivascular space in the basal ganglia to expand might not be caused by decreased cerebral perfusion.

We investigated the associations between inflammation biomarkers and the ALPS-index changes in asymptomatic patients with carotid plaque and control group to further evaluate the pathophysiological mechanism of the glymphatic system in individuals with cerebral arteriosclerosis before stroke and dementia, such as serum IL-6 and hsCRP. But the results showed that the ALPS-index was not a significant sign correlated with inflammation biomarkers mentioned above, which may be attributed to the insufficiency of sample size or the possibility that systemic inflammation may not affect the CSF along the ePVS.

In this pilot study, limitations included small sample size in our single center; further multiple center studies with larger samples are needed to assist in improving the usefulness of the DTI-ALPS parameter and whether it may be a biomarker of neuro-fluid dynamics in the glymphatic system. Due to the limited sample size, we failed to further analyze other different types of CAS, such as carotid vulnerable/stable plaque and carotid stenosis. Second, the ROIs were placed manually, and the ePVS score were counted manually, which might be a subjective factor of our measurement. Third, the method of the ALPS-index is theoretically deductive. In future, even if the components of carotid plaque are related to the function of the glymphatic system, it is necessary to combine the high-resolution MRI of carotid and high-level DTI parameter analysis, which will be a very meaningful task.

CONCLUSION

In summary, the present study provides elementary evidence that carotid plaque may reduce DTI-ALPS, damage the function of the glymphatic system, and promote the expansion of the PVs in the BG. This study revealed novel interesting evidence indicating that alterations in ALPS-index are associated with early high-risk cerebrovascular diseases, helping to find out the actual damage of carotid plaque in patients with early dysfunction of intracranial neurovascular unit, looking for the early pathophysiological changes from the micro level.

DATA AVAILABILITY STATEMENT

The raw data supporting the conclusions of this article will be made available by the authors, without undue reservation.

ETHICS STATEMENT

The studies involving human participants were reviewed and approved by the Ethics Committee of Xiangya Hospital of

Central South University. The patients/participants provided their written informed consent to participate in this study.

AUTHOR CONTRIBUTIONS

HL and SY: data analysis, statistical analysis, and manuscript preparation. WH and XL: data acquisition and data analysis. SS and SW: data acquisition. YW, XZ, TT, JX, and YL: data acquisition and definition of intellectual content. QH: study concepts, study design, and definition of intellectual content, guarantor of integrity of the entire study. All authors contributed to the article and approved the submitted version.

FUNDING

The study was funded by the National Natural Science Foundation of China (Grant No. 81400978) and the Youth Program of National Natural Science Foundation of China (No. 81801365).

REFERENCES

1. Al Hazzouri AZ, Vittinghoff E, Sidney S, Reis JP, Jacobs Jr DR, Yaffe K. Intima-media thickness and cognitive function in stroke-free middle-aged adults: findings from the coronary artery risk development in young adults study. *Stroke.* (2015) 46:2190–6. doi: 10.1161/STROKEAHA.115.008994
2. Meschia JF, Bushnell C, Boden-Albala B, Braun LT, Bravata DM, Chaturvedi S, et al. Guidelines for the primary prevention of stroke: a statement for healthcare professionals from the American Heart Association/American Stroke Association. *Stroke.* (2014) 45:3754–832. doi: 10.1161/STR.0000000000000046
3. Zhong WJ, Cruickshanks KJ, Schubert CR, Acher CW, Carlsson CM, Klein BEK, et al. Carotid atherosclerosis and 10-year changes in cognitive function. *Atherosclerosis.* (2012) 224:506–10. doi: 10.1016/j.atherosclerosis.2012.07.024
4. Suemoto CK, Santos IS, Bittencourt MS, Pereira AC, Goulart AC, Rundek T, et al. Subclinical carotid artery atherosclerosis and performance on cognitive tests in middle-aged adults: baseline results from the ELSA-Brasil. *Atherosclerosis.* (2015) 243:510–5. doi: 10.1016/j.atherosclerosis.2015.10.008
5. Barisano G, Sheikh-Bahaei N, Law M, Toga AW, Sepehrband F. Body mass index, time of day and genetics affect perivascular spaces in the white matter. *J Cereb Blood Flow Metab.* (2021) 41:1563–78. doi: 10.1177/0271678X20972856
6. Wardlaw JM, Benveniste H, Nedergaard M, Zlokovic BV, Mestre H, Lee H, et al. Perivascular spaces in the brain: anatomy, physiology and pathology. *Nat Rev Neurol.* (2020) 16:137–53. doi: 10.1038/s41582-020-0312-z
7. Hilal S, Tan CS, Adams HHH, Habes M, Mok V, Venketasubramanian N, et al. Enlarged perivascular spaces and cognition: a meta-analysis of 5 population-based studies. *Neurology.* (2018) 91:E832–42. doi: 10.1212/WNL.0000000000006079
8. Xia YW, Shen Y, Wang Y, Yang LM, Wang YQ Li Y, et al. White matter hyperintensities associated with progression of cerebral small vessel disease: a 7-year Chinese urban community study. *Aging.* (2020) 12:8506–22. doi: 10.18632/aging.103154
9. Li XD, Shen MX, Jin Y, Jia SH, Zhou Z, Han ZL, et al. The effect of cerebral small vessel disease on the subtypes of mild cognitive impairment. *Front Psychiatry.* (2021) 12:685965. doi: 10.3389/fpsyt.2021.685965
10. Iliff JJ, Wang MH, Liao YH, Plogg BA, Peng WG, Gundersen GA, et al. A paravascular pathway facilitates CSF flow through the brain parenchyma and the clearance of interstitial solutes, including amyloid beta. *Sci. Transl. Med.* (2012) 4:147ra11. doi: 10.1126/scitranslmed.3003748
11. Mestre H, Tithof J, Du T, Song W, Peng WG, Sweeney AM, et al. Flow of cerebrospinal fluid is driven by arterial pulsations and is reduced in hypertension. *Nat Commun.* (2018) 9:4878. doi: 10.1038/s41467-018-07318-3
12. Nedergaard M, Goldman SA. Glymphatic failure as a final common pathway to dementia. *Science.* (2020) 370:50–6. doi: 10.1126/science.abb8739
13. Mestre H, Mori Y, Nedergaard M. The brain's glymphatic system: current controversies. *Trends Neurosci.* (2020) 43:458–66. doi: 10.1016/j.tins.2020.04.003
14. Plog BA, Nedergaard M. The glymphatic system in central nervous system health and disease: past, present, and future. *Annu Rev Pathol.* (2018) 13:379–94. doi: 10.1146/annurev-pathol-051217-111018
15. Rasmussen MK, Mestre H, Nedergaard M. The glymphatic pathway in neurological disorders. *Lancet Neurol.* (2018) 17:1016–24. doi: 10.1016/S1474-4422(18)30318-1
16. Taoka T, Masutani Y, Kawai H, Nakane T, Matsuoka K, Yasuno F, et al. Evaluation of glymphatic system activity with the diffusion MR technique: diffusion tensor image analysis along the perivascular space (DTI-ALPS) in Alzheimer's disease cases. *Jpn JRadiol.* (2017) 35:172–8. doi: 10.1007/s11604-017-0617-z
17. Zhou W, Shen B, Shen WQ, Chen H, Zheng YF, Fei JJ. Dysfunction of the glymphatic system might be related to iron deposition in the normal aging brain. *Front Aging Neurosci.* (2020) 12:559603. doi: 10.3389/fnagi.2020.559603
18. Chen HL, Chen PC, Lu CH, Tsai NW Yu CC, Chou KH, et al. Associations among cognitive functions, plasma DNA, and diffusion tensor image along the perivascular space (DTI-ALPS) in patients with Parkinson's disease. *Oxid Med Cell Longev.* (2021) 2021:4034509. doi: 10.1155/2021/4034509
19. Yokota H, Vijayasarathi A, Cekic M, Hirata Y, Linetsky M, Ho M, et al. Diagnostic performance of glymphatic system evaluation using diffusion tensor imaging in idiopathic normal pressure hydrocephalus and mimickers. *Curr Gerontol Geriatr Res.* (2019) 2019:5675014. doi: 10.1155/2019/5675014
20. Yang GW, Deng N, Liu Y, Gu YJ, Yao X. Evaluation of glymphatic system using diffusion MR technique in T2DM cases. *Front Hum Neurosci.* (2020) 14:300. doi: 10.3389/fnhum.2020.00300
21. Steward CE, Venkatraman VK, Lui E, Malpas CB, Ellis KA, Cyarto EV, et al. Assessment of the DTI-ALPS parameter along the perivascular space in older adults at risk of dementia. *J Neuroimaging.* (2021) 31:569–78. doi: 10.1111/jon.12837
22. Vizcarra JA, Lang AE, Sethi KD, Espay AJ. Vascular parkinsonism: deconstructing a syndrome. *Mov Disord.* (2015) 30:886–94. doi: 10.1002/mds.26263
23. Folstein MF, Folstein SE, McHugh PR. "Mini-mental state". A practical method for grading the cognitive state of patients for the clinician. *J Psychiatr Res.* (1975) 12:189–98. doi: 10.1016/0022-3956(75)90026-6
24. Pignoli P, Tremoli E, Poli A, Oreste P, Paoletti R. Intimal plus medial thickness of the arterial wall: a direct measurement with ultrasound imaging. *Circulation.* (1986) 74:1399–406. doi: 10.1161/01.CIR.74.6.1399
25. Liu LH, Huang Q, Yang S, Wen YB, He W, Liu H, et al. Micro-structural white matter abnormalities and cognitive impairment in asymptomatic carotid plaque patients: a DTI study using TBSS analysis. *Clin Neurol Neurosurg.* (2020) 197:106096. doi: 10.1016/j.clineuro.2020.106096
26. Potter GM, Doubal FN, Jackson CA, Chappell FM, Sudlow CL, Dennis MS, et al. Enlarged perivascular spaces and cerebral small vessel disease. *Int J Stroke.* (2015) 10:376–81. doi: 10.1111/ijs.12054
27. Potter GM, Chappell FM, Morris Z, Wardlaw JM. Cerebral perivascular spaces visible on magnetic resonance imaging: development of a qualitative rating scale and its observer reliability. *Cerebrovasc Dis.* (2015) 39:224–31. doi: 10.1159/000375153
28. Taoka T, Ito R, Nakamichi R, Kamagata K, Sakai M, Kawai H, et al. Reproducibility of diffusion tensor image analysis along the perivascular space (DTI-ALPS) for evaluating interstitial fluid diffusivity and glymphatic function: CHanges in Alps index on Multiple conditiON acquIsition eXperiment (CHAMONIX) study. *Jpn JRadiol.* (2021). doi: 10.1007/s11604-021-01187-5
29. Bae YJ, Choi BS, Kim JM, Choi JH, Cho SJ, Kim JH. Altered glymphatic system in idiopathic normal pressure hydrocephalus. *Parkinsonism Relat Disord.* (2021) 82:56–60. doi: 10.1016/j.parkreldis.2020.11.009

30. Masutani Y, Aoki S, Abe O, Hayashi N, Otomo K. MR diffusion tensor imaging: recent advance and new techniques for diffusion tensor visualization. *Eur J Radiol.* (2003) 46:53–66. doi: 10.1016/S0720-048X(02)00328-5
31. Iliff JJ, Wang MH, Zeppenfeld DM, Venkataraman A, Plog BA, Liao YH, et al. Cerebral arterial pulsation drives paravascular CSF-interstitial fluid exchange in the murine brain. *J Neurosci.* (2013) 33:18190–9. doi: 10.1523/JNEUROSCI.1592-13.2013
32. Rennels ML, Gregory TF, Blaumanis OR, Fujimoto K, Grady PA. Evidence for a 'paravascular' fluid circulation in the mammalian central nervous system, provided by the rapid distribution of tracer protein throughout the brain from the subarachnoid space. *Brain Res.* (1985) 326:47–63. doi: 10.1016/0006-8993(85)91383-6
33. Zhai FF, Yang M, Wei Y, Wang M, Gui Y, Han F, et al. Carotid atherosclerosis, dilation, and stiffness relate to cerebral small vessel disease. *Neurology.* (2020) 94:E1811–9. doi: 10.1212/WNL.0000000000009319
34. Wang H, Nie ZY, Liu M, Li RR, Huang LH, Lu Z, et al. Clinical characteristics of perivascular space and brain CT perfusion in stroke-free patients with intracranial and extracranial atherosclerosis of different extents. *Ann Transl Med.* (2020) 8:215. doi: 10.21037/atm.2020.01.35
35. Tuo J, Huang Q, He W, Yang S, Liu LH, Liu XJ, et al. Disrupted topological organization of functional networks in asymptomatic carotid plaque without significant carotid stenosis: a resting-state fMRI study. *Front Hum Neurosci.* (2021) 15:685763. doi: 10.3389/fnhum.2021.685763
36. Berman SE, Wang X, Mitchell CC, Kundu B, Jackson DC, Wilbrand SM, et al. The relationship between carotid artery plaque stability and white matter ischemic injury. *Neuroimage Clin.* (2015) 9:216–22. doi: 10.1016/j.nicl.2015.08.011
37. Wang JQ, Huang R, Tian S, Lin HY, Guo D, An K, et al. Elevated plasma level of D-dimer predicts the high risk of early cognitive impairment in type 2 diabetic patients as carotid artery plaques become vulnerable or get aggravated. *Curr Alzheimer Res.* (2019) 16:396–404. doi: 10.2174/1567205016666190321164741
38. Williamson W, Lewandowski AJ, Forkert ND, Griffanti L, Okell TW, Betts J, et al. Association of cardiovascular risk factors with MRI indices of cerebrovascular structure and function and white matter hyperintensities in young adults. *JAMA.* (2018) 320:665–73. doi: 10.1001/jama.2018.11498
39. Mestre H, Kostrikov S, Mehta RI, Nedergaard M. Perivascular spaces, glymphatic dysfunction, and small vessel disease. *Clin Sci.* (2017) 131:2257–74. doi: 10.1042/CS20160381
40. Yang SN, Yuan JL, Zhang XY, Fan HM Li Y, Yin JM, et al. Higher ambulatory systolic blood pressure independently associated with enlarged perivascular spaces in basal ganglia. *Neurol Res.* (2017) 39:787–94. doi: 10.1080/01616412.2017.1324552
41. Paradise M, Crawford JD, Lam BP, Wen W, Kochan NA, Makkar S, et al. Association of dilated perivascular spaces with cognitive decline and incident dementia. *Neurology.* (2021) 96:E1501–11. doi: 10.1212/WNL.0000000000011537
42. Fang Y, Gu LY, Tian J, Dai SB, Chen Y, Zheng R, et al. MRI-visible perivascular spaces are associated with cerebrospinal fluid biomarkers in Parkinson's disease. *Aging.* (2020) 12:25805–18. doi: 10.18632/aging.104200
43. Schneider ALC, Rawlings AM, Sharrett AR, Alonso A, Mosley TH, Hoogeveen RC, et al. High-sensitivity cardiac troponin T and cognitive function and dementia risk: the atherosclerosis risk in communities study. *Eur Heart J.* (2014) 35:1817–24. doi: 10.1093/eurheartj/ehu124
44. Huang Q, Liu YH, Liao WH, Yang S, Shen L, Tang T, et al. Disruption of regional brain activity and functional connectivity in patients with asymptomatic vulnerable carotid plaque. *Neurosci Lett.* (2020) 716:134634. doi: 10.1016/j.neulet.2019.134634

Conflict of Interest: The authors declare that the research was conducted in the absence of any commercial or financial relationships that could be construed as a potential conflict of interest.

frontiers in Neurology

REVIEW
published: 09 February 2022
doi: 10.3389/fneur.2022.843386

MRI Features of Stroke-Like Episodes in Mitochondrial Encephalomyopathy With Lactic Acidosis and Stroke-Like Episodes

Weiqin Cheng, Yuting Zhang† and Ling He*†*

Ministry of Education Key Laboratory of Child Development and Disorders, Chongqing Key Laboratory of Pediatrics, National Clinical Research Center for Child Health and Disorders, China International Science and Technology Cooperation Base of Child Development and Critical Disorders, Department of Radiology, Children's Hospital of Chongqing Medical University, Chongqing, China

OPEN ACCESS

Edited by:
Xiaofei Hu,
Army Medical University, China

Reviewed by:
Jiuquan Zhang,
Chongqing University, China
Zhongwei Qiao,
Fudan University, China

***Correspondence:**
Yuting Zhang
zhangyuting@cqmu.edu.cn
Ling He
doctorheling@yeah.net

†These authors have contributed equally to this work

Specialty section:
This article was submitted to Applied Neuroimaging, a section of the journal Frontiers in Neurology

Received: *25 December 2021*
Accepted: *18 January 2022*
Published: *09 February 2022*

Citation:
Cheng W, Zhang Y and He L (2022) MRI Features of Stroke-Like Episodes in Mitochondrial Encephalomyopathy With Lactic Acidosis and Stroke-Like Episodes. Front. Neurol. 13:843386. doi: 10.3389/fneur.2022.843386

Mitochondrial myopathy encephalopathy lactic acidosis and stroke-like episodes (MELAS) is an important cause of stroke-mimicking diseases that predominantly affect patients before 40 years of age. MELAS results from gene mutations in either mitochondrial DNA (mtDNA) or nuclear DNA (nDNA) responsible for the wide spectrum of clinical symptoms and imaging findings. Neurological manifestations can present with stroke-like episodes (the cardinal features of MELAS), epilepsy, cognitive and mental disorders, or recurrent headaches. Magnetic resonance imaging (MRI) is an important tool for detecting stroke-like lesions, accurate recognition of imaging findings is important in guiding clinical decision making in MELAS patients. With the development of neuroimaging technologies, MRI plays an increasingly important role in course monitoring and efficacy assessment of the disease. In this article, we provide an overview of the neuroimaging features and the application of novel MRI techniques in MELAS syndrome.

Keywords: mitochondrial myopathy, encephalopathy, lactic acidosis and stroke-like episodes (MELAS), stroke-like episodes, MRI, neuroimaging, application

INTRODUCTION

Mitochondrial encephalomyopathy with lactic acidosis and stroke-like episodes (MELAS) is a maternally inherited disorder caused by mitochondrial DNA (mtDNA) or nuclear DNA (nDNA) mutations in a diffuse multisystemic fashion. MELAS varies widely in the disease onset, symptoms, severity and prognosis. Its broad clinical presentation includes stroke-like episodes (SLEs), epilepsy, lactic acidemia, myopathy, hearing impairment, diabetes, cardiomyopathy and short stature (1, 2). The strong dependence of the central nervous system on oxidative metabolism predisposes to mitochondrial damage (3), and SLEs are the predominant features of MELAS (4). Typical neurological manifestations of SLEs are very similar to ischemic stroke in the acute phase. The diagnosis of MELAS is not difficult when the clinical and imaging findings are typical. However, due to the variability of the disease, diagnosis remains challenging and MELAS is easily misdiagnosed as cerebral infarction, viral encephalitis and other brain diseases, especially the first attack.

At present, with the wide application of new magnetic resonance imaging (MRI) techniques in the clinic, such as hydrogen proton magnetic resonance spectroscopy (1H-MRS), perfusion-weighted imaging (PWI) and arterial spin labeling (ASL), MRI has also become one of the effective methods for diagnosis of MELAS in addition to muscle biopsy and pathogenic gene testing. Clinicians have also gradually gained a deeper understanding of MELAS. In this paper, we review the conventional findings and the latest application of MRI in MELAS syndrome (**Table 1**).

CLINICAL AND PATHOPHYSIOLOGICAL FEATURES

MELAS is commonly associated with the m.3243A>G tRNALeu (UUR) mutation. Childhood and early adulthood are typically the age of onset with 65–76% of cases occurring at or before the age of 20, but disease onset can occur at any age (1, 4). Yatsuga et al. (5) found the juvenile of MELAS was associated with significantly higher mortality and a more rapid disease progression than the adult. Generally the earlier the clinical phenotypes appear, the severer the disease develops (6). SLEs, as one of the cardinal symptoms, classically present as acute hemianopia, hemiparesis, or cortical blindness. SLEs are usually recurrent and can lead to serious long-term consequences, such as neurodegeneration, cognitive impairment (7).

Energy deficiency can stimulate the proliferation of mitochondria of smooth muscle and small vascular endothelial cells at the same time. In MELAS, a variety of factors can lead to the lack of nitric oxide that can maintain the relaxation function of vascular smooth muscle. Both can cause microvascular blood perfusion damage, lead to stroke like attack and other complications (1). The basic neuropathological changes of MELAS were comprised of spongiform degeneration, neuronal cell loss, glial proliferation, and demyelination (8, 9).

At present, the diagnosis of MELAS is a comprehensive diagnostic criterion combining imaging findings, pathological examination, genetic testing, or muscle biopsy results with clinical manifestations. Among them, the discovery of pathogenic mutations in mtDNA or nDNA genes and typical pathological changes in mitochondrial myopathy by muscle biopsy is the "gold standard" for the diagnosis (10).

CONVENTIONAL IMAGING FEATURES

SLEs appear as stroke-like lesions (SLLs) on MRI. In acute SLEs, MRI findings include cortex swelling presenting with hyperintensity on T2WI and T2 FLAIR, named as "bright thickened cortical band" (**Figures 1A,B**). Part of cortical lesions show patchy or linear enhancement on T1-weighted postcontrast images (**Figure 1C**), due to local exudation or circulation disorders caused by the breakdown of the blood-brain barrier and increased regional cerebral blood flow in the affected areas (11). In the sub-acute phase, SLLs may develop gyriform hyperintensity on T1WI and hypointensity on T2WI/T2FLAIR ("black toenail sign") because of cortical laminar necrosis. Whitehead et al. (12) found that the black toenail sign was a common imaging feature in MELAS, and the extent of gyral necrosis correlated with disease duration. A recent study observed that a cortical linear cystic lesion was a characteristic MR finding in MELAS patients (13), and it was defined as showing a linear or dotted cerebrospinal fluid signal in the deep layer of the affected cortex, and an iso-intensity line covered its surface. In the chronic stage, the affected areas gradually evolve into cerebral encephalomalacia, gliosis, and atrophy over time (**Figure 1D**).

Typical SLLs in MELAS mainly distribute in the cerebral cortex and subcortex white matter with a predilection to the posterior brain, although the deep gray matter such as the thalamus may also be affected probably reflecting its high metabolic demand (14). Lesions in the parietal and occipital lobe were twice as many as those in the temporal lobe and 4 times

TABLE 1 | The neuroimaging features of stroke-like lesions in MRI.

	Acute stage	No-acute stage	
		Sub-acute phase	**Chronic stage**
T1WI	Hypointensity	Hyperintensity	Hypointensity
T2WI	Hyperintensity (bright thickened cortical band)	Hypointensity (black toenail sign)	Hyperintensity
T2FLAIR	Hyperintensity	Hypo/hyperintensity	
T1WI C+	Patchy/linear enhancement	No enhancement	
DWI	Hyperintensity	Normal	
ADC	Hypo/iso/hyperintensity	Normal	
MRS	An increased lactate peak	An increased lactate peak	
PWI/ASL	Hyperperfusion	Hypoperfusion	
MRA	Major vessels dilation/ normal/stenosis	Normal	
Characteristics	Lesions mainly distribute in the cerebral cortex and subcortex white matter with a predilection to the posterior brain, not limited to arterial territories and migratory		

ADC, apparent diffusion coefficient; ASL, arterial spin labeling; DWI, diffusion-weighted imaging; MRA, magnetic resonance angiography; MRI, magnetic resonance imaging; MRS, magnetic resonance spectroscopy; PWI, perfusion-weighted imaging.

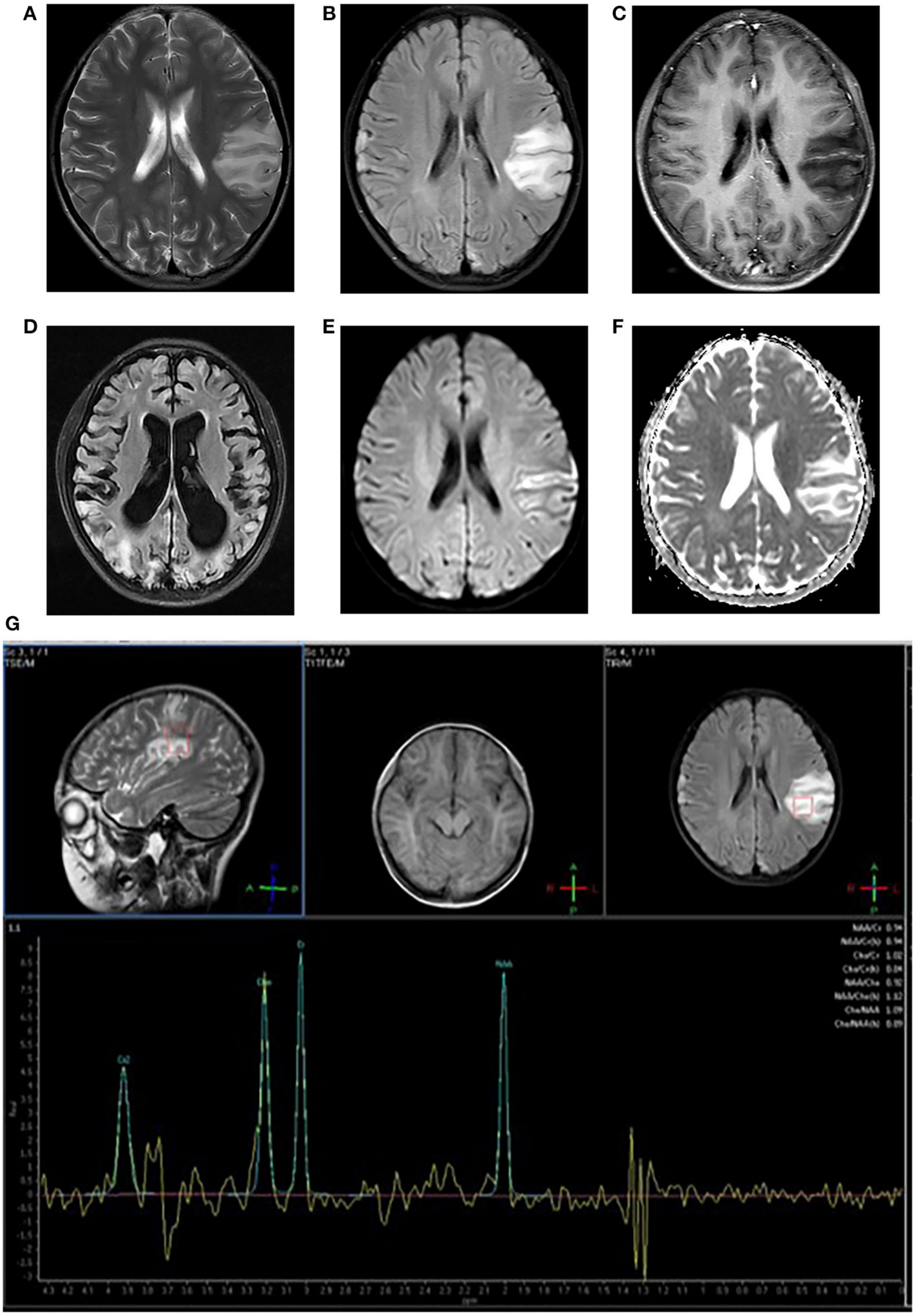

FIGURE 1 | Neuroimaging for an 8-year-old girl with MELAS who presented with intermittent fever, vomiting, convulsions. **(A,B)** Axial T2WI and T2FLAIR imaging reveal multiple hyperintensities in bilateral frontal and parietal cortex and subcortical white matter, especially in the left side; **(C)** Axial post-contrast T1WI imaging reveals linear enhancement of the left lesions; **(D)** T2FLAIR image 3 years later demonstrates new migrating lesions of both cerebral hemispheres along with old lesions, accompanied by evolving encephalomalacia, atrophy; **(E)** DWI imaging demonstrates hyperintensities in gyriform pattern in the lesion areas; **(F)** ADC sequence shows iso/hyperintensities corresponding to DWI lesions; **(G)** MRS imaging shows decreased NAA/Cho ratio and a large lactate peak.

as many as those in the frontal lobe (15). Tschampa et al. (16) reported that deep gray matter changes presented in the majority of m.3243A>G mutation carriers lacking SLEs. Cortical lesions are typically multiple and asymmetrical; however, more and more symmetric cases have been recognized (17, 18), Bhatia et al. (18) thought highly specific cortical symmetry should also raise the possibility of MELAS. SLLs frequently spread to the cortex of adjacent gyri in a migratory fashion over time, resulting in large regions of cortical involvement that are not limited to vascular territories (4, 15, 19). The migratory, increasing and decreasing pattern of SLLs on imaging is the main feature of MELAS.

FUNTIONAL MRI FINDINGS

Diffusion-Weighted Imaging and Apparent Diffusion Coefficient

Stroke-like lesions (SLLs) always present high signals on DWI (**Figure 1E**). Earlier reports suggested that the ADC value of SLLs was normal or increased (reflecting vasogenic edema) (20, 21), but now most studies have found that the ADC signals alternately change or mix in different periods (18, 22–24) (**Figure 1F**). Stoquart-Elsankari et al. (24) speculated that the changes in ADC might be related to the different levels of impairment of mitochondrial energy transport, correlated with cellular dysfunction. Moderate cellular dysfunction with vasogenic edema results from mild energy failure, and irreversible cellular failure responsible for cytotoxic edema is caused by severe energy failure. Besides, Xu et al. (25) reported a pattern of acute SLLs that DWI hyperintensity with decreased ADC along cortical area and increased ADC in most affected subcortical white matter. After the acute phase, the ADC value can return to normal.

1H-MRS

MELAS is characterized by an increased lactate peak in the lesion area, accompanied by a decreased N-acetylaspartate peak on 1H-MRS (**Figure 1G**). However, the characters are not specific and could also be found in other diseases, such as infarction. A lactate peak on MRS reflects anaerobic metabolism. Some reports have shown that a lactate peak even occurs in the normal-appearing region (brain parenchyma or cerebrospinal fluid area) on MRS (26, 27), which is of greater clinical significance for the disease. However, lactate signal could only be detected in normal cerebrospinal fluid in about one-third of patients (28).

Abe et al. (29) found that a patient 48 h after SLEs, a lactate peak on MRS could be seen much before the changes in DWI sequence, suggesting that MRS may have the predictive ability in displaying early lesions. Previous studies indicated that MRS might be more sensitive for detecting MELAS-associated preclinical abnormalities compared to conventional MRI (30, 31). Moreover, the lactate level varies at different stages of the disease. The lactate peak was bigger during onset than in intermission (30). Lactate in the lateral ventricles increased over time, and high lactate was associated with increased mortality (32). Weiduschat et al. (33) reported that lactate and total choline levels were reliable biomarkers for predicting the risk of individual A3243G mutation carriers to develop the MELAS. In addition, a recent study demonstrated the lactate peaks and ratios of N-acetylaspartate to choline were significantly improved that corresponded with clinical improvement after L-arginine therapy (34). To sum up, MRS may be a useful imaging biomarker for early diagnosis, course monitoring, and efficacy evaluation of MELAS.

PWI and ASL

Both PWI and ASL can reflect microscopic hemodynamic information of the brain and evaluate cerebral perfusion. And as a non-invasive technique, ASL provides new dimensions in the evaluation of cerebral perfusion. The general trend is hyperperfusion in the acute stage and hypoperfusion in the chronic phase of SLEs (35–38). Hyperperfusion might be caused by dilation of cerebral arteries and increased microvascular permeability in the lesion areas (39), and hypoperfusion could be associated with cerebral cytotoxic edema, cortical atrophy, and gliosis (40). Li et al. (41) identified focal hyperperfusion as an imaging hallmark in acute encephalopathy of MELAS. In addition, regional hyperperfusion was observed on ASL in the preclinical phase 3–5 months before the clinical onset of SLEs (40), similar results were also reported in two other teams (41, 42). These reports indicate that ASL has the potential for detecting latent SLLs and predicting the emergence of SLEs. Meanwhile, Rodan et al. (43) found that MELAS disease severity and mutation load were negatively correlated with interictal cerebrovascular reactivity and directly correlated with frontal cerebral blood flow on ASL, suggesting that these metrics could be used as non-invasive prognostic markers to stratify risk for SLEs.

Magnetic Resonance Angiography

MRA has not been routinely performed in MELAS in the past, because major cerebral vessels were considered to be the target of mitochondrial metabolism defects in these patients. However, more and more studies have found major cerebral vessels dilation (39, 44, 45) or stenosis (46, 47) on MRA in MELAS in the acute and chronic stages of the disease. Gramegna et al. (48) found that the proportion of cerebral major vessels dilation and stenosis was 40 and 19%, respectively, on MRA, and the middle cerebral artery was the most commonly involved. Among them, 88% of dilation was related to the acute SLEs, whereas only a few cases of stenosis were symptomatic for SLEs. Most alterations related to SLEs in the major cerebral vessels could be normalized completely after resolution of symptoms. These studies demonstrated that MRA could detect alterations in major cerebral vessels in MELAS patients. Furthermore, vasodilation by MRA had occasionally been detected in patients up to 3–5 months before the onset of SLEs (40, 44), indicating that MRA might be used as a possible tool for future onset of SLEs in selected patients. In a word, the macrovascular changes on MRA and underlying pathophysiology mechanism of MELAS need to be further investigated in large cohort studies.

Other Functional MRI

There are also a few reports on the application of other new MRI techniques in MELAS. Virtanen et al. (49) observed in patients that mild microstructural damage of white matter tracts with loss of directional organization and reduced brain volumes with diffusion tensor imaging. Mineral (calcium or iron) deposition in basal ganglia of MELAS could be demonstrated by susceptibility-weighted imaging (50). Furthermore, studies on monitoring the disease status and evaluating drug efficacy by blood oxygenation level dependent function magnetic resonance imaging (bold-fMRI) have also been reported. Wang et al. (51) reported that MELAS patients, particularly those at the acute stage, exhibited topological reorganization of the whole-brain functional network based on resting-state fMRI. They also found that MELAS patients spent more time in a state with weaker connectivity and less time in states with stronger connectivity, and patients at the acute stage exhibited that global efficiency was markedly increased while local efficiency was decreased, compared to the controls and the patients at the chronic period (52). Additionally, Rodan et al. (53) demonstrated that MELAS patients' fMRI activation in response to visual cortex stimulus was significantly increased in primary visual striate cortex V1 and extrastriate regions V2 to V5 after L-arginine treatment with task fMRI.

DIFFERENTIAL DIAGNOSIS

The diversity and complexity of clinical and radiological manifestations in patients with MELAS pose a challenge to the diagnosis. In imaging, the unilateral isolated cortical lesion is easily misdiagnosed as acute cerebral infarction, viral encephalitis, and low-grade glioma, etc., especially infarction. In acute SLLs, MRI differentiation of MELAS from other diseases mainly includes the following points: (1) lesions first involve the cortex and less deep white matter; (2) lesions commonly affect occipital and parietal lobes; (3) lesions are not limited to arterial territories and migrate over time; (4) a lactate peak appears in lesions, even in the normal-appearing region (brain parenchyma or cerebrospinal fluid area) on MRS, which is one of the indicators of diagnostic specificity; (5) lesions always present as hyperperfusion on PWI/ASL.

For acute ischemic stroke, patients are often accompanied by risk factors such as hypertension, diabetes, and hyperlipemia. The lesions of infarction are confined to the boundary of the vascular territories, and present hypoperfusion on PWI/ASL, effectively distinguishing it from MELAS. Chong et al. (54) discovered a new scoring criterion based on the vessel flow void sign and hyperintense vessel sign in T2FLAIR images was helpful to differentiate infarction from MELAS on conventional MRI, with sensitivity and specificity of 92.3 and 85.0%, respectively. Furthermore, cortical linear cystic lesions might help to distinguish the two diseases (13).

For viral encephalitis, patients may have a high fever, meningeal irritation with lymphocytic pleocytosis, and an elevated protein level on cerebrospinal fluid. On imaging, viral encephalitis usually involves the limbic system, such as the frontal orbital gyrus, hippocampus and temporal lobe, rather than the parietal, and temporal lobe. The diffusion restriction uninvolved the entire lesions might be an important differential diagnostic sign between them (55). Functional MRI techniques are also valuable for accurate diagnosis.

For low-grade glioma, patients often present with chronic onset. On imaging, the conventional MRI findings of low-grade glioma are sometimes similar to the single SLL, and MRS can help distinguish them. On MRS, low-grade glioma often presents with elevated choline peak and decreased N-acetylaspartate peak, but usually without an increased lactic acid peak, which is a characteristic of SLL.

CONCLUSIONS

In conclusion, MELAS is a rare progressive neurodegenerative disorder involving multi-organs. MELAS has obvious clinical heterogeneity as the clinical manifestations of different patients or the same patients vary in different phases, which makes the diagnosis a little arduous sometimes. However, neuroimaging of MRI demonstrates characteristic patterns of MELAS patients, including cortex swelling with a predilection for the posterior brain regions, not limited to arterial territories, hyperperfusion, and elevated lactate peak in both affected and non-affected regions, which may be found concurrently with encephalomalacia and atrophy. The recognition of these imaging features signs facilitates screening and early diagnosis of MELAS. Meanwhile, the novel MRI approaches have provided new dimensions in the evaluation of the disease. Multimodal MRI has shown great potential in risk stratification, course monitoring, progression, and efficacy evaluation of MELAS, and also provides a reference for understanding its neuropathological mechanism.

AUTHOR CONTRIBUTIONS

WC collected the data and wrote the manuscript. YZ and LH performed roles of the conception of this review and substantively revised it. All authors contributed to the article and approved the final manuscript.

FUNDING

This study was supported by grants from the joint Chongqing Health Commission and Chongqing Science and Technology Bureau Medical Research Project (No: 2020FYYX128) and Chongqing Science and Technology Bureau, Technology Foresight and System Innovation Project (No: cstc2021jsyj-yzysbAX0019).

REFERENCES

1. El-Hattab A, Adesina A, Jones J, Scaglia F. MELAS syndrome: clinical manifestations, pathogenesis, treatment options. *Mol Genet Metab.* (2015) 116:4–12. doi: 10.1016/j.ymgme.2015.06.004
2. Hsu YR, Yogasundaram H, Parajuli N, Valtuille L, Sergi C, Oudit GY. MELAS syndrome and cardiomyopathy: linking mitochondrial function to heart failure pathogenesis. *Heart Fail Rev.* (2016) 21:103–16. doi: 10.1007/s10741-015-9524-5
3. DiMauro S, Schon EA. Mitochondrial disorders in the nervous system. *Annu Rev Neurosci.* (2008) 31:91–123. doi: 10.1146/annurev.neuro.30.051606.094302
4. Wang YX, Le WD. Progress in diagnosing mitochondrial myopathy, encephalopathy, lactic acidosis, stroke-like episodes.

Chin Med J. (2015) 128:1820–5. doi: 10.4103/0366-6999.159360

5. Yatsuga S, Povalko N, Nishioka J, Katayama K, Kakimoto N, Matsuishi T, et al. MELAS: a nationwide prospective cohort study of 96 patients in Japan. *Biochim Biophys Acta.* (2012) 1820:619–24. doi: 10.1016/j.bbagen.2011.03.015
6. Ahmed ST, Craven L, Russell OM, Turnbull DM, Vincent AE. Diagnosis and treatment of mitochondrial myopathies. *Neurotherapeutics.* (2018) 15:943–53. doi: 10.1007/s13311-018-00674-4
7. Pizzamiglio C, Bugiardini E, Macken WL, Woodward CE, Hanna MG, Pitceathly RDS. Mitochondrial strokes: diagnostic challenges and chameleons. *Genes.* (2021) 12:1643. doi: 10.3390/genes12101643
8. Alston CL, Rocha MC, Lax NZ, Turnbull DM, Taylor RW. The genetics and pathology of mitochondrial disease. *J Pathol.* (2017) 241:236–50. doi: 10.1002/path.4809
9. Chen H, Hu Q, Raza HK, Chansysouphanthong T, Singh S, Rai P, et al. An analysis of the clinical and imaging features of mitochondrial encephalopathy, lactic acidosis, and stroke-like episodes (MELAS). *Somatosens Mot Res.* (2020) 37:45–9. doi: 10.1080/08990220.2020.1720636
10. Rare Diseases Branch of Beijing Medical Association, NDoNBoBMA, China national research collaborative group on mitochondrial disease. Chinese expert consensus on diagnosis and treatment of mitochondrial encephalomyopathy with lactic acidosis and stroke-like episodes. *Chin J Neurol.* (2020) 53:171–8. doi: 10.3760/cma.j.issn.1006-7876.2020.03.003
11. Yonemura K, Hasegawa Y, Kimura K, Minematsu K, Yamaguchi T. Diffusion-weighted MR imaging in a case of mitochondrial myopathy, encephalopathy, lactic acidosis, strokelike episodes. *AJNR Am J Neuroradiol.* (2001) 22:269–72.
12. Whitehead M, Wien M, Lee B, Bass N, Gropman A. Black toenail sign in MELAS syndrome. *Pediatr Neurol.* (2017) 75:61–5. doi: 10.1016/j.pediatrneurol.2017.06.017
13. Ishigaki H, Sato N, Kimura Y, Takeshita E, Komaki H, Chiba E, et al. Linear cortical cystic lesions: characteristic MR findings in MELAS patients. *Brain Dev.* (2021) 43:931–8. doi: 10.1016/j.braindev.2021.05.002
14. Goodfellow JA, Dani K, Stewart W, Santosh C, McLean J, Mulhern S, et al. Mitochondrial myopathy, encephalopathy, lactic acidosis and stroke-like episodes: an important cause of stroke in young people. *Postgrad Med J.* (2012) 88:326–34. doi: 10.1136/postgradmedj-2011-130326
15. Iizuka T, Sakai F. Pathogenesis of stroke-like episodes in MELAS: analysis of neurovascular cellular mechanisms. *Curr Neurovasc Res.* (2005) 2:29–45. doi: 10.2174/1567202052773544
16. Tschampa HJ, Urbach H, Greschus S, Kunz WS, Kornblum C. Neuroimaging characteristics in mitochondrial encephalopathies associated with the m. 3243A>G MTTL1 mutation. *J Neurol.* (2013) 260:1071–80. doi: 10.1007/s00415-012-6763-4
17. Pittet M, Idan R, Kern I, Guinand N, Van H, Toso S, et al. Acute cortical deafness in a child with MELAS syndrome. *J Inherit Metab Dis.* (2016) 39:465–6. doi: 10.1007/s10545-016-9929-x
18. Bhatia KD, Krishnan P, Kortman H, Klostranec J, Krings T. Acute cortical lesions in MELAS syndrome: anatomic distribution, symmetry, and evolution. *AJNR Am J Neuroradiol.* (2020) 41:167–73. doi: 10.3174/ajnr.A6325
19. Hongo Y, Kaneko J, Suga H, Ishima D, Kitamura E, Akutsu T, et al. A cluster of disseminated small cortical lesions in MELAS: its distinctive clinical and neuroimaging features. *J Neurol.* (2019) 266:1459–72. doi: 10.1007/s00415-019-09283-3
20. Ohshita T, Oka M, Imon Y, Watanabe C, Katayama S, Yamaguchi S, et al. Serial diffusion-weighted imaging in MELAS. *Neuroradiology.* (2000) 42:651–6. doi: 10.1007/s002340000335
21. Kolb S, Costello F, Lee A, White M, Wong S, Schwartz E, et al. Distinguishing ischemic stroke from the stroke-like lesions of MELAS using apparent diffusion coefficient mapping. *J Neurol Sci.* (2003) 216:11–5. doi: 10.1016/S0022-510X(03)00218-1
22. Tzoulis C, Bindoff LA. Serial diffusion imaging in a case of mitochondrial encephalomyopathy, lactic acidosis, stroke-like episodes. *Stroke.* (2009) 40:e15–7. doi: 10.1161/STROKEAHA.108.523118
23. Casimiro C, Martins J, Nunes C, Parreira T, Batista S, Cordeiro M, et al. Conventional and diffusion-weighted magnetic resonance imaging and proton spectroscopy in MELAS. *Acta Med Port.* (2012) 25:59–64.
24. Stoquart-Elsankari S, Lehmann P, Perin B, Gondry-Jouet C, Godefroy O. MRI and diffusion-weighted imaging followup of a stroke-like event in a patient with MELAS. *J Neurol.* (2008) 255:1593–5. doi: 10.1007/s00415-008-0968-6
25. Xu W, Wen J, Sun C, Cao J, Li Y, Geng D. Conventional and diffusional magnetic resonance imaging features of mitochondrial encephalomyopathy, lactic acidosis, and stroke-like episodes in Chinese patients: a study of 40 cases. *J Comput Assist Tomogr.* (2018) 42:510–6. doi: 10.1097/RCT.0000000000000712
26. Moller HE, Kurlemann G, Putzler M, Wiedermann D, Hilbich T, Fiedler B. Magnetic resonance spectroscopy in patients with MELAS. *J Neurol Sci.* (2005) 229–230:131–9. doi: 10.1016/j.jns.2004.11.014
27. Wilichowski E, Pouwels P, Frahm J, Hanefeld F. Quantitative proton magnetic resonance spectroscopy of cerebral metabolic disturbances in patients with MELAS. *Neuropediatrics.* (1999) 30:256–63. doi: 10.1055/s-2007-973500
28. Malhotra K, Liebeskind D. Imaging of MELAS. *Curr Pain Headache Rep.* (2016) 20:54. doi: 10.1007/s11916-016-0583-7
29. Abe K, Yoshimura H, Tanaka H, Fujita N, Hikita T, Sakoda S. Comparison of conventional and diffusion-weighted MRI and proton MR spectroscopy in patients with mitochondrial encephalomyopathy, lactic acidosis, stroke-like events. *Neuroradiology.* (2004) 46:113–7. doi: 10.1007/s00234-003-1138-2
30. Chen C, Xiong N, Wang Y, Xiong J, Huang J, Zhang Z, et al. A study of familial MELAS: evaluation of A3243G mutation, clinical phenotype, and magnetic resonance spectroscopy-monitored progression. *Neurol India.* (2012) 60:86–9. doi: 10.4103/0028-3886.93609
31. Castillo M, Kwock L, Green C. MELAS syndrome: imaging and proton MR spectroscopic findings. *AJNR Am J Neuroradiol.* (1995) 16:233–9.
32. Kaufmann P, Engelstad K, Wei Y, Kulikova R, Oskoui M, Sproule D, et al. Natural history of MELAS associated with mitochondrial DNA m. 3243A>G genotype. *Neurology*. (2011) 77:1965–71. doi: 10.1212/WNL.0b013e31823a0c7f
33. Weiduschat N, Kaufmann P, Mao X, Engelstad K, Hinton V, DiMauro S, et al. Cerebral metabolic abnormalities in A3243G mitochondrial DNA mutation carriers. *Neurology.* (2014) 82:798–805. doi: 10.1212/WNL.0000000000000169
34. Hovsepian D, Galati A, Chong R, Mazumder R, DeGiorgio C, Mishra S, et al. MELAS: Monitoring treatment with magnetic resonance spectroscopy. *Acta Neurol Scand.* (2019) 139:82–5. doi: 10.1111/ane.13027
35. Kim JH, Lim MK, Jeon TY, Rha JH, Eo H, Yoo S-Y, et al. Diffusion and perfusion characteristics of MELAS (Mitochondrial Myopathy, Encephalopathy, Lactic Acidosis, and Stroke-Like Episode) in thirteen patients. *Korean J Radiol.* (2011) 12:15. doi: 10.3348/kjr.2011.12.1.15
36. Ito H, Mori K, Harada M, Minato M, Naito E, Takeuchi M, et al. Serial brain imaging analysis of stroke-like episodes in MELAS. *Brain Dev.* (2008) 30:483–8. doi: 10.1016/j.braindev.2008.01.003
37. Takasu M, Kajima T, Ito K, Kato Y, Sakura N. A case of MELAS: hyperperfused lesions detected by non-invasive perfusion-weighted MR imaging. *Magn Reson Med Sci.* (2002) 1:50–3. doi: 10.2463/mrms.1.50
38. Tsujikawa T, Yoneda M, Shimizu Y, Uematsu H, Toyooka M, Ikawa M, et al. Pathophysiologic evaluation of MELAS strokes by serially quantified MRS and CASL perfusion images. *Brain Dev.* (2010) 32:143–9. doi: 10.1016/j.braindev.2008.12.003
39. Minobe S, Matsuda A, Mitsuhashi T, Ishikawa M, Nishimura Y, Shibata K, et al. Vasodilatation of multiple cerebral arteries in early stage of stroke-like episode with MELAS. *J Clin Neurosci.* (2015) 22:407–8. doi: 10.1016/j.jocn.2014.05.021
40. Ikawa M, Yoneda M, Muramatsu T, Matsunaga A, Tsujikawa T, Yamamoto T, et al. Detection of preclinically latent hyperperfusion due to stroke-like episodes by arterial spin-labeling perfusion MRI in MELAS patients. *Mitochondrion.* (2013) 13:676–80. doi: 10.1016/j.mito.2013.09.007
41. Li R, Xiao H, Lyu J, Wang DJJ, Ma L, Lou X. Differential diagnosis of mitochondrial encephalopathy with lactic acidosis and stroke-like episodes (MELAS) and ischemic stroke using 3D pseudocontinuous arterial spin labeling. *J Magn Reson Imaging.* (2017) 45:199–206. doi: 10.1002/jmri.25354
42. Li Y, Lin J, Sun C, Zhao C, Li H. Increased cerebral blood flow as a predictor of episodes in MELAS using multimodal MRI. *J Magn Reson Imag.* (2017) 46:915–8. doi: 10.1002/jmri.25592
43. Rodan L, Poublanc J, Fisher J, Sobczyk O, Wong T, Hlasny E, et al. Cerebral hyperperfusion and decreased cerebrovascular reactivity correlate with neurologic disease severity in MELAS. *Mitochondrion.* (2015) 22:66–74. doi: 10.1016/j.mito.2015.03.002

44. Li Y, Xu W, Sun C, Lin J, Qu J, Cao J, et al. Reversible dilation of cerebral macrovascular changes in MELAS episodes. *Clin Neuroradiol.* (2019) 29:321–9. doi: 10.1007/s00062-018-0662-8
45. Renard D, Ion I. Cerebral arterial and venous MRI abnormalities in MELAS. *Acta neurologica Belgica.* (2020) 120:455–6. doi: 10.1007/s13760-017-0867-7
46. Yoshida T, Ouchi A, Miura D, Shimoji K, Kinjo K, Sueyoshi T, et al. MELAS and reversible vasoconstriction of the major cerebral arteries. *Intern Med.* (2013) 52:1389–92. doi: 10.2169/internalmedicine.52.0188
47. Sun X, Jiang G, Ju X, Fu H. MELAS and macroangiopathy: a case report and literature review. *Medicine.* (2018) 97:e13866. doi: 10.1097/MD.0000000000013866
48. Gramegna LL, Cortesi I, Mitolo M, Evangelisti S, Lia T, Cirillo L, et al. Major cerebral vessels involvement in patients with MELAS syndrome: worth a scan? A systematic review. *J Neuroradiol.* (2021) 48:359–66. doi: 10.1016/j.neurad.2021.02.002
49. Virtanen SM, Lindroos MM, Majamaa K, Nuutila P, Borra RJ, Parkkola R. Voxelwise analysis of diffusion tensor imaging and structural MR imaging in patients with the m. 3243A>G mutation in mitochondrial DNA. *AJNR Am J Neuroradiol.* (2011) 32:522–6. doi: 10.3174/ajnr.A2309
50. Renard D, Taieb G. Neurological picture. Cortical susceptibility-weighted imaging hypointensity after stroke-like episode in MELAS. *J Neurol Neurosurg Psychiatry*. (2014) 85:1055–6. doi: 10.1136/jnnp-2013-306933
51. Wang R, Lin J, Sun C, Hu B, Liu X, Geng D, et al. Topological reorganization of brain functional networks in patients with mitochondrial encephalomyopathy with lactic acidosis and stroke-like episodes. *Neuroimage Clin.* (2020) 28:102480. doi: 10.1016/j.nicl.2020.102480
52. Wang R, Sun C, Lin J, Chen N, Hu B, Liu X, et al. Altered dynamic functional connectivity in patients with mitochondrial encephalomyopathy with lactic acidosis and stroke-like episodes (MELAS) at acute and chronic stages: shared and specific brain connectivity abnormalities. *J Magn Reson Imag.* (2021) 53:427–36. doi: 10.1002/jmri.27353
53. Rodan LH, Poublanc J, Fisher JA, Sobczyk O, Mikulis DJ, Tein I. L-arginine effects on cerebrovascular reactivity, perfusion and neurovascular coupling in MELAS (mitochondrial encephalomyopathy with lactic acidosis and stroke-like episodes) syndrome. *PLoS ONE.* (2020) 15:e0238224. doi: 10.1371/journal.pone.0238224
54. Chong L, Zhenzhou L, Daokun R, Yuankui W, Hui Z, Chao Y, et al. Vessel flow void sign and hyperintense vessel sign on FLAIR images distinguish between MELAS and AIS. *Mitochondrion.* (2021) 58:131–4. doi: 10.1016/j.mito.2021.02.015
55. Gieraerts C, Demaerel P, Van Damme P, Wilms G. Mitochondrial encephalomyopathy, lactic acidosis, and stroke-like episodes (MELAS) syndrome mimicking herpes simplex encephalitis on imaging studies. *J Comput Assist Tomogr.* (2013) 37:279–81. doi: 10.1097/RCT.0b013e3182811170

Conflict of Interest: The authors declare that the research was conducted in the absence of any commercial or financial relationships that could be construed as a potential conflict of interest.

frontiers in Neurology

CASE REPORT
published: 09 February 2022
doi: 10.3389/fneur.2022.818332

Case Report: Diffuse Cerebral Microbleeds in Cerebral Autosomal Recessive Arteriopathy With Subcortical Infarcts and Leukoencephalopathy

Lan Wen[1,2†], **Jichao Yuan**[2†], **Shuang Li**[3], **Jieyi Zhao**[1], **Congjun Li**[1], **Jiafei Li**[1], **Yuanyuan Han**[1], **Chaohua Wang**[1*] **and Guangjian Li**[2*]

[1] *Department of Neurosurgery, West China Hospital, Sichuan University, Chengdu, China,* [2] *Department of Neurology, Southwest Hospital, Third Military Medical University (Army Medical University), Chongqing, China,* [3] *Department of Neurology, The Affiliated Hospital of Southwest Medical University, Luzhou, China*

OPEN ACCESS

Edited by:
Yilei Zhao,
Zhejiang University, China

Reviewed by:
Alessandro Biffi,
Massachusetts General Hospital and Harvard Medical School, United States
Yongwei Zhang,
Changhai Hospital, China

***Correspondence:**
Guangjian Li
lgjian991139@163.com
Chaohua Wang
neuro_chaohua_wang@163.com

[†] *These authors have contributed equally to this work and share first authorship*

Specialty section:
This article was submitted to Applied Neuroimaging, a section of the journal Frontiers in Neurology

Received: *19 November 2021*
Accepted: *17 January 2022*
Published: *09 February 2022*

Citation:
Wen L, Yuan J, Li S, Zhao J, Li C, Li J, Han Y, Wang C and Li G (2022) Case Report: Diffuse Cerebral Microbleeds in Cerebral Autosomal Recessive Arteriopathy With Subcortical Infarcts and Leukoencephalopathy. Front. Neurol. 13:818332. doi: 10.3389/fneur.2022.818332

Cerebral autosomal recessive arteriopathy with subcortical infarcts and leukoencephalopathy (CARASIL) is a hereditary cerebral small vascular disease caused by a homozygous mutation in the high-temperature requirement A serine peptidase 1 (*HTRA1*) gene. Cerebral microbleeds (CMBs) are increasingly being recognized as neuroimaging findings occurring with cerebrovascular disease and have different etiologies. Mild to moderate CMBs are not unusual in CARASIL, and they are observed to affect cortical and subcortical structures; in contrast, diffuse CMBs, especially in the cerebellum, are rare. In this case, we report a novel mutation of *HTRA1* in a 43-year-old woman whose imaging indicated multiple CMBs in all lobes, brain stem, and cerebellum. The amount and location of CMBs vary in CARASIL cases, and the potential cause is not fully understood. This study revealed that specific imaging findings of this patient may be related to a new genetic mutation.

Keywords: CARASIL, cerebral microbleed, *HTRA1* mutation, leukoencephalopathy, cerebral small vessel disease

INTRODUCTION

Cerebral autosomal recessive arteriopathy with subcortical infarcts and leukoencephalopathy (CARASIL) is a very rare autosomal recessive non-hypertensive cerebral small vessel arteriopathy caused by biallelic mutations of the high-temperature requirement protease A1 (*HTRA1*) gene. Additionally, it is characterized by subcortical infarcts, alopecia, and spondylosis (1). Furthermore, leukoencephalopathy with multiple lacunar infarctions, brain atrophy, and cerebral microbleeds (CMBs) have been observed on magnetic resonance imaging (MRI) in previous studies (2–4). Presently, there are very few studies on CMBs in CARASIL, most of which are reported to be located in the cortex and subcortex, mainly in the basal ganglia region (5–9). Herein, we report a 43-year-old woman with a novel *HTRA1* gene mutation who presented widely distributed CMBs in the brain lobes and deep regions, especially the cerebellum.

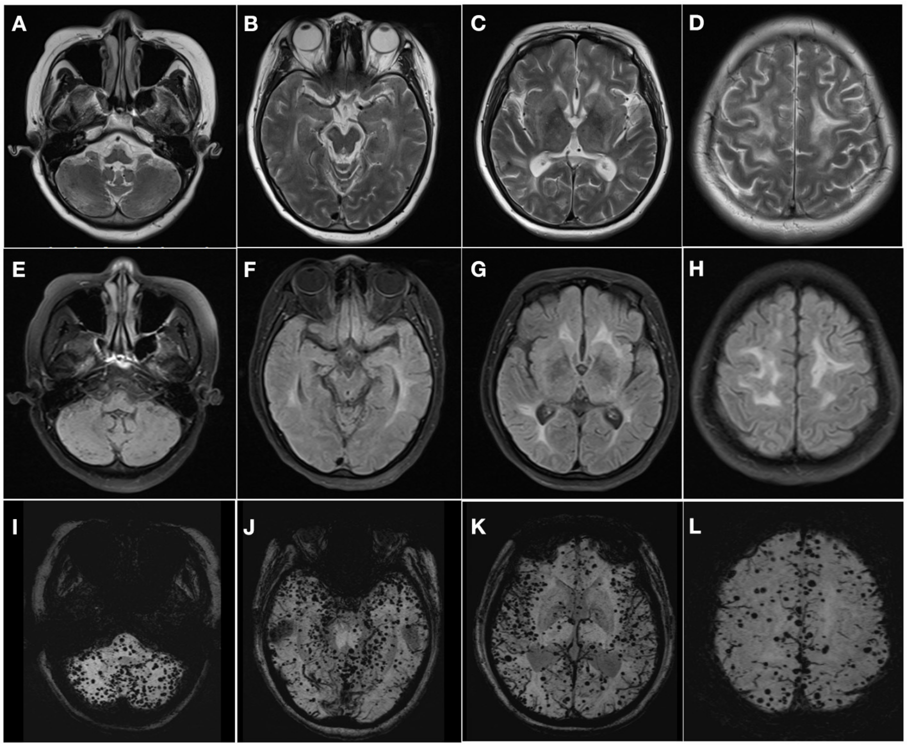

FIGURE 1 | Multiple hyperintensities in the cerebral white matter extending from supra- to infratentorial regions on T2-weighted **(A–D)** and fluid-attenuation inversion recovery images **(E–H)**. Susceptibility-weighted imaging shows diffuse microbleeds in the cerebellum, brain stem, subcortex, and cortex **(I–L)**.

CASE PRESENTATION

The proband was a 43-year-old woman with progressive gait disturbance and memory impairment for 1 year and inarticulate speech for 2 months. One year before admission, she developed walking instability and slight memory loss without any regular treatment. Since the last 2 months, slurred speech and comparatively obvious cognitive impairment have been observed. Additionally, the patient had no hypertension, diabetes, or other diseases except for mild hair loss at a young age. The positive sign of physical examination were mild alopecia, unsteady walking, ataxic gait, and inarticulate speech, accompany with moderate cognitive impairment and Mini-Mental State Exam score of 18 points (illiteracy), demonstrating majorly focused on orientation, memory, and computed function. Further neurological examination revealed normal muscle strength and tone, whereas exhibited positive bilateral Babinski signs. Moreover, she failed to complete the dysmetria and dysdiadochokinesia and underwent the Finger to-Nose test. MRI revealed white matter hyperintensities in the periventricular centrum semiovale and brain stem on T2-weighted and fluid-attenuation inversion recovery images; additionally, extensive microbleeds were observed in the frontal, temporal, and occipital lobes, brain stem, and cerebellum on magnetic susceptibility-weighted imaging (**Figure 1**). The imaging showed leukodystrophy and extensive CMBs tending toward cerebral small vascular disease (cSVD), which appeared similar to cerebral amyloid angiopathy (CAA) at first glance. However, deep CMBs in the cerebral and cerebellar regions were similarly observed; in contrast, other CAA-related features, such as convexity subarachnoid hemorrhage and cortical superficial siderosis, were absent. To further clarify the diagnosis, vasculitis markers were assessed, and angiography was performed, both of which showed negative findings. The blood pressure was noted an average at 136/80 mmHg. Considering the patient's hair loss, which is a symptom of CARASIL, we detected a genetic mutation linked to hereditary cSVD, and targeted panel-sequencing revealed a novel homozygous missense mutation (c.508 A>C, p.N170H, chr10:124248453) in the *HTRA1* gene, which exhibited heterozygous mutation in her father. Finally, the diagnosis was confirmed as CARASIL. Following the administration of donepezil and some neurotrophic treatments, the patient's symptoms did not improve but progressively worsened. At six months of follow-up after discharge, she could neither walk nor independently perform daily living activities.

DISCUSSION

CARASIL is an extremely rare cSVD, with most cases reported in Asia, mainly in Japan and China. A few reports on Caucasian patients have also been published in recent years (9–11). The clinical manifestations include early adult-onset subcortical infarcts, progressive motor and cognitive impairment, alopecia, and spondylosis; non-neurologic symptoms include special signs that distinguish CARASIL from other diseases (1, 3, 4). Due to the *HTRA1* mutation, dysregulation of the inhibition of signaling by members of the TGF-β family induces cerebral small vessel disease and has also been linked to alopecia and spondylosis. The central pathology involves the lack of vascular smooth muscle cells (VSMCs) in the media and adventitial fibrosis, which invades the small penetrating arteries and mainly affects the cerebral white matter and basal ganglia (12, 13). Loss of VSMCs is the primary feature of CARASIL, followed by deposition of granular materials in the media and fibrosis of the arterial wall, leading to ischemic and hemorrhagic consequences; consequently, diffuse white matter hyperintensity, lacunar infarctions, CMBs, and encephalatrophy are observed on MRI (14).

CMBs are increasingly being recognized as a characteristic marker of cSVD on neuroimaging and progressing in various locations for specific vascular pathologies among different etiology. For example, the lesions in leptomeningeal and cortical vessels contribute to strict lobar distribution, suggesting CAA, while the deep perforating arteries match with the hypertensive vasculopathy. Since the pial arteries, perforating arteries, and arterioles are affected in CARASIL, the lobes and deep brain regions are potentially involved in the pathologies simultaneously (4). Previously, mild to moderate CMBs were observed in patients with partial CARASIL, preferentially involving the juxtacortical hemispheric areas, thalamus, and brain stem (5–9). This patient showed multiple CMBs in all lobes, especially in the cerebellum, which is rarely reported. Since other vascular risk factors were absence, and the imaging findings, lacunar infarctions and atrophy, were less severe, such numerous CMBs and distinct locations may not be rationally explained by comorbidity or disease progression in this case. Additionally, it is unclear whether the presentation could be ascribed to coincidence or the new *HTRA1* gene mutation. Based on the available studies, the imagine features vary among different families in CARASIL, and the underlying mechanisms are unclear. Besides disease progression, different mutation sites may also a cause of differential imaging findings. A case in point is the various degrees and locations of microbleeds and white matter hyperintensities found in patients with different gene mutations (2, 3, 15). In some families, microbleeds were absent, while most families showed mild microbleeds in cortico-subcortica regions and thalamus. Even more, a few families exhibited extend regions were involvement, such as midbrain and pons. On the other hand, anterior temporal lobe immunity in a few familial cases, whereas contrary findings were observed in some other studies. However, there is no study on the relationship between gene loci and imaging features at present. Under these circumstances, accurate diagnosis may be difficult to establish based on imaging manifestations alone; therefore, non-neurological signs and proper molecular testing should be considered for an accurate diagnosis.

CONCLUSION

As a gene-associated orphan disease, the incidence of CARASIL in the general population is low, and there is limited knowledge about it. Our case describes a new genetic mutation that is not listed in the Exome Aggregation Consortium database. Our data further imply that different mutations could possibly lead to different imaging findings. The imaging features and potential mechanism of their versatility should be further investigated to gain deeper insights into this condition.

DATA AVAILABILITY STATEMENT

The original contributions presented in the study are included in the article/**Supplementary Material**, further inquiries can be directed to the corresponding author/s.

ETHICS STATEMENT

Written informed consent was obtained from the individual(s) for the publication of any potentially identifiable images or data included in this article.

AUTHOR CONTRIBUTIONS

GL and CW conceptualized the case report idea. LW and JY analyzed the case and drafted the manuscript for intellectual content. JZ, SL, JL, YH, and CL prepared the MRI scans and figure. All authors reviewed the manuscript and were involved inpatients' healthcare. All authors contributed to the article and approved it for publication.

ACKNOWLEDGMENTS

We acknowledge the support by west china hospital, Sichuan University and Third Military Medical University (Army Medical University).

SUPPLEMENTARY MATERIAL

The Supplementary Material for this article can be found online at: https://www.frontiersin.org/articles/10.3389/fneur.2022.818332/full#supplementary-material

REFERENCES

1. Hara K, Shiga A, Fukutake T, Nozaki H, Miyashita A, Yokoseki A, et al. Association of HTRA1 mutations and familial ischemic cerebral small-vessel disease. *N Engl J Med.* (2009) 360:1729–39. doi: 10.1056/NEJMoa0801560
2. Nozaki H, Sekine Y, Fukutake T, Nishimoto Y, Shimoe Y, Shirata A, et al. Characteristic features and progression of abnormalities on MRI for CARASIL. *Neurology.* (2015) 85:459–63. doi: 10.1212/WNL.0000000000001803
3. Nozaki H, Nishizawa M, Onodera O. Features of cerebral autosomal recessive arteriopathy with subcortical infarcts and leukoencephalopathy.

Stroke. (2014) 45:3447–53. doi: 10.1161/STROKEAHA.114.004236

4. Uemura M, Nozaki H, Kato T, Koyama A, Sakai N, Ando S, et al. HTRA1-related cerebral small vessel disease: a review of the literature. *Front Neurol.* (2020) 11:545. doi: 10.3389/fneur.2020.00545
5. Nozaki H, Kato T, Nihonmatsu M, Saito Y, Mizuta I, Noda T, et al. Distinct molecular mechanisms of HTRA1 mutants in manifesting heterozygotes with CARASIL. *Neurology.* (2016) 86:1964–74. doi: 10.1212/WNL.0000000000002694
6. Bianchi S, Di Palma C, Gallus GN, Taglia I, Poggiani A, Rosini F, et al. Two novel HTRA1 mutations in a European CARASIL patient. *Neurology.* (2014) 82:898–900. doi: 10.1212/WNL.0000000000000202
7. Preethish-Kumar V, Nozaki H, Tiwari S, Vengalil S, Bhat M, Prasad C, et al. CARASIL families from India with 3 novel null mutations in the HTRA1 gene. *Neurology.* (2017) 89:2392–4. doi: 10.1212/WNL.0000000000004710
8. Lee YC, Chung CP, Chao NC, Fuh JL, Chang FC, Soong BW, et al. Characterization of heterozygous HTRA1 mutations in Taiwanese patients with cerebral small vessel disease. *Stroke.* (2018) 49:1593–601. doi: 10.1161/STROKEAHA.118.021283
9. Menezes Cordeiro I, Nzwalo H, Sá F, Ferreira RB, Alonso I, Afonso L, et al. Shifting the CARASIL paradigm: report of a non-Asian family and literature review. *Stroke.* (2015) 46:1110–2. doi: 10.1161/STROKEAHA.114.006735
10. Ibrahimi M, Nozaki H, Lee A, Onodera O, Reichwein R, Wicklund M, et al. A CARASIL patient from Americas with novel mutation and atypical features: case presentation and literature review. *Cerebrovasc Dis.* (2017) 44:135–40. doi: 10.1159/000477358
11. Mendioroz M, Fernández-Cadenas I, Del Río-Espinola A, Rovira A, Solé E, Fernández-Figueras MT, et al. A missense HTRA1 mutation expands CARASIL syndrome to the Caucasian population. *Neurology.* (2010) 75:2033–5. doi: 10.1212/WNL.0b013e3181ff96ac
12. Liu J, Dong F, Hoh J. Loss of HtrA1-induced attenuation of TGF-beta signaling in fibroblasts might not be the main mechanism of CARASIL pathogenesis. *Proc Natl Acad Sci USA.* (2015) 112:E1693. doi: 10.1073/pnas.1500911112
13. Fasano A, Formichi P, Taglia I, Bianchi S, Di Donato I, Battisti C, et al. HTRA1 expression profile and activity on TGF-beta signaling in HTRA1 mutation carriers. *J Cell Physiol.* (2020) 235:7120–7. doi: 10.1002/jcp.29609
14. Pantoni L. Cerebral small vessel disease: from pathogenesis and clinical characteristics to therapeutic challenges. *Lancet Neurol.* (2010) 9:689–701. doi: 10.1016/S1474-4422(10)70104-6
15. Verdura E, Hervé D, Scharrer E, Amador Mdel M, Guyant-Maréchal L, Philippi A, et al. Heterozygous HTRA1 mutations are associated with autosomal dominant cerebral small vessel disease. *Brain.* (2015) 138:2347–58. doi: 10.1093/brain/awv155

Conflict of Interest: The authors declare that the research was conducted in the absence of any commercial or financial relationships that could be construed as a potential conflict of interest.

frontiers in Neurology

ORIGINAL RESEARCH
published: 23 February 2022
doi: 10.3389/fneur.2022.819055

Altered Brain Morphometry in Cerebral Small Vessel Disease With Cerebral Microbleeds: An Investigation Combining Univariate and Multivariate Pattern Analyses

Jing Li[1†‡], Hongwei Wen[2,3†‡], Shengpei Wang[4,5†], Yena Che[6†], Nan Zhang[7†] and Lingfei Guo[7†]*

[1] Department of Radiology, Beijing Friendship Hospital, Capital Medical University, Beijing, China, [2] Key Laboratory of Cognition and Personality (Ministry of Education), Chongqing, China, [3] School of Psychology, Southwest University, Chongqing, China, [4] Research Center for Brain-Inspired Intelligence, Institute of Automation, Chinese Academy of Sciences, Beijing, China, [5] University of Chinese Academy of Sciences, Beijing, China, [6] Department of Clinical Laboratory, Shandong Provincial Hospital Affiliated to Shandong First Medical University, Jinan, China, [7] Department of Radiology, Shandong Provincial Hospital Affiliated to Shandong First Medical University, Jinan, China

Purpose: The objective of this study was to evaluate whether altered gray matter volume (GMV) and white matter volume (WMV) are associated with the presence of cerebral microbleeds (CMBs) in cerebral small vessel disease (CSVD).

Materials and Methods: In this study, we included 26 CSVD patients with CMBs (CSVD-c), 43 CSVD patients without CMBs (CSVD-n) and 39 healthy controls. All participants underwent cognitive assessment testing. Both univariate analysis and multivariate pattern analysis (MVPA) approaches were applied to investigate differences in brain morphometry among groups.

Results: In univariate analysis, GMV and WMV differences were compared among groups using voxel-based morphometry (VBM) with diffeomorphic anatomical registration through exponentiated lie algebra (DARTEL). Compared to healthy controls, the CSVD-c group and CSVD-n group showed significantly lower GMV than the control group in similar brain clusters, mainly including the right superior frontal gyrus (medial orbital), left anterior cingulate gyrus, right inferior frontal gyrus (triangular part) and left superior frontal gyrus (medial), while the CSVD-n group also showed significantly lower WMV in the cluster of the left superior frontal gyrus (medial). No significant GMV or WMV differences were found between the CSVD-c group and the CSVD-n group. Specifically, we applied the multiple kernel learning (MKL) technique in MVPA to combine GMV and WMV features, yielding an average of >80% accuracy for three binary classification problems, which was a considerable improvement over the individual modality approach. Consistent with the univariate analysis, the MKL weight maps revealed default mode network and subcortical region damage associated with CSVD compared to controls. On the other hand, when classifying the CSVD-c group and CSVD-n group in the MVPA analysis, we found that some WMVs were highly weighted regions (left olfactory cortex

Edited by:
Xiaofei Hu,
Army Medical University, China

Reviewed by:
Iman Beheshti,
University of Manitoba, Canada
Swati Rane,
University of Washington, United States

Correspondence:
Lingfei Guo
glfsci@163.com

†ORCID:
Jing Li
orcid.org/0000-0001-9392-6600
Hongwei Wen
orcid.org/0000-0003-1717-7235
Shengpei Wang
orcid.org/0000-0001-6032-9578
Yena Che
orcid.org/0000-0003-4742-4778
Nan Zhang
orcid.org/0000-0002-6202-9349
Lingfei Guo
orcid.org/0000-0002-4885-625X

‡These authors have contributed equally to this work and share first authorship

Specialty section:
This article was submitted to Applied Neuroimaging, a section of the journal Frontiers in Neurology

Received: *20 November 2021*
Accepted: *31 January 2022*
Published: *23 February 2022*

Citation:
Li J, Wen H, Wang S, Che Y, Zhang N and Guo L (2022) Altered Brain Morphometry in Cerebral Small Vessel Disease With Cerebral Microbleeds: An Investigation Combining Univariate and Multivariate Pattern Analyses. Front. Neurol. 13:819055. doi: 10.3389/fneur.2022.819055

and right middle frontal gyrus), which hinted at the presence of different white matter alterations in the CSVD-c group.

Conclusion: Our findings not only suggested that the localized alterations in GMV and WMV appeared to be associated with the pathophysiology of CSVD but also indicated that altered brain morphometry could be a potential discriminative pattern to detect CSVD at the individual level.

Keywords: cerebral small vessel disease, cerebral microbleeds, gray matter volume, white matter volume, multivariate pattern analysis

INTRODUCTION

Cerebral small vessel disease (CSVD) refers to different pathologic changes involving small intracranial blood vessels, including small arteries, arterioles, capillaries, and small veins (1). CSVD plays a crucial role in lacunar stroke and brain hemorrhages and is a leading cause of functional loss and dementia in the elderly population (2). Neuroimaging is considered the gold standard for detecting CSVD, and the key neuroimaging markers include small cerebral infarctions, lacunes, white matter hyperintensities (WMH), enlarged perivascular spaces (PVS), cerebral microbleeds (CMBs), and brain atrophy (3). Among these, CMBs have been recognized to play a synergistic role in both cerebrovascular and neurodegenerative pathology occurring in the aging brain (4). CMBs are well-demarcated, hypointense, rounded lesions on magnetic susceptibility-sensitive sequences of magnetic resonance imaging (MRI). These hemosiderin-rich lesions form when the heme iron in red blood cells leaks out from brain micro-vessels and are then sequestered by macrophages for storage (5). Several large clinical studies have established an association of CMBs with vascular and systemic inflammation (6) as well as with cognitive decline in patients with vascular dementia and Alzheimer's disease (AD) (7) and in elderly subjects (8).

As one of the important neuroimaging markers of CSVD, CMBs have a significant impact on the cognitive function of patients with CSVD (9). Histopathologic studies have shown that the presence of CMBs indicates widespread damage in arterioles by hypertension, amyloid deposition and surrounding gliosis, infarction, or even necrosis, resulting in microstructural damage to the surrounding white matter. Therefore, CMBs may disrupt white matter tracts involved in cognitive function, leading to damage to neural networks (10). Therefore, cognitive impairment in patients with CMBs is thought to correlate with brain damage in white matter and gray matter structures, and exploring the relationship between CMBs and cerebral morphological changes with new techniques is a current hotspot for CSVD research.

WMH and lacunar infarct correspond to pathophysiological changes including neuron death, demyelination, and axon loss and these subcortical lesions may cause degenerative cortical atrophy in frontal and temporal area (11). Therefore, many studies reported reduced GMV and WMV in CSVD patients (11–13). However, few studies have investigated the relationship between brain volume and CMBs, particularly the relationship between CMBs and WM. A previous study findings speculated that higher CMBs were associated with WM atrophy but not associated with GM atrophy and concluded this caused by CMBs interrupting brain network connectivity (14). Another study found that CSVD subjects with deep or infratentorial CMBs had a lower amygdala GMV than the CSVD subjects with no CMBs after adjusting for age, sex, and total intracranial volume (TIV), although this significance was no longer present after further adjustment for other vascular risk factors (hypertension, diabetes, cigarette smoking, alcohol consumption, body mass index (BMI), and chronic kidney disease (CKD). On the other hand, subjects with strictly lobar CMBs had larger total, frontal, and occipital WMVs than the CSVD subjects with no CMBs (15). The results of previous studies were inconsistent in the relationship between CMBs and WMV morphological changes, but these results both gave us the hint that there existed WM changes in CSVD patients with CMBs compared with CSVD patients without CMBs. Meanwhile, no healthy subjects were included in these studies, and the brain morphological alterations between CSVD patients and healthy controls had not yet been investigated.

Using traditional mass-univariate analyses to quantify the alterations in GM or WM density or volume between groups in a voxel-wise manner has an important limitation in that mass-univariate analyses only aim to test whether there are any effects in one or more brain regions rather than to test whether the effects are large enough to have translational importance for clinical utility (15). Recently, researchers have developed a growing interest in applying multivariate pattern analysis (MVPA) to develop neuroimaging biomarkers for clinical diagnoses of brain diseases (16). MVPA is a promising machine-learning-based pattern recognition technique that can be used to classify neuroimaging data by discriminating between two or more classes (or groups). Relative to traditional univariate analysis, MVPA has two advantages. First, MVPA takes the intercorrelation between voxels into consideration and thus might be more sensitive in detecting subtle and spatially distributed alterations. Second, MVPA allows statistical inferences at the single-subject level and thus could be used to make diagnostic decisions regarding individual patients (17). MVPA and machine-learning methods have been successfully applied in the risk stratification of various diseases along with CSVD, including WMH and enlarged PVS (18–20). However, no study has investigated the utility of MVPA with brain morphometric features for the three binary classification problems in CSVD patients with CMBs (CSVD-c), CSVD patients without CMBs (CSVD-n) and healthy controls.

Therefore, we aimed to apply both mass-univariate and multivariate pattern analysis methods to evaluate brain morphological alterations in a relatively large sample of CSVD patients with or without CMBs. We hypothesized that (1) the CMBs accompanying CSVD will bring about specific brain morphological changes; (2) MVPA analysis would potentially be able to discriminate individual patients with CSVD from healthy controls; and (3) information will be provided on neurobiological changes that will potentially help to elucidate the potential pathogenesis of CSVD.

MATERIALS AND METHODS

Subjects

This was a cross-sectional study approved by the institutional review board of Shandong Provincial Hospital Affiliated to Shandong First Medical University. Between December 2018 and August 2019, 26 CSVD patients with CMBs (age: 67.08 ± 6.19 years; 10 females) and 43 CSVD patients without CMBs (age: 66.79 ± 5.19 years; 22 females) were recruited. We also included 39 healthy subjects (age: 63.90 ± 8.98 years; 22 females) in our study. The inclusion criteria for CSVD patients included diagnosis of recent small subcortical infarct, lacunes of presumed vascular origin, WMH of presumed vascular origin, enlarged PVS, CMBs, and brain atrophy, based on current MRI consensus standards (3). The severity of WMH was assessed using the Fazekas scale. The scale grades the severity from 0 to 3grade. 0 represents occasional or non-punctate WMH; grade 1, multiple punctate WMHs; grade 2, bridging of punctate WMHs leading to confluent lesions; and grade 3, widespread confluent WMH (21). The total CSVD disease burden was assessed by amended CSVD score (0–7 scale; scores calculated based on the severity of CMBs, lacunes, and WMH) that was recently recommended for predicting cognitive decline (22).

Image Acquisition

All subjects were imaged on a MAGNETOM Skyra 3.0 T MR scanner (Siemens Healthcare, Erlangen, Germany) using a product 32-channel head coil for signal reception. The brain scanning protocol consisted of a 3D T1-weighted (T1W) magnetization-prepared rapid gradient echo (MPRAGE) sequence for anatomical structure (repetition time (TR) = 7.3 ms, echo time (TE) = 2.4 ms, inversion time (TI) = 900 ms, flip angle = 9°, isotropic voxel size = 1 mm^3) and a 3D multi-echo gradient echo (mGRE) sequence for quantitative susceptibility mapping (QSM) (TR = 50 ms, first TE = 6.8 ms, TE interval = 4.1 ms, number of echoes = 10, flip angle = 15°, voxel size = $1 \times 1 \times 2$ mm^3). In addition, T2-weighted (T2W) turbo spin echo, T2W fluid-attenuated inversion recovery (FLAIR), diffusion-weighted, and susceptibility-weighted imaging (SWI) scans were acquired to detect brain abnormalities. Before the scan, all participants remained in a normal state of respiration and heart rate. All participants were required to be awake and quietly breathing until the end of the scan.

Diagnosis of CMBs in CSVD Patients

Through the conventional MRI sequence and SWI images, small subcortical infarct, lacune of presumed vascular origin, WMH of presumed vascular origin, PVS, CMBs, and brain atrophy were diagnosed by a senior neuroradiologist. CMBs are small (generally 2–5 mm in diameter) hypointense lesions that are visible on paramagnetic-sensitive MRI sequences such as T2*-weighted gradient-recalled echo (GRE) or susceptibility-weighted sequences and are most commonly located in the cortico-subcortical junction and deep gray or white matter in the cerebral hemispheres, brainstem, and cerebellum (23–25).

Cognitive Assessments

All participants underwent the Montreal Cognitive Assessment (MoCA) Beijing version (www.mocatest.org), which is a one-page 30-point test administered in 10 min (26). The optimal cutoff for detecting cognitive impairment was 13/14 points for illiterate individuals, 19/20 for individuals with 1–6 years of education, and 24/25 for individuals with 7 or more years of education (27). In addition, a variety of executive functions, including flexibility, working memory and inhibition, were assessed. Briefly, these tests included the following: the Rey auditory verbal learning test (AVLT) for assessing verbal memory abilities (28); the symbol digit modalities test (SDMT) for evaluating attention and information processing speed (29); the trail-making test (TMT) for evaluating attention, information processing speed, visual search and motor coordination (30); and the Stroop color-word test (SCWT) (31). The test implementer was professionally trained and qualified and had no knowledge of the subject grouping.

VBM-DARTEL Processing

After data acquisition, 3D T1W image processing was performed using VBM with Diffeomorphic Anatomical Registration Through Exponentiated Lie Algebra (DARTEL) (32) based on the statistical parametric mapping (SPM8, http://www.fil.ion.ucl.ac.uk/spm) toolbox (pipeline shown in **Figure 1**). DARTEL is a fully deformable registration and normalization method that provides precise inter-subject alignment throughout the iterative unified model. First, all the 3D T1W images were aligned to conventional AC-PC space using manually identified landmarks, including the anterior commissure (AC), the posterior commissure (PC), and the mid-sagittal plane. Then, the aligned images were segmented into GM, WM and cerebrospinal fluid (CSF) in native space with unified segmentation using the *New Segment* tool in SPM (16). Afterward, all the segmented GM and WM images were rigidly transformed to produce a series of aligned GM and WM images. The study-specific GM templates were then created by the DARTEL algorithm with the aligned serial images from all the subjects. During the template creation process, all aligned images were warped to the template, yielding a series of flow fields, which parameterized the deformation. After normalization and modulation, the modulated data were transformed into Montreal Neurological Institute (MNI) space. Finally, the gray matter volume (GMV) and white matter volume (WMV) and partitions were smoothed with an isotropic Gaussian kernel of 8-mm full-width at half-maximum (FWHM).

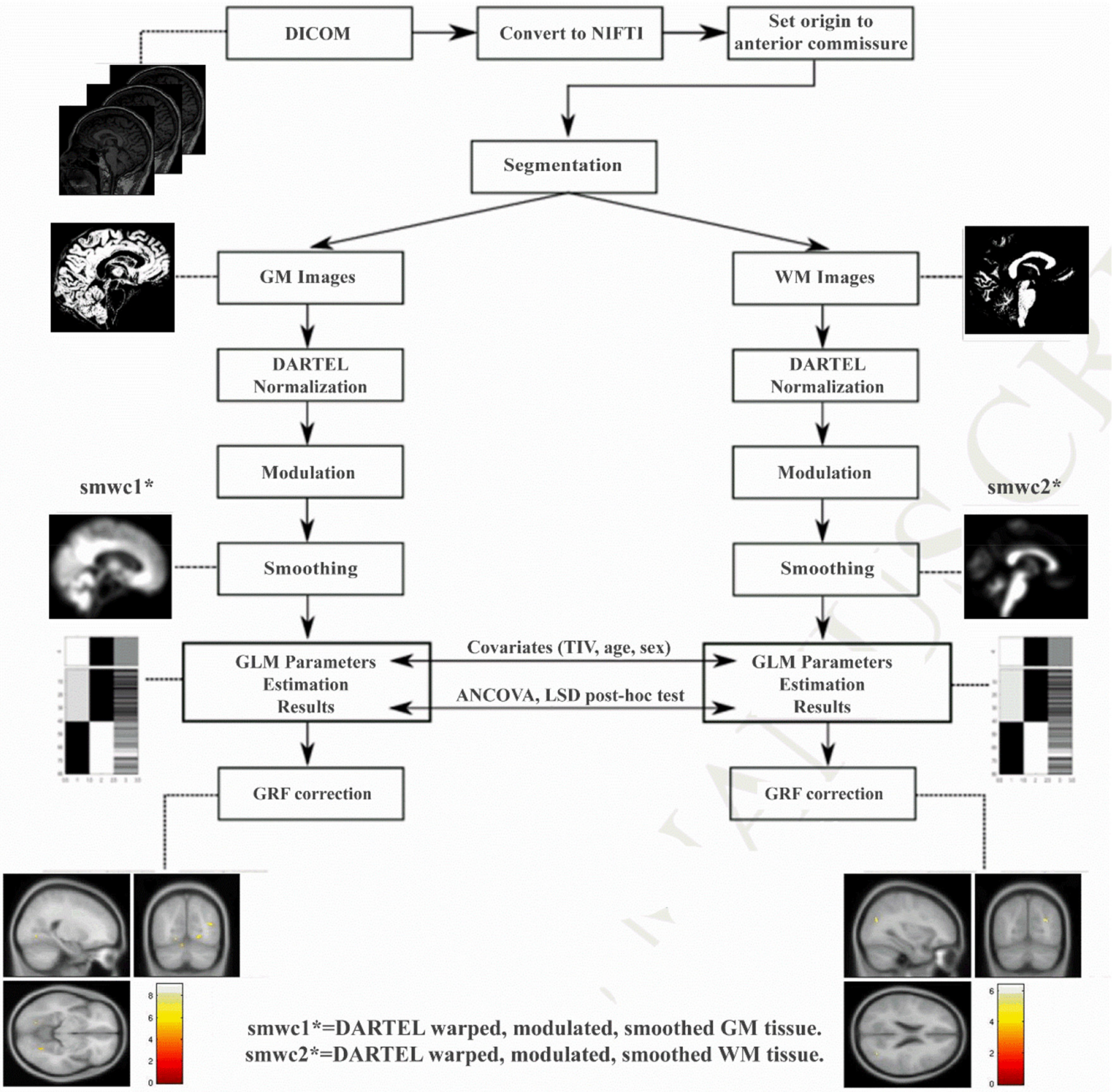

FIGURE 1 | The processing pipeline of VBM-DARTEL analysis using Statistical Parametric Mapping software. DARTEL, diffeomorphic anatomical registration through exponentiated lie algebra; GRF, Gaussian random field.

Univariate Analysis

To compare GMV and WMV and identify abnormalities among the three groups, one-way analysis of covariance ANCOVA was performed with age, sex and TIV as covariates using the *DPABI* toolbox. For *post-hoc* tests, the least-significant difference (LSD) method was applied, and the corrected *p*-values for comparing group means of any pairs were calculated (33). Then, the p maps were converted to Z maps, and using the Z maps, we performed Gaussian random field (GRF) correction (34) to correct for multiple comparisons. The statistical threshold was set at a voxel-level $p < 0.001$ with a cluster-level $p < 0.05$ (two-tailed) in the *DPAB*I toolbox (33). All coordinates are reported in MNI space. Brain regions with significant intergroup differences in GMV were defined as regions of interest (ROIs), and the mean GMV and WMV of these ROIs were extracted from CSVD patients. Pearson's correlations between mean GMV and clinical parameters were calculated using SPSS Version 24.0 (SPSS Inc, Chicago, IL, USA), and significance was set to $p < 0.05$.

Multivariate Pattern Analysis

MVPA was carried out to classify different groups based on GMV and WMV maps and investigate unique information that may be overlooked by univariate approaches. The Pattern Recognition Neuroimaging Toolbox (PRo-NTo) (35) was used to implement a binary classifier based on the multiple kernel learning (MKL) approach, which models the whole brain as a combination of regional patterns and therefore learns the contribution of different brain regions to the classification model (16). As an optimized MKL technique called "simple MKL" implemented in PRoNTo assumes sparsity in the kernel

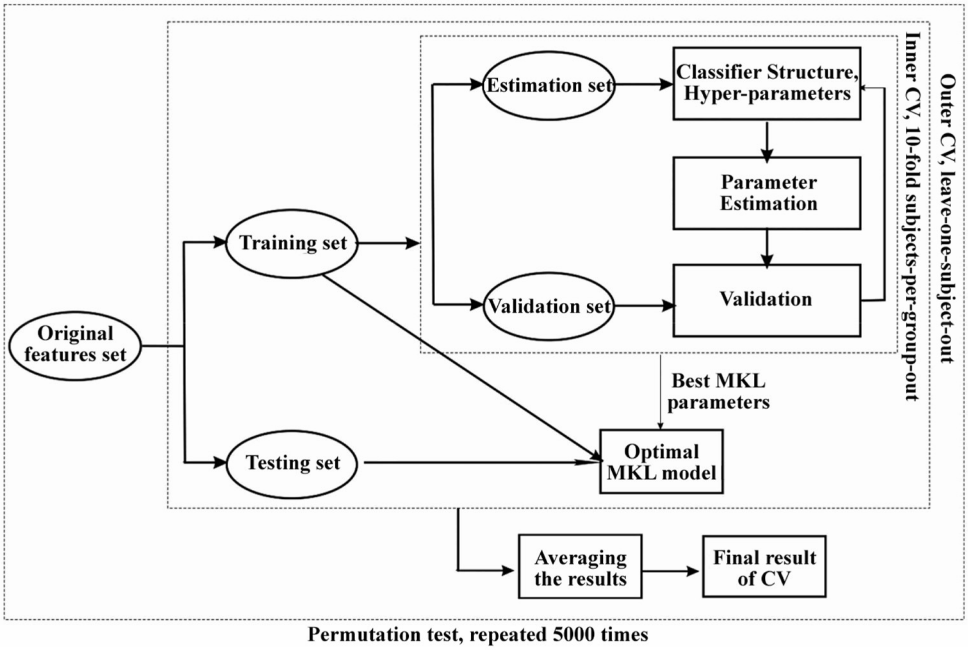

FIGURE 2 | The flow chart of machine learning based multivariate pattern analysis (MVPA) and nested cross-validation pipeline used in our study. Permutation test was used to evaluate the significance of the classification performance for 5,000 times randomly.

combination, this technique selects only a subset of brain regions to perform the classification, and the remaining regions have a null contribution to the model. Regions were defined using the automated anatomical labeling (AAL) atlas (36), which splits the brain into 90 cortical and subcortical regions (detailed shown in **Supplementary Table S1**). For each region and each modality, a linear kernel was computed based on the regional pattern containing all voxels within the region, and MKL was used to combine multiple (modalities × number of regions) kernels. Considering that the number of voxels varies among brain regions, the kernels were mean-centered and normalized using standard kernel operations implemented in PRoNTo. Age, sex and TIV were included as covariates.

Then, nested cross-validation (CV) with hyperparameter optimization was used to train the classification model and assess the generalization error (16). The outer loop was used to assess the model's performance, and the inner loop was used to optimize the model hyperparameters. For the inner loop, a 10-fold CV on subjects-per-group-out technique was used; for the outer loop, the leave-one-subject-out technique was used. As the simple MKL model employs a binary support vector machine (SVM) for classification, we used soft-margin hyperparameter optimization with the best configuration among $C = 0.01, 0.1, 1$ and 10. All C values were tested using a 10-fold CV (inner folds), and then the best C value was used for the outer loop (pipeline shown in **Figure 2**). As in our previous study (16), the statistics we used to evaluate classification performance are accuracy, sensitivity, specificity and the area under the curve (AUC) for the receiver operating characteristic (ROC) curve. Accuracy was defined as (TP+TN)/(TP+TN+FN+FP), where TP = true positive, TN =true negative, FP = false positive and FN = false negative. Sensitivity was defined as TP/(TP+FN), and specificity was defined as TN/(FP+TN).

After constructing the optimal classification model, we built weight maps representing the SVM weights per voxel and also maps summarizing the weights per ROI as defined by AAL atlas. As a simple kernel model was implemented by MKL-SVM, the weights per voxel will be averaged (in absolute value) within each region, and the regional weight maps were the spatial representation of the decision function that defined regional contributions to the classification process. Confidence intervals (*p*-values) generated by non-parametric permutation testing with 5000 randomizations were used to assure low variability in the outputs of classification models.

RESULTS

Demographic and Clinical Characteristics

The demographic and clinical characteristics of each group are summarized in **Table 1**. One-way analysis of variance (ANCOVA) with LSD *post-hoc* tests was performed to assess differences in age, TIV, and MoCA, AVLT, SDMT, SCWT, and TMT scores, and a chi-square test was used to assess differences in sex, lacunes and vascular risk factors (smoking, hypertension, treated hypercholesterolemia and diabetes mellitus) among groups. The rank sum test of

TABLE 1 | Demographic and clinical characteristics of CSVD patients and controls.

Characteristics	CSVD-c	CSVD-n	HC	*P*-value (ANOVA/χ^2)	*P*-value (*post-hoc*)		
					CSVD-c vs. HC	CSVD-c vs. CSVD-n	CSVD-n vs. HC
Gender	16 M/10 F	21 M/22 F	17 M/22 F	0.359$^{\chi 2}$	-	-	-
Age (y)	67.08 ± 6.19	66.68 ± 5.16	63.93 ± 8.87	0.105^{a}	-	-	-
Education (y)	11.56 ± 2.81	11.33 ± 2.68	12.97 ± 3.53	0.041^{a}			
smoking	10 (38.5%)	9 (20.9%)	10 (25.6%)	0.275$^{\chi 2}$	-	-	-
Hypertension	24 (92.3%)	38 (88.3%)	12 (30.8%)	<0.001$\chi 2$	<0.001	0.600	<0.001
Treated Hypercholesterolaemia	15 (57.7%)	13 (30.2%)	5 (12.8%)	0.001$^{\chi 2}$	0.024	<0.001	0.057
Diabetes Mellitus	9 (34.6%)	9 (20.9%)	4 (10.3%)	0.057$^{\chi 2}$	-	-	-
Amended CSVD score	4 (2, 5.25)	2 (1, 2)	0 (0.0)	<0.001^{b}	<0.001	<0.001	<0.001
WMH	2 (1, 3)	1 (1, 2)	0 (0.0)	<0.001^{b}	<0.001	0.079	<0.001
Lacune	14 (53.8%)	3 (7.0%)	0 (0.0%)	<0.001$^{\chi 2}$	<0.001	<0.001	0.093
MoCA	25.48 ± 2.67	27.58 ± 0.85	29.22 ± 3.27	<0.001^{a}	<0.001	0.001	0.003
AVLT	54.80 ± 16.01	64.38 ± 9.02	67.83 ± 8.49	<0.001^{a}	<0.001	<0.001	0.126
SDMT	23.96 ± 10.62	31.19 ± 7.55	41.95 ± 17.03	<0.001^{a}	<0.001	0.016	<0.001
SCWT	186.67 ± 68.53	145.24 ± 26.82	134.77 ± 37.42	<0.001^{a}	<0.001	<0.001	N.S.
TMT-A+B	332.92 ± 170.61	262.69 ± 74.01	208.58 ± 99.66	<0.001^{a}	<0.001	0.012	0.032
TIV	1.61 ± 0.13	1.56 ± 0.14	1.62 ± 0.16	0.187^{a}	-	-	-

$^{\chi}$2: chi-square test, ^{a}: one-way analysis of variance (ANOVA) test, ^{b}: Kruskal-Walllis test. WMH, white matter hyperintensities. MoCA, Montreal Cognitive Assessment; AVLT, sum of Rey auditory verbal learning test (N1-7); SDMT, symbol digit modalities test; SCWT, sum of Stroop color-word test (stroop1-3); TMT, the trail-making test; TMT A+B, sum of TMT-A and TMT-B; TIV, total intracranial volume; CSVD-c, CSVD with CMBs group; CSVD-n, CSVD without CMBs group; HC, control group; N.S., not significant.

TABLE 2 | Significant altered GMV and WMV among three groups.

Condition	Brain regions	Cluster size	z-score of peak voxel	MNI coordinates of peak voxel		
				x	y	z
GMV CSVD-c<control	Right superior frontal gyrus, medial orbital	271	5.17	1	43	−2
	Right inferior frontal gyrus, triangular part	22	4.18	50	24	1
	Left anterior cingulate gyrus	16	4.16	1	33	29
	Left superior frontal gyrus, medial	38	3.80	−2	44	32
GMV CSVD-n<control	Right superior frontal gyrus, medial orbital	267	4.82	1	48	−3
	Left anterior cingulate gyrus	16	4.36	1	32	30
	Left superior frontal gyrus, medial	58	5.09	−2	44	32
WMV CSVD-n<control	Left superior frontal gyrus, medial	50	4.88	−11	52	18

No significant differences were found between the two CSVD groups.

CSVD-c, CSVD with CMBs; CSVD-n, CSVD without CMBs.

Cluster size: the number of voxels in the (identified significant) cluster. ANOVA and LSD post-hoc test in a pair-wise manner within the areas identified by ANOVA were used to identify the GMV and WMV changes between groups with Gaussian random field (GRF) multiple comparison corrections (voxel level $p < 0.001$, cluster level $p < 0.05$).

multiple independent samples (Kruskal-Wallis test) was used to compare CSVD scores and the severity of WMH among groups. The CSVD-c group had significantly lower MoCA, AVLT, and SDMT scores and significantly higher SCWT and TMT scores than the other groups. The CSVD-c group had a higher percentage of hypertension and treated hypercholesterolemia. No significant differences were found in age, sex, smoking and diabetes mellitus status, or TIV among the three groups.

Univariate Analysis of GMV and WMV Differences

We performed univariate analyses to explore GMV and WMV alterations among groups. Compared with the control group, the CSVD-c group and CSVD-n group showed significantly (ANCOVA and LSD *post-hoc* test with GRF correction, voxel-level $p < 0.001$, cluster-level $p < 0.05$) decreased GMV in similar brain clusters, which mainly included the right superior frontal gyrus (medial orbital), left anterior cingulate gyrus, right inferior frontal gyrus (triangular part) and left superior frontal gyrus (medial). Meanwhile, the CSVD-n group also showed significantly decreased WMV in the cluster of the left medial superior frontal gyrus. The detailed results are shown in **Table 2** and **Figure 3**. No significant differences in GMV or WMV were found between the CSVD-c group and the CSVD-n group.

Multivariate Pattern Analysis and Classification Results

Regarding the three binary classification problems, the detailed statistics and ROC curves for evaluating classification performance are shown in **Table 3** and **Figure 4**. As the results show, the MKL models that combined GMV and WMV features enhanced the classification accuracy for each binary classification problem. Based on the optimal MKL model combining GMV and WMV features, regional weight maps obtained by MKL (per region) were also calculated. The CSVD-c group vs. control group contrast suggested high regional weight in the bilateral medial superior frontal gyri (12.96 and 5.94%), bilateral anterior cingulate gyri (6.48 and 5.45%), right gyrus rectus (7.91%), and right superior frontal gyrus (medial orbital) (5.04%) for GMV and in the left olfactory cortex (12.09%) and left parahippocampal gyrus (7.91%) for WMV (**Figure 5A**). Meanwhile, the CSVD-n group vs. control group contrast suggested high regional weight in the left medial superior frontal gyrus (7.02%), cuneus (5.98%), and precuneus (5.96%) for GMV and in the left anterior cingulate gyrus (8.02%) and left inferior temporal gyrus (7.15%) for WMV (**Figure 5B**). In addition, the CSVD-c group vs. CSVD-n group contrast suggested high regional weight in the right temporal pole of the middle temporal gyrus (11.21%), right temporal pole of the superior temporal gyrus (7.39%), and right parahippocampal gyrus (5.62%) for GMV and in the left olfactory cortex (12.42%) and right middle frontal gyrus (9.50%) for WMV (**Figure 5C**). The ROIs with high weight detected from two CSVD groups vs. control group contrasts were relatively analogous to the ROIs with significant differences in the univariate analyses. Of note, we achieved good classification accuracy (81.16%) in the CSVD-c group vs. CSVD-n group, despite no significant differences between groups, and the ROIs with high weights in the MKL model provided important supplementary information for the univariate analyses.

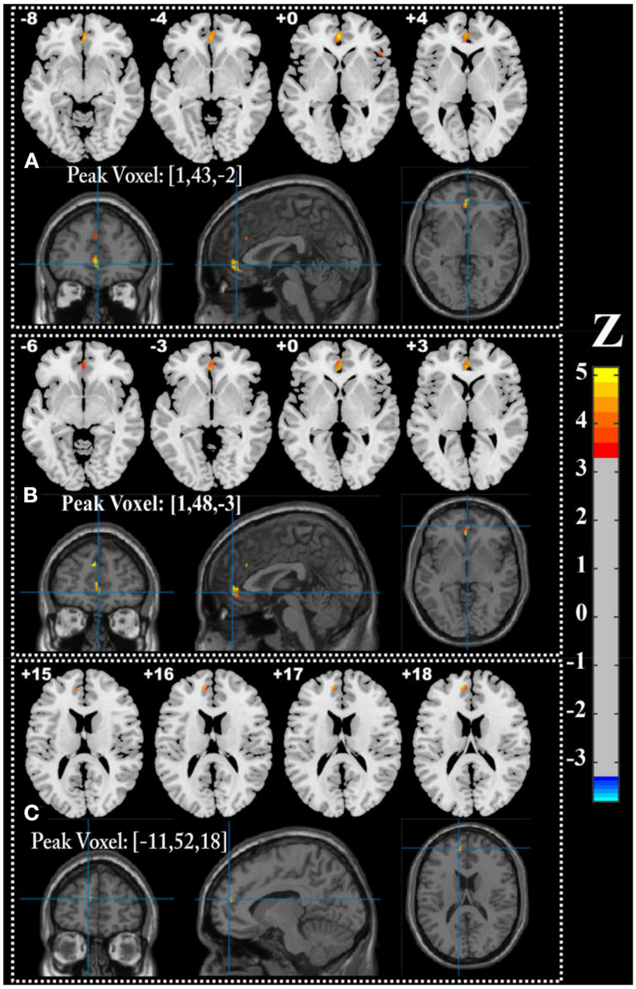

FIGURE 3 | Brain regions showing significantly decreased GMV in **(A)** CSVD-c group and **(B)** CSVD-n group (ANOVA and LSD *post-hoc* test with GRF correction, voxel level $p < 0.001$, cluster level $p < 0.05$), and **(C)** decreased WMV in CSVD-n group compared with control group.

DISCUSSION

The current study applied both univariate analyses and the MVPA approach to explore brain morphological alterations in a relatively large cohort of CSVD patients with or without CMBs. Our study revealed that compared with the control group, the CSVD-c and CSVD-n groups showed significantly decreased GMV in similar brain clusters, which mainly included the right superior frontal gyrus (medial orbital), left anterior cingulate gyrus, right inferior frontal gyrus (triangular part) and left superior frontal gyrus (medial). According to many previous researchers, these regions with decreased GMV are mainly involved in the default mode network (DMN) (37). At the same time, the CSVD-n group showed significantly decreased WMV in the cluster of the left superior frontal gyrus (medial) compared with controls. No significant GMV or WMV differences were found between the CSVD-c group and the CSVD-n group. Additionally, CSVD patients could be differentiated from healthy controls using the MKL model based on GMV and WMV maps with high classification accuracy (86.15%; $p < 0.05$). Brain regions involving the DMN and subcortical regions were identified to have high differentiating power in these MKL modles. Meanwhile, we achieved good classification accuracy (81.16%) in the CSVD-c group vs. CSVD-n group contrast using the MKL model.

Using univariate analyses, our results showed that the CSVD-c group and CSVD-n group had significantly decreased GMV in similar brain clusters compared with the healthy control group, mainly involving the DMN. The core mechanism underlying CSVD-related brain injury is diffuse cerebrovascular endothelial

TABLE 3 | The statistics for evaluating classification performance.

Modality	ACC	SEN	SPE	AUC	P
Condition:CSVD-c group vs. control group					
GMV	84.62%	76.92%	89.74%	0.857	<0.05
WMV	76.92%	69.23%	82.05%	0.817	<0.05
GMV+WMV	86.15%	80.77%	89.74%	0.926	<0.05
Condition:CSVD-n group vs. control group					
GMV	74.39%	67.44%	82.05%	0.815	<0.05
WMV	74.39%	65.12%	84.62%	0.804	<0.05
GMV+WMV	81.71%	69.77%	94.87%	0.891	<0.05
Condition:CSVD-c group vs. CSVD-n group					
GMV	68.12%	57.69%	74.42%	0.770	<0.05
WMV	79.71%	73.08%	83.72%	0.815	<0.05
GMV+WMV	81.16%	69.23%	88.37%	0.881	<0.05

ACC/SEN/SPE, accuracy/sensitivity/specificity; AUC, area under the ROC curve. P: p-values generated by non-parametric permutation testing with 5,000 randomizations.

failure. Endothelial damage leads to increased permeability with leakage of material into the vessel wall and perivascular tissue, leading to brain inflammation (38). Brain inflammation can lead to neuronal dysfunction and cell death (39, 40). In this study, we obtained similar results. We found that the TMT scores were significantly higher and the MoCA, AVLT and SDMT scores were significantly lower in the CSVD patients than in the healthy controls, suggesting that these related cognitive functions were significantly disrupted in CSVD patients. We thought this might be because the decreased GMV regions associated with CSVD mainly involved the DMN. The DMN is a set of functionally connected regions that plays crucial roles in internal cognitive processing. DMN connectivity strength has been positively correlated with individual cognitive performances (e.g., working memory, autobiographical memory, attention, and language) (41), and damage to the default network can cause cognitive impairment.

Compared to traditional univariate analysis, the MVPA approach can be used to make diagnostic decisions. Our results showed that the combination of GMV and WMV features improved the accuracy for each binary classification problem compared to using GMV or WMV features alone. For the classification of the CSVD and control groups, the high-weighted GMV feature areas included the bilateral superior frontal gyrus (medial part or medial orbital part) and bilateral anterior cingulate gyrus. More volume loss regions were identified compared to the univariate analyses. Meanwhile, many high-weighted WMV feature regions could also be found, such as the left anterior cingulate gyrus, left para-hippocampal gyrus and left inferior temporal gyrus.

The anterior cingulate gyrus is one of the important structures responsible for the executive function of the brain, and it mainly monitors ongoing directional behaviors and coordinates cognitive processes (42). The medial part of the superior frontal gyrus is commonly deactivated during the cognitive-related processing and has been ascribed to be a component of the default mode network and a study also found that the superior frontal gyrus is anatomically connected with the cingulate cortex (mostly the anterior cingulate gyrus and the mid-cingulate cortex) through resting-state functional connectivity analysis (43). These results suggest the injury of superior frontal gyrus and anterior cingulate gyrus related to decline of cognitive control. Our results also indicated that the impaired anterior cingulate gyrus and superior frontal gyrus were related with the decline of cognitive function. A study revealed damaged GMV and functional connectivity (FC) in the cerebellum in CSVD patients with WMH and reduced connectivity of cerebellar lobule VI to the left anterior cingulate gyrus owing to WMH (44). These results, similar to ours, showed WM lesions in CSVD. Furthermore, WMH can disrupt white matter tracts or U-fibers that mediate cortical–cortical or cortical–subcortical connections (45), which also provides evidence for our results.

The results of previous studies were inconsistent in the relationship between CMBs and WMV morphological changes, one showed reduced WMV (14), the other showed increased WMV (15). But using the MVPA approach could overcome this shortcoming came from the embarrassment of different conclusions, our analysis just concern existential WM changes, no matter WMV reduced or increased. Our results showed that CSVD should be considered a whole-brain disease and that GMV and WMV were both significantly altered, which was also hinted at by previous studies indicating that local white matter lesions may influence the gray matter in remote areas (46). Therefore, we combined between-group statistical comparison and MVPA-based individual classification to provide complementary information for revealing the potential pathogenesis of CSVD and assisting clinical diagnosis.

Notably, no significant GMV or WMV difference was found in univariate analysis between the CSVD-c and CSVD-n groups. This might reveal that the presence or absence of cerebral CMBs in patients with CSVD has little effect on changes in GMV, which is consistent with the findings of previous research (15). However, the MVPA analysis could mine multivoxel spatial pattern information and achieved a relatively good classification accuracy between the two CSVD groups (81.16%; $p < 0.05$). The classification of the CSVD-c and CSVD-n groups suggested that high-weighted regions were in the right temporal pole of the middle temporal gyrus, temporal pole of the superior temporal gyrus, right para-hippocampal gyrus for GMV and in the left olfactory cortex and right middle frontal gyrus for WMV. This result might have reflected more potential WM and GM changes in the CSVD-c group than in the CSVD-n group. CSVD-c patients have more severe inflammation in the brain because CMBs themselves could lead to a sustained local inflammatory response, characterized by initial activation and persistent increase in microglia and macrophages (47). Many investigations have reported that CMBs are associated with cognitive dysfunction in the elderly (48–50), and epidemiological studies have shown that CMBs adversely affect the cognitive function of patients with CSVD and are independent risk factors for cognitive decline (51). In our study, the CSVD-c patients had more serious cognitive problems than the CSVD-n patients. Hence, we speculated that more severe brain inflammation problems in CSVD-c patients

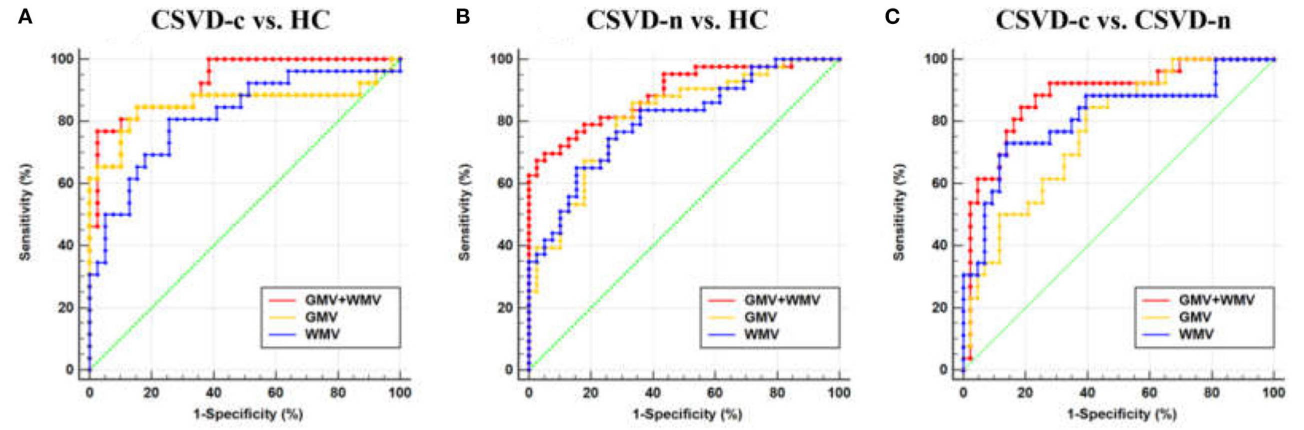

FIGURE 4 | Receiver operating characteristic (ROC) curve for **(A)** CSVD-c vs. HC, **(B)** CSVD-n vs. HC, and **(C)** CSVD-c vs. CSVD-n classification problems. HC, healthy controls.

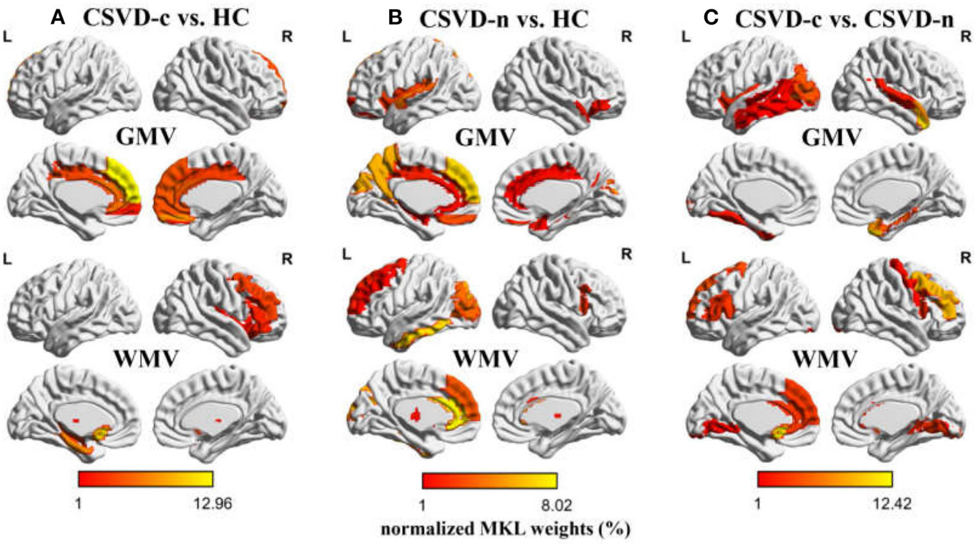

FIGURE 5 | Weight (per region) maps modeled by multi-kernel learning (MKL) combining GMV and WMV features. As a simple kernel model was implemented by MKL-SVM, the weights per voxel will be averaged (in absolute value) within each ROI as defined by AAL atlas. The regional MKL weights representing regional contribution to **(A)** CSVD-c vs. HC, **(B)** CSVD-n vs. HC, and **(C)** CSVD-c vs. CSVD-n classification problems were rendered on the ICBM152 template. Weights with lower (1% or less) contribution are not shown. HC, healthy controls.

might be the reason for them having poor cognitive scores. The middle temporal gyrus has been shown to be recruited during the processing of words and during the observation of actions (52). The human superior temporal gyrus is critical for extracting meaningful linguistic features from speech input (53). The hippocampus and surrounding medial temporal lobe structures play a key role in learning and memory formation (54). The hippocampus and parahippocampus were associated with olfactory ability (55). These previous studies showed the involved regions in CSVD-c patients correlated with cognitive function. Therefore, our results hinted the injury of right temporal lobe, right para-hippocampal gyrus and the left olfactory might be the reason why CSVD-c group had more serious congnitive decline.

In this study, we conducted VBM-DARTEL preprocessing using VBM8 within SPM8 toolbox. A recent study (56) has shown that VBM analysis through CAT12 within SPM12 toolbox is more robust to detect the small brain morphological changes than VBM8. Therefore, we also conducted VBM-DARTEL preprocessing using CAT12 as the supplementary experiment. The univariate results showed the number of significant voxels revealed by CAT12 method is more than VBM8 method, while the structural localization of peak voxels is similar between these two methods, and detailed results were shown in **Supplementary Materials**. In our future research, we will combine VBM and MVPA analysis based on CAT12. More longitudinal studies with a large sample size are needed in the future to understand the relationship between CMBs and the cerebral morphology changes. Besides, more specific features for neurodegeneration such as age, gender and cardiovascular risk factors should be included in future research to explore the neurodegeneration pathology of CSVD.

CONCLUSION

In conclusion, we found significantly lower decreased GMV and WMV in the frontal and anterior cingulate gyrus regions in CSVD patients. In addition, our work has shown that an appropriate a proper combination of MVPA and MKL methods can substantially improve the classification accuracy of CSVD patients. Our findings may clarify the potential pathogenesis of CSVD and provide further support in favor of machine-learning approaches in improving the clinical diagnosis of CSVD.

DATA AVAILABILITY STATEMENT

The original contributions presented in the study are included in the article/**Supplementary Material**, further inquiries can be directed to the corresponding author.

ETHICS STATEMENT

The studies involving human participants were reviewed and approved by the Institutional Review Board of Shandong Provincial Hospital Affiliated to Shandong First Medical University. The patients/participants provided their written informed consent to participate in this study.

AUTHOR CONTRIBUTIONS

JL and HW wrote the main manuscript text. HW prepared **Figures 1–5**. SW, YC, and NZ prepared the clinical data and imaging data. LG revised the main manuscript text. All authors reviewed the manuscript.

FUNDING

This work was supported by grants from the National Natural Science Foundation of China (81800840), the National Natural Science Foundation of China (32100902), the Fundamental Research Funds for the Central Universities (SWU118065), the Technology Development Plan of Jinan (201301049, 201602206, and 201907052), Medical and Health Science and Technology Development Project of Shandong Province (2016WS0529 and 2019WS544), Funding for Study Abroad Program by Shandong Province (201803059), and Shandong Provincial Natural Science Foundation (ZR2020MH288).

ACKNOWLEDGMENTS

We thank all of the volunteers and patients for their participation in our study.

SUPPLEMENTARY MATERIAL

The Supplementary Material for this article can be found online at: https://www.frontiersin.org/articles/10.3389/fneur.2022.819055/full#supplementary-material

REFERENCES

1. Yilmaz P, Ikram MK, Niessen WJ, Ikram MA, Vernooij MW. Practical small vessel disease score relates to stroke, dementia, and death. *Stroke.* (2018) 49:2857–65. doi: 10.1161/STROKEAHA.118.022485
2. Cuadrado-Godia E, Dwivedi P, Sharma S, Ois Santiago A, Roquer Gonzalez J, Balcells M, et al. Cerebral small vessel disease: a review focusing on pathophysiology, biomarkers, and machine learning strategies. *J Stroke.* (2018) 20:302–20. doi: 10.5853/jos.2017.02922
3. Wardlaw JM, Smith EE, Biessels GJ, Cordonnier C, Fazekas F, Frayne R, et al. Neuroimaging standards for research into small vessel disease and its contribution to ageing and neurodegeneration. *Lancet Neurol.* (2013) 12:822–38. doi: 10.1016/S1474-4422(13)70124-8
4. Schneider JA. Brain microbleeds and cognitive function. *Stroke.* (2007) 38:1730–1. doi: 10.1161/STROKEAHA.107.487173
5. Fazekas F, Kleinert R, Roob G, Kleinert G, Kapeller P, Schmidt R, et al. Histopathologic analysis of foci of signal loss on gradient-echo T2*-weighted MR images in patients with spontaneous intracerebral hemorrhage: evidence of microangiopathy-related microbleeds. *AJNR Am J Neuroradiol.* (1999) 20:637–42.
6. Shoamanesh A, Preis SR, Beiser AS, Vasan RS, Benjamin EJ, Kase CS, et al. Inflammatory biomarkers, cerebral microbleeds, and small vessel disease: framingham heart study. *Neurology.* (2015) 84:825–32. doi: 10.1212/WNL.0000000000001279
7. Li X, Yuan J, Yang L, Qin W, Yang S, Li Y, et al. The significant effects of cerebral microbleeds on cognitive dysfunction: an updated meta-analysis. *PLoS ONE.* (2017) 12:e0185145. doi: 10.1371/journal.pone.0185145
8. Takashima Y, Mori T, Hashimoto M, Kinukawa N, Uchino A, Yuzuriha T, et al. Clinical correlating factors and cognitive function in community-dwelling healthy subjects with cerebral microbleeds. *J Stroke Cerebrovasc Dis.* (2011) 20:105–10. doi: 10.1016/j.jstrokecerebrovasdis.2009.11.007
9. Yamashiro K, Tanaka R, Okuma Y, Shimura H, Ueno Y, Miyamoto N, et al. Cerebral microbleeds are associated with worse cognitive function in the nondemented elderly with small vessel disease. *Cerebrovasc Dis Extra.* (2014) 4:212–20. doi: 10.1159/000369294
10. Zhang J, Liu L, Sun H, Li M, Li Y, Zhao J, et al. Cerebral microbleeds are associated with mild cognitive impairment in patients with hypertension. *J Am Heart Assoc.* (2018) 7:e008453. doi: 10.1161/JAHA.117.008453
11. Liu C, Zhao L, Yang S, Luo Y, Zhu W, Zhu W, et al. Structural changes in the lobar regions of brain in cerebral small-vessel disease patients with and without cognitive impairment: an MRI-based study with automated brain volumetry. *Eur J Radiol.* (2020) 126:108967. doi: 10.1016/j.ejrad.2020.108967
12. Wang Q, Su N, Huang J, Liang X, Yuan J, Yao M, et al. White matter but not gray matter volumes are associated with cognition in community-dwelling Chinese Populations. *J Alzheimers Dis.* (2021) 84:367–75. doi: 10.3233/JAD-210367
13. Su N, Liang X, Zhai FF, Zhou LX, Ni J, Yao M, et al. The consequence of cerebral small vessel disease: linking brain atrophy to motor impairment in the elderly. *Hum Brain Mapp.* (2018) 39:4452–61. doi: 10.1002/hbm.24284

14. Su N, Liang X, Yao M, Zhou LX, Wang Q, Jin ZY, et al. Cerebral Microbleeds correlated with white matter and hippocampal volumes in community-dwelling populations. *J Alzheimers Dis.* (2019) 71:559–67. doi: 10.3233/JAD-190454
15. Wang PN, Chou KH, Peng LN, Liu LK, Lee WJ, Chen LK, et al. Strictly lobar cerebral microbleeds are associated with increased white matter volume. *Transl Stroke Res.* (2020) 11:29–38. doi: 10.1007/s12975-019-00704-z
16. Wen H, Liu Y, Rekik I, Wang S, Chen Z, Zhang J, et al. Multi-modal multiple kernel learning for accurate identification of Tourette syndrome children. *Pattern Recognit.* (2017) 63:601–11. doi: 10.1016/j.patcog.2016.09.039
17. Hu X, Zhang L, Bu X, Li H, Li B, Tang W, et al. Localized connectivity in obsessive-compulsive disorder: an investigation combining univariate and multivariate pattern analyses. *Front Behav Neurosci.* (2019) 13:122. doi: 10.3389/fnbeh.2019.00122
18. Lambert C, Narean JS, Benjamin P, Zeestraten E, Barrick TR, Markus HS. Characterising the grey matter correlates of leukoaraiosis in cerebral small vessel disease. *Neuroimage Clin.* (2015) 9:194–205. doi: 10.1016/j.nicl.2015.07.002
19. Ciulli S, Citi L, Salvadori E, Valenti R, Poggesi A, Inzitari D, et al. Prediction of impaired performance in trail making test in MCI patients with small vessel disease using DTI data. *IEEE J Biomed Health Inform.* (2016) 20:1026–33. doi: 10.1109/JBHI.2016.2537808
20. Gonzalez-Castro V, Valdes-Hernandez M, Chappell FM, Armitage PA, Wardlaw JM. Reliability of an automatic classifier for brain enlarged perivascular spaces burden and comparison with human performance. *Clin Sci.* (2017) 131:1465–81. doi: 10.1042/CS20170051
21. Cannistraro RJ, Badi M, Eidelman BH, Dickson DW, Middlebrooks EH, Meschia JF, et al. small vessel disease: a clinical review. *Neurology.* (2019) 92:1146–56. doi: 10.1212/WNL.0000000000007654
22. Amin Al, Olama A, Wason JMS, Tuladhar AM, van Leijsen EMC, Koini M, Hofer E, et al. Simple MRI score aids prediction of dementia in cerebral small vessel disease. *Neurology.* (2020) 94:e1294–302. doi: 10.1212/WNL.0000000000009141
23. Greenberg SM, Vernooij MW, Cordonnier C, Viswanathan A, Al-Shahi Salman R, Warach S, et al. Cerebral microbleeds: a guide to detection and interpretation. *Lancet Neurol.* (2009) 8:165–74. doi: 10.1016/S1474-4422(09)70013-4
24. Yakushiji Y. Cerebral microbleeds: detection, associations and clinical implications. *Front Neurol Neurosci.* (2015) 37:78–92. doi: 10.1159/000437115
25. Haller S, Scheffler M, Salomir R, Herrmann FR, Gold G, Montandon M-L, et al. MRI detection of cerebral microbleeds: size matters. *Neuroradiology.* (2019) 61:1209–13. doi: 10.1007/s00234-019-02267-0
26. Bergeron D, Flynn K, Verret L, Poulin S, Bouchard RW, Bocti C, et al. Multicenter validation of an MMSE-MoCA conversion table. *J Am Geriatr Soc.* (2017) 65:1067–72. doi: 10.1111/jgs.14779
27. Lu J, Li D, Li F, Zhou A, Wang F, Zuo X, et al. Montreal cognitive assessment in detecting cognitive impairment in Chinese elderly individuals: a population-based study. *J Geriatr Psychiatry Neurol.* (2011) 24:184–90. doi: 10.1177/0891988711422528
28. Putcha D, Brickhouse M, Wolk DA, Dickerson BC, Alzheimers dis neuroimaging I. Fractionating the rey auditory verbal learning test: distinct roles of large-scale cortical networks in prodromal Alzheimer's disease. *Neuropsychologia.* (2019) 129:83–92. doi: 10.1016/j.neuropsychologia.2019.03.015
29. Benedict RH, DeLuca J, Phillips G, LaRocca N, Hudson LD, Rudick R. Validity of the symbol digit modalities test as a cognition performance outcome measure for multiple sclerosis. *Mult Scler.* (2017) 23:721–33. doi: 10.1177/1352458517690821
30. Wei M, Shi J, Li T, Ni J, Zhang X, Li Y, et al. Diagnostic accuracy of the chinese version of the trail-making test for screening cognitive impairment. *J Am Geriatr Soc.* (2018) 66:92–9. doi: 10.1111/jgs.15135
31. Scarpina F, Tagini S. The stroop color and word test. *Front Psychol.* (2017) 8:557. doi: 10.3389/fpsyg.2017.00557
32. Ashburner J. A fast diffeomorphic image registration algorithm. *Neuroimage.* (2007) 38:95–113. doi: 10.1016/j.neuroimage.2007.07.007
33. Yan CG, Wang XD, Zuo XN, Zang YF. DPABI data processing & analysis for (resting-state) brain imaging. *Neuroinformatics.* (2016) 14:339–51. doi: 10.1007/s12021-016-9299-4
34. Bansal R, Peterson BS. Cluster-level statistical inference in fMRI datasets: the unexpected behavior of random fields in high dimensions. *Magn Reson Imaging.* (2018) 49:101–15. doi: 10.1016/j.mri.2018.01.004
35. Schrouff J, Rosa MJ, Rondina JM, Marquand AF, Chu C, Ashburner J, et al. PRoNTo: pattern recognition for neuroimaging toolbox. *Neuroinformatics.* (2013) 11:319–37. doi: 10.1007/s12021-013-9178-1
36. Tzourio-Mazoyer N, Landeau B, Papathanassiou D, Crivello F, Etard O, Delcroix N, et al. Automated anatomical labeling of activations in SPM using a macroscopic anatomical parcellation of the MNI MRI single-subject brain. *Neuroimage.* (2002) 15:273–89. doi: 10.1006/nimg.2001.0978
37. He Y, Wang J, Wang L, Chen ZJ, Yan C, Yang H, et al. Uncovering intrinsic modular organization of spontaneous brain activity in humans. *PLoS ONE.* (2009) 4:e5226. doi: 10.1371/journal.pone.0005226
38. Wardlaw JM, Smith C, Dichgans M. Mechanisms of sporadic cerebral small vessel disease: insights from neuroimaging. *Lancet.* (2013) 12:483–97. doi: 10.1016/S1474-4422(13)70060-7
39. Smith MA, Harris PL, Sayre LM, Perry G. Iron accumulation in Alzheimer disease is a source of redox-generated free radicals. *PNAS.* (1997) 94:9866–8. doi: 10.1073/pnas.94.18.9866
40. Li X, Lei P, Tuo Q, Ayton S, Li Q-X, Moon S, et al. Enduring elevations of hippocampal amyloid precursor protein and iron are features of β-amyloid toxicity and are mediated by tau. *Neurotherapeutics.* (2015) 12:862–73. doi: 10.1007/s13311-015-0378-2
41. Fan F, Liao X, Lei T, Zhao T, Xia M, Men W, et al. Development of the default-mode network during childhood and adolescence: a longitudinal resting-state fMRI study. *Neuroimage.* (2021) 226:117581. doi: 10.1016/j.neuroimage.2020.117581
42. Gu Z, Lu H, Zhou H, Zhang J, Xing W. The relationship between abnormal cortical activity in the anterior cingulate gyrus and cognitive dysfunction in patients with end- stage renal disease: a fMRI study on the amplitude of low- frequency fluctuations. *Ann Palliat Med.* (2020) 9:4187–93. doi: 10.21037/apm-20-2138
43. Li W, Qin W, Liu H, Fan L, Wang J, Jiang T, et al. Subregions of the human superior frontal gyrus and their connections. *Neuroimage.* (2013) 78:46–58. doi: 10.1016/j.neuroimage.2013.04.011
44. Cao S, Nie J, Zhang J, Chen C, Wang X, Liu Y, et al. The cerebellum is related to cognitive dysfunction in white matter hyperintensities. *Front Aging Neurosci.* (2021) 13:670463. doi: 10.3389/fnagi.2021.670463
45. Ward AM, Mormino EC, Huijbers W, Schultz AP, Hedden T, Sperling RA. Relationships between default-mode network connectivity, medial temporal lobe structure, and age-related memory deficits. *Neurobiol Aging.* (2015) 36:265–72. doi: 10.1016/j.neurobiolaging.2014.06.028
46. Wang Y, Yang Y, Wang T, Nie S, Yin H, Liu J. Correlation between white matter hyperintensities related gray matter volume and cognition in cerebral small vessel disease. *J Stroke Cerebrovasc Dis.* (2020) 29:105275. doi: 10.1016/j.jstrokecerebrovasdis.2020.105275
47. Yates PA, Villemagne VL, Ellis KA, Desmond PM, Masters CL, Rowe CC. Cerebral microbleeds: a review of clinical, genetic, and neuroimaging associations. *Front Neurol.* (2014) 4:205. doi: 10.3389/fneur.2013.00205
48. Koizumi K, Hattori Y, Ahn SJ, Buendia I, Ciacciarelli A, Uekawa K, et al. Apoε4 disrupts neurovascular regulation and undermines white matter integrity and cognitive function. *Nat Commun.* (2018) 9:3816. doi: 10.1038/s41467-018-06301-2
49. Sun J, Yu X, Jiaerken Y, Song R, Huang P, Wang C, et al. The relationship between microvasculature in white matter hyperintensities and cognitive function. *Brain Imaging Behav.* (2017) 11:503–11. doi: 10.1007/s11682-016-9531-8
50. Uchida Y, Kan H, Sakurai K, Arai N, Kato D, Kawashima S, et al. Voxel-based quantitative susceptibility mapping in Parkinson's disease with mild cognitive impairment. *Mov Disord.* (2019) 34:1164–73. doi: 10.1002/mds.27717
51. Seo SW, Lee BH, Kim EJ, Chin J, Cho YS, Yoon U, et al. Clinical significance of microbleeds in subcortical vascular dementia. *Stroke.* (2007) 38:1949–51. doi: 10.1161/STROKEAHA.106.477315
52. Papeo L, Agostini B, Lingnau A. The large-scale organization of gestures and words in the middle temporal gyrus. *J Neurosci.* (2019) 39:5966–74. doi: 10.1523/JNEUROSCI.2668-18.2019

53. Yi HG, Leonard MK, Chang EF. The encoding of speech sounds in the superior temporal gyrus. *Neuron.* (2019) 102:1096–110. doi: 10.1016/j.neuron.2019.04.023
54. Meda SA, Hawkins KA, Dager AD, Tennen H, Khadka S, Austad CS, et al. Longitudinal effects of alcohol consumption on the hippocampus and parahippocampus in college students. *Biol Psychiatry Cogn Neurosci Neuroimaging.* (2018) 3:610–7. doi: 10.1016/j.bpsc.2018.02.006
55. Kubota S, Masaoka Y, Sugiyama H, Yoshida M, Yoshikawa A, Koiwa N, et al. Hippocampus and parahippocampus volume reduction associated with impaired olfactory abilities in subjects without evidence of cognitive decline. *Front Hum Neurosci.* (2020) 14:556519. doi: 10.3389/fnhum.2020.556519
56. Farokhian F, Beheshti I, Sone D, Matsuda H. Comparing CAT12 and VBM8 for detecting brain morphological abnormalities in temporal lobe epilepsy. *Front Neurol.* (2017) 8:428. doi: 10.3389/fneur.2017.00428

Conflict of Interest: The authors declare that the research was conducted in the absence of any commercial or financial relationships that could be construed as a potential conflict of interest.

frontiers in Neurology

ORIGINAL RESEARCH
published: 24 March 2022
doi: 10.3389/fneur.2022.846348

Fully Automatic Classification of Brain Atrophy on NCCT Images in Cerebral Small Vessel Disease: A Pilot Study Using Deep Learning Models

*Jincheng Wang[1], Sijie Chen[2], Hui Liang[3], Yilei Zhao[1], Ziqi Xu[3], Wenbo Xiao[1], Tingting Zhang[1], Renjie Ji[3], Tao Chen[1], Bing Xiong[1], Feng Chen[1], Jun Yang[4] and Haiyan Lou[1]**

[1] Department of Radiology, First Affiliated Hospital, School of Medicine, Zhejiang University, Hangzhou, China, [2] State Key Laboratory of Medical Neurobiology and Collaborative Innovation Center for Brain Science, Institutes of Brain Science, Fudan University, Shanghai, China, [3] Department of Neurology, First Affiliated Hospital, School of Medicine, Zhejiang University, Hangzhou, China, [4] Taimei Medical Technology, Shanghai, China

Edited by:
Patrick Stroman,
Queen's University, Canada

Reviewed by:
Juha Koikkalainen,
Combinostics Oy, Finland
Suraj Mishra,
University of Notre Dame,
United States
Goo-Rak Kwon,
Chosun University, South Korea

****Correspondence:***
Haiyan Lou
loulan1988@zju.edu.cn

Specialty section:
This article was submitted to
Applied Neuroimaging,
a section of the journal
Frontiers in Neurology

Received: *31 December 2021*
Accepted: *24 February 2022*
Published: *24 March 2022*

Citation:
Wang J, Chen S, Liang H, Zhao Y, Xu Z, Xiao W, Zhang T, Ji R, Chen T, Xiong B, Chen F, Yang J and Lou H (2022) Fully Automatic Classification of Brain Atrophy on NCCT Images in Cerebral Small Vessel Disease: A Pilot Study Using Deep Learning Models. Front. Neurol. 13:846348. doi: 10.3389/fneur.2022.846348

Objective: Brain atrophy is an important imaging characteristic of cerebral small vascular disease (CSVD). Our study explores the linear measurement application on CT images of CSVD patients and develops a fully automatic brain atrophy classification model. The second aim was to compare it with the end-to-end Convolutional Neural Networks (CNNs) model.

Methods: A total of 385 subjects such as 107 no-atrophy brain, 185 mild atrophy, and 93 severe atrophy were collected and randomly separated into training set ($n = 308$) and test set ($n = 77$). Key slices for linear measurement were manually identified and used to annotate nine linear measurements and a binary classification of cerebral sulci widening. A linear-measurement-based pipeline (2D model) was constructed for two-types (existence/non-existence brain atrophy) or three-types classification (no/mild atrophy/severe atrophy). For comparison, an end-to-end CNN model (3D-deep learning model) for brain atrophy classification was also developed. Furthermore, age and gender were integrated to the 2D and 3D models. The sensitivity, specificity, accuracy, average F1 score, receiver operating characteristics (ROC) curves for two-type classification and weighed kappa for three-type classification of the two models were compared.

Results: Automated measurement of linear measurements and cerebral sulci widening achieved moderate to almost perfect agreement with manual annotation. In two-type atrophy classification, area under the curves (AUCs) of the 2D model and 3D model were 0.953 and 0.941 with no significant difference ($p = 0.250$). The Weighted kappa of the 2D model and 3D model were 0.727 and 0.607 according to standard classification they displayed, mild atrophy and severe atrophy, respectively. Applying patient age and gender information improved classification performances of both 2D and 3D models in two-type and three-type classification of brain atrophy.

Conclusion: We provide a model composed of different modules that can classify CSVD-related brain atrophy on CT images automatically, using linear measurement. It has similar performance and better interpretability than the end-to-end CNNs model and may prove advantageous in the clinical setting.

Keywords: brain atrophy, linear measurement, automated classification, convolutional neural networks, cerebral small vessel disease, computed tomography, deep learning

INTRODUCTION

Cerebral small vessel disease (CSVD), a disorder of cerebral microvessels, is an expanding epidemic all over the world. CSVD causes approximately a quarter of ischemic strokes and most hemorrhagic strokes. It is the most common cause of vascular dementia, and worsens the resulting cognitive impairment, thus contributing to about 50% of dementias worldwide, a massive health burden in reality (1, 2). In the context of CSVD, brain atrophy is one of the important radiological descriptions, according to the standards for reporting vascular changes on neuroimaging (STRIVE) (3). The neuropathological basis includes neuron loss, cortical thinning, subcortical vascular disease with white matter thinning and contraction, arteriolar sclerosis, venous collagen degeneration, and secondary neurodegenerative changes (4). Brain atrophy usually appears with other signs of CSVD, and it is an important measure in imaging studies that are done to assess the burden of vascular damage in the brain (5–7). The path analyses show that the impact of CSVD-related lesions on the clinical status is partly due to brain atrophy and changes in cortical morphology (8). Atrophy is thought to mediate, at least partially, the effects of vascular lesions on cognition, and is mainly observed in patients with accelerating cognitive decline (9, 10). Brain atrophy is suggested to impair the potential for functional recovery after stroke. Severe atrophy thus has lower brain reserve, making it less resilient to ischemic injury (11, 12).

Non-contrast computed tomography (NCCT) has the advantages of broader acceptability, lower cost, and faster scanning speed (less motion artifacts) compared to magnetic resonance imaging (MRI), and it plays a fundamental role in neuroimaging (13). Brain atrophy, such as cortical atrophy and central atrophy, has characteristic findings on NCCT images. The typical sign of central atrophy is the enlargement of the ventricular system. Correspondingly, enlarged Sylvian fissures, widened sulci, and narrowed gyrus are markers of cortical atrophy (14). The visual assessment of these discoveries of brain atrophy is simple and convenient (15), but its accuracy depends on the higher professional knowledge and rich clinical experience of raters. Although some scales based on visual findings have been developed, it is relatively coarse, subjective, and might be prone to floor and ceiling effects. In view of the low tissue contrast on NCCT images, accurate tissue segmentation and volume calculation are still imperfect and are constantly being improved (16). The challenge is believed to be tougher for some CSVD patients (17). The presence of white matter hypoattenuation or white matter hypodensities on NCCT further reduces tissue contrast. One-dimensional linear measurement, a mature and reliable way to assess the brain atrophy, has been widely used in clinical practice (18–20). Previous studies have shown that one-dimensional linear measurement and three-dimensional measurement results have achieved substantial correlation (21, 22). It does not have high requirements for tissue contrast and can be used on either MRI or NCCT.

A significant progress has been made in the development of fully automated structural image analysis and computer-aided diagnosis technology (23). The fully automatic method provides several advantages, including the ability to complete the set tasks independently without manual operation, and the measurement results can be quantified and further analyzed. This method has been beneficially applied to patients with CSVD (24). As a branch of machine learning, deep learning can extract hidden features within big data automatically and has achieved advanced performance across various fields (25). On the one hand, the underlying mechanism of deep learning is still a black box (26), and some researchers are focused on visualization and are dedicated to improving the interpretability of the algorithms (27). Building the model pipeline following the human medical approach rather than generating an end-to-end model is also a potentially advantageous protocol in relation to certain tasks. Yet, for the brain atrophy of CSVD patients, automatic analysis is mostly performed on MRI. The establishment of a fully automatic evaluation model on NCCT images is a useful supplement with clinical value.

In this study, we aimed to develop a fully automated brain atrophy classification model based on NCCT images for CSVD subjects, using one-dimensional line measurements to overcome the limitations of low tissue contrast. Several clinical information such as age and gender, were also included in the model to improve the accuracy of the model (2D-integrated model). For performance comparison, an end-to-end model (3D model and 3D-integrated model) has also been developed based on a pre-trained 3D CNN algorithm.

MATERIALS AND METHODS

Study Populations

An observational study based on a cohort of outpatients and inpatients was conducted at the Stroke Center of the First Affiliated Hospital of Zhejiang University, from March 1, 2019 to April 1, 2020. This retrospective study was approved by the ethics committee of the first affiliated hospital of Zhejiang University (approval number: 2019.1511). A total of 385 eligible patients were enrolled in this study. The inclusion criteria were set as follows: (1) Patients who have been clinically diagnosed as CSVD, and at least one of the following neuroimaging markers on MRI images: white matter hyperintensities, recent small subcortical infarcts, lacunes, enlarged perivascular spaces, cortical microinfarcts, cerebral microbleeds, and brain atrophy (8). (2) The both MRI and NCCT head/brain scans of patients

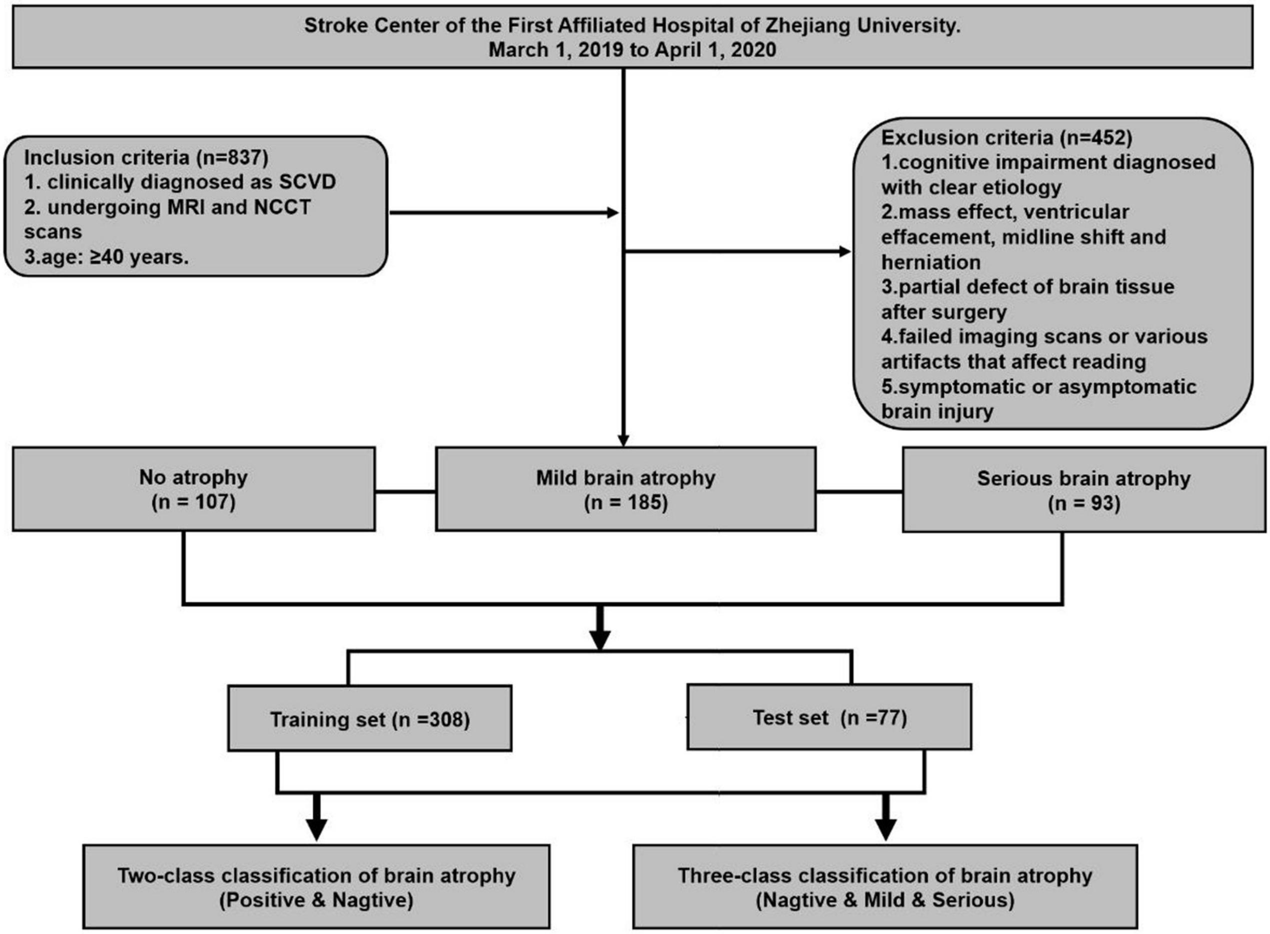

FIGURE 1 | Flowchart of patient enrollment and strategy of training and testing for brain atrophy classification.

were used to make a set of MRI–NCCT pairs for accurate training preparations, and the time interval between the MRI and NCCT scans were required to be <3 months to avoid differences in brain structures due to possible disease progression. (3) Age equal to or >40 years. The following patients were excluded: (1) cognitive impairment diagnosed with clear etiology, such as poisoning, infection, degeneration diseases (Parkinson's disease, multiple system atrophy, corticobasal degeneration, and dementia with Lewy bodies, etc.), and immune demyelination (multiple sclerosis, Balo's concentric sclerosis, etc.); (2) patients with any indications that may affect the linear measurement, such as of intracranial mass effect and local mass effect, ventricular effacement, midline shift, and herniation; (3) partial defect of brain tissue after surgery; (4) failed imaging scans or various artifacts that affect reading; and (5) symptomatic or asymptomatic brain injury. The study flowchart is shown in **Figure 1**.

Computed Tomography Image Dataset

All CT scans were performed using 64-rows helical CT scanners(Brilliance 64, Philips; LightSpeed VCT, GE Medical System) with a tube voltage of 20 kVp and a tube current of 180–200 mAs. The raw data of the Minimum slice thickness in the *Z* axis direction were 0.625 mm, and the reconstruction slice thickness was 5 mm with an image matrix of 512 × 512 pixels.

Data Pre-Processing

Each image was normalized to the same intensity range 0–255 (WW = 80 HU, WL = 40 HU) and when deemed necessary the brain midline was rotated vertically. For 2D model training, all images were resampled to 224 × 224 pixels to reduce the GPU memory usage.

Model Training and Testing

All NCCT scans were randomly separated into a training set ($n = 308$) and a test set ($n = 77$) for both two-type and three-type classification tasks. At first, all images were corrected by rotation on the X–Y plane, asserting the brains were perpendicular to the horizontal edges of image in each sample. A series of common data augmentation approaches were performed to increase training data diversity and size, such as random rotation (from −5 to 5 degrees), random shift, random zoom, left–right

TABLE 1 | Demographic information of the study subjects.

	No atrophy ($n = 107$)	Mild atrophy ($n = 185$)	Severe atrophy ($n = 93$)
Age (year)	48 (40 67)	74 (44 94)	81 (60 99)
Gender (male: female)	48:59	96:89	51:72

Age presented as median (range).

flipping, and adding Gaussian noise. We applied five-fold cross validation in the training set (the training set was randomly split into five subsets. A model was trained using the first four subsets, and then validated on the remaining subset. Five iterations were performed using each subset as validation set to optimize model parameters and to avoid overfitting. All models were trained only on the training set, and the testing set was reserved for performance evaluation of our models.

Ground Truth Label (Reference for Model Training)

A neuroscientist and a radiologist, both with more than 20 years of personal experience, will reach a consensus on MRI–NCCT image pairs. The CSVD-related brain atrophy is labeled by the visual assessment on MRI (28). No enlargement of the ventricular system (third and fourth ventricles) and no enlargement of the sulci and lateral fissure is defined as no brain atrophy ($n = 107$). The significant enlargement of the ventricular system, along with significantly widened parietal lobe sulci (at least 2 sulci were >5 mm in width), and a significantly widened lateral fissure cistern is defined as severe atrophy ($n = 93$). The rest did not meet the above conditions and were regarded as having mild atrophy ($n = 185$). The high atrophy ratio was retained in the dataset to ensure sufficient positive samples for the effective learning process and evaluation of 3-classification algorithms. The demographic characteristics of the dataset are shown in **Table 1**.

Manual Annotation on NCCT

The one-dimensional linear measurement was independently completed by another neuroradiologist on the four key slices of the NCCT images with ITK-SNAP software (US National Institutes of Health). This researcher was unaware of the label and clinical information of each subject. Results of the annotation were reviewed by the aforementioned two experts and a consensus was reached (**Figure 2**). Nine linear measurements included maximal frontal horn width (A), minimal intercaudate distance (B), maximal width of third ventricle (C), the choroid plexuses distance (D) on basal ganglion slice showing most prominently the heads of the caudate nuclei (key slice 1), minimal ventricular body width (E), maximal transversal intracranial width (F), and maximal transversal extracranial width (G) on a slice displaying most of the body of the lateral ventricle (key slice 2). The maximal width of Sylvian fissures (HR/HL) on the slice where measurement was most clearly visualized (key slice 3) (20, 29–31). It needs to be emphasized that enlargement of the parietal lobe sulci (at least 2 sulci being >5 mm in width) is a binary classification, implemented on the third slice above the top of the lateral ventricle (key slice 4), and still based on expert consensus as the ground truth.

Overview of Pipeline Modules of Brain Atrophy Classification Model

The pipeline of the classification model consists of four modules: (1) key slice detection module, (2) automatic measurement module, (3) identification module of cerebral sulci widening, and (4) classifier module (**Figure 3A**). Key slice detectors, linear measurement calculators and cerebral sulci enlargement identifiers were developed based on CNN algorithms, while the atrophy classifier was implemented by a logistic regression model. All included CT images after pre-processing were input into the pipeline: key slices were identified first, and then linear measurements and cerebral sulci information were automatically identified. Seven linear measurements such as the Huckman Number (A + B), ventricle index (D/A), lateral ventricular body index (F/E), width of lateral ventricular body index (G/E), ventricle forefoot index (G/A), maximum width of third ventricle (C), average width of Sylvian fissures ([HL + HR]/2) (20, 30, 31), along with cerebral sulci enlargement information were used to identify whether the subject had cerebral atrophy or not in the two-class classification, and no atrophy, mild atrophy, or severe atrophy in the three-class classification.

Module 1: Key Slice Detection

The ResNet34, consisting of four convolutional-pooling blocks and a fully connected layer, was used as the backbone model to detect four defined key slices (32). To train the proposed CNN model, momentum was applied as the optimizer to minimize the cross entropy between annotated key slices and the prediction outputs. The batch size was set to eight and the learning rate was applied with piecewise-scheduled decay with warming starting. We selected models for each key slice with the best accuracy in the validation set to construct the detector for each slice.

Module 2: Automatic Measurement

Models for nine linear measurements in key slices 1, 2, and 3 were developed based on the ResNet 18 backbone. As the structure and morphology of the brain are very similar on adjacent slices to the key slice, we fed the key slice and two adjacent slices into three channels of the RGB color image and generated a three-channel fused image to train the proposed model. We used the mean square error (MSE) as the cost function and Adam as the optimization algorithm. The batch size is 16, learning rate is 0.0001, and the value of decay is 0.8 with a decay step of 10,000.

Module 3: Cerebral Sulci of Parietal Lobe Enlargement Identification

Model for cerebral sulci of parietal lobe enlargement identification in key slice 4 was developed based on ResNet 18 backbone. Three channel fused image consisting of key slice 4 and adjacent slices was used to train the classification model. We used cross entropy as the loss function and momentum as the optimization algorithm. The batch size was 8 and the

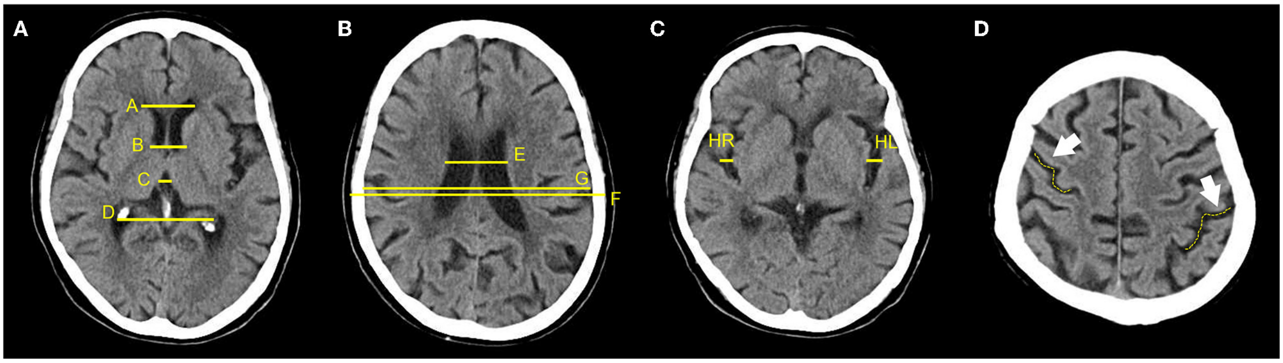

FIGURE 2 | Annotation of 9 linear measurements and cerebral sulci enlargement. **(A–D)** were four key slices defied for linear measurements and Cerebral sulci enlargement identification. **(A)**, A, B, C, and D were manually annotated on basal ganglion slice showing most prominently the heads of the caudate nuclei (Key slice 1); **(B)**, E, F, and G were annotated on slice displaying most of the body of the lateral ventricle (key slice 2); **(C)**. HL and HR were manually annotated on slice a that the Sylvian fissures were most clearly visualized (key slice 3); **(D)**, Binary classification of cerebral sulci widening on the third slice above the top of lateral ventricle was also annotated (key slice 4).

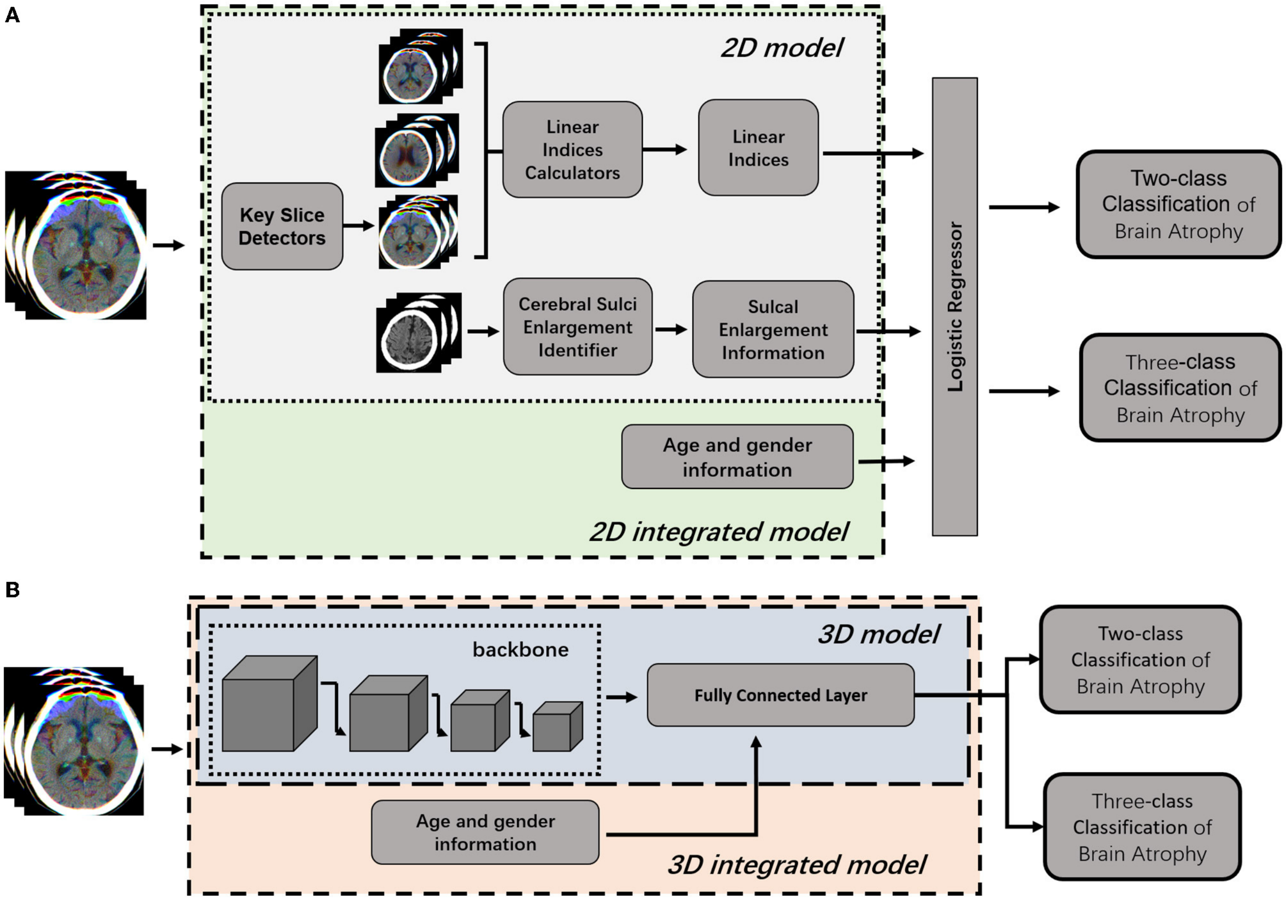

FIGURE 3 | Illustration of 2D model and 3D model for brain atrophy classification. **(A)** 2D model was consisted of four modules, such as key slice detectors, linear measurements calculators, cerebral sulci enlargement identifier, and atrophy classifier. Information of age and gender were integrated into the atrophy classifier of 2D model to generate 2D-integrated model. **(B)** 3D model was developed based on a 3D CNN model. Information of age and gender were integrated into the full connected layer to generate the 3D-integrated model.

learning rate was applied with piecewise-scheduled decay with warming starting.

Module 4: Brain Atrophy Classification

Seven linear measurements and cerebral sulci enlargement information were used to train a logistic regression classifier for no atrophy/atrophy two-class classification or no atrophy/mild atrophy/severe atrophy three-class classification. Furthermore, linear measurements, cerebral sulci of parietal lobe enlargement information as well as age and gender were utilized to build logistic regression as an integrated model.

These four modules had different outputs which were interconnected sequentially, and outputs from the last module were used as training inputs to the next module. The outputs of key slice detection module were the machine-selected four slices (key slice 1–4) from each subject's NCCT image set. The outputs of the automatic measurement module were eight straight lines automatically drawn by the machine and their length values (A-G, HR/HL). For better visualization, these lines were displayed on key slices in different colors. The sulcus enlargement recognition module outputted an automatic judgment result, with or without sulcus enlargement. The outputs of classifier module were obtained by the machine after integrating all the information; it could be binary classification (atrophy or no atrophy) or three classifications (no atrophy, mild atrophy, or severe atrophy).

Overview of End-To-End 3D CNN Model

To compare with the 2D model, an end-to-end deep learning algorithm for two-class and three-class classification were trained using Med3D, a heterogeneous three-dimensional network pretrained on the 3DSeg-8 dataset was employed as the backbone (**Figure 3B**). The batch size was set to four and the Adam algorithm was utilized to optimize model parameters with a learning rate of 0.0001 in the backbone and 0.001 in fully connected layers. Optimization of model parameters was considered to converge once the model's performance on the validation set stopped improving for 50 epochs. Age and gender information were integrated into the fully connected layer to generate the 3D-integrated model. The outputs of 3D model or 3D-integrated model directly generated classification results, either a binary classification (atrophy or no atrophy) or three classifications (no atrophy, mild atrophy, or severe atrophy).

Statistical Analysis

Paired t-test and Pearson correlation test were used to evaluate the performance of automatic linear measurements. The consistency of the cerebral sulci dichotomy was assessed on accuracy and Cohen's kappa. The model performance of two-class classification was evaluated by sensitivity, specificity, accuracy, F1 score, and area under the curve (AUC) with 95% *CI*. The 0.5 was set as the probability threshold of binarized class labels. The differences between Receiver Operating characteristic (ROC) curves were further analyzed using the DeLong test. For three-type classification, the model performance was evaluated based on accuracy, average F1 score, and weighted kappa. All statistical analyses were performed using the R programming language (version 3.6); the $p < 0.05$ was considered as statistically significant.

RESULTS

Module Performance

The performance of three modules, key slice detection, linear measurements, and cerebral sulci enlargement identification, were evaluated in the test set. The detection accuracy for key slices 1, 2, 3, and 4 were 0.887, 0.558, 0.934, and 0.574, respectively, and they were compared with the annotated ground truth. The accuracy of the detected key slice and its two adjacent slices reached 1 for all key slices (**Supplementary Table S1**). The correlation results of nine linear measurements between annotated ground truth and automated measurements were listed in **Table 2**. In the test set, no significant difference was found in the mean value of each linear measurement between automated and manual annotations. Automated measurements achieved a very good correlation with ground truth in the minimal intercaudate distance, maximal transversal intracranial width, and maximal transversal extracranial width (correlation coefficient $\geq$ 0.8), a strong correlation in maximal width of the third ventricle, minimal ventricular body width, and maximal width of Sylvian fissures in left and right (correlation coefficient $\geq$ 0.6), and a moderate correlation in maximal frontal horn width and the choroid plexuses distance (correlation coefficient $\geq$ 0.4). For the cerebral sulci dichotomy, the accuracy of the deep learning algorithm was 0.818, and the Cohen's kappa was 0.636.

Performance of the Two-Type Classification for Brain Atrophy With CSVD

The performance of four models for two-type classification in the test set was assessed (**Table 3** and **Figure 4**). The results showed that the 2D-integrated model yielded the highest sensitivity value (0.951), while the 3D-integrated model yielded the highest specificity value (0.943), accuracy value (0.943), F1 score (0.951), and AUC (0.981). Models with different strategies, all achieved great AUCs for two-type classification (>0.94). Furthermore, ROCs analysis showed the 2D model and 3D model, had no significant differences in statistics. Integration of age and gender information could significantly improve the model performance, while AUCs of the 2D-integrated model and 3D-integrated model had no significant differences (**Supplementary Table S2**). The representative cases of misclassifications showed key slice 3 (***** in **Figures 5A,B**) detected by the 2D model was the adjacent slice to the manually annotated slice (reference) in both cases, which led to shorter H (long arrows) and might be the reason for misclassifications.

Performance of the Three-Type Classification for Brain Atrophy With CSVD

The performance of four models for three-class classification tasks was shown (**Table 4**). In the test set, the 2D-integrated model achieved the highest accuracy (0.808) and kappa (0.786), while the 3D-integrated model showed the highest average F1 score. All models had a substantial agreement with experts

TABLE 2 | Correlation analysis between automated measurement and manual ground truth for linear measurements.

	GT	AI	t	*p*-Value	PCC	*p*-Value
A	35.999 ± 4.186	35.936 ± 2.686	0.363	0.717	0.584	<0.001
B	19.001 ± 4.151	18.808 ± 3.172	1.524	0.128	0.803	<0.001
C	8.215 ± 2.350	8.014 ± 1.536	1.867	0.063	0.618	<0.001
D	52.977 ± 5.858	52.970 ± 3.743	0.026	0.979	0.537	<0.001
E	34.223 ± 6.559	34.147 ± 4.452	−0.16	0.873	0.779	<0.001
F	142.290 ± 6.484	142.579 ± 5.642	−1.854	0.064	0.881	<0.001
G	123.591 ± 7.593	123.862 ± 6.810	−1.894	0.059	0.93	<0.001
HL	6.083 ± 3.078	6.365 ± 3.233	0.523	0.602	0.68	<0.001
HR	6.365 ± 3.229	6.159 ± 2.489	1.729	0.085	0.695	<0.001

GT, manual ground truth; AI, linear measurements achieved by 2D model; PCC, Pearson correlation coefficient.

TABLE 3 | Performance comparison for two-class classification of brain atrophy in test set, in terms of sensitivity, specificity, accuracy, F1 score, and area under the curve (AUC).

	Sensitivity	Specificity	Accuracy	F1 Score	AUC
2D model	0.931	0.854	0.899	0.916	0.953 (0.927–0.972)
2D integrated model	0.951	0.902	0.932	0.943	0.975 (0.954–0.988)
3D model	0.851	0.924	0.881	0.894	0.941 (0.912–0.962)
3D integrated model	0.943	0.943	0.943	0.951	0.981 (0.962–0.992)

AUC presented as the value of AUC (95% confident interval).

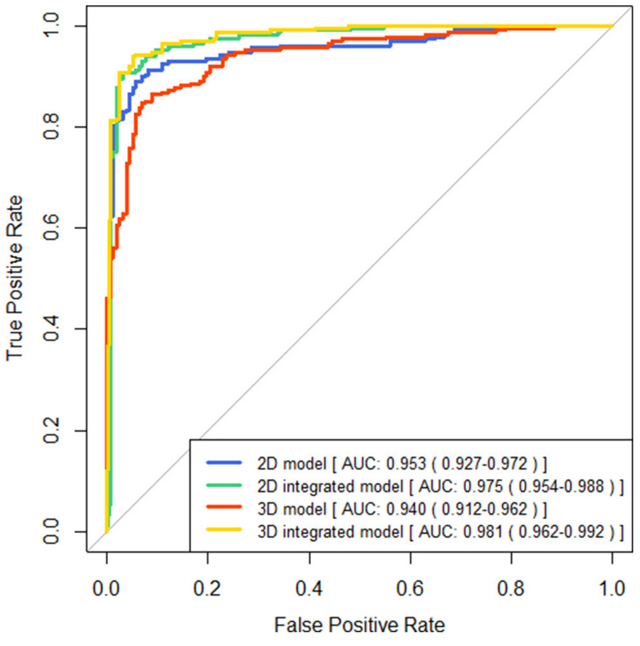

FIGURE 4 | Comparisons of receiver operating characteristics (ROC) curves generated by brain atrophy models for two-type classification.

in diagnosing and classifying the degree of brain atrophy. Furthermore, we evaluated the classification performance of no atrophy, mild atrophy, and severe atrophy, respectively (**Supplementary Table S3**). Consistent with the results of two-type classification, the models all achieved a high performance with the identification of no-atrophy subjects. The 2D-integrated model was the best-performed model with an accuracy of 0.932, F1 score of 0.917, and AUC of 0.978 (0.959–0.991). In mild and severe atrophy, the AUC of the 2D model was consistently higher than that of the 3D model. Integration of age and gender improved the AUC of the 2D model for mild atrophy classification but showed no significant difference from severe atrophy. Noticeably, all models achieved a low sensitivity (<0.6) and a high specificity (>0.93) for severe atrophy. The representative cases showed a longer H and were achieved by the linear measurement of the 2D model in the no-atrophy patient (**Figure 6A** short arrows). In the mild atrophy case, a shorter D (short arrows in **Figure 6A**) was achieved and the cerebral sulci on key slice 4 was misidentified as normal while manually annotated as enlargement (**Figure 6B***). In the severe atrophy case, shorter C and H (short arrows in **Figure 6C**) were achieved, which might be the reason for misclassification.

DISCUSSION

In this study, we developed and verified a new pipeline that is different from end-to-end. It is applicable to brain atrophy assessment, using linear measurement. On this basis, we provide a fully automatic brain atrophy classification model, which combines machine learning and deep learning, which can be applied to CSVD patients. In addition, by integrating limited clinical information and age and gender, the classification

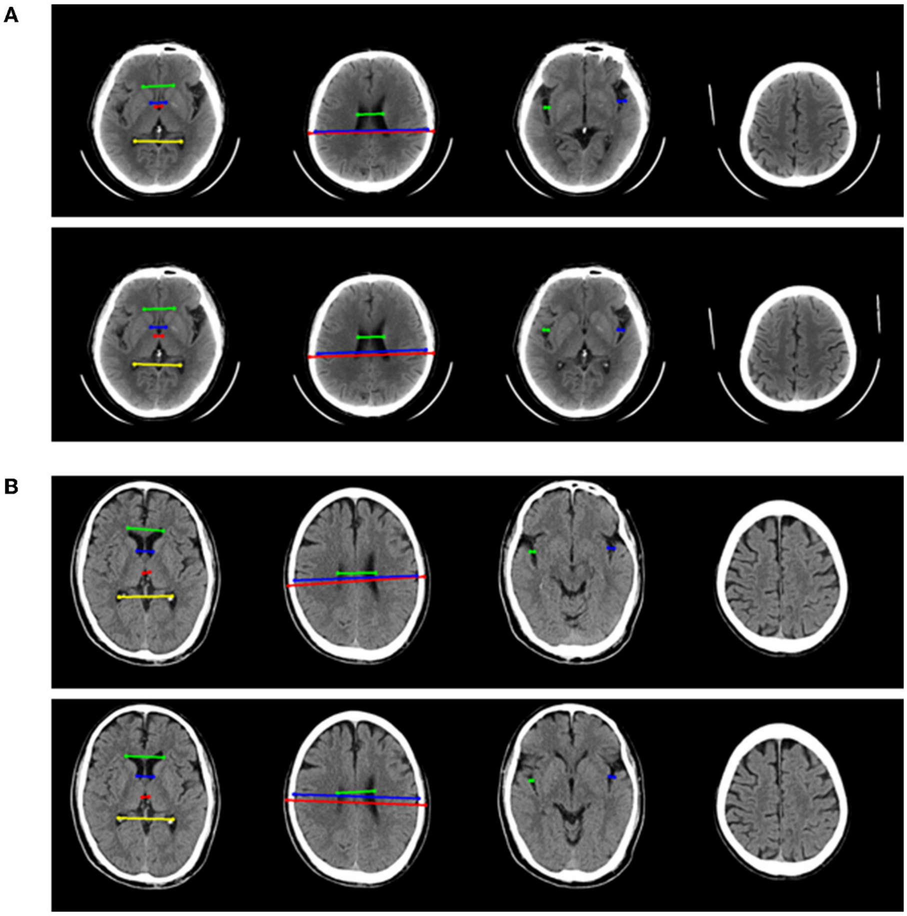

FIGURE 5 | Two representative examples of atrophy cases, which were misclassified. For each example, four key slices were presented from manual annotation (top) and detection of 2D model (bottom). On key slice 1, the green line represented A, the blue line represented B, the red line represented C and the yellow line represented D; On key slice 2, the green line represented E, the blue line represented F and the red line represented G; On key slice 3 (*in **Figures 5A,B**), the green line represented HL (long arrows), while the blue line represented HR (long arrows). **(A)** Example case was misclassified by 2D model but was correctly predicted by 3D model, 2D-integrated model, and 3D-integrated model. **(B)**. Example case was misclassified by both 2D model and 3D model but was correctly predicted by 2D-integrated model and 3D-integrated model.

TABLE 4 | Performance comparison for three-class classification of brain atrophy in test set, in terms of accuracy, average F1 score, and Weighted kappa coefficient.

	Accuracy	Average F1 score	Kappa
2D model	0.761	0.716	0.727
2D integrated model	0.808	0.74	0.786
3D model	0.73	0.657	0.607
3D integrated model	0.795	0.774	0.742

performance of the model is improved. It may be incorporated into clinical decision support tools in the future.

One of the motivations that drove our study is that brain atrophy has become an important risk factor for brain health with CSVD, and the effects of CSVD can be mediated through the development of brain atrophy (33). The increased white matter hypersignal burden undermines the integrity of the white matter and causes the loss of volume. CSVD-related cortical atrophy may result from secondary neurodegenerative processes elicited by degeneration to the WM tracts that disrupt the functional connections of the brain (8). In a longitudinal study, Jokinen H et al. visually assessed the severity of brain atrophy on MRI and confirmed that brain atrophy is independently related to cognitive decline in small vessel diseases (10). Medial temporal lobe atrophy (MTLA), subcortical and cortical atrophy increase the impact of white matter lesions (WML) and lacunae on cognitive decline. This evaluation conclusion was corroborated in another MRI study that used automated brain volume assessment (6). Brain atrophy is related to the adverse outcome of acute ischemic stroke after reperfusion therapy (34). It can be considered as an indicator of brain weakness and is more susceptible to ischemia (35). A study of automatic CT volume segmentation showed that brain atrophy reduces the possibility of functional recovery after acute ischemic stroke in

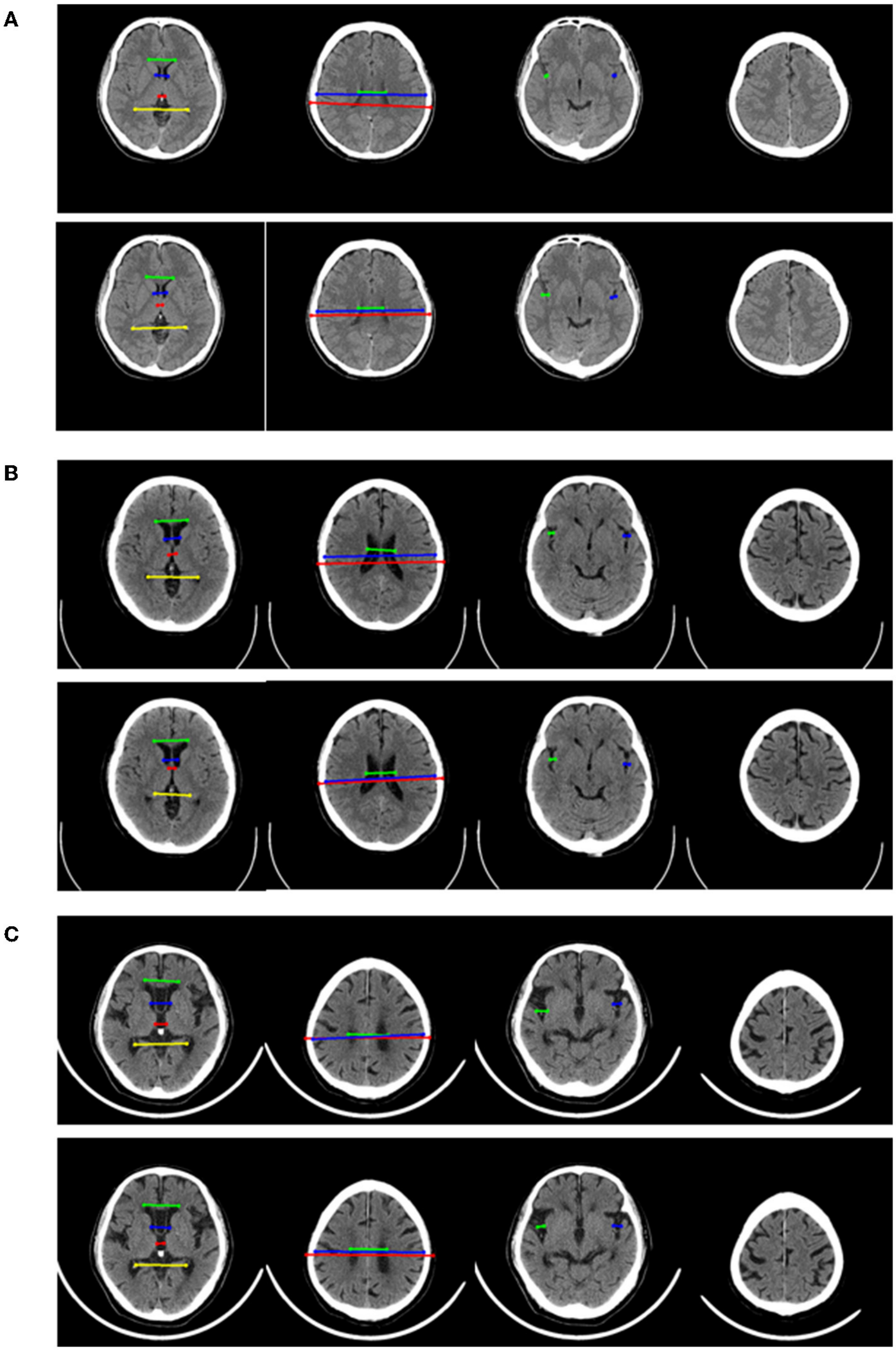

FIGURE 6 | Representative examples in no-atrophy, mild atrophy, and severe atrophy groups that were misclassified. For each example, 4 key slices were presented from manual annotation (top) and results of 2D model (bottom). On key slice 1, the green line represented A, the blue line represented B, the red line represented C and the yellow line represented D; On key slice 2, the green line represented E, the blue line represented F and the red line represented G; On key slice 3, the green line represented HL, while the blue line represented HR. **(A)**. Example case that was misclassified by 2D model but correctly predicted by 3D model, 2D-integrated model and 3D-integrated model in the no-atrophy group. **(B)**. Example case that was misclassified by 2D model, 3D model and 3D-integrated model but correctly predicted by the 2D-integrated model in mild atrophy group. **(C)**. Example case that was misclassified by all four models in severe atrophy group.

the anterior circulation (36). Our cross-sectional study of a group of CSVD subjects supports that the automatic assessment of brain atrophy is realistically achievable. Accurate clinical information (presence/absence and severity) of brain atrophy can be obtained through rapid and fully automatic linear measurement in NCCT. In the test set, the classification performance of the 2D integration model reached a significant agreement with the expert consensus (kappa = 0.786). This may be a friendly and effective assistant for young clinicians, involving decision-making and prognosis of CSVD.

Another important and original intention of our research is to realize and verify the method of fully automatic assessment of brain atrophy on NCCT images, which is also the reason why other neuroimaging features of CSVD patients were not involved in the study. As far as we know, this pilot study is the first attempt to automate linear measurement for the assessment of brain atrophy on NCCT. One-dimensional linear measurement is an effective and economical method for evaluating brain structure (29, 37). The linear index indirectly reflects the structural information of different brain regions. Based on the measured "Hackerman Number" and "ventricular index" data can reflect the degree of central atrophy (37, 38). The width of the Sylvian cistern and the sulci is related to the thickness of the cerebral cortex (39, 40). Linearity measurement is also suitable for evaluating patients with CSVD. Qin calculated the Sylvian fissure ratio (SFR) on the MRI axial image (29). It was defined as the average of the maximal Sylvian widths taken from the cut showing the widest Sylvian fissure divided by the transperineal coronal inner table diameter. In elderly patients with CSVD, SFR has clinical value in screening cognitive decline. Our linear measurement covers the lateral fissure cistern of the brain as well. What's more, we not only automate this linear measurement, but also include more one-dimensional measurements reflecting the brain structure, which will help improve the accuracy of the evaluation and also facilitate its application in different clinical scenarios.

Although the evaluation of CSVD relies on more advanced neuroimaging, mainly MRI structural and functional imaging, CT still plays an important role in primary healthcare centers. Hanning U quantitatively assessed the leukoaraiosis on NCCT images successfully (17). Subsequently, Chen and Pitkänen used machine learning and convolutional networks to further quantify white matter lesions on NCCT (41, 42). Recently, Kaipainen completed the simultaneous assessment of white matter lesions and brain atrophy, but the automated training is very complicated and requires MRI as template mapping (43). Moreover, the ventricular system has not been integrated. As one of many attempts to automate the analysis of CT images, our study can be a useful supplement to the automated evaluation of CSVD. In view of the difference in imaging principles, CT has a lower soft tissue contrast than MRI, and accurate three-dimensional volume measurement is a huge challenge. The presence of WM lesions affected segmentation-based brain volume measurements on MRI (44). For patients with CSVD, as the burden of white matter lesions increases, the density of white matter around the ventricular system decreases, and the segmentation and calculation of ventricle-white matter tissue relying on the difference of the Hounsfield unit threshold brings greater difficulties (17). On the subjects with CSVD, linear measurement is assumed to avoid the interference of white matter lesions. It has been proven that there is a correlation between one-dimensional measurement and three-dimensional measurement results.

Two different models of the underlying system design are presented in this study, one is the end-to-end pipeline, which is considered advanced, and the other is a pipeline composed of several modules. Although the accuracy of key slices detectors failed to reach 100%, the automatically detected key slice is the adjacent slice of manual annotated one in the rest of the cases. The cross-sectional anatomy on the adjacent CT slices of each key slice is similar to the key slice of the ground truth Information of measurements and cerebral sulci can also be obtained on the adjacent slices. We fed three consecutive slices into three channels of the RGB color image to ensure the features of defied key slices can be acquired. Furthermore, three consecutive slices would provide more anatomical information and contribute to generate robust models for the measurement of ventricle indices. The final results show that it is feasible to establish an atrophy classification model based on different modules. For the binary classification, the 2D model shows relatively higher sensitivity and lower specificity than the 3D model. The AUC is 0.953 (0.927–0.972) and 0.941 (0.912–0.962), respectively. In the three-classification task, the Kappa values of the two models were 0.727 and 0.607, respectively. Although both 2D and 3D models have application value in the future, we believe that some of the advantages of linear measurement modules are unique. Different from end-to-end, it is considered a black box between input and output, and the linear side measurement pipeline is artificially divided into four modules. Each module has a specific function and is visualized. This is closer to the thinking logic of human medicine, and therefore, has a greater clinical interpretability. In addition, this strategy improves the predictability of the model output. Adding or reducing the corresponding modules flexibly according to the specific clinical instructions is also easier to achieve. This can also reflect the significance of this pilot study.

There are several limitations in this study. First, this is a retrospective single-center study with a small sample size. Insufficient data will lead to the overfitting problem of deep learning algorithms and limit model performance. Although we have adjusted the ratio of no-atrophy and brain atrophy, the dataset is still imbalanced for a three-type task. Hence, a large and standard dataset is needed to improve model performance. And model robustness should be verified on diverse external datasets in future studies. Second, the present study excluded the atrophy of the cerebellum and brain stem and mainly focused on the assessment of cerebral atrophy, because image artifacts often present in the posterior cranial fossa of NCCT which may interfere with linear measurements and mislead classification. Third, the collected clinical information is limited. More demographic information, medical test results and medical history may be integrated into present models. Lastly, the lack of performance comparison between the automated algorithms and physicians with different training levels is also a limitation. The performance of physicians should be investigated to further elucidate the usefulness of our models.

In conclusion, we develop an end-to-end 3D CNN model and an automatic pipeline by using deep learning and machine learning algorithms to predict brain atrophy degree. The 2D model yields equivalent high performance when compared with the 3D model in predicting the presence of brain atrophy, while the 2D model is superior to the 3D model in predicting the degree of brain atrophy. Integration of age and gender can significantly improve the performance for brain atrophy classification. Compared to the end-to-end 3D CNN model, the 2D model follows the linear measurements approach which is more comprehensible to clinicians. Therefore, the application of our 2D linear measurement-based pipeline has the potential to assist physicians to reduce variants and improve efficiency.

DATA AVAILABILITY STATEMENT

The raw data supporting the conclusions of this article will be made available by the authors, without undue reservation.

ETHICS STATEMENT

The studies involving human participants were reviewed and approved by the Ethics Committee of the First Affiliated Hospital of Zhejiang University (2019.1511). Written informed consent for participation was not required for this study in accordance with the national legislation and the institutional requirements.

AUTHOR CONTRIBUTIONS

XZ, RJ, TZ, and TC collected clinical data of patients. JW, SC, HLi, HLo, and BX performed the image analysis. JW, SC, JY, and HLo analyzed the study data and build model. JW and SC wrote the paper. HLo, YZ, and JY reviewed and revised the manuscript. All authors contributed to the design of the study, gave advice, and reviewed the manuscript.

FUNDING

This study has received funding from National Natural Science Foundation of China (No. 81871428).

ACKNOWLEDGMENTS

The authors would like to thank Daqiang Ke and Huihui Wu for organizing the datasets and preparing supporting materials.

SUPPLEMENTARY MATERIAL

The Supplementary Material for this article can be found online at: https://www.frontiersin.org/articles/10.3389/fneur.2022.846348/full#supplementary-material

REFERENCES

1. Debette S, Schilling S, Duperron MG, Larsson SC, Markus HS. Clinical significance of magnetic resonance imaging markers of vascular brain injury: a systematic review and meta-analysis. *JAMA Neurol.* (2019) 76:81–94. doi: 10.1001/jamaneurol.2018.3122
2. Bos D, Wolters FJ, Darweesh S, Vernooij MW, de Wolf F, Ikram MA, et al. Cerebral small vessel disease and the risk of dementia: a systematic review and meta-analysis of population-based evidence. *Alzheimers Dement.* (2018) 14:1482–92. doi: 10.1016/j.jalz.2018.04.007
3. Wardlaw JM, Smith EE, Biessels GJ, Cordonnier C, Fazekas F, Frayne R, et al. Neuroimaging standards for research into small vessel disease and its contribution to ageing and neurodegeneration. *Lancet Neurol.* (2013) 12:822–38. doi: 10.1016/S1474-4422(13)70124-8
4. Wardlaw JM, Smith C, Dichgans M. Small vessel disease: mechanisms and clinical implications. *Lancet Neurol.* (2019) 18:684–96. doi: 10.1016/S1474-4422(19)30079-1
5. Yang J, Song Y, Huang J, Qu J, Jiao S, Wu P, et al. A pilot study of the association between leukoaraiosis and cerebral atherosclerosis using synthetic magnetic resonance imaging. *Acta Radiol.* (2021). doi: 10.1177/02841851211044970
6. Nitkunan A, Lanfranconi S, Charlton RA, Barrick TR, Markus HS. Brain atrophy and cerebral small vessel disease: a prospective follow-up study. *Stroke.* (2011) 42:133–8. doi: 10.1161/STROKEAHA.110.594267
7. Kloppenborg RP, Nederkoorn PJ, Grool AM, Vincken KL, Mali WP, Vermeulen M, et al. Cerebral small-vessel disease and progression of brain atrophy: the SMART-MR study. *Neurology.* (2012) 79:2029–36. doi: 10.1212/WNL.0b013e3182749f02
8. Ter Telgte A, van Leijsen E, Wiegertjes K, Klijn C, Tuladhar AM, de Leeuw FE. Cerebral small vessel disease: from a focal to a global perspective. *Nat Rev Neurol.* (2018) 14:387–98. doi: 10.1038/s41582-018-0014-y
9. Rizvi B, Narkhede A, Last BS, Budge M, Tosto G, Manly JJ, et al. The effect of white matter hyperintensities on cognition is mediated by cortical atrophy. *Neurobiol Aging.* (2018) 64:25–32. doi: 10.1016/j.neurobiolaging.2017.12.006
10. Jokinen H, Lipsanen J, Schmidt R, Fazekas F, Gouw AA, van der Flier WM, et al. Brain atrophy accelerates cognitive decline in cerebral small vessel disease: the LADIS study. *Neurology.* (2012) 78:1785–92. doi: 10.1212/WNL.0b013e3182583070
11. Diprose WK, Diprose JP, Wang M, Tarr GP, McFetridge A, Barber PA. Automated measurement of cerebral atrophy and outcome in endovascular thrombectomy. *Stroke.* (2019) 50:3636–8. doi: 10.1161/STROKEAHA.119.027120
12. Joutel A, Chabriat H. Pathogenesis of white matter changes in cerebral small vessel diseases: beyond vessel-intrinsic mechanisms. *Clin Sci.* (2017) 131:635–51. doi: 10.1042/CS20160380
13. Chhagan U, Burns JK. The clinical value of brain computerised tomography in a general hospital psychiatric service. *S Afr J Psychiatr.* (2017) 23:1050. doi: 10.4102/sajpsychiatry.v23i0.1050
14. Lockhart SN, DeCarli C. Structural imaging measures of brain aging. *Neuropsychol Rev.* (2014) 24:271–89. doi: 10.1007/s11065-014-9268-3
15. Park SW, Kim S, Park J, Jang JW, Kim S. A Comprehensive visual rating scale for predicting progression from mild cognitive impairment to dementia in patients with alzheimer's pathology or suspected non-alzheimer's pathology. *Dement Neurocogn Disord.* (2020) 19:129–39. doi: 10.12779/dnd.2020.19.4.129
16. Gupta V, Ambrosius W, Qian G, Blazejewska A, Kazmierski R, Urbanik A, et al. Automatic segmentation of cerebrospinal fluid, white and gray matter in unenhanced computed tomography images. *Acad Radiol.* (2010) 17:1350–8. doi: 10.1016/j.acra.2010.06.005
17. Hanning U, Sporns PB, Schmidt R, Niederstadt T, Minnerup J, Bier G, et al. Quantitative rapid assessment of leukoaraiosis in CT : comparison to gold standard MRI. *Clin Neuroradiol.* (2019) 29:109–15. doi: 10.1007/s00062-017-0636-2
18. van Niftrik C, Visser TF, Sebök M, Muscas G, El Amki M, Serra C, et al. Delayed cerebral atrophy after cerebellar stroke: topographical relation and clinical impact. *Brain Commun.* (2021) 3:fcab279. doi: 10.1093/braincomms/fcab279
19. Jain S, Vyvere TV, Terzopoulos V, Sima DM, Roura E, Maas A, et al. Automatic quantification of computed tomography features in acute traumatic brain injury. *J Neurotrauma.* (2019) 36:1794–803. doi: 10.1089/neu.2018.6183

20. Chrzan R, Gleń A, Bryll A, Urbanik A. Computed tomography assessment of brain atrophy in centenarians. *Int J Environ Res Public Health*. (2019) 16:3659. doi: 10.3390/ijerph16193659
21. Dunham CM, Cook AJ 2nd, Paparodis AM, Huang GS. Practical one-dimensional measurements of age-related brain atrophy are validated by 3-dimensional values and clinical outcomes: a retrospective study. *BMC Med Imaging*. (2016) 16:32. doi: 10.1186/s12880-016-0136-x
22. Turner B, Ramli N, Blumhardt LD, Jaspan T. Ventricular enlargement in multiple sclerosis: a comparison of three-dimensional and linear MRI estimates. *Neuroradiology*. (2001) 43:608–14. doi: 10.1007/s002340000457
23. Mateos-Pérez JM, Dadar M, Lacalle-Aurioles M, Iturria-Medina Y, Zeighami Y, Evans AC. Structural neuroimaging as clinical predictor: a review of machine learning applications. *Neuroimage Clin*. (2018) 20:506–22. doi: 10.1016/j.nicl.2018.08.019
24. Zhao L, Lee A, Fan YH, Mok V, Shi L. Magnetic resonance imaging manifestations of cerebral small vessel disease: automated quantification and clinical application. *Chin Med J*. (2020) 134:151–60. doi: 10.1097/CM9.0000000000001299
25. Zaharchuk G, Gong E, Wintermark M, Rubin D, Langlotz CP. Deep learning in neuroradiology. *AJNR Am J Neuroradiol*. (2018) 39:1776–84. doi: 10.3174/ajnr.A5543
26. Yasaka K, Akai H, Kunimatsu A, Kiryu S, Abe O. Deep learning with convolutional neural network in radiology. *Jpn J Radiol*. (2018) 36:257–72. doi: 10.1007/s11604-018-0726-3
27. Lee E, Choi JS, Kim M, Suk HI. Toward an interpretable Alzheimer's disease diagnostic model with regional abnormality representation via deep learning. *Neuroimage*. (2019) 202:116113. doi: 10.1016/j.neuroimage.2019.116113
28. Davies RR, Scahill VL, Graham A, Williams GB, Graham KS, Hodges JR. Development of an MRI rating scale for multiple brain regions: comparison with volumetrics and with voxel-based morphometry. *Neuroradiology*. (2009) 51:491–503. doi: 10.1007/s00234-009-0521-z
29. Qin Y, Ai D, Jordan AE, Guo X, Li T, Diao S, et al. Better screening value of sylvian fissure ratio on cognitive decline among female compared to male: an observational study in elderly patients with cerebral small vessel disease in soochow. *Front Neurosci*. (2021) 15:729782. doi: 10.3389/fnins.2021.729782
30. Butzkueven H, Kolbe SC, Jolley DJ, Brown JY, Cook MJ, van der Mei IA, et al. Validation of linear cerebral atrophy markers in multiple sclerosis. *J Clin Neurosci*. (2008) 15:130–7. doi: 10.1016/j.jocn.2007.02.089
31. Patra DP, Bir SC, Maiti TK, Kalakoti P, Cuellar H, Guthikonda B, et al. Role of radiological parameters in predicting overall shunt outcome after ventriculoperitoneal shunt insertion in pediatric patients with obstructive hydrocephalus. *Neurosurg Focus*. (2016) 41:E4. doi: 10.3171/2016.8.FOCUS16263
32. He K, Zhang X, Ren S, Sun J. Deep residual learning for image recognition. *Proceedings of the IEEE Conference on Computer Vision and Pattern Recognition*. (2016) 770–778. doi: 10.1109/CVPR.2016.90
33. Mayer C, Frey BM, Schlemm E, Petersen M, Engelke K, Hanning U, et al. Linking cortical atrophy to white matter hyperintensities of presumed vascular origin. *J Cereb Blood Flow Metab*. (2021) 41:1682–91. doi: 10.1177/0271678X20974170
34. Rastogi A, Weissert R, Bhaskar SM. Brain atrophy in acute ischaemic stroke patients treated with reperfusion therapy: a systematic review. *Acta Radiol*. (2021). doi: 10.1177/02841851211060427. [Epub ahead of print].
35. Rabinstein AA, Albers GW, Brinjikji W, Koch S. Factors that may contribute to poor outcome despite good reperfusion after acute endovascular stroke therapy. *Int J Stroke*. (2019) 14:23–31. doi: 10.1177/1747493018799979
36. Luijten SP, Compagne KC, van Es AC, Roos YB, Majoie CB, van Oostenbrugge RJ, et al. Brain atrophy and endovascular treatment effect in acute ischemic stroke: a secondary analysis of the MR CLEAN trial. *Int J Stroke*. (2021). doi: 10.1177/17474930211054964. [Epub ahead of print].
37. Marek M, Horyniecki M, Karpe J, Adamczyk-Sowa M, Walecki J, Kluczewska E. Relationship between stroke severity, extensity of leukoaraiosis, and brain atrophy in patients with ischaemic stroke. *Pol J Radiol*. (2019) 84:e80–5. doi: 10.5114/pjr.2019.82917
38. Wilk R, Kluczewska E, Syc B, Bajor G. Normative values for selected linear indices of the intracranial fluid spaces based on CT images of the head in children. *Pol J Radiol*. (2011) 76:16–25.
39. Dogan A, Bayar Muluk N, Sahan MH, Asal N, Inal M, Ergün U. Olfactory bulbus volume and olfactory sulcus depth in migraine patients: an MRI evaluation. *Eur Arch Otorhinolaryngol*. (2018) 275:2005–11. doi: 10.1007/s00405-018-5029-x
40. Jin K, Zhang T, Shaw M, Sachdev P, Cherbuin N. Relationship between sulcal characteristics and brain aging. *Front Aging Neurosci*. (2018) 10:339. doi: 10.3389/fnagi.2018.00339
41. Chen L, Carlton Jones AL, Mair G, Patel R, Gontsarova A, Ganesalingam J, et al. Rapid automated quantification of cerebral leukoaraiosis on CT images: a multicenter validation study. *Radiology*. (2018) 288:573–81. doi: 10.1148/radiol.2018171567
42. Pitkänen J, Koikkalainen J, Nieminen T, Marinkovic I, Curtze S, Sibolt G, et al. Evaluating severity of white matter lesions from computed tomography images with convolutional neural network. *Neuroradiology*. (2020) 62:1257–63. doi: 10.1007/s00234-020-02410-2
43. Kaipainen AL, Pitkänen J, Haapalinna F, Jääskeläinen O, Jokinen H, Melkas S, et al. A novel CT-based automated analysis method provides comparable results with MRI in measuring brain atrophy and white matter lesions. *Neuroradiology*. (2021) 63:2035–46. doi: 10.1007/s00234-021-02761-4
44. Battaglini M, Jenkinson M, De Stefano N. Evaluating and reducing the impact of white matter lesions on brain volume measurements. *Hum Brain Mapp*. (2012) 33:2062–71. doi: 10.1002/hbm.21344

Conflict of Interest: JY was employed by the Taimei Medical Technology.

The remaining authors declare that the research was conducted in the absence of any commercial or financial relationships that could be construed as a potential conflict of interest.

REVIEW
published: 25 April 2022
doi: 10.3389/fneur.2022.781063

Monocarboxylate Transporter 1 May Benefit Cerebral Ischemia *via* Facilitating Lactate Transport From Glial Cells to Neurons

Mao Zhang [†], **Yanyan Wang, Yun Bai, Limeng Dai and Hong Guo** [*†]

Department of Medical Genetics, College of Basic Medical Sciences, Army Medical University, Chongqing, China

Monocarboxylate transporter 1 (MCT1) is expressed in glial cells and some populations of neurons. MCT1 facilitates astrocytes or oligodendrocytes (OLs) in the energy supplement of neurons, which is crucial for maintaining the neuronal activity and axonal function. It is suggested that MCT1 upregulation in cerebral ischemia is protective to ischemia/reperfusion (I/R) injury. Otherwise, its underlying mechanism has not been clearly discussed. In this review, it provides a novel insight that MCT1 may protect brain from I/R injury *via* facilitating lactate transport from glial cells (such as, astrocytes and OLs) to neurons. It extensively discusses (1) the structure and localization of MCT1; (2) the regulation of MCT1 in lactate transport among astrocytes, OLs, and neurons; and (3) the regulation of MCT1 in the cellular response of lactate accumulation under ischemic attack. At last, this review concludes that MCT1, in cerebral ischemia, may improve lactate transport from glial cells to neurons, which subsequently alleviates cellular damage induced by lactate accumulation (mostly in glial cells), and meets the energy metabolism of neurons.

Keywords: monocarboxylate transporter 1 (MCT1), lactate transport, cerebral ischemia, astrocytes, oligodendrocytes (OLs)

OPEN ACCESS

Edited by:
Jan Kassubek,
University of Ulm, Germany

Reviewed by:
Mootaz M. Salman,
University of Oxford, United Kingdom
Zheng Wu,
Jinan University, China
Valentina Mosienko,
University of Exeter, United Kingdom

****Correspondence:***
Hong Guo
guohong02@gmail.com
orcid.org/0000-0002-3244-1340

[†] These authors have contributed equally to this work

Specialty section:
This article was submitted to Applied Neuroimaging, a section of the journal Frontiers in Neurology

Received: *22 September 2021*
Accepted: *15 March 2022*
Published: *25 April 2022*

Citation:
Zhang M, Wang YY, Bai Y, Dai LM and Guo H (2022) Monocarboxylate Transporter 1 May Benefit Cerebral Ischemia via Facilitating Lactate Transport From Glial Cells to Neurons. Front. Neurol. 13:781063. doi: 10.3389/fneur.2022.781063

INTRODUCTION

Cerebral ischemia is a worldwide public health issue that causes brain dysfunction and most frequently results in mortality (1). Ischemia/reperfusion (I/R) injury is the underlying pathogenesis of neurological damage in ischemic stroke (2). Intravenous injection of lactate offers neuroprotection at the reperfusion period of cerebral ischemia (3). Administration of lactate reduces brain lesion volume, ameliorates behavioral outcomes, and promotes long-term memory in neonatal hypoxia-ischemia (4, 5). These pieces of evidence point out that lactate plays a beneficial role in cerebral ischemia. In the work of Sylvain et al. (6) using a photothrombotic stroke model, they have shown a link between brain energy metabolism and increased glycogen level. Actually, lactate is not only an energetic source of neurons, but also acts as a signaling molecule in the regulation of neuronal excitotoxicity (7–9).

In the central nervous system (CNS), lactate is mainly produced by astrocytes and oligodendrocytes (OLs), and then metabolized in neurons to sustain neuronal growth (10, 11). In addition, Kitchen et al. (12) work demonstrates that the pharmacological inhibition of protein aquaporin-4 expressed in astrocytes prevents the development of cerebral edema and promotes functional recovery in injured rats. Therefore, the regulation of astrocytes and OLs in relation with neuronal injury, especially in the aspect of lactate transport, can benefit cerebral ischemia.

Monocarboxylate transporter 1 (MCT1) is an effective and the most abundant lactate transporter in the brain (11), which is expressed in OLs, astrocytes, and some population of neurons (13). Importantly, MCT1 promotes lactate transport from astrocytes and OLs to neurons (14). Moreover, neuronal MCT1 upregulation has a protective effect on cerebral I/R injury (15). Besides, the upregulation of astrocytic MCT1 expression improves neurological deficit in middle cerebral artery occlusion rats (16). MCT1, located in the inner mitochondrial membrane of astrocytes, facilitates lactate entry into tricarboxylic acid (TCA) cycle (17). Thus, MCT1 in the regulation of lactate transport from astrocytes and OLs to neurons can benefit cerebral ischemia.

In this work, it suggests that MCT1 can benefit cerebral ischemia *via* regulating lactate flow from glial cells to neurons. Specifically, this review introduces the structure and function of MCT family, and then discusses the regulation of MCT1 in lactate transport between glial cells, such as astrocytes, OLs, and neurons. Finally, it proposes that MCT1 benefits neuronal damage in cerebral ischemia. Besides, lactate efflux from astrocytes and OLs attenuates accumulated lactate-induced cellular response in these cells. Hence, this review concludes that the regulation of MCT1 in lactate balance among neural cells is protective to the neuronal I/R injury that should be a novel therapeutic target for cerebral ischemia.

STRUCTURE AND DISTRIBUTION OF MONOCARBOXYLATE TRANSPORTER FAMILY

Human SLC16 gene family, also known as MCT family, comprises 14 members (MCT1–MCT14) (13). The molecular identity of the first member of this family is MCT1, which was established by two parallel studies: specific labeling studies in erythrocytes of rats and rabbits (18); studies in the purification and N-termini sequencing of a 40- to 50-kDa protein (19). Besides, the structures of other MCT members were further identified, showing similar topography. Normally, MCT family has 10–12 α-helical transmembrane domains (TMDs) with intracellular N- and C-termini and a large intracellular loop between TMDs 6 and 7, already confirmed for MCT1 in erythrocytes (18). Especially, the cluster of differentiation 147 (CD147) is required by MCT1 and MCT4 (20). The proposed topology of MCT family is schemed (**Figure 1A**). Experimentally, it is demonstrated that MCT1–MCT4 catalyzes the proton-linked transport of metabolically important monocarboxylates, such as lactate, pyruvate, and ketone bodies. MCT8 has a high affinity for thyroid hormone, and MCT10 is a transporter of aromatic amino acid (21, 22). In addition, substrates transported by the other eight members (MCT5, MCT6, MCT7, MCT9, MCT11–MCT14) remain unknown (22). In non-mammalian, five members (MCT1–MCT5) in yeast are not responsible for lactate transport (23) (**Figure 1B**).

MCT1 IS EXPRESSED IN GLIAL CELLS AND NEURONS

The conceptual role of lactate in the brain has shifted from glycolytic waste product to supplemental fuel or signaling molecule (24). Four members of MCT family (MCT1, MCT2, MCT3, and MCT4) facilitate cerebral lactate transport, while the cerebral distribution of them is quite different. According to the brain-RNAseq database (http://www.brainrnaseq.org/), MCT1 is predominantly expressed by endothelial cells, MCT2 is equally expressed by all major brain cell types, and MCT3 and MCT4 are mainly expressed by microglia. Particularly, MCT1 is recognized as a lactate transporter of erythrocyte, and then found in energy-costing tissues, such as Chinese hamster ovary, Xenopus laevis oocyte and brain (25, 26). In the brain, MCT1 is distributed in the most of neural cells, such as astrocytes, OLs, and neurons (26). In addition, MCT1 expression can be merely recognized in activated microglia, which is merely correlated with inflammation (27). It is identified that MCT1 mainly localizes to OLs, astrocytes, and some specific neuronal populations, such as hippocampal, brainstem trigeminal ganglion, and cerebellar Purkinje neurons (11, 28, 29) (**Table 1**).

In cerebral ischemia, an increased expression of MCT1 is protective to neuronal damage (2, 4). Redistribution of MCT1 also protects OLs from ischemic stress (29). Brain cost 10 times higher than what should be expected from its weight alone (30). Lactate, transported by MCT1, is an indispensable energy source of neurons (31). Moreover, the developmental expression of oligodendrocyte MCT1 has a regulative effect on neuronal amounts in medial prefrontal cortex (mPFC) during 12 months (32). Thus, MCT1 protects neurons from I/R injury through mediating lactate balance among neural cells.

MCT1 COUPLES ASTROCYTE-TO-NEURON LACTATE FLOW

Astrocytes exhibit a high glycolytic rate and release large amounts of lactate to neurons (11). In 1994, Pellerin and Magistretti has proposed a hypothesis of astrocyte-neuron lactate shuttle (ANLS). In ANLS, astrocytes serve as a "lactate source" whereas neurons serve as a "lactate sink" (33). Moreover, the opposition by Bak et al. (34) who argued that the oxidative metabolism of lactate in neurons only occurs during repolarization (and in the period between depolarization) rather than during neurotransmission activity. Hence, it still exists a debate in ANLS hypothesis. Until recently, it is discussed that the lactate supplement of astrocytes is a necessary energetic source of neurons (35). Furthermore, the glycolytic capability of astrocytes can be stimulated under various conditions, such as hypoxia, acidosis, and ATP deficiency (36). As an example, glutamate,

---

Abbreviations: BBB, blood brain barrier; CD147, cluster of differentiation 147; CNS, central nervous system; GSH, glutathione; IL23/IL17, interleukin 23/ interleukin 17; I/R, ischemia/reperfusion; MCT, monocarboxylate transporter; MCTs, monocarboxylate transporters; mPFC, medial prefrontal cortex; NAD+, nicotinamide adenine dinucleotide; NADH, nicotinamide adenine dinucleotide; NADPH, methylenetetrahydrofolate reductase; NMDARs, receptors of the N-methyl-D-aspartate type; OL, oligodendrocyte; OLs, oligodendrocytes; TCA, tricarboxylic acid; TLR2/TLR4, toll-like receptor 2/toll-like receptor 4; TMDs, transmembrane domains.

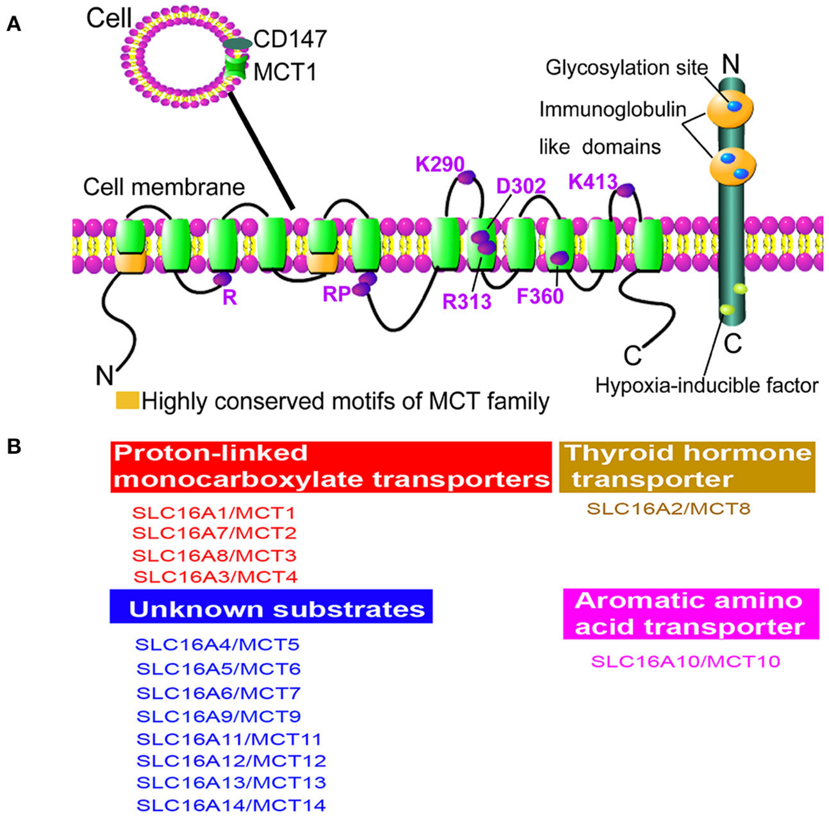

FIGURE 1 | Structure and function of monocarboxylate transporter (MCT) family. **(A)** The proposed topology of MCT family. There are 10–12 α-helical transmembrane domains (TMDs) for MCT family membranes in the presence of N- and C-termini located within cytoplasm. Besides, it shows the greatest variation at N- and C-termini and the large loop between TMDs 6 and 7 among family members, while the TMDs themselves are highly conserved. Importantly, two highly conserved motifs can be identified as the characteristic of the MCT family (green). Cluster of differentiation 147 (CD147) is an ancillary protein of MCT1 and MCT4, which is a cell surface glycoprotein containing a signal transmembrane span, two immunoglobulin-like domains in the extracellular region, and a short C-terminal cytoplasmic tail. The marked amino acids are significant for the structure conservation of MCT family. Specifically, R represents Arg; RP represents Arg and Pro; K290 represents Lys290; D302 represents Asp302; R313 represents Arg313; F360 represents Phe360; K413 represents Lys413; E218 represents Glu218. **(B)** Functions of MCT family members. MCT1, MCT2, MCT3, and MCT4 are proton-dependent transporters, which transport lactate, pyruvate, D-β-hydroxybutyrate, and acetoacetate (1). MCT8 can transport thyroid hormone and MCT10 is a transporter of aromatic amino acids, while the substrates of other MCT members are still unknown.

TABLE 1 | Expression and Distribution of MCT1.

Distribution	Time
MCT1 Expression	
Erythrocyte, Endothelial cell	1992 (17)
Chinese hamster ovary	1994 (26)
Xenopus laevis oocyte	1998 (27)
Astrocyte, Oligodendrocyte, Microglia, Neuron	1999 (28, 29)
Oligodendrocyte, Astrocyte, Some population of neuron	2012 (16, 29, 30)

released from activated neurons, is considered as a stimulus of glycolysis in astrocytes (37).

Lactate release is enhanced during glycogenolysis and glycolysis (38). A glucose flow exists between astrocytes and neurons. Glucose passes through blood brain barrier (BBB), and then transported and stored in a form of glycogen in astrocytes (39, 40). Glycogen is not only a component of brain energetics during sensory stimulation (41, 42), but also a regulator of K^+ inflow, glutamate uptake, and calcium homeostasis (43, 44). Particularly, glycogen can be rapidly converted to pyruvate/lactate, or used for glutamate biosynthesis and glucose production (45, 46). Either glucose or lactate can be exported from astrocytes to neurons and used as an energetic substrate (47). Otherwise, under ischemia or hypoxia condition, lactate becomes the main energetic source of neurons (48). At this moment, lactate is converted from glycogen in astrocytes, and transported into neurons (49). In an experiment *in vitro*, astrocytic lactate release is stimulated by glutamate (50).

In the CNS, MCT1 arouses much attention because of its unique localization, which is expressed in astrocytes and neurons (11). Meanwhile, MCT2 restrictively localizes to neurons (7) and MCT4 is mainly expressed by astrocytes (31). Such a cellular distribution of cerebral MCT1, MCT2, and MCT4 may associate with their functional characteristics. *In vitro*, it was observed in cultured tanycytes that MCT1

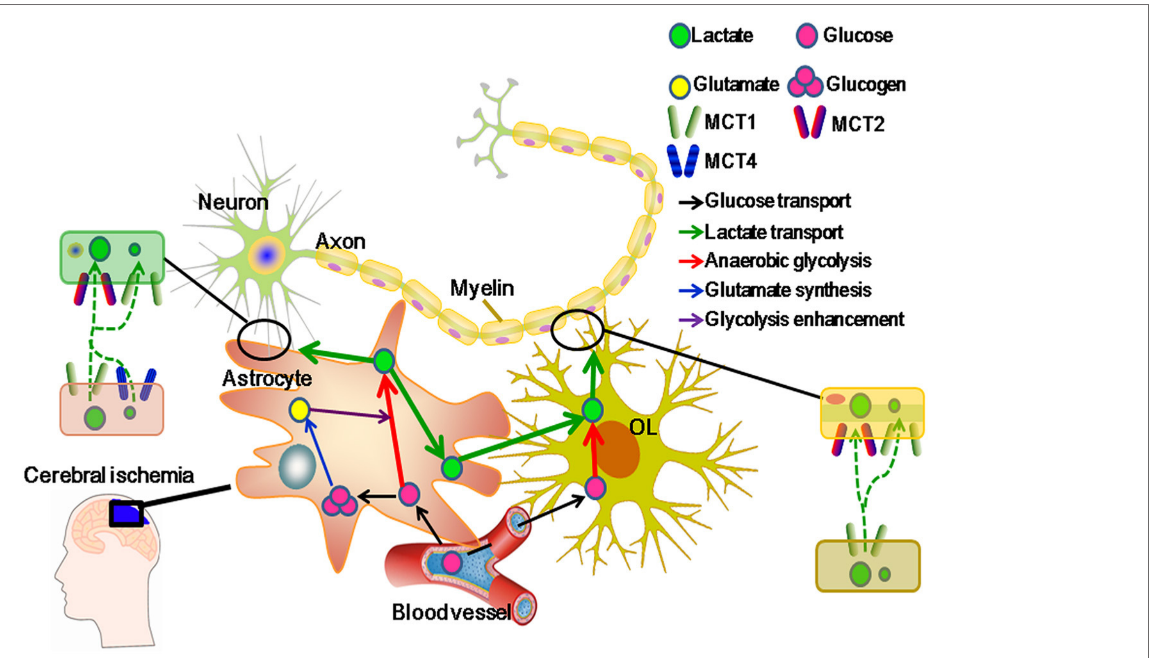

FIGURE 2 | Monocarboxylate transporter 1 (MCT1) regulatively facilitates lactate transport from glial cells to neurons in cerebral ischemia. MCT1 is expressed in glial cells, such as astrocytes and oligodendrocytes (OLs), and some populations of neurons in the areas of hippocampus, brainstem, trigeminal ganglion, and cerebellar Purkinje. Meanwhile, another three lactate transporters (MCT2, MCT3, and MCT4) are restricted to cell types: MCT2 in neurons, MCT3 in epithelial cells, and MCT4 in astrocytes. Moreover, MCT1 can regulate lactate influx and efflux among neural cells. MCT2 can merely regulate lactate influx and MCT4 mainly functions in lactate efflux from neural cells. In cerebral ischemia, MCT1 upregulation protects neurons from I/R injury through regulating lactate transport (2). Generally, glucose is transported from capillaries to glial cells, and then to be polymerized into glucogen (stored in astrocytes) or aerobically metabolized. Otherwise, increased glutamate is released from neurons and activates glial glycolysis in cerebral ischemia. As a result, glucose is metabolized into lactate in glial cells. At this moment, lactate becomes the main energetic substrate of neurons. To adapt the changed microenvironment, e.g., increased acidosis, MCT1 activity is strengthened, which not only facilitates the accumulated lactate efflux from glial cells, but also improves the lactate influx to neurons (11).

is functional for lactate influx, displaying a Km of 7.7 mM (51, 52) and MCT2 has a Km of 0.8 mM for lactate influx (53), while MCT4 displays a Km of 34 mM for lactate efflux (54). Notably, MCT1 can also export lactate from astrocytes into extracellular space (55). Actually, both MCT1 and MCT4 can convey astrocyte-released lactate, while MCT1 is involved in basal lactate release, and MCT4 is required for enhanced lactate export (56–58). MCT2, predominantly expressed in neurons (59), mainly regulates the lactate uptake of neurons whose activity can be stimulated by glutamate (60).

Here, it is suggested that glucose is crossed over BBB, and then polymerized and stored in astrocytes in a form of glycogen. Once energetic supplements are rapidly required for neurons, e.g., under ischemic attack, astrocytic glycogen is activated and metabolized into lactate and glutamate. Besides, glutamate can further stimulate glycolysis, enhancing astrocytic lactate release. At this moment, MCT1 couples lactate flow from astrocytes to neurons, which exports lactate from astrocytes, and possibly imports lactate into neurons. Moreover, MCT4 can further enhance astrocytic lactate release in the presence of MCT1-mediated lactate efflux, and MCT2 facilitates lactate influx into neurons (**Figure 2**).

MCT1 FACILITATES LACTATE TRANSPORT FROM OLS TO NEURONS

Myelin wraps up 99% of axons, which is critical for an efficient impulse conduction of axons. Otherwise, myelin limits the contact between axons and extracellular space, and restricts the access of energetic metabolites into axons (61). Besides, it is postulated that axons derive metabolic energy from OLs (62). *In vitro*, oligodendrocyte MCT1 metabolically supports neuronal survival, and its deficiency leads to cell death (11). *In vivo*, OLs and myelin benefit the neurodegeneration, axonal energy metabolism, and structural integrity of axons. In addition, lactate supports oligodendrocyte development and myelination (63). The promotion of MCT1 in lactate transport from OLs to axons encourages neuronal conduction (62, 64).

Monocarboxylate transporter 1 was first found in the endothelial cells of capillaries and astrocytes (62, 65, 66). Until recently, MCT1 expressed in OLs was discussed. It is suggested that lactate is released from OLs through MCT1, and utilized by axons as an energetic substrate (62). Indeed, MCT1 is highly enriched within OLs, whose disruption or downregulation induces axon damage and neuron loss in an animal or a cell culture model (15, 62). In addition, MCT2 is expressed in neurons and MCT4 in astrocytes (67–69). MCT1 is indispensable for glycolytic OLs in supporting neuronal metabolism (70). On one hand, oligodendroglial MCT1 regulates lactate efflux and prevents the intracellular accumulation of lactate in OLs. On the other hand, MCT1 guarantees sufficient lactate to be transported and metabolized in neuronal axons (11). Furthermore, capillaries provide a constant source of glucose which enters astrocytes or OLs, and undergoes glycolysis. Then, glycolytic products (lactate or pyruvate) in OLs diffuse through cytoplasmic ("myelinic") channels and reach the periaxonal space *via* MCT1 (15, 63). Moreover, MCT1, expressed in astrocytes, especially in the population closely located to OLs, constantly supplies lactate to neurons (71). Above all, MCT1 regulates lactate flow released from OLs to neurons that energetically supports the neuronal activity (**Figure 2**).

MCT1 PROTECTS BRAIN FROM I/R INJURY *VIA* REGULATING LACTATE TRANSPORT

Glycolysis is significant for neuronal metabolism in cerebral ischemia (72). Glucose enters brain parenchyma *via* glucose transporters, which was partially converted to lactate in astrocytes and OLs to meet the energetic demand of neurons (62, 67). It was proved that the given of exogenous lactate rescues impaired long-term memory (73, 74). In addition, lactate supports electrically evoked action potentials in brain slices when suffering oxygen and glucose deprivation (75). Indeed, lactate oxidation can support cellular functions under specific experimental conditions, e.g., lactate infusions or strenuous exercise (76). Even, lactate may "jump start" neuronal recovery after the restoration of blood flow and oxygen delivery (77). Therefore, lactate is an obligatory energy substrate for neurons under I/R injury (78).

Furthermore, the expressions of MCT1, MCT2, and MCT4 are cell-specifically modulated to adapt the changed metabolic state in cerebral ischemia (12). Particularly, MCT1 expression is strongly enhanced both at 1 and 24 h post-ischemia, which is supposed to regulate the lactate supplement from microvessels to ischemic brain and redistribute lactate between glial cells (astrocytes and OLs) and neurons (15). Besides, it has been recognized that post-ischemic modulation of MCT1 in rat hippocampal CA1 neurons can benefit their survival (79). Lactate is released in larger quantities from "resting" cultured astrocytes than that from neurons despite both of them can produce lactate under various conditions, e.g., high K^+ or dinitrophenol (an uncoupling agent that suppresses oxidative respiratory chain) exposure (52, 53). Besides, OLs provide lactate to support neuronal survival and axonal energy metabolism (11). Here, it proposes a novel concept that in cerebral ischemia, MCT1 can metabolically support the neuronal survival and activity through regulating lactate transport (80).

In cerebral ischemia, the dysfunction of MCT1 is a critical determinant of acid-related cell damage (16, 81). Otherwise, MCT1 upregulation can alleviate cellular damage, and further improve the neurological deficit following experimental transient focal cerebral ischemia (16). The demonstrated utilization of lactate in hypoxic hippocampal slices suggests that MCT1 can meet the metabolic needs of the injured neurons (82). In ischemic heart, it showed that the increased MCT1 expression is a regulator in restoring cardiac pH through lactate export (83). Similarly, in ischemic brain, enhanced MCT1 immunoreactivity was observed in astrocytes, endothelial cells, and adjacent ependymal lining, which plays a protective role in the initial and long-term neuronal survival in hippocampus (84). Therefore, MCT1 potentially mediates the extent of lactic acidosis and lactate metabolism during cerebral ischemia, through which, neurons can sustain I/R injury.

Ischemia/reperfusion injury includes inflammatory reaction, oxidative stress (85, 86), apoptosis (87), and excitotoxicity (88). Overproduced lactate in ischemic brain plays as a mediator to activate proinflammatory pathways, e.g., interleukin 23/interleukin 17 (IL23/IL17) signaling pathway, which further activates toll-like receptor 2/toll-like receptor 4 (TLR2/TLR4) and then induces inflammatory response (89, 90). Additionally, changes in glycolytic intermediates contribute to reductions in the form of nicotinamide adenine dinucleotide (NADH), and glutathione (GSH) (91). Besides, high intracellular lactate level can impede the coupled oxidation of NADH to nicotinamide adenine dinucleotide (NAD^+) in MCT1 inhibitor-treated cells (92). As a result, GSH reduction facilitates the production of hypoxia-enhanced superoxide radicals and hydrogen peroxide (92, 93). Then, more cytochrome C is released from mitochondria, which further contributes to the cell death through an apoptotic pathway (87). Furthermore, high NADH level favors glycolysis, but not aerobic glycolysis. When glycolysis is enhanced, ATPase activity is suppressed and lactate is overproduced (86). On one hand, the overproduced lactate can exacerbate lactic acidosis. On the other hand, the suppressed activity of ATPase decreases ATP production (87), and promotes an overload of intracellular Ca^{2+}, eventually resulting in cell death (87, 88). In addition, the excessive accumulation of intracellular Ca^{2+} coexists with glutamate-induced excitotoxicity and overstimulation N-methyl-D-aspartate type (NMDARs) (94, 95). Both Ca^{2+} overload and excitotoxicity exacerbate cellular damage during cerebral ischemia (**Figure 3**).

CONCLUSIONS AND PERSPECTIVES

Glucose is an obligatory fuel of brain, which is metabolized mostly in a manner of aerobic glycolysis, but not anaerobic glycolysis (82). Anaerobic glycolysis and increased lactate production can be extensively enhanced when facing oxygen deficit (92). In glia-neuron metabolic crosstalk, lactate is produced mainly by glial cells, such as astrocytes and OLs, and further utilized by neurons (63). In ANLS model, glutamate depolarizes neurons by its receptors, which is terminated by an efficient glutamate uptake system in astrocytes (96). Especially, glutamate-cotransported Na^+ can activate Na^+/K^+ ATPase, which fuels glycolytic enzymes and stimulates glycolysis in astrocytes. Lactate, once released from astrocytes, can be taken up and utilized by neurons (96). Besides, OLs are critical intermediaries for lactate transport to neurons (97), which

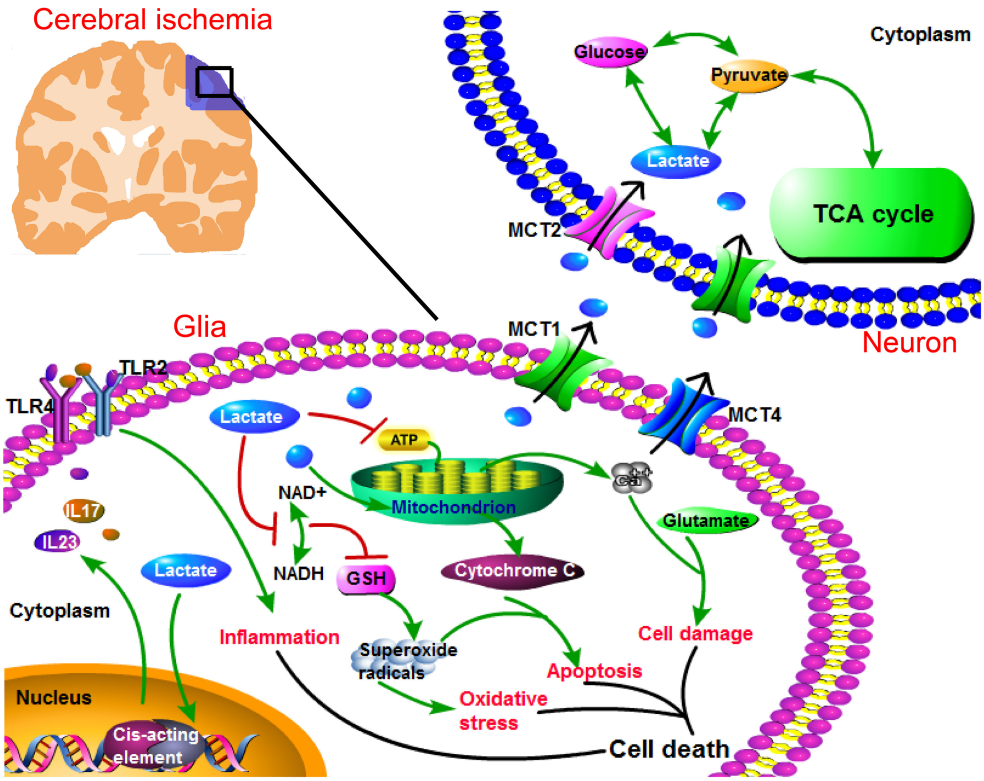

FIGURE 3 | Regulation of MCT1 in lactate transport promotes neuronal energy supplement, and suppresses cellular damage under ischemic attack. In ischemic brain, anaerobic glycolysis is largely enhanced and leads to lactate overproduction. Lactate becomes the main energy resource for neurons, while its intracellular accumulation (in glial cells) leads to toxic response. Specifically, lactate accumulation associates with cellular responses, such as inflammation, oxidative stress, apoptosis, Ca^{2+} overload, and glutamate-induced excitotoxicity. Especially, lactate can promote the transcription of proinflammatory factors (interleukin 23/interleukin 17 (IL23/IL17)), which triggers inflammation *via* toll-like receptor 2/toll-like receptor 4 (TLR2/TLR4). In addition, lactate can suppress the production of glutathione (GSH) which is an indispensable anti-oxidative enzyme, and GSH deficit leads to the increased superoxide radicals. Then, superoxide radicals can further activate oxidative stress. Again, superoxide radicals contribute to apoptosis in the presence of mitochondrial cytochrome C. Furthermore, lactate decreases adenosine triphosphate (ATP) level, resulting in Ca^{2+} overload. Ca^{2+} overload coexists with glutamate-induced excitotoxicity which leads to cellular damage. Collectively, intracellular lactate accumulation contributes to these cellular responses, leading to cell death. Therefore, a timely and rightly utilization of lactate protects brain from I/R injury. MCT1 can facilitate lactate efflux from glial cells, and assist lactate influx into neurons. Besides, neuronal MCT2 assists lactate entries into neurons, and then lactate is efficiently utilized by neurons.

potentially impact energy-dependent processes in axons (98). Actually, energetic interactions exist among astrocytes, OLs, and neurons: astrocytes can transfer energetic metabolites directly to neurons, or to OLs which in turn support neuronal axons (47).

Research over the last couple of decades has provided novel insights into lactate neurobiology and the implications of lactate transport-driven neuroenergetics in the health and diseases of peripheral nerve and CNS. Lactate transporters in peripheral nerves are important for the maintenance of axon and myelin integrity, motor end-plate integrity, the development of diabetic peripheral neuropathy (DPN), and the functional recovery following nerve injuries (99). This review discusses that the regulation of MCT1 in ANSL and oligodendrocyte-neuron lactate flow are necessary for the functional recovery of neurons under I/R injury. Especially, MCT1 can peculiarly facilitate astrocytic and oligodendroglial lactate transport to neurons (11). Conversely, the dysfunction of MCT1 may impede lactate transport from glial cells to neurons, leading to intracellular lactate accumulation (in glial cells) and insufficient energy supplement (of neurons).

During cerebral ischemia, lactate is a significant fuel for neurons (100). Otherwise, the intracellular accumulation of lactate overproduced in glial cells can trigger inflammation, oxidative stress, apoptosis, and excitotoxicity (87). In this review, it suggests that the timely utilization of lactate not only benefits the neuronal energy supplement, but also prevents harmful cell response resulted from glial lactate accumulation. MCT1 upregulation in ischemic brain plays a protective role in I/R injury (14, 16). Specifically, lactate is overproduced as a result of enhanced glycolysis, and MCT1 can possibly regulate lactate transport and balance its distribution among neural cells in cerebral ischemia. For one aspect, MCT1 metabolically supports neuronal survival. For another, MCT1 probably alleviates the intracellular accumulation of overproduced lactate and rescues the risk factors of I/R injury (**Figure 3**). Otherwise, the dysfunction of MCT1 leads to its incapability in the regulation of lactate transport and contributes to the activation of cellular response under I/R injury. Therefore, this review provides a promising preventive strategy for cerebral ischemia—lactate metabolism and MCT1.

AUTHOR CONTRIBUTIONS

MZ drafted the manuscript. YYW and YB assisted with the revise of manuscript. LMD assisted with the draft the manuscript. HG critically revised the manuscript. All authors contributed to the article and approved the submitted version.

FUNDING

This work was supported by grants from the National Natural Science Foundation of China (Grant No. 82171840) and Natural Science Foundation of Chongqing (Grant No. cstc2021jcyj-msxmX0281).

ACKNOWLEDGMENTS

The authors would like to acknowledge Xingying Guan and Jia Li for critically reading the manuscript.

REFERENCES

1. Zhao Q, Wang S, Li Y, Wang P, Li S, Guo Y, et al. The role of the mitochondrial calcium uniporter in cerebral ischemia/reperfusion injury in rats involves regulation of mitochondrial energy metabolism. *Mol Med Rep.* (2013) 7:1073–80. doi: 10.3892/mmr.2013.1321
2. Deng HJ, Zhang S, Ge HF, Liu L, Liu LT, Feng H, et al. The effect of cyclosporin a on ischemia-reperfusion damage in a mouse model of ischemic stroke. *Neurol Res.* (2020) 42:721–9. doi: 10.1080/01616412.2020.1762353
3. Castillo X, Rosafio K, Wyss MT, Drandarov K, Buck A, Pellerin L, et al. A probable dual mode of action for both L- and D-lactate neuroprotection in cerebral ischemia. *J Cereb Blood Flow Metab.* (2015) 35:1561–9. doi: 10.1038/jcbfm.2015.115
4. Tassinari ID, Andrade MKG, Rosa LAD, Hoff MLM, Nunes RR, Vogt EL, et al. Lactate administration reduces brain injury and ameliorates behavioral outcomes following neonatal hypoxia-ischemia. *Neuroscience.* (2020) 448:191–205. doi: 10.1016/j.neuroscience.2020.09.006
5. Roumes H, Dumont U, Sanchez S, Mazuel L, Blanc J, Raffard G, et al. Neuroprotective role of lactate in rat neonatal hypoxia-ischemia. *J Cereb Blood Flow Metab.* (2021) 41:342–58. doi: 10.1177/0271678X20908355
6. Sylvain NJ, Salman MM, Pushie MJ, Hou H, Meher V, Herlo R, et al. The effects of trifluoperazine on brain edema, aquaporin-4 expression and metabolic markers during the acute phase of stroke using photothrombotic mouse model. *Biochim Biophys Acta Biomembr.* (2021) 1863:183573. doi: 10.1016/j.bbamem.2021.183573
7. Rosafio K, Castillo X, Hirt L, Pellerin L. Cell-specific modulation of monocarboxylate transporter expression contributes to the metabolic reprograming taking place following cerebral ischemia. *Neuroscience.* (2016) 317:108–20. doi: 10.1016/j.neuroscience.2015.12.052
8. Berthet C, Lei HX, Thevenet J, Gruetter R, Pierre JM, Lorenz H. Neuroprotective role of lactate after cerebral ischemia. *J Cereb Blood Flow Metab.* (2009) 29:1780–9. doi: 10.1038/jcbfm.2009.97
9. Jourdain P, Allaman I, Rothenfusser K, Fiumelli H, Marquet P, Magistretti PJ. L-Lactate protects neurons against excitotoxicity: implication of an ATP-mediated signaling cascade. *Sci Rep.* (2016) 6:21250. doi: 10.1038/srep21250
10. Lee Y, Morrison BM, Li Y, Lengacher S, Farah MH, Hoffman PN, et al. Oligodendroglia metabolically support axons and contribute to neurodegeneration. *Nature.* (2012) 87:443–438. doi: 10.1038/nature11314
11. Alberini CM, Cruz E, Descalzi G, Bessières B, Gao V. Astrocyte glycogen and lactate: new insights into learning and memory mechanisms. *Glia.* (2018) 66:1244–62. doi: 10.1002/glia.23250
12. Kitchen P, Salman MM, Halsey AM, Bland CC, MacDonald JA, Ishida H, et al. Targeting aquaporin-4 subcellular localization to treat central nervous system edema. *Cell.* (2020) 181:784–99.e19. doi: 10.1016/j.cell.2020.03.037
13. Felmlee MA, Jones RS, Cruz VR, Follman KE, Morris ME. Monocarboxylate transporters (SLC16): function, regulation, and role in health and disease. *Pharmacol Rev.* (2020) 72:466–85. doi: 10.1124/pr.119.018762
14. Xu SY, Jiang XL, Liu Q, Xu J, Huang J, Gan SW, et al. Role of rno-miR-124-3p in regulating MCT1 expression in rat brain after permanent focal cerebral ischemia. *Genes Dis.* (2019) 6:398–406. doi: 10.1016/j.gendis.2019.01.002
15. Hyacinthe JN, Buscemi L, Lê TP, Lepore M, Hirt L, Mishkovsky M, et al. Evaluating the potential of hyperpolarised [1-13C] L-lactate as a neuroprotectant metabolic biosensor for stroke. *Sci Rep.* (2020) 10:5507. doi: 10.1038/s41598-020-62319-x
16. Lu Y, Zhao HJ, Wang Y, Han BB, Wang T, Zhao H, et al. Electro-acupuncture up-regulates astrocytic MCT1 expression to improve neurological deficit in middle cerebral artery occlusion rats. *Life Sci.* (2015) 134:68–72. doi: 10.1016/j.lfs.2015.05.014
17. Rose J, Brian C, Pappa A, Panayiotidis MI, Franco R. Mitochondrial metabolism in astrocytes regulates brain bioenergetics, neurotransmission and redox balance. *Front Neurosci.* (2020) 14:536682. doi: 10.3389/fnins.2020.536682
18. Poole RC, Halestrap AP. N-Terminal protein sequence analysis of the rabbit erythrocyte lactate transporter suggests identity with the cloned monocarboxylate transport protein MCT1. *Biochem J.* (1994) 303:755–9. doi: 10.1042/bj3030755
19. Poole RC, Sansom CE, Halestrap AP. Studies of the membrane topology of the rat erythrocyte H+/lactate cotransporter (MCT1). *Biochem J.* (1996) 320:817–824. doi: 10.1042/bj3200817
20. Li S, Nguyen TT, Bonanno JA. CD147 required for corneal endothelial lactate transport. *Invest Ophthalmol Vis Sci.* (2014) 55:4673–81. doi: 10.1167/iovs.14-14386
21. Visser WE, Friesema EC, Visser TJ. Minireview: thyroid hormone transporters: the knowns and the unknowns. *Mol Endocrinol.* (2011) 25:1–14. doi: 10.1210/me.2010-0095
22. Halestrap AP. The monocarboxylate transporter family–Structure and functional characterization. *IUBMB Life.* (2012) 64:1–9. doi: 10.1002/iub.573
23. Makuc J, Paiva S, Schauen M, Kramer R, Andre B, Casal M, et al. The putative monocarboxylate permeases of the yeast Saccharomyces cerevisiae do not transport monocarboxylic acids across the plasma membrane. *Yeast.* (2001) 18:1131–43. doi: 10.1002/yea.763
24. Magistretti PJ, Allaman I. Lactate in the brain: from metabolic end-product to signalling molecule. *Nat Rev Neurosci.* (2018) 19:235–49. doi: 10.1038/nrn.2018.19
25. Bröer S, Schneider HP, Bröer A, Rahman B, Hamprecht B, Deitmer JW, et al. Characterization of the monocarboxylate transporter 1 expressed in Xenopus laevis oocytes by changes in cytosolic pH. *Biochem J.* (1998) 333:67–174. doi: 10.1042/bj3330167
26. Halestrap AP, Price NT. The proton-linked monocarboxylate transporter (MCT) family: structure, function and regulation. *Biochem J.* (1999) 343:281–99. doi: 10.1042/bj3430281
27. Kong L, Wang Z, Liang X, Wang Y, Gao L, Ma C. Monocarboxylate transporter 1 promotes classical microglial activation and pro-inflammatory effect via 6-phosphofructo-2-kinase/fructose-2, 6-biphosphatase 3. *J Neuroinflammation.* (2019) 16:240. doi: 10.1186/s12974-019-1648-4
28. Dong F, Liu Y, Zhang Z, Guo R, Ma L, Qu X, et al. Postnatal alteration of monocarboxylate transporter 1 expression in the rat corpus callosum. *Physiol Res.* (2017) 66:345–55. doi: 10.33549/physiolres.933365
29. Zhou P, Guan T, Jiang Z, Namaka M, Huang QJ, Kong JM. Monocarboxylate transporter 1 and the vulnerability of oligodendrocyte lineage cells to metabolic stresses. *CNS Neurosci Ther.* (2018) 24:126–34. doi: 10.1111/cns.12782
30. Raichle ME, Gusnard DA. Appraising the brain's energy budget. *Proc Natl Acad Sci USA.* (2002) 99:10237–9. doi: 10.1073/pnas.172399499

31. Welling LC, Welling MS, Teixeira MJ, Figueiredo EG. Fueling the brain-a new role in lactate metabolism. *World Neurosurg.* (2015) 84:611–2. doi: 10.1016/j.wneu.2015.07.063
32. Zhang M, Ma ZY, Qin HC, Yao ZX. Monocarboxylate transporter 1 in the medial prefrontal cortex developmentally expresses in oligodendrocytes and associates with neuronal amounts. *Mol Neurobiol.* (2016) 54:2315-2326. doi: 10.1007/s12035-016-9820-7
33. Pellerin L, Magistretti PJ. Glutamate uptake into astrocytes stimulates aerobic glycolysis: a mechanism coupling neuronal activity to glucose utilization. *PNAS.* (1994) 91:10625–9. doi: 10.1073/pnas.91.22.10625
34. Bak LK, Walls AB, Schousboe A, Ring A, Sonnewald U, Waagepetersen HS. Neuronal glucose but not lactate utilization is positively correlated with NMDA-induced neurotransmission and fluctuations in cytosolic Ca^{2+} levels. *J Neurochem.* (2009) 109:87–93. doi: 10.1111/j.1471-4159.2009.05943.x
35. Bordone MP, Salman MM, Titus HE, Amini E, Andersen JV, Chakraborti B, et al. The energetic brain-a review from students to students. *J Neurochem.* (2019) 151:139–65. doi: 10.1111/jnc.14829
36. Dienel GA. Brain glucose metabolism: Integration of energetics with function. *Physiol Rev.* (2019) 99:949–1045. doi: 10.1152/physrev.00062.2017
37. Shen Y, Tian Y, Shi X, Yang J, Ouyang L, Gao J, et al. Exposure to high glutamate concentration activates aerobic glycolysis but inhibits ATP-linked respiration in cultured cortical astrocytes. *Cell Biochem Funct.* (2014) 32:530–7. doi: 10.1002/cbf.3047
38. Pellerin L, Bouzier Sore AK, Aubert A, Serres S, Merle M, Costalat R, et al. Activity-dependent regulation of energy metabolism by astrocytes: an update. *Glia.* (2007) 55:1251–62. doi: 10.1002/glia.20528
39. Vilchez D, Ros S, Cifuentes D, Pujadas L, Vallès J, García Fojeda B, et al. Mechanism suppressing glycogen synthesis in neurons and its demise in progressive myoclonus epilepsy. *Nat Neurosci.* (2007) 10:1407–13. doi: 10.1038/nn1998
40. Dienel GA, Cruz NF. Contributions of glycogen to astrocytic energetic during brain activation. *Metab Brain Dis.* (2015) 30:281–98. doi: 10.1007/s11011-014-9493-8
41. Gibbs ME, Hutchinson DS. Rapid turnover of glycogen in memory formation. *Neurochem Res.* (2012) 37:2456–63. doi: 10.1007/s11064-012-0805-2
42. Gilbert E, Tang JM, Ludvig N, Bergold PJ. Elevated lactate suppresses neuronal firing in vivo and inhibits glucose metabolism in hippocampal slice. *Brain Res.* (2006) 1117:213–323. doi: 10.1016/j.brainres.2006.07.107
43. Hertz L, Xu J, Song D, Du T, Li B, Yan E, et al. Astrocytic glycogenolysis: mechanisms and functions. *Metab Brain Dis.* (2015) 30:317–33. doi: 10.1007/s11011-014-9536-1
44. Muller MS. Functional impact of glycogen degradation on astrocytic signaling. *Biochem Soc Trans.* (2014) 42:1311–5. doi: 10.1042/BST20140157
45. Hamprecht B, Verleysdonk S, Wiesinger H. Enzymes of carbohydrate and energy metabolism. In: Kettenmann H, Ransom BR, editots. *Neuroglia 2nd* ed. New York, NY: Oxford University Press (2005). p. 202–15. doi: 10.1093/acprof:oso/9780195152227.003.0015
46. Ghosh A, Cheung YY, Mansfield BC, Chou JY. Brain contains a functional glucose-6-phosphatase complex capable of endogenous glucose production. *J Biol Chem.* (2005) 280:11114–9. doi: 10.1074/jbc.M410894200
47. Brown AM, Baltan Tekkok S, Ransom BR. Energy transfer from astrocytes to axons: the role of CNS glycogen. *Neurochem Int.* (2004) 45:529–36. doi: 10.1016/j.neuint.2003.11.005
48. Brooks GA. Lactate: link between glycolytic and oxidative metabolism. *Sports Med.* (2007) 37:341–3. doi: 10.2165/00007256-200737040-00017
49. DiNuzzo M, Mangia S, Maraviglia B, Giove F. Glycogenolysis in astrocytes supports blood-borne glucose channeling not glycogen-derived lactate shuttling to neurons: evidence from mathematical modeling. *J Cereb Blood Flow Metab.* (2010) 30:1895–904. doi: 10.1038/jcbfm.2010.151
50. Dienel GA. Lack of appropriate stoichiometry: strong evidence against an energetically important astrocyte-neuron lactate shuttle in brain. *J Neurosci Res.* (2017) 95:2103–25. doi: 10.1002/jnr.24015
51. Broer S, Rahman B, Pellegri G, Pellerin L, Martin JL, Verleysdonk S, et al. Comparison of lactate transport in astroglial cells and monocarboxylate transporter 1 (MCT 1) expressing Xenopus laevis oocytes. expression of two different monocarboxylate transporters in astroglial cells and neurons. *J Biol Chem.* (1997) 272:30096–102. doi: 10.1074/jbc.272.48.30096
52. Cortés Campos C, Elizondo R, Llanos P, Uranga RM, Nualart F, García MA. MCT expression and lactate influx/efflux in tanycytes involved in glia-neuron metabolic interaction. *PLoS ONE.* (2011) 6:e16411. doi: 10.1371/journal.pone.0016411
53. Garcia CK, Brown MS, Pathak RK, Goldstein JL. cDNA cloning of MCT2, a second monocarboxylate transporter expressed in different cells than MCT1. *J Biol Chem.* (1995) 270:1843–9. doi: 10.1074/jbc.270.4.1843
54. Dimmer KS, Friedrich B, Lang F, Deitmer JW, Broer S. The low-affinity monocarboxylate transporter MCT4 is adapted to the export of lactate in highly glycolytic cells. *Biochem J.* (2000) 350:219–27. doi: 10.1042/bj3500219
55. Korn T, Magnus T, Jung S. Interaction with antigen-specific T cells regulates expression of the lactate transporter MCT1 in primary rat astrocytes: specific link between immunity and homeostasis. *Glia.* (2005) 49:73–83. doi: 10.1002/glia.20101
56. Maekawa F, Minehira K, Kadomatsu K, Pellerin L. Basal and stimulated lactate fluxes in primary cultures of astrocytes are differentially controlled by distinct proteins. *J Neurochem.* (2008) 107:789–98. doi: 10.1111/j.1471-4159.2008.05650.x
57. Rosafio K, Pellerin L. Oxygen tension controls the expression of the monocarboxylate transporter MCT4 in cultured mouse cortical astrocytes via a hypoxia-inducible factor-1alpha-mediated transcriptional regulation. *Glia.* (2013) 62:477–90. doi: 10.1002/glia.22618
58. Pérez Escuredo J, Van Hée VF, Sboarina M, Falces J, Payen VL, Pellerin L, et al. Monocarboxylate transporters in the brain and in cancer. *Biochim Biophys Acta.* (2016) 1863:2481–97. doi: 10.1016/j.bbamcr.2016.03.013
59. Pierre K, Magistretti PJ, Pellerin L. MCT2 is a major neuronal monocarboxylate transporter in the adult mouse brain. *J Cereb Blood Flow Metab.* (2002) 22:586–95. doi: 10.1097/00004647-200205000-00010
60. Pierre K, Chatton JY, Parent A, Repond C, Gardoni F, Di Luca M, et al. Linking supply to demand: the neuronal monocarboxylate transporter MCT2 and the alpha-amino-3-hydroxyl-5-methyl-4-isoxazole-propionic acid receptor GluR2/3 subunit are associated in a common trafficking process. *Eur J Neurosci.* (2009) 29:1951–63. doi: 10.1111/j.1460-9568.2009.06756.x
61. Nave KA. Myelination and support of axonal integrity by glia. *Nature.* (2010) 468:244–52. doi: 10.1038/nature09614
62. Morrison BM, Lee Y, Rothstein JD. Oligodendroglia: metabolic supporters of axons. *Trends Cell Biol.* (2013) 23:644–51. doi: 10.1016/j.tcb.2013.07.007
63. Saab AS, Tzvetanova ID, Nave KA. The role of myelin and oligodendrocytes in axonal energy metabolism. *Curr Opin Neurobiol.* (2013) 23:1065–72. doi: 10.1016/j.conb.2013.09.008
64. Rinholm JE, Hamilton NB, Kessaris N, Richardson WD, Bergersen LH, Attwell D. Regulation of oligodendrocyte development and myelination by glucose and lactate. *J Neurosci.* (2011) 31:538–48. doi: 10.1523/JNEUROSCI.3516-10.2011
65. Vannucci SJ, Simpson IA. Developmental switch in brain nutrient transporter expression in the rat. *Am J Physiol Endocrinol Metab.* (2003) 285:E1127–34. doi: 10.1152/ajpendo.00187.2003
66. Nunez Parra A, Cortes Campos C, Bacigalupo J, Garcia Mde L, Nualart F, Reyes JG. Expression and distribution of facilitative glucose (GLUTs) and monocarboxylate/H+ (MCTs) transporters inrat olfactory epithelia. *Chem Senses.* (2011) 36:771–80. doi: 10.1093/chemse/bjr052
67. Pellerin L, Pellegri G, Bittar PG, Charnay Y, Bouras C, Martin JL, et al. Evidence supporting the existence of an activity-dependent astrocyte–neuron lactate shuttle. *Dev Neurosci.* (1998) 20:291–9. doi: 10.1159/000017324
68. Bergersen L, Rafiki A, Ottersen OP. Immunogold cytochemistry identifies specialized membrane domains for monocarboxylate transport in the central nervous system. *Neurochem Res.* (2002) 27:89–96. doi: 10.1023/A:1014806723147
69. Rafiki A, Boulland JL, Halestrap AP, Ottersen OP, Bergersen L. Highly differential expression of the monocarboxylate transporters MCT2 and MCT4 in the developing rat brain. *Neuroscience.* (2003) 122:677–88. doi: 10.1016/j.neuroscience.2003.08.040
70. Klosinski LP, Yao J, Yin F, Fonteh AN, Harrington MG, Christensen TA, et al. White matter lipids as a ketogenic fuel supply in aging female

brain: implications for Alzheimer's disease. *EBioMedicine.* (2015) 2:1888–904. doi: 10.1016/j.ebiom.2015.11.002

71. Amaral AI, Meisingset TW, Kotter MR, Sonnewald U. Metabolic aspects of neuron-oligodendrocyte-astrocyte interactions. *Front Endocrinol*. (2013) 4:54. doi: 10.3389/fendo.2013.00054
72. Zhao X, Li S, Mo Y, Li R, Huang S, Zhang A, et al. DCA protects against oxidation injury attributed to cerebral ischemia-reperfusion by regulating glycolysis through PDK2-PDH-Nrf2 axis. *Oxid Med Cell Longev*. (2021) 2021:5173035. doi: 10.1155/2021/5173035
73. Newman LA, Korol DL, Gold PE. Lactate produced by glycogenolysis in astrocytes regulates memory processing. *PLoS ONE.* (2011) 6:e28427. doi: 10.1371/journal.pone.0028427
74. Suzuki A, Stern SA, Bozdagi O, Huntley GW, Walker RH, Magistretti PJ, et al. Astrocyte-neuron lactate transport is required for long-term memory formation. *Cell.* (2011) 144:810–23. doi: 10.1016/j.cell.2011.02.018
75. Schurr A, West CA, Rigor BM. Lactate-supported synaptic function in the rat hippocampal slice preparation. *Science.* (1988) 240:1326–8. doi: 10.1126/science.3375817
76. Dienel GA. Brain lactate metabolism: the discoveries and the controversies. *J Cereb Blood Flow Metab.* (2012) 32:1107–38. doi: 10.1038/jcbfm.2011.175
77. Schurr A. Lactate: the ultimate cerebral oxidative energy substrate? *J Cereb Blood Flow Metab.* (2006) 26:142–52. doi: 10.1038/sj.jcbfm.9600174
78. Zhu Y, Wu J, Yuan SY. MCT1 and MCT4 expression during myocardial ischemic-reperfusion injury in the isolated rat heart. *Cell Physiol Biochem.* (2013) 32:663–74. doi: 10.1159/000354470
79. Tseng MT, Chan SA, Schurr A. Ischemia-induced changes in monocarboxylate transporter 1 reactive cells in rat hippocampus. *Neurol Res.* (2003) 25:83–6. doi: 10.1179/016164103101200978
80. Magistretti PJ, Pellerin L, Rothman DL, Shulman RG. Energy on demand. *Science.* (1999) 283:496–7. doi: 10.1126/science.283.5401.496
81. Lengacher S, Sitayeb TN, Steiner N, Carneiro L, Favrod C, Preitner F, et al. Resistance to diet-induced obesity and associated metabolic perturbations in haploinsufficient monocarboxylate transporter 1 mice. *PLoS ONE.* (2013) 8:e82505. doi: 10.1371/journal.pone.0082505
82. Schurr A, Payne RS, Miller JJ, Rigor BM. Glia are the main source of lactate utilized by neurons for recovery of function posthypoxia. *Brain Res.* (1997) 774:221–4. doi: 10.1016/S0006-8993(97)81708-8
83. Martinov V, Rizvi SM, Weiseth SA, Sagave J, Bergersen LH, Valen G. Increased expression of monocarboxylate transporter 1 after acute ischemia of isolated, perfused mouse hearts. *Life Sci.* (2009) 85:379–85. doi: 10.1016/j.lfs.2009.07.001
84. Murakami R, Chiba Y, Nishi N, Matsumoto K, Wakamatsu K, Yanase K, et al. Immunoreactivity of receptor and transporters for lactate located in astrocytes and epithelial cells of choroid plexus of human brain. *Neurosci Lett.* (2021) 741:135479. doi: 10.1016/j.neulet.2020.135479
85. Wong CH, Crack PJ. Modulation of neuro-inflammation and vascular response by oxidative stress following cerebral ischemia-reperfusion injury. *Curr Med Chem.* (2008) 15:1–14. doi: 10.2174/092986708783330665
86. Huang J, Upadhyay UM, Tamargo RJ. Inflammation in stroke and focal cerebral ischemia. *Surg Neurol.* (2006) 66:232–45. doi: 10.1016/j.surneu.2005.12.028
87. Chen SD, Yang DI, Lin TK, Shaw FZ, Liou CW, Chuang YC. Roles of oxidative stress, apoptosis, PGC-1α and mitochondrial biogenesis in cerebral ischemia. *Int J Mol Sci.* (2011) 12:7199–215. doi: 10.3390/ijms12107199
88. Schurr A. Energy metabolism, stress hormones and neural recovery from cerebral ischemia/hypoxia. *Neurochem Int.* (2002) 41:1–8. doi: 10.1016/S0197-0186(01)00142-5
89. Brea D, Blanco M, Ramos Cabrer P, Moldes O, Arias S, Pérez Mato M, et al. Toll-like receptors 2 and 4 in ischemic stroke: outcome and therapeutic values. *J Cereb Blood Flow Metab.* (2011) 31:1424–31. doi: 10.1038/jcbfm.2010.231
90. Shime H, Yabu M, Akazawa T, Kodama K, Matsumoto M, Seya T, et al. Tumor-secreted lactic acid promotes IL-23/IL-17 proinflammatory pathway. *J Immunol*. (2008) 180:7175–83. doi: 10.4049/jimmunol.180.11.7175
91. Doherty JR, Yang C, Scott KE, Cameron MD, Fallahi M, Li W, et al. Blocking lactate export by inhibiting the Myc target MCT1 Disables glycolysis and glutathione synthesis. *Cancer Res.* (2014) 74:908–20. doi: 10.1158/0008-5472.CAN-13-2034
92. Schurr A, Rigor BM. Brain anaerobic lactate production: a suicide note or a survival kit? *Dev Neurosci.* (1998) 20:348–57. doi: 10.1159/000017330
93. Schurr A, Payne RS, Miller JJ, Rigor BM. Brain lactate, not glucose, fuels the recovery of synaptic function from hypoxia upon reoxygenation: an in vitro study. *Brain Res.* (1997) 744:105–11. doi: 10.1016/S0006-8993(96)01106-7
94. Lee WT, Lin MH, Lee EJ, Hung YC, Tai SH, Chen HY, et al. Magnolol reduces glutamate-induced neuronal excitotoxicity and protects against permanent focal cerebral ischemia up to 4 hours. *PLoS ONE.* (2012) 7:e39952. doi: 10.1371/journal.pone.0039952
95. Fan J, Vasuta OC, Zhang LY, Wang L, George A, Raymond LA. N-methyl-D-aspartate receptor subunit- and neuronal-type dependence of excitotoxic signaling through post-synaptic density 95. *J Neurochem.* (2010) 115:1045–56. doi: 10.1111/j.1471-4159.2010.06994.x
96. Pellerin L, Magistretti PJ. Sweet sixteen for ANLS. *J Cereb Blood Flow Metab*. (2012) 32:1152–66. doi: 10.1038/jcbfm.2011.149
97. Fünfschilling U, Supplie LM, Mahad D, Boretius S, Saab AS, Edgar J, et al. Glycolytic oligodendrocytes maintain myelin and long-term axonal integrity. *Nature.* (2012) 485:517–21. doi: 10.1038/nature11007
98. Nave KA, Trapp BD. Axon-glial signaling and the glial support of axon function. *Annu Rev Neurosci*. (2008) 31:535–61. doi: 10.1146/annurev.neuro.30.051606.094309
99. Jha MK, Morrison BM. Lactate transporters mediate Glia-Neuron metabolic crosstalk in homeostasis and disease. *Front Cell Neurosci.* (2020) 14:589582. doi: 10.3389/fncel.2020.589582
100. Schurr A, Payne RS, Miller JJ, Rigor BM. Brain lactate is an obligatory aerobic energy substrate for functional recovery after hypoxia: further in vitro validation. *J Neurochem.* (1997) 69:423–6. doi: 10.1046/j.1471-4159.1997.69010423.x

Conflict of Interest: The authors declare that the research was conducted in the absence of any commercial or financial relationships that could be construed as a potential conflict of interest.

frontiers | Frontiers in Neurology

REVIEW
published: 03 May 2022
doi: 10.3389/fneur.2022.844938

Perivascular Spaces, Glymphatic System and MR

Linya Yu[1†], **Xiaofei Hu**[2†], **Haitao Li**[2*] and **Yilei Zhao**[1*]

[1] Department of Radiology, The First Affiliated Hospital, School of Medicine, Zhejiang University, Hangzhou, China,
[2] Department of Radiology, Southwest Hospital, Third Military Medical University (Army Medical University), Chongqing, China

The importance of the perivascular space (PVS) as one of the imaging markers of cerebral small vessel disease (CSVD) has been widely appreciated by the neuroradiologists. The PVS surrounds the small blood vessels in the brain and has a signal consistent with the cerebrospinal fluid (CSF) on MR. In a variety of physio-pathological statuses, the PVS may expand. The discovery of the cerebral glymphatic system has provided a revolutionary perspective to elucidate its pathophysiological mechanisms. Research on the function and pathogenesis of this system has become a prevalent topic among neuroradiologists. It is now believed that this system carries out the similar functions as the lymphatic system in other parts of the body and plays an important role in the removal of metabolic waste and the maintenance of homeostatic fluid circulation in the brain. In this article, we will briefly describe the composition of the cerebral glymphatic system, the influencing factors, the MR manifestations of the PVS and the related imaging technological advances. The aim of this research is to provide a reference for future clinical studies of the PVS and glymphatic system.

Keywords: perivascular space (PVS), CSVD, glymphatic system, magnetic resonance imaging, aquaporin 4 (AQP4)

OPEN ACCESS

Edited by:
Alberto L. Vazquez,
University of Pittsburgh, United States

Reviewed by:
Davneet S. Minhas,
University of Pittsburgh, United States
Xingfeng Shao,
University of Southern California,
United States
Nagesh C. Shanbhag,
Lund University, Sweden

***Correspondence:**
Yilei Zhao
1309035@zju.edu.cn
Haitao Li
13883818704@163.com

†These authors have contributed equally to this work

Specialty section:
This article was submitted to Applied Neuroimaging, a section of the journal Frontiers in Neurology

Received: *29 December 2021*
Accepted: *28 March 2022*
Published: *03 May 2022*

Citation:
Yu LY, Hu XF, Li HT and Zhao YL (2022) Perivascular Spaces, Glymphatic System and MR. Front. Neurol. 13:844938. doi: 10.3389/fneur.2022.844938

INTRODUCTION

Approximately 150 years ago, German pathologist Rudolf Virchow (1821–1902) and French anatomist Charles Philippe Robin (1821–1885) described the perivascular space in detail. As a tribute to them, perivascular space was named Virchow-Robin space (VRS). A VR space is a space filled with interstitial fluid (ISF) surrounding the cerebral small vessels (CSV). They penetrate the brain parenchyma from the brain surface, and are covered with leptomeninges. PVS is an emerging and early imaging marker of CSVD and can be considered a risk factor for CSVD. The STandards for ReportIng Vascular changes on nEuroimaging (STRIVE) (1) lists PVS together with recent small subcortical infarct (RSSI), lacunae, white matter hyperintensity (WMH), cerebral microbleed (CMB) and cerebral atrophy as the six major imaging manifestations of CSVD. Besides CSVD, many neurodegenerative disorders are associated with dilated PVS, such as Alzheimer's Disease (AD), Parkinson's Disease (PD), multiple sclerosis (MS), idiopathic normal pressure hydrocephalus (iNPH), brain trauma, central nervous system (CNS) cryptococcal infection and mucopolysaccharidosis.

While the function of PVS has been debated, the current literature consensus suggests that PVS acts as a conduit for lymphatic drainage, exchange between CSF and ISF, and waste removal from the brain, and it is the anatomic basis of the glymphatic system (2).

In the following review, we provide a brief description of the glymphatic system in terms of its function and possible mechanisms. We also discuss MR imaging features of VRS. In addition, we focus on the novel MR imaging techniques for evaluating the glymphatic system, some of which are currently in development but likely to become available soon in clinical settings.

ANATOMY OF PVS

VR spaces surround the walls of arteries, arterioles, capillaries, veins, and venules as they pass through the brain parenchyma from the subarachnoid space. The outer limits of VR spaces are the glia limitans of the underlying brain, and inner limits are the endothelial basement membranes of the vessel (**Figure 1**) (3). Penetrating arterioles are completely wrapped in a sheet of pia mater. It can be observed under electron microscopy that when the penetrating arterioles branch into the level of capillaries, the basement membrane of the pial sheath and the basement membranes of the astrocytes (glia limitans) fuse together to create a perivascular compartment (4). The compartment separates the vessel from surrounding brain tissue and fill with ISF.

The perforating arteries in the basal ganglia (BG) are covered with two coats of leptomeninges, and the spaces between these two layers connect to the subarachnoid space directly (**Figure 1**) (3). Cortical arterioles and all venules are surrounded by only one leptomeningeal layer, so they connect directly to the subpial space and indirectly to the subarachnoid space in some way (**Figure 1**) (3).

VR spaces are accessory structures that are not actually a part of the blood vessel. It has been demonstrated that VR spaces function as pathways for waste removal and fluid drainage in the brain, similarly to the lymphatic drainage system in the body (2, 5).

GLYMPHATIC SYSTEM AND PVS

Glymphatic System Hypothesis

Although the existence of perivascular spaces has been confirmed by pathologists for more than 150 years and MR has made it possible to clearly visualize enlarged perivascular spaces (EPVS), the function and clinical significance of perivascular spaces continued to be debated until 2012, when Iliff et al. (5) uncovered a new mechanism of brain metabolism-a unique para-vascular pathway of brain metabolism, thus gradually unraveling the mystery of perivascular spaces. Their study revealed the presence of interstitial solute clearance structures dependent on astrocyte podocyte aquaporins 4 (AQP4) in the perivascular space of the

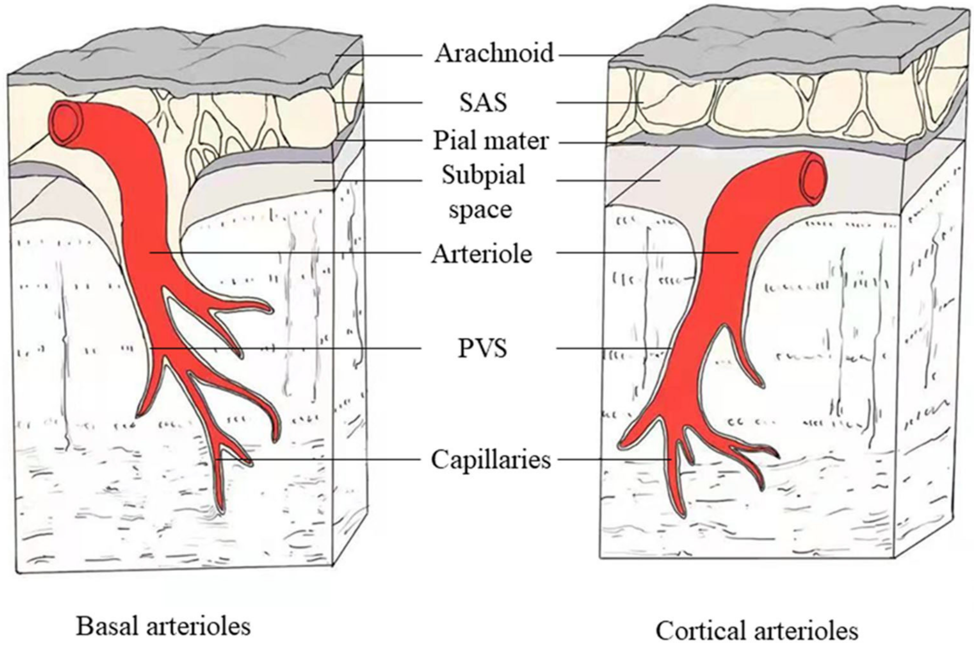

FIGURE 1 | Schematic drawing of PVS around basal and cortical perforating arterioles. The perivascular spaces surround the cerebral small perforating vessels as they pass through the brain parenchyma from the subarachnoid space (SAS). The outer limits of PVS are the glia limitans of the underlying brain, and inner limits are the endothelial basement membranes of the vessel. The basal perforating arterioles are covered by two layers of leptomeninges, with the inner membrane tightly adhering to the arteriolar wall, and the outer layer extending from the pia mater (left). The spaces between these two meningeal membranes connect to the SAS directly (left). Cortical arterioles are surrounded by only one leptomeningeal layer, closely applied to the vessel wall, so the cortical perivascular spaces connect directly to the subpial space and indirectly to the SAS in some way (right).

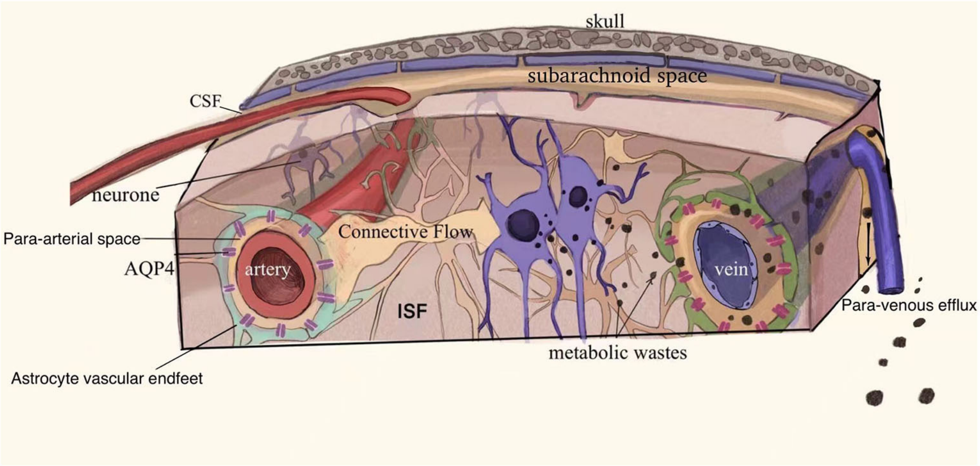

FIGURE 2 | Schematic drawing of the glymphatic system. The glymphatic system may consist of the following three principal segments (1) a para-arterial CSF influx, (2) an astrocyte end-foot water channel protein AQP4 mediated convection of CSF and ISF, and (3) a para-venous ISF efflux. Neuronal metabolites are carried into the perivascular space and drain through the meningeal lymphatic vessels and soft tissues surrounding the skull to the cervical and nasal lymph nodes and are eventually removed from the general circulation. Adapted with permission from Nedergaard (2).

rodent brain and termed it the "glymphatic system" (5). Iliff et al. also found that soluble amyloid β (Aβ) protein injected into the striatum of mice was cleared from this para-vascular pathway (5). In their subsequent study, the exchange of CSF with ISF in the live rat brain was observed by dynamic contrast-enhanced MRI through intrathecal injection of two different molecular weights of MRI contrast agents. Both contrast agents passed largely similarly through the para-arterial space in the rats, but the smaller molecular weight contrast agent entered the brain parenchyma more extensively, while the larger one was sparsely distributed in the brain parenchyma (6). This finding points to the molecular size-selective nature of the glymphatic system for clearing substances, which may explain the tendency of large molecular Aβ protein to be deposited around blood vessels. The discovery of meningeal lymphatic vessels in 2015 was even stronger evidence for the existence of brain glymphatic system (7).

The precise drainage pathways and mechanisms of the glymphatic system are not known. It is hypothesized that the system consists of three principal segments (2, 8): (1) a para-arterial CSF influx, (2) an astrocyte end-foot water channel protein AQP4 mediated convection of CSF and ISF, and (3) a para-venous ISF efflux (**Figure 2**). The possible circulation pathways of the system are as follows: neuronal metabolites are carried to the perivascular space via convection of CSF and ISF facilitated by AQP4, from where they are transported directed into lymphatic vessels located in meninges and in the soft tissue surrounding the skull and eventually return to the general circulation for clearance by the kidneys and liver via cervical and nasal lymph nodes (**Figure 2**) (2, 7, 8).

Drivers of Glymphatic Transport

The possible factors driving ISF through perivascular spaces are continuous production of CSF (8), vascular pulsation (9, 10), respiratory movement (11), the sleep–wake cycle (12–14), and AQP4 water channel protein (15).

The power source for this fluid drainage system is generated by the continuous CSF flow. The production of CSF from the choroid plexus drives the fluid from the ventricular system into the subarachnoid space and along the perivascular space into the cerebral interstitium. The driving force generated by CSF flow is important for the exchange between CSF and ISF and helps to flush out metabolites within perivascular spaces (8).

Cerebrovascular pulsatility drives fluid transport along this pathway. Rodent studies have shown that increased intracranial vascular pulsation is associated with increased PVS, and that vascular pulsation, particularly in the small cerebral arteries, is directly involved in the production of enlargement of perivascular spaces in the brain (9, 10). The elevation of blood pressure and the increase in the amplitude of pulsation of the arterial wall, although the arterial diameter remains constant, causes a decrease in the net flow of PVS and a decrease in debris clearance (10). Spontaneous low-frequency oscillations were observed in the arteries of awake mice which drives the drainage of solutes from the PVS (16). In mice with cerebral amyloid angiopathy (CAA), impaired vascular reactivity resulted in reduced solute clearance (16).

The similar effect of vascular pulsation on the glymphatic function of the human brain is derived from phase contrast MR. Lower cerebrovascular reactivity (CVR) was associated with higher WMH volume and increased PVS visibility in the basal ganglia (17). Furthermore, increased intracranial vascular pulsatility was associated with lower CSF stroke volume at the foramen magnum and, in turn, with increased PVS burden at the basal ganglia (17).

Respiratory movements affect the fluid drainage within the PVS by influencing CSF transport. Forced inspiration causes the CSF to move cephalad, while the venous blood draws away caudally (11). The movement of CSF from breathing might also flush perivascular spaces.

The glymphatic system is more effective during sleep. Using real-time assessment of tetramethylammonium diffusion and two-photon imaging, a recent study evaluated tracer clearance in live mice during wakefulness, natural sleep, and anesthesia. They found that the rate of clearance was highest during sleep, with the same performance under anesthesia, and a 95% reduction in tracer flux into the perivascular spaces of the mouse brain during wakefulness (12). Similarly, the clearance of Aβ by mice doubled during sleep (12). The study also shows a 60% increase in interstitial space under natural sleep or anesthesia, thus explaining the significant increase in the convection between CSF and ISF. Sleep may be involved in perivascular clearance in ischemic encephalopathy (13). CSF uptake and ISF drainage from the PVS increases during sleep, and poor sleep quality may affect the clearance of neurotoxins, interrupting ISF drainage and possibly leading to enlarged perivascular spaces (13). Hablitz et al. studied the relationship between the sleep timing and the glymphatic function in mice and found that the influx and clearance of glymphatic fluid had a circadian rhythm and peaked in efficiency during the mid-rest phase (14). The peak of perivascular AQP4 polarization occured simultaneously during the resting phase in mice, and the absence of AQP4 eliminated diurnal differences in glymphatic flow and drainage (14). Therefore, they concluded that the distribution of CSF is controlled by the diurnal rhythm, and AQP4 is involved.

AQP4 is a water channel protein on the feet of perivascular astrocytes and is a regulator of normal glymphatic function (15, 18), which facilitates the exchange of CSF and ISF in the VR spaces and the active outflow of ISF (5). Although AQP4 is the major water channel protein in mammals, it is only expressed in astrocytes and ventricular meningeal cells. The outer wall of the VR space is composed of astrocyte end-feet with abundant AQP4, which allows water in this interstitial space to move into the ISF, making the transport of small molecules and ions possible. In AQP4 knockout mice and rats, the transport of tracers in the CSF and ISF was significantly reduced, suggesting that the AQP4 gene is necessary for the fluid transport in the brain (5, 15). But the importance of AQP4 in the glymphatic system remains controversial. Smith et al. founded that uptake of CSF tracers and transport of fluorescent dextrans from subarachnoid space to brain parenchyma were unaffected by AQP4 gene knockout in rats or mices (19). They suggested that AQP4 does not appear to be necessary for fluid movement within the glymphatic system in rodent brains, and this movement applies more to diffusion than to convection. These conflicting findings may be due to the use of different techniques or anesthetics by different investigators (3, 20).

Substances Cleared by the Glymphatic System

Glymphatic clearance is a molecular size selective mechanism (5, 6). Soluble Aβ (5), tau (3) and lactate (21) can be selectively removed through this system. The system also contributes to the delivery of apolipoprotein E (ApoE) (22), lipids (23) and signaling molecules (23). AQP4 plays a major role in the transport of ions and small molecules. Polarized AQP4 can fold toward the center and constitute highly selective water pores, allowing the smooth passage of water molecules (2, 5, 6, 8). The abundance of AQP4 on the astrocyte end-foot, which forms the outer wall of the perivascular space, provides for the transport of small molecules and ions. At the same time, the cleft between astrocyte end-feet allows the passage of macromolecular compounds, and most of the solutes with molecular weight <100 kDa will leave the perivascular spaces through this cleft (8). Today's research is increasingly focused on the glymphatic clearance mechanisms, hoping to develop new therapeutic strategies for associated neurological disorders in the future.

PVS Enlargement

The PVS, as the main conduit for the drainage of ISF from brain tissues, is responsible for the exchange between CSF and ISF, the removal of intracerebral waste, and the maintenance of brain homeostasis (2). PVS also acts as a conduit for delivering various signaling molecules and metabolic factors (2, 18). The precise causes and mechanisms of PVS enlargement are not yet known. As the anatomical basis of the glymphatic system, the increased visibility and enlargement of PVS on imaging may be potentially linked to the dysfunction of the glymphatic system. Theoretically, PVS enlargement should be caused by fluid accumulation due to imbalance between CSF inflow and outflow, but direct evidence is still lacking (24). Altered blood flow and blood-brain barrier (BBB) dysfunction are also believed to be involved in PVS dysfunction (24, 25).

It is controversial whether the visible PVS on MRI refers only to the periarterial spaces or to both the periarterial and perivenous spaces. Most of the evidence suggests that visible PVS on MR are around arteries (3). However, the answer to the question of whether the absence of visibility on MR equates to the absence of enlargement of the perivenous spaces or the absence of venular dysfunction is no. Histopathological studies of autopsy specimens confirm the presence of many visible perivenous spaces in areas of collagenization of deep penetrating veins (3, 26). However, the extent to which this venous collagenization contributes to the visibility of PVS on MR, and the incidence and severity of venous collagenization in small vessel disease are unknown. Furthermore, the available studies do not find that the main pathway of solute efflux in the glymphatic system is along perivenous routes, but rather there is much evidence that solute inflow and efflux occur along periarterial routes (27). If the main pathway of solute efflux is not perivenous routes, could this explain to some extent why enlarged perivenous spaces are usually not observed on MR.

Patients with dilated VRS are generally asymptomatic, but multiple enlarged VRS or giant VRS may occasionally show the following symptoms or signs: headache, dizziness, cognitive impairment, inattention, visual impairment, epilepsy. PVS may be aggravated by aging, hypertension, inflammation, lacunar stroke, and dementia (3).

The enlarged perivascular space (EPVS) at different sites may have different pathophysiological basis and pathogenic mechanisms. EPVS often coexists with lacunar infarction. EPVS tends to be more pronounced in the basal ganglia region in patients with lacunar stroke than in those with non-lacunar stroke (28). Ischemic stroke patients with a higher EPVS load in the basal ganglia region have a higher risk of stroke recurrence (24). Small artery occlusion stroke subtypes have a relatively higher risk of high load EPVS in the hippocampus (29). Patients with CAA have a higher total cortical Aβ load and impaired Aβ clearance leading to enlarged perivascular spaces, especially in the centrum semiovale (30, 31). In patients with spontaneous cerebral hemorrhage, basal ganglia EPVS severity is associated with hypertensive arteriopathy (31), and high EPVS load in the centrum semiovale is associated with cerebral hemorrhage recurrence in patients with CAA (32). Post-stroke depression (PSD) is a common psychiatric symptom after stroke, occurring in approximately 1/3 of patients (33). EPVS is thought to be associated with the development of PSD. Researchers found that centrum semiovale rather than basal ganglia EPVS is more severe in patients with PSD and is associated with poor antidepressant response (34).

There are conflicting data on MR regarding the relationship between perivascular spaces and cognitive decline. Most studies have concluded that the burden of EPVS in both the basal ganglia and centrum semiovale is associated with cognitive decline (3). However, some studies did not find an association between EPVS in the basal ganglia region and cognitive dysfunction (3), whereas Arba et al. came to the opposite conclusion, suggesting that EPVS in the basal ganglia region, but not in the centrum semiovale, was associated with cognitive decline (35). Three other studies showed no independent association between EPVS and cognitive impairment (36, 37) and that EPVS was not a predictor of cognitive decline (38). These contradictory data may be related to the differences in the enrollment and assessment methods of each study. In addition, due to the wide range of cognitive functions included, EPVS may affect only some of these cognitive domains and not necessarily the overall cognitive function of the whole brain.

In addition, CADASIL 45, PD, cerebral trauma, idiopathic normal pressure hydrocephalus, mucopolysaccharidosis (39), neuropsychiatric retardation, autism (40), systemic lupus erythematosus (SLE) (41, 42), multiple sclerosis, primary angiitis of the central nervous system (43, 44), and cryptococcal infection (45, 46) are often accompanied with EPVS. For example, in patients with mucopolysaccharidosis, transient sieve-like PVS can appear in the white matter in the early stages of the disease and can increase, decrease or remain stable depending on the progression of the disease (39). In patients with cryptococcal infection, multiple EPVS can be found in the cerebral hemispheres, parietal ventricles, midbrain, bilateral cerebellar hemispheres, and especially in the basal ganglia, which is considered the most common early sign of cryptococcal infection and is associated with intracranial dissemination and proliferation of cryptococci (45, 46).

EPVS is not a specific disease, but should be considered as one of the imaging markers for the development of multiple diseases, and its mechanism of action and corresponding clinical relevance in neurological diseases are still unclear and need further investigation.

MR IMAGING OF PERIVASCULAR SPACES

Appropriate MR Imaging Sequence

Based on STRIVE (1), PVS were referred to as a neuroimaging marker of CSVD. MRI instead of CT is recommended for detecting PVS. The recommended sequences include T1-weighted imaging (T1WI), T2-weighted imaging (T2WI), fluid attenuated inversion recovery sequence (FLAIR), diffusion-weighted imaging (DWI) and apparent diffusion coefficient map (ADC). VRS are best detected using T2WI. DWI is the most sensitive sequence for RSSI. FLAIR is used to identify VRS from WMHs and lacunes. A field strength of 1.5T is often of a similarly high resolution as 3.0T (47). It is generally believed that the VRS seen on conventional magnetic field strength (1.5T or 3.0T) MR is the peri-arteriolar space (48).

MR Manifestation

The signal intensity of perivascular spaces is consistent with CSF on all MRI sequences showing hypointense on T1WI and FLAIR, hyperintense on T2WI, without enhancement and generally no mass effect (1, 49). The diffusion of PVS is unrestricted. The signal of the surrounding brain is generally normal.

PVS appears striped when the penetrating artery is parallel to the imaging plane and rounded or ovoid when perpendicular to the imaging plane (**Figures 3A–F**) (1, 49). PVS is typically <3 mm in diameter (1). The distribution of PVS is usually bilaterally symmetrical. Sometimes, high-resolution MRI can reveal microscopic structures within the PVS: a central vessel can be observed in the cystic space and is defined as the "vessel sign", which could be possibly helpful for differentiating the spaces from lacunes (**Figure 3B**) (1, 49). VR spaces can show a solitary round cyst, multiple strips and lines, unilateral predominantly dense cysts, or even a spider web-like appearance on MRI (**Figure 3C**).

PVS are commonly located in the basal ganglia, the centrum semiovale, the subcortical white matter of brain convexity, and the brainstem, however, the space is rarely seen in the cerebellum (1, 49). Large PVS is often first seen around the penetrating artery in the precribrum even in young people.

Perivascular spaces of 1–2 mm appear in all age groups (49, 50). Mildly enlarged PVS can also be detected in routine MR examination in healthy individuals of all ages, however, the burden of EPVS becomes increasingly apparent with advancing age (50). PVS of >3 mm can be observed in approximately one-third of elderly people (50). Increased visibility of VRS in the BG and white matter is significantly associated with age, and the VRS burden in the BG is heavier in men than in women (50). PVS with a diameter >3 mm must be distinguished from small lacunes. Lacunes tend to be 3–15 mm in diameter with a hyperintense rim around the vesicular cavity on FLAIR sequence (**Figures 3D,E**) (1). Sometimes, PVS can be especially enlarged with a diameter larger than 15 mm, even with mass effect, which is named as giant PVS or tumefactive PVS (**Figure 3F**) (51).

Type of PVS

VR spaces are traditionally classified into three types based on their location. Type I-basal ganglia type: PVS courses with

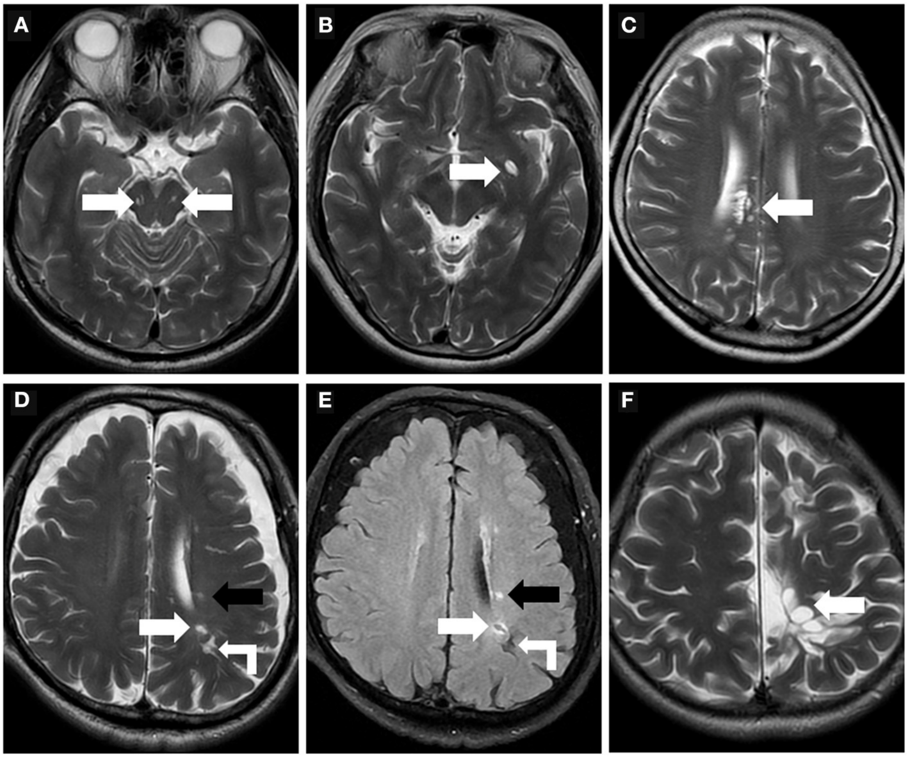

FIGURE 3 | Morphologic characteristics of the perivascular spaces. **(A)** Type III-midbrain type: Axial T2WI showed multiple linear EPVS (white arrow) with high intensity in the midbrain, which were generally symmetrically distributed on both sides and consistent with the course of the penetrating arteries. **(B)** In a 62-year-old woman, axial T2WI showed a large EPVS in the left precribrum with sac-like high intensity, within which a linear hypointense vessel can be seen, namely "vessel sign" (white arrow). **(C)** Axial T2WI revealed multiple linear and ovoid EPVS clustered locally near the right lateral ventricle (white arrow). **(D,E)** In a 76-year-old man with a history of hypertension and diabetes mellitus for many years, EPVS (white right angle arrow), WMH (black arrow), and small lacune (white arrow) were simultaneously present in the left centrum semiovale. The lacune (white arrow) showed a hyperintense rim around the vesicular cavity on FLAIR sequence, which can be distinguished from EPVS. **(F)** A 32-year-old male with cerebral cleft malformation combined with hypoplasia of the corpus callosum in the left cerebral hemisphere, who had recurrent headaches for many years. Multiple tumefactive PVS (white arrow) were seen in the subcortical white matter areas, and the lesions were unchanged on follow-up reviews of brain MR.

the lenticulostriate artery entering the basal ganglia through the precribrum (52); This is the most prevalent type. Type II-Hemispheric type: PVS follows the course of the medullary arteries into the white matter of brain convexity and extends into the subcortical white matter (52). Type III-midbrain type (**Figure 3A**): PVS lies in the midbrain following the path of penetrating artery from the posterior cerebral artery.

Similarly, giant VR spaces or tumefactive VR Spaces can be categorized into the three types described above, but type II and type III are more common (53). Type II VR spaces rarely cause clinical symptoms, but when they are diffuse, they may mimic PD or dementia (53). They are also seen in patients with neurofibromatosis and neuropsychiatric retardation (54, 55). Due to its special location, Type III VR spaces are more likely to compress the middle cerebral aqueduct or third ventricle, causing hydrocephalus. In some cases, tumefactive PVS can also cause pulsatile tinnitus (56), homonymous quadrantanopia (57), paralysis of the extremities (58), and reversible focal dystonia (59). Unlike the small PVS, the brain parenchyma surrounding the giant PVS has an abnormal signal intensity in 32.3% of type II cases and 3.8% of type III cases (53). They are often misdiagnosed as other pathologic processes, especially cystic neoplasms (49).

A recent study described an enlarged perivascular space located in the anterior temporal lobe with unique neuroimaging features (60). It occured in association with the vascular loop of the middle cerebral artery (MCA) branch and often compressed the adjacent cortex, with edema around the lesion. The clinical presentation was very similar to that of a cystic tumor and was often misdiagnosed and surgically removed as such. The author suggested that it should be considered as a separate subtype of perivascular spaces, namely type IV perivascular spaces, and proposed the term "opercular perivascular cyst" as naming. This type of PVS exhibits the same internal signal characteristics as CSF in all MRI sequences, without contrast enhancement or magnetic susceptibility artifacts, and the brain parenchyma surrounding the lesion shows variable high signal on T2WI and FLAIR (60).

Quantification of Perivascular Spaces

Visual Scoring

Visual scoring is frequently used to assess the severity of PVS, but there is currently no uniform grading system for radiologists. The most widely used method is Potter scoring. PVS are divided into 0–4 grades (grade 0 none; grade 1 <1–10; grade 2 11–20; grade 3 21–40; grade 4 > 40) according to their number in the BG and centrum semiovale, by counting the side of the cerebral hemisphere with the heavier PVS burden, and 0 to 1 grades for the midbrain according to the presence or absence of PVS (**Figure 4**) (51). The hippocampus was not involved in the Potter scoring, which has numerous methods of grading. Chinese IntraCranial AtheroSclerosis (CICAS) study group graded the hippocampal region based on the number of PVS as follows: grade 1 < 5; grade 2 5–10; grade 3 > 10 (29). Heier classified the PVS based on its diameter as: (mild) grade 1<2 mm, (moderate) grade 2 2–3 mm, and (severe) grade 3 > 3 mm (52).

These scores are handy, practical, reliable and repeatable to use in clinical settings (51). Several studies, including some involving thousands of participants, have utilized these scoring methods (29). However, the intra- and inter-observer consistency of visual scores may be less than optimal, particularly in the centrum semiovale, as PVS coexists with other imaging markers of CSVD such as WMH and lacunae, making it difficult to distinguish between them (51). Visual scores are also subject to ceiling/flooring effects (3).

Automatic Computerized Quantification

With the development of computer image recognition technology, automatic computerized quantification of the perivascular space became feasible in clinical settings (61–63). Recently, Dubost et al. attempted to use 3D regression neural network for the quantification of dilated PVS, and the result was encouraging. The consistency between their automatic quantitative scoring and the experts' visual scores was high, with an intraclass correlation coefficient (ICC) of 0.74 and the reproducibility of the neural network was higher than the intra-rater agreement (ICC 0.93 vs. 0.80) (63). In addition, computational PVS counts correlate with age in a similar way to visual scores (63). Lian et al. presented a novel fully convolutional neural network to segment PVS efficiently without requiring any hand-drawing features or regions of interest (ROIs) (64). In addition to number, several morphological characteristics of perivascular spaces were also analyzed in some studies, including volume, size, length, width and linearity (65, 66). Interestingly, these studies showed that computational PVS morphological features were strongly associated with cerebrovascular risk factors and CSVD than PVS count or visual score (65, 66). The size and width of PVS in the centrum semiovale and deep corona radiata were associated with hypertension and stroke, but not with diabetes, hypercholesterolemia, or cardiovascular disease, while computational descriptors of PVS were associated with WMH severity in white matter region and with lacunes and microbleeds in basal ganglia (66).

Most of these automatic quantification methods focus on using computer technology in an effort to improve the efficiency and accuracy of automatic image segmentation. PVS is still mainly quantified visually and is usually limited to large-aperture PVS, and little has been done to improve its visibility and contrast with surrounding tissue through image postprocessing (67). Sepehrband et al. described an enhanced PVS contrast (EPC) multimodal approach to intensify the visibility of the PVS on

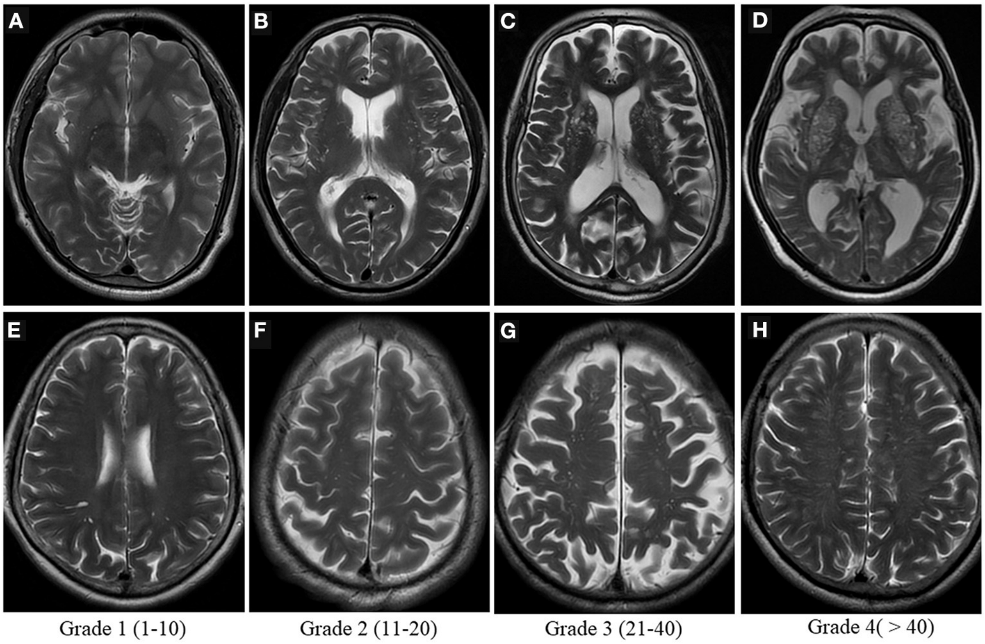

FIGURE 4 | Visual scoring of PVS. Potter scoring-Axial T2WI demonstrates the different severity of EPVS in the basal ganglia [top row, **(A–D)**] and in the centrum semiovale [bottom row, **(E–H)**], with the corresponding scores (1–4) shown at the bottom.

MRI. An EPC image was created by fusing T1- and T2-weighted images and removing "non-structured high frequency spatial noise" using a dedicated filtering algorithm. This technique can significantly improve the consuity of the PVS and is effectively used for subsequent automatic quantification of the PVS (67).

These computational quantification methods are 100% automatic and do not have any inter- or intra-rater variability. This makes them more suitable for longitudinal studies. It seems that these methods have shown high consistency between manual assessment and computerized counts, but their value requires further testing. We expect that this automatic segmentation technique will be applied in the clinic in the near future, similarly to the AI software for lung nodule assessment that is widely used in radiology today. It will provide a wealth of basic data on the evolution of perivascular spaces with age and disease.

Application of Ultra-High-Field MRI

It is likely, in the near future, that ultra-high-field strength MRI will have an increased clinical impact. Ultra-high-field strengths are expected to improve spatial resolution and image contrast, making it possible to visualize the internal structure of VR spaces on MR images. Using 7T MRI in the human brain, small penetrating vessels within the PVS of the BG and centrum semiovale were successfully detected (48). Additionally, 7T MRI has been used to assess the asymmetric distribution of PVS in epileptic patients' brains (68), the number and size of VRS in multiple sclerosis patients (69), and the quantitative description of PVS in young and middle-aged healthy individuals (70, 71). Ultra-high-field MRI may help in the precise localization of onset areas of neurological disorders (68). Clearly, it is an effective tool for the non-invasive assessment of CSVD. It can detect atheromatous plaques in lenticulostriate arteries (72), assess post-stroke revascularization (73) and measure cerebral microvessel velocity (74).

Nevertheless, ultra-high field MRI also has its limitations. Typically, increased spatial resolution entails an increase in sensitivity to motion. An object scanned may exhibit artifacts caused by physiological involuntary movements, such as respiration or heartbeat, or spontaneous movements, such as slight head movements. By utilizing motion correction procedures, this issue can be greatly alleviated (75). The transmit radiofrequency (RF) magnetic field (B1) inhomogeneity also increases, resulting in a lower signal-to-noise ratio (SNR), especially in the periphery of the brain (75). Peripheral SNR loss may significantly limit detection of the subcortical perivascular spaces. In addition, the radiofrequency specific absorption rate (SAR) is significantly increased, which raises questions about the safety of the examination and the more limited compatibility with medical implants and devices (75). Parallel RF transmission (pTx) technology is an effective and most commonly applied solution for mitigating B1 inhomogeneities (76). Due to advances in pTx techniques in ultra-high magnetic field environments, combined with optimization of MR pulse sequences, black blood imaging techniques, non-contrast enhanced MR angiography (MRA) and arterial spin labeling (ASL) perfusion are able to achieve isotropic sub-millimeter resolution, which is very useful for high-resolution neurovascular imaging studies (76). Using optimized high-resolution black-blood T1-weighted 3D turbo spin-echo with variable flip angles (T1w TSE-VFA) sequences at 3T and 7T, Ma et al. successfully characterized the morphology of tonsillar arteries in healthy volunteers (77). As compared to 3T ASL, 7T ASL has a significantly better SNR, thus enabling whole-brain high-resolution perfusion imaging (76). Furthermore, ASL-based four-dimensional MRA (4D MRA) has been developed with a significantly higher SNR than ASL-based perfusion. 4D MRA at 7T enables detailed characterization of vascular structures and dynamic flow patterns (76). Regarding the safety of the examination at 7T, a recently proposed safety guideline can be helpful in future clinical settings for healthcare professionals (78).

IMAGING OF BRAIN GLYMPHATIC SYSTEM

In the following section we will briefly discuss imaging techniques for assessing the glymphatic system, most of which are in development.

Two-Photon Imaging and Fluorescent Tracing

Early studies of the cerebral glymphatic system were mostly carried out using two-photon imaging and fluorescence tracers. Iliff et al. used this technique to visualize the glymphatic pathway for the first time in rodents and showed that Aβ, the causative peptide of AD, was cleared from this pathway (5). The system is more effective during sleep (12, 14). A recent study explored the mechanisms of brain edema formation after stroke using radiolabeled tracers and multiphoton imaging coupled with DWI-MRI. According to the study, post-stroke cerebral edema is caused by an accelerated influx of CSF into the brain parenchyma via perivascular spaces within minutes of an ischemic insult (79). The finding overturns the traditional understanding of poststroke edema and provides a new concept for the development of alternative treatment strategies.

Researchers are continually innovating existing photo-microscopy techniques in order to obtain more accessible, minimally invasive, and higher definition images. Using a multiband filter cube, tunable LED light source, and CMOS camera, Sweeney et al. presented a transcranial fluorescence macroscopic imaging method to visualize CSF transport within perivascular spaces through the intact skull of living mice (80). In addition, a novel method for qualitative and quantitative estimation of glymphatic flux in rats using Evans blue-labeled albumin (EBA) was proposed that does not require radioactive labeling (81).

However, due to its drawbacks such as narrow field of view, shallow penetration depth, invasiveness to the study subject and the need for small cranial openings, this technique is not applicable to human brains. A real-time image of the entire human brain is not possible. Human brain researches are mainly focused on postmortem tissue assessment. Researchers evaluated the postmortem frontal cortex using Western blotting and immune-fluorescence from a total of 79 cognitively competent and histo-pathologically proven AD patients, and found a significant association between AQP4 expression and advancing age in all the participants (82). Individuals with AD had reduced AQP4 perivascular localization, and loss of perivascular localization slowed the clearance of Aβ and promoted its deposition (82). This may be one of the most successful applications of microscopy techniques in the human brain glymphatic system.

MRI for Assessment of the Glymphatic System

MRI's sensitive, non-invasive nature has made it possible to bring the study of the glymphatic system from the laboratory to the clinic. Researchers today are becoming more and more interested in the application of novel MR imaging techniques for assessing the human glymphatic system.

Dynamic Contrast-Enhanced MRI, DCE-MRI

Similar to animal experiments, non-invasive direct *in vivo* imaging of the human glymphatic system has been mainly accomplished through intrathecal administration of contrast agents. Intrathecal injection of gadolinium-based contrast agents (GBCA) has been considered safe at doses <1.0 mmol (83, 84). Serious neurotoxic complications were associated with significantly higher GBCA doses (84).

Researchers have also tried to assess the glymphatic system using the faster and more convenient intravenous GBCA method, thus avoiding the need for intrathecal injections. For a long time, it has been widely assumed that GBCA does not cross an intact BBB (85). However, recent studies questioned this dogma (85–87). Today, it is generally accepted that gadolinium, even with intact BBB and competent renal function, can gradually accumulate in the human CSF after intravenous injection. Based on this consideration, one study utilized heavy T2-weighted fluid-attenuated inversion recovery imaging (hT2W-FLAIR), a technique they call delayed T2-weighted gadolinium enhancement imaging, to assess GBCA distribution in the brain at different time points after intravenous administration in a cohort of 33 healthy subjects and 7 patients with brain metastases, and confirmed that hT2W-FLAIR allows the observation of the pathway of GBCA into and out of the glymphatic system (88). There are at least two routes were found for GBCA to enter the glymphatic system: through the blood-aqueous barrier of the ciliary body, as well as through the choroid plexus into the CSF circulation, from where GBCA was eventually removed along the PVS of penetrating arteries and the cranial perineural sheath (88). Further comparative analysis revealed no significant differences in signal intensity at any of the observed locations between patients with brain metastases and subjects without neurological disease, while patients with severe deep and periventricular WMHs (Fazekas score $= 3$) had significantly higher signals in the PVS, aqueous chamber, choroid plexus and ventricles than patients with minimal white matter lesions (Fazekas score ≤ 1) (88). With MRI, Absinta and colleagues found a way to visualize lymphatic vessels in people and common marmoset monkeys' dura mater. High-resolution 3D cranial T1-Magnetization Prepared Rapid Acquisition of Gradient Echoes (T1-MPRAGE), limited T2-FLAIR, T1 black blood technique and T1-Sampling Perfection with Application optimized Contrasts using different flip angle Evolution (T1-SPACE) were applied to visualize human and primate meningeal lymphatic vessels by intravenous injection of two chemically different contrast agents, gadobutrol and gadofosveset (89). Gadobutrol is a macrocyclic contrast agent with a high propensity for extravasation and gadofosveset is a blood-pool agent. The results show that lymphatic vessels enhance with gadobutrol, but not with gadofosveset (89). Their achievement is an important step toward noninvasive visualization of human dural lymphatic vessels, and it offers hope for improving our knowledge of CNS' glymphatic drainage physiology. If this result can be repeatedly validated in future studies, in combination with suitable MR sequences, gadobutrol may prove excellent for the examination of downstream drainage channels in the human glymphatic system. Would it also be possible to observe the perivascular spaces with the appropriate adjustments to the experimental design?

Diffusion Imaging

DCE-MRI for the human glymphatic system has its own drawbacks (90): (1) the potential adverse effects of GBCA accumulation in the brain, and (2) the long time required for the GBCA to reach and transit through the PVS after injection, which may limit its clinical utility. Furthermore, GBCA-free imaging of the glymphatic system is becoming increasingly popular. DWI allows for indirectly assessing the movement of intracranial interstitial extracellular spaces (iECS) (90). Diffusion tensor image analysis along the perivascular space (DTI-ALPS) was applied to assess the glymphatic activity in AD cases. Impaired water diffusivity along PVS in the white matter with dense projection or association fibers was associated with lower mini-mental state examination (MMSE) score and AD severity (91). Similar results have been observed in Parkinson's patients (92). Another study in a community-dwelling population of non-demented older adults showed that a higher DTI-ALPS index was associated with higher scores on the neuropsychological performance test and also with higher gray matter volume (93). Meanwhile, the significant association between glymphatic function and sleep was reconfirmed (93). These studies suggest the promise of the DTI-ALPS index as an imaging marker for assessing cognitive impairment. Two other researches on sleep disorders found that the DTI-ALPS index was significantly lower in patients with obstructive sleep apnea (OSA) and isolated rapid eye movement sleep behavior disorder (iRBD) than in healthy controls (94, 95).

Intravoxel incoherent motion diffusion weighted imaging (IVIM-DWI) has also been extended to assess for glymphatic function. This noninvasive DWI technique is considered suitable for the measurement of both Brownian motion and microvascular perfusion of brain tissues. In the region surrounding EPVS and WMHs, an additional diffusion was detected independent of brain parenchymal diffusion and microvascular perfusion, using non-negative least squares IVIM-MRI spectral diffusion analysis (96). With increasing EPVS and WMH burden, the volume fraction of this additional intermediate diffusion increased (96).

Other Imaging Methods

As a novel MR perfusion imaging technique by using blood as its own tracer, instead of an exogenous contrast agent, arterial spin labeling (ASL) allows noninvasive assessment of cerebral perfusion (97). In terms of the brain glymphatic system, ASL was mainly used to evaluate BBB water permeability (97–99). A recent study utilized a diffusion prepared arterial spin labeling (DP-ASL) MRI approach to quantify the fluid exchange across the BBB [k(w)] among 40 cognitively normal older individuals, and found a positive correlation between BBB k(w) and CSF Aβ42 concentration levels in multiple brain regions (98). Current MRI techniques for detecting water exchange across BBB are summarized in a review paper by Dickie et al. and are divided into three categories. One is ASL-based methods mentioned above, including (1) Multi-TE ASL, (2) Diffusion-weighted ASL, (3) Magnetization transfer weighted ASL, (4) Contrast-enhanced ASL and (5) Phase- contrast ASL; second, contrast-based methods, including (1) Dose ramping at steady state with a varied infusion rate, (2) First pass methods, (3) Water exchange index (WEI) method and (4) Multiple flip angle multi-echo (MFAME)-MRI; third, methods based on the injection of MRI-detectable water tracers, including (1) Indirect detection of ^{17}O-labeled water via its effect on ^{1}H T_2 and (2) Indirect detection of ^{2}H-labeled water by proton replacement (100). These may be good alternative methods to study the aquaporin function at the level of capillaries. At the capillary level, the BBB and the glymphatic system have overlapping structural bases, and they may have synergistic and complementary roles in maintaining neuronal stability and the homeostasis of the intracerebral environment.

Chemical exchange saturation transfer (CEST) is a magnetic resonance spectroscopic imaging technique used to detect compounds at low concentrations, two orders of magnitude lower than standard magnetic resonance spectroscopy (MRS) imaging (90). By adding a saturation RF pulse to compounds with exchangeable hydrogen protons, the saturated hydrogen protons are transferred to the free water pool by chemical exchange, which results in a decrease in the free water signal. Information on compounds is thus obtained indirectly by detecting the free water signal changes. This emerging MRI technology can be used to detect body temperature, pH, enzyme activity and metabolites (glucose, glutamate, creatine and inositol) (101). In a porcine model of impaired glymphatic function, intrinsic compounds in the blood, lymph, and CSF were distinguished using CEST MRI at 7 Tesla, and the CEST effect of lymph is extremely significant compared to that of blood and CSF, which the author refers to as the "Lym-CEST" effect (102). In the subsequent animal experiment, this "Lym-CEST" effect was used to assess the impaired status of the glymphatic system in a rat model with unilateral cervical lymph node ligation. Results indicated that the ipsilateral hippocampus had a significantly higher signal intensity than the contralateral hippocampus, and this altered signal was strongly correlated with behavioral scores (102). According to these results, CEST MRI could be a useful tool to analyze metabolites and detect glymphatic function changes in the glymphatic system *in vivo*. To date, the application of CEST for the analysis of compounds within human brain lymph fluid has not been documented, but this does not prevent its great potential for exploring the glymphatic function and pathogenic mechanisms.

A combination of MRI and other imaging techniques can significantly improve sensitivity and accuracy, and provide a wide range of options for studying the glymphatic system. A combination of *in vivo* MRI and PET in a 4.2-year-old dog found that the pial-glial basement membranes were significantly thicker in the midbrain compared to other parts of the brain, indicating that CSF influx through perivascular pathway is most efficient in the midbrain (103). This finding was confirmed in a 12-year-old dog using a post-mortem electron microscopy study. This result offers a novel potential target for intrathecal drug delivery. It has been reported that MRI-guided Focused UltraSound (MRgFUS) can disrupt the local BBB integrity and facilitate gadobutrol contrast penetration into the brain parenchyma (104). The accumulation of gadobutrol in the PVS, subarachnoid space, and surrounding large draining veins has been detected in a few patients with AD or amyotrophic lateral sclerosis (ALS) using MRgFUS (104). Ultra-fast Magnetic Resonance EncephaloGraphy (MREG) is a less commonly used route to evaluate glymphatic pulsation mechanisms (105). With this technique, Kiviniemi et al. detected three types of physiological mechanisms that affect CSF pulsations: cardiac, respiratory, and very low frequency pulsations (105). According to another study, near-infrared spectroscopy (NIRS) can be used to study the water dynamics within the human brain, to monitor the brain function over time (including sleep period) and in conjunction with various magnetic neuroimaging techniques, particularly MREG (106). These researches provide novel approaches to noninvasively study glymphatic function *in vivo*.

CONCLUSION AND OUTLOOK

Enlargement of the perivascular space is considered to be one of the early imaging signs of CSVD and neurodegenerative disease. With the advance in imaging techniques, its pathophysiological mechanisms have been studied in depth. What is known is that the PVS, as the anatomical basis of the glymphatic system, plays a crucial role in removing cerebral waste, participating in water circulation, and maintaining brain homeostasis. Knowledge of the structure, function, influencing factors and associated diseases of this system is also being constantly updated. MRI overcomes the shortcomings of microscopic imaging and provides noninvasive visualization of the whole glymphatic system, which holds great promise for the clinical study of the glymphatic system. It may be useful for the early diagnosis, monitoring, treatment and prognosis of diseases related to the glymphatic system.

In addition to providing an innovative theory of metabolite clearance, future studies of the glymphatic system will have to address many important questions, such as (1) the form of fluid exchange in the glymphatic system, the specific components that can enter the system and the mechanisms of entry, the specific types of waste products that can be removed, and whether iron excretion after cerebral hemorrhage also occurs through this conduit? (2) What are the exogenous regulatory approaches of the system? Research into the intrinsic mechanisms of operation, the factors involved, and how they are regulated needs to be further developed. (3) Its effects on CSF circulation need to be taken into account. The effects on non-neurological diseases need further study. For example, it has been tentatively demonstrated that the development of glaucoma is associated with dysfunction of the cerebral glymphatic system (107). (4) What is the utility of sleep therapy? (5) Can intrathecal drug delivery be an effective route of administration for CNS diseases? What is its safety profile? Can drugs that previously failed to cross the BBB by oral or intravenous routes be administered intrathecally, thus providing new perspectives for the development of new drugs. (6) Given the existence of the lymphatic system in CNS, why is it still rare for intracranial tumors to metastasis to the neck via this route and what are the reasons for this? (7) Longitudinal studies of perivascular spaces enlargement in large samples are still lacking. Is the perivascular spaces burden during childhood and youth associated with the development of AD or any other cognitive decline in the future? The study of the brain glymphatic system opens up new ideas for neurological disease research and brings new treatment strategies for patients, and we believe that with joint efforts, these questions will be overcome one by one.

AUTHOR CONTRIBUTIONS

All authors listed have made a substantial, direct, and intellectual contribution to the work and approved it for publication.

FUNDING

This work was supported by Zhejiang Natural Science Foundation Association of Mathematical and Physical Medicine (No. LSY19H180014) and Zhejiang Basic Public Welfare Research Project (No. LGF19H220003).

ACKNOWLEDGMENTS

We thank Mr. Jilin Tan for illustrating this article.

REFERENCES

1. Wardlaw JM, Smith EE, Biessels GJ, Cordonnier C, Fazekas F, Frayne R, et al. Neuroimaging standards for research into small vessel disease and its contribution to ageing and neurodegeneration. *Lancet Neurol.* (2013) 12:822–38. doi: 10.1016/S1474-4422(13)70124-8
2. Nedergaard M. Neuroscience. Garbage truck of the brain. *Science.* (2013) 340:1529–30. doi: 10.1126/science.1240514
3. Wardlaw JM, Benveniste H, Nedergaard M, Zlokovic BV, Mestre H, Lee H, et al. Perivascular spaces in the brain: anatomy, physiology and pathology. *Nat Rev Neurol.* (2020) 16:137–53. doi: 10.1038/s41582-020-0312-z
4. Agarwal N, Carare RO. Cerebral Vessels: An overview of anatomy, physiology, and role in the drainage of fluids and solutes. *Front Neurol.* (2021) 11:611485. doi: 10.3389/fneur.2020.611485
5. Iliff JJ, Wang M, Liao Y, Plogg BA, Peng W, Gundersen GA, et al. A paravascular pathway facilitates CSF flow through the brain parenchyma and the clearance of interstitial solutes, including amyloid β. *Sci Transl Med.* (2012) 4:147ra111. doi: 10.1126/scitranslmed.3003748
6. Iliff JJ, Lee H, Yu M, Feng T, Logan J, Nedergaard M, et al. Brain-wide pathway for waste clearance captured by contrast-enhanced MRI. *J Clin Invest.* (2013) 123:1299–309. doi: 10.1172/JCI67677
7. Louveau A, Smirnov I, Keyes TJ, Eccles JD, Rouhani SJ, Peske JD, et al. Structural and functional features of central nervous system lymphatic vessels. *Nature.* (2015) 523:337–41. doi: 10.1038/nature14432
8. Jessen NA, Munk AS, Lundgaard I, Nedergaard M. The Glymphatic System: a beginner's guide. *Neurochem Res.* (2015) 40:2583–99. doi: 10.1007/s11064-015-1581-6
9. Shi Y, Thrippleton MJ, Blair GW, Dickie DA, Marshall I, Hamilton I, et al. Small vessel disease is associated with altered cerebrovascular pulsatility but not resting cerebral blood flow. *J Cereb Blood Flow Metab.* (2020) 40:85–99. doi: 10.1177/0271678X18803956
10. Mestre H, Tithof J, Du T, Song W, Peng W, Sweeney AM, et al. Flow of cerebrospinal fluid is driven by arterial pulsations and is reduced in hypertension. *Nat Commun.* (2018) 9:4878. doi: 10.1038/s41467-018-07318-3
11. Dreha-Kulaczewski S, Joseph AA, Merboldt KD, Ludwig HC, Gärtner J, Frahm J. Identification of the upward movement of human CSF in vivo and its relation to the brain venous system. *J Neurosci.* (2017) 37:2395–402. doi: 10.1523/JNEUROSCI.2754-16.2017
12. Xie L, Kang H, Xu Q, Chen MJ, Liao Y, Thiyagarajan M, et al. Sleep drives metabolite clearance from the adult brain. *Science.* (2013) 342:373–7. doi: 10.1126/science.1241224
13. Berezuk C, Ramirez J, Gao F, Scott CJ, Huroy M, Swartz RH, et al. Virchow-robin spaces: correlations with polysomnography-derived sleep parameters. *Sleep.* (2015) 38:853–8. doi: 10.5665/sleep.4726
14. Hablitz LM. PláV, Giannetto M, Vinitsky HS, Stæger FF, Metcalfe T, et al. Circadian control of brain glymphatic and lymphatic fluid flow. *Nat Commun.* (2020) 11:4411. doi: 10.1038/s41467-020-18115-2
15. Mestre H, Hablitz LM, Xavier AL, Feng W, Zou W, Pu T, et al. Aquaporin-4-dependent glymphatic solute transport in the rodent brain. *eLife.* (2018) 7. doi: 10.7554/eLife.40070
16. van Veluw SJ, Hou SS, Calvo-Rodriguez M, Arbel-Ornath M, Snyder AC, Frosch MP, et al. Vasomotion as a driving force for paravascular clearance in the awake mouse brain. *Neuron.* (2020) 105:549–61.e5. doi: 10.1016/j.neuron.2019.10.033
17. Blair GW, Thrippleton MJ, Shi Y, Hamilton I, Stringer M, Chappell F, et al. Intracranial hemodynamic relationships in patients with cerebral small vessel disease. *Neurology.* (2020) 94:e2258–69. doi: 10.1212/WNL.0000000000009483
18. Mestre H, Kostrikov S, Mehta RI, Nedergaard M. Perivascular spaces, glymphatic dysfunction, and small vessel disease. *Clin Sci (Lond).* (2017) 131:2257–74. doi: 10.1042/CS20160381
19. Smith AJ, Yao X, Dix JA, Jin BJ, Verkman AS. Test of the 'glymphatic' hypothesis demonstrates diffusive and aquaporin-4-independent solute transport in rodent brain parenchyma. *eLife.* (2017) 6:e27679. doi: 10.7554/eLife.27679
20. Benveniste H, Liu X, Koundal S, Sanggaard S, Lee H, Wardlaw J. The glymphatic system and waste clearance with brain aging: a review. *Gerontology.* (2019) 65:106–19. doi: 10.1159/000490349
21. Lundgaard I, Lu ML, Yang E, Peng W, Mestre H, Hitomi E, et al. Glymphatic clearance controls state-dependent changes in brain lactate concentration. *J Cereb Blood Flow Metab.* (2017) 37:2112–24. doi: 10.1177/0271678X16661202
22. Achariyar TM Li B, Peng W, Verghese PB, Shi Y, McConnell E, et al. Glymphatic distribution of CSF-derived apoE into brain is isoform

specific and suppressed during sleep deprivation. *Mol Neurodegener.* (2016) 11:74. doi: 10.1186/s13024-016-0138-8

23. Rangroo Thrane V, Thrane AS, Plog BA, Thiyagarajan M, Iliff JJ, Deane R, et al. Paravascular microcirculation facilitates rapid lipid transport and astrocyte signaling in the brain. *Sci Rep.* (2013) 3:2582. doi: 10.1038/srep02582
24. Brown R, Benveniste H, Black SE, Charpak S, Dichgans M, Joutel A, et al. Understanding the role of the perivascular space in cerebral small vessel disease. *Cardiovasc Res.* (2018) 114:1462–73. doi: 10.1093/cvr/cvy113
25. Li Y, Li M, Yang L, Qin W, Yang S, Yuan J, et al. The relationship between blood-brain barrier permeability and enlarged perivascular spaces: a cross-sectional study. *Clin Interv aging.* (2019) 14:871–78. doi: 10.2147/CIA.S204269
26. Pettersen JA, Keith J, Gao F, Spence JD, Black SE. CADASIL accelerated by acute hypotension: Arterial and venous contribution to leukoaraiosis. *Neurology.* (2017) 88:1077–80. doi: 10.1212/WNL.0000000000003717
27. Hladky SB, Barrand MA. The glymphatic hypothesis: the theory and the evidence. *Fluids Barriers CNS.* (2022) 19:9. doi: 10.1186/s12987-021-00282-z
28. Doubal FN, MacLullich AM, Ferguson KJ, Dennis MS, Wardlaw JM. Enlarged perivascular spaces on MRI are a feature of cerebral small vessel disease. *Stroke.* (2010) 41:450–4. doi: 10.1161/STROKEAHA.109.564914
29. Zhang C, Chen Q, Wang Y, Zhao X, Wang C, Liu L, et al. Chinese IntraCranial AtheroSclerosis (CICAS) Study Group. Risk factors of dilated Virchow-Robin spaces are different in various brain regions. *PLoS ONE.* (2014) 9:e105505. doi: 10.1371/journal.pone.0105505
30. Charidimou A, Hong YT, Jäger HR, Fox Z, Aigbirhio FI, Fryer TD, et al. White matter perivascular spaces on magnetic resonance imaging: marker of cerebrovascular amyloid burden? *Stroke.* (2015) 46:1707–9. doi: 10.1161/STROKEAHA.115.009090
31. Charidimou A, Meegahage R, Fox Z, Peeters A, Vandermeeren Y, Laloux P, et al. Enlarged perivascular spaces as a marker of underlying arteriopathy in intracerebral haemorrhage: a multicentre MRI cohort study. *J Neurol Neurosurg Psychiatry.* (2013) 84:624–9. doi: 10.1136/jnnp-2012-304434
32. Boulouis G, Charidimou A, Pasi M, Roongpiboonsopit D, Xiong L, Auriel E, et al. Hemorrhage recurrence risk factors in cerebral amyloid angiopathy: comparative analysis of the overall small vessel disease severity score versus individual neuroimaging markers. *J Neurol Sci.* (2017) 380:64–7. doi: 10.1016/j.jns.2017.07.015
33. Hackett ML, Pickles K. Part I: frequency of depression after stroke: an updated systematic review and meta-analysis of observational studies. *Int J Stroke.* (2014) 9:1017–25. doi: 10.1111/ijs.12357
34. Liang Y, Chan YL, Deng M, Chen YK, Mok V, Wang F, et al. Enlarged perivascular spaces in the centrum semiovale are associated with poststroke depression: a 3-month prospective study. *J Affect Disord.* (2018) 228:166–72. doi: 10.1016/j.jad.2017.11.080
35. Arba F, Quinn TJ, Hankey GJ, Lees KR, Wardlaw JM, Ali M, et al. Enlarged perivascular spaces and cognitive impairment after stroke and transient ischemic attack. *Int J Stroke.* (2018) 13:47–56. doi: 10.1177/1747493016666091
36. Hurford R, Charidimou A, Fox Z, Cipolotti L, Jager R, Werring DJ. MRI-visible perivascular spaces: relationship to cognition and small vessel disease MRI markers in ischaemic stroke and TIA. *J Neurol Neurosurg Psychiatry.* (2014)85:522–5. doi: 10.1136/jnnp-2013-305815
37. Smeijer D, Ikram MK, Hilal S. Enlarged Perivascular Spaces and Dementia: A Systematic Review. *J Alzheimers Dis.* (2019) 72:247–56. doi: 10.3233/JAD-190527
38. Benjamin P, Trippier S, Lawrence AJ, Lambert C, Zeestraten E, Williams OA, et al. Lacunar infarcts, but not perivascular spaces, are predictors of cognitive decline in cerebral small-vessel disease. *Stroke.* (2018) 49:586–93. doi: 10.1161/STROKEAHA.117.017526
39. Zafeiriou DI, Batzios SP. Brain and spinal MR imaging findings in mucopolysaccharidoses: a review. *AJNR Am J Neuroradiol.* (2013)34:5–13. doi: 10.3174/ajnr.A2832
40. Zeegers M, Van Der Grond J, Durston S, Nievelstein RJ, Witkamp T. Van Daalen E,et al. Radiological findings in autistic and developmentally delayed children. *Brain Dev.* (2006) 28:495–9. doi: 10.1016/j.braindev.2006.02.006
41. Ota Y, Srinivasan A, Capizzano AA, Bapuraj JR, Kim J, Kurokawa R, et al. Central nervous system systemic lupus erythematosus: pathophysiologic, clinical, and imaging features. *Radiographics.* (2022) 42:212–32. doi: 10.1148/rg.210045
42. Miyata M, Kakeda S, Iwata S, Nakayamada S, Ide S, Watanabe K, et al. Enlarged perivascular spaces are associated with the disease activity in systemic lupus erythematosus. *Sci Rep.* (2017) 7:12566. doi: 10.1038/s41598-017-12966-4
43. Campi A, Benndorf G, Filippi M, Reganati P, Martinelli V, Terreni MR. Primary angiitis of the central nervous system: serial MRI of brain and spinal cord. *Neuroradiology.* (2001) 43:599–607. doi: 10.1007/s002340100561
44. Salvarani C, Brown RD Jr, Huston J 3rd, Hunder GG. Prominent perivascular enhancement in primary central nervous system vasculitis. *Clin Exp Rheumatol.* (2008) 26(Suppl. 49):S111.
45. Sarkis RA, Mays M, Isada C, Ahmed M, MRI. findings in cryptococcal meningitis of the non-HIV population. *Neurologist.* (2015) 19:40–5. doi: 10.1097/NRL.0000000000000000
46. Tan ZR, Long XY, Li GL, Zhou JX, Long L. Spectrum of neuroimaging findings in cryptococcal meningitis in immunocompetent patients in China - a series of 18 cases. *J Neurol Sci.* (2016) 368:132–7. doi: 10.1016/j.jns.2016.06.069
47. Wardlaw JM, Brindle W, Casado AM, Shuler K, Henderson M, Thomas B, et al. A systematic review of the utility of 15 versus 3 Tesla magnetic resonance brain imaging in clinical practice and research. *Eur Radiol.* (2012) 22:2295–303. doi: 10.1007/s00330-012-2500-8
48. Bouvy WH, Biessels GJ, Kuijf HJ, Kappelle LJ, Luijten PR, Zwanenburg JJ. Visualization of perivascular spaces and perforating arteries with 7 T magnetic resonance imaging. *Invest Rdiol.* (2014) 49:307–13. doi: 10.1097/RLI.0000000000000027
49. Kwee RM, Kwee TC. Virchow-robin spaces at MR imaging. *Radiographics.* (2007) 27:1071–86. doi: 10.1148/rg.274065722
50. Zhu YC, Dufouil C, Mazoyer B. SoumaréA, Ricolfi F, Tzourio C, et al. Frequency and location of dilated Virchow-Robin spaces in elderly people: a population-based 3D MR imaging study. *AJNR Am J Neuroradiol.* (2011) 32:709–13. doi: 10.3174/ajnr.A2366
51. Potter GM, Chappell FM, Morris Z, Wardlaw JM. Cerebral perivascular spaces visible on magnetic resonance imaging: development of a qualitative rating scale and its observer reliability. *Cerebrovasc Dis.* (2015) 39:224–31. doi: 10.1159/000375153
52. Heier LA, Bauer CJ, Schwartz L, Zimmerman RD, Morgello S, Deck MD. Large Virchow-Robin spaces: MR-clinical correlation. *AJNR Am J Neuroradiol.* (1989) 10:929–36.
53. Kwee RM, Kwee TC. Tumefactive Virchow-Robin spaces. *Eur J Radiol.* (2019) 111:21–33. doi: 10.1016/j.ejrad.2018.12.011
54. Li P, Zhao F, Liu P. Multiple large dilated Virchow-Robin spaces in a 12-year-old with neurofibromatosis type 2. *Pediatr Neurol.* (2014) 51:856–7. doi: 10.1016/j.pediatrneurol.2014.08.018
55. Härtel C, Bachmann S, Bönnemann C, Meinecke P, Sperner J. Familial megalencephaly with dilated Virchow-Robin spaces in magnetic resonance imaging: an autosomal recessive trait? *Clin Dysmorphol.* (2005) 14:31–4. doi: 10.1097/00019605-200501000-00007
56. Donaldson C, Chatha G, Chandra RV, Goldschlager T. Obstructive hydrocephalus secondary to enlarged Virchow-Robin spaces: a rare cause of pulsatile tinnitus. *World neurosurg.* (2017) 101:815.e1–e3. doi: 10.1016/j.wneu.2017.02.119
57. Rivet A, Gauthier AS, Chatain M, Billon-Grand R, Thines L, Delbosc B, et al. Giant tumefactive Virchow-Robin space: a rare cause of a homonymous quadrantanopia. *J Neuroophthalmol.* (2017) 37:75–6. doi: 10.1097/WNO.0000000000000478
58. Ayele B, Zenebe G, Mengesha A, Teshale Y. Symptomatic giant Virchow-Robin spaces: a rare cause of spastic quadriparesis in 43-year-old ethiopian patient: a case report. *Ethiop J Health Sci.* (2020) 30:843–6. doi: 10.4314/ejhs.v30i5.24
59. De Schlichting E, Zaldivar-Jolissaint JF, Castrioto A, Reyns N, Chabardès S. Reversible focal dystonia secondary to giant perivascular spaces. *Stereotact Funct Neurosurg.* (2020) 98:80–4. doi: 10.1159/000505711
60. McArdle DJT, Lovell TJH, Lekgabe E, Gaillard F. Opercular perivascular cysts: a proposed new subtype of dilated perivascular spaces. *Eur J Radiol.* (2020) 124:108838. doi: 10.1016/j.ejrad.2020.108838

61. Ballerini L, Lovreglio R, Valdés Hernández MDC, Ramirez J, MacIntosh BJ, Black SE, et al. Perivascular spaces segmentation in brain MRI using optimal 3D filtering. *Sci Rep*. (2018) 8:2132. doi: 10.1038/s41598-018-19781-5
62. González-Castro V, Valdés Hernández MDC, Chappell FM, Armitage PA, Makin S, Wardlaw JM. Reliability of an automatic classifier for brain enlarged perivascular spaces burden and comparison with human performance. *Clin Sci.* (2017) 131:1465–81. doi: 10.1042/CS20170051
63. Dubost F, Adams H, Bortsova G, Ikram MA, Niessen W, Vernooij M, et al. 3D regression neural network for the quantification of enlarged perivascular spaces in brain MRI. *Med Image Anal.* (2019) 51:89–100. doi: 10.1016/j.media.2018.10.008
64. Lian C, Zhang J, Liu M, Zong X, Hung SC, Lin W, et al. Multi-channel multi-scale fully convolutional network for 3D perivascular spaces segmentation in 7T MR images. *Med Image Anal.* (2018) 46:106–17. doi: 10.1016/j.media.2018.02.009
65. Wang S, Huang P, Zhang R, Hong H, Jiaerken Y, Lian C, et al. Quantity and morphology of perivascular spaces: associations with vascular risk factors and cerebral small vessel disease. *J Magn Reson Imaging*. (2021) 54:1326–36. doi: 10.1002/jmri.27702
66. Ballerini L, Booth T, Valdés Hernández MDC, Wiseman S, Lovreglio R, Muñoz Maniega S, et al. Computational quantification of brain perivascular space morphologies: associations with vascular risk factors and white matter hyperintensities. a study in the lothian birth cohort 1936. *Neuroimage Clin*. (2020) 25:102120. doi: 10.1016/j.nicl.2019.102120
67. Sepehrband F, Barisano G, Sheikh-Bahaei N, Cabeen RP, Choupan J, Law M, et al. Image processing approaches to enhance perivascular space visibility and quantification using MRI. *Sci Rep*. (2019) 9:12351. doi: 10.1038/s41598-019-48910-x
68. Feldman RE, Rutland JW, Fields MC, Marcuse LV, Pawha PS, Delman BN, et al. Quantification of perivascular spaces at 7T: a potential MRI biomarker for epilepsy. *Seizure.* (2018) 54:11. doi: 10.1016/j.seizure.2017.11.004
69. Kilsdonk ID, Steenwijk MD, Pouwels PJ, Zwanenburg JJ, Visser F, Luijten PR, et al. Perivascular spaces in MS patients at 7 Tesla MRI: a marker of neurodegeneration? *Mult Scler.* (2015) 21:155–62. doi: 10.1177/1352458514540358
70. Zong X, Lian C, Jimenez J, Yamashita K, Shen D, Lin W. Morphology of perivascular spaces and enclosed blood vessels in young to middle-aged healthy adults at 7T: dependences on age, brain region, and breathing gas. *NeuroImage*. (2020) 218:116978. doi: 10.1016/j.neuroimage.2020.116978
71. Zong X, Park SH, Shen D, Lin W. Visualization of perivascular spaces in the human brain at 7T: sequence optimization and morphology characterization. *Neuroimage.* (2016) 125:895–902. doi: 10.1016/j.neuroimage.2015.10.078
72. Kong Q, Zhang Z, Yang Q, Fan Z, Wang B, An J, et al. 7T TOF-MRA shows modulated orifices of lenticulostriate arteries associated with atherosclerotic plaques in patients with lacunar infarcts. *Eur J Radiol.* (2019) 118:271–6. doi: 10.1016/j.ejrad.2019.07.032
73. Suzuki T, Natori T, Sasaki M, Miyazawa H, Narumi S, Ito K, et al. Evaluating recanalization of relevant lenticulostriate arteries in acute ischemic stroke using high-resolution MRA at 7T. *Int J Stroke.* (2021) 16:1039–46. doi: 10.1177/1747493019897868
74. Kang CK, Park CA, Lee DS, Lee YB, Park CW, Kim YB, et al. Velocity measurement of microvessels using phase-contrast magnetic resonance angiography at 7 Tesla MRI. *Magn Reson Med.* (2016) 75:1640–6. doi: 10.1002/mrm.25600
75. Barisano G, Law M, Custer RM, Toga AW, Sepehrband F. Perivascular space imaging at ultrahigh field MR imaging. *Magn Reson Imaging Clin N Am.* (2021) 29:67–75. doi: 10.1016/j.mric.2020.09.005
76. Shao X, Yan L, Ma SJ, Wang K, Wang DJJ. High-resolution neurovascular imaging at 7T: arterial spin labeling perfusion, 4-dimensional MR angiography, and black blood MR imaging. *Magn Reson Imaging Clin N Am.* (2021) 29:53–65. doi: 10.1016/j.mric.2020.09.003
77. Ma SJ, Sarabi MS, Yan L, Shao X, Chen Y, Yang Q, et al. Characterization of lenticulostriate arteries with high resolution black-blood T1-weighted turbo spin echo with variable flip angles at 3 and 7 Tesla. *Neuroimage.* (2019) 199:184–93. doi: 10.1016/j.neuroimage.2019.05.065
78. Barisano G, Culo B, Shellock FG, Sepehrband F, Martin K, Stevens M, et al. 7-Tesla MRI of the brain in a research subject with bilateral, total knee replacement implants: case report and proposed safety guidelines. *Magn Reson Imaging.* (2019) 57:313–6. doi: 10.1016/j.mri.2018.11.016
79. Mestre H, Du T, Sweeney AM, Liu G, Samson AJ, Peng W, et al. Cerebrospinal fluid influx drives acute ischemic tissue swelling. *Science.* (2020) 367:eaax7171. doi: 10.1126/science.aax7171
80. Sweeney AW, Plá V, Du T, Liu G, Sun Q, Peng S, et al. In vivo imaging of cerebrospinal fluid transport through the intact mouse skull using fluorescence macroscopy. *J Vis Exp*. (2019) 149:10.3791/59774. doi: 10.3791/59774
81. Wolf MS, Chen Y, Simon DW, Alexander H, Ross M, Gibson GA, et al. Quantitative and qualitative assessment of glymphatic flux using Evans blue albumin. *J Neurosci Methods.* (2019) 311:436–41. doi: 10.1016/j.jneumeth.2018.09.031
82. Zeppenfeld DM, Simon M, Haswell JD, D'Abreo D, Murchison C, Quinn JF, et al. Association of perivascular localization of aquaporin-4 with cognition and Alzheimer disease in aging brains. *JAMA Neurol.* (2017) 74:91–9. doi: 10.1001/jamaneurol.2016.4370
83. Edeklev CS, Halvorsen M, Løvland G, Vatnehol SAS, Gjertsen Ø, Nedregaard B, et al. Intrathecal use of gadobutrol for glymphatic MR imaging: prospective safety study of 100 patients. *AJNR Am J Neuroradiol.* (2019) 40:1257–64. doi: 10.3174/ajnr.A6136
84. Patel M, Atyani A, Salameh JP, McInnes M, Chakraborty S. Safety of intrathecal administration of gadolinium-based contrast agents: a systematic review and meta-analysis. *Radiology.* (2020) 297:75–83. doi: 10.1148/radiol.2020191373
85. Rasschaert M, Weller RO, Schroeder JA, Brochhausen C, Idée IM. Retention of gadolinium in brain parenchyma: pathways for speciation, access, and distribution. a critical review. *J Magn Reson Imaging.* (2020) 52:1293–305. doi: 10.1002/jmri.27124
86. Nehra AK, McDonald RJ, Bluhm AM, Gunderson TM, Murray DL, Jannetto PJ, et al. Accumulation of gadolinium in human cerebrospinal fluid after gadobutrol-enhanced MR imaging: a prospective observational cohort study. *Radiology.* (2018) 288:416–23. doi: 10.1148/radiol.2018171105
87. Berger F, Kubik-Huch RA, Niemann T, Schmid HR, Poetzsch M, Froehlich JM, et al. Gadolinium distribution in cerebrospinal fluid after administration of a gadolinium-based MR contrast agent in humans. *Radiology.* (2018) 288:703–9. doi: 10.1148/radiol.2018171829
88. Deike-Hofmann K, Reuter J, Haase R, Paech D, Gnirs R, Bickelhaupt S, et al. Glymphatic pathway of gadolinium-based contrast agents through the brain: overlooked and misinterpreted. *Invest Radiol.* (2019) 54:229–37. doi: 10.1097/RLI.0000000000000533
89. Absinta M, Ha SK, Nair G, Sati P, Luciano NJ, Palisoc M, et al. Human and nonhuman primate meninges harbor lymphatic vessels that can be visualized noninvasively by MRI. *eLife*. (2017) 6:e29738. doi: 10.7554/eLife.29738
90. Klostranec JM, Vucevic D, Bhatia KD, Kortman HGJ, Krings T, Murphy KP, et al. Current concepts in intracranial interstitial fluid transport and the glymphatic system: part II-imaging techniques and clinical applications. *Radiology.* (2021) 301:516–32. doi: 10.1148/radiol.2021204088
91. Taoka T, Masutani Y, Kawai H, Nakane T, Matsuoka K, Yasuno F, et al. Evaluation of glymphatic system activity with the diffusion MR technique: diffusion tensor image analysis along the perivascular space (DTI-ALPS) in Alzheimer's disease cases. *Jpn J Radiol.* (2017) 35:172–8. doi: 10.1007/s11604-017-0617-z
92. Ma X, Li S, Li C, Wang R, Chen M, Chen H, et al. Diffusion tensor imaging along the perivascular space index in different stages of Parkinson's disease. *Front Aging Neurosci.* (2021) 13:773951. doi: 10.3389/fnagi.2021.773951
93. Siow TY, Toh CH, Hsu JL, Liu GH, Lee SH, Chen NH, et al. Association of sleep, neuropsychological performance, and gray matter volume with glymphatic function in community-dwelling older adults. *Neurology.* (2022) 98:e829mmunidoi: 10.1212/WNL.0000000000013215
94. Lee HJ, Lee DA, Shin KJ, Park KM. Glymphatic system dysfunction in obstructive sleep apnea evidenced by DTI-ALPS. *Sleep Med.* (2022) 89:176–81. doi: 10.1016/j.sleep.2021.12.013
95. Lee DA, Lee HJ, Park KM. Glymphatic dysfunction in isolated REM sleep behavior disorder. *Acta Neurol Scand.* (2022) 145:464–70. doi: 10.1111/ane.13573
96. Wong SW, Backes WH, Drenthen GS, Zhang CE, Voorter PHM, Staals J, et al. Spectral diffusion analysis of intravoxel incoherent motion MRI

in cerebral small vessel disease. *J Magn Reson Imaging.* (2020) 51:1170–80. doi: 10.1002/jmri.26920

97. Joseph CR. Utilizing 3D arterial spin labeling to identify cerebrovascular leak and glymphatic obstruction in neurodegenerative disease. *Diagnostics.* (2021) 11:1888. doi: 10.3390/diagnostics11101888
98. Gold BT, Shao X, Sudduth TL, Jicha GA, Wilcock DM, Seago ER, et al. Water exchange rate across the blood-brain barrier is associated with CSF amyloid-β 42 in healthy older adults. *Alzheimers Dement.* (2021). doi: 10.1002/alz.12357
99. Joseph CR. Novel MRI techniques identifying vascular leak and paravascular flow reduction in early Alzheimer disease. *Biomedicines.* (2020) 8:228. doi: 10.3390/biomedicines8070228
100. Dickie BR, Parker GJM, Parkes LM. Measuring water exchange across the blood-brain barrier using MRI. *Prog Nucl Magn Reson Spectrosc.* (2020) 116:19c.atedoi: 10.1016/j.pnmrs.2019.09.002
101. Tang Y, Xiao G, Shen Z, Zhuang C, Xie Y, Zhang X, et al. Noninvasive detection of extracellular pH in human benign and malignant liver tumors using CEST MRI. *Front Oncol.* (2020) 10:578985. doi: 10.3389/fonc.2020.578985
102. Chen Y, Dai Z, Fan R, Mikulis DJ, Qiu J, Shen Z, et al. Glymphatic system visualized by chemical-exchange-saturation-transfer magnetic resonance imaging. *ACS Chem Neurosci.* (2020) 11:1978–84. doi: 10.1021/acschemneuro.0c00222
103. Dobson H, Sharp MM, Cumpsty R, Criswell TP, Wellman T, Finucane C, et al. The perivascular pathways for influx of cerebrospinal fluid are most efficient in the midbrain. *Clin Sci.* (2017) 131:2745–52. doi: 10.1042/CS20171265
104. Meng Y, Abrahao A, Heyn CC, Bethune AJ, Huang Y, Pople CB, et al. Glymphatics visualization after focused ultrasound-induced blood-brain barrier opening in humans. *Ann Neurol.* (2019) 86:975–80. doi: 10.1002/ana.25604
105. Kiviniemi V, Wang X, Korhonen V, Keinänen T, Tuovinen T, Autio J, et al. Ultra-fast magnetic resonance encephalography of physiological brain activity - Glymphatic pulsation mechanisms? *J Cereb Blood Flow Metab.* (2016) 36:1033–45. doi: 10.1177/0271678X15622047
106. Myllylä T, Harju M, Korhonen V, Bykov A, Kiviniemi V, Meglinski I. Assessment of the dynamics of human glymphatic system by near-infrared spectroscopy. *J Biophotonics.* (2018) 11:e201700123. doi: 10.1002/jbio.201700123
107. Wostyn P, Killer HE, De Deyn PP. Glymphatic stasis at the site of the lamina cribrosa as a potential mechanism underlying open-angle glaucoma. *Clin Exp Ophthalmol.* (2017) 45:539–47. doi: 10.1111/ceo.12915

Conflict of Interest: The authors declare that the research was conducted in the absence of any commercial or financial relationships that could be construed as a potential conflict of interest.

frontiers | Frontiers in Neurology

ORIGINAL RESEARCH
published: 20 June 2022
doi: 10.3389/fneur.2022.913241

The Clustering Analysis of Time Properties in Patients With Cerebral Small Vessel Disease: A Dynamic Connectivity Study

Wenwen Yin[1†], Xia Zhou[1†], Chenchen Li[1], Mengzhe You[1], Ke Wan[1], Wei Zhang[1], Wenhao Zhu[1], Mingxu Li[1], Xiaoqun Zhu[1], Yinfeng Qian[2] and Zhongwu Sun[1]*

[1] Department of Neurology, The First Affiliated Hospital of Anhui Medical University, Hefei, China, [2] Department of Radiology, The First Affiliated Hospital of Anhui Medical University, Hefei, China

Edited by:
Xiaofei Hu,
Army Medical University, China

Reviewed by:
Maria Del Carmen Valdés Hernández,
University of Edinburgh,
United Kingdom
Valentina Ciullo,
Santa Lucia Foundation (IRCCS), Italy

***Correspondence:**
Zhongwu Sun
sunzhwu@126.com

[†] These authors have contributed equally to this work and share first authorship

Specialty section:
This article was submitted to Applied Neuroimaging, a section of the journal Frontiers in Neurology

Received: *05 April 2022*
Accepted: *27 May 2022*
Published: *20 June 2022*

Citation:
Yin W, Zhou X, Li C, You M, Wan K, Zhang W, Zhu W, Li M, Zhu X, Qian Y and Sun Z (2022) The Clustering Analysis of Time Properties in Patients With Cerebral Small Vessel Disease: A Dynamic Connectivity Study. Front. Neurol. 13:913241. doi: 10.3389/fneur.2022.913241

Purpose: This study aimed to investigate the dynamic functional connectivity (DFC) pattern in cerebral small vessel disease (CSVD) and explore the relationships between DFC temporal properties and cognitive impairment in CSVD.

Methods: Functional data were collected from 67 CSVD patients, including 35 patients with subcortical vascular cognitive impairment (SVCI) and 32 cognitively unimpaired (CU) patients, as well as 35 healthy controls (HCs). The DFC properties were estimated by k-means clustering analysis. DFC strength analysis was used to explore the regional functional alterations between CSVD patients and HCs. Correlation analysis was used for DFC properties with cognition and SVD scores, respectively.

Results: The DFC analysis showed three distinct connectivity states (state I: sparsely connected, state II: strongly connected, state III: intermediate pattern). Compared to HCs, CSVD patients exhibited an increased proportion in state I and decreased proportion in state II. Besides, CSVD patients dwelled longer in state I while dwelled shorter in state II. CSVD subgroup analyses showed that state I frequently occurred and dwelled longer in SVCI compared with CSVD-CU. Also, the internetwork (frontal-parietal lobe, frontal-occipital lobe) and intranetwork (frontal lobe, occipital lobe) functional activities were obviously decreased in CSVD. Furthermore, the fractional windows and mean dwell time (MDT) in state I were negatively correlated with cognition in CSVD but opposite to cognition in state II.

Conclusion: Patients with CSVD accounted for a higher proportion and dwelled longer mean time in the sparsely connected state, while presented lower proportion and shorter mean dwell time in the strongly connected state, which was more prominent in SVCI. The changes in the DFC are associated with altered cognition in CSVD. This study provides a better explanation of the potential mechanism of CSVD patients with cognitive impairment from the perspective of DFC.

Keywords: cerebral small vessel disease, dynamic functional connectivity, sliding window, clustering analysis, cognitive impairment

INTRODUCTION

Cerebral small vessel disease (CSVD) is a common neurological disease in elderly individuals and is clinically characterized by progressive cognitive impairment, especially executive dysfunction (1). The mechanism of CSVD and the consequential cognitive impairment have been explored from various perspectives (2, 3). Notably, previous studies have tried to explore the underlying pathogenesis of CSVD from the perspective of the brain functional network, indicating that CSVD is a "disconnection syndrome" (3), with the characteristics of extensive structural and functional connectivity disruption in large-scale brain networks, such as the default mode (4–6), dorsal attention (5), frontoparietal control (6) and salience networks (7). Most of these studies were based on resting-state functional MRI (rs-fMRI), which reflects the spontaneous activity of the brain (7). Rs-fMRI has been consistently considered a promising measurement to investigate brain connectivity alterations in both the resting state and during the execution of specific tasks. Nevertheless, increasing evidence has shown that the functional activity of the brain in the resting state is not static but constantly dynamic during scanning (8, 9), and the dynamic fluctuations of brain connectivity analysis could reveal more information that cannot be observed in the static state.

Dynamic functional connectivity (DFC) analysis is widely utilized to explore the time-varying profiles of functional connectivity and has been used in the study of several neurodegenerative diseases (10–17). For example, Fu et al. presented that language, attention, and processing speeds were negatively correlated with weakly connected states and positively correlated with strongly connected states in Alzheimer's disease (AD) patients (10). Moreover, the temporal properties and spatial pattern of the cognitive control network were suggested to serve as biomarkers that could differentiate the stages of AD (11). The changes in DFC strength in different frequency bands were reported to be related to both positive and negative symptoms in patients with schizophrenia (12, 13). The DFC states were also suggested to be associated with cognitive decline in Parkinson's disease, specifically, increased mean dwell time (MDT) in the segregated state and reduced number of transitions between states are associated with dementia in Parkinson's disease (16, 17). These studies presented the valuable roles of DFC analysis in elucidating the mechanisms underlying cognition and mental symptoms. However, few studies have focused on CSVD from the perspective of DFC. A recent functional network study showed that patients with subcortical ischaemic vascular disease (SIVD), which resembles the disease of CSVD, dwelled longer in the weakly connected state, which may be a feature of SIVD (10). However, whether patients with subcortical vascular cognitive impairment (SVCI) and cognitively unimpaired CSVD (CSVD-CU) exhibit similar DFC changes and whether the altered DFC is associated with cognitive impairment in CSVD patients or can be seemed as a biomarker remain unclear.

Herein, the differences in dynamic connectivity between healthy controls (HCs) and patients with CSVD were systematically investigated and the relationships between dynamic connectivity changes with cognitive impairment were also explored. The CSVD patients were hypothesized with a higher proportion and longer MDT in the sparsely connected state, while a lower proportion and shorter MDT in the strongly connected state in CSVD patients, which may be correlated with cognitive impairment.

MATERIALS AND METHODS

Subjects

This cross-sectional study included 67 consecutive CSVD patients recruited from the First Affiliated Hospital of Anhui Medical University between July 2018 and July 2021, with 35 HCs (patient's spouse or other family members) matched by age, gender, and education. The general information, comorbidities, and histories of smoking and drinking were collected from all participants.

The inclusion criteria for CSVD patients were as follows: (a) aged 50–80; (b) presented at least one common symptom of CSVD, including cognitive decline, gait, and balance disorders, mood or sleep disorders, and urinary and stool disorders; or a history of symptomatic stroke (lacunar stroke syndrome, symptoms lasting more than 24 h and occurring more than 6 months before visiting; or transient ischaemic attack lasting <24 h, with limb weakness, semisensory loss or dyskinesia in the preceding 6 months); and (c) met any of the following brain MRI marker criteria for CSVD, such as white matter hyperintensities (WMH), lacunar infarction (LI), and enlarged perivascular spaces (EPVS) using daily routine brain MRI scan (18, 19). The WMH was defined as the hyperintensities on fluid-attenuated inversion-recovery (FLAIR) and was further graded according to the Fazekas scale (20). The Fazekas score was calculated as the sum of periventricular and deep WMH, ranging from 0 to 6. The severity of WMH was categorized as follows: none to mild WMH (Fazekas scale score 0–2) and moderate to severe WMH (Fazekas scale score 3–6) (18); LI was defined as round or ovoid fluid-filled cavities of 3–15 mm on T2 weight and FLAIR images (21). EPVS was defined as small (3 mm) punctate (if perpendicular) and linear (if longitudinal to the plane of scan) hyperintensities on T2 images in the basal ganglia or centrum semiovale, and they were rated on a previously described, validated semiquantitative scale from 0 to 4. The severity of EPVS was categorized as follows: none to mild (grade 0–1) and moderate to severe (grade 2–4) (21).

Then, CSVD with subcortical vascular cognitive impairment (SVCI) was defined as having either mild cognitive impairment or dementia (22) according to impairment in MMSE as follows: MMSE scores were based on the following educational levels of Chinese people: illiteracy ≤ 19, primary school ≤ 22, junior middle school, and above ≤ 26 (23).

The exclusion criteria were as follows: (a) patients with brain tumors or other systemic malignant tumors; (b) history of brain trauma; (c) large area of new infarction with a diameter > 2 cm; (d) dysfunction of liver, kidney, heart, lung, or other vital organs; (e) history of craniocerebral surgery; (f) CT or other imaging examinations of cerebral hemorrhage; (g) acute ischaemic stroke caused by atrial fibrillation and cardiogenic embolism; (h) other CSVD etiologies secondary to heredity, infection, autoimmune inflammation, poisoning, radiation, metabolic encephalopathy, and sporadic cerebral amyloid vascular disease; (i) history of psychiatry disease or history of using psychiatry drugs within the past 3 months; and (g) history of diseases that may affect cognition, such as Parkinson's disease, dementia with Lewy bodies, frontotemporal dementia, and AD. The exclusion and inclusion processes of participants are shown in **Supplementary Figure S1**.

The present study was approved by the First Affiliated Hospital of Anhui Medical University Subcommittee on Human Studies (Ethics ref. Quick-PJ2021-15-33). Written informed consent was obtained from all study subjects after a full explanation of the procedure.

Total MRI Burden of CSVD

According to the previous study (24), the total MRI burden of SVD was rated from 0 to 4 by counting the presence of 4 traditional MRI features of SVD, including WMH (1 point), LI (1 point), cerebral microbleed (CMB) (1 point) and EPVS (1 point). However, the CMB had not been evaluated in our study due to the lack of susceptibility weighted imaging (SWI) sequences (19). Therefore, the total scores of SVD in our study were 3. The presence of WMH was defined as periventricular Fazekas score = 3 or subcortical Fazekas score ≥ 2 (1 point if present). The presence of LI was defined as the presence of one or more lacunes (1 point if present). The presence of EPVS was counted as 1 point if there were moderate to severe (grade 2–4) EPVS in the basal ganglia.

Neuropsychological Assessment

Cognition assessment of both CSVD patients and HCs was performed by two trained neuropsychological technicians within 1 week after the MRI scan. All participants were evaluated by the Mini-Mental State Examination (MMSE) (25), Montreal Cognitive Assessment (MoCA) (26), Cambridge Cognitive Examination-Chinese version (CAMCOG-C) (27–29), and Activities of Daily Living (ADL) scales (30). The impairments in specific cognition domains were further extracted by the subscores of CAMCOG-C. Moreover, executive function was further assessed using the Stoop Color-Word Test (31) (SCWT-A dot, SCWT-B words, SCWT-C dot-word).

Image Acquisition

All images of participants were collected on a 3.0 Tesla GE Signa HDxt MRI scanner (GE, Milwaukee, WI, USA) with an 8-channel head coil. During the scanning, the participants were instructed to remain quiet, close their eyes, and not think of anything as much as possible. The scanning sequences included high-resolution 3D T1-weighted (3D-T1) structural images, T2 FLAIR images, and resting-state blood oxygen level-dependent (BOLD) fMRI. The 3D-T1 structural images were acquired by employing a spoiled gradient recalled echo sequence with the following parameters: repetition time (TR) = 9.5 ms; echo time (TE) = 3.9 ms; flip angle (FA) = 20°; field of view (FOV) = 256 mm × 256 mm; matrix size = 512 × 512; slice thickness = 1 mm. The parameters of T2 FLAIR images were as follows: TR = 11 s; TE =120 ms; FA = 90; 22 contiguous, 5-mm-thick axial slices; matrix size = 512 × 512; and FOV = 230 × 230 mm^2. Functional MRI images were collected using echo-planar imaging (EPI) at 2-s interval sequences with the following parameters: TR = 2,000 ms; TE = 30 ms; flip angle = 80°; FOV = 240 mm × 240 mm; matrix size = 64 × 64; slice thickness = 4 mm; and slice ga$p$ = 0.6 mm. The total BOLD duration was 8 min, with a total of 240 time points.

Data Preprocessing

The rs-fMRI data were preprocessed by Data Processing and Analysis for Brain Imaging (http://rfmri.org/dpabi) (32). The following preprocessing steps were taken: (a) the first 10 volumes were removed to allow the signal to reach equilibrium, and the remaining 230 time points were then processed; (b) the remaining volumes were corrected for acquisition time delay between slices; (c) all volumes were then realigned to the mean volume to correct for head motion; (d) functional images were spatially normalized to the Montreal Neurological Institute space with resampled voxel size = 3 × 3 × 3 mm^3; (e) detrending was performed to remove the linear trends; (f) temporal bandpass filtering (0.01–0.08 Hz) was used to reduce high-frequency physiology noise and low frequency drift; and (g) white matter, cerebrospinal fluid, and head motion nuisance variables were removed using a Friston 24-parameter model. Participants were excluded if their head motion parameters exceeded 2.5 mm translation and/or 2.5° rotation. The mean framewise displacement (FD) value was calculated by averaging the FD of each subject across the time points, and no significant differences were found between CSVD patients and HCs (p = 0.887). Furthermore, the mean FD value was calculated as an additional motion correction.

Construction of Dynamic Functional Connectivity

The dynamic brain connectome analysis toolbox (http://restfmri.net/forum/ DynamicBC) was applied to compute the DFC. The average time courses were extracted from 90 regions of interest (ROIs) of Anatomical Automatic Labeling atlas (AAL) (excluding the cerebellum) to calculate the functional connectivity, and the widely used sliding window approach was adopted to calculate DFC alterations, with a width of 50 TR (100 s) slides in steps of 1 TR (2 s) according to previous studies. Then, the functional connectivity in each window was calculated, resulting in a time series of functional connectivity matrices (90 × 90) for the next analysis. The average DFC strength was calculated as follows:

$$\text{DFC} - \text{Strength}\left(i,j\right) = \frac{1}{T}\sum_{t=1}^{T} Z\left(i,j\right)_t$$

where $Z\left(i,j\right)_t$ is the value of functional connectivity (Fisher-z transformed) between ROI i and ROI j in time window t, and T is the number of windows (33).

Clustering Analysis

K-means clustering was applied to estimate the reoccurring functional connectivity states over time using the squared Euclidean distance. The optimal number of clusters estimated using the elbow criterion was 3 (k = 3), which was computed

TABLE 1 | Demographic and clinical data of the CSVD and HC groups.

	HC (N=35)	CSVD (N=67)	t/χ2	*P* value	Cohen's d/*Φ*
Age, years	64.89 ± 7.80	67.51 ± 7.52	−1.65	0.102[a]	−0.344
Female, *n* (%)	19(54%)	31(46%)	0.591	0.442[b]	0.076
Education, years	9.19 ± 4.49	9.12 ± 3.67	0.08	0.936[a]	0.017
BMI, kg/m^2	23.46 ± 2.51	24.61 ± 2.83	−2.025	0.045[a]	−0.422
Alcohol abuse, *n* (%)	9(26%)	13(19%)	0.541	0.462[b]	−0.073
Current smoking, *n* (%)	6(17%)	16(24%)	0.617	0.432[b]	0.078
Commorbidities					
Hypertension, *n* (%)	13(37%)	30(45%)	0.549	0.459[b]	0.073
Diabetes mellitus, *n* (%)	2(6%)	9(13%)	0.734	0.391[b]	0.118
Dyslipidaemia, *n* (%)	5(14%)	11(16%)	0.079	0.779[b]	0.028
CAD, *n* (%)	2(6%)	11(16%)	1.504	0.22[b]	0.152
MMSE	27.71 ± 1.64	25.75 ± 2.90	3.713	<0.001[a]	0.774
MoCA	24.06 ± 3.23	21.51 ± 4.58	2.932	0.004[a]	0.612
CAMCOG-C	89.87 ± 7.48	83.11 ± 11.04	3.250	0.002[a]	0.678
Orientation	9.62 ± 0.61	9.21 ± 1.18	1.916	0.058[a]	0.400
Language	26.72 ± 2.12	25.34 ± 3.03	2.400	0.018[a]	0.500
Memory	18.86 ± 3.33	17.13 ± 4.31	2.077	0.040[a]	0.433
Attention	6.38 ± 1.01	6.02 ± 1.35	1.364	0.176[a]	0.285
Praxis	11.24 ± 1.23	10.12 ± 1.98	3.065	0.003[a]	0.639
Calculation	2.07 ± 0.23	1.92 ± 0.26	2.782	0.006[a]	0.580
Abstraction	6.41 ± 1.18	5.58 ± 1.74	2.526	0.013[a]	0.527
Perception	8.00 ± 1.03	7.12 ± 1.36	3.365	0.001[a]	0.702
SCWT-A (s)	20.78 ± 7.00	24.62 ± 9.70	−2.071	0.041[a]	−0.432
SCWT-B (s)	23.14 ± 6.69	29.14 ± 8.81	−3.532	0.001[a]	−0.737
SCWT-C (s)	35.08 ± 10.53	42.36 ± 15.77	−2.455	0.016[a]	−0.512
ADL	20.54 ± 1.67	21.16 ± 2.79	−1.208	0.154[a]	−0.252
Mean FD	0.10 ± 0.05	0.10 ± 0.10	0.142	0.887[a]	0.030
WMH			31.637	<0.001[b]	0.577
None to mild, *n* (%)	35(100%)	29(43%)			
Moderate to severe, *n* (%)	0	38(57%)			
LI, *n* (%)	0	16(24%)	9.913	0.002[b]	0.312
EPVS, *n* (%)			31.637	<0.001[b]	0.577
None to mild, *n* (%)	35	49(73%)			
Moderate to severe, *n* (%)	0	18 (27%)			

BMI, body mass index; CAD, Coronary artery disease; MMSE, Mini-Mental State Examination; MoCA, Montreal Cognitive Assessment; CAMCOG-C, Cambridge Cognitive Examination–Chinese version; SCWT, Stroop Color-Word Test; ADL, activities of daily living scale; FD, framewise displacement; WMH, white matter hyperintensity; LI, lacunar infarction; EPVS, enlarged perivascular space. [a]two sample T-test, [b]chi square test.

as the ratio between the within-cluster distance and between-cluster distances (34). Three temporal properties of the DFC states were evaluated, the fractional windows (proportion of total time window for each state in all participants), MDT (the time the subject stayed in the specific state before changing to another state), and the total number of transitions (the number of changes between the 3 connectivity states).

Validation Analysis

To validate the robustness of the temporal properties, different window sizes (20 TRs, 30 TRs, 40 TRs and 60 TRs) and a range of cluster sizes were applied to retest the results ($k = 2$, 4, 5 and 6).

Blinding

All assessments were performed by two trained neurologists who were blinded to the subjects' diagnoses. When the two neurologists had questions or disputes about the subject's cognitive function scores or imaging classification, a third experienced neurology expert was invited to make the final decision.

Statistical Analysis

Two-sample *t*-tests and χ^2 tests were used to compare demographic data between the CSVD and HC groups with SPSS version 23.0. A general linear model (GLM) was used to evaluate between-group differences of all metrics extracted from DFC (fractional windows, MDT, number of transitions) with age, gender, education, and mean FD as covariates (Bonferroni correction, $P < 0.05$). To identify the altered DFC strength between CSVD patients and HCs, two-sample t-tests with age, gender, education, and mean FD as covariates were performed in GRETNA (http://www.nitrc.org/projects/Gretna) (35) with network-based statistics (NBS) correction (edge $P < 0.001$, component $P < 0.05$, 1,000 iterations). Partial correlation analysis was conducted between DFC temporal properties and cognition scales in CSVD patients with age, gender, education, and mean FD as covariates ($P < 0.05$). The Spearman's correlation was conducted between SVD scores and temporal properties ($P < 0.05$).

RESULTS

Demographics, Clinical and Cognitive Characteristics

The participants' demographic and neuroimaging characteristics are provided in **Table 1**. For the neuropsychological scale, the general cognitive function of the CSVD patients was worse than that of the HCs, indicated by decreased MMSE and COMCOG-C scores, especially in the SVCI subgroup. In the CAMCOG-C subitems, CSVD patients showed decreased language, memory, praxis, calculation, abstraction, and perception, indicating extensive cognitive impairment. Furthermore, executive dysfunction was found in the CSVD group, as indicated by their worse performance on the SCWT. CSVD scores were presented in **Table 2.** The SVD scores of 35 HCs were 0, 46 patients with CSVD were scored 1, 17 patients were scored 2, and 4 patients were scored 3.

TABLE 2 | SVD scores for all participants across 3 small vessel disease components.

SVD scores	0	1	2	3
Total, *n* (%)	35 (34%)	46 (45%)	17 (17%)	4 (4%)

SVD, small vessel disease.

Dynamic Functional Connectivity State Characteristics

Here, three patterns of structured functional connectivity states recurring during individual scans across subjects were identified (**Figure 1**). Notably, state I (53.69%) was a more frequent and relatively sparse connected state; state II (27.98%) was a less frequent and stronger interconnected state, and state III (18.33%) was an intermediate pattern. As shown in the above three states, state I occurred most frequently.

Temporal Properties Comparison

As shown in **Figure 2** and **Supplementary Figure S2**, state II (39.35%) was more frequently observed than state I (36.09%) and state III (24.56%) in the HCs, while in the CSVD group, state I occurred much more frequently (62.90%) than state II (22.03%) and state III (15.07%). When comparing the fractional windows after correcting for age, gender, education, and mean FD, state II was less frequent in the CSVD group than in the HC group ($P = 0.015$), and the opposite pattern was observed for state I ($P = 0.001$). Furthermore, state I was more common in the SVCI group (74.38%) than in the CSVD-CU group (50.33%) ($P = 0.021$, Bonferroni correction), while state II was less frequent in the SVCI group (12.27%) than in the CSVD-CU group (32.72%) ($P = 0.049$, Bonferroni correction). In total, the CSVD group exhibited a decreased reoccurrence fraction in state II and an increased reoccurrence fraction in state I compared with those of the HCs.

Significant differences in the MDT in state I were observed between the CSVD group and HC group after correcting for age, gender, education, and mean FD ($P = 0.01$). The MDT in state II was shorter in the CSVD group than in the HC group ($P = 0.035$). Between-group comparisons among CSVD subgroups revealed that SVCI patients spent significantly more time in state I than CSVD-CU patients ($P = 0.006$, Bonferroni correction) and less time in state II than CSVD-CU patients, but

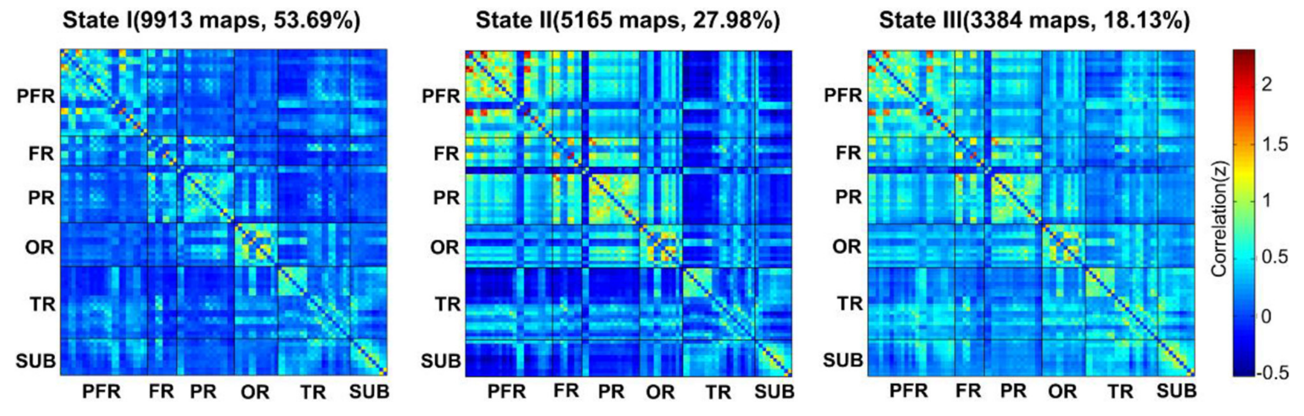

FIGURE 1 | The total numbers and percentages of three state occurrences in all subjects. PFR, prefrontal region; FR, other regions of the frontal lobe; PR, parietal region; OR, occipital region; TR, temporal region; SUB, subcortical region.

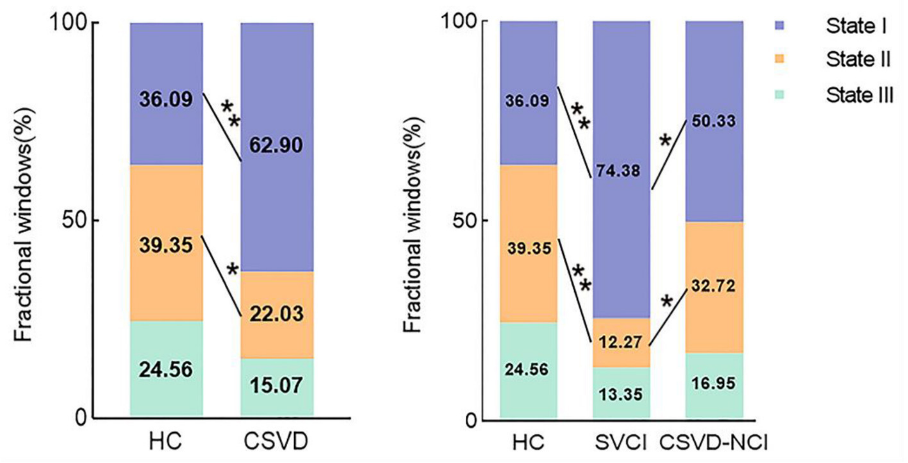

FIGURE 2 | Comparison of the fractional windows in each state between the CSVD and HC groups as well as among the CSVD subgroups by GLM. GLM, general linear model. * $P < 0.05$, ** $P < 0.01$.

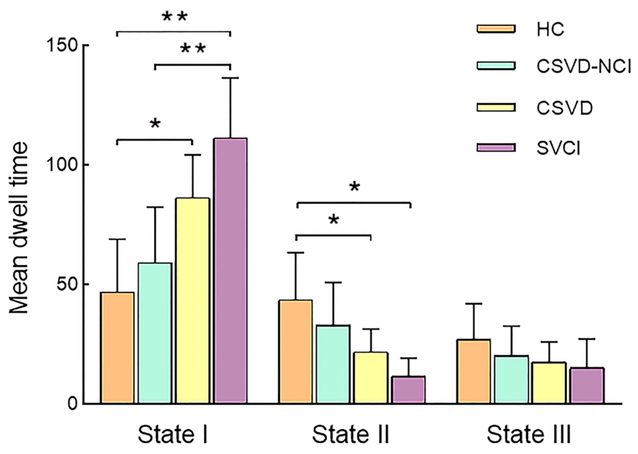

FIGURE 3 | Comparison of the mean dwell time in each state between the CSVD and HC groups as well among the CSVD subgroups by GLM. GLM, general linear model. * $P < 0.05$, ** $P < 0.01$.

the latter difference was not significant ($P = 0.216$). Overall, these changes in properties showed that CSVD patients, especially SVCI patients, stayed longer in weakly connected state I and dwelled for a shorter period in strongly interconnected state II (**Figure 3**). The number of transitions was not significantly different between the CSVD group and HC group or among the CSVD subgroups (**Supplementary Figures S3, S4**).

Altered DFC Strength Between the CSVD and HC Groups

When comparing the DFC strength in regions between the two groups, the CSVD group showed greatly decreased internetwork and intranetwork functional activity in the frontal lobe, parietal lobe, and occipital lobe (NBS correction) compared to those in the HC groups (**Figure 4**).

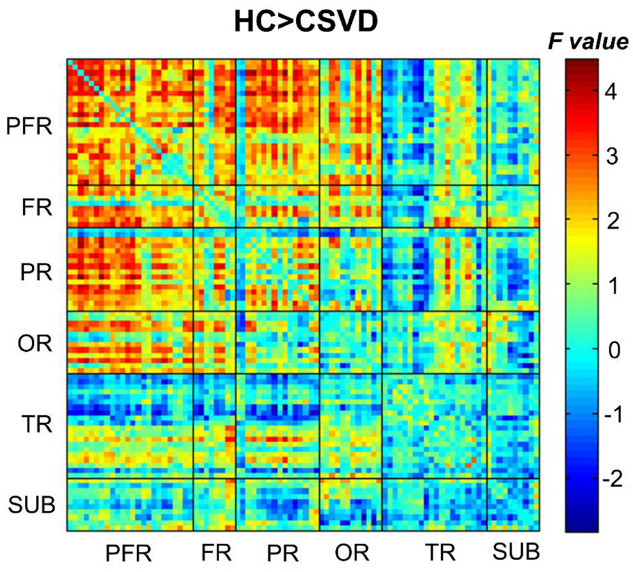

FIGURE 4 | Comparison of the DFC strengths between CSVD patients and HCs (HCs > CSVD) (NBS correction, edge $P < 0.001$, component $P < 0.05$, 1,000 iterations). NBS, network-based statistic.

Validation Analyses

As shown in **Figures 5**, **6**, the additional sliding window lengths were set at 20 TRs, 30 TRs, 40 TRs, and 60 TRs, and the numbers of clusters were set at 2, 4, 5 and 6. The differences in the fractional windows and MDT in state I and state II between the two groups (CSVD and HCs) and among the three groups (CSVD-CU, SVCI, and HCs) were almost consistent, which indicated the stable results of the DFC analysis.

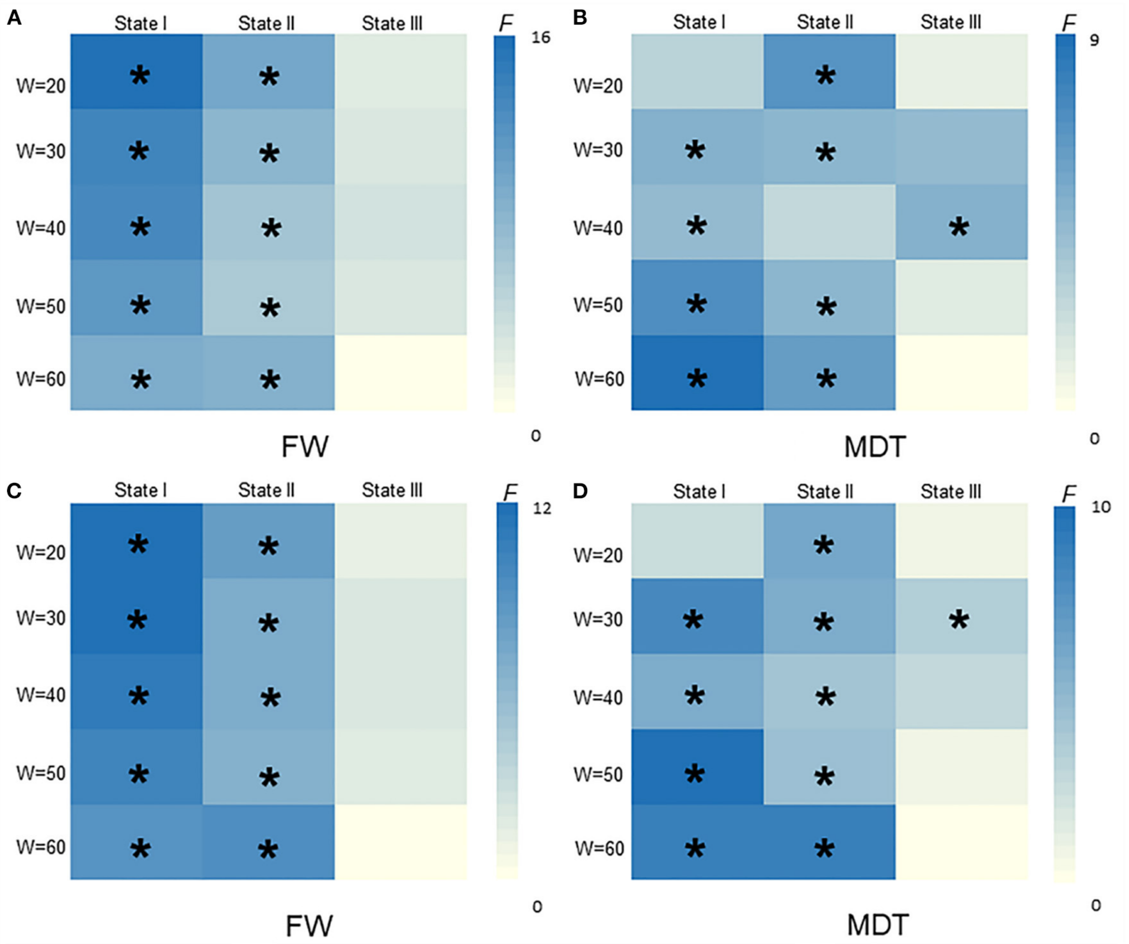

FIGURE 5 | The difference of FW and MDT in different widths of window size among HCs, CSVD-CU, SVCI (20TRs, 30TRs, 40TRs, 50TRs, 60TRs). **(A)** Comparison of FW between HCs and CSVD by GLM. **(B)** Comparison of MDT between HCs and CSVD by GLM. **(C)** Comparison of FW among HCs, CSVD-CU and SVCI by GLM. **(D)** Comparison of MDT among HCs, CSVD-CU and SVCI by GLM. GLM, general linear model; FW, fractional windows; MDT, mean dwell time. * $P < 0.05$.

Correlation Between Cognition and Temporal Properties

The fractional windows in state I were negatively related to global cognitive function in the CSVD group (**Figure 7A**), while the fractional windows in state I were positively associated with time consumption when performing the SCWT-A and SCWT-B tests (**Figures 7B,C**). Clearly, the results showed that a higher frequency in state I was associated with worse executive function. Moreover, the frequency of state II was positively correlated with global cognitive function (**Figures 7D,E**). In addition, global cognitive function was negatively related to the MDT in state I (**Figure 7F**) but positively related to the MDT in state II (**Figures 7G,H**). Furthermore, a significant positive correlation was shown between the MDT in state I and time consumption when performing the SCWT-B test (**Figure 7I**).

Correlation Between SVD Scores and Temporal Properties

Here, no statistical significance was shown between the temporal properties and SVD scores of CSVD group in state I, state II, and state III ($P > 0.05$) (**Supplementary Table S1**).

DISCUSSION

The extensively used sliding window approach, combined with straightforward metrics of temporal variability and clustering results for DFC analysis, was utilized. Three states of all subjects were identified by k-means clustering analysis (state I: sparsely connected, state II: strongly connected, state III: intermediate pattern). CSVD patients showed a higher percentage of DFC states in weakly connected state I but a lower percentage of DFC states in strongly connected state II. Moreover, patients with

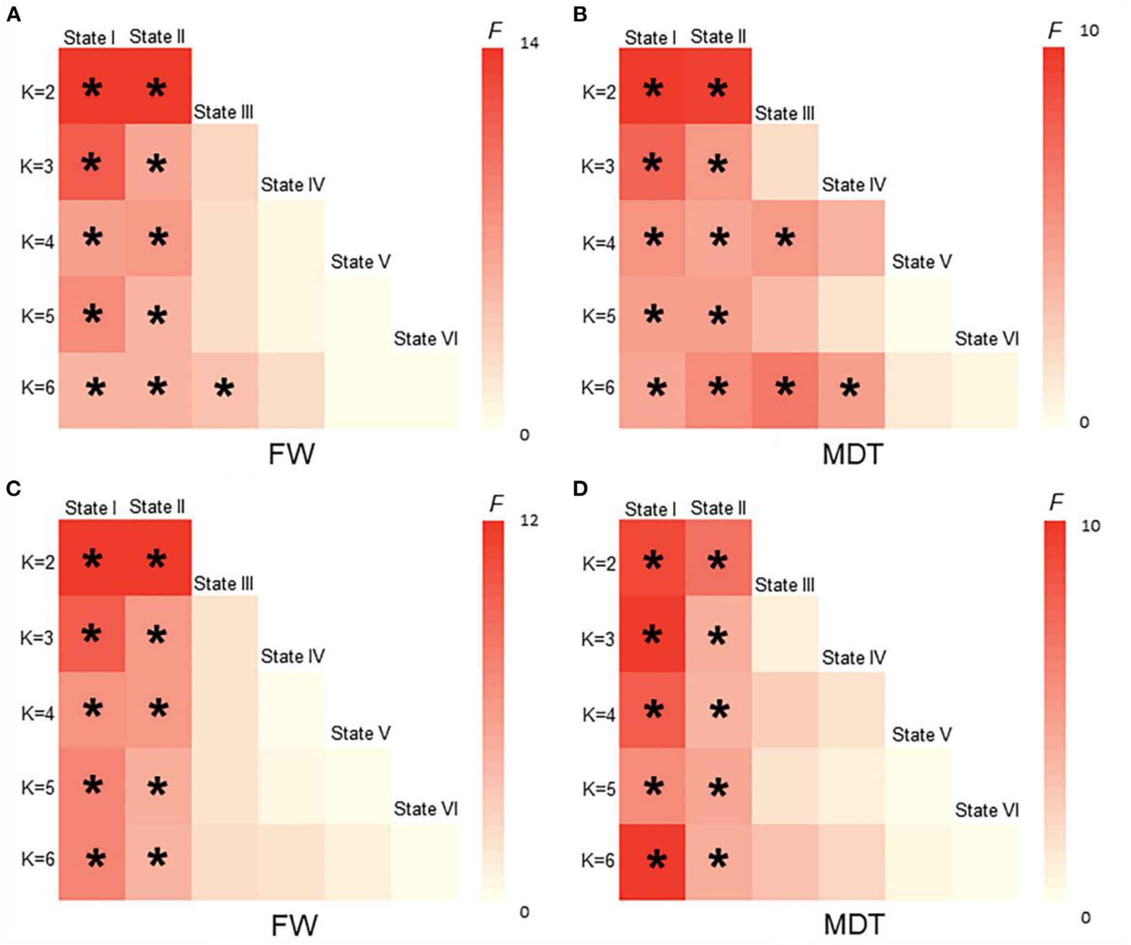

FIGURE 6 | The difference of FW and MDT in different K values among HCs, CSVD, CSVD-CU and SVCI. ($K = 2$, $K = 3$, $K = 4$, $K = 5$, $K = 6$). **(A)** Comparison of FW between HCs and CSVD by GLM. **(B)** Comparison of MDT between HCs and CSVD by GLM. **(C)** Comparison of FW among HCs, CSVD-CU and SVCI by GLM. **(D)** Comparison of MDT among HCs, CSVD-CU and SVCI by GLM. GLM, general linear model; FW, fractional windows; MDT, mean dwell time. * $P < 0.05$.

CSVD dwelled significantly longer in state I and for a shorter period in state II than HCs. Notably, these alterations were more significant in the SVCI subgroup. The analysis of DFC strength showed that the CSVD group exhibited substantially decreased internetwork functional activity in the frontal-parietal lobe and frontal-occipital lobe and decreased intranetwork in the frontal lobe and occipital lobe. In addition, a negative correlation was found between cognition and the DFC properties in state I in the CSVD group, while the opposite was found in state II.

Altered Temporal Properties of Dynamic Functional Connectivity States

In previous research, hypoconnectivity within several large-scale brain networks in CSVD patients compared with HCs has been reported (36, 37). Similarly, a significant hypoconnected pattern in the DFC clustering analysis of CSVD patients was found in this study, especially in the SVCI subgroup. These results indicated that CSVD could transit into the sparse pattern with a higher probability and dwell longer than the HC group. Hypoconnectivity in state I means widespread disruption of the whole brain network, which might result from the disruption of the focal lesion on the traditional imaging or from the cascade effect that spread from the initial focus to remote brain areas (3). Moreover, similar findings have been reported in other neuropsychiatric diseases, such as depression (38, 39), AD (17, 40), and dementia with Lewy bodies (40), as these patients spent more time in the sparsely connected state. Prior studies have revealed the characteristics of disconnection of structural and functional brain networks at a resting state. Therefore, the increased occurrence and longer duration in state I may indicate severe disruption of the brain networks, which leads to an increase in cognitive impairment. The results obtained in this paper could provide more evidence elucidating the disruption mechanism of CSVD from the perspective of DFC.

State II was characterized by highly integrated connections, which showed tightly positive connectivities within regions. When further comparing the DFC properties in the SVCI

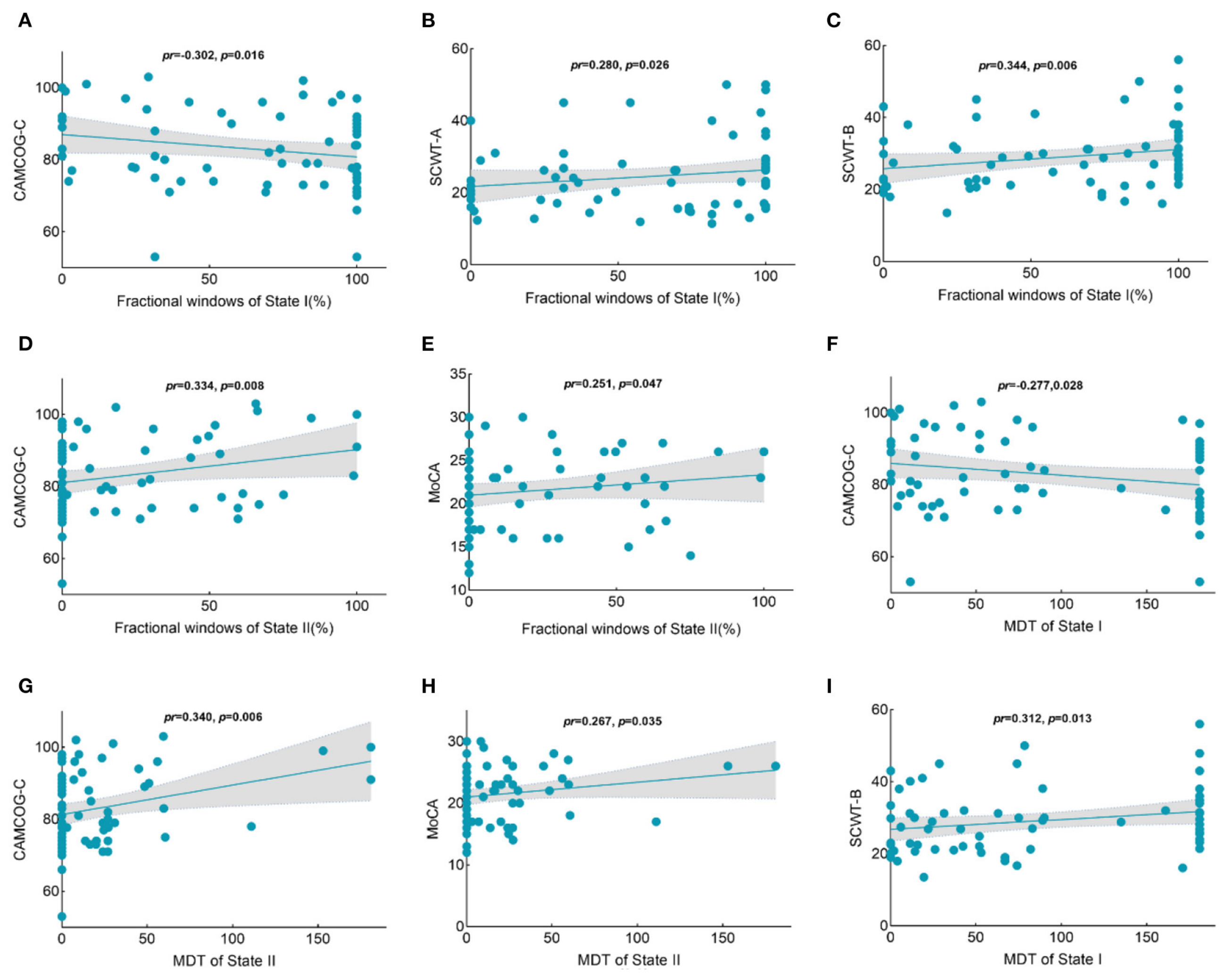

FIGURE 7 | Correlations between the temporal properties with intergroup differences and the cognition scores in the CSVD group. **(A)** A negative relationship was observed between the percentage of state I and the CAMCOG-C scores. **(B)** A positive relationship was observed between the percentage of state I and time consumption in SCWT-A performances. **(C)** A positive relationship was observed between the percentage of state I and time consumption in SCWT-B performances. **(D)** A positive relationship was observed between the percentage of state II and the CAMCOG-C scores. **(E)** A positive relationship was observed between the percentage of state II and MoCA scores. **(F)** A negative relationship was observed between the MDT in state I and CAMCOG-C scores. **(G)** A positive relationship was observed between the MDT in state I and time consumption in SCWT-B performances. **(H)** A positive relationship was observed between the MDT in state II and CAMCOG-C scores. **(I)** A positive relationship was observed between the MDT in state II and MoCA scores. CAMCOG-C, Cambridge Cognitive Examination–Chinese version; SCWT, Stroop Color-Word test; MoCA, Montreal Cognitive Assessment; MDT, mean dwell time.

and CSVD-CU groups, the SVCI group presented an even lower frequency of state II than the CSVD-CU group. The strongly connected state may play a role in cognition processing (41), decreased fractional window and MDT in strongly connected state in CSVD patients suggested that an important connectivity pattern was disrupted in CSVD patients during spontaneous neural activity. Therefore, the lower percentage of DFC occurrence in state II meant lower efficiency in information conveyance, resulting in disruption of integration in specific cognition domains, finally leading to cognitive impairment. The lower frequency of the hyperconnected state implied decreased information transmission and exchange, which was in line with previous studies, thus showing the disconnection of either structural or functional brain networks in CSVD (42–44).

Altered Average Dynamic Functional Connectivity Strength

The regions with decreased DFC strength were mainly distributed in regions of the frontal lobe, parietal lobe and occipital lobe in CSVD patients, consistent with previous studies (45, 46). In recent decades, disrupted functional activity in the frontal lobe of CSVD patients has been confirmed. The frontal lobe plays pivotal roles in execution and processing and is generally considered to be the initial region involved in the prefrontal-subcortical loop. The frontal-parietal areas are also believed to be associated with several executive control processes related to working memory (45). The decreased DFC strength in the frontal and parietal lobes might be related to reduced flexibility in executive functions, which is in line with a previous study (47). For the occipital lobe, the decreased temporary variability might be associated with impaired visuospatial functions, which have gradually been elucidated to be a vital clinical characteristic (48). Chen et al. reported white matter tract disruption in the inferior frontal-occipital fasciculus in WMH patients, which was in line with our results, indicating the important roles of the occipital lobe in CSVD (49). These results indicated that connectivity impairment in frontal-parietal-occipital areas may be crucial for the pathophysiology of CSVD-related cognitive impairment.

Relationship Between Temporal Properties and Cognition

Both general cognition and the sub-cognition of executive function were negatively correlated with the proportion of fractional windows and MDT in state I, while positively correlated with fractional windows and MDT in state II. Moreover, better cognitive function was associated with a higher MDT in the strongly connected state II in CSVD. The MDT in hypoconnected state I was negatively related to global cognition, which was characterized by CAMCOG-C scores. Executive function exhibited longer time consumption in SCWT performance. The relevant studies have confirmed hypofunctional connectivity in widespread brain networks in CSVD with cognitive impairment (50, 51). General cognition and executive function were negatively correlated with the occurrence of sparse states, which was consistent with our findings (16). The association of cognitive function with altered dynamic functional connectivity has also been demonstrated in other disease studies (10, 52). These results showed that strongly connected state means more efficient information integration and transmission, thus facilitating the cognition process, whereas sparsely connected states have the opposite effect (10, 41). Here, no significant relationship was found between SVD scores and temporal properties, which indicated that the structural alteration was hard to fully explain the aberrant functional activity, even though the temporal properties were associated with cognition. This study may provide a potential mechanism of CSVD with cognitive impairment from the perspective of dynamic functional connectivity.

Validation Analyses

In the validation analyses, the results of this work were well replicated when using various analytical parameters, including different parameters of sliding window lengths and k-means clusters. With the number of clusters increasing, the brain variability between the groups was still readily apparent. These observations indicated that the abnormal temporal features and network topological properties in patients with CSVD remained stable, indicating that these parameters can be used as neuroimaging markers to distinguish patients with CSVD from healthy people as well as to distinguish SVCI patients from CSVD-CU patients. Herein, the findings validate the results obtained by DFC, which were consistent with previous studies and further confirmed the reliability and repeatability of DFC analysis (53, 54).

Limitations

However, the current research still has several limitations. First, the specific differences in DFC according to the different imaging features of CSVD or the severity of cognitive impairment were not investigated due to the relatively small sample size. Moreover, none of the participants underwent susceptibility-weighted imaging or T2* imaging; therefore, the cerebral microbleed information remains unclear. In addition, the widely used sliding-window approach was adopted to extract the dynamics of functional connectivity in the current study. Furthermore, these results should be validated by other methods, such as Bayesian and frequentist methods, in the future. Finally, longitudinal and large sample studies are required to confirm the alteration of DFC in CSVD and its relationship with cognitive impairment.

CONCLUSION

In this study, the temporal property alterations of functional connectivity in CSVD and cognitive impairment analyses were emphatically investigated from the perspective of DFC. The patients with CSVD spent more time in a sparsely connected state and less time in a strongly connected state in all reoccurring states, which might have been associated with cognitive impairment. All the results herein could facilitate a deeper understanding of the potential neural mechanisms of cognitive impairment in CSVD.

DATA AVAILABILITY STATEMENT

The raw data supporting the conclusions of this article will be made available by the authors, without undue reservation.

ETHICS STATEMENT

The present study was approved by the First Affiliated Hospital of Anhui Medical University Subcommittee on Human Studies (Ethics Ref. Quick-PJ2021-15-33). The patients/participants provided their written informed consent to participate in this study.

AUTHOR CONTRIBUTIONS

WY and XZho: conceptualization, methodology, data analysis, visualization, and writing of the original draft. CL, MY, KW, WZha, WZhu, and ML: investigation, execution, data collection, and revision of the manuscript. ZS, YQ, and XZhu: conceptualization, funding acquisition, and revision of the manuscript. All authors read and approved the final version of the manuscript.

FUNDING

This work was supported by Key Research and Development Projects of Anhui Province (202104j07020031), the Natural Science Foundation of Anhui Province (1908085QH322), the Basic and Clinical Cooperative Research Promotion Plan of Anhui Medical University (2020xkjT026), and the National Natural Science Foundation of China (81771154).

ACKNOWLEDGMENTS

The authors sincerely thank all the volunteers and patients for their participation in our study.

SUPPLEMENTARY MATERIAL

The Supplementary Material for this article can be found online at: https://www.frontiersin.org/articles/10.3389/fneur.2022.913241/full#supplementary-material

REFERENCES

1. Wardlaw JM, Smith C, Dichgans M. Small vessel disease: mechanisms and clinical implications. *Lancet Neurol.* (2019) 18:684–96. doi: 10.1016/S1474-4422(19)30079-1
2. Hamilton OKL, Cox SR, Okely JA, Conte F, Ballerini L, Bastin ME, et al. Cerebral small vessel disease burden and longitudinal cognitive decline from age 73 to 82: the Lothian birth cohort 1936. *Transl Psychiatry.* (2021) 11:376. doi: 10.1038/s41398-021-01495-4
3. Ter Telgte A, van Leijsen EMC, Wiegertjes K, Klijn CJM, Tuladhar AM, de Leeuw FE. Cerebral small vessel disease: From a focal to a global perspective. *Nat Rev Neurol.* (2018) 14:387–98. doi: 10.1038/s41582-018-0014-y
4. Chen X, Huang L, Ye Q, Yang D, Qin R, Luo C, et al. Disrupted functional and structural connectivity within default mode network contribute to WMH-related cognitive impairment. *Neuroimage Clin.* (2019) 24:102088. doi: 10.1016/j.nicl.2019.102088
5. Liu R, Chen H, Qin R, Gu Y, Chen X, Zou J, et al. The altered reconfiguration pattern of brain modular architecture regulates cognitive function in cerebral small vessel disease. *Front Neurol.* (2019) 10:324. doi: 10.3389/fneur.2019.00324
6. Liu R, Wu W, Ye Q, Gu Y, Zou J, Chen X, et al. Distinctive and pervasive alterations of functional brain networks in cerebral small vessel disease with and without cognitive impairment. *Dement Geriatr Cogn Disord.* (2019) 47:55–67. doi: 10.1159/000496455
7. Schulz M, Malherbe C, Cheng B, Thomalla G, Schlemm E. Functional connectivity changes in cerebral small vessel disease - a systematic review of the resting-state mri literature. *BMC Med.* (2021) 19:103. doi: 10.1186/s12916-021-01962-1
8. Gonzalez-Castillo J, Bandettini PA. Task-based dynamic functional connectivity: recent findings and open questions. *Neuroimage.* (2018) 180:526–33. doi: 10.1016/j.neuroimage.2017.08.006
9. Marusak HA, Calhoun VD, Brown S, Crespo LM, Sala-Hamrick K, Gotlib IH, et al. Dynamic functional connectivity of neurocognitive networks in children. *Hum Brain Mapp.* (2017) 38:97–108. doi: 10.1002/hbm.23346
10. Fu Z, Caprihan A, Chen J, Du Y, Adair JC, Sui J, et al. Altered static and dynamic functional network connectivity in alzheimer's disease and subcortical ischemic vascular disease: shared and specific brain connectivity abnormalities. *Hum Brain Mapp.* (2019) 40:3203–21. doi: 10.1002/hbm.24591
11. Sendi MSE, Zendehrouh E, Fu Z, Liu J, Du Y, Mormino E, et al. Disrupted dynamic functional network connectivity among cognitive control networks in the progression of alzheimer's disease. *Brain Connect.* (2021). doi: 10.1089/brain.2020.0847
12. Luo Y, He H, Duan M, Huang H, Hu Z, Wang H, et al. Dynamic functional connectivity strength within different frequency-band in schizophrenia. *Front Psychiatry.* (2019) 10:995. doi: 10.3389/fpsyt.2019.00995
13. Sun F, Zhao Z, Lan M, Xu Y, Huang M, Xu D. Abnormal dynamic functional network connectivity of the mirror neuron system network and the mentalizing network in patients with adolescent-onset, first-episode, drug-naïve schizophrenia. *Neurosci Res.* (2021) 162:63–70. doi: 10.1016/j.neures.2020.01.003
14. Marchitelli R, Paillère-Martinot ML, Bourvis N, Guerin-Langlois C, Kipman A, Trichard C, et al. Dynamic functional connectivity in adolescence-onset major depression: relationships with severity and symptom dimensions. *Biol Psychiatry Cogn Neurosci Neuroimag.* (2021) 7:385–96. doi: 10.1016/j.bpsc.2021.05.003
15. Zhu DM, Yang Y, Zhang Y, Wang C, Wang Y, Zhang C, et al. Cerebellar-cerebral dynamic functional connectivity alterations in major depressive disorder. *J Affect Disord.* (2020) 275:319–28. doi: 10.1016/j.jad.2020.06.062
16. Fiorenzato E, Strafella AP, Kim J, Schifano R, Weis L, Antonini A, et al. Dynamic functional connectivity changes associated with dementia in parkinson's disease. *Brain.* (2019) 142:2860–72. doi: 10.1093/brain/awz192
17. Gu Y, Lin Y, Huang L, Ma J, Zhang J, Xiao Y, et al. Abnormal dynamic functional connectivity in alzheimer's disease. *CNS Neurosci Ther.* (2020) 26:962–71. doi: 10.1111/cns.13387
18. Zhu S, Qian S, Xu T, Peng H, Dong R, Wang D, et al. White matter hyperintensity, immediate antihypertensive treatment, and functional outcome after acute ischemic stroke. *Stroke.* (2020) 51:1608–12. doi: 10.1161/STROKEAHA.119.028841
19. Staals J, Makin SD, Doubal FN, Dennis MS, Wardlaw JM. Stroke subtype, vascular risk factors, and total mri brain small-vessel disease burden. *Neurology.* (2014) 83:1228–34. doi: 10.1212/WNL.0000000000000837
20. Fazekas F, Chawluk JB, Alavi A, Hurtig HI. Zimmerman RA. Mr signal abnormalities at 15 t in alzheimer's dementia and normal aging. *AJR Am J Roentgenol.* (1987) 149:351–6. doi: 10.2214/ajr.149.2.351
21. Wardlaw JM, Smith EE, Biessels GJ, Cordonnier C, Fazekas F, Frayne R, et al. Neuroimaging standards for research into small vessel disease and its contribution to ageing and neurodegeneration. *Lancet Neurol.* (2013) 12:822–38. doi: 10.1016/S1474-4422(13)70124-8
22. Park JH, Seo SW, Kim C, Kim SH, Kim GH, Kim ST, et al. Effects of cerebrovascular disease and amyloid beta burden on cognition in subjects with subcortical vascular cognitive impairment. *Neurobiol Aging.* (2014) 35:254–60. doi: 10.1016/j.neurobiolaging.2013.06.026
23. Zhang Z, Hong X, Li H, Zhao J, Huang J, Wei J, et al. Distribution characteristics of mini-mental state examination test results of residents aged 55 or above in urban and rural beijing. *Chin J Neurol.* (1999):20–24.
24. Klarenbeek P, van Oostenbrugge RJ, Rouhl RP, Knottnerus IL, Staals J. Ambulatory blood pressure in patients with lacunar stroke: Association with total mri burden of cerebral small vessel disease. *Stroke.* (2013) 44:2995–9. doi: 10.1161/STROKEAHA.113.002545
25. Folstein M, Anthony JC, Parhad I, Duffy B, Gruenberg EM. The meaning of cognitive impairment in the elderly. *J Am Geriatr Soc.* (1985) 33:228–35. doi: 10.1111/j.1532-5415.1985.tb07109.x
26. Nasreddine ZS, Phillips NA, Bédirian V, Charbonneau S, Whitehead V, Collin I, et al. The montreal cognitive assessment, moca: a brief screening tool for mild cognitive impairment. *J Am Geriatr Soc.* (2005) 53:695–9. doi: 10.1111/j.1532-5415.2005.53221.x
27. Roth M, Tym E, Mountjoy CQ, Huppert FA, Hendrie H, Verma S, et al. Camdex. A standardised instrument for the diagnosis of mental disorder in the elderly with special reference to the early detection of dementia. *Br J Psychiatry.* (1986) 149:698–709. doi: 10.1192/bjp.149.6.698
28. Wang QS, Zhou JN. Retrieval and encoding of episodic memory in normal aging and patients with mild cognitive impairment. *Brain Res.* (2002) 924:113–5. doi: 10.1016/S0006-8993(01)03200-0

29. Wouters H, van Gool WA, Schmand B, Zwinderman AH, Lindeboom R. Three sides of the same coin: Measuring global cognitive impairment with the mmse, adas-cog and camcog. *Int J Geriatr Psychiatry*. (2010) 25:770–9. doi: 10.1002/gps.2402
30. Mlinac ME, Feng MC. Assessment of activities of daily living, self-care, and independence. *Arch Clin Neuropsychol.* (2016) 31:506–16. doi: 10.1093/arclin/acw049
31. Lansbergen MM, Kenemans JL, van Engeland H. Stroop interference and attention-deficit/hyperactivity disorder: a review and meta-analysis. *Neuropsychology*. (2007) 21:251–62. doi: 10.1037/0894-4105.21.2.251
32. Yan CG, Wang XD, Zuo XN, Zang YF. Dpabi: Data processing & analysis for (resting-state) brain imaging. *Neuroinformatics.* (2016) 14:339–51. doi: 10.1007/s12021-016-9299-4
33. Li Y, Zhu Y, Nguchu BA, Wang Y, Wang H, Qiu B, et al. Dynamic functional connectivity reveals abnormal variability and hyper-connected pattern in autism spectrum disorder. *Autism Res.* (2020) 13:230–43. doi: 10.1002/aur.2212
34. Allen EA, Damaraju E, Plis SM, Erhardt EB, Eichele T, Calhoun VD. Tracking whole-brain connectivity dynamics in the resting state. *Cereb Cortex.* (2014) 24:663–76. doi: 10.1093/cercor/bhs352
35. Wang J, Wang X, Xia M, Liao X, Evans A, He Y. Gretna: a graph theoretical network analysis toolbox for imaging connectomics. *Front Hum Neurosci.* (2015) 9:386. doi: 10.3389/fnhum.2015.00386
36. Gesierich B, Tuladhar AM, Ter Telgte A, Wiegertjes K, Konieczny MJ, Finsterwalder S, et al. Alterations and test-retest reliability of functional connectivity network measures in cerebral small vessel disease. *Hum Brain Mapp.* (2020) 41:2629–41. doi: 10.1002/hbm.24967
37. Lawrence AJ, Tozer DJ, Stamatakis EA, Markus HS, A. comparison of functional and tractography based networks in cerebral small vessel disease. *Neuroimage Clin.* (2018) 18:425–32. doi: 10.1016/j.nicl.2018.02.013
38. Yao Z, Shi J, Zhang Z, Zheng W, Hu T, Li Y, et al. Altered dynamic functional connectivity in weakly-connected state in major depressive disorder. *Clin Neurophysiol.* (2019) 130:2096–104. doi: 10.1016/j.clinph.2019.08.009
39. Zhi D, Ma X, Lv L, Ke Q, Yang Y, Yang X, et al. Abnormal dynamic functional network connectivity and graph theoretical analysis in major depressive disorder. *Annu Int Conf IEEE Eng Med Biol Soc.* (2018) 2018:558–61. doi: 10.1109/EMBC.2018.8512340
40. Schumacher J, Peraza LR, Firbank M, Thomas AJ, Kaiser M, Gallagher P, et al. Dynamic functional connectivity changes in dementia with lewy bodies and alzheimer's disease. *Neuroimage Clin.* (2019) 22:101812. doi: 10.1016/j.nicl.2019.101812
41. Cohen JR. The behavioral and cognitive relevance of time-varying, dynamic changes in functional connectivity. *Neuroimage.* (2018) 180:515–25. doi: 10.1016/j.neuroimage.2017.09.036
42. Du J, Zhu H, Zhou J, Lu P, Qiu Y, Yu L, et al. Structural brain network disruption at preclinical stage of cognitive impairment due to cerebral small vessel disease. *Neuroscience.* (2020) 449:99–115. doi: 10.1016/j.neuroscience.2020.08.037
43. Madden DJ, Parks EL, Tallman CW, Boylan MA, Hoagey DA, Cocjin SB, et al. Sources of disconnection in neurocognitive aging: Cerebral white-matter integrity, resting-state functional connectivity, and white-matter hyperintensity volume. *Neurobiol Aging.* (2017) 54:199–213. doi: 10.1016/j.neurobiolaging.2017.01.027
44. Tuladhar AM, van Dijk E, Zwiers MP, van Norden AG, de Laat KF, Shumskaya E, et al. Structural network connectivity and cognition in cerebral small vessel disease. *Hum Brain Mapp.* (2016) 37:300–10. doi: 10.1002/hbm.23032
45. Liu C, Shi L, Zhu W, Yang S, Sun P, Qin Y, et al. Fiber connectivity density in cerebral small-vessel disease patients with mild cognitive impairment and cerebral small-vessel disease patients with normal cognition. *Front Neurosci.* (2020) 14:83. doi: 10.3389/fnins.2020.00083
46. Ye Q, Bai F. Contribution of diffusion, perfusion and functional mri to the disconnection hypothesis in subcortical vascular cognitive impairment. *Stroke Vasc Neurol.* (2018) 3:131–9. doi: 10.1136/svn-2017-000080
47. Naghavi HR, Nyberg L. Common fronto-parietal activity in attention, memory, and consciousness: Shared demands on integration? *Conscious Cogn.* (2005) 14:390–425. doi: 10.1016/j.concog.2004.10.003
48. Wu X, Lai Y, Zhang Y, Yao L, Wen X. Breakdown of sensorimotor network communication in leukoaraiosis. *Neurodegener Dis.* (2015) 15:322–30. doi: 10.1159/000435918
49. Chen HF, Huang LL Li HY, Qian Y, Yang D, Qing Z, et al. Microstructural disruption of the right inferior fronto-occipital and inferior longitudinal fasciculus contributes to wmh-related cognitive impairment. *CNS Neurosci Ther.* (2020) 26:576–88. doi: 10.1111/cns.13283
50. Qin Y, Zhu W, Liu C, Wang Z, Zhu W. Functional brain connectome and its relation to mild cognitive impairment in cerebral small vessel disease patients with thalamus lacunes: a cross-sectional study. *Medicine (Baltimore).* (2019) 98:e17127. doi: 10.1097/MD.0000000000017127
51. Wang J, Chen Y, Liang H, Niedermayer G, Chen H, Li Y, et al. The role of disturbed small-world networks in patients with white matter lesions and cognitive impairment revealed by resting state function magnetic resonance images (rs-fmri). *Med Sci Monit.* (2019) 25:341–56. doi: 10.12659/MSM.913396
52. Chen Q, Lu J, Zhang X, Sun Y, Chen W, Li X, et al. Alterations in dynamic functional connectivity in individuals with subjective cognitive decline. *Front Aging Neurosci.* (2021) 13:646017. doi: 10.3389/fnagi.2021.646017
53. Wang Y, Wang C, Miao P, Liu J, Wei Y, Wu L, et al. An imbalance between functional segregation and integration in patients with pontine stroke: a dynamic functional network connectivity study. *Neuroimage Clin.* (2020) 28:102507. doi: 10.1016/j.nicl.2020.102507
54. Wu X, He H, Shi L, Xia Y, Zuang K, Feng Q, et al. Personality traits are related with dynamic functional connectivity in major depression disorder: a resting-state analysis. *J Affect Disord.* (2019) 245:1032–42. doi: 10.1016/j.jad.2018.11.002

Conflict of Interest: The authors declare that the research was conducted in the absence of any commercial or financial relationships that could be construed as a potential conflict of interest.

frontiers | Frontiers in Neurology

REVIEW
published: 24 June 2022
doi: 10.3389/fneur.2022.841521

Clinical, Radiological and Pathological Characteristics Between Cerebral Small Vessel Disease and Multiple Sclerosis: A Review

Bijia Wang[1†], Xuegang Li[2†], Haoyi Li[2], Li Xiao[1], Zhenhua Zhou[1], Kangning Chen[1], Li Gui[1], Xianhua Hou[1], Rong Fan[1], Kang Chen[3], Wenjing Wu[3], Haitao Li[3*] and Xiaofei Hu[3*]

[1] Department of Neurology, First Affiliated Hospital, Army Medical University (Third Military Medical University), Chongqing, China, [2] Department of Neurosurgery, First Affiliated Hospital, Army Medical University (Third Military Medical University), Chongqing, China, [3] Department of Radiology, First Affiliated Hospital, Army Medical University (Third Military Medical University), Chongqing, China

OPEN ACCESS

Edited by:
Jie Lu,
Capital Medical University, China

Reviewed by:
Wei Zhang,
Sichuan Armed Police Corps Hospital, China
Katsuhisa Masaki,
University of Chicago Medical Center, United States

***Correspondence:**
Haitao Li
13883818704@163.com
Xiaofei Hu
harryzonetmmu@163.com

† These authors have contributed equally to this work

Specialty section:
This article was submitted to Applied Neuroimaging, a section of the journal Frontiers in Neurology

Received: *22 December 2021*
Accepted: *19 May 2022*
Published: *24 June 2022*

Citation:
Wang B, Li X, Li H, Xiao L, Zhou Z, Chen K, Gui L, Hou X, Fan R, Chen K, Wu W, Li H and Hu X (2022) Clinical, Radiological and Pathological Characteristics Between Cerebral Small Vessel Disease and Multiple Sclerosis: A Review. Front. Neurol. 13:841521. doi: 10.3389/fneur.2022.841521

Cerebral small vessel disease (CSVD) and multiple sclerosis (MS) are a group of diseases associated with small vessel lesions, the former often resulting from the vascular lesion itself, while the latter originating from demyelinating which can damage the cerebral small veins. Clinically, CSVD and MS do not have specific signs and symptoms, and it is often difficult to distinguish between the two from the aspects of the pathology and imaging. Therefore, failure to correctly identify and diagnose the two diseases will delay early intervention, which in turn will affect the long-term functional activity for patients and even increase their burden of life. This review has summarized recent studies regarding their similarities and difference of the clinical manifestations, pathological features and imaging changes in CSVD and MS, which could provide a reliable basis for the diagnosis and differentiation of the two diseases in the future.

Keywords: cerebral small vessel disease, multiple sclerosis, magnetic resonance imaging, pathological features, review

INTRODUCTION

Cerebral small vessel disease (CSVD) belongs to a group of diseases involving cerebral arterioles, venules and capillaries. CSVD accounts for about 25% of ischemic stroke, and its etiology remains unclear. The pathogenesis may be related to vascular endothelial injury, hypoperfusion and ischemia, and impaired blood-brain barrier function (1, 2). Currently, CSVD can be divided into 6 categories according to different pathological characteristics: atherosclerosis, cerebral amyloid angiopathy, hereditary vascular diseases [such as cerebral autosomal dominant arteriopathy with subcortical infarcts and leukoencephalopathy (CADASIL), Fabry disease, etc.], inflammatory vascular diseases (such as primary angiitis of the central nervous system (PACNS), Susac syndrome, etc.), venous collagen deposition lesion and other types (3, 4). The imaging features included recent small subcortical infarcts, lacune of presumed vascular origin, white matter hyperintensities of presumed vascular origin, perivascular space (PVS), cerebral microbleed (CMB) and brain atrophy. Some patients may obtain CSVD-related symptoms, but many patients lack symptom and the occurrence of such imaging features appears more problematic within individuals above the age of 50. However, after repeated small vessel events, patients often show abnormal gait, numbness of limbs, cognitive decline and etc., which can seriously result in cognitive dysfunction and physical disability. It has been reported that the etiology of 45% patients with dementia is CSVD, which ranks second only to Alzheimer's disease (3, 5). Therefore, a series of complications caused by CSVD bring immeasurable burden and cost to society.

Multiple sclerosis (MS) is an autoimmune disease characterized by inflammatory demyelination of white matter centered on the central nervous system. The etiology and pathogenesis of MS remains to be unknown. In terms of anatomical structure, MRI showed that the white matter lesions of MS were often distributed around the paracele, subcortex, thalamus, brainstem, and others, showing hyperintensity signal lesions on T2-weighted images (6). MS is an important cause of non-traumatic nervous system dysfunction in young people. Epidemiologically, the incidence of MS shows obvious differences in different regions of the world, and the incidence of MS in Europe and America is higher than that in Asia and Africa. The incidence of MS in females is higher than that in males. Usually, the clinical onset age ranges from 20 to 40 years old, and its clinical manifestations are non-specific. The main symptoms include limb numbness, limb weakness, dizziness, ataxia, blurred vision and others, which are often similar to the clinical manifestations of other inflammatory-related diseases and non-inflammatory-related diseases, thus making them difficult to be distinguished. If patients cannot be correctly diagnosed and treated in the early stage of MS progression, more than half of patients will lose their independent exercise ability after 20 years (7, 8). It not only seriously affects the quality of life of patients, but also brings more medical burden to all sectors of society.

In clinical work, CSVD and MS often have similar characteristics in clinical manifestations, imaging features and pathological changes, which brings many difficulties to the identification, early diagnosis and treatment intervention of clinical diseases, and further delays the effective treatment time window of patients. Therefore, it is helpful to improve our diagnosis, comprehensive evaluation and formulate treatment strategies in clinical work through in-depth understanding of the similarities and differences in clinical symptoms, imaging changes and pathological features of these two diseases. This review intends to summarize and discuss the similarities and differences between CSVD and MS from three aspects, such as clinical features, imaging changes, and pathological features, so as to provide a strong basis for the subsequent clinical diagnosis and treatment.

CSVD

Clinical, Pathological, and Imaging Features of CSVD

CSVD refers to a series of clinical, imaging, and pathological syndromes resulting from various etiologies affecting small intracerebral arteries and their distal branches, microarteries, capillaries, microvenules, and small veins. The current definition of CSVD is broader and includes not only the small vessels mentioned above, but also the vascular structures within the brain parenchyma and subarachnoid space 2–5 mm surrounding these small vessels (9). CSVD is one of the important causes of white matter lesions. Due to the occult onset and mild symptoms, it is difficult to be diagnosed by screening in clinic. However, repeated cerebrovascular events will eventually result in the limb dysfunction and seriously affect the quality of life. Pathologically, cerebrovascular arteriosclerosis often occurs in CSVD, which is highly correlated with age and vascular risk factors (VRFs) (e.g., hypertension) (10). The results of pathological sections indicated that fibrinoid necrosis in the vascular wall, lipohyalinotic degeneration, atherosclerotic plaque, thickening of vessel wall and narrowing of vascular lumen could all promote the formation of cerebral arteriolar sclerosis. The loss of smooth muscle cells in the vessel wall will lead to the dysfunction of vascular autonomic regulation and the formation of microaneurysms. In view of the fact that arteriosclerosis is a systemic pathological process, similar pathological findings exist in target organs with more small blood vessels, such as retina and kidney (5). Although many previous studies on CSVD have made some achievements, the pathogenesis of CSVD remains to be unclear. Imaging can not only assist the diagnosis of CSVD and reflect the degree of involvement, but also help to understand its pathological basis. However, imaging description has individual heterogeneity (3). Therefore, an expert consensus was organized and drafted by the international working group, which classified the imaging features of CSVD as recent small subcortical infarcts, lacune of presumed vascular origin, white matter hyperintensities of presumed vascular origin, perivascular space (PVS), cerebral microbleed (CMB) and brain atrophy (3, 9) (**Figure 1**).

Classification of CSVD Based on Imaging

Recent Small Subcortical Infarcts

The infarct foci usually smaller than 20 mm are considered as the imaging features of recent small subcortical infarcts or acute lacuna infarction. These lesions progress to potential lacunae or white matter hyperintensities without cavities over time, and may also disappear (11). These lacunae are generally round or oval, with a diameter of about 3 to 15 mm, and their signal strength is consistent with CSF (3). The blood supply area of perforating arterioles is the predilection site of recent small subcortical infarcts, which can gradually evolve into lacuna and usually appear with white matter hyperintensities in chronic stage, suggesting that lacuna and white matter hyperintensities may have interrelated pathological basis (12). Another distinguishing feature is that in the fluid attenuated inversion recovery (FLAIR), the lesion area can be seen with hyperintensity at the edge, which suggests that the lesion is more likely to be a lacuna than a perivascular space. Multiple perivascular spaces in basal ganglia are called "sieve state," which is usually related to brain atrophy and brain degenerative disease (3, 5).

Lacune of Presumed Vascular Origin

Lacune of presumed vascular origin are generally small cavities that remain in the brain tissue after removal of the necrotic tissue of a subcortical infarction. Most symptoms

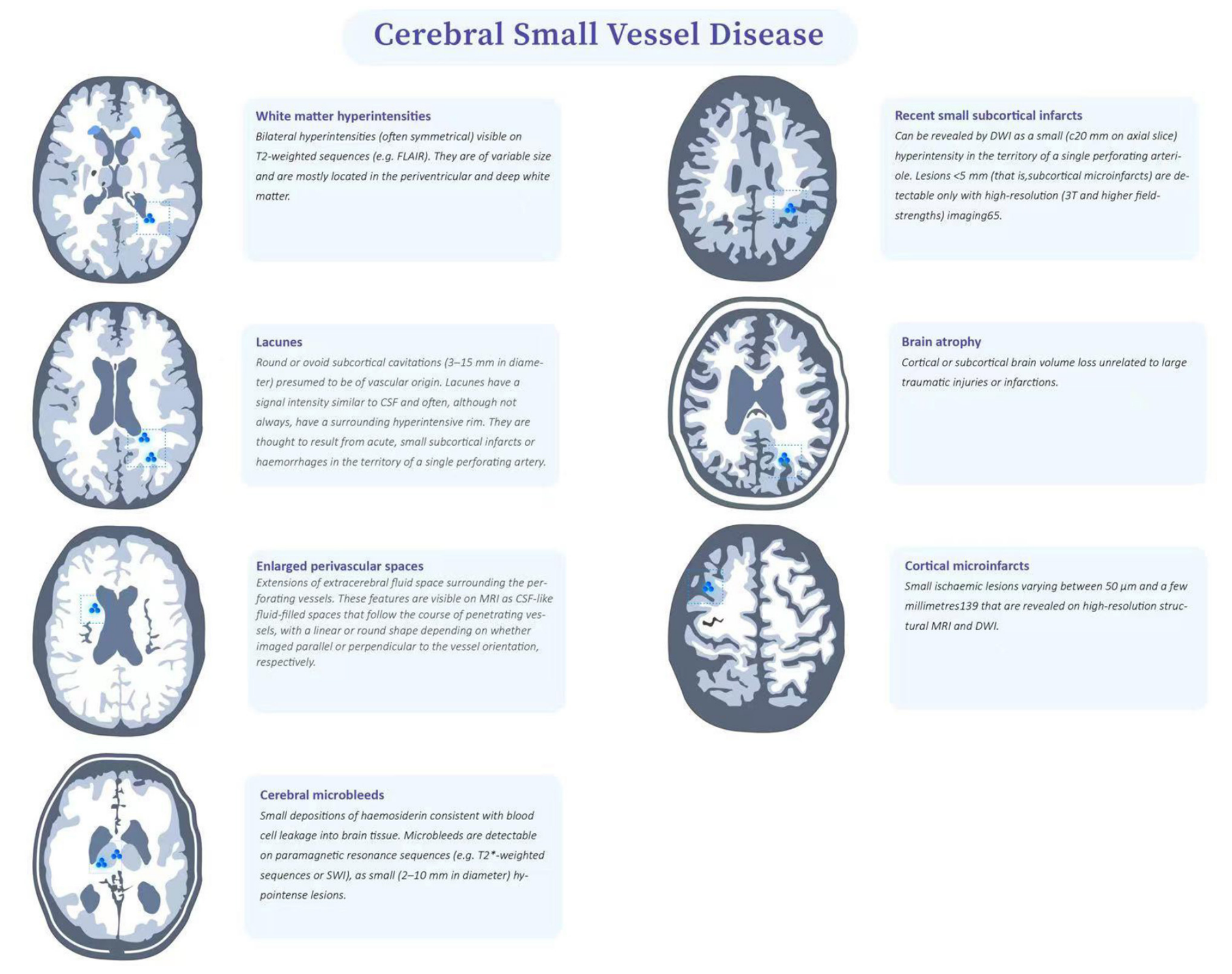

Cerebral Small Vessel Disease

White matter hyperintensities
Bilateral hyperintensities (often symmetrical) visible on T2-weighted sequences (e.g. FLAIR). They are of variable size and are mostly located in the periventricular and deep white matter.

Lacunes
Round or ovoid subcortical cavitations (3–15 mm in diameter) presumed to be of vascular origin. Lacunes have a signal intensity similar to CSF and often, although not always, have a surrounding hyperintensive rim. They are thought to result from acute, small subcortical infarcts or haemorrhages in the territory of a single perforating artery.

Enlarged perivascular spaces
Extensions of extracerebral fluid space surrounding the perforating vessels. These features are visible on MRI as CSF-like fluid-filled spaces that follow the course of penetrating vessels, with a linear or round shape depending on whether imaged parallel or perpendicular to the vessel orientation, respectively.

Cerebral microbleeds
Small depositions of haemosiderin consistent with blood cell leakage into brain tissue. Microbleeds are detectable on paramagnetic resonance sequences (e.g. T2-weighted sequences or SWI), as small (2–10 mm in diameter) hypointense lesions.*

Recent small subcortical infarcts
Can be revealed by DWI as a small (c20 mm on axial slice) hyperintensity in the territory of a single perforating arteriole. Lesions <5 mm (that is,subcortical microinfarcts) are detectable only with high-resolution (3T and higher field-strengths) imaging65.

Brain atrophy
Cortical or subcortical brain volume loss unrelated to large traumatic injuries or infarctions.

Cortical microinfarcts
Small ischaemic lesions varying between 50 μm and a few millimetres139 that are revealed on high-resolution structural MRI and DWI.

FIGURE 1 | Features of CSVD.

lack clear corresponding clinical manifestations and may lead to progressive neurological decline such as cognitive decompensation or even vascular dementia (13), balance disorders, gait disturbances, urinary incontinence and affective disorders after several episodes of mild hemiparesis. The cognitive decrements caused by lacunae are dominated by executive function decrements. For motor impairment, an increased number of lacunae is associated with slower gait speed, wider step base and reduced balance; thalamic and frontal lacunae are associated with slower gait speed, reduced stride length and slower gait frequency (14).

White Matter Hyperintensities of Presumed Vascular Origin

Frontal lobe and parietal lobe are the predilection sites of WMHs (15), and about 80% of white people over 60 years old suffer from WMHs. According to the scope of WMH, it can be divided into three types: focal, initial fusion and extensive fusion (16, 17). The terminal region of WMHs blood supply is the predilection site of WMHs. In the supratentorial region, it is more common in basal ganglia, corona radiata and centrum semiovale (12). In the brain stem position, it is more found in the center of brainstem (18). Previous studies have shown that the progress of WMHs is related to cognitive impairment, behavioral impairment, gait abnormality and urination disorder, and develops with time (4, 19, 20).

PVS

The PVS is an extension of the extracerebral fluid gap surrounding the arteries, small arteries, veins, and small veins. Since the PVS enters from the brain surface or through the brain parenchyma, it can be traced through the lamellar soft meninges (21, 22). As patients age, PVS becomes increasingly evident and especially PVS at the base of the brain (21). Several studies have shown that enlarged PVS is associated with reduced cognitive function (22). The clinical symptoms associated with PVS are still in the exploratory stage. Several cross-sectional studies have found that PVS is associated with reduced information processing speed, reduced executive function, and increased risk of vascular dementia (23). However a meta-analysis that included five large studies found that PVS was not associated with cognitive function in healthy older adults (21). There is limited research on PVS and movement disorders. Previous case reports have suggested that severe striatal area PVS is associated with motor symptoms in Parkinson's disease, possibly because severe PVS affects striatal structure and function, which in turn leads to extrapyramidal symptoms.

CMB

SWI (susceptibility weighted imaging) or GRE (gradient recalled echo) is relatively sensitive to the exploration of cerebral microhemorrhage. The lesions are <5 mm in diameter on images, but not visible on other MRI sequences or CT (computed tomography, CT) (24). When complicated with chronic hypertension and atherosclerosis, microhemorrhage usually occurs in deep gray matter, and should be distinguished from calcification, normal blood vessels, iron deposition from other causes, hemorrhagic metastasis and brain trauma (3, 25).

Brain Atrophy

Brain atrophy is also an important imaging manifestation of CSVD, and ventricular enlargement can be seen on imaging. Usually, the T1 sequence is the most suitable for evaluation, and the corresponding rating scale can also be used (26). However, atrophy caused by large vascular infarction, trauma and other focal lesions is not attributed to brain atrophy caused by CSVD (3).

Classification of CSVD Based on Pathological Features

Cerebral Amyloid Angiopathy

Based on the pathological characteristics of CSVD, cerebral amyloid angiopathy (CAA) is considered to be a vascular disease caused by β-amyloid protein deposition in the middle and adventitia of cortex and pia mater artery. This disease occurs in the white matter of occipital lobe and frontal lobe. Different from systemic amyloidosis, CAA commonly occurs in middle-aged and elderly people, and the proportion of CAA over 55 years old is as high as 10–40% (27). In addition, 80% of AD patients also coexist with CAA lesions. The pathological features of this disease include the occurrence of hemorrhage foci of different sizes in cerebral lobes, subcortex and cortex with time changes, and the signs of subarachnoid hemorrhage in the past (28). Histochemical staining (such as Congo red staining) showed that β-amyloid protein was deposited on the vascular wall, and the thinning and loosening of the vascular wall, vascular dilatation and perivascular inflammation were another important pathological features of CAA (29). Increased vascular fragility is often one of the important reasons for bleeding tendency. Previous imaging studies suggest that chronic hypoperfusion is one of the risk factors of leukoencephalopathy, Therefore, lobar hemorrhage, non-traumatic subarachnoid hemorrhage and WMH are also common imaging manifestations of CAA (30). According to the revised Boston Diagnostic Criteria, the results of imaging examination are suggestive for diagnosis, but autopsy is still needed to make a definite diagnosis (31, 32).

CADASIL

CADASIL is an autosomal dominant disease associated with a mutation in the NOTCH3 gene on chromosome 19. The incidence rate reaches 2–4/100000, which has no significant correlation with gender. Clinically, it usually occurs at the age of 30–40 years old, with various clinical manifestations, including migraine, recurrent ischemic stroke, progressive cognitive dysfunction in young people and etc. Pathology suggests that the disease is a non-atherosclerotic CSVD without amyloid deposition (33). CADASIL is the most common genetic factor of subcortical vascular dementia. Under electron microscope, granular osmiophilic material (GOM) was found deposited in the smooth muscle layer of pia mater artery and perforator vessels. This abnormal deposition causes the loss of smooth muscle cells, which leads to the narrowing and even occlusion of the official lumen of small blood vessels (34–36).

The imaging features of the disease show a dynamic evolution process with the age of patients. First of all, WMHs can be found in temporal pole in most CADASIL patients around 30 years old, which is a characteristic different from other microangiopathy. At the age of 40, WMHs gradually progressed to the posterior temporal region, frontal region, parietal region, basal ganglia and thalamus (37). Subcortical U-shaped fibers can be involved, and subcortical lacunar infarction can often be found. The outer capsule and corpus callosum are also involved, which are important landmark lesions of CADASIL. At the age of 50, cerebral microhemorrhage appeared in the white matter area of the patient's brain and gradually developed. Subsequently, at the age of 50–60, large areas of WMHs, lacunae and Cerebral microhemorrhage were often seen on imaging examination. Due to the high risk of complications in CADASIL patients, invasive procedures such as angiography should be avoided as much as possible to aggravate the disease progression (36). Since CADASIL is a non-atherosclerotic type of CSVD without amyloid deposition, we further summarized the characteristics of CADASIL, small atherosclerotic CSVD and MS (**Table 1**).

PACNS

PACNS is a kind of CSVD characterized by idiopathic vasculitis, which is more common in patients aged 50–60 years, and its lesions are limited to the white matter area of brain and spinal cord. There is no obvious specific clinical manifestation of this disease, and headache is the common first symptom in clinic (38). Laboratory examination can find that the levels of inflammatory markers and proteins in cerebrospinal fluid are increased. The pathological manifestations of PACNS include inflammation, intimal hyperplasia, small and medium artery occlusion and necrosis and others, which often involve pia mater and cortical vessels (39). Although there are no specific imaging features in PACNS, some imaging features including multiple cortical-subcortical infarction, hemorrhage, enhancement of brain parenchyma and pia mater also provide some evidence

TABLE 1 | Identification and comparison of CADASIL, small arteriolosclerosis CSVD and MS.

	CADASIL	Small arteriolosclerosis CSVD	MS
Clinical course	Progressive	Progressive	Multiphase course
Pathological manifestation	Deposition of osmiophilic particles in vascular smooth muscle	Small arteriosclerosis, lipohyalinosis, fibrinoid necrosis	Small perivenous inflammation
Paraventricular	Involved	The lesion is symmetrical and less likely to be adjacent to the ventricular canal	The lesion is asymmetric and often adjacent to the ventricular canal
Temporal pole	Early involvement with a characteristic lesion site	Rarely involved	Involved
Corpus callosum	Commonly involved	Rarely involved	Frequently involved
U-shaped fiber bundle	Involved	Not involved	Involved
Cortex	Not commonly involved	Not commonly involved	Involved
Optical nerve	Not involved	Not involved	Involved
Brainstem	Early stages are less frequently involved and late stages can involve	Central part of the pons	Peripheral part of the pons (dorsal and ventral), asymmetric
Spine	Not involved	Not involved	Focally located in the periphery of the spinal cord, short segments, posterior and lateral cords are common
Laboratory tests	Genetic testing	VRFs	OCB, IgG in the sheath

for clinical diagnosis of PACNS. Clinical routine angiography can sometimes find multiple stenosis of small and medium-sized vessels, but brain biopsy is the gold standard for the diagnosis of this disease (38, 40).

MS

Clinical Features of MS

MS disease pedigree includes radiologically isolated syndrome (RIS), clinically isolated syndrome (CIS), and clinically diagnosed MS. According to the different characteristics of the course of disease, the clinically diagnosed MS can be classified as follows: relapsing-remitting multiple sclerosis (RRMS); secondary progressive multiple sclerosis (SPMS); primary progressive multiple sclerosis (PPMS); progressive relapsing multiple sclerosis (PRMS). Among them, RRMS is the most common in clinic, while PRMS is the rarest (41).

Pathological Features of MS

Generally, macular demyelination changes in white matter can be found in typical non-specific MS pathology. Classic MS lesions are considered to be slender or oblate lesions, usually distributed around venules (42). This demyelination lesion is thought to be associated with macrophage infiltration, perivascular cuff-like lymphocytes, accumulation of fibrin, and proliferation of reactive microglia. The white matter of MS patients is usually accompanied by abnormal deposition of hair iron, which is related to disease activity and usually deposited in the white matter where perivenous inflammation exists (43).

MS Imaging Features

MRI is the most important tool to assist clinical diagnosis and disease monitoring of MS (44). McDonald criteria revised in 2010 have proposed the spatial and temporal multiplicity of MS lesions: spatial multiplicity requires white matter hyperintensity (WMH) in at least two of the four typical sites: paraventricular, juxtacortical, subtentorial and spinal cord; Multiple timing requires the presence of both enhanced and non-enhanced lesions in a single MRI scan or the discovery of new lesions in follow-up MRI (45, 46). During follow-up, the new white matter hyperintensity of T2 image and the white matter hyperintensity enhanced by contrast medium are related to the activity of inflammation; the average sustainable time of enhancement is about 3 weeks (47).

On MRI, Dawson fingers sign is a classic lesion shape of paraventricular WMH in MS patients, which is usually perpendicular to ventricle, oval and distributed around venules, adjacent to ependyma. This has certain significance for differential diagnosis with non-specific WMHs and CSVD. The lesions of CSVD often appear in the posterior horn of paracele, and similar lesions may appear in MS. In the early stage of MS, specific lesions can be found at the junction of corpus callosum and ependyma. These lesions have both local patchy changes and discrete distribution. We named this distribution feature as "dot-line sign," which is usually easier to observe on sagittal T2-weighted imaging. This lesion is more likely to appear in the knee and body of corpus callosum (48). Of course, this kind of MS also needs to be differentiated from other types of diseases, including other primary or secondary demyelination diseases [neuromyelitis optica (NMO), acute disseminated encephalomyelitis (ADEM), CADASIL, Susac syndrome, progressive multifocal leukoencephalopathy (PML), etc.]; tumor diseases [lymphoma, glioma, gliomatosis cerbri (GC)-the latter is easily confused with leukoplakia due to its diffuse lesion]; traumatic injury (traumatic/diffuse axonal injury). The corpus callosum lesions of MS were enhanced in the acute phase while the corpus callosum lesions of CADASIL were not usually enhanced. Another typical lesion of MS is that WMHs

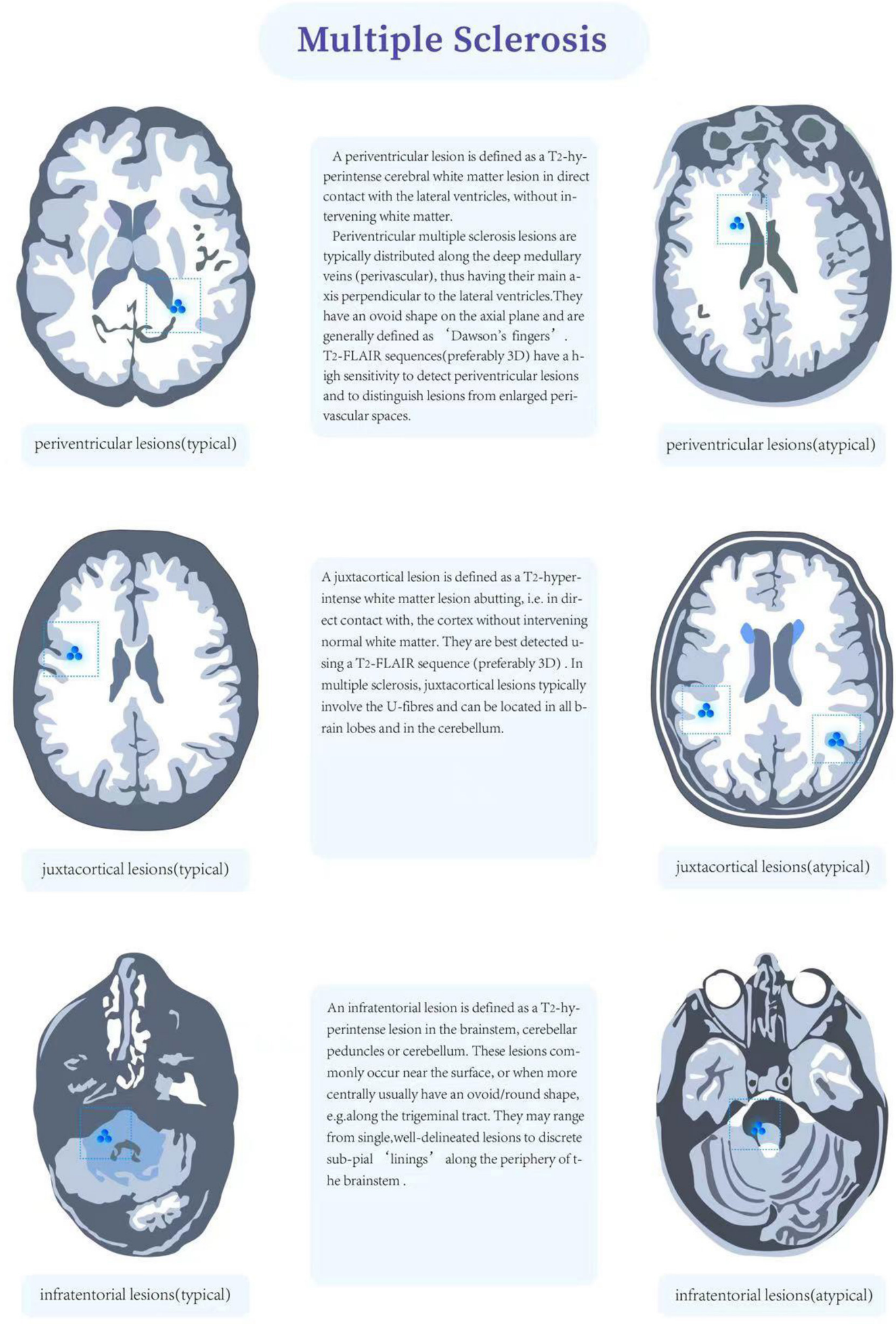

A periventricular lesion is defined as a T2-hyperintense cerebral white matter lesion in direct contact with the lateral ventricles, without intervening white matter.

Periventricular multiple sclerosis lesions are typically distributed along the deep medullary veins (perivascular), thus having their main axis perpendicular to the lateral ventricles.They have an ovoid shape on the axial plane and are generally defined as ‘Dawson's fingers’. T2-FLAIR sequences(preferably 3D) have a high sensitivity to detect periventricular lesions and to distinguish lesions from enlarged perivascular spaces.

A juxtacortical lesion is defined as a T2-hyperintense white matter lesion abutting, i.e. in direct contact with, the cortex without intervening normal white matter. They are best detected using a T2-FLAIR sequence (preferably 3D) . In multiple sclerosis, juxtacortical lesions typically involve the U-fibres and can be located in all brain lobes and in the cerebellum.

An infratentorial lesion is defined as a T2-hyperintense lesion in the brainstem, cerebellar peduncles or cerebellum. These lesions commonly occur near the surface, or when more centrally usually have an ovoid/round shape, e.g.along the trigeminal tract. They may range from single,well-delineated lesions to discrete sub-pial ‘linings’ along the periphery of the brainstem .

FIGURE 2 | Charateristics of multiple sclerosis lesion that that are typical **(right)** and atypical **(left)**.

near cortex involve U-shaped fibers under cortex. Generally, cortical lesions appear in the early stage of MS, which is related to cognitive dysfunction. Cortical lesions are usually smaller, and the contrast is more obvious under double inversion recovery sequence and high magnetic field intensity (49–51) (**Figure 2**).

Summary of MS

The McDonald diagnostic criteria have suggested spatial and temporal multiplicity in the distribution of MS lesions: spatial multiplicity requires the presence of white matter hyperintensity in at least two of the four typical locations in the paraventricular, subcortical, subepicentral and spinal cord regions; temporal multiplicity requires the presence of both enhancing and non-enhancing lesions on a single MRI scan or new lesions on follow-up MRI (45, 46). New white matter hyperintensities on follow-up T2 image and contrast-enhanced white matter hyperintensities correlate with the activity of inflammation; enhancement can persist for an average of about 3 weeks (47). Dawson's finger sign is the classic lesion pattern of paraventricular white matter hyperintensity in MS patients; these lesions are usually perpendicular to the ventricles, ovoid in shape and distributed around small veins. They are contiguous with the ventricular canal, which is important in relation to the non-specific These lesions are usually perpendicular to the ventricles, ovoid and distributed around small veins (52). Early in MS, specific callosal lesions can be found at the junction of the corpus callosum and the ventricular canal, and these lesions These lesions are both localized and discrete, forming a subcallosal "dotted line sign" that is usually more easily observed on sagittal T2 weighted images in the sagittal plane are more easily observed. Such lesions are more likely to be found in the knee and body of the corpus callosum (48). In MS, the corpus callosum lesions are enhanced in the acute phase, whereas in CADASIL the corpus callosum lesions are usually not enhanced. Proximal cortical white matter hyperintensities in MS patients involve subcortical U-shaped fibers, which is also a classical lesion location. On the other hand, there is a growing awareness of cortical lesions in MS, which may have more prognostic and diagnostic value in the future. The prognostic and diagnostic value of these lesions may increase in the future. For MR spectroscopy, previous studies summarized that patients with MS have shown increased glutamate concentrations in acute MS lesions, indicating hypoxic condition (53–55).

McDonald criteria also included the subtentorial area. Among them, MS occurring in the brainstem has certain characteristics. The lesions are usually located in the periphery of the brainstem (CSVD brainstem lesions are usually located in the middle of the brainstem), and the lesions are asymmetric or located on one side of the brainstem with clear boundaries (56). Cerebellar lesions usually affect larger white matter structures, such as the pontine arm (middle-cerebellar peduncle), although middle-cerebellar peduncle and white matter in cerebellar hemisphere may also be affected. Spinal cord lesions are present in 30 to 40% of CIS cases and up to 90% of clinically confirmed MS patients (52).

MS also often involves cervical spinal cord, such patients are in dangerous condition, and even die in severe cases. Normally, the spinal cord lesions have a clear boundary, which is less than one or two spinal segments in longitudinal direction, <50% of the cross-sectional area of spinal cord in axial plane, and the spinal cord lesions are usually located in the white matter around the spinal cord. Extensive spinal cord swelling is rare. Active lesions may be enhanced, although less frequently than brain lesions. Spinal cord atrophy can be seen occasionally in long course and progressive MS, especially in the upper segment (57). The similar disease of MS in peripheral organs is chronic inflammatory demyelination polyradiculoneuropathy (CIDP), which is a chronic multiphase disease involving peripheral nervous system (PNS).

To sum up, the diagnosis of MS should be based on the comprehensive analysis of patients' clinical data, laboratory examinations and auxiliary examinations, including the analysis of patients' medical history, cerebrospinal fluid components, such as oligoclonal bands (OCB) and intrathecal immunoglobulin G (IgG) synthesis, abnormal visual evoked potential (VEP) and imaging analysis. However, MS is often misdiagnosed due to atypical imaging features. About 25% of patients received MS treatment without suffering from MS. The imaging features of CSVD, NMO and ADEM are often confused with MS (58), but there is still no effective means to distinguish them, which poses great challenges for clinical diagnosis and treatment.

RELATIONSHIP BETWEEN CSVD AND MS

Currently, it is thought that there may be interaction between CSVD and MS, because the progression of CSVD and MS is positively correlated with age. Advanced age means that glial cells may have hypoxia (59), mitochondrial dysfunction (60), iron deposition (61) and other dysfunctions. These changes are obviously related to neurodegenerative changes. Recently, Geraldes et al. summarized that CSVD shares some features with MS and has been shown to contribute to the neuronal damage seen in vascular cognitive impairment (62). In addition, CSVD (35) has been found to be associated with neurodegeneration in young people with VRFs (63), which may also promote age-related neurodegeneration in MS. Therefore, we summarized the main possible reasons for the interaction value between MS and age-related CSVD: (i) the life expectancy of MS patients is longer (64), over 60 years old (65), and the risk of vascular complications is higher; (ii) vascular complications can promote the disease progression of MS (66), shorten the expected survival time (67–69), aggravate WML load and brain atrophy (70); (iii) the focal demyelination lesions in the watershed area of MS (71) are characterized by hypoperfusion and hypoxia (72–74), suggesting that there is an important relationship between the pathology of MS and cerebral artery perfusion. In addition, Lucchinetti et al. previously reported MS lesions divided into four patterns, in which two patterns (I and II) showed close similarities to T-cell-mediated or T-cell plus antibody-mediated autoimmune encephalomyelitis, and the other patterns (III and IV) were highly suggestive of a primary oligodendrocyte dystrophy, reminiscent of virus- or toxin-induced demyelination rather than autoimmunity. The pattern III is distal oligodendrogliopathy which means oligodendrocytic apoptosis due to hypoxia or viral infection (75, 76). Similar observations are reported independent researchers (77, 78). Santiago Martinez Sosa et al. also reported that The deep and periventricular white matter is preferentially affected in several neurological disorders, including CSVD and MS, suggesting that common pathogenic mechanisms may be involved in this injury and considered the potential pathogenic role of tissue hypoxia in lesion development, arising partly from the vascular anatomy of the affected white matter (1); (iv) chronic inflammatory microenvironment of MS can promote CSVD, furthermore, Robin et al. found that shared mechanism of white matter damage in ischemia and MS and reported that inflammation acts in distinct pathways because of the differing nature of the primary insult (79); (v) some MS patients benefit from using drugs targeting microvascular system (80–82). Furthermore, Chitnis et al. reported a case of Balo's concentric sclerosis, a variant of MS, with CADASIL mutation and suggested systematic testing for the CADASIL mutation in patients with a demyelinating presentation consistent with Balo concentric sclerosis or significant restricted diffusion on MRI (83) (**Table 1**).

The influencing mechanism of CSVD on the imaging features of MS remains to be unclear. It is possible that the increased load of T2 phase lesions in MS patients with VRFs is due to the superposition effect of paraventricular vascular WML, lacuna and microhemorrhage. Similarly, the more severe brain atrophy associated with VRFs in MS patients may also be due to the superposition of VRFs on MS basis (84). Although the previous understanding of MS is that multiple demyelination areas are found in pathological sections, and axons in these areas are relatively preserved, imaging and pathological studies have found that neuron/axon damage can occur at an early stage and is related to active inflammatory activity and demyelination (85, 86). However, age and duration of disease can affect the inflammatory response of WM and gray matter (GM) in lesion and non-lesion areas of MS, and the inflammatory response seems to decrease in elderly patients with longer course of disease (87, 88). In these patients, neurodegeneration may be related not only to persistent low-intensity inflammatory activity, but also to various mechanisms such as energy deficiency, oxidative damage, hypoxia, and energy reserve failure (72). Energy failure is an important concept for MS pathogenesis. Glucose and lactate transporters and connexin gap junctions have a crucial roles for energy transport among glial cells in MS (89–93). Recently, Philips et al. summarized oligodendrocytes transfer energy metabolites to neurons through cytoplasmic "myelinic" channels and monocarboxylate transporters, which allow for the fast delivery of short-carbon-chain energy metabolites like pyruvate and lactate to neurons. These substrates are metabolized and contribute to ATP synthesis in neurons (93). But this deficient process may be a cause of pathogenesis for MS. Age-related pathological processes, such as AD or vascular disease, may amplify the effects of these mechanisms and lead to increased neuronal damage (87).

The presence of CSVD in MS patients may mean an additional blow to the compensatory mechanism. In this case, chronic hypoxia caused by vascular dysfunction and hypoperfusion can cause neuron death and aggravate neurological dysfunction. In neurodegenerative diseases such as AD (94, 95) and vascular cognitive impairment (96), cerebral vascular lesions promote neuronal damage, aggravate pericyte and astrocyte dysfunction caused by chronic hypoperfusion and BBB permeability changes, oxidative stress, inflammation and mitochondrial damage (97). The theory of "blood vessel-neuron-inflammation" centered on NVU dysfunction in neurodegenerative diseases is also applicable to MS (95). Energy deficiency and tissue hypoxia caused by mitochondrial dysfunction in MS will lead to ion disorder and axonal degeneration, and the accompanying CSVD may aggravate this process, especially in watershed area (72). Not only the lesions related to MS and arteries and veins need further study (72), but also the characterization and quantification of CSVD, including the score of arterial wall changes, microbleeding and microinfarction, which is conducive to further exploring the relationship between CSVD and MS. Moreover, Geraldes et al. based on post-mortem study reported that an excess burden of cerebral small vessel disease in multiple sclerosis may explain the link between vascular comorbidity and accelerated irreversibility disability (98).

SUMMARY

In conclusion, this review compares and summarizes the clinical, pathological and imaging features of MS and CSVD and the effect of vascular diseases on MS, which is conducive to deepening our understanding of these two diseases, making correct differential diagnosis and giving patients correct treatment strategies in time.

AUTHOR CONTRIBUTIONS

BW, HaoL, and XL contributed to the conceptualization of the manuscript. BW, HaoL, XL, XH, LG, RF, KangC, and WW contributed to the writing of the manuscript. XH, HaiL, KangnC, ZZ, and LX contributed to the editing and revising of the manuscript. All authors contributed to the article and approved the submitted version.

REFERENCES

1. Martinez Sosa S, Smith KJ. Understanding a role for hypoxia in lesion formation and location in the deep and periventricular white matter in small vessel disease and multiple sclerosis. *Clin Sci.* (2017) 131:2503–24. doi: 10.1042/CS20170981
2. Thrippleton MJ, Backes WH, Sourbron S, Ingrisch M, van Osch MJP, Dichgans M, et al. Quantifying blood-brain barrier leakage in small vessel disease: review and consensus recommendations. *Alzheimers Dement.* (2019) 15:840–58. doi: 10.1016/j.jalz.2019.01.013
3. Pantoni L. Cerebral small vessel disease: from pathogenesis and clinical characteristics to therapeutic challenges. *Lancet Neurol.* (2010) 9:689–701. doi: 10.1016/S1474-4422(10)70104-6
4. Wardlaw JM, Smith EE, Biessels GJ, Cordonnier C, Fazekas F, Frayne R, et al. Neuroimaging standards for research into small vessel disease and its contribution to ageing and neurodegeneration.

Lancet Neurol. (2013) 12:822–38. doi: 10.1016/S1474-4422(13)70124-8

5. Wardlaw JM, Smith C, Dichgans M. Mechanisms of sporadic cerebral small vessel disease: insights from neuroimaging. *Lancet Neurol.* (2013) 12:483–97. doi: 10.1016/S1474-4422(13)70060-7
6. Lassmann H, Bruck W, Lucchinetti CF. The immunopathology of multiple sclerosis: an overview. *Brain Pathol.* (2007) 17:210–8. doi: 10.1111/j.1750-3639.2007.00064.x
7. Karussis D. The diagnosis of multiple sclerosis and the various related demyelinating syndromes: a critical review. *J Autoimmun.* (2014) 48-49:134–42. doi: 10.1016/j.jaut.2014.01.022
8. Ragonese P, Aridon P, Salemi G, D'Amelio M, Savettieri G. Mortality in multiple sclerosis: a review. *Eur J Neurol.* (2008) 15:123–7. doi: 10.1111/j.1468-1331.2007.02019.x
9. Cannistraro RJ, Badi M, Eidelman BH, Dickson DW, Middlebrooks EH, Meschia JF. Cns small vessel disease: a clinical review. *Neurology.* (2019) 92:1146–56. doi: 10.1212/WNL.0000000000007654
10. Solomon AJ, Bourdette DN, Cross AH, Applebee A, Skidd PM, Howard DB, et al. The contemporary spectrum of multiple sclerosis misdiagnosis: a multicenter study. *Neurology.* (2016) 87:1393–9. doi: 10.1212/WNL.0000000000003152
11. Doubal FN, Dennis MS, Wardlaw JM. Characteristics of patients with minor ischaemic strokes and negative MRI: a cross-sectional study. *J Neurol Neurosurg Psychiatry.* (2011) 82:540–2. doi: 10.1136/jnnp.2009.190298
12. Duering M, Csanadi E, Gesierich B, Jouvent E, Herve D, Seiler S, et al. Incident lacunes preferentially localize to the edge of white matter hyperintensities: insights into the pathophysiology of cerebral small vessel disease. *Brain.* (2013) 136:2717–26. doi: 10.1093/brain/awt184
13. Chen X, Wang J, Shan Y, Cai W, Liu S, Hu M, et al. Cerebral small vessel disease: neuroimaging markers and clinical implication. *J Neurol.* (2019) 266:2347–62. doi: 10.1007/s00415-018-9077-3
14. Litak J, Mazurek M, Kulesza B, Szmygin P, Litak J, Kamieniak P, et al. Cerebral small vessel disease. *Int J Mol Sci.* (2020) 21:9729. doi: 10.3390/ijms21249729
15. Wardlaw JM. Prevalence of cerebral white matter lesions in elderly people: a population based magnetic resonance imaging study: the Rotterdam scan study. *J Neurol Neurosurg Psychiatry.* (2001) 70:2–3. doi: 10.1136/jnnp.70.1.2
16. Fazekas F, Chawluk JB, Alavi A, Hurtig HI, Zimmerman RA. Mr Signal abnormalities at 1.5 T in Alzheimer's dementia and normal aging. *AJR Am J Roentgenol.* (1987) 149:351–6. doi: 10.2214/ajr.149.2.351
17. Wahlund LO, Barkhof F, Fazekas F, Bronge L, Augustin M, Sjogren M, et al. A new rating scale for age-related white matter changes applicable to MRI and CT. *Stroke.* (2001) 32:1318–22. doi: 10.1161/01.STR.32.6.1318
18. Erro ME, Gallego J, Herrera M, Bermejo B. Isolated pontine infarcts: etiopathogenic mechanisms. *Eur J Neurol.* (2005) 12:984–8. doi: 10.1111/j.1468-1331.2005.01119.x
19. Maillard P, Fletcher E, Harvey D, Carmichael O, Reed B, Mungas D, et al. White matter hyperintensity penumbra. *Stroke.* (2011) 42:1917–22. doi: 10.1161/STROKEAHA.110.609768
20. Schmidt R, Schmidt H, Haybaeck J, Loitfelder M, Weis S, Cavalieri M, et al. Heterogeneity in age-related white matter changes. *Acta Neuropathol.* (2011) 122:171–85. doi: 10.1007/s00401-011-0851-x
21. Brown R, Benveniste H, Black SE, Charpak S, Dichgans M, Joutel A, et al. Understanding the role of the perivascular space in cerebral small vessel disease. *Cardiovasc Res.* (2018) 114:1462–73. doi: 10.1093/cvr/cvy113
22. Wardlaw JM, Benveniste H, Nedergaard M, Zlokovic BV, Mestre H, Lee H, et al. Perivascular spaces in the brain: anatomy, physiology and pathology. *Nat Rev Neurol.* (2020) 16:137–53. doi: 10.1038/s41582-020-0312-z
23. Gertje EC, van Westen D, Panizo C, Mattsson-Carlgren N, Hansson O. Association of enlarged perivascular spaces and measures of small vessel and Alzheimer disease. *Neurology.* (2021) 96:e193–202. doi: 10.1212/WNL.0000000000011046
24. Shuaib A, Akhtar N, Kamran S, Camicioli R. Management of cerebral microbleeds in clinical practice. *Transl Stroke Res.* (2019) 10:449–57. doi: 10.1007/s12975-018-0678-z
25. Greenberg SM, Vernooij MW, Cordonnier C, Viswanathan A, Al-Shahi Salman R, Warach S, et al. Cerebral microbleeds: a guide to detection and interpretation. *Lancet Neurol.* (2009) 8:165–74. doi: 10.1016/S1474-4422(09)70013-4
26. Sarria-Estrada S, Acevedo C, Mitjana R, Frascheri L, Siurana S. Reproducibility of qualitative assessment of temporal lobe atrophy in MRI studies. *Radiologia.* (2015) 57:225–8. doi: 10.1016/j.rxeng.2014.04.007
27. Banerjee G, Carare R, Cordonnier C, Greenberg SM, Schneider JA, Smith EE, et al. The increasing impact of cerebral amyloid angiopathy: essential new insights for clinical practice. *J Neurol Neurosurg Psychiatry.* (2017) 88:982–94. doi: 10.1136/jnnp-2016-314697
28. Biessels GJ. Cerebral amyloid angiopathy: still a syndromal diagnosis. *Stroke.* (2020) 51:3487–8. doi: 10.1161/STROKEAHA.120.032703
29. Charidimou A, Boulouis G, Gurol ME, Ayata C, Bacskai BJ, Frosch MP, et al. Emerging concepts in sporadic cerebral amyloid angiopathy. *Brain.* (2017) 140:1829–50. doi: 10.1093/brain/awx047
30. Charidimou A, Gang Q, Werring DJ. Sporadic cerebral amyloid angiopathy revisited: recent insights into pathophysiology and clinical spectrum. *J Neurol Neurosur Ps.* (2012) 83:124–37. doi: 10.1136/jnnp-2011-301308
31. Knudsen KA, Rosand J, Karluk D, Greenberg SM. Clinical diagnosis of cerebral amyloid angiopathy: validation of the Boston criteria. *Neurology.* (2001) 56:537–9. doi: 10.1212/WNL.56.4.537
32. Zhang HL, Linn J, Bruckmann H, Greenberg SM. Prevalence of superficial siderosis in patients with cerebral amyloid angiopathy. *Neurology.* (2010) 75:1571. doi: 10.1212/WNL.0b013e3181f002c1
33. Di Donato I, Bianchi S, De Stefano N, Dichgans M, Dotti MT, Duering M, et al. Cerebral autosomal dominant arteriopathy with subcortical infarcts and leukoencephalopathy (Cadasil) as a model of small vessel disease: update on clinical, diagnostic, and management aspects. *BMC Med.* (2017) 15:41. doi: 10.1186/s12916-017-0778-8
34. Chabriat H, Vahedi K, Iba-Zizen MT, Joutel A, Nibbio A, Nagy TG, et al. Clinical spectrum of cadasil: a study of 7 families. Cerebral autosomal dominant arteriopathy with subcortical infarcts and leukoencephalopathy. *Lancet.* (1995) 346:934–9. doi: 10.1016/S0140-6736(95)91557-5
35. Singhal S, Rich P, Markus HS. The spatial distribution of MR Imaging abnormalities in cerebral autosomal dominant arteriopathy with subcortical infarcts and leukoencephalopathy and their relationship to age and clinical features. *AJNR Am J Neuroradiol.* (2005) 26:2481–7.
36. van den Boom R, Lesnik Oberstein SA, Ferrari MD, Haan J, van Buchem MA. Cerebral autosomal dominant arteriopathy with subcortical infarcts and leukoencephalopathy: MR imaging findings at different ages—3rd-6th Decades. *Radiology.* (2003) 229:683–90. doi: 10.1148/radiol.2293021354
37. Wang MM. Cadasil. *Handb Clin Neurol.* (2018) 148:733–43. doi: 10.1016/B978-0-444-64076-5.00047-8
38. Mandal J, Chung SA. Primary angiitis of the central nervous system. *Rheum Dis Clin North Am.* (2017) 43:503–18. doi: 10.1016/j.rdc.2017.06.001
39. Godasi R, Pang G, Chauhan S, Bollu PC. *Primary Central Nervous System Vasculitis*. Treasure Island, FL: Statpearls (2022).
40. Abdel Razek AA, Alvarez H, Bagg S, Refaat S, Castillo M. Imaging spectrum of Cns vasculitis. *Radiographics.* (2014) 34:873–94. doi: 10.1148/rg.344135028
41. Okuda DT. Unanticipated demyelinating pathology of the Cns. *Nat Rev Neurol.* (2009) 5:591–7. doi: 10.1038/nrneurol.2009.157
42. Dobson R, Giovannoni G. Multiple sclerosis - a review. *Eur J Neurol.* (2019) 26:27–40. doi: 10.1111/ene.13819
43. Williams R, Buchheit CL, Berman NE, LeVine SM. Pathogenic implications of iron accumulation in multiple sclerosis. *J Neurochem.* (2012) 120:7–25. doi: 10.1111/j.1471-4159.2011.07536.x
44. Filippi M, Evangelou N, Kangarlu A, Inglese M, Mainero C, Horsfield MA, et al. Ultra-high-field MR imaging in multiple sclerosis. *J Neurol Neurosurg Psychiatry.* (2014) 85:60–6. doi: 10.1136/jnnp-2013-305246
45. Montalban X, Tintore M, Swanton J, Barkhof F, Fazekas F, Filippi M, et al. Mri criteria for MS in patients with clinically isolated syndromes. *Neurology.* (2010) 74:427–34. doi: 10.1212/WNL.0b013e3181cec45c
46. Thompson AJ, Banwell BL, Barkhof F, Carroll WM, Coetzee T, Comi G, et al. Diagnosis of multiple sclerosis: 2017 revisions of the Mcdonald criteria. *Lancet Neurol.* (2018) 17:162–73. doi: 10.1016/S1474-4422(17)30470-2
47. Cotton F, Weiner HL, Jolesz FA, Guttmann CR. Mri contrast uptake in new lesions in relapsing-remitting ms followed at weekly intervals. *Neurology.* (2003) 60:640–6. doi: 10.1212/01.WNL.0000046587.83503.1E
48. Lisanti CJ, Asbach P, Bradley WG Jr. The ependymal "Dot-Dash" Sign: an MR imaging finding of early multiple sclerosis. *AJNR Am J Neuroradiol.* (2005) 26:2033–6.

49. de Graaf WL, Kilsdonk ID, Lopez-Soriano A, Zwanenburg JJ, Visser F, Polman CH, et al. Clinical application of multi-contrast 7-T Mr imaging in multiple sclerosis: increased lesion detection compared to 3 T confined to grey matter. *Eur Radiol.* (2013) 23:528–40. doi: 10.1007/s00330-012-2619-7
50. Filippi M, Rocca MA, Calabrese M, Sormani MP, Rinaldi F, Perini P, et al. Intracortical lesions: relevance for new MRI diagnostic criteria for multiple sclerosis. *Neurology.* (2010) 75:1988–94. doi: 10.1212/WNL.0b013e3181ff96f6
51. Roosendaal SD, Moraal B, Pouwels PJ, Vrenken H, Castelijns JA, Barkhof F, et al. Accumulation of cortical lesions in MS: relation with cognitive impairment. *Mult Scler.* (2009) 15:708–14. doi: 10.1177/1352458509102907
52. Filippi M, Rocca MA. Mr imaging of multiple sclerosis. *Radiology.* (2011) 259:659–81. doi: 10.1148/radiol.11101362
53. Srinivasan R, Sailasuta N, Hurd R, Nelson S, Pelletier D. Evidence of elevated glutamate in multiple sclerosis using magnetic resonance spectroscopy at 3 T. *Brain.* (2005) 128(Pt. 5):1016–25. doi: 10.1093/brain/awh467
54. Srinivasan R, Cunningham C, Chen A, Vigneron D, Hurd R, Nelson S, et al. Te-averaged two-dimensional proton spectroscopic imaging of glutamate at 3 T. *Neuroimage.* (2006) 30:1171–8. doi: 10.1016/j.neuroimage.2005.10.048
55. Trapp BD, Stys PK. Virtual hypoxia and chronic necrosis of demyelinated axons in multiple sclerosis. *Lancet Neurol.* (2009) 8:280–91. doi: 10.1016/S1474-4422(09)70043-2
56. Lu Z, Zhang B, Qiu W, Kang Z, Shen L, Long Y, et al. Comparative brain stem lesions on MRI of acute disseminated encephalomyelitis, neuromyelitis optica, and multiple sclerosis. *PLoS ONE.* (2011) 6:e22766. doi: 10.1371/journal.pone.0022766
57. Muccilli A, Seyman E, Oh J. Spinal cord MRI in multiple sclerosis. *Neurol Clin.* (2018) 36:35–57. doi: 10.1016/j.ncl.2017.08.009
58. Solomon AJ, Klein EP, Bourdette D. "Undiagnosing" multiple sclerosis: the challenge of misdiagnosis in Ms. *Neurology.* (2012) 78:1986–91. doi: 10.1212/WNL.0b013e318259e1b2
59. Raz L, Knoefel J, Bhaskar K. The neuropathology and cerebrovascular mechanisms of dementia. *J Cereb Blood Flow Metab.* (2016) 36:172–86. doi: 10.1038/jcbfm.2015.164
60. Currais A. Ageing and inflammation - a central role for mitochondria in brain health and disease. *Ageing Res Rev.* (2015) 21:30–42. doi: 10.1016/j.arr.2015.02.001
61. Ward RJ, Zucca FA, Duyn JH, Crichton RR, Zecca L. The role of iron in brain ageing and neurodegenerative disorders. *Lancet Neurol.* (2014) 13:1045–60. doi: 10.1016/S1474-4422(14)70117-6
62. Geraldes R, Esiri MM, DeLuca GC, Palace J. Age-related small vessel disease: a potential contributor to neurodegeneration in multiple sclerosis. *Brain Pathol.* (2017) 27:707–22. doi: 10.1111/bpa.12460
63. Fazekas F, Schmidt R, Kleinert R, Kapeller P, Roob G, Flooh E. The spectrum of age-associated brain abnormalities: their measurement and histopathological correlates. *J Neural Transm Suppl.* (1998) 53:31–9. doi: 10.1007/978-3-7091-6467-9_4
64. Marrie RA, Elliott L, Marriott J, Cossoy M, Blanchard J, Leung S, et al. Effect of comorbidity on mortality in multiple sclerosis. *Neurology.* (2015) 85:240–7. doi: 10.1212/WNL.0000000000001718
65. Solaro C, Ponzio M, Moran E, Tanganelli P, Pizio R, Ribizzi G, et al. The changing face of multiple sclerosis: prevalence and incidence in an aging population. *Mult Scler.* (2015) 21:1244–50. doi: 10.1177/1352458514561904
66. Marrie RA, Horwitz RI. Emerging effects of comorbidities on multiple sclerosis. *Lancet Neurol.* (2010) 9:820–8. doi: 10.1016/S1474-4422(10)70135-6
67. Capkun G, Dahlke F, Lahoz R, Nordstrom B, Tilson HH, Cutter G, et al. Mortality and comorbidities in patients with multiple sclerosis compared with a population without multiple sclerosis: an observational study using the us department of defense administrative claims database. *Mult Scler Relat Dis.* (2015) 4:546–54. doi: 10.1016/j.msard.2015.08.005
68. Goodin DS, Corwin M, Kaufman D, Golub H, Reshef S, Rametta MJ, et al. Causes of death among commercially insured multiple sclerosis patients in the United States. *PloS ONE.* (2014) 9:e105207. doi: 10.1371/journal.pone.0105207
69. Marrie RA, Rudick R, Horwitz R, Cutter G, Tyry T, Campagnolo D, et al. Vascular comorbidity is associated with more rapid disability progression in multiple sclerosis. *Neurology.* (2010) 74:1041–7. doi: 10.1212/WNL.0b013e3181d6b125
70. Kappus N, Weinstock-Guttman B, Hagemeier J, Kennedy C, Melia R, Carl E, et al. Cardiovascular risk factors are associated with increased lesion burden and brain atrophy in multiple sclerosis. *J Neurol Neurosurg Psychiatry.* (2016) 87:181–7. doi: 10.1136/jnnp-2014-310051
71. Haider L, Zrzavy T, Hametner S, Hoftberger R, Bagnato F, Grabner G, et al. The topograpy of demyelination and neurodegeneration in the multiple sclerosis brain. *Brain.* (2016) 139(Pt. 3):807–15. doi: 10.1093/brain/awv398
72. Correale J, Gaitan MI, Ysrraelit MC, Fiol MP. Progressive multiple sclerosis: from pathogenic mechanisms to treatment. *Brain.* (2017) 140:527–46. doi: 10.1093/brain/aww258
73. Davies AL, Desai RA, Bloomfield PS, McIntosh PR, Chapple KJ, Linington C, et al. Neurological deficits caused by tissue hypoxia in neuroinflammatory disease. *Ann Neurol.* (2013) 74:815–25. doi: 10.1002/ana.24006
74. Desai RA, Davies AL, Tachrount M, Kasti M, Laulund F, Golay X, et al. Cause and prevention of demyelination in a model multiple sclerosis lesion. *Ann Neurol.* (2016) 79:591–604. doi: 10.1002/ana.24607
75. Lucchinetti C, Bruck W, Parisi J, Scheithauer B, Rodriguez M, Lassmann H. Heterogeneity of multiple sclerosis lesions: implications for the pathogenesis of demyelination. *Ann Neurol.* (2000) 47:707–17. doi: 10.1002/1531-8249(200006)47:6<707::AID-ANA3>3.0.CO;2-Q
76. Aboul-Enein F, Rauschka H, Kornek B, Stadelmann C, Stefferl A, Bruck W, et al. Preferential loss of myelin-associated glycoprotein reflects hypoxia-like white matter damage in stroke and inflammatory brain diseases. *J Neuropathol Exp Neurol.* (2003) 62:25–33. doi: 10.1093/jnen/62.1.25
77. Barnett MH, Prineas JW. Relapsing and remitting multiple sclerosis: pathology of the newly forming lesion. *Ann Neurol.* (2004) 55:458–68. doi: 10.1002/ana.20016
78. Masaki K, Suzuki SO, Matsushita T, Matsuoka T, Imamura S, Yamasaki R, et al. Connexin 43 astrocytopathy linked to rapidly progressive multiple sclerosis and neuromyelitis optica. *PLoS ONE.* (2013) 8:e72919. doi: 10.1371/journal.pone.0072919
79. Brown RB, Traylor M, Burgess S, Sawcer S, Markus HS. Do cerebral small vessel disease and multiple sclerosis share common mechanisms of white matter injury? *Stroke.* (2019) 50:1968–72. doi: 10.1161/STROKEAHA.118.023649
80. Chataway J, Schuerer N, Alsanousi A, Chan D, MacManus D, Hunter K, et al. Effect of high-dose simvastatin on brain atrophy and disability in secondary progressive multiple sclerosis (Ms-Stat): a randomised, placebo-controlled, phase 2 trial. *Lancet.* (2014) 383:2213–21. doi: 10.1016/S0140-6736(13)62242-4
81. Miller H, Newell DJ, Ridley A. Multiple sclerosis. Trials of maintenance treatment with prednisolone and soluble aspirin. *Lancet.* (1961) 1:127–9. doi: 10.1016/S0140-6736(61)91308-3
82. Nofer JR, Bot M, Brodde M, Taylor PJ, Salm P, Brinkmann V, et al. Fty720, a synthetic sphingosine 1 phosphate analogue, inhibits development of atherosclerosis in low-density lipoprotein receptor-deficient mice. *Circulation.* (2007) 115:501–8. doi: 10.1161/CIRCULATIONAHA.106.641407
83. Chitnis T, Hollmann TJ. Cadasil mutation and Balo concentric sclerosis: a link between demyelination and ischemia? *Neurology.* (2012) 78:221–3. doi: 10.1212/WNL.0b013e31823fcd3c
84. Launer LJ, Lewis CE, Schreiner PJ, Sidney S, Battapady H, Jacobs DR, et al. Vascular factors and multiple measures of early brain health: cardia brain MRI study. *PLoS ONE.* (2015) 10:e0122138. doi: 10.1371/journal.pone.0122138
85. Ferguson B, Matyszak MK, Esiri MM, Perry VH. Axonal damage in acute multiple sclerosis lesions. *Brain.* (1997) 120 (Pt. 3):393–9. doi: 10.1093/brain/120.3.393
86. Trapp BD, Peterson J, Ransohoff RM, Rudick R, Mork S, Bo L. Axonal transection in the lesions of multiple sclerosis. *N Engl J Med.* (1998) 338:278–85. doi: 10.1056/NEJM199801293380502
87. Fieschi C, Gottlieb A, De Carolis V. ischaemic lacunae in the spinal cord of arteriosclerotic subjects. *J Neurol Neurosurg Psychiatry.* (1970) 33:138–46. doi: 10.1136/jnnp.33.2.138
88. Frischer JM, Bramow S, Dal-Bianco A, Lucchinetti CF, Rauschka H, Schmidbauer M, et al. The relation between inflammation and neurodegeneration in multiple sclerosis brains. *Brain.* (2009) 132(Pt. 5):1175–89. doi: 10.1093/brain/awp070
89. Cambron M, D'haeseleer M, Laureys G, Clinckers R, Debruyne J, De Keyser J. White-matter astrocytes, axonal energy metabolism, and axonal

degeneration in multiple sclerosis. *J Cerebr Blood F Met.* (2012) 32:413–24. doi: 10.1038/jcbfm.2011.193

90. Nijland PG, Michailidou I, Witte ME, Mizee MR, van der Pol SMA, van het Hof B, et al. Cellular distribution of glucose and monocarboxylate transporters in human brain white matter and multiple sclerosis lesions. *Glia.* (2014) 62:1125–41. doi: 10.1002/glia.22667
91. Masaki K. Early disruption of glial communication via connexin gap junction in multiple sclerosis, Balo's disease and neuromyelitis optica. *Neuropathology.* (2015) 35:469–80. doi: 10.1111/neup.12211
92. Nijland PG, Molenaar RJ, van der Pol SM, van der Valk P, van Noorden CJ, de Vries HE, et al. Differential expression of glucose-metabolizing enzymes in multiple sclerosis lesions. *Acta Neuropathol Commun.* (2015) 3:79. doi: 10.1186/s40478-015-0261-8
93. Philips T, Rothstein JD. Oligodendroglia: metabolic supporters of neurons. *J Clin Invest.* (2017) 127:3271–80. doi: 10.1172/JCI90610
94. Di Marco LY, Venneri A, Farkas E, Evans PC, Marzo A, Frangi AF. Vascular dysfunction in the pathogenesis of Alzheimer's disease–a review of endothelium-mediated mechanisms and ensuing vicious circles. *Neurobiol Dis.* (2015) 82:593–606. doi: 10.1016/j.nbd.2015.08.014
95. Zlokovic BV. Neurovascular pathways to neurodegeneration in alzheimer's disease and other disorders. *Nat Rev Neurosci.* (2011) 12:723–38. doi: 10.1038/nrn3114
96. Prins ND, Scheltens P. White matter hyperintensities, cognitive impairment and dementia: an update. *Nat Rev Neurol.* (2015) 11:157–65. doi: 10.1038/nrneurol.2015.10
97. Szolnoki Z, Szekeres M, Szaniszlo I, Balda G, Bodor A, Kondacs A, et al. Decreased number of mitochondria in leukoaraiosis. *Arch Med Res.* (2015) 46:604–8. doi: 10.1016/j.arcmed.2015.11.002
98. Geraldes R, Esiri MM, Perera R, Yee SA, Jenkins D, Palace J, et al. Vascular disease and multiple sclerosis: a post-mortem study exploring their relationships. *Brain.* (2020) 143:2998–3012. doi: 10.1093/brain/awaa255

Conflict of Interest: The authors declare that the research was conducted in the absence of any commercial or financial relationships that could be construed as a potential conflict of interest.

frontiers | Frontiers in Neurology

ORIGINAL RESEARCH
published: 29 June 2022
doi: 10.3389/fneur.2022.851735

Excessive Visit-to-Visit Small and Dense Low-Density Lipoproteins Elevate Cerebral Small Vessel Disease Progression Risk in the Elderly

Weike Liu*[1]*, Jing Xu*[1]*, Huajing Song*[2,3]*, Chunju Zhang*[2,3]*, Yanli Yao*[2,3]*, Hua Zhang*[2,3]*, Yue-Chun Li*[1]** and Zhendong Liu*[2,3]**

[1] Department of Cardiology, Second Affiliated Hospital and Yuying Children's Hospital of Wenzhou Medical University, Wenzhou, China, [2] Department of Cardiology, Shandong Provincial Hospital Affiliated to Shandong First Medical University, Jinan, China, [3] School of Basic Medicine, Shandong First Medical University and Shandong Academy of Medical Sciences, Jinan, China

Objective: Small and dense low-density lipoprotein (sdLDL) elevation may be among the most sensitive early biomarkers for nascent cardiovascular disease. This study, therefore, investigated the association between visit-to-visit changes in sdLDL and cerebral small vessel disease (CSVD) progression in older individuals, and the influence of *Apolipoprotein E* (*APOE*) genotype on this association.

Methods: Between April 2007 and July 2009, 1,143 participants ≥60 years old were recruited from the Shandong region of China, and sdLDL was measured at baseline and at each follow-up visit. White matter hyperintensities (WMHs), lacunes, microbleeds, and enlarged perivascular spaces (EPVSs) were assessed by magnetic resonance imaging. The *APOE* genotype was determined and participants were stratified as $\varepsilon 4$-positive or $\varepsilon 4$-negative.

Results: During an average follow-up of 86.0 months, 225 participants (19.7%) developed WMH progression, 193 (16.9%) lacune progression, 170 (14.9%) microbleed progression, and 185 (16.2%) EPVS progression. Compared with patients in the first (lowest) tertile of visit-to-visit mean sdLDL, those in the second and third tertiles demonstrated significantly greater risks of WMH progression (53.5 and 105.3% higher), lacune progression (53.3 and 60.8%), microbleed progression (47.2 and 127.6%), and EPVS progression (54.0 and 135.0%) after adjustment for confounders (all adjusted P values for trends <0.001). Compared with patients in the first tertile of visit-to-visit sdLDL SD, those in the second and third tertiles also demonstrated significantly greater risks of WMH progression (49.9% and 143.6%), lacune progression (75.3 and 178.0%), microbleed progression (12.7 and 64.7%), and EPVS progression (41.7 and 114.6%) after adjustment (all $P < 0.001$). There were significant and positive visit-to-visit mean sdLDL × visit-to-visit sdLDL SD, visit-to-visit mean sdLD×$\varepsilon 4$-positive, visit-to-visit sdLDL SD×$\varepsilon 4$-positive, and visit-to-visit mean sdLDL×visit-to-visit sdLDL

OPEN ACCESS

Edited by:
Tao Liu,
Hainan General Hospital, China

Reviewed by:
Cheryl Wellington,
University of British Columbia, Canada
Haiqing Song,
Capital Medical University, China
Cui Yi,
Shandong University, China

***Correspondence:**
Yue-Chun Li
liyuechun1980@sina.com
Zhendong Liu
zhendongliu876@126.com

Specialty section:
This article was submitted to
Applied Neuroimaging,
a section of the journal
Frontiers in Neurology

Received: *28 January 2022*
Accepted: *01 June 2022*
Published: *29 June 2022*

Citation:
Liu W, Xu J, Song H, Zhang C, Yao Y, Zhang H, Li Y-C and Liu Z (2022) Excessive Visit-to-Visit Small and Dense Low-Density Lipoproteins Elevate Cerebral Small Vessel Disease Progression Risk in the Elderly. Front. Neurol. 13:851735. doi: 10.3389/fneur.2022.851735

SD×*ε4*-positive interactions influencing CSVD progression after confounder adjustment (all $P<0.05$).

Conclusion: Large and variable visit-to-visit changes in sdLDL are independent predictors of aggressive CSVD progression, and this association is strongly influenced by *APOE ε4* allele genotype.

Keywords: lipid, variability, Apolipoprotein E, risk factor, cerebral small vessel disease

INTRODUCTION

Cerebral small vessel disease (CSVD) is a major contributor to stroke and dementia in older individuals (1, 2). Indeed, CSVD is implicated in 25%−30% of strokes and up to 45% of dementia cases. The MRI hallmarks of CSVD are well-established, namely, white matter hyperintensities (WMHs), lacunes, microbleeds, and enlarged perivascular spaces (EPVSs) (1–3). Nonetheless, the exact etiology of CSVD is not fully understood, which has impeded the development of effective strategies for prevention and control (4).

Elevated serum low-density lipoprotein cholesterol (LDL-C) is widely regarded as the primary risk factor for macroangiopathic cardiovascular diseases, including myocardial infarction and stroke (5, 6), and several guidelines recommend LDL-C-lowering medication as the primary preventive therapy (7–9). However, the efficacy of LDL-C-lowering medications, such as statins, on CSVD progression is still controversial (10–14), possibly due to the paucity of data on the associations between various LDL-C fractions and CSVDs (15).

Low-density lipoprotein cholesterol particles are heterogeneous and fractionated based on size and density into large buoyant and small dense particles (16, 17). The small dense particles, constituting the so-called small and dense low-density lipoprotein (sdLDL) fraction, are more atherogenic than the large buoyant particles due to greater susceptibility to oxidation, higher cell membrane permeability, and reduced affinity for the LDL receptor (17, 18). Therefore, sdLDL has been suggested as a sensitive predictive biomarker for the early diagnosis of cardiovascular diseases, particularly atherosclerosis (17, 19–21). However, the association between sdLDL and CSVD progression remains unclear. In this study, our major objective was to investigate the association between CSVD progression and visit-to-visit changes in mean sdLDL among older individuals.

METHODS

Study Participants and Design

To clarify the role of sdLDL in CSVD progression, 1,143 participants aged ≥60 years old were recruited between April 2007 and July 2009 from the Shandong area of China for a prospective and population-based cohort study (identifier at www.chictr.org.cn/, ChiCTR–EOC−17013598) (10, 22). The exclusion criteria were as follows: history of stroke/transient ischemic attack, Alzheimer's disease, Parkinson's disease, schizophrenia, seizures, claustrophobia, bipolar disorder, myocardial infarction, congestive heart failure, liver and renal diseases, dialysis treatment, drug and alcohol abuse, malignancy, contraindications to MRI, less than two annual sdLDL measurements and one brain MRI assessments during follow-up, and unwilling to provide informed consent.

The research ethics committee of the Institute of Basic Medicine, Shandong Academy of Medical Sciences, Shandong, China approved the study protocol. Each participant provided informed written consent and the study was conducted in compliance with the Declaration of Helsinki.

Follow-UP

As previously described (10, 22), participants were examined at six-month intervals after the baseline measurements with the help of family physicians. Demographic and clinical characteristics including current medications such as antidyslipidemic, antihypertensive, antidiabetic, and antiplatelet drugs were recorded at every clinical visit. Total cholesterol (TCHO), triglyceride, high-density lipoprotein cholesterol (HDL-C), LDL-C, sdLDL, and fasting plasma glucose were assessed at baseline and at annual follow-up visits. After corresponding sdLDL assessments, respectively, white matter hyperintensities, lacunes, microbleeds, and EPVS were determined by MRI at baseline (2007–2009) and at three subsequent visits during the periods 2009–2012, 2013–2015, and 2016–2018.

Measurements of Visit-to-Visit Mean and Variation in SdLDL

Venous blood samples were collected from each participant in the morning after overnight fasting. Blood plasma and mononuclear cells were separated and stored at −80°C for lipid assessment and *APOE* genotype determination, respectively. Plasma TCHO, triglycerides, HDL-C, LDL-C, and glucose were assessed using routine laboratory methods and sdLDL was determined using an sdLDL "Seiken" kit (Denka Seiken Co. Ltd, Tokyo, Japan) and Hitachi 7600 automatic biochemical analyzer (Hitachi, Japan) (23, 24). The participants received at least two annual sdLDL measurements during follow-up. The mean and SD in sdLDL of each participant were estimated from these serial sdLDL measurements.

Abbreviations: APOE, Apolipoprotein E; CSVD, cerebral small vessel disease; EPVS, enlarged perivascular spaces; FLAIR, fluid-attenuated inversion recovery; HDL-C, high-density lipoprotein cholesterol; ICV, intracranial volume; LDL-C, low-density lipoprotein cholesterol; sdLDL, small and dense low-density lipoprotein; TCHO, total cholesterol; WMH, white matter hyperintensities.

Brain MRI Assessment

Neuroimaging markers for CSVD were assessed on 3.0-Tesla scanners (GE Medical Systems, Pittsburgh, PA, USA; GE Systems, Milwaukee, WI, USA; or Siemens Medical, Erlangen, Germany) using protocols described previously (11, 22). Briefly, scans were acquired using T1-weighted 3-dimensional magnetization-prepared rapid gradient echo, T2-weighted 3-dimensional fast spin-echo, fluid-attenuated inversion recover (FLAIR), and T2*-weighted gradient-echo sequences. Montreal Neurological Institute templates were applied to normalize MRIs and then spatial transformation matrices were obtained. The International Consortium for Brain Mapping template for East Asian Brains was used to correct for differences in individual MRI features during the normalization. Images were then smoothed and the variability in local anatomy among subjects was minimized using a Gaussian filter.

White matter hyperintensities volume was computed from periventricular regions (frontal, parietal, occipital, and temporal), subcortical regions (frontal, parietal, occipital, and temporal), basal ganglia, and infratentorial regions on segmented T2-weighted and FLAIR axial images using FreeSurfer. The WMH-to-intracranial volume (ICV) ratio ([WMH (ml)/total intracranial volume (ml)] × 100%) was calculated to normalize individual WMH volumes. Volumetric analysis was conducted using the brain extraction tool of the FSL software package (FMRIB Software Library, Oxford, UK, www.fmrib.ox.ac.uk/fsl, version 4.19). The individual WMH pattern was graded on FLAIR images according to the Fazekas scale as none, punctuate, early confluent, and confluent.

Lacunes, microbleeds, and EPVSs were determined according to the diagnostic criteria defined in STRIVE v1 (STandards for ReportIng Vascular changes on nEuroimaging version 1). A lacune was defined as a 3–15 mm cavity with cerebrospinal-fluid-like signal intensity involving the white matter, internal capsule, basal ganglia, thalamus, or brain stem on a combination of T1-weighted, T2-weighted, and FLAIR images. Microbleeds in the brain parenchyma were defined on T2*-weighted images as oval or round homogenous and hypointense foci of diameter 2–10 mm. Mimics of microbleeds arising from signal averaging of bone, calcifications, and sulcal vessel signals on T2*-weighted images were systematically distinguished and excluded. Enlarged perivascular spaces were defined as visible fluid-filled spaces adjacent to cerebral vessels on T2-weighted and FLAIR images and distinguished from small lacunes of presumed vascular origin.

Each available scan was rated in a side-by-side fashion by experienced neuroradiologists initially blinded to clinical details, and consensus meetings were held to resolve disagreements among raters. A total of one hundred and forty randomly selected MRI scans were scored first to assess interrater and intrarater reliability. The interrater and intrarater coefficients of variation for WMH volume were 0.94 and 0.92, and the weighted Cohen's kappa values were 0.88 and 0.87 for the Fazekas scale, 0.84 and 0.83 for lacunes, 0.85 and 0.83 for microbleeds, and 0.79 and 0.80 for EPVSs, respectively, indicating good reliability.

Identification of CSVD Progression

The progression of each CSVD neuroimaging hallmark was determined from at least two MRI assessments during follow-up. The WMH progression was assessed by volume change and visual rating. The volume change during the follow-up period was defined as the difference between each successive follow-up WMH volume measurement minus the baseline volume, while the visual rating of absence or presence of progression was assessed using the modified Rotterdam Progression scale (scores of 0 and 1, respectively) (25, 26). For lacunes, microbleeds, and EPVSs, progression was defined as the presence of any new lesions on follow-up scans (presence = 1 and absence = 0) (27). The progression of total CSVD burden was defined as the new incident of coexistence of WMH, lacune, microbleeds, and EPVSs in this study. It was rated as 1 if one of the four markers occurred, and the total score ranged from 1 to 4.

Apolipoprotein E (APOE) Genotyping

All participants were genotyped for the *APOE* rs429358 and rs7412 single-nucleotide polymorphisms by PCR using the TaqMan genotyping kit (Applied Biosystems, Foster City, CA, USA), forward primer 5'-TTG AAG GCC TAC AAA TCG GAA CTG-3', and reverse primer 5'-CCG GCT GCC CAT CTC CAT CCG-3' (11, 28, 29). Participants with the *ε2/ε4*, *ε3/ε4*, or *ε4/ε4* genotype were categorized as *ε4*-positive carriers, while participants with the *ε2/ε2*, *ε2/ε3*, or *ε3/ε3* genotype were categorized as *ε4*-negative carriers (11, 28).

Statistical Analysis

Participants were divided into three tertiles of visit-to-visit mean sdLDL and sdLDL SD. Variables are presented as mean (SD), median [interquartile range (IQR)], or number (percentage) as appropriate. The normality of continuous variables was determined using the Kolmogorov–Smirnov test. Mean baseline characteristics were compared among groups by one-way ANOVA with *post hoc* Bonferroni's correction, Kruskal–Wallis test with *post hoc* Wilcoxon rank-sum test, or chi-square test as indicated. Differences in the trends of WMH volume and WMH-to-ICV ratio were assessed using a linear mixed model and differences in CSVD progression risk by Kaplan–Meier analysis and log-rank test among groups. The hazard ratio (HR) with 95% CI was estimated using the Cox proportional hazards model. Models were initially adjusted for age and sex (model 1). Model 2 adjusted for smoking; alcohol consumption; the initial body mass index, blood pressure, lipids, and fasting plasma glucose at baseline; the histories of hypertension, diabetes, and dyslipidemia; medications; and the initial WMH volume (for the changes in WMH volume analysis) and WMH-to-ICV ratio (for the changes in WMH fraction analysis) at baseline base on model 1. Model 3 adjusted for visit-to-visit mean sdLDL (for the models grouped by the tertile of variability in sdLDL), variability in sdLDL (for the models grouped by the tertile of visit-to-visit mean sdLDL), and *APOE* genotype. We also conducted an exploratory investigation on the influences of visit-to-visit mean sdLDL×sdLDL SD, visit-to-visit mean sdLD×*APOE ε4* genotype, visit-to-visit sdLDL SD×*APOE ε4* genotype, and visit-to-visit mean sdLDL×sdLDL SD×*APOE ε4* genotype interactions on CSVD progression. Missing data were imputed using chained equations. All statistical analyses were performed using SPSS v.24.0 (SPSS Inc., Chicago, IL, USA). A $P < 0.05$ (two-tailed) was considered statistically significant for all tests.

RESULTS

Baseline Characteristics

There were 1,309 initial enrolled individuals at baseline in this study. Among them, 69 failed in less than two annual sdLDL measurements and 51 failed in at least one brain MRI assessment during the follow-up period, and 46 failed to identify APOE genotype. Finally, 1,143 participants were eligible and used for further analyses. **Table 1** summarizes the baseline characteristics of the eligible participants, including brain MRI parameters and *APOE* genotype. **Supplementary Figure 1** presents the changes in sdLDL during the follow-up period. The median visit-to-visit mean sdLDL was 0.60 mmol/l [IQR, 0.49–0.72 mmol/l] and the median visit-to-visit sdLDL SD was 0.25 mmol/l [0.17–0.34 mmol/l]. The tertiles of visit-to-visit mean sdLDL were <0.53, 0.53–0.66, and ≥0.67 mmol/l and the tertiles for visit-to-visit sdLDL SD were <0.20, 0.20–0.30, and ≥0.31 mmol/l.

Outcomes

During an average 86.0 [IQR, 84.0–90.0] months of follow-up, WMH volume increased by 1.72 [IQR, 1.44–2.03] ml and WMH-to-ICV ratio by 0.14% [IQR, 0.11%−0.17%]. During follow-up, 225 participants (19.7%) developed WMH progression, 193 (16.9%) lacune progression, 170 (14.9%) microbleed progression, and 185 (16.2%) developed EPVS progression. The average of CSVD new burden was 0.67 (IQR, 0–1).

Contributions of Visit-to-Visit Mean SdLDL to CSVD Progression Risk

To examine the contributions of sdLDL to CSVD progression rise, we first compared the trends in WMH volume and WMH-to-ICV ratio changes and CSVD new burden among visit-to-visit mean sdLDL tertile groups (defined in the previous section) and found that compared to the first tertile group, the second and third groups demonstrated significantly greater increases in WMH volume, WMH-to-ICV ratio, and CSVD new burden (all $P < 0.05$). Furthermore, increases in WMH volume, WMH-to-ICV ratio, and CSVD new burden were significantly greater in the third tertile group than in the second (all $P<0.05$), and these differences remained significant after values were adjusted for confounders including baseline WMH volume and baseline WMH-to-ICV ratio (adjusted *P* values for trends <0.05, **Figure 1** and **Supplementary Figure 2**). Visit-to-visit increases in mean sdLDL were also associated with greater risks of WMH, lacune, microbleed, and EPVS progression. Compared with the first tertile group, the second and third tertile groups showed significantly greater risks of WMH progression (53.5% and 105.3% greater), lacune progression (53.3% and 60.8%), microbleed progression (47.2% and 127.6%), and EPVS progression (54.0% and 135.0%) (all adjusted *P* values for trends <0.001). The HRs and 95% CIs resulting from analysis model 3 are provided in **Figure 2** and **Supplementary Table 1**.

Contributions of Visit-to-Visit SdLDL Variability to CSVD Progression Risk

We also compared the trends in WMH volume and WMH-to-ICV ratio changes and CSVD new burden among tertile groups stratified by the visit-to-visit sdLDL SD, and again found the WMH volume and WMH-to-ICV ratio changes and CSVD new burden were significantly greater in the third tertile group than in the first and second tertile groups, and greater in the second than the first tertile group (all $P<0.05$). Furthermore, these differences among tertile groups remained significant after adjustment for confounders including the baseline WMH volume and WMH-to-ICV ratio (all adjusted *P* values for trend <0.05, **Figure 3**).

Like increased mean sdLDL, greater visit-to-visit sdLDL SD was associated with significantly higher risks of WMH progression (49.9% higher in the second tertile and 143.6% higher in the third tertile group compared with the first), lacune progression (75.3 and 178.0% higher, respectively), microbleed progression (12.7 and 64.7% higher, respectively), and EPVS progression (41.7 and 114.6% higher, respectively), and these increases were still significant after adjustment for confounders (all adjusted *P* values for trends <0.001). The HRs and 95% CIs resulting from analysis model 3 are provided in **Figure 4** and **Supplementary Table 1**.

Contributions of Interactions Among Visit-to-Visit Mean SdLDL, Visit-to-Visit SdLDL Variability, and *APOE* Genotype to CSVD Progression Risk

We also identified significant positive visit-to-visit mean sdLDL×visit-to-visit sdLDL SD, visit-to-visit mean sdLDL×*APOE ε4* allele, visit-to-visit sdLDL SD×*APOE ε4* allele, and visit-to-visit mean sdLDL×visit-to-visit sdLDL SD×*APOE ε4* allele interaction effects on CSVD progression after adjustment for confounders (adjusted *P* values <0.05). The details are shown in **Table 2**.

DISCUSSION

In this prospective longitudinal cohort study, we found that visit-to-visit mean sdLDL and visit-to-visit sdLDL SD were independently associated with the risk of CSVD progression over a mean duration of 86.0 months in older adults. Specifically, greater visit-to-visit mean sdLDL and sdLDL SD predicted more aggressive progression of the CSVD manifestations WMH volume, lacunes, microbleeds, and EPVS. Furthermore, there were significant positive mutual interaction effects of visit-to-visit mean sdLDL and visit-to-visit sdLDL SD and positive interaction effects of both with *APOE ε4* genotype on CSVD progression.

The sdLDL faction of LDL is strongly associated with atherosclerotic disease (19, 20, 30, 31), possibly due to the greater susceptibility of sdLDL particles to oxidation, higher cell membrane permeability than other fractions, and lower

TABLE 1 | Participant demographic and baseline clinical characteristics.

	All (*n* = 1,143)	Grouped by tertile of visit-to-visit mean sdLDL				Grouped by tertile of visit-to-visit sdLDL SD			
		First tertile group (*n* = 384)	Second tertile group (*n* = 381)	Third tertile group (*n* = 378)	*P* value	First tertile group (*n* = 381)	Second tertile group (*n* = 381)	Third tertile group (*n* = 381)	*P* value
Clinical parameters									
Age (years)	67.35 ± 5.50	67.15 ± 5.39	67.52 ± 5.59	67.46 ± 5.51	0.611	66.76 ± 5.41	67.61 ± 5.43	67.76 ± 5.60*	0.024
Female [*n* (%)]	652 (57.0)	196 (51.0)	205 (53.8)	251 (66.4) *,†	<0.001	217 (57.0)	214 (56.2)	221 (58.0)	0.876
Smoking [*n* (%)]	368 (32.2)	96 (25.0)	125 (32.8)*	147 (38.9)*	<0.001	109 (28.6)	122 (32.0)	137 (36.0)	0.094
Alcohol consumption [*n* (%)]	382 (33.4)	109 (28.4)	125 (32.8)	148 (39.2)*	0.007	107 (28.1)	138 (36.2)*	137 (36.0)*	0.026
Hypertension [*n* (%)]	797 (69.7)	256 (66.7)	263 (69.0)	278 (73.5)	0.111	266 (69.8)	257 (67.5)	274 (71.9)	0.407
Antihypertensive medication [*n* (%)]	624 (54.6)	214 (55.7)	209 (54.9)	201 (53.2)	0.772	212 (55.6)	208 (54.6)	204 (53.5)	0.844
Diabetes [*n* (%)]	172 (15.0)	48 (12.5)	61 (16.0)	63 (16.7)	0.223	53 (13.9)	55 (14.4)	64 (16.8)	0.494
Anti-diabetes medication [*n* (%)]	159 (13.9)	56 (14.6)	54 (14.2)	49 (13.0)	0.789	59 (15.5)	51 (13.4)	49 (12.9)	0.541
Dyslipidemia [*n* (%)]	329 (28.8)	103 (26.8)	107 (28.1)	119 (31.5)	0.341	104 (27.3)	104 (27.3)	121 (31.8)	0.291
Antidyslipidemia medication [*n* (%)]	80 (7.0)	31 (8.1)	26 (6.8)	23 (6.1)	0.553	31 (8.1)	28 (7.3)	21 (5.5)	0.346
Antiplatelet medication [*n* (%)]	99 (8.7)	38 (9.9)	32 (8.4)	29 (7.7)	0.538	34 (8.9)	33 (8.7)	32 (8.4)	0.967
Heart rate (bpm)	70.12 ± 8.11	69.70 ± 8.12	69.86 ± 7.49	70.81 ± 8.67	0.122	69.13 ± 8.25	70.38 ± 8.16	70.86 ± 7.86*	0.009
Body mass index (kg/m^2)	24.94 ± 2.39	24.86 ± 2.46	24.71 ± 2.43	24.94 ± 2.39†	0.006	25.00 ± 2.35	24.78 ± 2.45	25.03 ± 2.37	0.304
Blood pressure (mm Hg)									
Systolic blood pressure	146.32 ± 15.53	146.13 ± 15.96	145.51 ± 15.09	147.34 ± 15.52	0.257	144.09 ± 15.72	146.52 ± 15.22	148.35 ± 15.39*	0.001
Diastolic blood pressure	76.69 ± 8.08	76.80 ± 7.69	76.38 ± 8.35	76.89 ± 8.21	0.651	76.04 ± 8.15	76.77 ± 7.78	77.26 ± 8.28	0.112
Biochemical parameters (mmol/L)									
Total cholesterol	4.72 ± 0.75	4.37 ± 0.70	4.69 ± 0.69*	5.09 ± 0.69*,†	<0.001	4.52 ± 0.75	4.77 ± 0.73*	4.86 ± 0.74*	<0.001
Triglycerides	1.60 ± 0.52	1.54 ± 0.52	1.57 ± 0.50	1.68 ± 0.54*,†	0.001	1.57 ± 0.51	1.61 ± 0.52	1.61 ± 0.54	0.361
HDL-C	1.16 ± 0.42	1.27 ± 0.49	1.11 ± 0.38*	1.09 ± 0.37*	<0.001	1.20 ± 0.45	1.16 ± 0.42	1.11 ± 0.40*	0.019
LDL-C	2.83 ± 0.69	2.41 ± 0.62	2.86 ± 0.60*	3.24 ± 0.57*,†	<0.001	2.61 ± 0.68	2.88 ± 0.64*	3.02 ± 0.69*,†	<0.001
sdLDL	0.64 (0.44, 0.89)	0.47 (0.33, 0.65)	0.63 (0.46, 0.81)*	0.89 (0.67, 1.09)*,†	<0.001	0.56 (0.42, 0.72)	0.69 (0.44, 0.90)*	0.75 (0.46, 1.04)*,†	<0.001
FPG	5.66 ± 1.49	5.61 ± 1.41	5.63 ± 1.42	5.76 ± 1.64	0.321	5.63 ± 1.42	5.64 ± 1.47	5.73 ± 1.58	0.545

(Continued)

TABLE 1 | Continued

	All (*n* = 1,143)	Grouped by tertile of visit-to-visit mean sdLDL				Grouped by tertile of visit-to-visit sdLDL SD			
		First tertile group (*n* = 384)	**Second tertile group (*n* = 381)**	**Third tertile group (*n* = 378)**	***P* value**	**First tertile group (*n* = 381)**	**Second tertile group (*n* = 381)**	**Third tertile group (*n* = 381)**	***P* value**
Brain magnetic resonance imaging									
WMH volume (mL)	4.69 (3.16, 6.16)	4.19 (2.68, 5.59)	4.63 (3.18, 6.18)*	5.22 (3.81, 6.67)*†	<0.001	4.09 (2.72, 5.47)	4.56 (3.06, 5.93)*	5.55 (3.92, 6.95)*†	<0.001
WMH-to-ICV ratio (%)	0.36 (0.24, 0.48)	0.31 (0.21, 0.45)	0.36 (0.25, 0.48)*	0.40 (0.30, 0.52)*†	<0.001	0.31 (0.21, 0.43)	0.35 (0.24, 0.45)*	0.44 (0.31, 0.54)*†	<0.001
Incidence of Fazekas scale ≥2 [*n* (%)]	114 (10.0)	27 (7.0)	33 (8.7)	54 (14.3)*†	0.002	19 (5.0)	29 (7.6)	66 (17.3)* †	<0.001
Incidence of lacunes [*n* (%)]	96 (8.4)	24 (6.3)	28 (7.3)	44 (11.6)*†	0.018	15 (3.9)	23 (6.0)	58 (15.2)*†	<0.001
Incidence of microbleeds [*n* (%)]	71 (6.2)	16 (4.2)	19 (5.0)	36 (9.5)*†	0.004	16 (4.2)	19 (5.0)	36 (9.4)*†	0.005
Incidence of EPVS [*n* (%)]	124 (10.8)	38 (9.9)	36 (9.4)	50 (13.2)	0.188	36 (9.4)	40 (10.5)	48 (12.6)	0.363
***APOE* genotype**									
ε4-positive carriers [*n* (%)]	297 (26.0)	80 (20.8)	105 (27.6)*	112 (29.6)*	0.015	81 (21.3)	100 (26.2)	116 (30.4)*	0.015

Compared with the First tertile group.

**P <0.05; compared with the Second tertile group, †P <0.05.*

sdLDL, small and dense low-density lipoproteins; SD, standard deviation; HDL-c, high-density lipoprotein cholesterol; LDL-c, low-density lipoprotein cholesterol; FPG, fasting plasma glucose; WMH, white matter hyperintensities; ICV, intracranial volume; EPVS, enlarged perivascular space; APOE, apolipoprotein E.

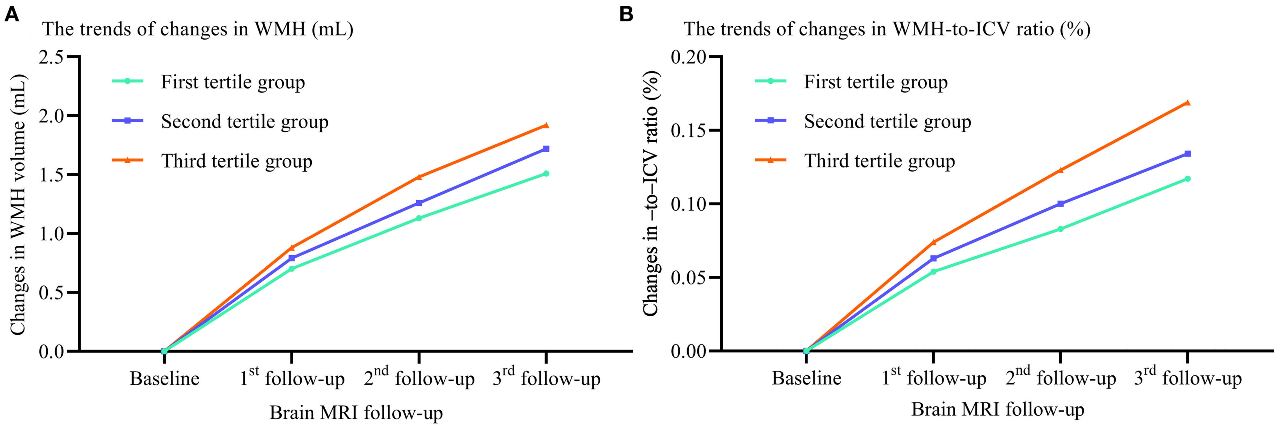

FIGURE 1 | Differences in WMH volume and WMH-to-ICV ratio changes among tertile groups stratified by visit-to-visit mean sdLDL during the follow-up period. **(A)** Changes in WMH. **(B)** Changes in WMH-to-ICV ratio. WMH, white matter hyperintensities; ICV, intracranial volume.

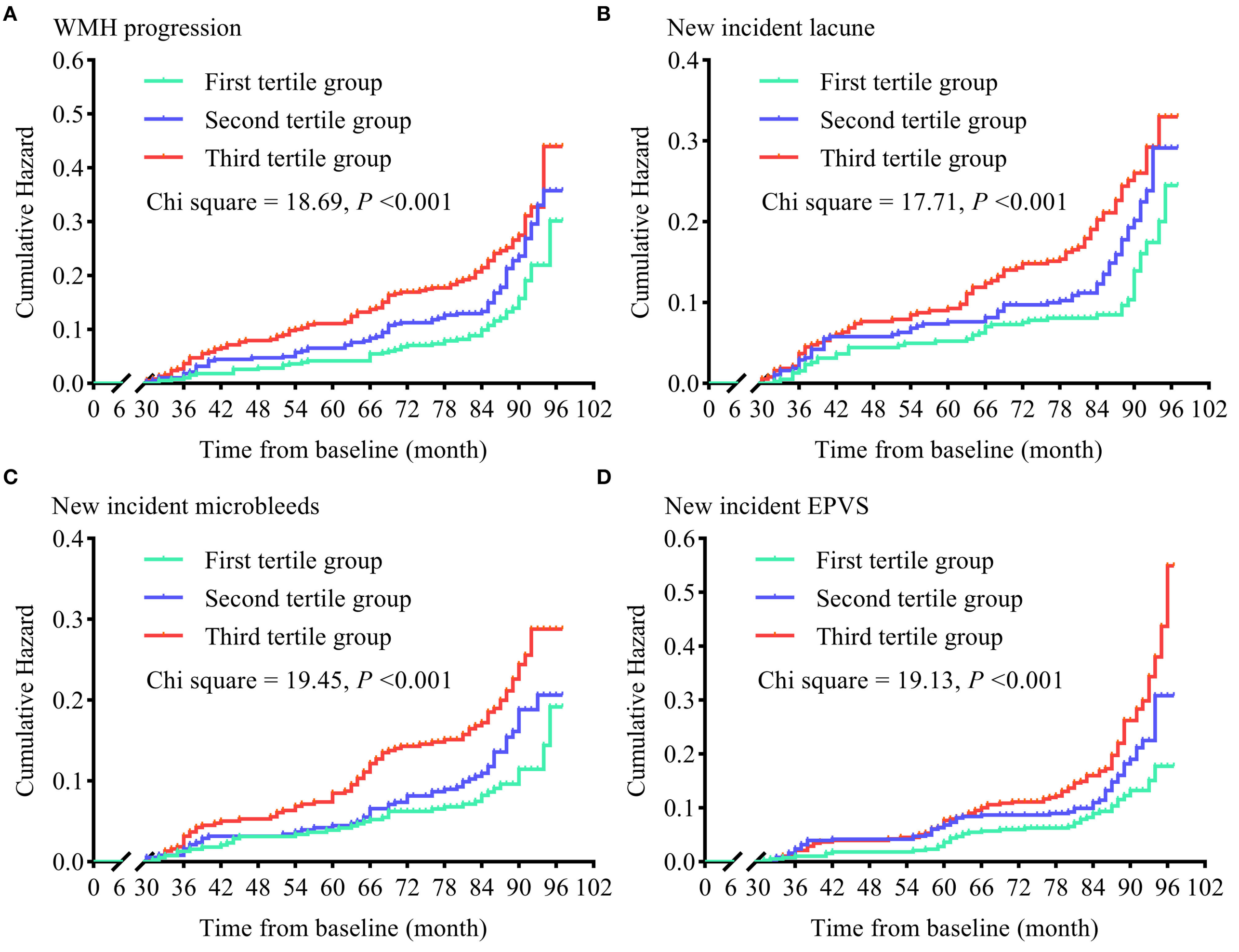

FIGURE 2 | Cumulative hazards of cerebral small vessel disease progression in tertile groups stratified by visit-to-visit mean sdLDL during the follow-up period. **(A)** Cumulative hazards of WMH progression. **(B)** Cumulative hazards of new-incident lacunes. **(C)** Cumulative hazards of new-incident microbleeds. **(D)** Cumulative hazards of new-incident EPVS. WMH, white matter hyperintensities; EPVS, enlarged perivascular space.

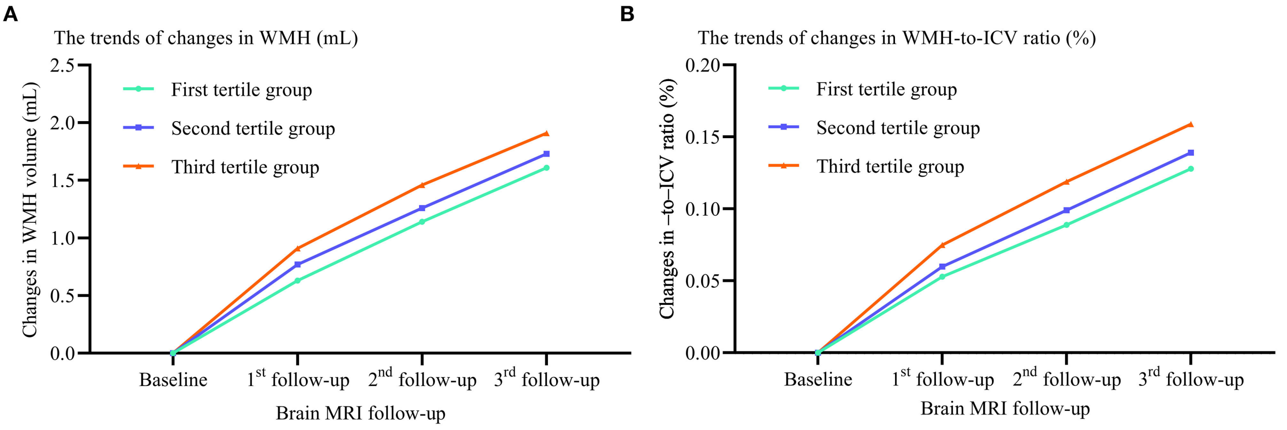

FIGURE 3 | Differences in WMH volume and WMH-to-ICV ratio changes among tertile groups stratified by visit-to-visit sdLDL SD during the follow-up period. **(A)** Changes in WMH. **(B)** Changes in WMH-to-ICV ratio. WMH, white matter hyperintensities; ICV, intracranial volume.

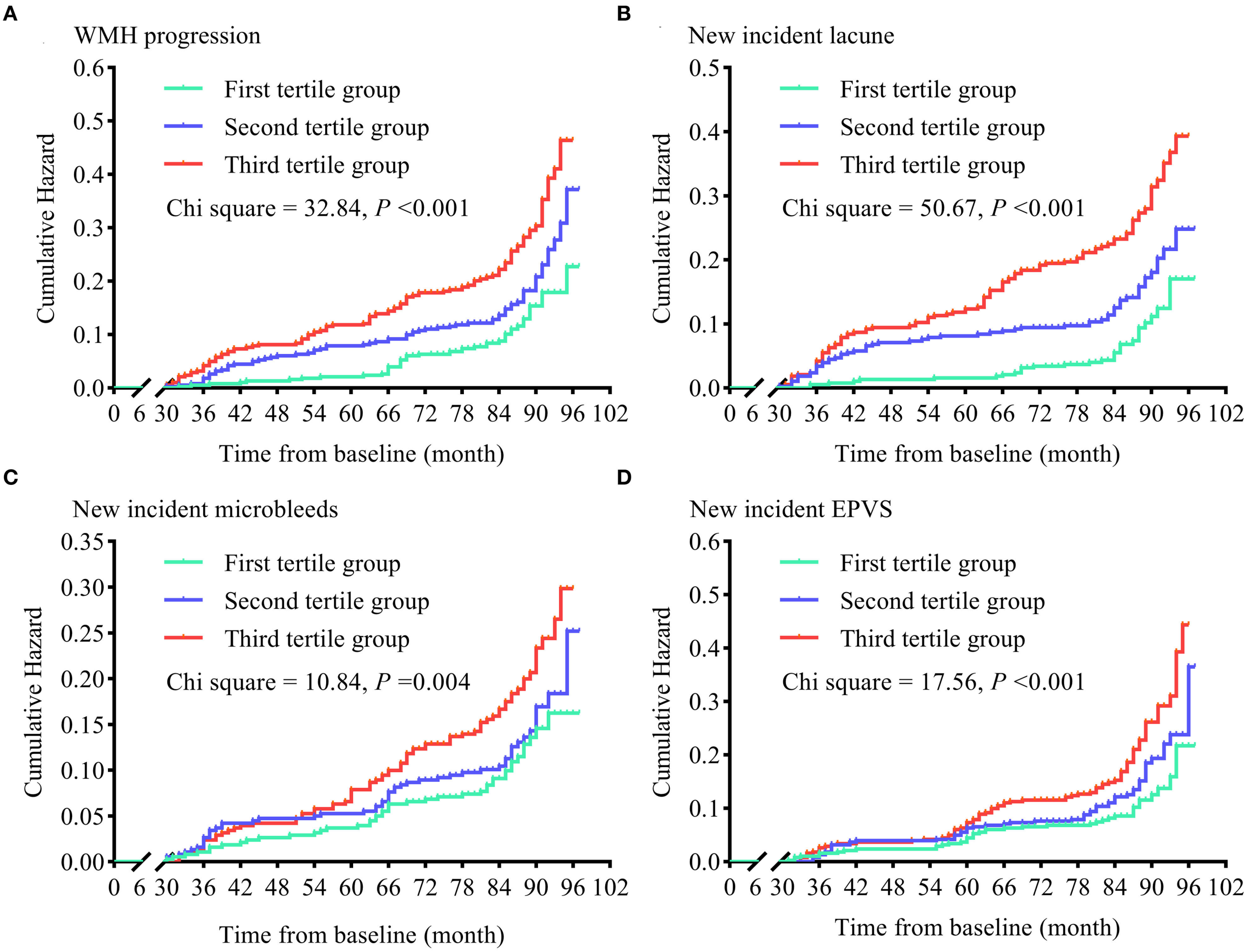

FIGURE 4 | Cumulative hazards of cerebral small vessel disease progression in tertile groups stratified by visit-to-visit sdLDL SD during the follow-up period. **(A)** Cumulative hazards of WMH progression. **(B)** Cumulative hazards of new-incident lacunes. **(C)** Cumulative hazards of new-incident microbleeds. **(D)** Cumulative hazards of new-incident EPVS. WMH, white matter hyperintensities; EPVS, enlarged perivascular space.

TABLE 2 | Interactions among visit-to-visit mean sdLDL, visit-to-visit sdLDL variability, and *APOE* genotype influencing cerebral small vessel disease progression.

	WMH progression		Lacune progression		Microbleed progression		EPVS progression	
	HR (95% CI)	***P* value**	**HR (95% CI)**	***P* value**	**HR (95% CI)**	***P* value**	**HR (95% CI)**	***P* value**
Model 1								
Visit-to-visit mean sdLDL× visit-to-visit sdLDL SD	1.173 (1.113,1.236)	<0.001	1.197 (1.131, 1.266)	<0.001	1.141 (1.074, 1.212)	<0.001	1.191 (1.120, 1.267)	<0.001
Visit-to-visit mean sdLDL×*APOE ε4* genotype	1.509 (1.359, 1.675)	<0.001	1.456 (1.300, 1.631)	<0.001	1.593 (1.416, 1.792)	<0.001	1.349 (1.191, 1.527)	<0.001
Visit-to-visit sdLDL SD ×*APOE ε4* genotype	1.497 (1.351, 1.695)	<0.001	1.434 (1.282, 1.605)	<0.001	1.576 (1.395, 1.781)	<0.001	1.298 (1.147, 1.469)	<0.001
Visit-to-visit mean sdLDL×visit-to-visit sdLDL SD ×*APOE ε4* genotype	1.159 (1.115, 1.206)	<0.001	1.147 (1.098, 1.197)	<0.001	1.186 (1.136, 1.239)	<0.001	1.121 (1.066, 1.178)	<0.001
Model 2								
Visit-to-visit mean sdLDL×visit-to-visit sdLDL SD	1.145 (1.094, 1.198)	<0.001	1.176 (1.120, 1.235)	<0.001	1.132 (1.074, 1.193)	<0.001	1.178 (1.111, 1.248)	<0.001
Visit-to-visit mean sdLDL×*APOE ε4* genotype	1.504 (1.350, 1.674)	<0.001	1.417 (1.262, 1.591)	<0.001	1.569 (1.396, 1.763)	<0.001	1.349 (1.190, 1.530)	<0.001
Visit-to-visit sdLDL SD×*APOE ε4* genotype	1.500 (1.348, 1.669)	<0.001	1.421 (1.265, 1.595)	<0.001	1.575 (1.394, 1.778)	<0.001	1.298 (1.145, 1.472)	<0.001
Visit-to-visit mean sdLDL×visit-to-visit sdLDL SD ×*APOEε4*genotype	1.160 (1.113, 1.210)	<0.001	1.140 (1.090, 1.193)	<0.001	1.188 (1.134, 1.245)	<0.001	1.120 (1.067, 1.176)	<0.001
Model 3								
Visit-to-visit mean sdLDL×visit-to-visit sdLDL SD	1.088 (1.030, 1.149)	<0.001	1.063 (1.003, 1.127)	0.039	1.103 (1.035, 1.175)	0.003	1.139 (1.083, 1.197)	<0.001
Visit-to-visit mean sdLDL×*APOE ε4* genotype	1.431 (1.283, 1.596)	<0.001	1.294 (1.150, 1.456)	<0.001	1.510 (1.334, 1.708)	<0.001	1.341 (1.188, 1.513)	<0.001
Visit-to-visit sdLDL SD ×*APOE ε4* genotype	1.396 (1.255, 1.554)	<0.001	1.259 (1.121, 1.413)	<0.001	1.488 (1.315, 1.683)	<0.001	1.286 (1.140, 1.451)	<0.001
Visit-to-visit mean sdLDL×visit-to-visit sdLDL SD ×*APOE ε4* genotype	1.127 (1.081, 1.175)	<0.001	1.083 (1.035, 1.133)	0.001	1.167 (1.113, 1.224)	<0.001	1.114 (1.063, 1.167)	<0.001

Model 1 is adjusted for age and sex. Model 2 is adjusted for smoking, alcohol consumption, initial body mass index, blood pressure, serum lipids, and fasting plasma glucose at baseline, and either the initial WMH volume (for WMH volume change analysis) and WMH-to-ICV ratio (for WMH-to-ICV ratio change analysis) at baseline. Model 3 is adjusted for visit-to-visit mean sdLDL (for the models grouped by tertile of sdLDL variability), variability in sdLDL (for the models grouped by visit-to-visit mean sdLDL tertile), and APOE genotype. WMH, white matter hyperintensities; EPVS, enlarged perivascular space; HR, hazard ratio; sdLDL, small and dense low-density lipoproteins; SD, standard deviation.

LDL receptor affinity (17, 18). Several reports have document associations between sdLDL level and both carotid artery intima-media thickness and plaque progression (32–34). The Atherosclerosis Risk in Communities study also found that the risk of coronary artery disease was 1.5-fold higher in individuals with sdLDL in the four quartiles (≥75th percentile) compared to the lowest quartile (20), while a Chinese cohort study with an average 9.5-year follow-up identified sdLDL level as an independent risk factor for major adverse cardiovascular events in hypertensive subjects (24). Here, we extend these findings by demonstrating a significant association of sdLDL with CSVD. To the best of our knowledge, only one previous study has reported an association between sdLDL and a CSVD sign (brain WMH volume) (35) but the cross-sectional design precluded evaluation of an association with disease progression. In the current prospective longitudinal cohort study, we show that long-term sdLDL elevation and greater variability are strongly associated with CSVD progression, particularly in *APOE ε4* carriers. We also found that greater visit-to-visit mean sdLDL and sdLDL SD were associated with higher risks of lacune, microbleed, and EPVS progression and WMH volume progression, even after adjustment for multiple confounders including baseline sdLDL, LDL-C, and WMH volume and also lacune, microbleed, and EPVS incidence.

Serum lipid levels and sdLDL levels are influenced by numerous factors, namely, diet, exercise level, medication adherence and dose, season, and mood (18, 36–40). Relationships between high serum LDL-C variability and increased cardiovascular and cerebrovascular disease risks are well established (36, 41–43). Thus, we hypothesized that sdLDL variability would also be closely associated with CSVD progressions, and indeed higher tertile of sdLDL SD predicted WMH, lacune, microbleed, and EPVS progression after adjustment for confounders including visit-to-visit mean sdLDL.

In addition, visit-to-visit sdLDL SD interacted synergistically with visit-to-visit mean sdLDL to further increase CSVD risk.

One of the major functions of *APOE* is to regulate lipid metabolism, especially of TCHO and LDL-C (11, 28, 44). Apolipoprotein E is abundantly expressed in the brain and accumulation on vessel walls is strongly associated with CSVD severity (45–47). Our exploratory analysis showed that the *APOE ε4* allele significantly and positively interacted with both higher visit-to-visit mean sdLDL and visit-to-visit sdLDL SD to enhance CSVD progressions risk. Thus, the *APOE* genotype is an important mediator of the association between serum sdLDL and CSVD progression in older individuals.

The major strengths of this study include the prospective longitudinal cohort design with long-term follow-up and a large sample size. In addition, we examined the effects of both higher long-term mean sdLDL and greater long-term sdLDL variability on CSVD progression and the interaction between these factors and *APOE* genotype. On the other hand, many critical confounders were not examined, such as lifestyle, diet, season, mood changes, and medication adherence, all of which can significantly influence serum lipid levels and variability (18, 37–40). Second, all participants were of Han ethnicity, so applicability to other ethnicities is uncertain. Third, we did not examine many additional pathogenic factors that could directly influence disease progression or the effects of serum sdLDL, such as oxidative stress, endothelial dysfunction, and inflammatory status.

In conclusion, serum sdLDL level and variation are critical independent and synergistically acting risk factors for CSVD progression in older individuals. Moreover, the *APOE* genotype strongly influences the association of sdLDL level with CSVD progression. However, further multinational studies involving additional ethnic groups and controlling for factors such as lifestyle, diet, and medication adherence are needed to validate our results.

DATA AVAILABILITY STATEMENT

The original contributions presented in the study are included in the article/**Supplementary Material**, further inquiries can be directed to the corresponding authors.

ETHICS STATEMENT

The studies involving human participants were reviewed and approved by the Research Ethics Committee of the Institute of Basic Medicine, Shandong Academy of Medical Sciences, Shandong, China. The patients/participants provided their written informed consent to participate in this study.

AUTHOR CONTRIBUTIONS

WL wrote the manuscript with input from all authors. WL, JX, HS, CZ, YY, and HZ were responsible for data collection. WL and HZ performed the statistical analysis. Y-CL and ZL designed and supervised the study, drafting, and editing of the manuscript. All authors contributed to a critical review of the manuscript.

FUNDING

This work was supported by the National Natural Science Foundation of China (Grant Nos. 81870281, 81670432, and 81973139), the Zhejiang Provincial Natural Science Foundation of China (Grant Nos. LY18H020011 and LQ19H020005), the Key Technology Research and Development Project of Shandong Province (Grant Nos. 2019GSF108079 and 2018GSF118044), the Medical and Health Science and Technology Development Plan Project of Shandong, China (Grant No. 202103010686), and the Innovation Project of Shandong Academy of Medical Sciences, and the Academic Promotion Program of Shandong First Medical University.

ACKNOWLEDGMENTS

The authors thank the participants, family physicians, and nurses involved in this study and all individuals who offered their assistance.

SUPPLEMENTARY MATERIAL

The Supplementary Material for this article can be found online at: https://www.frontiersin.org/articles/10.3389/fneur.2022.851735/full#supplementary-material

REFERENCES

1. Wardlaw JM, Smith EE, Biessels GJ, Cordonnier C, Fazekas F, Frayne R, et al. STandards for ReportIng Vascular changes on nEuroimaging (STRIVE v1). Neuroimaging standards for research into small vessel disease and its contribution to ageing and neurodegeneration. *Lancet Neurol.* (2013) 12:822–38. doi: 10.1016/S1474-4422(13)70124-8
2. Wardlaw JM, Smith C, Dichgans M. Mechanisms of sporadic cerebral small vessel disease: insights from neuroimaging. *Lancet Neurol.* (2013) 12:483–97. doi: 10.1016/S1474-4422(13)70060-7
3. Graff-Radford J, Aakre JA, Knopman DS, Schwarz CG, Flemming KD, Rabinstein AA, et al. Prevalence and heterogeneity of cerebrovascular disease imaging lesions. *Mayo Clin Proc.* (2020) 95:1195–205. doi: 10.1016/j.mayocp.2020.01.028
4. Georgakis MK, Malik R, Anderson CD, Parhofer KG, Hopewell JC, Dichgans M. Genetic determinants of blood lipids and cerebral small vessel disease: role of high-density lipoprotein cholesterol. *Brain.* (2020) 143:597–610. doi: 10.1093/brain/awz413
5. National Cholesterol Education Program (NCEP) Expert Panel on Detection, Evaluation, and Treatment of High Blood Cholesterol in Adults (Adult Treatment Panel III). (2002). Third Report of the National Cholesterol Education Program (NCEP) Expert Panel on Detection, Evaluation, and Treatment of High Blood Cholesterol in Adults (Adult Treatment Panel III) final report. *Circulation*. 106:3143–421. doi: 10.1161/circ.106.25.3143
6. Ference BA, Ginsberg HN, Graham I, Ray KK, Packard CJ, Bruckert E, et al. Low-density lipoproteins cause atherosclerotic cardiovascular disease. 1.

Evidence from genetic, epidemiologic, clinical studies. A consensus statement from the European Atherosclerosis Society Consensus Panel. *Eur. Heart J.* (2017) 38:2459–72. doi: 10.1093/eurheartj/ehx144

7. Arnett DK, Blumenthal RS, Albert MA, Buroker AB, Goldberger ZD, Hahn EJ, et al. 2019 ACC/AHA Guideline on the primary prevention of cardiovascular disease: a report of the American College of Cardiology/American Heart Association Task Force on Clinical Practice Guidelines. *Circulation.* (2019) 140:e596–646. doi: 10.1161/CIR.0000000000000678
8. Mortensen MB, Nordestgaard BG. Comparison of five major guideline for statin use in primary prevention in a contemporary general population. *Ann Intern Med.* (2018) 168:85–92. doi: 10.7326/M17-0681
9. US Preventive Services Task Force, Bibbins-Domingo K, Grossman DC, Curry SJ, Davidson KW, Epling JW, et al. Statin use for the primary prevention of cardiovascular disease in adults: US Preventive Services Task Force Recommendation Statement. *JAMA*. (2016) 316:1997–2007. doi: 10.1001/jama.2016.15450
10. Guo Y, Li Y, Liu X, Cui Y, Zhao Y, Sun S, et al. Assessing the effectiveness of statin therapy for alleviating cerebral small vessel disease progression in people ≥75 years of age. *BMC Geriatr*. (2020) 20:292. doi: 10.1186/s12877-020-01682-w
11. Ji T, Zhao Y, Wang J, Cui Y, Duan D, Chai Q, et al. Effect of low-dose statins and Apolipoprotein E genotype on cerebral small vessel disease in older hypertensive patients: a subgroup analysis of a randomized clinical trial. *J Am Med Dir Assoc*. (2018) 19:995–1002.e4. doi: 10.1016/j.jamda.2018.05.025
12. Kim JS. Role of blood lipid levels and lipid-lowering therapy in stroke patients with different levels of cerebral artery diseases: reconsidering recent stroke guidelines. *J Stroke.* (2021) 23:149–61. doi: 10.5853/jos.2021.01249
13. Sillesen H, Amarenco P, Hennerici MG, Callahan A, Goldstein LB, Zivin J, et al. Atorvastatin reduces the risk of cardiovascular events in patients with carotid atherosclerosis: a secondary analysis of the Stroke Prevention by Aggressive Reduction in Cholesterol Levels (SPARCL) trial. *Stroke.* (2008) 39:3297–302. doi: 10.1161/STROKEAHA.108.516450
14. Zhang H, Cui Y, Zhao Y, Dong Y, Duan D, Wang J, et al. Effects of sartans and low-dose statins on cerebral white matter hyperintensities and cognitive function in older patients with hypertension: a randomized, double-blind and placebo-controlled clinical trial. *Hypertens Res.* (2019) 42:717–29. doi: 10.1038/s41440-018-0165-7
15. Mitaki S, Nagai A, Oguro H, Yamaguchi S. Serum Lipid Fractions and Cerebral Microbleeds in a Healthy Japanese Population. *Cerebrovasc Dis.* (2017) 43:186–91. doi: 10.1159/000456623
16. Hayashi T, Fukui T, Nakanishi N, Yamamoto S, Tomoyasu M, Osamura A, et al. Dapagliflozin decreases small dense low-density lipoprotein-cholesterol and increases high-density lipoprotein 2-cholesterol in patients with type 2 diabetes: comparison with sitagliptin. *Cardiovasc Diabetol*. (2017) 16:8. doi: 10.1186/s12933-016-0491-5
17. Nakayama A, Morita H, Sato T, Kawahara T, Takeda N, Kato S, et al. Small dense low-density lipoprotein cholesterol is a potential marker for predicting laser treatment for retinopathy in diabetic patients. *J Atheroscler Thromb*. (2021) 14. doi: 10.21203/rs.3.rs-53274/v1
18. Alizadeh-Fanalou S, Nazarizadeh A, Alian F, Faraji P, Sorori B, Khosravi M. Small dense low-density lipoprotein-lowering agents. *Biol Chem.* (2020) 401:1101–21. doi: 10.1515/hsz-2019-0426
19. Ai M, Otokozawa S, Asztalos BF, Ito Y, Nakajima K, White CC, et al. Small dense LDL cholesterol and coronary heart disease: results from the Framingham Offspring Study. *Clin Chem.* (2010) 56:967–76. doi: 10.1373/clinchem.2009.137489
20. Hoogeveen RC, Gaubatz JW, Sun W, Dodge RC, Crosby JR, Jiang J, et al. Small dense low-density lipoprotein-cholesterol concentrations predict risk for coronary heart disease: the Atherosclerosis Risk In Communities (ARIC) study. *Aterioscler Thromb Vasc Biol.* (2014) 34:1069–77. doi: 10.1161/ATVBAHA.114.303284
21. Ivanova EA, Myasoedova VA, Melnichenko AA, Grechko AV, Orekhov AN. Small dense low-density lipoprotein as biomarker for atherosclerotic diseases. *Oxid Med Cell Longev*. (2017) 2017:1273042. doi: 10.1155/2017/1273042
22. Zhang H, Cui Y, Zhao Y, Dong Y, Wang J, Duan D, et al. Association of circadian rhythm of blood pressure and cerebral small vessel disease in community-based elderly population. *J Gerontol A Biol Sci Med Sci.* (2019) 74:1322–30. doi: 10.1093/gerona/gly212
23. Sekimoto T, Koba S, Mori H, Sakai R, Arai T, Yokota Y, et al. Small Dense Low-Density Lipoprotein Cholesterol: A Residual Risk for Rapid Progression of Non-Culprit Coronary Lesion in Patients with Acute Coronary Syndrome. *J Atheroscler Thromb.* (2021) 28:1161–74. doi: 10.5551/jat.60152
24. Wang X, Wang L, Cao R, Yang X, Xiao W, Zhang Y, et al. Correlation between small and dense low-density lipoprotein cholesterol and cardiovascular events in Beijing community population. *J Clin Hypertens (Greenwich).* (2021) 23:345–51. doi: 10.1111/jch.14150
25. Gouw AA, van der Flier WM, Fazekas F, van Straiten EC, Pantoni L, Poggesi A, et al. LADIS Study Group. Progression of white matter hyperintensities and incidence of new lacunes over a 3-year period: the Leukoaraiosis and Disability study. *Stroke.* (2008) 39:1414–20. doi: 10.1161/STROKEAHA.107.498535
26. Prins ND, van Straaten EC, van Dijk EJ, Simoni M, van Schijndel RA, Vrooman HA, et al. Measuring progression of cerebral white matter lesions on MRI: visual rating and volumetrics. *Neurology.* (2004) 62:1533–9. doi: 10.1212/01.WNL.0000123264.40498.B6
27. Kan CN, Gyanwali B, Hilal S, Ng KP, Venketasubramanian N, Chen CL, et al. Neuropsychiatric correlates of small vessel disease progression in incident cognitive decline: independent and interactive effects. *J Alzheimers Dis.* (2020) 73:1053–62. doi: 10.3233/JAD-190999
28. Hu W, Li Y, Zhao Y, Dong Y, Cui Y, Sun S, et al. Telmisartan and rosuvastatin synergistically ameliorate dementia and cognitive impairment in older hypertensive patients with Apolipoprotein E genotype. *Front Aging Neurosci.* (2020) 12:154. doi: 10.3389/fnagi.2020.00154
29. Molinuevo JL, Gramunt N, Gispert JD, Fauria K, Esteller M, Minguillon C, et al. The ALFA project: a research platform to identify early pathophysiological features of Alzheimer's disease. *Alzheimers Dement.* (2016) 2:82–92. doi: 10.1016/j.trci.2016.02.003
30. Jin JL, Zhang HW, Cao YX, Liu HH, Hua Q, Li YF, et al. Association of small dense low-density lipoprotein with cardiovascular outcome in patients with coronary artery disease and diabetes: a prospective, observational cohort study. *Cardiovasc Diabetol.* (2020) 19:45. doi: 10.1186/s12933-020-01015-6
31. Tsai MY, Steffen BT, Guan W, McClelland RL, Warnick R, McConnell J, et al. New automated assay of small dense low-density lipoprotein cholesterol identifies risk of coronary heart disease: the multi-ethnic study of atherosclerosis. *Arterioscler Thromb Vasc Biol.* (2014) 34:196–201. doi: 10.1161/ATVBAHA.113.302401
32. Maeda S, Nakanishi S, Yoneda M, Awaya T, Yamane K, Hirano T, et al. Associations between small dense LDL, HDL subfractions (HDL2, HDL3) and risk of atherosclerosis in Japanese-Americans. *J Atheroscler Thromb.* (2012) 19:444–52. doi: 10.5551/jat.11445
33. Norata GD, Raselli S, Grigore L, Garlaschelli K, Vianello D, Bertocco S, et al. Small dense LDL and VLDL predict common carotid artery IMT and elicit an inflammatory response in peripheral blood mononuclear and endothelial cells. *Atherosclerosis.* (2009) 206:556–62. doi: 10.1016/j.atherosclerosis.2009.03.017
34. Qi Y, Liu J, Wang W, Wang M, Zhao F, Sun J, et al. High sdLDL cholesterol can be used to reclassify individuals with low cardiovascular risk for early intervention: findings from the Chinese multi-provincial cohort study. *J Atheroscler Thromb.* (2019) 27:695–710. doi: 10.5551/jat.49841
35. Hawkins KA, Emadi N, Pearlson GD, Winkler AM, Taylor B, Dulipsingh L, et al. Hyperinsulinemia and elevated systolic blood pressure independently predict white matter hyperintensities with associated cognitive decrement in the middle-aged offspring of dementia patients. *Metab Brain Dis.* (2017) 32:849–57. doi: 10.1007/s11011-017-9980-9
36. Dong Y, Liu X, Zhao Y, Chai Q, Zhang H, Gao Y, et al. Attenuating the variability of lipids is beneficial for the hypertension management to reduce the cardiovascular morbidity and mortality in older adults. *Front Cardiovasc Med.* (2021) 8:692773. doi: 10.3389/fcvm.2021.692773
37. Izumida T, Nakamura Y, Sato Y, Ishikawa S. Association among age, gender, menopausal status and small dense low-density lipoprotein cholesterol: a cross-sectional study. *BMJ Open.* (2021) 11:e041613. doi: 10.1136/bmjopen-2020-041613
38. Rizzo M, Berneis K. Small, dense low-density-lipoproteins and the metabolic syndrome. *Diabetes Metab Res Rev.* (2007) 23:14–20. doi: 10.1002/dmrr.694

39. Simpson WG. Biomarker variability and cardiovascular disease residual risk. *Curr Opin Cardiol.* (2019) 34:413–7. doi: 10.1097/HCO.0000000000000627
40. Urahama N, Iguchi G, Shimizu M, Fujihira K, Kobayashi S, Baba H. Smoking and small, dense low-density lipoprotein particles: cross-sectional study. *Nicotine Tob Res*. (2008) 10:1391–5. doi: 10.1080/14622200802238852
41. Bangalore S, Breazna A, DeMicco DA, Wun CC, Messerli F. H., N T. T., Steering Committee, and Investigators. Visit-to-visit low-density lipoprotein cholesterol variability and risk of cardiovascular outcomes: insights from the TNT trial. *J Am Coll Cardiol.* (2015) 65:1539–48. doi: 10.1016/j.jacc.2015.02.017
42. Smit R. A., Trompet S, Sabayan B, le Cessie S, van der Grond J, van Buchem MA, et al. Higher visit-to-visit low-density lipoprotein cholesterol variability is associated with lower cognitive performance, lower cerebral blood flow, and greater white matter hyperintensity load in older subjects. *Circulation.* (2016) 134:212–21. doi: 10.1161/CIRCULATIONAHA.115.020627
43. Cholesterol Treatment Trialists' (CTT) Collaboration, Baigent C, Blackwell L, Emberson J, Holland LE, Reith C, et al. Efficacy and safety of more intensive lowering of LDL cholesterol: A meta-analysis of data from 170,000 participants in 26 randomised trials. *Lancet*. (2010) 376:1670–81. doi: 10.1016/S0140-6736(10)61350-5
44. Dergunov AD. Apolipoprotein E genotype as a most significant predictor of lipid response at lipid-lowering therapy: mechanistic and clinical studies. *Biomed Pharmacother*. (2011) 65:597–603. doi: 10.1016/j.biopha.2011.04.003
45. Lahiri DK. Apolipoprotein E as a target for developing new therapeutics for Alzheimer's disease based on studies from protein, RNA, and regulatory region of the gene. *J Mol Neurosci.* (2004) 23:225–33. doi: 10.1385/JMN:23:3:225
46. Mahley RW, Huang Y. Apolipoprotein E: from atherosclerosis to Alzheimer's disease and beyond. *Curr Opin Lipidol.* (1999) 10:207–17. doi: 10.1097/00041433-199906000-00003
47. Utter S, Tamboli IY, Walter J, Upadhaya AR, Birkenmeier G, Pietrzik CU, et al. Cerebral small vessel disease-induced apolipoprotein E leakage is associated with Alzheimer disease and the accumulation of amyloid beta-protein in perivascular astrocytes. *J Neuropathol Exp Neurol.* (2008) 67:842–56. doi: 10.1097/NEN.0b013e3181836a71

Conflict of Interest: The authors declare that the research was conducted in the absence of any commercial or financial relationships that could be construed as a potential conflict of interest.

The reviewer CY declared a shared parent affiliation with the authors HS, CZ, HZ, YY, and ZL to the handling editor at the time of review.

frontiers | Frontiers in Neurology

REVIEW
published: 07 July 2022
doi: 10.3389/fneur.2022.865920

Research Progress on MRI for White Matter Hyperintensity of Presumed Vascular Origin and Cognitive Impairment

Fanhua Meng[1], **Ying Yang**[2] **and Guangwei Jin**[2]*

[1] North China University of Science and Technology, Tangshan, China, [2] Department of Radiology, China Emergency General Hospital, Beijing, China

White matter hyperintensity of presumed vascular origin (WMH) is a common medical imaging manifestation in the brains of middle-aged and elderly individuals. WMH can lead to cognitive decline and an increased risk of cognitive impairment and dementia. However, the pathogenesis of cognitive impairment in patients with WMH remains unclear. WMH increases the risk of cognitive impairment, the nature and severity of which depend on lesion volume and location and the patient's cognitive reserve. Abnormal changes in microstructure, cerebral blood flow, metabolites, and resting brain function are observed in patients with WMH with cognitive impairment. Magnetic resonance imaging (MRI) is an indispensable tool for detecting WMH, and novel MRI techniques have emerged as the key approaches for exploring WMH and cognitive impairment. This article provides an overview of the association between WMH and cognitive impairment and the application of dynamic contrast-enhanced MRI, structural MRI, diffusion tensor imaging, 3D-arterial spin labeling, intravoxel incoherent motion, magnetic resonance spectroscopy, and resting-state functional MRI for examining WMH and cognitive impairment.

Keywords: white matter hyperintensities of presumed vascular origin, cerebral small vascular disease, cognitive impairment, magnetic resonance imaging, neuroimaging, white matter

Edited by:
Xiaofei Hu,
Army Medical University, China

Reviewed by:
Henk J. M. M. Mutsaerts,
VU University
Amsterdam, Netherlands
Feng Chen,
Hainan General Hospital, China
Wen Qin,
Tianjin Medical University General
Hospital, China

***Correspondence:**
Guangwei Jin
guangweijin@sina.com

Specialty section:
This article was submitted to
Applied Neuroimaging,
a section of the journal
Frontiers in Neurology

Received: *30 January 2022*
Accepted: *14 June 2022*
Published: *07 July 2022*

Citation:
Meng F, Yang Y and Jin G (2022)
Research Progress on MRI for White
Matter Hyperintensity of Presumed
Vascular Origin and Cognitive
Impairment. Front. Neurol. 13:865920.
doi: 10.3389/fneur.2022.865920

INTRODUCTION

With the growth in aging populations worldwide and the high incidence of risk factors for cerebrovascular diseases, comorbid neurodegenerative diseases such as Alzheimer's disease (AD) and cerebrovascular diseases are common, resulting in a heavy burden on families and society (1). White matter hyperintensity of presumed vascular origin (WMH) is an imaging marker of cerebral small vessel disease (CSVD) and its common imaging manifestation in the brains of middle-aged and elderly individuals (2, 3). The reported prevalence of WMH varies due to the differences in patient's characteristics, imaging techniques, and rating methods (4). The prevalence of WMH ranges from 39 to 100% and increases with age (5). Of individuals aged 60–70 years, 87% have deep WMH (DWMH), and 68% have periventricular WMH (PVWMH), whereas of individuals aged 80–90 years, 100% have DWMH, and 95% have PVWMH (5). Several factors contribute to the formation of WMH, including age, hypertension, apolipoprotein E ε4 allele, diabetes, hyperlipidemia, race, female sex, smoking, and alcohol consumption (5, 6). Studies have demonstrated that WMH is associated with cognitive decline, dementia, depression, stroke, gait disorder, and urinary system problems (5, 6).

Extensive evidence indicates that WMH is associated with cognitive impairment (4, 7, 8). WMH increases the risk of all-cause dementia, AD, and vascular dementia by 14, 25, and 73%, respectively (8). Notably, the nature and severity of related cognitive impairment depend on the volume and location of WMH and the patient's cognitive reserve (4, 7). Compared to conventional MRI, the application of novel MRI techniques to explore the relationship between WMH and cognitive impairment may facilitate early diagnosis of WMH and predict its progression, which is critical to enhancing our understanding of the pathogenesis of WMH and associated cognitive impairment.

WMH

Definition of WMH

Before 2013, the medical imaging diagnostic terms for WMH were not unified. Wardlaw et al. (2) summarized the terms used in WMH, including leukoaraiosis, white matter lesions, white matter hyperintensity, leukoencephalopathy, and white matter disease. Standards for Reporting Vascular Changes on Neuroimaging (STRIVE) recommended the term "white matter hyperintensity of presumed vascular origin" and defined WMH in 2013. WMH is hyperintense on T_2-weighted and T_2-fluid attenuated inversion recovery sequences; it may appear as isointense or hypointense (less hypointense than cerebrospinal fluid) on T_1-weighted image (T_1WI) sequences, depending on the severity of pathological changes and sequence parameters. Notably, lesions of the subcortical gray matter and brainstem should not be classified as WMH, and subcortical hyperintensities can be used as an alternative collective term (2).

Possible Pathogenesis of WMH

The pathogenesis of WMH is complex and multifactorial. Currently, WMH pathogenesis remains unclear. The pathological manifestations of WMH include demyelination, oligodendrocyte apoptosis, axonal damage, and gliosis (9, 10). Several acquired risk factors (such as age and hypertension) interact with WMH susceptibility caused by congenital risk factors (such as the apolipoprotein Eε4 allele), resulting in arterial and venous diseases. Cerebral arteriolar stenosis, arteriosclerosis, and endothelial dysfunction lead to diffuse loss of dynamic cerebral autoregulation.

In contrast, venous collagenosis, such as venous ischemia, periventricular small vein collagen deposition, jugular vein reflux, and pulse wave encephalopathy, causes venous reflux limitation and leads to venous hypertension. The loss of dynamic cerebral autoregulation and venous collagenosis can lead to white matter hypoperfusion, blood–brain barrier (BBB) damage, and ependyma damage. Further, hypoperfusion causes white matter ischemia and damage to the BBB and ependyma, resulting in the leakage of plasma or cerebrospinal fluid components into the brain parenchyma. These cause inflammation and apoptosis, demyelination, oligodendrocyte apoptosis, axonal injury, and gliosis, which may eventually lead to WMH (9, 10).

WMH AND COGNITIVE IMPAIRMENT

WMH Volume and Cognitive Impairment

White matter hyperintensity of presumed vascular origin volume is associated with cognitive impairment, whereby a larger WMH volume is associated with a greater decline in cognitive function (4, 8). Patients with confluent WMH have a greater decrease in annual Mini-Mental State Examination scores; patients with mild cognitive impairment (MCI) and confluent WMH are more likely to develop AD (11). Moreover, WMH volumes are significantly increased in patients with MCI that evolve to AD (12). Studies on the relationship between total WMH volume and cognitive impairment have yet to reach a consensus. Some scholars believe that total WMH volume is negatively correlated with executive function, memory, and speed performance (5, 13, 14). However, Melazzini et al. (15) propose that there is no correlation between total WMH volume and cognitive ability. The presence of WMH does not necessarily lead to cognitive impairment, indicating that patients with WMH may be asymptomatic (16). Decarl highlighted that WMH volume was associated with decreased cognitive scores only when $>0.5\%$ of the total intracranial volume (17). These findings suggest that WMH volume is closely associated with cognitive impairment. Nevertheless, the relationship between total WMH volume and cognitive impairment requires further investigation.

WMH and Cognitive Impairment in Different Locations and T_1WI Signal Intensity

White matter hyperintensity of presumed vascular origin location is associated with specific cognitive impairment and spatial specificity (7, 8). The correlation between PVWMH and cognitive impairment is stronger than that between PVWMH and DWMH. PVWMH is associated with various types of cognitive impairment, whereas DWMH is negatively correlated with motion speed (8, 14, 15). A possible pathogenic mechanism involves PVWMH-mediated disruption of long-distance white matter connectivity, leading to cognitive decline in several locations. DWMH disrupts short-distance connections and impairs cognitive abilities in specific brain regions (18, 19). One study reported that frontal WMH near the frontal ventricles affected executive function and parieto-temporal WMH near the posterior horns resulted in memory deterioration (14). Kaskikallio et al. demonstrated that the parieto-occipital region was associated with processing speed and speech memory

---

Abbreviations: AD, Alzheimer's disease; ALFF, low-frequency fluctuations; BBB, blood–brain barrier; CBF, cerebral blood flow; CSVD, cerebral small vessel disease; DCE-MRI, enhanced magnetic resonance imaging; DTI, diffusion tensor imaging; DWMH, deep WMH; FC, functional connectivity; IVIM, intravoxel incoherent motion; MCI, mild cognitive impairment; MRI, magnetic resonance imaging; MRS, magnetic resonance spectroscopy; NAWM, normal-appearing white matter; OEF, oxygen extraction fraction; PVWMH, periventricular WMH; Rs-fMRI, resting-state functional magnetic resonance imaging; sMRI, structural magnetic resonance imaging; T_1WI T_1, weighted image; WMH, white matter hyperintensity of presumed vascular origin; 3D-ASL, 3D-arterial spin labeling.

disorders, whereas WMH in the upper deep white matter compromised motor speed performance. Temporal lobe WMH is associated with processing speed impairment, and the processing speed of patients with MCI and AD with temporal lobe WMH is significantly decreased (20).

Recently, Luca et al. (15) employed a novel classification method to classify WMH into four types: T_1-hypointense PVWMH, non-T_1-hypointense PVWMH, T_1-hypointense DWMH, and non-T_1-hypointense DWMH. They reported that WMH with T_1WI hypointensity was associated with poorer cognitive ability, and WMH with T_1WI hypointensity around the ventricle was significantly associated with cognitive impairment. These results suggest that PVWMH is more closely associated with cognitive impairment than DWMH and that WMH in different brain regions is associated with distinct cognitive impairment. WMH with T_1WI hypointensity may be the most severe WMH. In this regard, combining the traditional classification of WMH with the location and intensity of lesions in T_1WI may be more valuable than previous classification approaches (12, 15).

Changes in WMH and Cognitive Impairment

White matter hyperintensity of presumed vascular origin may progress or regress; these processes may even occur simultaneously (4, 10, 21). The volume and severity of WMH increase over time (4, 5). One study showed that 25.5% of participants had regression of WMH, 19.1% had no change in WMH, and 55.4% had progression of WMH (22). In the 2008 Rotterdam Scan Study, 39% of participants had increased WMH volume within 3.4 years. In the 2009 Oregon Brain Aging Study, 84% of patients developed WMH progression within 9.1 years. Overall, the annual growth rate of WMH volume was 4.4–37.2% (5). When patients with MCI evolved to AD, the T_1WI hypointense intensity of paracortical WMH was significantly decreased, and the T_1WI hypointense intensity of other regions decreased significantly with age (12). Large-scale longitudinal MRI studies have demonstrated that increased WMH volume can lead to an accelerated decline in cognitive function (4, 10). The mean annual decline in cognitive function is $\sim$2-folds for each standard deviation increase in WMH volume (13). An increase in PVWMH and DWMH volumes is associated with a decrease in Mini-Mental State Examination scores (4, 23). In addition, an increase in DWMH volume is significantly correlated with a change in language fluency score (23), and an increase in PVWMH volume is correlated with a decrease in information processing speed and general cognitive ability (4).

Studies have also reported a reduction in WMH. In a previous study (24), 71 participants (37%) exhibited a decrease in WMH within 1 year. Another study evaluated middle-aged and elderly participants living in the community three times over 9 years. During the first follow-up, 26 participants (9.4%) exhibited a decrease in WMH volume, but only 1 participant (0.4%) exhibited a decrease in WMH volume throughout the follow-up period (21). A recent study reported that 87 patients with subcortical vascular cognitive impairment had WMH progression, and 17 had WMH regression over a 3-year period (25). The cognitive function of the two groups decreased, and there was no difference in the rate of decline of language, visuospatial function, memory, executive function, or general cognitive function. These results may be due to the severe WMH burden at baseline and the small sample size of the study. Although the net amount of WMH was generally reduced in the WMH regression group, severe WMH may have perturbed network connections and continued to progress, resulting in a significant decline in cognitive function (25). These findings suggest that the changes in WMH are non-linear, which can accelerate over time, or their progress may be attenuated or interrupted for various reasons (21). In summary, WMH progression can lead to an accelerated decline in cognitive ability.

APPLICATION OF MULTIMODAL MRI TECHNIQUES FOR WMH AND COGNITIVE IMPAIRMENT

Structural Magnetic Resonance Imaging

White matter hyperintensity of presumed vascular origin, cognitive impairment, and brain atrophy often coexist in older adults. Voxel-based morphometry enables quantitative measurement of the volume of whole-brain white matter and gray matter and accurate analysis of the difference in volume and density of gray matter. Gray matter defects are associated with reduced cognitive function in patients with WMH (26). A recent study demonstrated that WMH was associated with a decrease in gray matter in the middle temporal gyrus, right medial frontal gyrus, and left parahippocampal gyrus (27). This agrees with another study that reported significantly lower cortical and subcortical widespread gray matter density in participants with WMH with cognitive impairment/AD than in control participants; Moreover, white matter volume was significantly different between participants with WMH with cognitive impairment/AD and the control group (26). In addition, Ashwati's results revealed non-unidirectional relationships between WMH burden, gray matter volume, and cognition in MCI. At a high burden, WMH and gray matter volume were negatively correlated, whereas at a low burden, WMH and gray matter volume were positively correlated. The negative correlation between WMH and memory and executive function is regulated by regional gray matter volume (28).

Previous studies have demonstrated that cortical thinning and WMH are associated with cognitive impairment (29, 30). Longitudinal studies have revealed that parietal WMH is associated with left entorhinal cortical and right frontal atrophy, and total WMH volume is associated with cortical thinning in the right frontal and parietal regions. Moreover, cortical thinning is associated with poorer memory (29), and WMH progression is associated with faster cortical thinning (25). These results suggest that WMH may promote brain atrophy, leading to cognitive decline. These data may deepen our understanding of the pathogenesis of cognitive impairment in patients with WMH.

Dynamic Contrast-Enhanced Magnetic Resonance Imaging

Blood–brain barrier dysfunction is one of the pathophysiological mechanisms of WMH (9, 10). Dynamic contrast-enhanced magnetic resonance imaging (DCE-MRI) is widely used as an indicator of WMH, as well as for assessing the functional integrity of the BBB (31). Studies have shown that BBB leakage was greater in patients with WMH than in those without WMH (32, 33). Among participants with higher WMH load, the leakage rate of BBB in normal-appearing white matter (NAWM), WMH, and gray matter was significantly higher (31), and there was no significant difference in the leakage rate of NAWM, WMH, and cortical gray matter (33). Another study found that a lower leakage rate in WMH was associated with a larger WMH volume. This may be due to the decreased perfusion of WMH, which needs further study (34). BBB leakage increased with increased hypertension and the load of WMH and NAWM (35). Higher BBB permeability is associated with higher WMH burden and decreased cognitive ability (31). Higher BBB leakage at baseline was associated with stronger cognitive decline, especially in executive function (32). BBB dysfunction may be the mechanism of CSVD and cognitive impairment. The increase of BBB leakage in the WMH area indicates the deterioration of cognitive function in the future (31, 33, 36). These results suggest that DCE-MRI may help to evaluate the permeability of BBB in WMH and its relationship with cognitive impairment. Impaired BBB integrity may be a key factor in the pathogenesis of WMH and part of a series of pathological processes that eventually lead to cognitive impairment.

Diffusion Tensor Imaging

Diffusion tensor imaging is widely used to evaluate the microstructural integrity of the matter. Common DTI parameters include fractional anisotropy (FA), mean diffusivity (MD), axial diffusivity, and radial diffusivity (37). It is generally believed that lower FA and higher MD reflect poor microstructural integrity of white matter (38, 39). Cognitive function is closely associated with white matter integrity detected by DTI (40, 41). The related injury is not limited to visible lesions but also exists in NAWM around the WMH. Over time, abnormal changes in NAWM precede the progression of WMH, referred to as the WMH penumbra (42). In a study by Zhong et al. (43), patients with WMH underwent DTI and 3D-arterial spin labeling (3D-ASL). The results demonstrated that FA and MD of NAWM were significantly correlated with WMH volume, and multiple linear regression analysis indicated that overall cognitive function was independently correlated with WMH-FA and NAWM-FA but not with cortical cerebral blood flow (CBF). This suggests that the relationship between overall cognitive function and white matter integrity may be closer than that with blood supply.

Cognitive impairment in patients with WMH is associated with the microstructural destruction of various white matter fibers, which may include "disconnection" of cortical-subcortical pathways (40, 41). Yuan et al. (40) reported that compared with that in NAWM and control groups, FA in the WMH group was significantly decreased, and MD was significantly increased. The MD values of the periventricular white matter and corpus callosum in the NAWM group were significantly higher than those in the control group, suggesting the destruction of the nerve fiber bundles. A recent study (39) demonstrated that in patients with WMH, the MD values of several fiber bundles, including the bilateral anterior thalamic radiation, left inferior fronto-occipital fasciculus, right inferior longitudinal fasciculus, and right superior longitudinal fasciculus, were negatively correlated with memory function. The anterior part of the right inferior fronto-occipital fasciculus and the posterior and middle parts of the right inferior longitudinal fasciculus were negatively correlated with Mini-Mental State Examination scores and episodic memory. These results suggest that WMH pathogenesis may be related to the microstructural integrity of the white matter. In this regard, cognitive impairment in patients with WMH may be due to the "disconnection" of cortical-subcortical pathways.

3D-ASL

Cerebral perfusion decreases throughout the life cycle and changes in the early stages of age-related neuropathies (44). 3D-ASL permits non-invasive quantification of CBF and has good reliability and repeatability (45). One study reported that greater WMH severity was associated with lower average CBF of whole-brain white matter and CBF at and around the lesion (42, 46). A quantitative study of CBF in patients with different degrees of WMH using 3D-ASL revealed that CBF in WMH was lower than that in the surrounding tissues, and whole-brain CBF in patients with confluent WMH was 20% lower than that in patients with spotted or newly confluent WMH (47). CBF is significantly reduced in patients with cognitive impairment (48). A longitudinal study reported that a decrease in whole-brain CBF was associated with a decrease in processing speed, and better baseline perfusion was associated with better executive function. A decrease in whole-brain perfusion is also associated with deterioration of brain structure and a decrease in processing speed (44). Brain perfusion may significantly impact the maintenance of white matter integrity in patients with WMH (43). Patients with MCI with WMH exhibit reduced regional cerebral blood flow in the frontal, parietal, and medial temporal lobes and putamen compared to those without WMH (49). The decrease in CBF is related to the volume of WMH (50). Among patients with AD, patients with WMH have less local CBF and a wider range than patients without WMH, especially in the frontal and middle temporal lobes (51). Crucially, a larger volume of WMH is associated with lower whole-brain and cortical CBF (50, 52). In a study on patients with AD and control patients without AD (53), whole-brain CBF and CBF in different brain regions were significantly reduced in the AD group. Meanwhile, whole-brain CBF, PVWMH, and DWMH were positively correlated with Montreal Cognitive Assessment Scale scores.

Arterial spin labeling permits the detection of CBF changes in the penumbra (42). A study compared the penumbra of WMH structure with that of CBF using FLAIR, pulsed arterial spin labeling, and DTI. The variation in DTI parameters extended to 2–9 mm around the WMH, whereas the variation in CBF extended to 13–14 mm. This suggests that the CBF penumbra may be more extensive than the structural penumbra in WMH tissues, with or without microstructural changes (54). Collectively, these results suggest that WMH severity is negatively correlated with CBF, which may contribute to the early diagnosis and prediction of WMH. These data provide help to the pathogenesis of WMH and cognitive impairment in patients with WMH.

Intravoxel Incoherent Motion

Intravoxel incoherent motion enables the simultaneous evaluation of microvasculature and microstructure. Accordingly, this approach provides insight into the interplay between brain tissue and vessels. Moreover, it does not rely on tracer delivery (55, 56). IVIM has revealed increased parenchymal diffusivity and decreased perfusion in patients with CSVD and a correlation between cognitive decline and WMH (56). Sun et al. (55) demonstrated that both PVWMH and DWMH are associated with decreased fast diffusion and increased slow diffusion. An increased perfusion fraction in PWMH is associated with improved cognitive function. The observed association between decreased microvascular perfusion of NAWM and decreased cognitive function supports previous findings that NAWM in CSVD may be affected before pathological abnormalities (i.e., WMH) become apparent and perfusion abnormalities may precede structural abnormalities (57).

Nevertheless, this result is not fully consistent with previously reported results. One study demonstrated that both perfusion volume fraction and parenchymal diffusivity were higher than those in the control group and increased with an increase in WMH burden (58). Further research is warranted to clarify the relationship between perfusion volume fraction and blood flow. Nevertheless, findings from IVIM imaging indicate that increases in perfusion fraction and parenchymal diffusivity in WMH are both associated with disease severity, highlighting the potential of IVIM imaging as a surrogate marker for CSVD.

Magnetic Resonance Spectroscopy

Magnetic resonance spectroscopy technology is an MR technology used for the non-invasive evaluation of metabolic changes in brain tissue. 1H-MRS is currently the most widely used method. Its main metabolites are N-acetylaspartate, choline, creatine, and phosphocreatine (59). Reports suggest that cognitive function in patients with WMH is associated with neurometabolite levels (60). One study reported that in patients with vascular cognitive impairment, creatine was significantly correlated with executive function, memory, attention, and overall cognitive scores; N-acetylaspartate was significantly correlated with executive function and overall cognitive scores; changes were observed in metabolic concentrations in both WMH and NAWM (61). The assessment of neurometabolite levels in patients with WMH provides additional information about vascular cognitive impairment and cognitive function, which may not be readily available by measuring WMH volume (61). Another study (62) reported that the N-acetylaspartate/creatine and N-acetylaspartate/choline ratios in WMH were significantly decreased, and cognitive function score was positively correlated with N-acetylaspartate/choline and N-acetylaspartate/creatine ratios in WMH and N-acetylaspartate choline ratios in NAWM. In addition, Xing et al. (60) proposed that the N-acetylaspartate/creatine and choline/creatine ratios in 1H-MRS can be used to diagnose early WMH and evaluate cognitive impairment in patients with WMH. In sum, MRS is a useful technique for the early diagnosis of WMH and cognitive impairment, which may help to elucidate WMH pathogenesis.

Resting-State Functional Magnetic Resonance Imaging

Resting-state functional magnetic resonance imaging reflects the activity of brain regions by relying on MR signals generated by the changes in the blood oxygen levels of brain tissues in the resting state (63). The oxygen extraction fraction (OEF) is an important parameter of brain metabolism and a key biomarker of tissue vitality, detecting oxygen utilization rate to oxygen delivery rate (64). Compared with patients without WMH, patients with WMH have significantly lower CBF values and significantly higher OEF values (65, 66). This may be due to increased oxygen extraction due to abnormally reduced blood flow (67). With the increase of WMH density, CBF decreased, and OEF increased. In addition, in concentric contours close to WMH, OEF gradually increased, and CBF decreased (66). WMH is related to OEF, but it will change due to the existence of cognitive impairment (68). The lower the OEF, the more severe the cognitive impairment, possibly due to reduced oxygen consumption resulting from reduced neural activity (67). The recent studies have shown that WMH is related to OEF, but it will change due to the existence of cognitive impairment (68). The OEF of cognitively impaired subjects was higher than that of those with cognitive integrity. The increase of WMH load in cognitive impairment subjects was significantly correlated with the decrease of OEF, but not in the cognitively intact (68).

The amplitude of low-frequency fluctuations (ALFF) of rs-fMRI signals can be used to detect spontaneous brain activity under physiological conditions. ALFF has been used to study WMH and associated cognitive impairment (69, 70). Cognitive impairment in patients with WMH may be associated with different amplitude fluctuations in rs-fMRI signals (69). A previous study (71) reported the large differences in ALFF predominantly in the posterior cingulate cortex, posterior precuneus, and right inferior temporal gyrus. The ALFF value of the inferior temporal gyrus was significantly higher in the WMH-MCI group than in the WMH-AD and control groups, and the change in ALFF was positively correlated with the executive function score. Moreover, the ALFF value of the temporal posterior cingulate cortex was significantly lower, and the ALFF value of the precuneus was significantly higher in patients with WMH-AD than in the control group. Another study (69) demonstrated that ALFF values in the right inferior occipital gyrus, left precuneus, right superior frontal gyrus, and right superior occipital gyrus were significantly higher in the non-cognitive WMH group than in the normal control group. Further, the ALFF values of the right inferior occipital gyrus, superior occipital gyrus, left middle temporal gyrus, and precuneus were significantly lower in the cognitively impaired WMH group than in the non-cognitively impaired WMH group.

Cognitive impairment in patients with WMH may be associated with abnormal functional connectivity (FC) (72, 73). In one study (73), FC in subcortical nuclei and central cortical areas of cognitive networks was decreased in patients with WMH-MCI, especially in the cingulate cortex. Another study reported that (72), compared with the control group, the MCI group exhibited decreased FC between the precuneus seeds and bilateral lateral temporal cortex, medial prefrontal cortex, posterior cingulate cortex, and parietal lobe. There was a significant regional correlation between WMH volume and default mode network (DMN) FC in the MCI group. FC of the DMN is lower in patients with MCI than in cognitively healthy elderly, and its degree is distinct from that of WMH. These findings suggest that WMH plays a key role in the destruction of DMN in patients with cognitive impairment. In a recent study by Chen et al. (74), participants underwent DTI and rs-fMRI. The results revealed that participants with a higher WMH load had higher FC in the DMN of the medial frontal gyrus and lower FC in the DMN of the thalamus. The increase in radial diffusivity in the white matter bundle between the hippocampus and posterior cingulate cortex was identified as an independent indicator of poor memory. These abnormal FC and structural connections were independently associated with slower processing speed and poor memory. Collectively, these results suggest that OEF, ALFF, and FC obtained by rs-fMRI can be used to explore WMH and cognitive impairment, which may help to deepen our understanding of the pathogenesis of cognitive impairment in patients with WMH.

DISCUSSION AND CONCLUSION

The pathogenesis of WMH is heterogeneous. Studies have shown that the vascular anatomy and pathogenesis of PVWMH and DWMH are different, but ischemia is both involved (9, 10). It should be noted that the smooth halo hyperintensity adjacent to the ventricle is associated with ependymal rupture, ependymal gliosis, and myelin loss but is not caused by ischemia (75). WMH induced by arterial stenosis usually shows dot or patchy hyperintensity with an obvious dividing line. Arteriosclerosis-related WMH is mainly characterized by symmetrical hyperintensity around the basal ganglia. However, venous white matter lesions may have symmetrical cloud patterns around bilateral periventricular (signal intensity is often lower than WMH). Multiple ischemic foci may be caused by asymptomatic cardiogenic embolism; cerebral amyloid angiopathy-related WMH may be unevenly distributed, but it is more likely to occur in the occipital lobe (76).

In conclusion, WMH is closely associated with cognitive impairment, which is related to the location, size, and progression of WMH. In addition, WMH with T_1WI hypointensity seems more detrimental than WMH without T_1WI hypointensity, and the former is closely related to cognitive impairment. Structural MRI research suggests that WMH may accelerate changes in brain structure, promote neurodegenerative changes, and affect cognitive ability. DTI and 3D-ASL are the useful tools for the early clinical diagnosis and prediction of WMH. Pathogenesis identified by DTI may be related to the integrity of white matter microstructure, whereas 3D-ASL enables CBF quantification. CBF abnormalities in patients with WMH precede microstructural changes, which may be due to the integrity of white matter microstructure requires maintenance of CBF. IVIM imaging indicates that the increase in WMH perfusion fraction and parenchymal dispersion is associated with disease severity. In this regard, IVIM imaging may be harnessed as a novel marker of CSVD. MRS can provide additional information through the evaluation of neurometabolite levels in patients, which is useful for the early diagnosis of WMH and cognitive impairment as well as for understanding the pathogenesis of WMH. Rs-fMRI permits the detection of spontaneous brain activity and FC to explore WMH and cognitive dysfunction.

The research is currently limited to single pathogenic mechanisms, and the relationship between different mechanisms should not be overlooked. Simultaneously, treatment measures are limited by research on pathogenesis. In the future, molecular biology can be harnessed as a bridge in combination with multimodal MRI imaging, neurobiology, and other disciplines to further explore the pathogenesis and treatment of WMH and cognitive impairment by expanding clinical sample sizes, increasing follow-up time, and exploring novel biomarkers.

AUTHOR CONTRIBUTIONS

FM, YY, and GJ have made a substantial, direct, and intellectual contribution to the work and were involved in the preparation, correction, and modification of the manuscript. All authors contributed to the article and approved the submitted version.

FUNDING

This study was funded by Medical Development Scientific Research Fund of China Emergency General Hospital (K202106).

ACKNOWLEDGMENTS

We would like to thank Editage (www.editage.com) for English language editing.

REFERENCES

1. Badji A, Westman E. Cerebrovascular pathology in Alzheimer's disease: hopes and gaps. *Psychiatry Res Neuroimaging.* (2020) 306:111184. doi: 10.1016/j.pscychresns.2020.111184
2. Wardlaw JM, Smith EE, Biessels GJ, Cordonnier C, Fazekas F, Frayne R, et al. Neuroimaging standards for research into small vessel disease and its contribution to ageing and neurodegeneration. *Lancet Neurol.* (2013) 12:822–38. doi: 10.1016/S1474-4422(13)70124-8
3. Litak J, Mazurek M, Kulesza B, Szmygin P, Litak J, Kamieniak P, et al. Cerebral Small Vessel Disease. *Int J Mol Sci.* (2020) 21:9729. doi: 10.3390/ijms21249729

4. Prins ND, Scheltens P. White matter hyperintensities, cognitive impairment and dementia: an update. *Nat Rev Neurol.* (2015) 11:157–65. doi: 10.1038/nrneurol.2015.10
5. Alber J, Alladi S, Bae HJ, Barton DA, Beckett LA, Bell JM, et al. White Matter Hyperintensities in Vascular Contributions to Cognitive Impairment and Dementia (Vcid): Knowledge Gaps and Opportunities. *Alzheimers Dement.* (2019) 5:107–17. doi: 10.1016/j.trci.2019.02.001
6. Frey BM, Petersen M, Mayer C, Schulz M, Cheng B, Thomalla G. Characterization of white matter hyperintensities in large-scale mri-studies. *Front Neurol.* (2019) 10:238. doi: 10.3389/fneur.2019.00238
7. Biesbroek JM, Weaver NA, Biessels GJ. Lesion location and cognitive impact of cerebral small vessel disease. *Clin Sci.* (2017) 131:715–28. doi: 10.1042/CS20160452
8. Hu HY, Ou YN, Shen XN, Qu Y, Ma YH, Wang ZT, et al. White matter hyperintensities and risks of cognitive impairment and dementia: a systematic review and meta-analysis of 36 prospective studies. *Neurosci Biobehav Rev.* (2021) 120:16–27. doi: 10.1016/j.neubiorev.2020.11.007
9. Lin J, Wang D, Lan L, Fan Y. Multiple factors involved in the pathogenesis of white matter lesions. *Biomed Res Int.* (2017) 2017:9372050. doi: 10.1155/2017/9372050
10. Wardlaw JM, Smith C, Dichgans M. Small vessel disease: mechanisms and clinical implications. *Lancet Neurol.* (2019) 18:684–96. doi: 10.1016/S1474-4422(19)30079-1
11. Heng LC, Lim SH, Foo H, Kandiah N. Confluent white matter in progression to Alzheimer dementia. *Alzheimer Dis Assoc Disord.* (2021) 35:8–13. doi: 10.1097/WAD.0000000000000409
12. Dadar M, Maranzano J, Ducharme S, Collins DL, Alzheimer's Disease Neuroimaging I. White Matter in Different Regions Evolves Differently During Progression to Dementia. *Neurobiol Aging.* (2019) 76:71–9. doi: 10.1016/j.neurobiolaging.2018.12.004
13. Dhamoon MS, Cheung YK, Moon Y, DeRosa J, Sacco R, Elkind MSV, et al. Cerebral white matter disease and functional decline in older adults from the northern manhattan study: a longitudinal cohort study. *PLoS Med.* (2018) 15:e1002529. doi: 10.1371/journal.pmed.1002529
14. Lampe L, Kharabian-Masouleh S, Kynast J, Arelin K, Steele CJ, Loffler M, et al. Lesion location matters: the relationships between white matter hyperintensities on cognition in the healthy elderly. *J Cereb Blood Flow Metab.* (2019) 39:36–43. doi: 10.1177/0271678X17740501
15. Melazzini L, Mackay CE, Bordin V, Suri S, Zsoldos E, Filippini N, et al. White matter hyperintensities classified according to intensity and spatial location reveal specific associations with cognitive performance. *Neuroimage Clin.* (2021) 30:102616. doi: 10.1016/j.nicl.2021.102616
16. Das AS, Regenhardt RW, Vernooij MW, Blacker D, Charidimou A, Viswanathan A. Asymptomatic cerebral small vessel disease: insights from population-based studies. *J Stroke.* (2019) 21:121–38. doi: 10.5853/jos.2018.03608
17. DeCarli C, Murphy DG, Tranh M, Grady CL, Haxby JV, Gillette JA, et al. The effect of white matter hyperintensity volume on brain structure, cognitive performance, and cerebral metabolism of glucose in 51 healthy adults. *Neurology.* (1995) 45:2077–84. doi: 10.1212/WNL.45.11.2077
18. Griffanti L, Jenkinson M, Suri S, Zsoldos E, Mahmood A, Filippini N, et al. Classification and characterization of periventricular and deep white matter hyperintensities on Mri: a study in older adults. *Neuroimage.* (2018) 170:174–81. doi: 10.1016/j.neuroimage.2017.03.024
19. Bolandzadeh N, Davis JC, Tam R, Handy TC, Liu-Ambrose T. The association between cognitive function and white matter lesion location in older adults: a systematic review. *BMC Neurol.* (2012) 12:126. doi: 10.1186/1471-2377-12-126
20. Kaskikallio A, Karrasch M, Koikkalainen J, Lotjonen J, Rinne JO, Tuokkola T, et al. White matter hyperintensities and cognitive impairment in healthy and pathological aging: a quantified brain Mri study. *Dement Geriatr Cogn Disord.* (2020) 48:297–307. doi: 10.1159/000506124
21. van Leijsen EMC, van Uden IWM, Ghafoorian M, Bergkamp MI, Lohner V, Kooijmans ECM, et al. Nonlinear temporal dynamics of cerebral small vessel disease: the run Dmc study. *Neurology.* (2017) 89:1569–77. doi: 10.1212/WNL.0000000000004490
22. Al-Janabi OM, Bauer CE, Goldstein LB, Murphy RR, Bahrani AA, Smith CD, et al. White matter hyperintensity regression: comparison of brain atrophy and cognitive profiles with progression and stable groups. *Brain Sci.* (2019) 9:170. doi: 10.3390/brainsci9070170
23. Hirao K, Yamashita F, Tsugawa A, Haime R, Fukasawa R, Sato T, et al. Association of white matter hyperintensity progression with cognitive decline in patients with amnestic mild cognitive impairment. *J Alzheimers Dis.* (2021) 80:877–83. doi: 10.3233/JAD-201451
24. Wardlaw JM, Chappell FM, Valdes Hernandez MDC, Makin SDJ, Staals J, Shuler K, et al. White matter hyperintensity reduction and outcomes after minor stroke. *Neurology.* (2017) 89:1003–10. doi: 10.1212/WNL.0000000000004328
25. Kim SJ, Lee DK, Jang YK, Jang H, Kim SE, Cho SH, et al. The effects of longitudinal white matter hyperintensity change on cognitive decline and cortical thinning over three years. *J Clin Med.* (2020) 9:2663. doi: 10.3390/jcm9082663
26. Wang J, Liang Y, Chen H, Wang W, Wang Y, Liang Y, et al. Structural changes in white matter lesion patients and their correlation with cognitive impairment. *Neuropsychiatr Dis Treat.* (2019) 15:1355–63. doi: 10.2147/NDT.S194803
27. Celle S, Boutet C, Annweiler C, Ceresetti R, Pichot V, Barthelemy JC, et al. Leukoaraiosis and gray matter volume alteration in older adults: the proof study. *Front Neurosci.* (2021) 15:747569. doi: 10.3389/fnins.2021.747569
28. Vipin A, Wong BYX, Kumar D, Low A, Ng KP, Kandiah N. Association between white matter hyperintensity load and grey matter atrophy in mild cognitive impairment is not unidirectional. *Aging.* (2021) 13:10973–88. doi: 10.18632/aging.202977
29. Rizvi B, Lao PJ, Chesebro AG, Dworkin JD, Amarante E, Beato JM, et al. Association of regional white matter hyperintensities with longitudinal alzheimer-like pattern of neurodegeneration in older adults. *JAMA Netw Open.* (2021) 4:e2125166. doi: 10.1001/jamanetworkopen.2021.25166
30. Rizvi B, Narkhede A, Last BS, Budge M, Tosto G, Manly JJ, et al. The effect of white matter hyperintensities on cognition is mediated by cortical atrophy. *Neurobiol Aging.* (2018) 64:25–32. doi: 10.1016/j.neurobiolaging.2017.12.006
31. Li Y, Li M, Zhang X, Shi Q, Yang S, Fan H, et al. Higher blood-brain barrier permeability is associated with higher white matter hyperintensities burden. *J Neurol.* (2017) 264:1474–81. doi: 10.1007/s00415-017-8550-8
32. Kerkhofs D, Wong SM, Zhang E, Uiterwijk R, Hoff EI, Jansen JFA, et al. Blood-brain barrier leakage at baseline and cognitive decline in cerebral small vessel disease: a 2-year follow-up study. *Geroscience.* (2021) 43:1643–52. doi: 10.1007/s11357-021-00399-x
33. Zhang CE, Wong SM, van de Haar HJ, Staals J, Jansen JF, Jeukens CR, et al. Blood-brain barrier leakage is more widespread in patients with cerebral small vessel disease. *Neurology.* (2017) 88:426–32. doi: 10.1212/WNL.0000000000003556
34. Zhang CE, Wong SM, Uiterwijk R, Backes WH, Jansen JFA, Jeukens C, et al. Blood-brain barrier leakage in relation to white matter hyperintensity volume and cognition in small vessel disease and normal aging. *Brain Imaging Behav.* (2019) 13:389–95. doi: 10.1007/s11682-018-9855-7
35. Munoz Maniega S, Chappell FM, Valdes Hernandez MC, Armitage PA, Makin SD, Heye AK, et al. Integrity of normal-appearing white matter: influence of age, visible lesion burden and hypertension in patients with small-vessel disease. *J Cereb Blood Flow Metab.* (2017) 37:644–56. doi: 10.1177/0271678X16635657
36. Chen Y, Wang X, Guan L, Wang Y. Role of white matter hyperintensities and related risk factors in vascular cognitive impairment: a review. *Biomolecules.* (2021) 11:1102. doi: 10.3390/biom11081102
37. Lope-Piedrafita S. Diffusion tensor imaging (Dti). *Methods Mol Biol.* (2018) 1718:103–16. doi: 10.1007/978-1-4939-7531-0_7
38. Power MC, Su D, Wu A, Reid RI, Jack CR, Knopman DS, et al. Association of white matter microstructural integrity with cognition and dementia. *Neurobiol Aging.* (2019) 83:63–72. doi: 10.1016/j.neurobiolaging.2019.08.021
39. Chen HF, Huang LL, Li HY, Qian Y, Yang D, Qing Z, et al. Microstructural disruption of the right inferior fronto-occipital and inferior longitudinal

fasciculus contributes to wmh-related cognitive impairment. *CNS Neurosci Ther.* (2020) 26:576–88. doi: 10.1111/cns.13283

40. Yuan JL, Wang SK, Guo XJ, Teng LL, Jiang H, Gu H, et al. Disconnections of cortico-subcortical pathways related to cognitive impairment in patients with leukoaraiosis: a preliminary diffusion tensor imaging study. *Eur Neurol.* (2017) 78:41–7. doi: 10.1159/000477899
41. Lu T, Wang Z, Cui Y, Zhou J, Wang Y, Ju S. Disrupted structural brain connectome is related to cognitive impairment in patients with ischemic leukoaraiosis. *Front Hum Neurosci.* (2021) 15:654750. doi: 10.3389/fnhum.2021.654750
42. Wu X, Ge X, Du J, Wang Y, Sun Y, Han X, et al. Characterizing the penumbras of white matter hyperintensities and their associations with cognitive function in patients with subcortical vascular mild cognitive impairment. *Front Neurol.* (2019) 10:348. doi: 10.3389/fneur.2019.00348
43. Zhong G, Zhang R, Jiaerken Y, Yu X, Zhou Y, Liu C, et al. Better correlation of cognitive function to white matter integrity than to blood supply in subjects with leukoaraiosis. *Front Aging Neurosci.* (2017) 9:185. doi: 10.3389/fnagi.2017.00185
44. Staffaroni AM, Cobigo Y, Elahi FM, Casaletto KB, Walters SM, Wolf A, et al. A longitudinal characterization of perfusion in the aging brain and associations with cognition and neural structure. *Hum Brain Mapp.* (2019) 40:3522–33. doi: 10.1002/hbm.24613
45. Alsop DC, Detre JA, Golay X, Gunther M, Hendrikse J, Hernandez-Garcia L, et al. Recommended implementation of arterial spin-labeled perfusion mri for clinical applications: a consensus of the ismrm perfusion study group and the european consortium for Asl in dementia. *Magn Reson Med.* (2015) 73:102–16. doi: 10.1002/mrm.25197
46. Huang H, Zhao K, Zhu W, Li H, Zhu W. Abnormal cerebral blood flow and functional connectivity strength in subjects with white matter hyperintensities. *Front Neurol.* (2021) 12:752762. doi: 10.3389/fneur.2021.752762
47. Dolui S, Tisdall D, Vidorreta M, Jacobs DR, Nasrallah IM, Bryan RN, et al. Characterizing a perfusion-based periventricular small vessel region of interest. *Neuroimage Clin.* (2019) 23:101897. doi: 10.1016/j.nicl.2019.101897
48. Zhang N, Gordon ML, Goldberg TE. Cerebral blood flow measured by arterial spin labeling mri at resting state in normal aging and Alzheimer's disease. *Neurosci Biobehav Rev.* (2017) 72:168–75. doi: 10.1016/j.neubiorev.2016.11.023
49. Ishibashi M, Kimura N, Aso Y, Matsubara E. Effects of white matter lesions on brain perfusion in patients with mild cognitive impairment. *Clin Neurol Neurosurg.* (2018) 168:7–11. doi: 10.1016/j.clineuro.2018.02.030
50. Kim CM, Alvarado RL, Stephens K, Wey HY, Wang DJJ, Leritz EC, et al. Associations between cerebral blood flow and structural and functional brain imaging measures in individuals with neuropsychologically defined mild cognitive impairment. *Neurobiol Aging.* (2020) 86:64–74. doi: 10.1016/j.neurobiolaging.2019.10.023
51. Hanaoka T, Kimura N, Aso Y, Takemaru M, Kimura Y, Ishibashi M, et al. Relationship between white matter lesions and regional cerebral blood flow changes during longitudinal follow up in Alzheimer's disease. *Geriatr Gerontol Int.* (2016) 16:836–42. doi: 10.1111/ggi.12563
52. Benedictus MR, Binnewijzend MAA, Kuijer JPA, Steenwijk MD, Versteeg A, Vrenken H, et al. Brain volume and white matter hyperintensities as determinants of cerebral blood flow in Alzheimer's disease. *Neurobiol Aging.* (2014) 35:2665–70. doi: 10.1016/j.neurobiolaging.2014.06.001
53. Li RR, He YS, Liu M, Nie ZY, Huang LH, Lu Z, et al. Analysis of correlation between cerebral perfusion and kim score of white matter lesions in patients with Alzheimer's disease. *Neuropsychiatr Dis Treat.* (2019) 15:2705–14. doi: 10.2147/NDT.S207069
54. Promjunyakul NO, Lahna DL, Kaye JA, Dodge HH, Erten-Lyons D, Rooney WD, et al. Comparison of cerebral blood flow and structural penumbras in relation to white matter hyperintensities: a multi-modal magnetic resonance imaging study. *J Cereb Blood Flow Metab.* (2016) 36:1528–36. doi: 10.1177/0271678X16651268
55. Sun J, Yu X, Jiaerken Y, Song R, Huang P, Wang C, et al. The relationship between microvasculature in white matter hyperintensities and cognitive function. *Brain Imaging Behav.* (2017) 11:503–11. doi: 10.1007/s11682-016-9531-8
56. Raja R, Rosenberg G, Caprihan A. Review of diffusion Mri studies in chronic white matter diseases. *Neurosci Lett.* (2019) 694:198–207. doi: 10.1016/j.neulet.2018.12.007
57. Zhang CE, Wong SM, Uiterwijk R, Staals J, Backes WH, Hoff EI, et al. Intravoxel incoherent motion imaging in small vessel disease: microstructural integrity and microvascular perfusion related to cognition. *Stroke.* (2017) 48:658–63. doi: 10.1161/STROKEAHA.116.015084
58. Wong SM, Zhang CE, van Bussel FC, Staals J, Jeukens CR, Hofman PA, et al. Simultaneous investigation of microvasculature and parenchyma in cerebral small vessel disease using intravoxel incoherent motion imaging. *Neuroimage Clin.* (2017) 14:216–21. doi: 10.1016/j.nicl.2017.01.017
59. Rhodes CJ. Magnetic resonance spectroscopy. *Sci Prog.* (2017) 100:241–92. doi: 10.3184/003685017X14993478654307
60. Xing Y, Fang F, Zhang X, Hou LL, Zheng ZS, Sheikhali M. Proton magnetic resonance spectroscopy and cognitive impairment in patients with ischemic white matter lesions. *J Res Med Sci.* (2013) 18:1061–6. Available online at: https://www.ncbi.nlm.nih.gov/pmc/articles/PMC3908527/?report=classic
61. Gasparovic C, Prestopnik J, Thompson J, Taheri S, Huisa B, Schrader R, et al. 1h-Mr Spectroscopy metabolite levels correlate with executive function in vascular cognitive impairment. *J Neurol Neurosurg Psychiatry.* (2013) 84:715–21. doi: 10.1136/jnnp-2012-303878
62. Wang S, Yuan J, Guo X, Peng P, Gu H, Niu S, et al. Neurochemical correlates of cognitive dysfunction in patients with leukoaraiosis: a proton magnetic resonance spectroscopy study. *Neurol Res.* (2012) 34:989–97. doi: 10.1179/1743132812Y.0000000104
63. Smitha KA, Akhil Raja K, Arun KM, Rajesh PG, Thomas B, Kapilamoorthy TR, et al. Resting state Fmri: a review on methods in resting state connectivity analysis and resting state networks. *Neuroradiol J.* (2017) 30:305–17. doi: 10.1177/1971400917697342
64. Yang Y, Yin Y, Lu J, Zou Q, Gao JH. Detecting resting-state brain activity using Oef-weighted imaging. *Neuroimage.* (2019) 200:101–20. doi: 10.1016/j.neuroimage.2019.06.038
65. Yamaji S, Ishii K, Sasaki M, Imamura T, Kitagaki H, Sakamoto S, et al. Changes in cerebral blood flow and oxygen metabolism related to magnetic resonance imaging white matter hyperintensities in Alzheimer's disease. *J Nucl Med.* (1997) 38:1471–4. Available online at: https://jnm.snmjournals.org/content/38/9/1471.long
66. Kang P, Ying C, Chen Y, Ford AL, An H, Lee JM. Oxygen metabolic stress and white matter injury in patients with cerebral small vessel disease. *Stroke.* (2022) 53:1570–9. doi: 10.1161/STROKEAHA.121.035674
67. Jiang D, Lin Z, Liu P, Sur S, Xu C, Hazel K, et al. Brain oxygen extraction is differentially altered by Alzheimer's and vascular diseases. *J Magn Reson Imaging.* (2020) 52:1829–37. doi: 10.1002/jmri.27264
68. Chiang GC, Cho J, Dyke J, Zhang H, Zhang Q, Tokov M, et al. Brain oxygen extraction and neural tissue susceptibility are associated with cognitive impairment in older individuals. *J Neuroimag.* (2022). doi: 10.1111/jon.12990. [Epub ahead of print].
69. Li C, Yang J, Yin X, Liu C, Zhang L, Zhang X, et al. Abnormal intrinsic brain activity patterns in leukoaraiosis with and without cognitive impairment. *Behav Brain Res.* (2015) 292:409–13. doi: 10.1016/j.bbr.2015.06.033
70. Cheng R, Qi H, Liu Y, Zhao S, Li C, Liu C, et al. Abnormal amplitude of low-frequency fluctuations and functional connectivity of resting-state functional magnetic resonance imaging in patients with leukoaraiosis. *Brain Behav.* (2017) 7:e00714. doi: 10.1002/brb3.714
71. Wang J, Chen H, Liang H, Wang W, Liang Y, Liang Y, et al. Low-frequency fluctuations amplitude signals exhibit abnormalities of intrinsic brain activities and reflect cognitive impairment in leukoaraiosis patients. *Med Sci Monit.* (2019) 25:5219–28. doi: 10.12659/MSM.915528
72. Wang Z, Williams VJ, Stephens KA, Kim CM, Bai L, Zhang M, et al. The effect of white matter signal abnormalities on default mode network connectivity in mild cognitive impairment. *Hum Brain Mapp.* (2020) 41:1237–48. doi: 10.1002/hbm.24871
73. Zhu W, Huang H, Yang S, Luo X, Zhu W, Xu S, et al. Dysfunctional architecture underlies white matter hyperintensities with and without cognitive impairment. *J Alzheimers Dis.* (2019) 71:461–76. doi: 10.3233/JAD-190174
74. Chen X, Huang L, Ye Q, Yang D, Qin R, Luo C, et al. Disrupted functional and structural connectivity within default mode network

contribute to wmh-related cognitive impairment. *Neuroimage Clin.* (2019) 24:102088. doi: 10.1016/j.nicl.2019.102088

75. Kim KW, MacFall JR, Payne ME. Classification of white matter lesions on magnetic resonance imaging in elderly persons. *Biol Psychiatry*. (2008) 64:273–80. doi: 10.1016/j.biopsych.2008.03.024
76. Wu X, Ya J, Zhou D, Ding Y, Ji X, Meng R. Pathogeneses and imaging features of cerebral white matter lesions of vascular origins. *Aging Dis.* (2021) 12:2031–51. doi: 10.14336/AD.2021.0414

Conflict of Interest: The authors declare that the research was conducted in the absence of any commercial or financial relationships that could be construed as a potential conflict of interest.

frontiers | Frontiers in Neurology

TYPE Original Research
PUBLISHED 24 August 2022
DOI 10.3389/fneur.2022.889884

EDITED BY
Xiaofei Hu,
Army Medical University, China

REVIEWED BY
Ruiting Zhang,
Zhejiang University, China
Joan Jiménez-Balado,
University of Southern California,
United States

*CORRESPONDENCE
Maria del C. Valdés Hernández
m.valdes-hernan@ed.ac.uk

SPECIALTY SECTION
This article was submitted to
Applied Neuroimaging,
a section of the journal
Frontiers in Neurology

RECEIVED 04 March 2022
ACCEPTED 01 August 2022
PUBLISHED 24 August 2022

CITATION
Barnes A, Ballerini L, Valdés Hernández MdC, Chappell FM, Muñoz Maniega S, Meijboom R, Backhouse EV, Stringer MS, Duarte Coello R, Brown R, Bastin ME, Cox SR, Deary IJ and Wardlaw JM (2022) Topological relationships between perivascular spaces and progression of white matter hyperintensities: A pilot study in a sample of the Lothian Birth Cohort 1936.
Front. Neurol. 13:889884.
doi: 10.3389/fneur.2022.889884

Topological relationships between perivascular spaces and progression of white matter hyperintensities: A pilot study in a sample of the Lothian Birth Cohort 1936

Abbie Barnes[1], Lucia Ballerini[2], Maria del C. Valdés Hernández[2]*, Francesca M. Chappell[2], Susana Muñoz Maniega[2], Rozanna Meijboom[2], Ellen V. Backhouse[2], Michael S. Stringer[2], Roberto Duarte Coello[2], Rosalind Brown[2], Mark E. Bastin[2], Simon R. Cox[3], Ian J. Deary[3] and Joanna M. Wardlaw[2]

[1]College of Medicine and Veterinary Medicine, University of Edinburgh, Edinburgh, United Kingdom, [2]Department of Neuroimaging Sciences, Centre for Clinical Brain Sciences, University of Edinburgh, Edinburgh, United Kingdom, [3]Department of Psychology, University of Edinburgh, Edinburgh, United Kingdom

Enlarged perivascular spaces (PVS) and white matter hyperintensities (WMH) are features of cerebral small vessel disease which can be seen in brain magnetic resonance imaging (MRI). Given the associations and proposed mechanistic link between PVS and WMH, they are hypothesized to also have topological proximity. However, this and the influence of their spatial proximity on WMH progression are unknown. We analyzed longitudinal MRI data from 29 out of 32 participants (mean age at baseline = 71.9 years) in a longitudinal study of cognitive aging, from three waves of data collection at 3-year intervals, alongside semi-automatic segmentation masks for PVS and WMH, to assess relationships. The majority of deep WMH clusters were found adjacent to or enclosing PVS (waves—1: 77%; 2: 76%; 3: 69%), especially in frontal, parietal, and temporal regions. Of the WMH clusters in the deep white matter that increased between waves, most increased around PVS (waves—1–2: 73%; 2–3: 72%). Formal statistical comparisons of severity of each of these two SVD markers yielded no associations between deep WMH progression and PVS proximity. These findings may suggest some deep WMH clusters may form and grow around PVS, possibly reflecting the consequences of impaired interstitial fluid drainage *via* PVS. The utility of these relationships as predictors of WMH progression remains unclear.

KEYWORDS

perivascular spaces, Virchow-Robin Spaces, white matter hyperintensities, aging, longitudinal, MRI, brain, small vessel disease

Introduction

Enlarged perivascular spaces (PVS) and white matter hyperintensities (WMH) are two of the most common neuroradiological signatures of cerebral small vessel disease (cSVD) (1) in older age, a condition resulting from pathological processes affecting the small arteries, veins, and capillaries in the brain (2). cSVD is identified by the coexistence of microhaemorrhages, WMH, and/or lacunes/lacunar infarcts, usually accompanied by enlarged PVS, in brain magnetic resonance imaging (MRI) scans. PVS are fluid-filled spaces that surround small penetrating blood vessels (1), which provide a route for the clearance of brain waste products (3). When enlarged, they become visible in brain MRI with the appearance of small linear or round structures depending on how they are positioned (i.e., parallel or perpendicular) with respect to the imaging plane. The cause of PVS enlargement is not fully understood but is thought to be related to impaired fluid drainage (4), as a consequence of several pathological processes that affect the cerebral microvasculature, including blood–brain barrier dysfunction, vessel stiffening, and reduced vessel pulsatility (5, 6). MRI-visible PVS, although seen also in scans of healthy adults without cSVD, have been associated with age, vascular risk factors, especially hypertension (7, 8), and WMH (1). WMH, on the contrary, are considered neuropathological features and appear in a wide spectrum of disorders. They have traditionally been associated with de-/dysmyelination processes and axonal degeneration (9), but advances in MRI have revealed that their presence may also reflect changes in interstitial fluid flow and increased water content in the white matter, especially in the earlier stages of cSVD (10). Like PVS, our understanding of WMH pathogenesis is poor, but they are strongly associated with vascular risk factors (11, 12), other imaging features of cSVD (13), cognitive decline, gait disturbance, and an increased risk of stroke and dementia (14).

Although PVS and WMH are commonly seen together in brain MRI scans of cognitively normal older individuals, they are clinically silent, and only a few studies have analyzed their relationship with conflicting results. Thus far, these studies have based their analyses on PVS and WMH severity, as determined by visual rating scores, for which subjectivity may have contributed to the conflicting findings. For instance, two cross-sectional studies found an association between the severity of enlarged PVS with WMH in two different clinical groups: lacunar stroke patients (15) and community-dwelling septuagenarian individuals (16); yet a recent meta-analysis including these studies and six others found no statistically significant associations between the two imaging markers (8).

Computational methods have been developed to quantify a PVS burden from MRI scans, helping to overcome the subjectivity associated with these scoring systems [e.g., (17–22), for mentioning just a few]. A recent study found stronger positive associations between computationally derived PVS metrics and WMH severity than visual scores (23). These cross-sectional associations suggest that widening of PVS might reflect small vessel endothelial dysfunction and impaired interstitial fluid drainage that contributes to a greater WMH burden and accumulating brain damage in aging and cSVD (23). Longitudinal associations between these PVS metrics and WMH have not been studied. However, a high burden of PVS in the basal ganglia (determined by visual rating) has been associated with WMH progression after adjusting for age, sex at birth, and vascular risk factors (24).

There is a growing interest in topological relationships between PVS and WMH. Understanding how PVS and WMH are spatially related to one another in the brain may reveal important insights into their underlying mechanisms and formation. It has been observed that WMH appear to form around PVS in stroke patients (25), typically in the parietal and posterior and lateral temporal regions. A recent study (26) explored the topological associations between WMH and PVS in randomly selected WMH clusters identified in a cross-sectional sample of 136 adults without previous history of stroke, brain trauma, or any neurological or systemic disease and reported that most of the randomly selected deep WMH clusters analyzed were spatially connected to PVS. But longitudinal data are required to directly characterize the within-person temporal dynamics of the processes related to the evolution of WMH and PVS and their possible synergy. The findings from Huang et al. (26), if confirmed in a longitudinal and more heterogeneous sample in terms of vascular disease, would provide further evidence to support a mechanistic link between both cSVD features and reveal whether PVS could predict WMH progression. Being able to identify patients with WMH that are more likely to progress may help to prevent development of associated neurological symptoms and conditions through earlier clinical intervention (27). We hypothesize that in cognitively normal older adults, (1) more deep WMH clusters would probably be spatially close to PVS (than not close) and increase in size around them and (2) those WMH clusters close to PVS, with time, will increase in size more than the WMH clusters that are distant from PVS.

Materials and methods

Subjects and clinical data

We utilized brain MRI, clinical, and demographic data from a randomly selected sample of participants of the Lothian Birth Cohort 1936 Study (https://en.wikipedia.org/wiki/Lothian_birth-cohort_studies), a longitudinal study of cognitive aging comprising community-dwelling individuals from in and around Edinburgh born in 1936. All participants provided written consent to take part in the study under protocols approved by Lothian (REC 07/MRE00/58) and Scottish

Multicentre (MREC/01/0/56) Research Ethics Committees. The methods used for MRI acquisition and clinical data in this cohort have been reported previously (28–30). Participants had their first brain MRI scan at the second wave of testing at a mean age of 72.6 years and subsequent MRI examinations spaced at 3-year intervals (30). For this study, we randomly (i.e., using a random number generator function in MATLAB R2019b) selected a sample of 32 participants with brain MRI available for the first three consecutive scanning waves (i.e., a total of 96 individual MRI scans) with high-quality image data. Vascular risk factors, which included presence or absence of hypertension, hypercholesterolaemia, diabetes mellitus, stroke, and history of cardiovascular disease, were self-reported at each wave (30).

Image acquisition

All brain images were acquired at the Western General Hospital of Edinburgh in a GE Signa Horizon HDx 1.5-T clinical scanner (General Electric, Milwaukee, WI) following the research acquisition protocol described in Wardlaw et al. (29) and ensuring full-brain coverage. In brief, the 3D T1-weighted sequence (160 slices) had an acquisition matrix of 192 × 192 and a voxel size of 1 × 1 × 1.3 mm^3. The axial T2-weighted fast spin echo sequence (TR/TE = 11,320/102 ms, 80 slices) was acquired with a 256 × 256 matrix and a voxel size of 1 × 1 × 2 mm^3. The axial fluid-attenuated inversion recovery (FLAIR) fast spin echo sequence (TR/TE/TI = 9,000/140/2,200 ms, 40 slices) was acquired with a 256 × 192 matrix and a voxel size of 1 × 1 × 4 mm^3. The axial T2*-weighted gradient echo sequence (TR/TE = 940/15 ms, 80 slices) was also acquired with a 256 × 192 matrix, but with a voxel size of 1 × 1 × 2 mm^3. None of the sequences had an inter-slice gap.

Image processing

Each study participant's image data were processed and checked individually. For each participant, all image sequences from all waves were co-registered to the T2-weighted image acquired in the first scanning wave using rigid-body registration (linear, six degrees of freedom) through FSL-FLIRT (31). We used existent binary masks of WMH from the three waves and PVS in the centrum semiovale from the first imaging wave generated as previously published (23, 32, 33) (Supplementary Figure 1). In brief, for the first scanning wave (i.e., referred hereby as wave 1) WMH masks were generated using a multispectral method that combines T2*-weighted and FLAIR images mapped in the red–green color space and quantised to facilitate a robust thresholding using minimum variance quantisation (32). For the other two waves, WMH binary masks were generated from a statistical analysis of the FLAIR-normalized intensities, seeking full compatibility with the semi-automatic approach applied in the first wave, and a higher level of automation: while in the multispectral approach the Gaussians that describe the intensity distribution of the tissue classes in the FLAIR image were adjusted by the observer aided by a combination with another T2-weighted-based image, in the other this adjustment was performed automatically. In brief, hyperintense voxels on FLAIR were identified by thresholding intensity values equal to 1.69*standard deviation above the mean, using an adjusted implementation from Zhan et al. (34). The resulting hyperintense areas unlikely to reflect pathology (i.e., artifacts and cortex) were removed automatically using a lesion distribution template generated from the segmentation results of the first wave. Further refinement was achieved by applying Gaussian smoothing, followed by the removal of voxels with intensity values below 0.1 and *z*-scores below 0.95. All WMH masks were checked and manually edited to ensure the segmentation was as accurate as possible. Bland–Altman analyses yielded a mean WMH volume difference (SD) of 0.38 (1.29) ml and an intra-class correlation coefficient of 0.938, in 15 randomly selected individual datasets that were segmented with both implementation approaches. Voxel-wise reliability analyses comparing the WMH masks manually edited after applying both approaches show only scattered differences in the periventricular boundaries and Dice similarity coefficient of 0.6 (SD = 0.128), similar to the published inter-observer differences using the same method (35). No clusters (i.e., of three or more voxels) of differences were identified.

Segmentation masks for PVS in the deep normal-appearing white matter (i.e., excluding the internal and external capsules that are part of the region clinically defined as basal ganglia for the purposes of PVS identification) were generated using a computational method described previously (23, 36), on T2-weighted images. Succinctly, images were resampled from 256 × 256 × 80 to 256 × 256 × 160, using spline interpolation, to perform the PVS segmentation in images with 1-mm^3 isotropic voxels. According to Wardlaw et al. (1) and Valdés Hernández et al. (37), PVS were identified as tubular structures with lengths between 3 and 50 mm. Tubular structures in the "isotropic" T2-weighted images were enhanced using the Frangi filter in its 3D version, optimized for this purpose with the parameters described by Ballerini et al. (36), which, according to Ballerini et al. (23), enhances structures with widths above 0.5 and below 2.5 voxels. The output from the filter was thresholded, binarised, and quantified in the region of interest. We used 3D connected component analysis to computationally identify and assess the PVS. Segmentation masks for PVS inside WMH were generated using the same method (i.e., thresholding the output of the 3D Frangi filter) but in a fused image obtained by subtracting the FLAIR image from the T2-weighted image after both being corrected for bias-field inhomogeneities using FSL-FAST (38) and their intensities being normalized. This is to discern whether the low-intensity voxels within the WMH

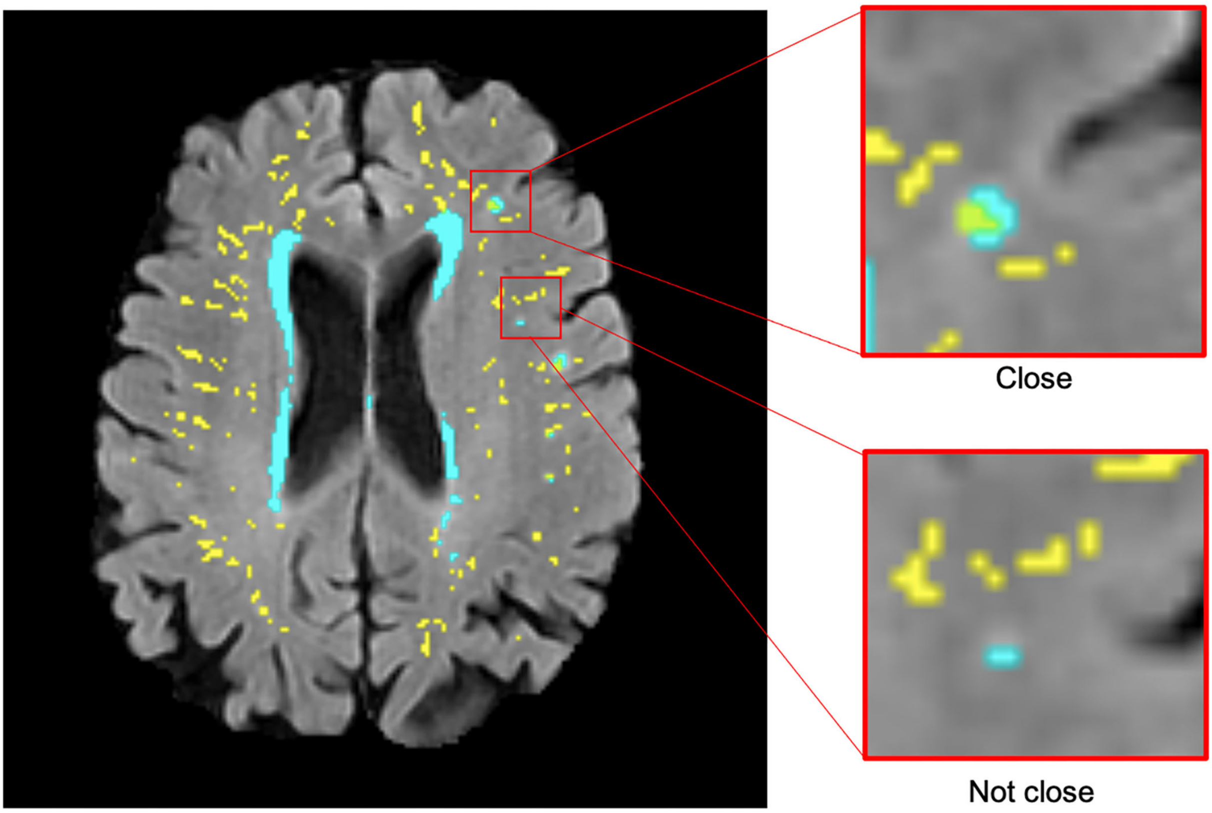

FIGURE 1
Examples of deep WMH in the baseline scan that would be classified as "close" and "not close" to baseline PVS when determining cross-sectional topological relationships (segmentation masks for WMH in cyan and PVS in yellow, overlaid on FLAIR MRI).

in FLAIR correspond to the PVS-like hyperintense structures identified using the T2-weighted image. Combining sequences to increase distinction of PVS-like structures is a well-established procedure (17, 21). The images were individually checked for noise and other artifacts that would affect accuracy of PVS segmentation. To avoid errors in misclassifying small lacunes resembling PVS as PVS, neuroradiological reports were checked.

Visual assessments

Adjacency/closeness (or not) of PVS with WMH clusters [minimum size 3 mm diameter according to Wardlaw et al. (1)] was recorded while/by visually inspecting all slices where PVS were segmented. Initially, the inspection was done in axial slices, and they were double-checked in all radiological orientations throughout the sample in all waves. All visual assessments, performed with MRIcron v1.0.20190902 (https://www.nitrc.org/projects/mricron/), were blinded to visual rating scores for PVS and WMH and participants' clinical and demographic information. These were repeated by the same observer to ensure a perfect intra-observer agreement [mean differences in PVS count ± 95% confidence interval are equal to −0.207 ± 1.637, intra-class correlation coefficient (ICC) 0.99917 for wave 1 and −0.034 ± 1.361, ICC = 0.99961 for wave 2, see Bland–Altman plot in Supplementary Figure 2]. Deep WMH clusters were defined as regions or voxel clusters of WMH not contiguous with the WMH located in the periventricular lining. Periventricular WMH caps surrounding the horns of the lateral ventricles were counted as deep WMH clusters if they extend more than 13 mm from the ventricular surface into the deep white matter (39). Cross-sectional topological relationships were assessed on the first scanning wave. Each deep WMH cluster was recorded and classified as either "close" or "not close" to a perivascular spaces (PVS) in the first scan in co-registered T2-weighted and FLAIR images after superimposing the PVS and WMH binary masks in different contrasting colors (Figure 1). Deep WMH were defined as "close" to a PVS if their segmentation was overlapping or contiguous with a PVS and "not close" if it was not overlapping or contiguous. Adjacent slices were carefully inspected to ensure

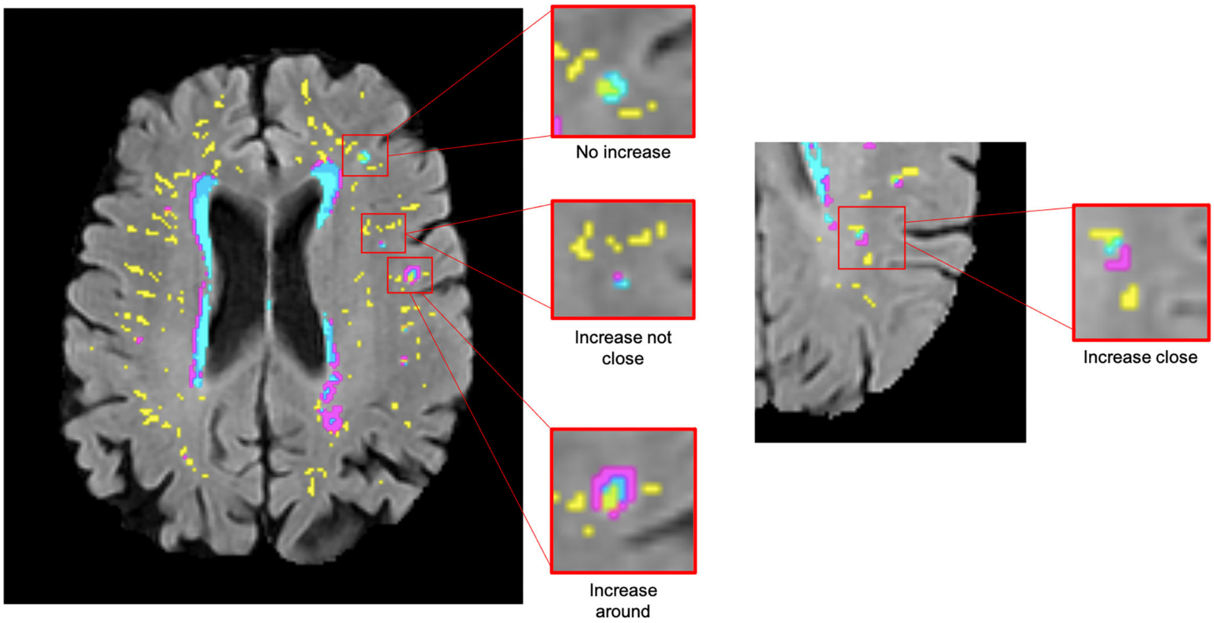

FIGURE 2
Examples of deep WMH for each of the different categories used to determine longitudinal topological relationships (segmentation masks for WMH in cyan, change in WMH in violet, and PVS in yellow, overlaid on FLAIR MRI).

not to miss or double-count any PVS. Each deep WMH cluster was also labeled, and the region of the brain it was found in was recorded—either frontal, parietal, temporal, or occipital, determined by examining lobar segmentations from a digital anatomical atlas (40).

To identify topological relationships longitudinally, the total number of deep WMH clusters was counted again. This time, each was classified according to how their morphology changed relative to baseline PVS between consecutive waves (e.g., waves 1 and 2 and waves 2 and 3) in each participant. A further mask that represented the change in WMH between waves was also overlaid in the FLAIR image to facilitate this assessment (Figure 2). These relationships were defined as follows: "increase around"—deep WMH cluster increased so that more voxels of the WMH mask became contiguous with a PVS; "increase close"—deep WMH cluster previously considered "close" to a PVS, increased in size, but no more of it became contiguous with a PVS (i.e., the adjacency between both—PVS and WMH—masks observed was owed to the same number of voxels as in the previous wave); "increase not close"—deep WMH cluster increased but it was still not contiguous with a PVS; and "no increase"—no visible change in the deep WMH cluster (Figure 2). To avoid WMH cluster change in size being influenced by differences in WMH segmentation algorithms, this was only considered if the change was perceived as nearly having doubled (or halved) or more the original cluster size. Again, all deep WMH clusters counted were recorded according to the lobar brain region.

Statistical analysis

A statistical analysis was performed in R (version 3.6.2). First, the counted data per overall individual brain scan were summarized to show the median count and distribution within the sample, per category. Cross-sectional and longitudinal topological relationships were analyzed by calculating percentages per category, both overall and per brain region. To allow a longitudinal analysis of the cross-sectional relationships, a change in count of deep WMH clusters "close" and "not close" to baseline PVS between waves was simplified into a binary variable where "1" indicates an increase in the number of deep WMH clusters and "0" indicates otherwise (i.e., no change or a decrease). A binary logistic regression with random effects was used to model the association between the change in the number of deep WMH clusters and their location relative to a PVS. Random effects accounted for variation between participants and for correlation within participants, i.e., an individual could contribute more than one row of data to the analysis. Data per overall brain were used, and separate models were performed for waves 1–2 and waves 2–3. In addition to unadjusted models, we evaluated models that corrected for sex at birth and vascular risk factors, including hypertension, hypercholesterolaemia, diabetes mellitus, and history of cardiovascular disease, with a maximum of three predictors per model. We estimated our sample size guided by the only study that visually assessed the topological relationships between WMH and PVS (26), which randomly selected 600 deep WMH clusters from a cross-sectional sample for analysis. In our sample, at baseline (i.e., only in wave 1), the total number of deep WMH clusters counted surpasses 600. Resources available for this study allowed us to process data from 29 individuals. Nevertheless, given the exploratory nature of this study, the complexity, and nature of the assessments, to ensure reproducibility, comparability, trustworthiness, and objectivity in the analyses, this estimate was considered appropriate (41). We consider the primary value of this study to be an indication of feasibility. Moreover, although the LBC 1936 Study, which provided data for the current analysis, enrolls 728 individuals in its first MRI scanning wave, it is inappropriate to use own data for a sample size calculation for an analysis with the same data (41).

To further evaluate whether the spatial relationship between deep WMH clusters and PVS could have been (or not) influenced by the PVS burden, we analyzed the R^2 value of the univariate linear regression models that had the number of PVS close to WMH clusters as independent variables and the WMH volume at each wave as a dependent variable, and we further compared these with the R^2 values of the models that have, instead, the PVS volume and the average PVS size as dependent variables. As R^2 measures the strength of the relationship between the set of independent variables and the dependent variable, if the spatial relationship between PVS and WMH is determined by the PVS burden we would expect higher R^2 values (i.e., less variance around the fitted line) in the models that relate the PVS burden (i.e., total volume, mean PVS size) to the WMH volume. In addition, we calculated the density of PVS "close" and PVS "not close" to WMH at the three scanning waves and conducted a paired t-test (two-tailed) at each wave comparing the densities of PVS "close" and PVS "not close". If our hypothesis on the existence of a spatial relationship between deep WMH clusters and PVS is true, the PVS density (i.e., number per ml) close to deep WMH clusters will be greater than (and significantly different from) the PVS density not close to WMH.

Results

Sample characteristics

Data from three participants were excluded due to inaccuracies in their PVS segmentations mainly due to the presence of motion artifacts in the T2-weighted images. One participant was not included in the models performed between waves 1 and 2 as no deep WMH clusters were counted in either of these waves. The mean age of the sample at baseline was 71.87 years (SD = 0.38). The follow-up MRI scans from waves 2 and 3 were obtained three and six years later, respectively (i.e., at a mean age ~75 and 78 years). Table 1 shows the baseline characteristics of the sample including sex at birth, vascular risk factors, and Fazekas visual rating scores of WMH.

TABLE 1 Baseline participant characteristics, $n = 29$ (CVD = cardiovascular disease).

	Male/Female
Gender	17/12 (58.62%/41.38%)
	Deep/Periventricular
WMH Fazekas scores (median [QR1 QR3])	1 [1 1]/1[1 2]
Diabetes	1 (3.45%)
Hypertension	14 (48.28%)
Hypercholesterolaemia	9 (31.03%)
Stroke	0 (0.00%)
History of CVD	9 (31.03%)

Cross-sectional topological relationships

Figure 3 illustrates the variations in the cross-sectional topologies observed. For deep WMH clusters classed as "close" to a PVS, most bordered a PVS with a small area of overlap (Figure 3A). Within deep WMH clusters that were classed as "not close" to a PVS, there was considerable variability in the distance separating them (Figure 3D). Many of these different topologies existed simultaneously in the same participant (Figure 4).

The median count of deep WMH clusters "close" to baseline PVS (i.e., PVS identified at the first scanning wave) was greater than the median count of those "not close" at all time points (Figure 5). The counts were not normally distributed in this sample, with several participants having zero or very low counts of deep WMH clusters (see individual data in Supplementary files). A higher percentage of WMH clusters in wave 1 were found close to PVS (Table 2). In the rest of the waves, this pattern was also observed (wave 1: 77% "close," 23% "not close"; wave 2: 76% "close," 24% "not close"; wave 3: $n =$ 69% "close," 31% "not close"; Figure 6, Table 2). Despite far fewer deep WMH clusters being counted in the parietal and temporal regions than in the frontal region (Table 2), the percentages of these that were found "close" to baseline PVS (i.e., PVS identified at the first wave) were higher than those found "not close" in these regions (Figure 7; e.g., wave 1—frontal: 75% "close," 25% "not close"; parietal: 81% "close," 19% "not close"; temporal: 86% "close," 14% "not close"). The occipital region was not included in Figure 7 as only one deep WMH cluster was counted in wave 1.

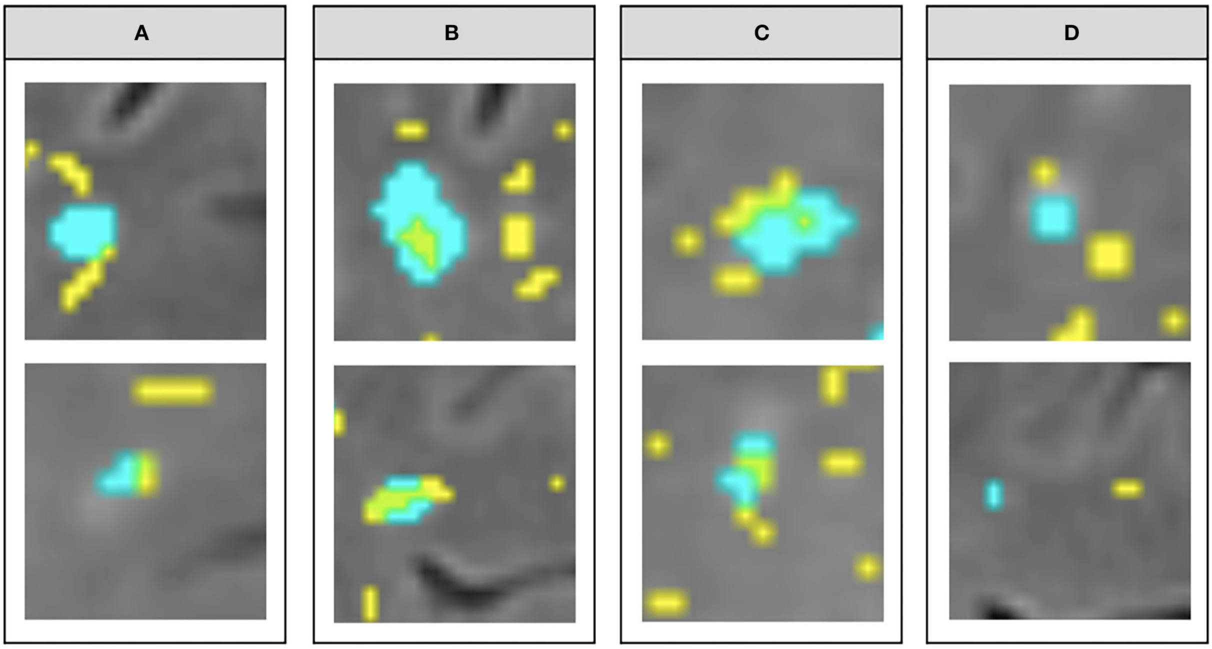

FIGURE 3
Examples of the different topological types observed within the "close" vs. "not close" classification used for describing cross-sectional topological relationships. **(A–C)** show variations within deep WMH classed as "close," while **(D)** shows variations within those classed as "not close" (segmentation masks for WMH in cyan and PVS in yellow, overlaid on FLAIR MRI).

Associations between progression of deep WMH clusters and proximity to PVS at wave 1

Between waves 1 and 2, the number of deep WMH clusters changed in 28 participants. There was a median increase of 2 in deep WMH clusters spatially close to baseline PVS (i.e., PVS detected at wave 1) and 1 in those not close. Between waves 2 and 3, the number of deep WMH clusters changed in all 29 participants. The median change in number spatially close to a PVS increased in 10, while the median change for those "not close" increased in 6. Logistic regression models with random effects found no significant associations between progression (defined by an increase in number) of deep WMH clusters and proximity of these clusters to PVS (i.e., either "close" or "not close") at wave 1. Table 3 shows the odds ratios, 95% confidence intervals, and *p*-values for all models performed.

Longitudinal topological relationships

Figure 8 shows the counts of changes in deep WMH clusters' morphology in relation to baseline PVS. The percentages of the different changes between waves 1 and 2 and waves 2 and 3 are displayed in Figure 9 and Table 4. A greater percentage of deep WMH clusters increased in size (waves 1–2: 70% increased and 30% did not increase; waves 2–3: 77% increased and 23% did not increase). Of those that increased, the most frequent change was an increase in size around the location of the already existent (i.e., "baseline") PVS (waves 1–2: 73% "increased around," 10% "increased close," 17% "increased not close"; waves 2–3: 72% "increased around," 10% "increased close," 18% "increased not close"). When lobar regions were analyzed separately, these trends were also observed (Figure 10, Table 4). The occipital region was not included in Figure 10 because, as previously referred, only one WMH cluster was identified in this region at wave 1.

Although far fewer deep WMH clusters were counted in the parietal and temporal regions compared with the frontal region, we more frequently observed larger WMH clusters forming around multiple PVS in the parietal and posterior temporal regions (Figure 11). Deep WMH clusters in the frontal region were typically smaller in volume with a small area of continuity with a PVS.

Influence of the PVS burden and WMH cluster size in the spatial relationships found

The PVS volume and mean size did not seem to have influenced the spatial relationships found.

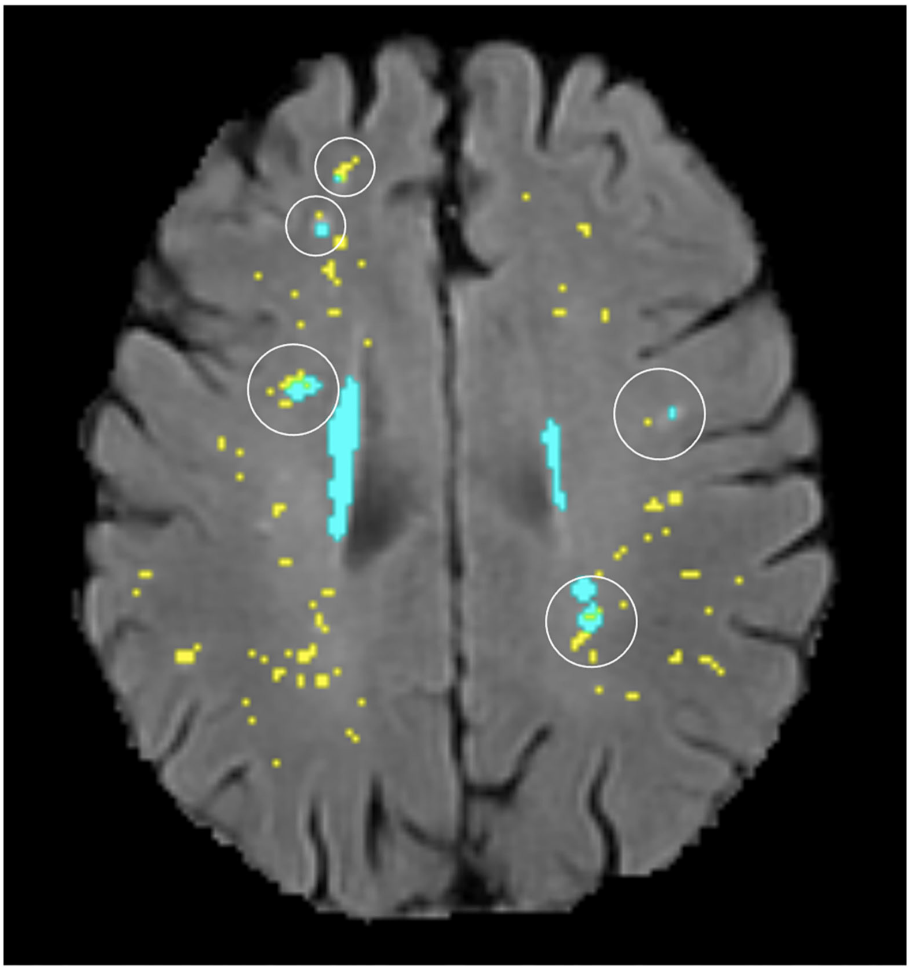

FIGURE 4
Illustration of several different topological types (circled) existing in the same participant (segmentation masks for WMH in cyan and PVS in yellow, overlaid on FLAIR MRI).

As shown in the Supplementary data spreadsheet "PVSandWMHburden_analysis.xlsx," the R^2 value for the linear regression between number of CSO PVS "close" to WMH and WMH volume for the scanning wave 1 was 0.484, for wave 2 it was 0.421, and for wave 3 it was 0.542. On the contrary, the R^2 value for the linear regression between CSO PVS volume and WMH volume for wave 1 was 0.0539, and between mean CSO PVS size and WMH volume, it was 0.049, thus indicating that approximately half of the variation in WMH volume at each wave can be rather explained by the number of PVS "close" to WMH instead of by the PVS burden. Similar results were obtained while evaluating the univariate association between the number of PVS considered "close" or "around" WMH that increased from waves 1 to 2 ($R^2 = 0.581$) and from waves 2 to 3 ($R^2 = 0.512$), and the WMH volume at waves 2 and 3, respectively. Paired t-test analysis of the density of PVS "close" vs. "not close" showed significant differences between both variables at all waves [wave 1: mean (SD) PVS "close" = 0.114 (0.103) ml^{-1}, mean (SD) PVS "not close" = 0.0349 (0.0406) ml^{-1}, $p = 1.259 \times 10^{-6}$; wave 2: mean (SD) PVS "close" = 0.140 (0.117) ml^{-1}, mean (SD) PVS "not close" = 0.0450 (0.0560) ml^{-1}, $p = 2.443 \times 10^{-7}$; wave 3: mean (SD) PVS "close" = 0.216 (0.163) ml^{-1}, mean (SD) PVS "not close" = 0.100 (0.113) ml^{-1}, $p = 1.133 \times 10^{-8}$).

To classify the WMH clusters into "big" or "small" while avoiding inter-/intra-observer bias, we looked at the deep Fazekas scores (provided as part of the Supplementary data) given by the neuroradiologist. As defined in Fazekas et al. (49), the deep WMH scores are equal to 1 if small punctate and very few, 2 if bigger and in higher number, and 3 if large and confluent with the periventricular WMH. From the whole sample, only one subject (subject no. 16) has deep Fazekas scores equal to 3 and two subjects (subject nos. 7 and 11) have deep Fazekas scores equal to 2. Therefore, it is unlikely that the spatial relationship

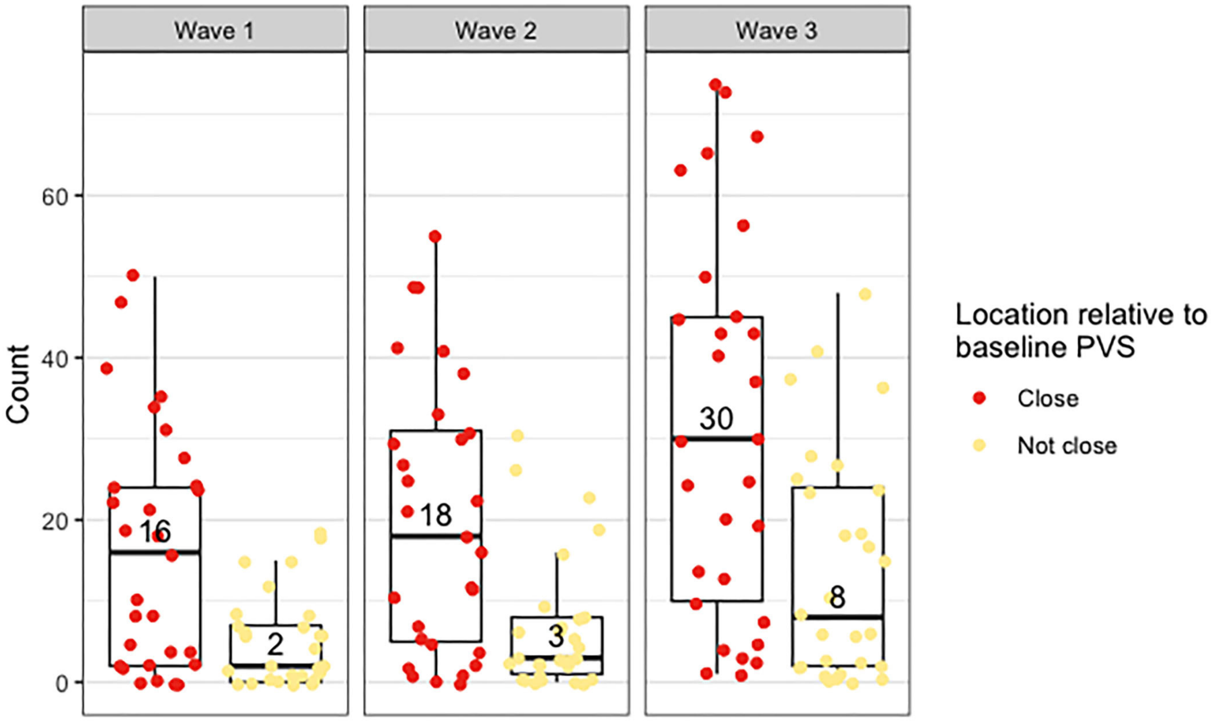

FIGURE 5
Distribution of counts of deep WMH in waves 1, 2, and 3, found close and not close to baseline (i.e., wave 1) PVS. The points plotted on each boxplot represent a different participant in the sample, and the numbers inside the boxplots correspond to the median count.

TABLE 2 Total number of deep WMH counted across the sample in waves 1, 2, and 3 that were found "close" and "not close" to baseline PVS, per lobar region and overall.

	Close (%)	Not close (%)	Total (%)
Wave 1			
Frontal	343 (54.88)	114 (18.24)	457 (73.12)
Parietal	109 (17.44)	26 (4.16)	135 (21.60)
Temporal	25 (4.00)	4 (0.64)	29 (4.64)
Occipital	1 (0.16)	0 (0.00)	1 (0.16)
Overall	479 (76.64)	146 (23.36)	625 (100.00)
Wave 2			
Frontal	401 (51.87)	125 (16.17)	526 (68.05)
Parietal	146 (18.89)	42 (5.43)	188 (24.32)
Temporal	34 (4.40)	14 (1.81)	48 (6.21)
Occipital	3 (0.39)	5 (0.65)	8 (1.03)
Overall	585 (75.68)	188 (24.32)	773 (100.00)
Wave 3			
Frontal	633 (48.14)	264 (20.08)	897 (68.21)
Parietal	206 (15.66)	74 (5.63)	280 (21.29)
Temporal	60 (4.56)	42 (0.03)	102 (7.76)
Occipital	10 (0.76)	22 (1.67)	32 (2.43)
Overall	909 (69.12)	406 (30.87)	1,315 (100.00)

between WMH and PVS would have been driven by the size of the WMH clusters.

Discussion

This pilot study in a sample of participants from a community-dwelling Scottish cohort is the first longitudinal study to date that evaluated the topological spatial relationship between PVS and deep WMH clusters. By carefully analyzing data across six years acquired in three equally spaced time points, our study provides further insights into this novel area of research by corroborating the hypothesis that some deep WMH may increase in size and form around PVS, previously inferred from cross-sectional data. Our results, therefore, suggest that in normal aging, WMH formation may be linked to impaired brain clearance mechanisms in addition to the vascular origin referred to in the current literature (42). From our observations, it is possible to infer that worsening interstitial fluid drainage over time can cause further accumulation of fluid in the white matter immediately adjacent to where drainage *via* PVS was previously impaired. This is consistent with the proposed mediating role of free water in the brain in the association seen between

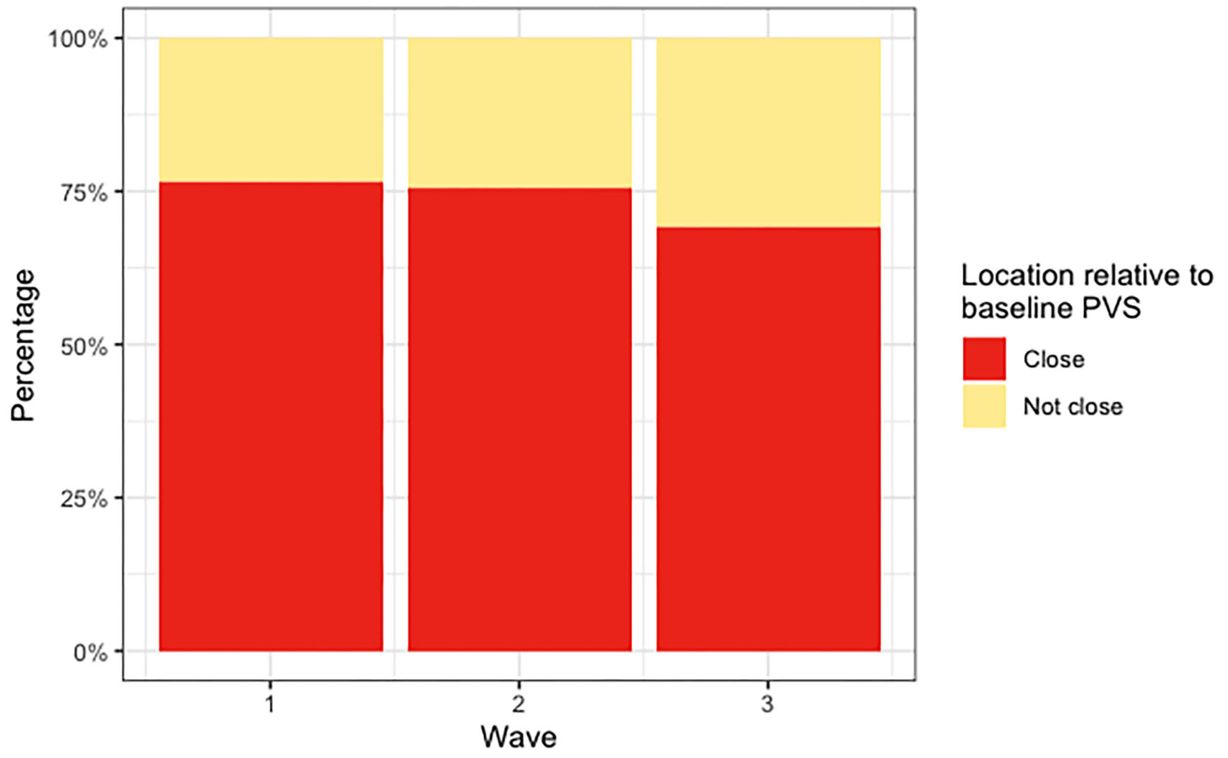

FIGURE 6
Percentages of deep WMH in waves 1, 2, and 3 that were found "close" and "not close" to baseline (i.e., wave 1) PVS.

PVS and deep WMH clusters by a previous cross-sectional study (26).

Moreover, our results indicate that the spatial relationships found are not likely to be artificially driven by the PVS volume and mean size or by the size of WMH clusters. Clinical reviews have previously proposed that WMH may preferentially form around PVS (5, 42). Another review that examined the pathological evidence for the failure of the brain clearance mechanisms as a significant cause of the overall pathology found particularly in the aging brain, stated that enlarged PVS reflect impaired interstitial fluid drainage and lead to the development of WMH (43). Our study for the first time provides evidence to support this claim, by analyzing the spatial proximity, distribution, and evolution of WMH in relation to PVS in brain scans from an age-homogeneous cohort representative of normal aging across 6 years within the eight decade of life.

Previously published data on topological relationships observed a marked difference between the percentages of WMH clusters spatially connected and not connected to PVS (26) when compared with those of our study. However, this may be due to several differences in study design. The age of the sample utilized by Huang et al. (26) was younger, with an inter-quartile range of 56–65 years, compared with that of our sample, where participants were aged ∼72, 75, and 78 years when relationships were analyzed. As both PVS and WMH are independently correlated with increasing age (44, 45), this may have influenced the differences seen. In terms of vascular disease, our sample is also more heterogeneous as it includes individuals with cardiovascular disease and total Fazekas scores ranging from 1 to 5. Also, different from our study, Huang et al. analyzed a random sample of deep WMH clusters rather than all present. While this was more feasible in a larger sample and allowed better appreciation of relationships in 3D, it may have introduced within-subject sampling error.

Although our longitudinal analysis revealed an increase in size of the WMH clusters close to or overlapping with the PVS identified at the first wave of scanning, our statistical analysis suggests that the number of deep WMH clusters spatially close to PVS was no more likely to increase than those spatially not close and that the location of deep WMH clusters in relation to PVS at the first scan was not a predictor for WMH progression in this sample. There are several possible reasons why no statistically significant associations were found. The baseline scan, obtained at a mean age close to 72 years, already showed most of the WMH clusters being located close to PVS, and most of these clusters experienced a growth over the periods evaluated. Therefore, it is reasonable that they would appear around or close to PVS at follow-up scans without necessarily meaning

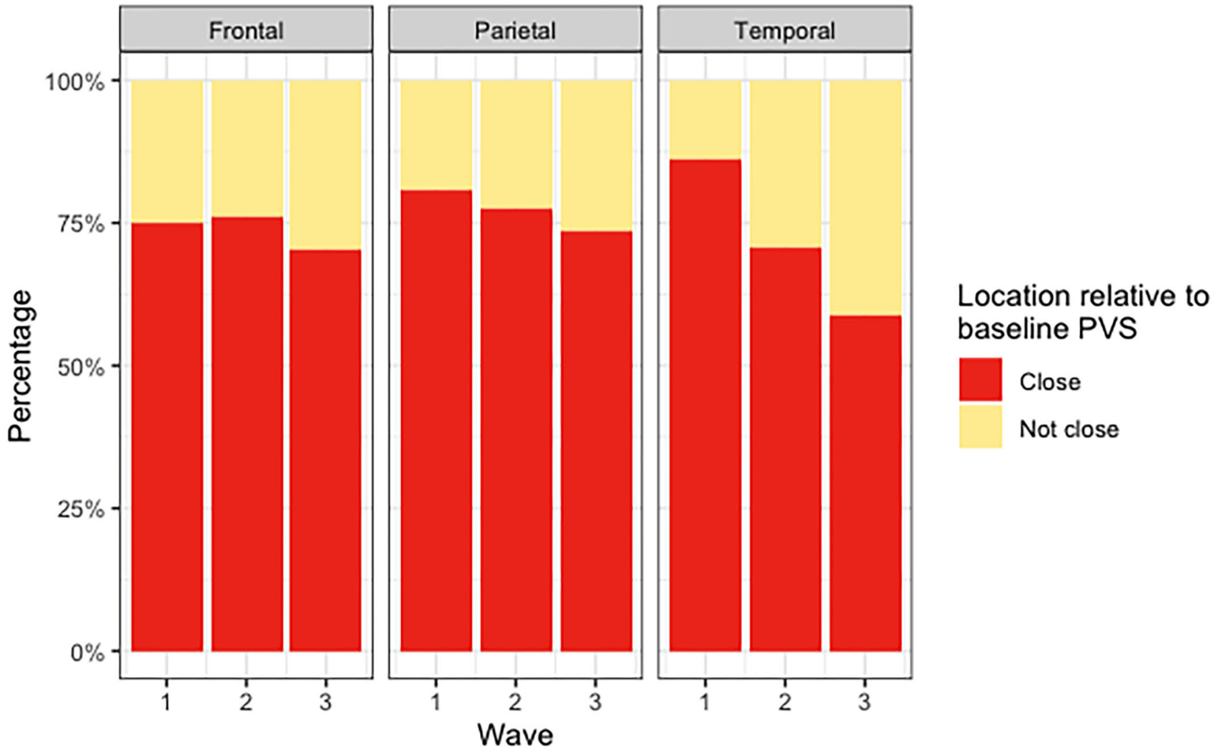

FIGURE 7
Percentages of deep WMH in waves 1, 2, and 3 that were found close and not close to baseline PVS in the frontal, parietal, and temporal regions.

TABLE 3 Association between proximity of deep WMH to PVS and deep WMH progression by binary logistic regression with random effects.

OR
(95% CI; *p*-value)

	Unadjusted	**Adjusted for sex and VRF**
Wave 1–2		
Not close	1.00	1.00
Close	1.93 (0.58–6.83; $p = 0.28$)	2.44 (0.68–8.82; $p = 0.17$)
Wave 2–3		
Not close	1.00	1.00
Close	4.05 (0.09–176.00; $p = 0.47$)	2.00 (0.16–25.10; $p = 0.59$)

OR, odds ratio; 95% CI, 95% confidence interval; VRF, vascular risk factors.

that the proximity to a PVS was related to their enlargement. The homogeneity of the sample in terms of age compensated the likelihood of biasedness of the adjusted statistical models, as age was not a factor needed to account for. Nevertheless, given the small size of the sample, the number of outcome events per predictor variable was slightly less than the recommended 10 (46). A Binary logistic regression with random effects was chosen because the alternatives were deemed beyond the scope of this study due to the complexity and number of assessments, which such a small sample size would be unlikely to support. A larger study would use more sophisticated analysis methods, such as Poisson's regression, to fully exploit the count nature of the data (47). Defining deep WMH clusters' progression as an increase in their number for statistical analyses was a further limitation as it did not take into account change in volume of individual clusters and the possibility of multiple clusters coalescing into one over time, which was observed in some cases. For such a detailed analysis to be performed computationally, it would have required access to a large "ground-truth" databank currently non-existent. Also, the analysis of the odds of deep WMH clusters close to PVS increasing in number to those not close to PVS is complex as it is unclear what deep WMH clusters not close to PVS represent. Although their appearance is unlikely to be related to the consequences of impaired interstitial fluid drainage, they may be just as likely to increase in number for different reasons.

Another limitation of our study is the relatively low spatial resolution of the images for the assessment of these types of structures (i.e., 1 × 1 × 2 mm^3 at 1.5 tesla), which, despite resampling, may have introduced an error in counting

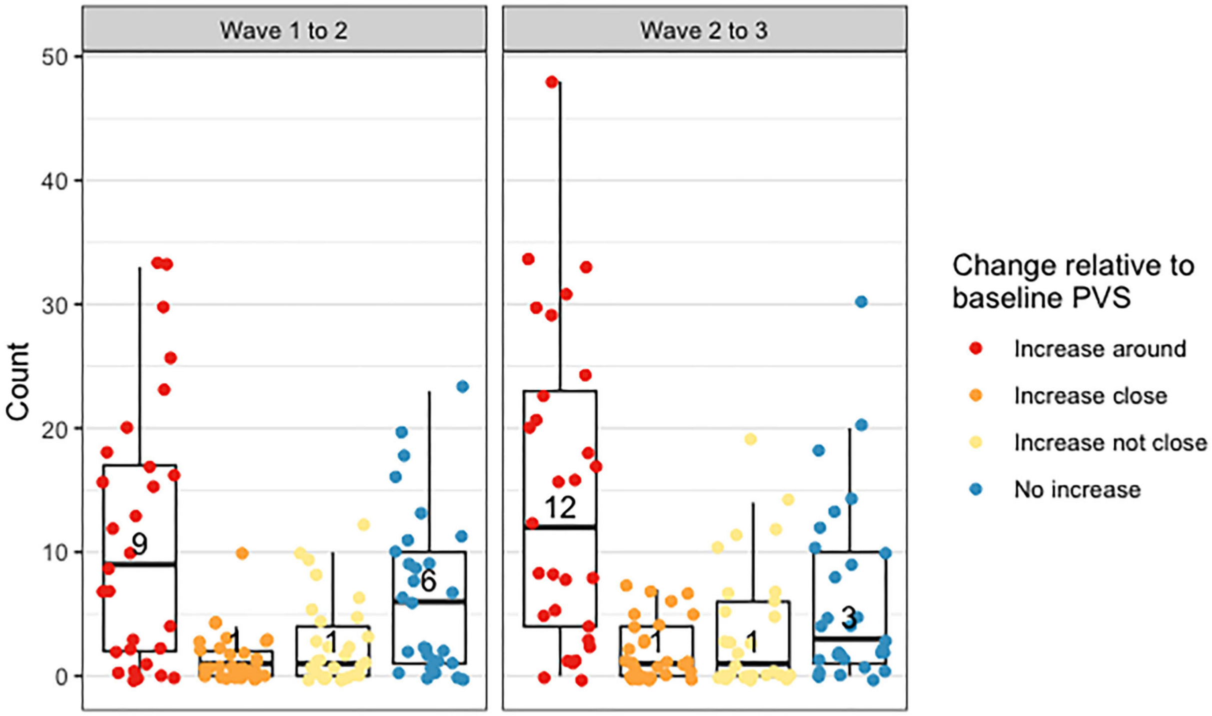

FIGURE 8
Distribution of counts of deep WMH that increased around, close and not close to baseline PVS, and did not increase between waves 1 and 2 and waves 2 and 3. The points plotted on each boxplot represent a different participant in the sample, and the numbers represent the median count.

the PVS that occur parallel to the axial plane. Relying on segmentation to define the relationships seen, despite improving the reliability and reproducibility in the assessments, meant that accuracy of the data collected was dependent on the accuracy of segmentation, particularly for PVS for which manual edit of each of these small features individually is impractical and highly prone to individual observer's considerations, especially for cases with a high burden of them. Inaccuracies in the segmentation of baseline PVS in this cohort as a whole have been recognized (23), but the sample analyzed was double-checked visually to ensure quality in the analyses. The reliance in the segmentation could have also meant that small increase (or decrease) in the number of voxels (e.g., one or two voxels) recognized by the algorithm could have been considered an actual biological change. The filtering method used in the PVS segmentation is widely recognized for its robustness, and given the image normalization steps also conducted, an artificial increase in the number of connected voxels considered PVS is not highly likely. The change in WMH volume, however, could have been artificially generated by the algorithms, especially given the undefined borders of some lesions and the differences in defining the thresholds by the two methods used to segment them. To overcome this limitation, the change in the WMH cluster size was evaluated visually and considered as such only if this was perceived nearly as two times (or half) or more the original cluster size. Also, it is not clear whether punctate WMH that pathology studies recognize as WMH composed of and characterized by enlarged PVS (48–50) are segmented as PVS, WMH, or both. This may have also affected how accurately deep WMH clusters were classified. Lastly, due to the visual and 3D nature of the assessments, despite the high intra-observer reliability, one cannot discard the possibility of potentially mistaken classification of WMH clusters close to PVS diagonally across slices, or double counting of the same cluster in different planes. Once the segmentations are done, distance from each cluster to PVS masks could have been calculated computationally, for example, using the Euclidean or Manhattan distances, but anyway they would have needed to be checked visually, because to avoid considering PVS proximities to more than one WMH cluster, arbitrary limits would have needed to be imposed, complicating the interpretability of the results.

The fact that only one observer performed the visual assessments limited the sources of variation in the dataset. Counting all deep WMH clusters is very time-consuming, especially in participants with a high WMH burden, so the methodology used here would not be feasible in large samples. Nonetheless, it proved a useful way of obtaining data on topological relationships between deep WMH clusters and PVS, both cross-sectionally and longitudinally, to test our hypotheses. Due to the novelty of this research, there are no reliably

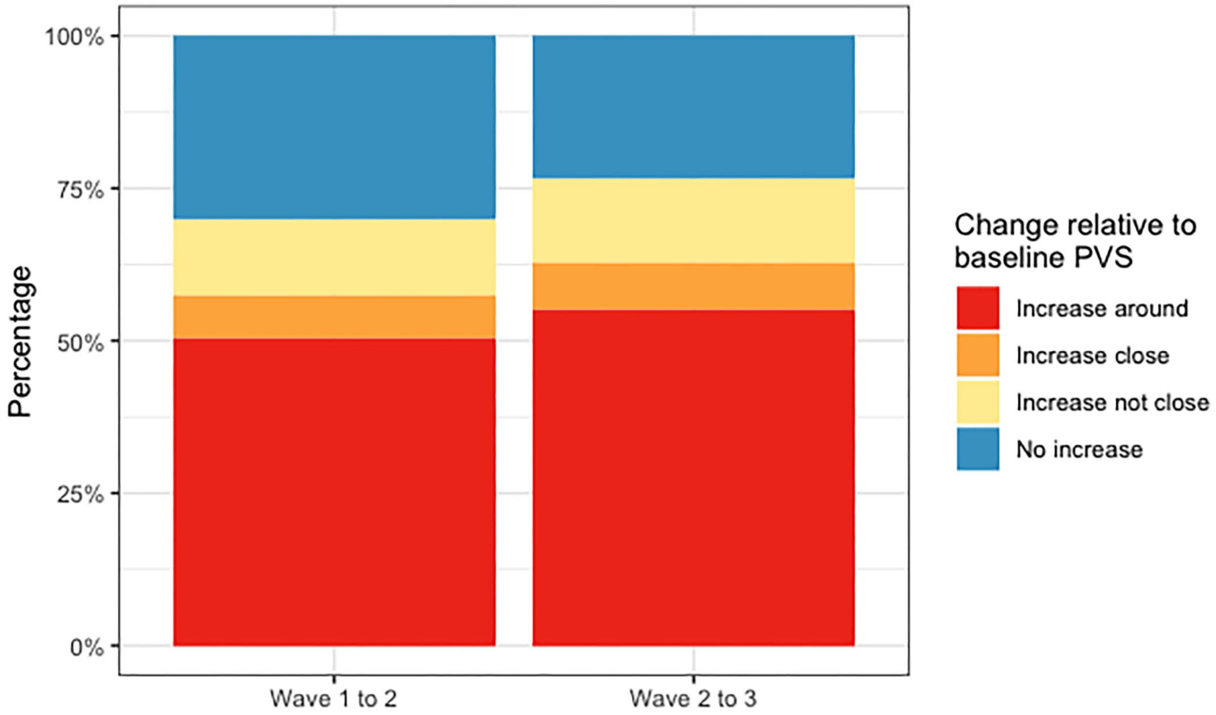

FIGURE 9
Percentages of deep WMH that increased around, close and not close to baseline PVS, and did not increase between waves 1 and 2 and waves 2 and 3.

TABLE 4 Total number and percentages of deep WMH counted across the sample that increased around, close and not close to baseline PVS, and number of those that did not increase between waves 1 and 2 and waves 2 and 3, per region and overall.

	Increase around (%)	Increase close (%)	Increase not near (%)	No increase (%)	Total (%)
Wave 1–2					
Frontal	227 (36.09)	33 (5.25)	62 (9.86)	139 (22.10)	461 (73.29)
Parietal	74 (11.76)	8 (1.27)	12 (1.91)	44 (6.99)	138 (21.94)
Temporal	17 (2.70)	4 (0.64)	2 (0.32)	6 (0.95)	29 (4.61)
Occipital	1 (0.16)	0 (0.00)	0 (0.00)	0 (0.00)	1 (0.16)
Overall	319 (50.71)	45 (7.15)	76 (12.08)	189 (30.05)	629 (100.00)
Wave 2–3					
Frontal	283 (36.66)	42 (5.44)	79 (10.23)	124 (16.06)	528 (68.39)
Parietal	110 (14.25)	17 (2.20)	23 (2.98)	40 (5.18)	190 (24.61)
Temporal	29 (3.76)	1 (0.13)	4 (0.52)	12 (1.55)	46 (5.96)
Occipital	3 (0.39)	0 (0.00)	2 (0.26)	3 (0.39)	8 (1.04)
Overall	425 (55.05)	60 (7.77)	108 (13.99)	179 (23.18)	772 (100.00)

annotated data to train any machine learning algorithm to reliably classify large data fully automatically across the whole brain. Existent automatic classifiers that demand less or no data at all have a suboptimal accuracy for being applied in clinical studies or test clinically relevant hypotheses. Therefore, future research should continue to use the methodology developed for this study to generate ground-truth data in a larger sample, reassess the relationships seen, and re-evaluate the utility of the presented paradigm to determine its usefulness in predicting WMH progression. Moreover, future studies should include in the analyses participants with history of previous strokes to investigate differences in tendencies over time (if they exist) between individuals who had a stroke against those who did not. It will be also useful to validate the results against the percentage overlap between segmentation masks for PVS and WMH, which would better take into account differences in

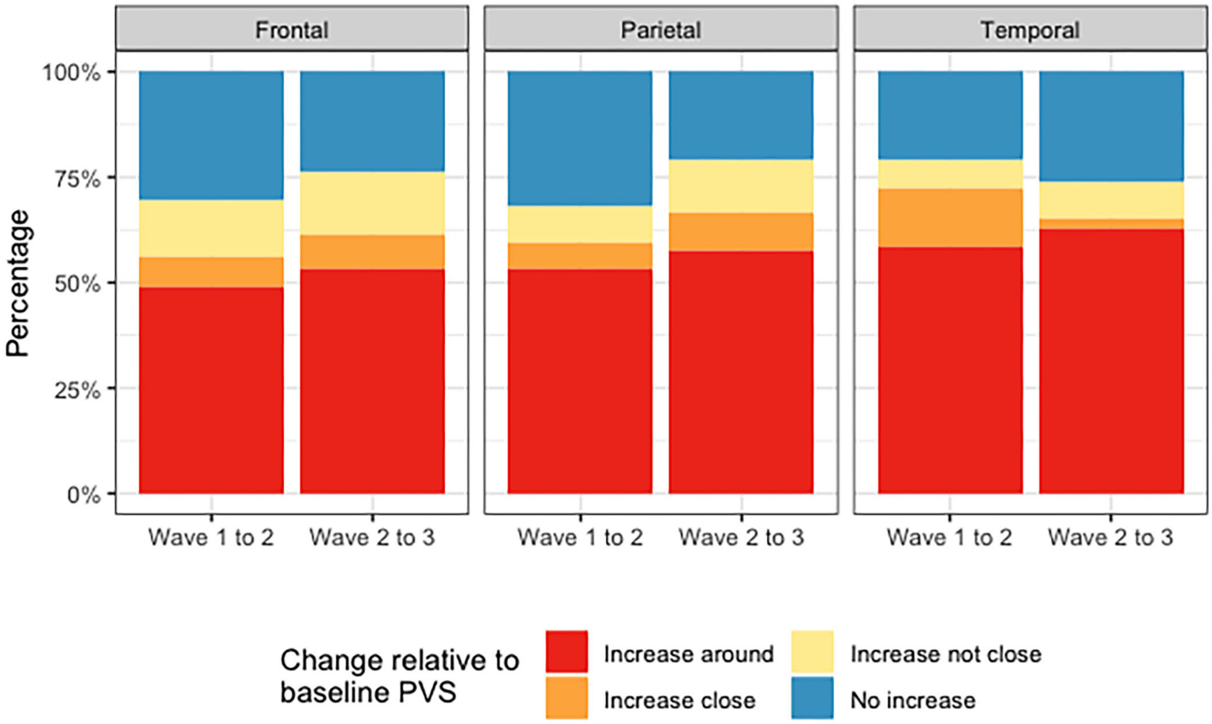

FIGURE 10
Percentages of deep WMH that increased around, close and not close to baseline PVS, and did not increase in the frontal, parietal, and temporal regions between waves 1 and 2 and waves 2 and 3.

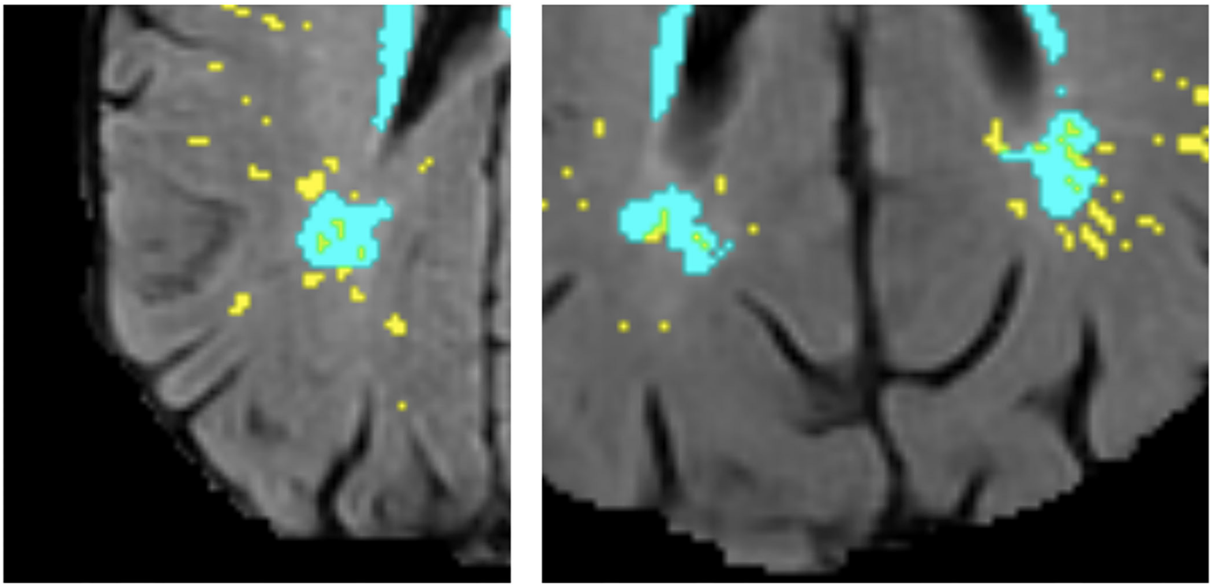

FIGURE 11
Examples of large deep WMH in the parietal region that were found spatially close to multiple PVS (segmentation masks for WMH in cyan and PVS in yellow, overlaid on FLAIR MRI).

volume. As described in Materials and Methods section and in previous publications from this cohort, WMH binary masks separately for periventricular and deep regions are not currently available. Therefore, with the data available at present such computational analysis would have been misleading.

As our findings support the idea that PVS enlargement (i.e., for PVS to be visible in MRI) may precede WMH development, future research on better understanding what causes PVS enlargement would be important. MRI-visible PVS in the centrum semiovale are linked to amyloid deposition (51, 52); therefore, ways to prevent this would be clinically beneficial.

Conclusion

In this pilot study, more deep WMH clusters were found spatially close to a baseline PVS than distant, and more than half progressed with time, increasing around a baseline PVS. Although this sample is very small, these findings support a mechanistic link between these two cSVD features that may improve our understanding of the mechanisms involved in cSVD and WMH development to help reduce and prevent associated symptoms and neurological conditions. Formal statistical comparisons of severity of these two SVD markers yielded no associations between deep WMH clusters progression and the location of these clusters relative to PVS. The sample size should be increased to confirm these associations. Future research should also explore more feasible ways of analyzing these relationships (i.e., automatically) and the causes of PVS enlargement to continue furthering our understanding of the mechanisms involved in cSVD.

Data availability statement

The original contributions presented in the study are included in the article/Supplementary material, further inquiries can be directed to the corresponding author.

Ethics statement

The studies involving human participants were reviewed and approved by Lothian (REC 07/MRE00/58) and Scottish Multicentre (MREC/01/0/56) Research Ethics Committees. The patients/participants provided their written informed consent to participate in this study.

Author contributions

LB, MV, JW, and FC were involved in conceptualization. AB, LB, MV, SM, RM, EB, and MS were involved in data curation. AB was involved in formal analysis and visualization. SC, MB, ID, and JW were involved in funding acquisition. AB, LB, JW, and FC were involved in investigation. AB, LB, RD, MV, FC, and JW contributed to methodology. LB, RB, RM, and JW were involved in project administration. LB, JW, SC, ID, and MB contributed to supervision and resources. LB, RD, MV, and FC contributed to software. AB, MV, and LB were involved in validation. AB and MV were involved in writing—original draft preparation. All authors were involved in writing—review and editing. All authors contributed to the article and approved the submitted version.

Funding

This study was partially funded by the Selfridges Group Foundation under the Novel Biomarkers 2019 scheme (ref UB190097) administered by the Weston Brain Institute. The LBC1936 is supported by Age UK as The Disconnected Mind Project (http://www.disconnectedmind.ed.ac.uk), the Medical Research Council [G1001245/96099] and The University of Edinburgh. LBC1936 MRI brain imaging was supported by Medical Research Council (MRC) grants [G0701120], [G1001245], [MR/M013111/1], and [MR/R024065/1]. Magnetic Resonance Image acquisition and analyses were conducted at the Brain Research Imaging Centre, Neuroimaging Sciences, University of Edinburgh (www.bric.ed.ac.uk) which is part of SINAPSE (Scottish Imaging Network—A Platform for Scientific Excellence) collaboration (www.sinapse.ac.uk) funded by the Scottish Funding Council and the Chief Scientist Office. This work was supported by the Centre for Cognitive Ageing and Cognitive Epidemiology, funded by the Medical Research Council and the Biotechnology and Biological Sciences Research Council (MR/K026992/1), the Row Fogo Charitable Trust (BRO-D.FID3668413), the European Union Horizon 2020, (PHC-03-15, project No 666881), SVDs@Target, the Fondation Leducq Transatlantic Network of Excellence for the Study of Perivascular Spaces in Small Vessel Disease, ref no. 16 CVD 05, the US National Institutes of Health (R01AG054628), a Sir Henry Dale Fellowship jointly funded by the Wellcome Trust, the Royal Society (SRC, Grant Number 221890/Z/20/Z), and the Medical Research Council UK Dementia Research Institute at the University of Edinburgh. None of the funders have any role in the collection and processing of the data or the content presented in this manuscript.

Acknowledgments

We thank all those involved in the Lothian Birth Cohort 1936 Study, including the participants, nurses, clinicians, researchers, and support staff, without whom the data utilized in this project would not have been available. We especially thank David Alexander Dickie, Stewart Wiseman, and Benjamin S. Aribisala for their contributions to the development or generation of WMH segmentations throughout the different waves of the LBC 1936 Study.

Conflict of interest

The authors declare that the research was conducted in the absence of any commercial or financial relationships that could be construed as a potential conflict of interest.

Publisher's note

Supplementary material

The Supplementary Material for this article can be found online at: https://www.frontiersin.org/articles/10.3389/fneur.2022.889884/full#supplementary-material

References

1. Wardlaw JM, Smith EE, Biessels GJ, Cordonnier C, Fazekas F, Frayne R, et al. Neuroimaging standards for research into small vessel disease and its contribution to ageing and neurodegeneration. *Lancet Neurol.* (2013) 12:822–38. doi: 10.1016/S1474-4422(13)70124-8

2. Shi Y, Wardlaw JM. Update on cerebral small vessel disease: a dynamic whole-brain disease. *BMJ.* (2016) 1:83–92. doi: 10.1136/svn-2016-000035

3. Iliff JJ, Wang M, Liao Y, Plogg BA, Peng W, Gundersen GA, et al. A paravascular pathway facilitates CSF flow through the brain parenchyma and the clearance of interstitial solutes, including amyloid. *Sci Transl Med.* (2012) 4:147ra111. doi: 10.1126/scitranslmed.3003748

4. Brown R, Benveniste H, Black SE, Charpak S, Dichgans M, Joutel A, et al. Understanding the role of the perivascular space in cerebral small vessel disease. *Cardiovasc Res.* (2018) 114:1462–73. doi: 10.1093/cvr/cvy113

5. Wardlaw JM. Blood-brain barrier and cerebral small vessel disease. *J Neurol Sci.* (2010) 299:66–71. doi: 10.1016/j.jns.2010.08.042

6. Kress BT, Iliff JJ, Xia M, Wang M, Wei HS, Zeppenfeld D, et al. Impairment of paravascular clearance pathways in the aging brain. *Ann Neurol.* (2014) 76:845–61. doi: 10.1002/ana.24271

7. Debette S, Schilling S, Duperron MG, Larsson SC, Markus HS. Clinical significance of magnetic resonance imaging markers of vascular brain injury. *JAMA Neurol.* (2019) 76:81–94. doi: 10.1001/jamaneurol.2018.3122

8. Francis F, Ballerini L, Wardlaw JM. Perivascular spaces and their associations with risk factors, clinical disorders and neuroimaging features: a systematic review and meta-analysis. *Int J Stroke.* (2019) 14:359–71. doi: 10.1177/1747493019830321

9. Sarbu N, Shih RY, Jones RV, Horkayne-Szakaly I, Oleaga L, Smirniotopoulos JG, et al. White matter diseases with radiologic-pathologic correlation. *RadioGraphics.* (2016) 36:1426–47. doi: 10.1148/rg.2016160031

10. Wardlaw JM, Valdés Hernández MC, Muñoz-Maniega S. What are white matter hyperintensities made of? Relevance to vascular cognitive impairment. *J Am Heart Assoc.* (2015) 4:001140. doi: 10.1161/JAHA.114.001140

11. Dufouil C, De Kersaint-Gilly A, Besancon V, Levy C, Auffray E, Brunnereau L, et al. Longitudinal study of blood pressure and white matter hyperintensities: the EVA MRI cohort. *Neurology.* (2001) 56:921–6. doi: 10.1212/WNL.56.7.921

12. Ferguson SC, Blane A, Perros P, McCrimmon RJ, Best JJK, Wardlaw J, et al. Cognitive ability and brain structure in type 1 diabetes: relation to microangiopathy and preceding severe hypoglycemia. *Diabetes.* (2003) 52:149–56. doi: 10.2337/diabetes.52.1.149

13. Ghaznawi R, Geerlings MI, Jaarsma-Coes MG, Zwartbol MH, Kuijf HJ, Van Der Graaf Y, et al. The association between lacunes and white matter hyperintensity features on MRI: the SMART-MR study. *J Cereb Blood Flow Metab.* (2019) 39:2486–96. doi: 10.1177/0271678X18800463

14. Debette S, Markus HS. The clinical importance of white matter hyperintensities on brain magnetic resonance imaging: systematic review and meta-analysis. *BMJ.* (2010) 341:c3666. doi: 10.1136/bmj.c3666

15. Doubal FN, Maclullich AMJ, Ferguson KJ, Dennis MS, Wardlaw JM. Enlarged perivascular spaces on MRI are a feature of cerebral small vessel disease. *Stroke.* (2010) 41:450–4. doi: 10.1161/STROKEAHA.109.564914

16. Aribisala BS, Wiseman S, Morris Z, Valdés-Hernández MC, Royle NA, Maniega SM, et al. Circulating inflammatory markers are associated with magnetic resonance imaging-visible perivascular spaces but not directly with white matter hyperintensities. *Stroke.* (2014) 45:605–7. doi: 10.1161/STROKEAHA.113.004059

17. Sepehrband F, Barisano G, Sheikh-Bahaei N, Cabeen RP, Choupan J, Law M, et al. Image processing approaches to enhance perivascular space visibility and quantification using MRI. *Sci Rep.* (2019) 9:12351. doi: 10.1038/s41598-019-48910-x

18. Dubost F, Yilmaz P, Adams H, Bortsova G, Ikram MA, Niessen W, et al. Enlarged perivascular spaces in brain MRI: automated quantification in four regions. *Neuroimage.* (2019) 185:534–44. doi: 10.1016/j.neuroimage.2018.10.026

19. Boutinaud P, Tsuchida A, Laurent A, Adonias F, Hanifehlou Z, Nozais V, et al. 3D segmentation of perivascular spaces on T1-weighted 3 Tesla MR images with a convolutional autoencoder and a U-shaped neural network. *Front Neuroinform.* (2021) 15:641600. doi: 10.3389/fninf.2021.641600

20. Ballerini L, Lovreglio R, Valdés Hernández MDC, Ramirez J, Macintosh BJ, Black SE, et al. Perivascular spaces segmentation in brain MRI using optimal 3D filtering. *Sci Rep.* (2018) 8:2132. doi: 10.1038/s41598-018-19781-5

21. Boespflug EL, Schwartz DL, Lahna D, Pollock J, Iliff JJ, Kaye JA, et al. MR Imaging–based multimodal autoidentification of perivascular spaces (mMAPS): automated morphologic segmentation of enlarged perivascular spaces at clinical field strength. *Radiology.* (2018) 286:632–42. doi: 10.1148/radiol.2017170205

22. Ramirez J, Berezuk C, McNeely A, Scott C, Gao F, Black S, et al. Visible Virchow-Robin spaces on magnetic resonance imaging of Alzheimer's disease patients and normal elderly from the Sunnybrook Dementia Study. *J Alz Dis.* (2015) 43:415–24. doi: 10.3233/JAD-132528

23. Ballerini L, Booth T, Valdes Hernandez MDC, Wiseman S, Lovreglio R, Munoz Maniega S, et al. Computational quantification of brain perivascular space morphologies: associations with vascular risk factors and white matter hyperintensities. A study in the Lothian Birth Cohort 1936. *Neuroimage Clin.* (2020) 25:102120. doi: 10.1016/j.nicl.2019.102120

24. Loos CMJ, Klarenbeek P, Van Oostenbrugge RJ, Staals J. Association between perivascular spaces and progression of white matter hyperintensities in lacunar stroke patients. *PLoS ONE.* (2015) 10:e0137323. doi: 10.1371/journal.pone.0137323

25. Wardlaw JM, Benveniste H, Nedergaard M, Zlokovic BV, Mestre H, Lee H, et al. Perivascular spaces in the brain: anatomy, physiology and pathology. *Nat Rev Neurol.* (2020) 16:137–53. doi: 10.1038/s41582-020-0312-z

26. Huang P, Zhang R, Jiaerken Y, Wang S, Yu W. Hong,H, et al. Deep white matter hyperintensity is associated with the dilation of perivascular space. *J Cereb Blood Flow Metab.* (2021) 41:2370–80. doi: 10.1177/0271678X211002279

27. Clancy U, Appleton J, Arteaga C, Doubal FN, Bath PM, Wardlaw JM, et al. Clinical management of cerebral small vessel disease: a call for a holistic approach. *Chin Med J.* (2021) 134:127–42. doi: 10.1097/CM9.0000000000001177

28. Deary IJ, Gow AJ, Taylor MD, Corley J, Brett C, Wilson V, et al. The Lothian Birth Cohort 1936: a study to examine influences on cognitive ageing from age 11 to age 70 and beyond. *BMC Geriatr.* (2007) 7:28. doi: 10.1186/1471-2318-7-28

29. Wardlaw JM, Bastin ME, Valdés Hernández MC, Munoz Maniega S, Royle NA, Morris Z, et al. Brain aging, cognition in youth and old age and vascular disease in the Lothian Birth Cohort 1936: rationale, design and methodology of the imaging protocol. *Int J Stroke.* (2011) 6:547–59. doi: 10.1111/j.1747-4949.2011.00683.x

30. Taylor AM, Pattie A, Deary IJ. Cohort profile update: the Lothian Birth Cohorts of 1921 and 1936. *Int J Epidemiol.* (2018) 2018:47. doi: 10.1093/ije/dyy022

31. Jenkinson M, Bannister PR, Brady JM, Smith SM. Improved optimisation for the robust and accurate linear registration and motion correction of brain images. *NeuroImage.* (2002) 17:825–41. doi: 10.1006/nimg.2002.1132

32. Valdés Hernández MDC, Ferguson KJ, Chappell FM, Wardlaw JM. New multispectral MRI data fusion technique for white matter lesion segmentation: method and comparison with thresholding in FLAIR images. *Eur Radiol.* (2010) 20:1684–91. doi: 10.1007/s00330-010-1718-6

33. Valdés Hernández MDC, Ballerini L, Glatz A, Muñoz Maniega S, Gow AJ, Bastin ME, et al. Perivascular spaces in the centrum semiovale at the beginning of the 8th decade of life: effect on cognition and associations with mineral deposition. *Brain Imaging Behav.* (2020) 14:1865–75. doi: 10.1007/s11682-019-00128-1

34. Zhan T, Zhan Y, Liu Z, et al. Automatic method for white matter lesion segmentation based on T1-fluid-attenuated inversion recovery images. *IET Comput Vis.* (2015) 9:447–55. doi: 10.1049/iet-cvi.2014.0121

35. Agan MLF, Valdés Hernández MC. *Manual segmentations of white matter hyperintensities from a subset of 7 ADNI subjects scanned three consecutive* years, *for inter-/intra-observer reliability analyses* [dataset]. Edinburgh: University of Edinburgh, Centre for Clinical Brain Sciences (2017).

36. Ballerini L, Lovreglio R, Valdés Hernández MDC, Gonzalez-Castro V, Munoz Maniega S, Pellegrini E, et al. Application of the ordered logit model to optimising frangi filter parameters for segmentation of perivascular spaces. *Procedia Comput Sci.* (2016) 90:61–7. doi: 10.1016/j.procs.2016.07.011

37. Valdés Hernandez MC, Piper RJ, Wang X, Deary IJ, Wardlaw JM. Towards the automatic computational assessment of enlarged perivascular spaces on brain magnetic resonance images: a systematic review. *J Mag Res Imag.* (2013) 38:774–85. doi: 10.1002/jmri.24047

38. Zhang Y, Brady M, Smith S. Segmentation of brain MR images through a hidden Markov random field model and the expectation-maximization algorithm. *IEEE Trans Med Imag.* (2001) 20:45–57. doi: 10.1109/42.906424

39. Kim KW, Macfall JR, Payne ME. Classification of white matter lesions on magnetic resonance imaging in elderly persons. *Biol Psychiat.* (2008) 64:273–80. doi: 10.1016/j.biopsych.2008.03.024

40. Debowski M. Brain lobes – annotated MRI (2018). Available online at: https://radiopaedia.org/cases/brain-lobes-annotated-mri-1?lang=us (accessed February, 2021).

41. Hoenig JM, Heisei DM. The abuse of power: the pervasive fallacy of power calculations for data analysis. *Am Stat.* (2001) 55:6. doi: 10.1198/000313001300339897

42. Wardlaw JM, Smith C, Dichgans M. Mechanisms of sporadic cerebral small vessel disease: insights from neuroimaging. *Lancet Neurol.* (2013) 12:483–97. doi: 10.1016/S1474-4422(13)70060-7

43. Weller RO, Hawkes CA, Kalaria RN, Werring DJ, Carare RO. White matter changes in dementia: role of impaired drainage of interstitial fluid. *Brain Pathol.* (2015) 25:63–78. doi: 10.1111/bpa.12218

44. De Leeuw FE, De Groot JC, Achten E, Oudkerk M, Ramos LMP, Heijboer R, et al. Prevalence of cerebral white matter lesions in elderly people: a population based magnetic resonance imaging study. The Rotterdam Scan Study. *J Neurol Neurosurg Psychiatr.* (2001) 70:9–14. doi: 10.1136/jnnp.70.1.9

45. Zhu YC, Dufouil C, Mazoyer B, Soumaré A, Ricolfi F, Tzourio C, et al. Frequency and location of dilated Virchow-Robin spaces in elderly people: a population-based 3D MR imaging study. *Am J Neuroradiol.* (2011) 32:709–13. doi: 10.3174/ajnr.A2366

46. Peduzzi P, Concato J, Kemper E, Holford TR, Feinstein ARA. simulation study of the number of events per variable in logistic regression analysis. *J Clin Epidemiol.* (1996) 49:1373–9. doi: 10.1016/S0895-4356(96)00236-3

47. Coxe S, West SG, Aiken LS. The analysis of count data: a gentle introduction to poisson regression and its alternatives. *J Pers Assess.* (2009) 91:121–36. doi: 10.1080/00223890802634175

48. Chimowitz MI, Estes ML, Furlan AJ, Awad IA. Further observations on the pathology of subcortical lesions identified on magnetic resonance imaging. *Arch Neurol.* (1992) 49:747–52. doi: 10.1001/archneur.1992.00530310095018

49. Fazekas F, Kleinert R, Offenbacher H, Schmidt R, Kleinert G, Payer F, et al. Pathologic correlates of incidental MRI white matter signal hyperintensities. *Neurology*. (1993) 43:1683–9. doi: 10.1212/wnl.43.9.1683

50. Munoz DG, Hastak SM, Harper B, Lee D, Hachinski VC. Pathologic correlates of increased signals of the centrum ovale on magnetic resonance imaging. *Arch Neurol.* (1993) 50:492–7. doi: 10.1001/archneur.1993.00540050044013

51. Charidimou A, Hong YT, Jäger HR, Fox Z, Aigbirhio FI, Fryer TD, et al. White matter perivascular spaces on magnetic resonance imaging. *Stroke.* (2015) 46:1707–9. doi: 10.1161/STROKEAHA.115.009090

52. Martinez-Ramirez S, Van Rooden S, Charidimou A, Van Opstal AM, Wermer M. Guro lME, et al. Perivascular spaces volume in sporadic and hereditary (Dutch-type) cerebral amyloid angiopathy. *Stroke.* (2018) 49:1913–9. doi: 10.1161/STROKEAHA.118.021137

frontiers | Frontiers in Neurology

TYPE Original Research
PUBLISHED 23 September 2022
DOI 10.3389/fneur.2022.922320

OPEN ACCESS

EDITED BY
Tao Liu,
Hainan General Hospital, China

REVIEWED BY
Nan Wang,
Stanford University, United States
Jan Egger,
University Hospital Essen, Germany

*CORRESPONDENCE
ZhiYou Cai
caizhiyou@ucas.ac.cn

SPECIALTY SECTION
This article was submitted to
Applied Neuroimaging,
a section of the journal
Frontiers in Neurology

RECEIVED 17 April 2022
ACCEPTED 01 August 2022
PUBLISHED 23 September 2022

CITATION
Zhong T, Qi Y, Li R, Zhou H, Ran B, Wang J and Cai Z (2022) Contribution of intracranial artery stenosis to white matter hyperintensities progression in elderly Chinese patients: A 3-year retrospective longitudinal study. *Front. Neurol.* 13:922320. doi: 10.3389/fneur.2022.922320

Contribution of intracranial artery stenosis to white matter hyperintensities progression in elderly Chinese patients: A 3-year retrospective longitudinal study

Tingting Zhong[1,2,3,4], Yunwen Qi[1,3,4], Rui Li[5], Huadong Zhou[6], Boli Ran[2], Jiao Wang[2] and ZhiYou Cai[1,3,4]*

[1]Chongqing Medical University, Chongqing, China, [2]Department of Cardiology, Chongqing General Hospital, Chongqing, China, [3]Department of Neurology, Chongqing General Hospital, Chongqing, China, [4]Chongqing Key Laboratory of Neurodegenerative Diseases, Chongqing, China, [5]Stroke Center and Department of Neurology, The First Affiliated Hospital of USTC, Division of Life Sciences and Medicine, University of Science and Technology of China, Hefei, China, [6]Department of Neurology and Centre for Clinical Neuroscience, Daping Hospital, Third Military Medical University, Chongqing, China

Background and purpose: There have been controversial results in previous studies for the association between intracranial artery stenosis (ICAS) and white matter hyperintensities (WMHs), and the correlation of ICAS with the progression of WMHs is uncertain. The aim of this study was to investigate the association between ICAS and the progression of WMHs.

Methods: In this retrospective longitudinal study, we enrolled 302 patients aged 60 years and older who had received two brain MRI scans with a 3-year interval and was examined by CTA in the first MRI scan. We measured the stenosis of major intracranial arteries by CTA and assessed the progression of WMHs using the modified Rotterdam Progression scale (mRPS). We performed binary logistic regression analyses and established linear regression model to determine the relationship between the degree of ICAS and the progression of WMHs.

Results: A total of 302 patients were enrolled, of which 48.3% experienced WMHs progression. After adjustment for confounding factors, the patients with Grade 2 ICAS had an OR of 2.8 (95% CI 1.4–5.5), and those with Grade 3 ICAS had an OR of 3.0 (95% CI 1.2–7.3) for the progression of WMHs. The ICAS degree remained associated with PVWMHs but had an attenuated relation to SCWMHs. ICAS severity was significantly associated with WMHs progression scores, higher for Grade 3 ICAS [β (SE) $= 0.18$ (0.18)] followed by Grade 2 ICAS [β (SE) $= 0.10$ (0.15)] compared with Grade 1 ICAS.

Conclusions: Patients with more severe ICAS are more likely to have WMHs progression and have distinct relevancy to PVWMHs and SCWMHs, which may provide clues for understanding mechanisms of WMHs progression.

KEYWORDS

intracranial artery stenosis, white matter hyperintensities, magnetic resonance imaging, computed tomography angiography, retrospective longitudinal study

Introduction

White matter hyperintensities (WMHs) are frequently found on brain MRI of older individuals and substantially predict an increased risk of dementia, stroke, mortality, and physical disability (1, 2). Some evidence considers WMHs as small-vessel disease-related lesions (3, 4), but the exact etiology is poorly understood. Proposed mechanisms include that chronic hypoperfusion, diffuse cerebrovascular endothelial failure, and blood-brain barrier alterations (4, 5) alone or simultaneously contribute to the damage of cerebral vessels and parenchyma. Postmortem studies have shown that WMHs correlate with various degrees of demyelination, arteriolosclerosis, and mild gliosis (6). Pathologically, most WMHs lesions are ischaemic in origin.

Inefficient blood supply to brain due to luminal narrowing by atherosclerotic arterial stenosis in the upstream may be contributory to the presence and development of WMHs (7). The correlation between carotid arteriosclerosis and WMHs is still a matter of controversy, even though a large number of studies have been dedicated to identifying it (8). Most of these studies have reported no definitive association between vascular risk factors (VRFs) and WMHs (9). Intracranial- and Extracranial atherosclerosis (ICAS and ECAS) have been suggested to have different pathogeneses. Intracranial arteries might have less opportunity to be hemodynamically compensated by the circle of Willis and is related to weaker cerebral autoregulation, because they are less elastic and result in pressure-passive cerebral blood flow (10). Some cross-sectional studies have suggested that patients with ICAS, rather than ECAS, may particularly have heavier WMHs burden (7, 11, 12), while others failed to demonstrate the relevance (13, 14). Additionally, WMHs may progress insidiously rather than staying unalterable, and the risk factors for progression are uncertain. To our knowledge, only one study assessed the effects of statins on the progression of WMHs, but regrettably, it mentioned no significant correlation between ICAS and the progression of WMHs (15). Further exploration of the relationship between ICAS and WMHs is warranted.

We therefore sought to conduct the present retrospective longitudinal study in patients without acute stroke or ECAS, aiming to determine whether stenosis in major intracranial arteries could serve as a predictor for WMHs progression within a period of 3 years.

Methods

Study population

This study was retrospectively performed on inpatients admitted to the Department of Neurology of Daping Hospital in the city of Chongqing, China, from January 1, 2010 to December 31, 2015. Eligibility criteria included: (1) patients aged 60 years and older; (2) patients who had undergone cerebral magnetic resonance imaging (MRI) scans twice in this period with a 3-year interval; and (3) patients who had been examined by CT angiography (CTA) in the first MRI scan. Exclusion criteria were: (1) patients with a leukoencephalopathy of non-vascular origin (e.g., infectious, toxic, immunological-demyelinating); (2) patients with a diagnosis of brain tumors, acute stroke within 2 weeks, or new stroke during the 3-year interval; (3) patients with a stenosis of ≥20% in the extracranial internal carotid artery and vertebral artery (ECAS); and (4) patients without adequate clinical information. The study protocols were approved by the Institutional Review Board of the Third Military Medical University, and all patients signed written informed consent before the study started.

Clinical assessment

The clinical data were obtained from reliable medical records, physical examinations and structured clinical interview, and consisted of demographic data, medical history, and vascular risk factors (VRFs). The demographic data collected were comprised of age and sex. Each patient's systolic and diastolic blood pressures (BP) were measured using an aneroid sphygmomanometer with a 10-min relaxing. Body mass index (BMI) was measured. Use of anti-hypertensive, antiplatelet agents, statin and anti-diabetic medications, including oral hypoglycemic agents or insulin injection, were ascertained. The VRFs included in our study were hypertension, diabetes, coronary heart disease, dyslipidaemia, previous stroke, and current smoking and alcohol habit. Individuals with hypertension were defined as those with systolic/diastolic BP measures >140/90 mmHg in three consecutive measurements, or current use of anti-hypertensive agents, or a prior diagnosis of hypertension. Diabetes was defined as fasting blood glucose >7.0 mM or currently undergoing treatment with hypoglycemic medicine or insulin. Coronary heart disease (CHD) was determined by coronary angiography or cardiac CTA after being screened by electrocardiography or echocardiography according to the protocols for cardiac risk assessment. Dyslipidaemia was defined by a total cholesterol concentration >5.2 mM and a low-density lipoprotein cholesterol concentration >3.4 mM. Previous stroke defined by history were confirmed before a definitive diagnosis was made. Current smoking and daily alcohol use were investigated as previously described (16).

CTA scans and determination of ICAS

CTA scanning from the aortic arch to the cranial vessels was performed on a 64-slice CT scanner (Light Speed VCT

64-slice Scanner; General Electric, Milwaukee, WI). Details of the CTA protocols have been reported previously (17). All intracranial artery stenosis in the CTA images were reviewed and calculated as percent stenosis = $[(1 - (D_{stenosis}/D_{normal})] \times 100$ ($D_{stenosis}$ = the diameter of the artery at the site of the most severe stenosis, D_{normal} = the diameter of the proximal normal artery) (18) by two researchers (Zhong and Zhou) who were blinded to the patients' clinical information and WMHs scoring. The final stenosis percent for each vessel was defined according to the maximum value of all sites if multiple stenotic lesions were simultaneously existent. The vessels inspected include the intracranial internal carotid arteries; the proximal portions of anterior, middle, and posterior cerebral arteries (e.g., A1, M1, and P1, as well as distal segments or the communicating arteries, if present); intracranial vertebral arteries and basilar artery (19). The degree of ICAS was determined according to our previous study (19) and rated as: Grade 1 required stenosis of $<20\%$ in any vessel; Grade 3 required stenosis of $\geq 40\%$ in two or more vessels; Grade 2 was assigned as intermediate lesions, which predominantly included single-vessel disease or multiple low-grade stenosis (20).

MRI scans and WMHs grading

MRI scans were performed using a 3.0 T magnet (MAGNETOM Verio 3.0T; Siemens, Erlangen, Germany) with three high-resolution axial scans, i.e., T1- and T2-weighted and fluid attenuated inversion recovery sequences (FLAIR). The degree of WMHs severity was rated visually on axial FLAIR images by two trained investigators (Li and Cai) blinded to clinical data and ICAS assessment, using both the Age-related white matter changes (ARWMC) scale (range, 0–30) (21) and the four-class modified Fazekas scale (WMHs grade = none, mild, moderate, and severe) stratified separately for periventricular white matter hyperintensities (PVWMHs) and subcortical white matter hyperintensities (SCWMHs) (22). In brief, the ARWMC scale graded WMHs severity by giving scores 0 to 3 in bilateral five brain regions (frontal lobe, parietal-occipital lobe, temporal lobe, infratentorial region, and basal ganglia). PVWMHs were graded as: none, absent; mild, small caps or pencil-thin lining; moderate, large caps or thick smooth halo; severe, irregular PVWMHs extending into the subcortical white matter. SCWMHs were graded as: none, absent; mild, punctuate foci; moderate, beginning confluence of foci; severe, large confluent areas. Standards for Reporting Vascular Changes on Neuroimaging (STRIVE v1) (3) was consulted for identifying WMHs from other signs of cerebral small vessel disease (e.g., recent small subcortical infarcts, lacunes, prominent perivascular spaces and cerebral microbleeds).

Visual rating of WMHs progression was performed in a side-by-side fashion blinded to clinical and image details. WMH progression was rated on FLAIR images against the modified Rotterdam Progression scale (mRPS) (range, 0–9) (23), in which absence or presence of progression (0 and 1, respectively) was rated in three periventricular regions (frontal caps, occipital caps, bands), four subcortical white matter regions (frontal, parietal, occipital, temporal), basal ganglia, and infratentorial region. Progression of WMHs was defined as an increase in one point or more on the 3-year interval, which was further stratified into PVWMHs progression and SCWMHs progression with one point or more in periventricular and subcortical areas on mRPS, separately. The progression of basal ganglia and infratentorial regions was not further studied in the subgroup analysis because the sample size was too small. Disagreements over imaging assessment were resolved by discussion and consensus was reached.

Statistical analysis

The normal distribution of the data for numerical variables was evaluated with the Shapiro–Wilk normality test or Q–Q plot test. In the univariate analyses, continuous variables which were independent and normally distributed were expressed as mean ± SD and analyzed using Student *t*-test, or were expressed as median and interquartile range and compared using the Mann–Whitney *U* test when those were not normally distributed; and χ^2 tests were analyzed for categorical data. Binary logistic regression analyses with adjustment for age and sex and additionally for VRFs (e.g., hypertension, diabetes, CHD, dyslipidaemia, previous stroke, current smoking and daily alcohol use), and finally baseline WMHs (ARWMC scores) were performed to determine the relationship between ICAS degrees and WMHs progression. Furthermore, a linear regression model was established to describe the associations between ICAS degrees and WMHs progression scores. Then, we reapplied binary logistic regression analyses adjusting for age, gender, VRFs, and baseline PVWMHs or SCWMHs (Fazekas scores) separately to stratify the association of ICAS degrees and PVWMHs or SCWMHs progression. All *P*-values were two-tailed, and those <0.05 were considered statistically significant. The statistical analyses were performed by using SPSS22.0 for Windows (SPSS Inc., Chicago, IL, USA).

Results

Characteristics of the study participants

From January 1, 2010 to December 31, 2015, a total of 578 patients aged 60 years or above who met the criterion that they

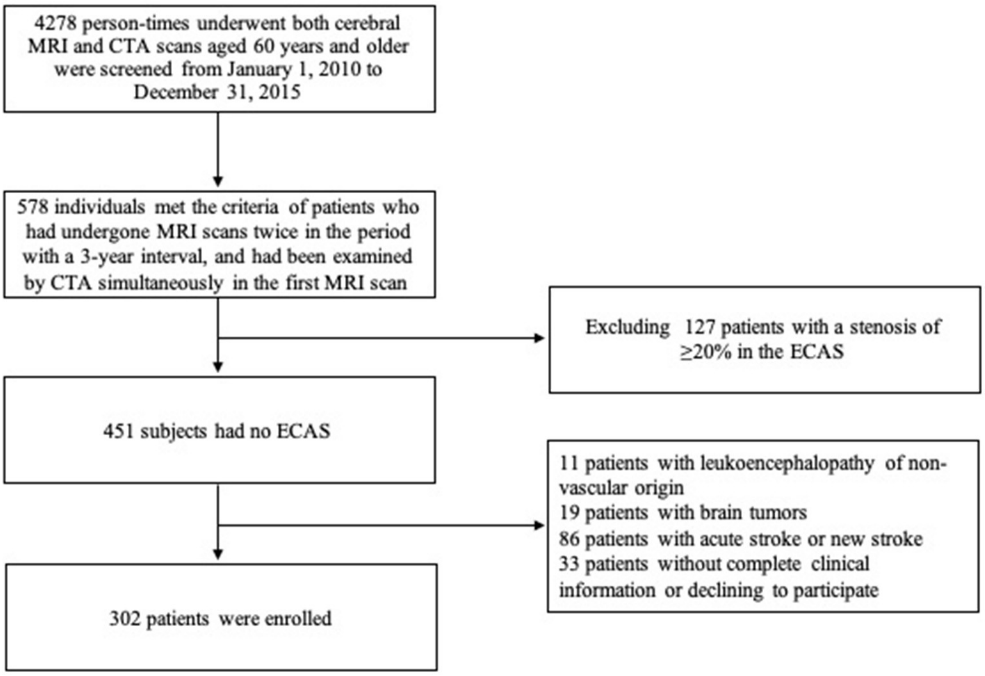

FIGURE 1
Flow chart of patient screening for the present study.

received two MRI scans 3 years apart and a CTA examination in their first MRI scan in our center were screened. Among them, the following patients were excluded from this study: 11 patients with leukoencephalopathy of non-vascular origin, 19 with brain tumors, 86 with acute stroke at the first MRI scan within 2 weeks or new stroke during the 3-year interval, 127 with a stenosis of ≥20% in the ECAS and vertebral artery, and 33 patients without complete clinical information or who refused to participate. Finally, a total of 302 patients (139 men and 163 women) with mean age of 69.7 ± 8.2 years were enrolled (flow chart shown in Figure 1). Amongst the enrolled patients, 186 complained of non-specific neurological symptoms (e.g., dizziness, vertigo, and numbness), 17 of headache, 5 of sleep disorders, 6 of cognitive impairment, 33 of Parkinson's disease, 20 of movement disorders, 20 of peripheral neuropathy, and 15 of other neurological conditions. Among them, 146 (48.3%) had a progression of WMHs within 3 years and showed 2.04 ± 1.14 points increase on the mRPS (one-sample *t*-test: $P < 0.001$).

Characteristics of patients with and without WMHs progression are shown in Table 1. Compared with the patients who had no WMHs progression, those who progressed were older, displayed significantly higher incidence of hypertension and diabetes, and were more likely to have a previous stroke ($P < 0.05$). The baseline WMHs score (ARWMC scale), proportion of patients who already had PVWMHs and SCWMHs (Fazekas scale) at baseline, and as well as the severity of ICAS were higher in the patients who had WMHs progression compared with those who did not progress ($P < 0.001$). Unexpected association also appeared with antihypertensive use ($P = 0.010$).

Association between baseline ICAS severity and risk of WMHs progression

We used binary logistic regression analyses to calculate the ORs for ICAS severity with the progression of WMHs, as shown in Table 2. Compared to the patients with Grade 1 ICAS, those with Grade 2 ICAS had an OR of 4.8, and those with Grade 3 ICAS had an OR of 9.4 (unadjusted model in Table 2). The association remained statistically significant after adjusting for age and sex (model 1 in Table 2) with declined ORs [3.7 (95% CI 2.0–6.8) for Grade 2 ICAS; 6.4 (95% CI 2.9–14.2) for Grade 3 ICAS; $P < 0.001$, separately]. The effect magnitudes were changeless after additional adjustment for VRFs (model 2 in Table 2). It remained significant but with a slightly faded impact when further correcting for baseline WMHs (OR 2.8, 95% CI 1.4–5.5 for Grade 2 ICAS; OR 3.0, 95% CI 1.2–7.3 for Grade 3 ICAS; $P < 0.001$, separately; model 3 in Table 2). The correlation for age and baseline WMHs (ARWMC scores) with WMHs progression was weaker, but still significant (OR

TABLE 1 Characteristics of patients with and without WMHs progression.

Patient characteristics	**All patients ($n = 302$)**	**WMHs**		
		Non-progression ($n = 156$)	**Progression ($n = 146$)**	***P***
Age (years)	69.7 ± 8.2	67.0 ± 8.5	72.6 ± 6.7	<0.001**
Gender (male)	139 (46.0%)	68 (43.6%)	71 (48.6%)	0.380
BMI (kg/m^2)	23.6 ± 3.4	23.4 ± 3.4	23.8 ± 3.4	0.283
Systolic BP (mmHg)	136.0 ± 18.4	134.8 ± 18.8	137.3 ± 18.0	0.236
Diastolic BP (mmHg)	76.4 ± 12.1	77.0 ± 13.0	75.7 ± 11.0	0.378
Hypertension	173 (57.3%)	73 (46.8%)	100 (68.5%)	<0.001**
Diabetes	46 (15.2%)	15 (9.6%)	31 (21.2%)	0.005**
Coronary heart disease	84 (27.8%)	43 (27.6%)	41 (28.1%)	0.920
Dyslipidaemia	47 (15.6%)	30 (19.2%)	17 (11.6%)	0.069
Previous stroke	39 (12.9%)	12 (7.7%)	27 (18.5%)	0.005**
Current smoking	23 (7.6%)	11 (7.1%)	12 (8.2%)	0.702
Daily alcohol use	6 (2.0%)	4 (2.6%)	2 (1.4%)	0.457
Antihypertensive use	122 (40.4%)	52 (33.3%)	70 (47.9%)	0.010**
Anti-diabetic use	37 (12.3%)	15 (9.6%)	22 (15.1%)	0.149
Antiplatelet use	59 (19.5%)	32 (20.5%)	27 (18.5%)	0.658
Statin use	33 (10.9%)	20 (12.8%)	13 (8.9%)	0.276
Baseline WMHs-ARWMC scores*	3 (0.00–7.00)	0 (0.00–3.00)	7 (4.00–10.00)	<0.001**
Baseline PVWMHs-Fazekas scores				<0.001**
None	124 (41.1%)	105 (67.3%)	19 (13.0%)	
Mild	92 (30.5%)	37 (23.7%)	55 (37.7%)	
Moderate	59 (19.5%)	11 (7.1%)	48 (32.9%)	
Severe	27 (8.9%)	3 (1.9%)	24(16.4%)	
Baseline SCWMHs-Fazekas scores				<0.001**
None	138 (45.7%)	111 (71.2%)	27 (18.5%)	
Mild	83 (27.5%)	32 (20.5%)	51 (34.9%)	
Moderate	54 (17.9%)	9 (5.8%)	45 (28.8%)	
Severe	27 (8.9%)	4 (2.6%)	23 (15.8%)	
Baseline ICAS				<0.001**
Grade 1	178 (58.9%)	123 (78.8%)	55 (37.7%)	
Grade 2	72 (23.8%)	23 (14.7%)	49 (33.6%)	
Grade 3	52 (17.2%)	10 (6.4%)	42 (28.8%)	

BMI, body mass index; BP, blood pressure; PVWMHs, periventricular white matter hyperintensities; SCWMHs, subcortical white matter hyperintensities; ICAS, intracranial atherosclerotic stenosis.

*Median (interquartile range), using Mann–Whitney *U* test.

**Significant variables.

ARWMC scores, Age-related White Matter Changes (ARWMC) rating scale scores; WMHs progression, increase in one point or more on the modified Rotterdam Progression scale (mRPS).

1.1, 95% CI 1.0–1.1, $P = 0.010$; OR 1.3, 95% CI 1.2–1.4, $P < 0.001$; respectively).

Effect of baseline ICAS severity on WMHs progression scores on MRPS

Results of the linear regression analysis for ICAS degrees were described in Table 3. Patients with Grade 2 and 3 ICAS, in comparison with Grade 1 ICAS, gained higher increase on mRPS (Figure 2), and showed a significant influence on WMHs progression in univariate linear regression ($P < 0.001$). Therefore, we performed a multiple linear regression analysis and found that: ICAS severity was significantly associated with WMHs progression scores, higher for Grade 3 ICAS [β (SE) $= 0.18$ (0.18), $P = 0.001$] followed by Grade 2 ICAS [β (SE) $= 0.10$ (0.15), $P = 0.044$] compared with Grade 1 ICAS; and it remained notably significant in terms of baseline WMHs (ARWMC scores) relating to increase of mRPS scores [β (SE) $= 0.53$ (0.01), $P < 0.001$].

TABLE 2 Logistic regression analysis of baseline ICAS severity with risk of WMHs progression.

	Unadjusted Model		Adjusted OR (95% CI)					
	OR (95% CI)	*p*	Model 1	*p*	Model 2	*p*	Model 3	*p*
Age	1.1 (1.1–1.2)	<0.001	1.1 (1.1–1.1)	<0.001	1.1 (1.1–1.1)	<0.001	1.1 (1.0–1.1)	0.010
Hypertension	2.5 (1.5–4.0)	<0.001	–	–	1.6 (0.9–2.8)	0.116	1.4 (0.8–2.6)	0.270
Diabetes	2.5 (1.3–4.9)	0.006	–	–	1.6 (0.7–3.4)	0.275	2.1 (0.9–5.0)	0.105
Previous stroke	2.7 (1.3–5.6)	0.007	–	–	1.6 (0.7–3.9)	0.254	0.9 (0.3–2.4)	0.818
Baseline WMHs*	1.4 (1.3–1.5)	<0.001	–	–	–	–	1.3 (1.2–1.4)	<0.001
Baseline ICAS								
Grade 1	1.0 (reference)		1.0 (reference)		1.0 (reference)		1.0 (reference)	
Grade 2	4.8 (2.6–8.6)	<0.001	3.7 (2.0–6.8)	<0.001	3.2 (1.7–6.2)	<0.001	2.8 (1.4–5.5)	0.003
Grade 3	9.4 (4.4–20.1)	<0.001	6.4 (2.9–14.2)	<0.001	5.1 (2.1–12.1)	<0.001	3.0 (1.2–7.3)	0.015
Ptrend	3.5 (2.4–5.0)	<0.001	2.8 (1.9–4.1)	<0.001	2.5 (1.6–3.7)	<0.001	1.8 (1.1–2.8)	0.002

OR, odds ratio; CI, confidence interval; WMHs, white matter hyperintensities; ICAS, intracranial atherosclerotic stenosis.
Model 1, adjusted for age and sex; Model 2, additionally adjusted for vascular risk factors (e.g., hypertension, diabetes, coronary heart disease, dyslipidaemia, previous stroke, current smoking and daily alcohol use); Model 3: additionally adjusted for baseline WMHs.
*Baseline WMHs, measured by Age-related White Matter Changes (ARWMC) rating scale; WMHs progression, increase in one point or more on the modified Rotterdam Progression scale (mRPS).

TABLE 3 Linear regression for the association between baseline ICAS severity and the WMHs progression scores.

	Univariate linear regression		Multiple linear regression	
	β (SE)	*p*	β (SE)	*p*
Age	0.30 (0.01)	<0.001	0.06 (0.01)	0.202
Hypertension	0.23 (0.15)	<0.001	0.05 (0.13)	0.342
Dyslipidaemia	−0.12 (0.20)	0.032	−0.01 (0.17)	0.767
Previous stroke	0.19 (0.22)	0.001	−0.00 (0.19)	0.981
Baseline WMHs*	0.61 (0.01)	<0.001	0.53 (0.01)	<0.001
Baseline ICAS				
Grade 2 vs. Grade 1	0.13 (0.17)	<0.001	0.10 (0.15)	0.044
Grade 3 vs. Grade 1	0.36 (0.18)	<0.001	0.18 (0.18)	0.001

β, standardized regression coefficient; SE, standard error; WMHs, white matter hyperintensities; ICAS, intracranial atherosclerotic stenosis.
*Baseline WMHs, measured by Age-related White Matter Changes (ARWMC) rating scale.
WMHs progression scores, the modified Rotterdam Progression scale (mRPS) scores.

Risk for WMHs progression subtypes associated with ICAS severity at baseline

Presence of WMHs progression was stratified separately into PVWMHs (n = 104), SCWMHs (n = 106), basal ganglia (n = 39), and infratentorial region (n = 5) progress according to mRPS (including coexistence of two or more regions). To search for a detail relationship of ICAS degree with WMHs progression subtypes, we repeated the logistic regression analysis with separate PVWMHs and SCWMHs progression in Table 4 and found that: after adjusting for confounding variables [age, sex, VRFs and baseline WMHs (Fazekas scores of PVWMHs and SCWMHs, respectively)], the ORs associated with Grade 2 and Grade 3 ICAS at baseline were 2.31 (95% CI 1.21–4.39, P = 0.011) and 2.50 (95% CI 1.18–5.32, P = 0.017) for PVWMHs progression, respectively, and remained significant but slightly weakened to 1.92 (95% CI 1.01–3.68, P = 0.048) and 2.47 (95% CI 1.14–5.34, P = 0.022) for SCWMHs progression, respectively. Figure 3 shows several cases with different WMHs and ICAS.

Discussion

Although the pathophysiology of WMHs remains hypothetical, there is evidence that WMHs may have correlation with cerebral ischemia. Chronic hypoperfusion of brain parenchyma could render white matter in loss of myelin and axons and tissue rarefaction (24), somewhat analogous to pathological manifestations of WMHs. Reduced cerebral blood flow was found in white matter instead of gray matter among individuals with WMHs and the local circulatory deficiency was related to WMHs volume of the same lobe (25). White matter is particularly vulnerable to hypotension-induced low flow effects because it is supplied by long, non-anastomosing arterioles with deficient autoregulatory capacity. Intracranial arteries, as the vessel most neighboring to upstream, play a critical role in distal perfusion into cerebral small vessels and parenchyma, and exhibit distinct metabolism and relatively blunted autoregulation compared with extracranial arteries for lacking vasa vasorum and external elastic lamina (26). Hence, there have been reasons to believe that ICAS plays a role in the pathogenesis and deterioration of WMHs, which is the purpose of our study.

In our analysis, the progression of WMHs measured by mRPS occurred in 48.3% of Chinese patients and could be trebled by Grade 3 ICAS in 3 years. Remarkably, a dose-response relationship between ICAS degrees and mRPS scores was found additionally in a linear regression, which undoubtedly adds weight to the strong impact of ICAS on WMHs burden increase. In previous cross-sectional studies, greater prevalence of WMHs were elucidated in ICAS rather than ECAS (11) and the former could act as an independent factor associated with greater WMH burden in Korean patients (12), while these were not in agreement with another study in American crowd (14). As a fact, those studies took acute stroke patients as research objects and had no age-matched group with stroke-free participants, which may cause indeterminate validity and inevitably bias for the association. A recent Chinese cohort study found that WMHs were prone to be hemodynamically compromised by the impact of ICAS, but it did not consider the influence of isolated or concurrent extracranial stenosis (7). Regrettably, no study on WMHs progression has been performed so far. Thus, our results provide new insights into understanding the mechanisms underlying WMHs recruitment and the likelihood

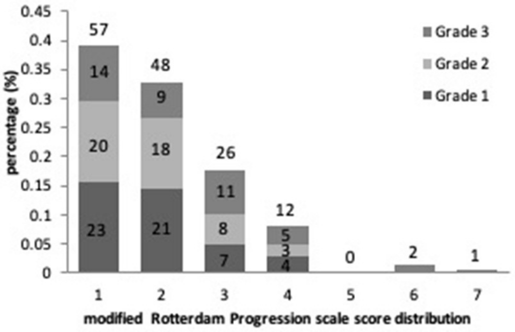

FIGURE 2
The proportional frequency of modified Rotterdam Progression scale (mRPS) scores and its distribution with ICAS severity are depicted.

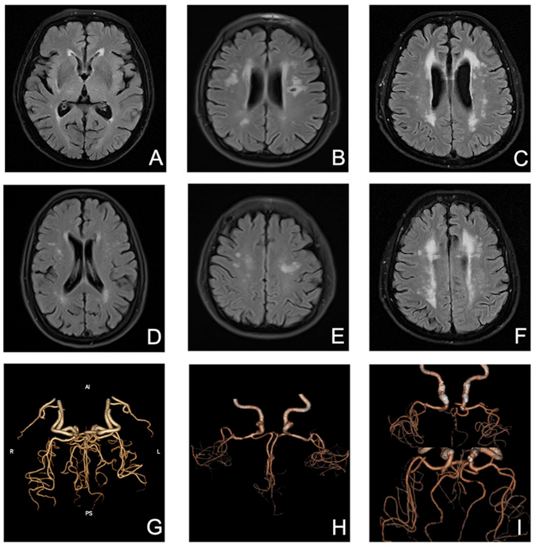

FIGURE 3
Several cases with different WMHs and ICAS. **(A)** mild PVWMHs; **(B)** moderate PVWMHs; **(C)** severe PVWMHs; **(D)** mild SCWMHs; **(E)** moderate SCWMHs; **(F)** severe SCWMHs; **(G)** Grade 1 ICAS; **(H)** Grade 2 ICAS; **(I)** Grade 3 ICAS.

TABLE 4 Risk for progression of PVWMHs and SCWMHs associated with ICAS severity at baseline.

	Risk for PVWMHs progression				Risk for SCWMHs progression			
	Unadjusted		Adjusted*		Unadjusted		Adjusted*	
	OR (95% CI)	*p*	OR (95% CI)	*p*	OR (95% CI)	*p*	OR (95% CI)	*p*
Baseline PVWMHs	3.10 (2.30–4.17)	<0.001	2.64 (1.94–3.62)	<0.001	–	–	–	–
Baseline SCWMHs	–	–	–	–	3.44 (2.53–4.67)	<0.001	3.08 (2.24–4.22)	<0.001
ICAS								
Grade 1	1.00 (reference)	–	1.00 (reference)		1.00 (reference)		1.00 (reference)	
Grade 2	3.81 (2.12–2.90)	<0.001	2.31 (1.21–4.39)	0.011	2.83 (1.58–5.05)	<0.001	1.92 (1.01–3.68)	0.048
Grade 3	5.63 (2.90–10.9)	<0.001	2.50 (1.18–5.32)	0.017	5.35 (2.77–10.3)	<0.001	2.47 (1.14–5.34)	0.022

PVWMHs, periventricular white matter hyperintensities; SCWMHs, subcortical white matter hyperintensities; ICAS, intracranial atherosclerotic stenosis.
*Adjusted for age, sex, vascular risk factors (e.g., hypertension, diabetes, coronary heart disease, dyslipidaemia, previous stroke, current smoking and daily alcohol use) and baseline PVWMHs and SCWMHs (measured by Fazekas scores), respectively.
Progression for PVWMHs and SCWMHs, increase in one point or more on the PVWMHs and SCWMHs part of modified Rotterdam Progression sc scale (mRPS), respectively.

of ICAS in determining the severity of WMHs progression in ECAS free patients.

We found that more severe ICAS remained relevant with PVWMHs progression but was with an attenuated relation to the SCWMH progression even after adjusting for confounding variables. Periventricular white matter is prone to be more vulnerable to hemodynamic disturbance than subcortical white matter, since this area is supplied by non-collateralizing subependymal arteries with unstable blood supply. However, previous cross-sectional studies showed that SCWMHs gained more influence by chronic hypoperfusion secondary to atherosclerotic stenosis than PVWMHs (12, 27), which were not in complete agreement with our study. Moreover, Sachdev et al. (28) also discovered that the deep white matter and anterior brain regions performed a greater rate of progression. Interestingly, as a notable result in our analysis, baseline SCWMHs themselves manifested a stronger power on WMHs progression than PVWMHs, which corresponds with the results reported by Umemura et al. (29) that higher mRPS scores were found in SCWMHs with relation to baseline SCWMHs severity. These may suggest that PVWMHs and SCWMHs have dissimilar pathogenic mechanisms as the burden of lesions increases.

There are limited longitudinal studies investigating the severity of ICAS in elderly patients with relation to WMHs progression. We used CTA as a non-invasive examination method for the diagnosis and assessment of ICAS to enhance methodological effectiveness. In addition, we categorized WMHs progression into PVWMHs and SCWMHs and found the potential distinctive features between them. ECAS (with a stenosis of ≥20%) was eliminated in our study due to the controversial relationship between carotid stenosis/plaque and WMHs (30) and to avoid confounding interfere with blood flow.

Several limitations to the present study should be addressed. First, as our study retrospectively utilized inpatients from a single center who sought medical service for various reasons, it may be insufficiently representative of community-based cohorts who appear to have fewer risk factors. Nevertheless, the longitudinal data and blinded assessment may strengthen its reliability. An extrapolation to other ethnic individuals could be tested in future studies. Second, although automated assessment of WMHs burden was preferred over a visual scales in single center studies, visual rating scales have proven to be reliable and showed good correlation with volumetrics and interobserver agreement for WMHs assessment (23). We also expect that computerized appraisal procedure would be available in our future studies. Third, a much lower prevalence of ICAS is presented in our study, mainly the Grade 2 ICAS with a prevalence of 23.8% than that of 42.0% reported by Dolan et al. (20) by postmortem. However, the participants who had completed body autopsies had a mean age of 87.6 years at death which was definitely older than that in our study, and the subjects with ECAS and acute stroke who share more risk factors were eliminated from our analysis.

In summary, our results demonstrate the association of ICAS severity to WMHs progression in elderly Chinese patients and additionally have distinct relevancy to PVWMHs and SCWMHs, which may provide clues for understanding atherosclerotic stenosis of relatively large intracranial vessels as an indicator of widespread microvascular lesions and microcirculation defects not only potential responsible vessels resulting in deficit cerebral perfusion. Further studies with a larger sample size are needed to confirm the conclusions and to investigate the role of ICAS in prevention of WMHs progression.

Data availability statement

The raw data supporting the conclusions of this article will be made available by the authors, without undue reservation.

Ethics statement

The studies involving human participants were reviewed and approved by the Institutional Review Board of the Third Military Medical University. The patients/participants provided their written informed consent to participate in this study.

Author contributions

All authors contributed to the article and approved the submitted version.

Funding

This work was supported by the Construction Project of Capacity Improvement Plan for Chongqing Municipal Health Commission Affiliated Unit (2019NLTS001)-ZS03174, the Operating Grant to Chongqing Key Laboratory of Neurodegenerative Diseases (1000013), Chongqing Talent Project (2000062), Overseas Students Entrepreneurial Fund (2000079), and Plan for High-level Talent Introduction (2000055).

Acknowledgments

We would like to thank all the clinicians for participating in this study.

Conflict of interest

The authors declare that the research was conducted in the absence of any commercial or financial relationships that could be construed as a potential conflict of interest.

Publisher's note

References

1. Debette S, Markus H. The clinical importance of white matter hyperintensities on brain magnetic resonance imaging: systematic review and meta-analysis. *BMJ Clin Res Edn.* (2010) 341:c3666. doi: 10.1136/bmj.c3666

2. Roseborough A, Saad L, Goodman M, Cipriano L, Hachinski V, Whitehead S. White matter hyperintensities and longitudinal cognitive decline in cognitively normal populations and across diagnostic categories: a meta-analysis, systematic review, and recommendations for future study harmonization. *Alzheimer's Dement J Alzheimer's Assoc.* (2022). doi: 10.1002/alz.12642. [Epub ahead of print].

3. Wardlaw J, Smith E, Biessels G, Cordonnier C, Fazekas F, Frayne R, et al. Neuroimaging standards for research into small vessel disease and its contribution to ageing and neurodegeneration. *Lancet Neurol.* (2013) 12:822–38. doi: 10.1016/S1474-4422(13)70124-8

4. Pantoni L. Cerebral small vessel disease: from pathogenesis and clinical characteristics to therapeutic challenges. *Lancet Neurol.* (2010) 9:689–701. doi: 10.1016/S1474-4422(10)70104-6

5. Simpson J, Wharton S, Cooper J, Gelsthorpe C, Baxter L, Forster G, et al. Alterations of the blood-brain barrier in cerebral white matter lesions in the ageing brain. *Neurosci Lett.* (2010) 486:246–51. doi: 10.1016/j.neulet.2010.09.063

6. Fazekas F, Kleinert R, Offenbacher H, Schmidt R, Kleinert G, Payer F, et al. Pathologic correlates of incidental mri white matter signal hyperintensities. *Neurology.* (1993) 43:1683–9. doi: 10.1212/WNL.43.9.1683

7. Fang H, Leng X, Pu Y, Zou X, Pan Y, Song B, et al. Hemodynamic significance of middle cerebral artery stenosis associated with the severity of ipsilateral white matter changes. *Front Neurol.* (2020) 11:214. doi: 10.3389/fneur.2020.00214

8. Rundek T, Della-Morte D, Gardener H, Dong C, Markert M, Gutierrez J, et al. Relationship between carotid arterial properties and cerebral white matter hyperintensities. *Neurology.* (2017) 88:2036–42. doi: 10.1212/WNL.0000000000003951

9. Wardlaw J, Allerhand M, Doubal F, Valdes Hernandez M, Morris Z, Gow A, et al. Vascular risk factors, large-artery atheroma, and brain white matter hyperintensities. *Neurology.* (2014) 82:1331–8. doi: 10.1212/WNL.0000000000000312

10. Ritz K, Denswil N, Stam O, van Lieshout J, Daemen M. Cause and mechanisms of intracranial atherosclerosis. *Circulation.* (2014) 130:1407–14. doi: 10.1161/CIRCULATIONAHA.114.011147

11. Lee S, Kim J, Chung S, Kim B, Ahn K, Lee K. White matter hyperintensities (Wmh) are associated with intracranial atherosclerosis rather than extracranial atherosclerosis. *Arch Gerontol Geriat.* (2011) 53:e129–32. doi: 10.1016/j.archger.2010.07.008

12. Park J, Kwon H, Lee J, Kim D, Ovbiagele B. Association of intracranial atherosclerotic stenosis with severity of white matter hyperintensities. *Eur J Neurol.* (2015) 22:44–52, e2–3. doi: 10.1111/ene.12431

13. Li H, Xu G, Xiong Y, Zhu W, Yin Q, Fan X, et al. Relationship between cerebral atherosclerosis and leukoaraiosis in aged patients: results from Dsa. *J Neuroimag Off J Am Soc Neuroimag.* (2014) 24:338–42. doi: 10.1111/jon.12047

14. Chutinet A, Biffi A, Kanakis A, Fitzpatrick K, Furie K, Rost N. Severity of leukoaraiosis in large vessel atherosclerotic disease. *AJNR Am J Neuroradiol.* (2012) 33:1591–5. doi: 10.3174/ajnr.A3015

15. Mok V, Lam W, Fan Y, Wong A, Ng P, Tsoi T, et al. Effects of statins on the progression of cerebral white matter lesion: post hoc analysis of the rocas (regression of cerebral artery stenosis) study. *J Neurol.* (2009) 256:750–7. doi: 10.1007/s00415-009-5008-7

16. Zhou S, Zhou R, Zhong T, Li R, Tan J, Zhou H. Association of smoking and alcohol drinking with dementia risk among elderly men in China. *Curr Alzheimer Res.* (2014) 11:899–907. doi: 10.2174/1567205011666141001123356

17. Yu K, Zhong T, Li L, Wang J, Chen Y, Zhou H. Significant association between carotid artery kinking and leukoaraiosis in middle-aged and elderly Chinese patients. *J Stroke Cerebrovasc Dis Off J Natl Stroke Assoc.* (2015) 24:1025–31. doi: 10.1016/j.jstrokecerebrovasdis.2014.12.030

18. Samuels O, Joseph G, Lynn M, Smith H, Chimowitz M. A standardized method for measuring intracranial arterial stenosis. *AJNR Am J Neuroradiol.* (2000) 21:643–6.

19. Zhu J, Wang Y, Li J, Deng J, Zhou H. Intracranial artery stenosis and progression from mild cognitive impairment to alzheimer disease. *Neurology.* (2014) 82:842–9. doi: 10.1212/WNL.0000000000000185

20. Dolan H, Crain B, Troncoso J, Resnick S, Zonderman A, Obrien R. Atherosclerosis, dementia, and alzheimer disease in the baltimore longitudinal study of aging cohort. *Ann Neurol.* (2010) 68:231–40. doi: 10.1002/ana.22055

21. Wahlund L, Barkhof F, Fazekas F, Bronge L, Augustin M, Sjögren M, et al. A new rating scale for age-related white matter changes applicable to Mri and Ct. *Stroke.* (2001) 32:1318–22. doi: 10.1161/01.STR.32.6.1318

22. Fazekas F, Chawluk J, Alavi A, Hurtig H. Zimmerman R. Mr signal abnormalities at 15 T in Alzheimer's dementia and normal aging. *AJR Am J Roentgenol.* (1987) 149:351–6. doi: 10.2214/ajr.149.2.351

23. Prins N, van Straaten E, van Dijk E, Simoni M, van Schijndel R, Vrooman H, et al. Measuring progression of cerebral white matter lesions on Mri: visual rating and volumetrics. *Neurology.* (2004) 62:1533–9. doi: 10.1212/01.WNL.0000123264.40498.B6

24. Pantoni L, Garcia J, Gutierrez J. Cerebral white matter is highly vulnerable to ischemia. *Stroke.* (1996) 27(9):1641–6; discussion 7. doi: 10.1161/01.STR.27.9.1641

25. Wen W, Sachdev P, Shnier R, Brodaty H. Effect of white matter hyperintensities on cortical cerebral blood volume using perfusion mri. *Neuroimage.* (2004) 21:1350–6. doi: 10.1016/j.neuroimage.2003.11.015

26. Masuoka T, Hayashi N, Hori E, Kuwayama N, Ohtani O, Endo S. Distribution of internal elastic lamina and external elastic lamina in the internal carotid artery: possible relationship with atherosclerosis. *Neurol Med Chir.* (2010) 50:179–82. doi: 10.2176/nmc.50.179

27. Ni L, Zhou F, Qing Z, Zhang X, Li M, Zhu B, et al. The asymmetry of white matter hyperintensity burden between hemispheres is associated with intracranial atherosclerotic plaque enhancement grade. *Front Aging Neurosci.* (2020) 12:163. doi: 10.3389/fnagi.2020.00163

28. Sachdev P, Wen W, Chen X, Brodaty H. Progression of white matter hyperintensities in elderly individuals over 3 years. *Neurology.* (2007) 68:214–22. doi: 10.1212/01.wnl.0000251302.55202.73

29. Umemura T, Kawamura T, Umegaki H, Mashita S, Kanai A, Sakakibara T, et al. Endothelial and inflammatory markers in relation to progression of ischaemic cerebral small-vessel disease and cognitive impairment: a 6-year longitudinal study in patients with type 2 diabetes mellitus. *J Neurol Neurosurg Psychiatry.* (2011) 82:1186–94. doi: 10.1136/jnnp.2010.217380

30. Altaf N, Morgan P, Moody A, MacSweeney S, Gladman J, Auer D. Brain white matter hyperintensities are associated with carotid intraplaque hemorrhage. *Radiology.* (2008) 248:202–9. doi: 10.1148/radiol.2481070300

Frontiers in
Neurology

Explores neurological illness to improve patient care

The third most-cited clinical neurology journal explores the diagnosis, causes, treatment, and public health aspects of neurological illnesses. Its ultimate aim is to inform improvements in patient care.

Discover the latest Research Topics

See more →

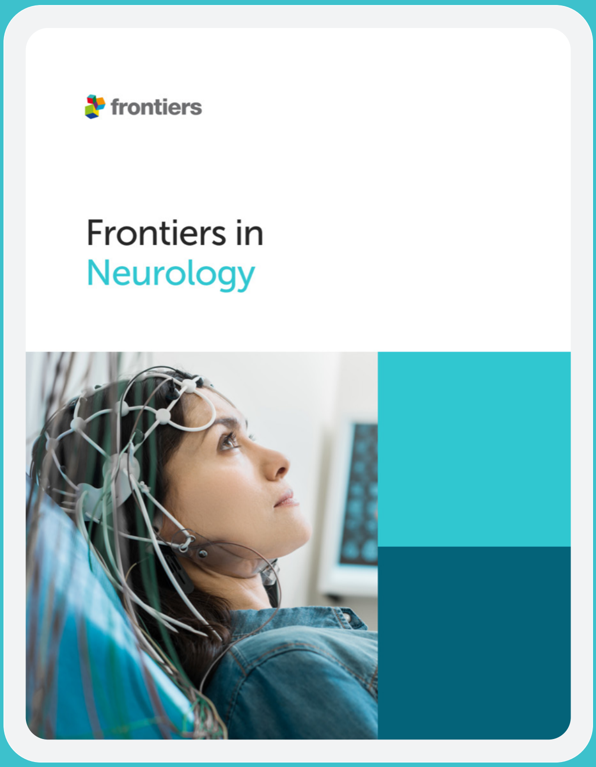

frontiers

Frontiers in
Neurology

Frontiers

Avenue du Tribunal-Fédéral 34
1005 Lausanne, Switzerland
frontiersin.org

Contact us

+41 (0)21 510 17 00
frontiersin.org/about/contact